Azimuthal decorrelation between leptons in the Drell-Yan process as a probe of infrared QCD: Phenomenology, predictions and measurement of a novel collider observable using perturbative resummation techniques

The following correspondingly numbered figures and tables should replace those appearing in Sections 13.1 and 13.3 of the aforementioned PhD thesis by Lee Tomlinson. None of the associated text in the thesis requires modification.

Lee Tomlinson
March 2015

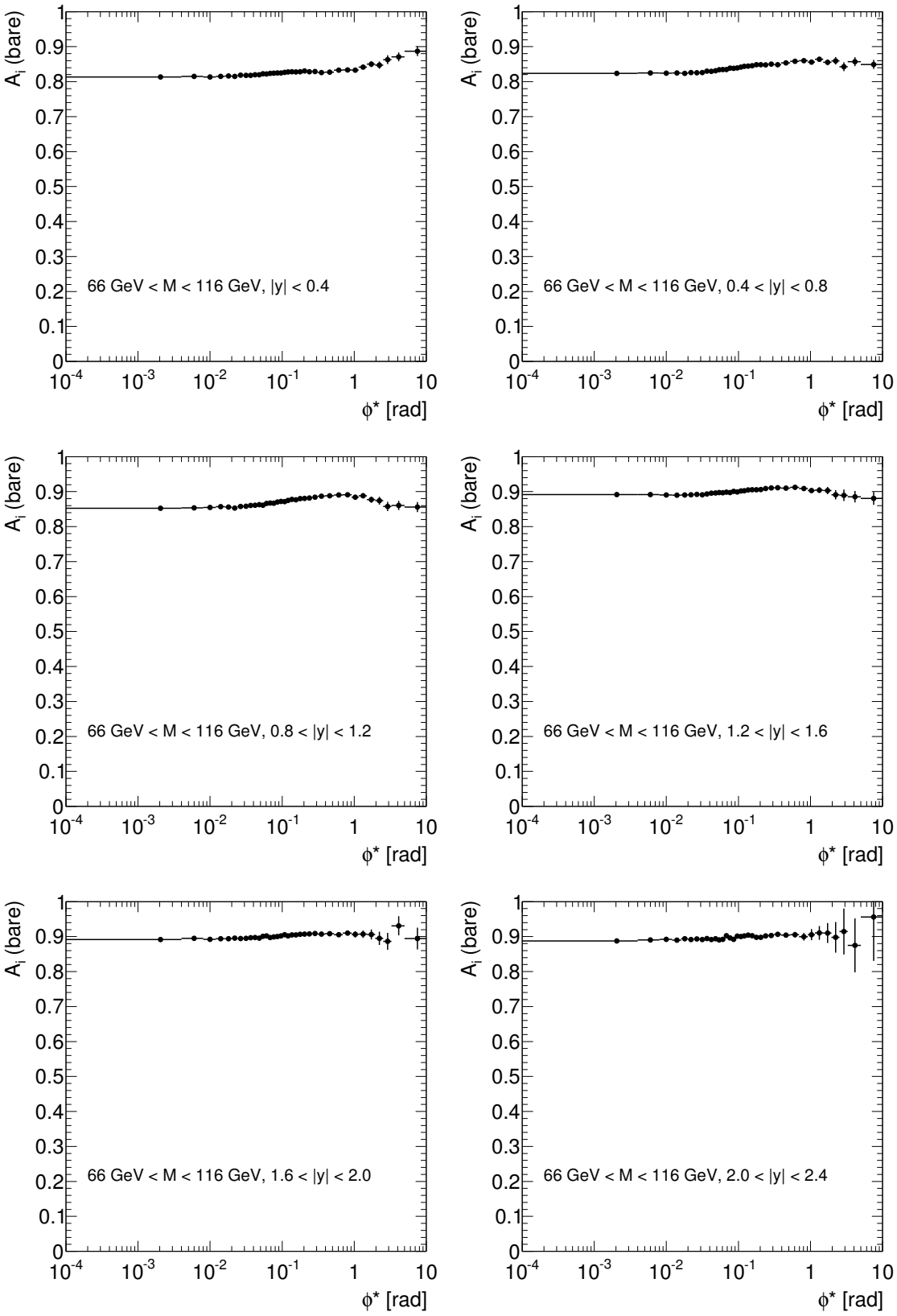

FIGURE 13.1. Bin-by-bin correction factors for the ϕ^* distributions in the 66 GeV $< M <$ 116 GeV region, in different $|y|$ bins. These factors are to be applied to the background-subtracted distributions of the number of candidate events in data.

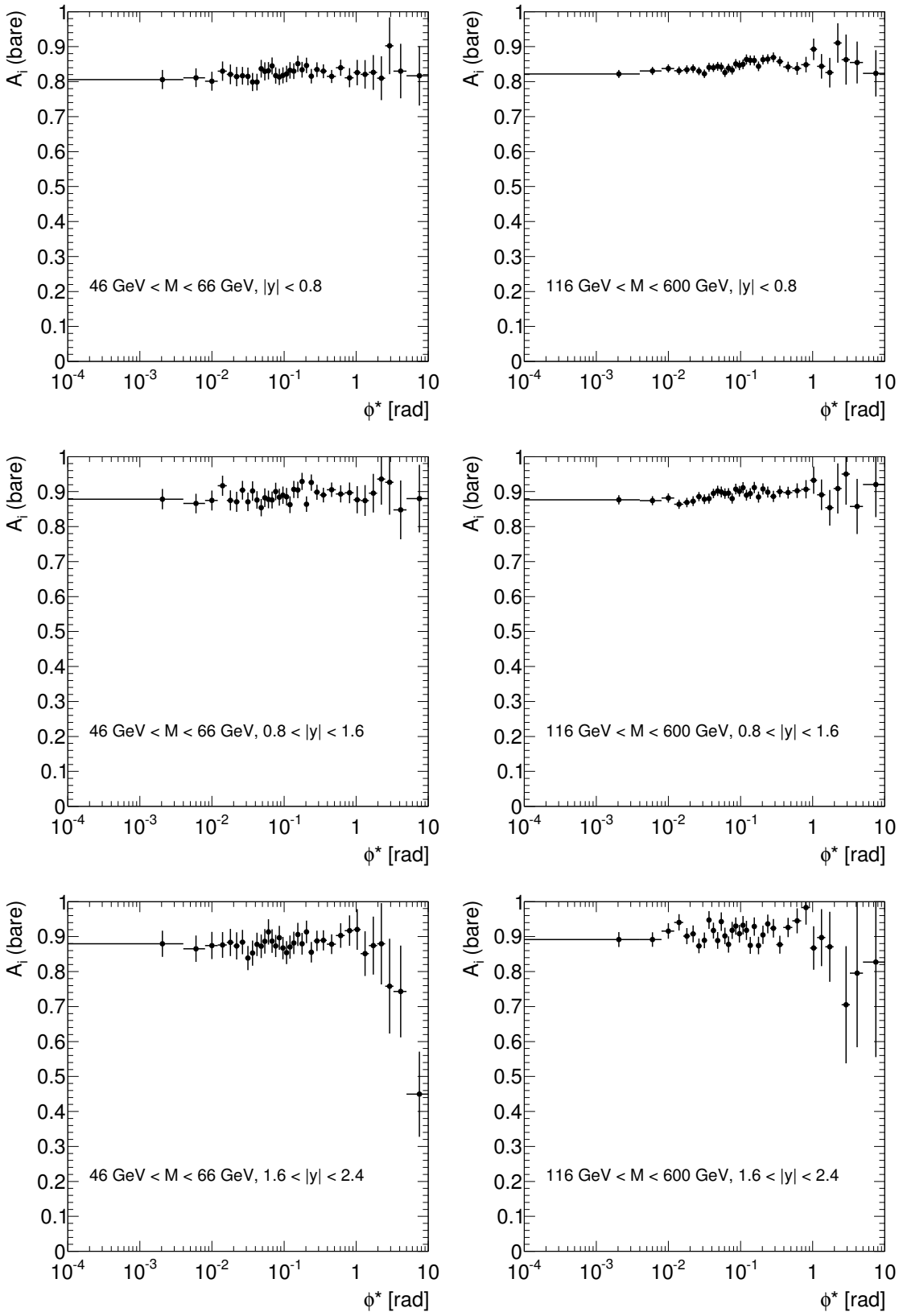

FIGURE 13.2. Bin-by-bin correction factors for the ϕ^* distributions in the 46 GeV $< M <$ 66 GeV (left) and 116 GeV $< M <$ 150 GeV (right) regions, in different $|y|$ bins. These factors are to be applied to the background-subtracted distributions of the number of candidate events in data.

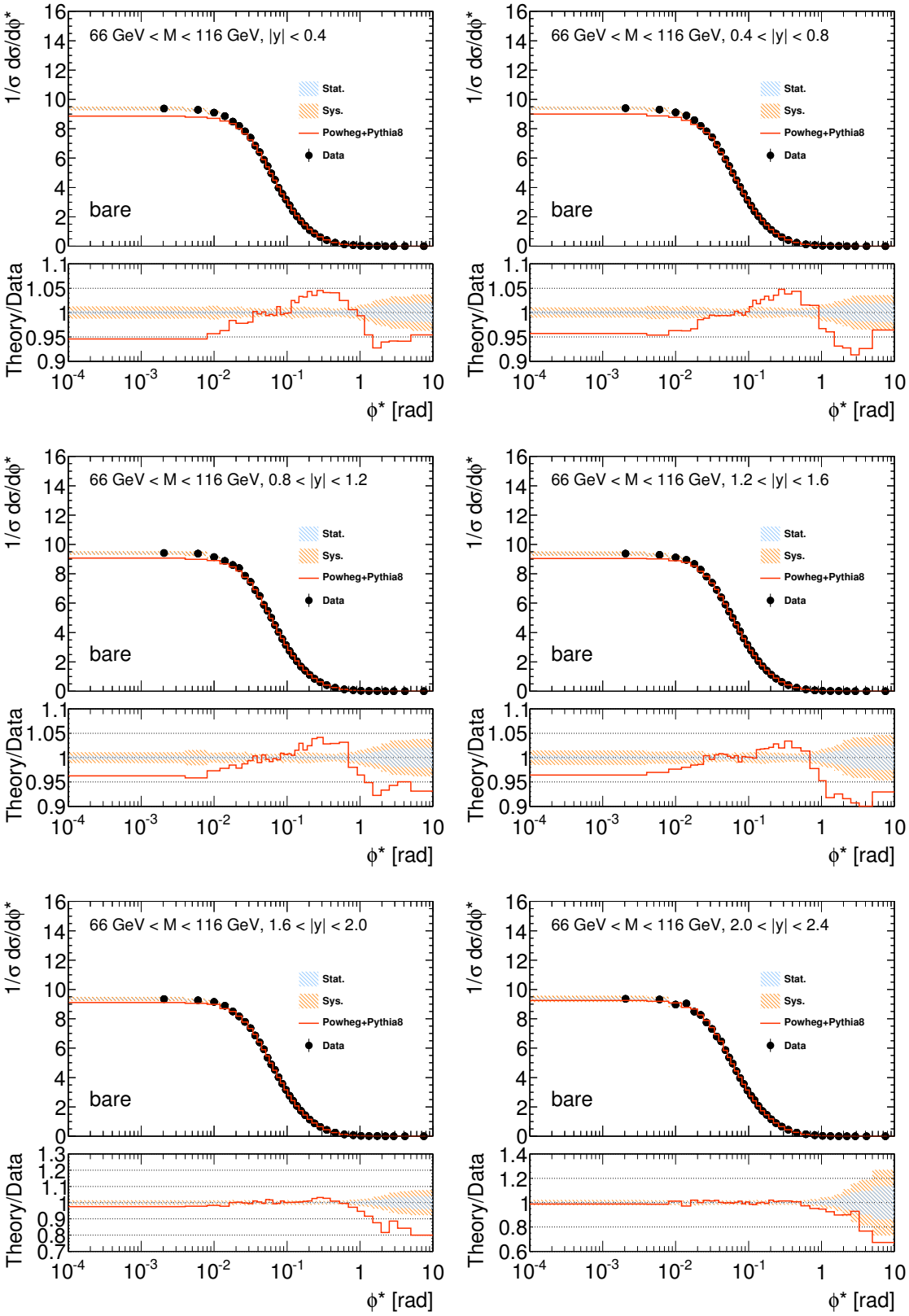

FIGURE 13.7. The results of the ATLAS ϕ^* analysis in the $Z \to \mu\mu$ channel. These distributions are background-subtracted and corrected for detector effects to the *bare-level* distribution, before being individually normalized. The mass region shown is 66 GeV $< M <$ 116 GeV, and each distribution corresponds to one of the six equally-sized rapidity bins across the total range $|y| < 2.4$.

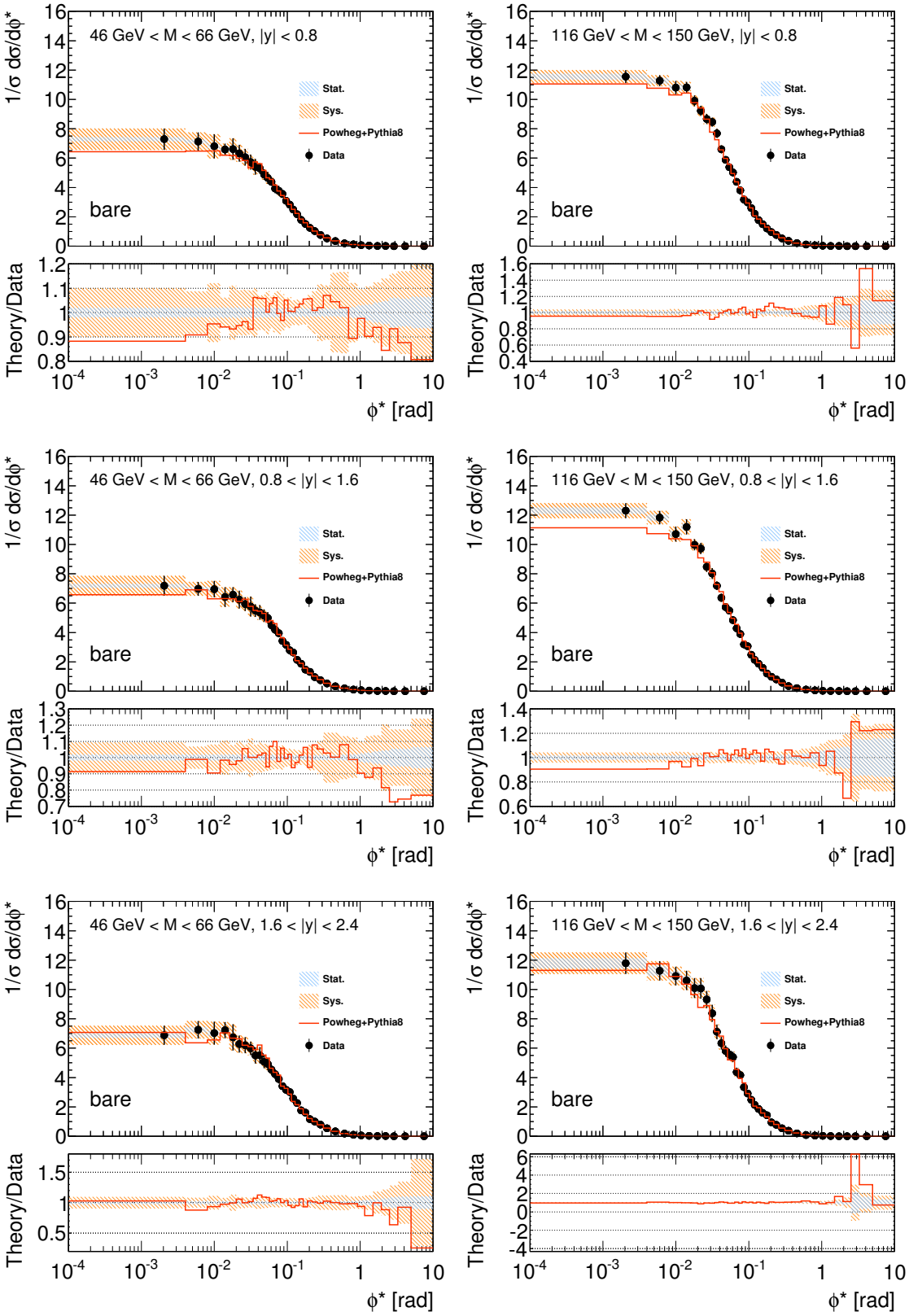

FIGURE 13.8. The results of the ATLAS ϕ^* analysis in the $Z \to \mu\mu$ channel. These distributions are background-subtracted and corrected for detector effects to the *bare-level* distribution, before being individually normalized. The mass regions shown are 46 GeV $< M <$ 66 GeV (left) and 116 GeV $< M <$ 150 GeV (right), and each left-right pair of distributions corresponds to one of the three equally-sized rapidity bins across the total range $|y| < 2.4$.

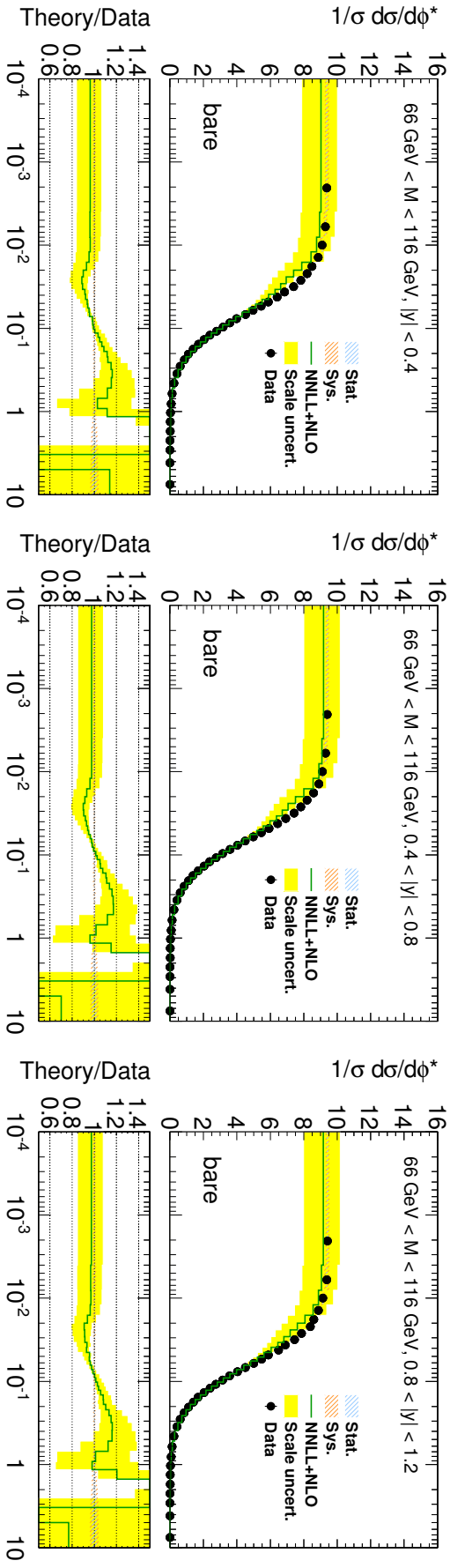

FIGURE 13.9. ATLAS data compared with NNLL+NLO prediction at 8 TeV (66 GeV $< M <$ 116 GeV, $|y| < 1.2$)

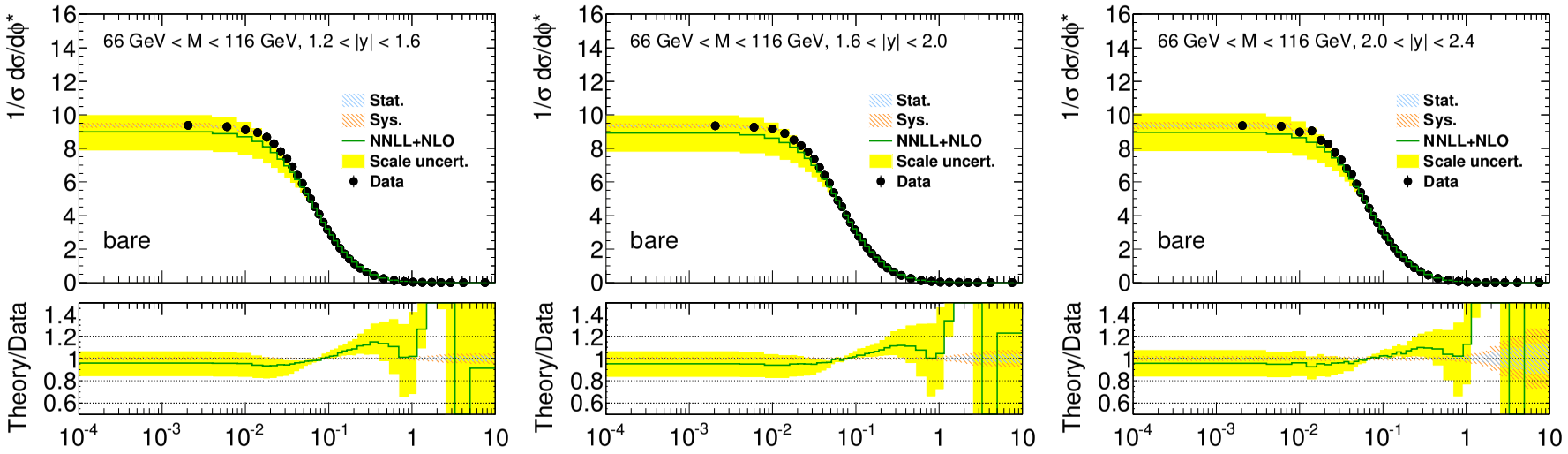

FIGURE 13.10. ATLAS data compared with NNLL+NLO prediction at 8 TeV (66 GeV $< M <$ 116 GeV, $1.2 < |y| < 2.4$)

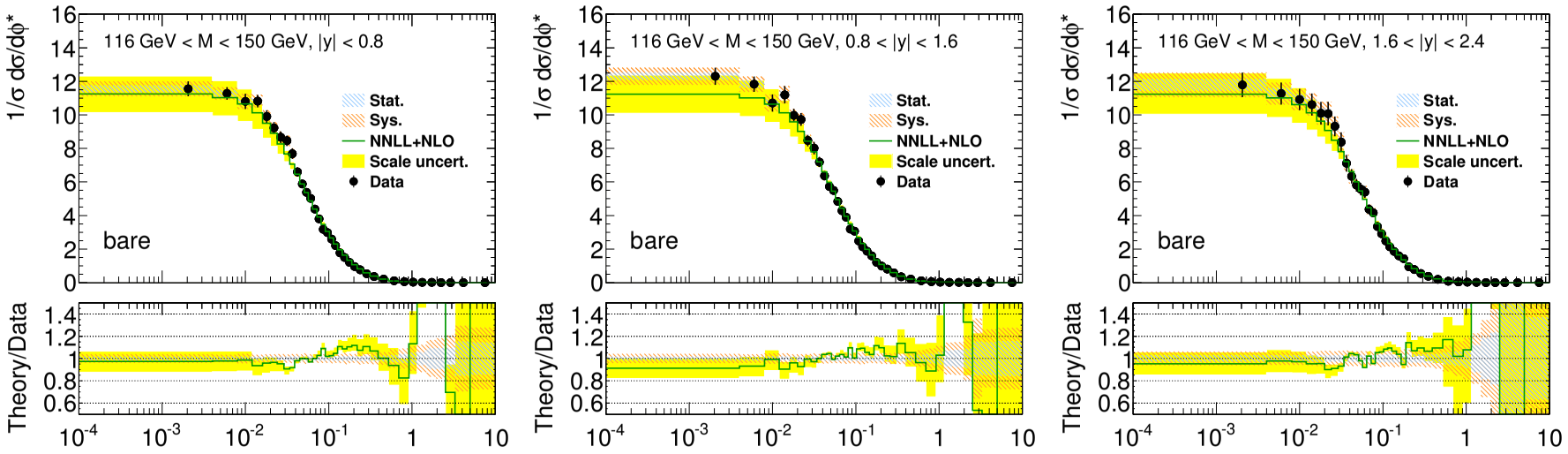

FIGURE 13.11. ATLAS data compared with NNLL+NLO prediction at 8 TeV (116 GeV $< M <$ 150 GeV)

TABLE 13.1. Tabulation of ϕ^* distributions, along with corresponding systematic and statistical uncertainties, for the on-peak analysis: $66\,\text{GeV} < M < 116\,\text{GeV}$. The relative dominance of the uncertainties for each bin are indicated using a red-blue spectrum: red = more dominant, blue = less dominant.

		$\lvert y\rvert < 0.4$			$0.4 < \lvert y\rvert < 0.8$			$0.8 < \lvert y\rvert < 1.2$			$1.2 < \lvert y\rvert < 1.6$			$1.6 < \lvert y\rvert < 2.0$			$2.0 < \lvert y\rvert < 2.4$		
low	high	$(1/\sigma)\,d\sigma/d\phi^*$	$\delta\phi^*_{\text{sys}}$[%]	$\delta\phi^*_{\text{stat}}$[%]	$(1/\sigma)\,d\sigma/d\phi^*$	$\delta\phi^*_{\text{sys}}$[%]	$\delta\phi^*_{\text{stat}}$[%]	$(1/\sigma)\,d\sigma/d\phi^*$	$\delta\phi^*_{\text{sys}}$[%]	$\delta\phi^*_{\text{stat}}$[%]	$(1/\sigma)\,d\sigma/d\phi^*$	$\delta\phi^*_{\text{sys}}$[%]	$\delta\phi^*_{\text{stat}}$[%]	$(1/\sigma)\,d\sigma/d\phi^*$	$\delta\phi^*_{\text{sys}}$[%]	$\delta\phi^*_{\text{stat}}$[%]	$(1/\sigma)\,d\sigma/d\phi^*$	$\delta\phi^*_{\text{sys}}$[%]	$\delta\phi^*_{\text{stat}}$[%]
0.0001	0.004	9.38	0.855	0.402	9.4	0.645	0.399	9.42	0.719	0.397	9.37	1.07	0.421	9.35	0.849	0.519	9.36	1.27	0.903
0.004	0.008	9.3	0.786	0.398	9.31	0.944	0.395	9.37	1.18	0.393	9.29	0.819	0.418	9.26	0.733	0.515	9.32	1.05	0.892
0.008	0.012	9.1	1	0.403	9.12	0.673	0.4	9.15	0.621	0.397	9.11	0.898	0.422	9.15	0.856	0.518	8.98	0.99	0.909
0.012	0.016	8.86	0.7	0.408	8.9	0.965	0.404	8.88	0.698	0.403	8.95	0.714	0.426	8.89	0.721	0.526	9.04	0.851	0.906
0.016	0.02	8.48	0.686	0.416	8.58	0.708	0.412	8.6	0.73	0.409	8.66	0.974	0.433	8.5	1.08	0.537	8.49	1.28	0.933
0.02	0.024	8.2	0.785	0.424	8.2	0.729	0.421	8.38	0.548	0.415	8.29	0.906	0.443	8.16	0.559	0.548	8.26	1.19	0.947
0.024	0.029	7.82	0.513	0.387	7.83	0.629	0.386	7.87	0.845	0.382	7.81	0.486	0.407	7.8	1.05	0.502	7.75	1.11	0.874
0.029	0.034	7.39	0.645	0.399	7.42	0.404	0.396	7.44	0.466	0.393	7.39	0.436	0.419	7.37	0.925	0.516	7.31	0.808	0.9
0.034	0.039	6.85	0.524	0.414	6.92	0.486	0.409	6.89	0.421	0.408	6.9	0.536	0.433	6.86	0.471	0.534	6.8	0.865	0.932
0.039	0.045	6.4	0.515	0.391	6.43	0.512	0.387	6.49	0.325	0.383	6.39	0.514	0.41	6.4	0.444	0.505	6.46	0.85	0.874
0.045	0.051	5.88	0.379	0.408	5.92	0.346	0.403	5.88	0.422	0.402	5.9	0.36	0.427	5.92	0.546	0.525	5.87	0.905	0.916
0.051	0.057	5.45	0.334	0.423	5.47	0.331	0.419	5.47	0.406	0.418	5.42	0.372	0.445	5.36	0.484	0.551	5.37	0.808	0.96
0.057	0.064	4.97	0.411	0.41	4.98	0.327	0.407	5.01	0.344	0.403	4.99	0.367	0.43	4.9	0.622	0.533	4.95	0.764	0.925
0.064	0.072	4.52	0.466	0.401	4.49	0.335	0.4	4.51	0.374	0.397	4.52	0.717	0.422	4.52	0.557	0.52	4.44	0.851	0.908
0.072	0.081	3.98	0.402	0.403	4.04	0.354	0.397	4.03	0.377	0.396	4.07	0.416	0.419	4.03	0.549	0.519	3.97	0.809	0.909
0.081	0.091	3.58	0.404	0.403	3.59	0.47	0.4	3.56	0.699	0.399	3.58	0.678	0.423	3.58	0.524	0.522	3.57	0.777	0.911
0.091	0.102	3.18	0.653	0.408	3.14	0.576	0.407	3.15	0.462	0.405	3.17	0.593	0.43	3.16	1.06	0.529	3.12	1.14	0.924
0.102	0.114	2.79	0.603	0.417	2.76	0.703	0.416	2.75	0.639	0.414	2.78	0.708	0.439	2.76	0.7	0.541	2.77	0.988	0.94
0.114	0.128	2.39	0.913	0.417	2.37	0.653	0.415	2.39	0.48	0.41	2.43	0.686	0.435	2.42	0.75	0.536	2.45	0.864	0.924
0.128	0.145	2.04	0.662	0.409	2.04	0.704	0.405	2.03	0.608	0.404	2.05	0.724	0.429	2.06	0.829	0.526	2.07	1.3	0.913
0.145	0.165	1.7	0.641	0.413	1.7	0.827	0.409	1.68	0.779	0.409	1.71	0.832	0.433	1.73	0.713	0.529	1.72	0.843	0.922
0.165	0.189	1.39	0.811	0.417	1.38	0.612	0.414	1.4	0.728	0.409	1.4	0.827	0.436	1.43	0.868	0.532	1.46	0.8	0.918
0.189	0.219	1.1	0.663	0.419	1.11	0.697	0.413	1.11	0.686	0.41	1.13	0.561	0.435	1.14	0.74	0.532	1.15	1.32	0.923
0.219	0.258	0.855	0.582	0.417	0.848	0.587	0.415	0.845	0.621	0.413	0.856	0.6	0.437	0.875	0.513	0.533	0.888	0.92	0.92
0.258	0.312	0.615	0.47	0.419	0.612	0.627	0.414	0.612	0.536	0.412	0.624	0.559	0.435	0.633	0.663	0.532	0.646	0.842	0.917
0.312	0.391	0.412	0.581	0.424	0.41	0.412	0.419	0.409	0.402	0.416	0.41	0.412	0.444	0.426	0.54	0.537	0.438	0.774	0.919
0.391	0.524	0.239	0.364	0.429	0.236	0.427	0.425	0.236	0.352	0.422	0.238	0.396	0.45	0.246	0.456	0.545	0.254	0.815	0.932
0.524	0.695	0.124	0.421	0.525	0.125	0.444	0.516	0.122	0.492	0.518	0.122	0.462	0.554	0.127	0.57	0.672	0.133	0.964	1.14
0.695	0.918	0.0631	0.539	0.647	0.0625	0.591	0.639	0.0619	0.563	0.639	0.061	0.604	0.69	0.0613	0.904	0.845	0.0612	1.35	1.47
0.918	1.15	0.0329	0.773	0.875	0.0333	0.844	0.858	0.0323	0.724	0.866	0.0309	0.855	0.948	0.03	0.992	1.18	0.0283	2.22	2.11
1.15	1.5	0.0176	0.82	0.986	0.0174	0.884	0.979	0.0167	0.914	0.996	0.0158	0.979	1.1	0.0148	1.21	1.39	0.0127	2.19	2.6
1.5	1.95	0.00883	1.34	1.21	0.00875	1.14	1.21	0.00845	1.06	1.23	0.00732	1.24	1.41	0.00639	1.88	1.85	0.00481	3.21	3.68
1.95	2.52	0.00445	1.29	1.51	0.00438	1.29	1.51	0.00411	1.35	1.56	0.00357	1.83	1.79	0.00295	2.27	2.42	0.00154	5.3	5.79
2.52	3.28	0.00233	1.54	1.8	0.00229	1.6	1.84	0.0021	1.6	1.93	0.00174	1.92	2.24	0.00127	2.96	3.24	0.000536	7.44	8.53
3.28	5	0.00104	1.5	1.78	0.00102	1.69	1.81	0.000913	1.64	1.93	0.000784	1.93	2.22	0.000497	3.66	3.34	0.000183	8.94	9.83
5	10	0.000302	1.83	1.92	0.000304	1.61	1.96	0.000274	1.74	2.08	0.000209	2.12	2.53	0.00013	3.76	3.91	3.1e-05	13.5	13.6

TABLE 13.2. Tabulation of ϕ^* distributions, along with corresponding systematic and statistical uncertainties, for the off-peak analyses: $46\,\text{GeV} < M < 66\,\text{GeV}$ and $116\,\text{GeV} < M < 150\,\text{GeV}$. The relative dominance of the uncertainties for each bin are indicated using a red-blue spectrum: red = more dominant, blue = less dominant.

		$46\,\text{GeV} < M < 66\,\text{GeV}$									$116\,\text{GeV} < M < 150\,\text{GeV}$								
		$\lvert y\rvert < 0.8$			$0.8 < \lvert y\rvert < 1.6$			$1.6 < \lvert y\rvert < 2.4$			$\lvert y\rvert < 0.8$			$0.8 < \lvert y\rvert < 1.6$			$1.6 < \lvert y\rvert < 2.4$		
low	high	$(1/\sigma)\,d\sigma/d\phi^*$	$\delta\phi^*_{\text{sys}}$[%]	$\delta\phi^*_{\text{stat}}$[%]	$(1/\sigma)\,d\sigma/d\phi^*$	$\delta\phi^*_{\text{sys}}$[%]	$\delta\phi^*_{\text{stat}}$[%]	$(1/\sigma)\,d\sigma/d\phi^*$	$\delta\phi^*_{\text{sys}}$[%]	$\delta\phi^*_{\text{stat}}$[%]	$(1/\sigma)\,d\sigma/d\phi^*$	$\delta\phi^*_{\text{sys}}$[%]	$\delta\phi^*_{\text{stat}}$[%]	$(1/\sigma)\,d\sigma/d\phi^*$	$\delta\phi^*_{\text{sys}}$[%]	$\delta\phi^*_{\text{stat}}$[%]	$(1/\sigma)\,d\sigma/d\phi^*$	$\delta\phi^*_{\text{sys}}$[%]	$\delta\phi^*_{\text{stat}}$[%]
0.0001	0.004	7.29	8.06	1.98	7.19	7.59	1.87	6.88	6.9	2.59	11.6	2.07	1.76	12.3	2.37	1.79	11.8	3.37	2.91
0.004	0.008	7.13	6.73	1.99	6.98	4.9	1.91	7.25	5.73	2.43	11.3	1.57	1.75	11.8	2.03	1.82	11.3	2.91	2.94
0.008	0.012	6.81	10	2.06	6.95	6.14	1.88	7.02	8.67	2.49	10.8	2.45	1.78	10.7	2.86	1.9	10.9	2.86	2.95
0.012	0.016	6.58	4.09	2.05	6.42	8.57	1.93	7.22	5.22	2.46	10.8	1.73	1.78	11.2	2.77	1.88	10.6	3.28	2.94
0.016	0.02	6.62	9.06	2.03	6.57	5.91	1.95	6.73	10.7	2.55	9.9	1.92	1.86	9.98	1.86	1.98	10.1	3.67	3.09
0.02	0.024	6.33	7.01	2.12	6.24	7.75	2.02	6.28	6.62	2.67	9.22	1.82	1.92	9.73	1.93	2	10.1	3.88	3.08
0.024	0.029	6.06	7.45	1.93	5.94	6.23	1.8	6.2	6.51	2.39	8.67	2.17	1.79	8.47	2.16	1.91	9.32	3.4	2.92
0.029	0.034	5.73	7.01	2	5.77	9.94	1.88	5.99	5.25	2.5	8.46	1.88	1.82	8.02	2.71	1.98	8.38	3.91	3.05
0.034	0.039	5.4	7.9	2.1	5.49	6.02	1.88	5.51	7.42	2.58	7.69	2.12	1.88	7.19	2.02	2.08	7.11	3.91	3.21
0.039	0.045	5.3	5.12	1.93	5.36	7.55	1.76	5.52	7.77	2.29	6.6	2.24	1.86	6.37	2.44	2.01	6.34	3.63	3.16
0.045	0.051	4.88	5.45	1.95	5.15	6.55	1.83	5.08	6.45	2.4	5.88	1.75	1.97	5.73	2.21	2.11	5.8	3.27	3.35
0.051	0.057	4.65	6.82	1.99	4.99	6.27	1.81	4.92	6.21	2.4	5.38	2.61	2.06	5.5	1.92	2.15	5.58	3.34	3.31
0.057	0.064	4.39	4.61	1.87	4.5	5.84	1.77	4.54	5.07	2.3	5.02	1.85	2	4.84	2.06	2.14	5.4	3.38	3.19
0.064	0.072	3.92	6.23	1.86	4.18	5.24	1.72	4.23	5.46	2.24	4.38	1.64	1.99	4.28	2.19	2.12	4.37	3.44	3.37
0.072	0.081	3.78	7.1	1.81	3.95	5.38	1.64	3.9	5.84	2.22	3.81	1.86	2.02	3.9	2.65	2.11	4.17	3.25	3.18
0.081	0.091	3.56	5.82	1.76	3.43	5.7	1.69	3.41	5.13	2.23	3.18	1.72	2.09	3.19	2.09	2.19	3.34	3.12	3.35
0.091	0.102	3.09	4.3	1.81	3.16	3.87	1.66	3.16	4.79	2.28	2.99	1.8	2.05	3.06	2.25	2.14	2.91	4.14	3.48
0.102	0.114	2.83	4.54	1.79	2.79	3.89	1.7	3.01	5.47	2.2	2.59	2.22	2.13	2.48	2.77	2.26	2.49	3.6	3.57
0.114	0.128	2.49	3.32	1.76	2.63	3.45	1.63	2.56	5.34	2.2	2.2	1.87	2.12	2.13	3.28	2.29	2.13	3.35	3.59
0.128	0.145	2.18	3.54	1.71	2.14	3.01	1.61	2.26	4.44	2.1	1.77	1.85	2.16	1.88	1.97	2.23	1.86	4.17	3.63
0.145	0.165	1.78	3.16	1.73	1.88	2.88	1.58	1.77	5.15	2.2	1.5	2.95	2.18	1.6	1.96	2.21	1.59	4.06	3.46
0.165	0.189	1.51	3.14	1.74	1.47	3.79	1.61	1.61	4.87	2.1	1.21	1.9	2.26	1.21	1.97	2.36	1.43	4.79	3.44
0.189	0.219	1.24	5.48	1.7	1.32	6.25	1.58	1.17	5.99	2.18	0.954	1.7	2.26	0.979	2.36	2.34	0.944	4.15	3.74
0.219	0.258	1.02	7.06	1.67	0.949	6.14	1.58	0.991	7.45	2.15	0.76	3.19	2.25	0.804	2.61	2.29	0.771	3.5	3.61
0.258	0.312	0.767	10	1.62	0.754	8.54	1.53	0.787	9.71	1.97	0.531	2.36	2.33	0.582	2.54	2.32	0.543	3.41	3.65
0.312	0.391	0.527	9.53	1.64	0.529	13.9	1.53	0.545	9.55	1.96	0.361	2.8	2.41	0.342	2.4	2.59	0.367	3.99	3.85
0.391	0.524	0.341	14.7	1.59	0.335	13.9	1.47	0.335	10.2	1.97	0.212	3.08	2.56	0.203	3.18	2.65	0.199	5.15	3.98
0.524	0.695	0.197	14.9	1.84	0.193	11.5	1.74	0.182	9.88	2.34	0.108	4.94	3.3	0.104	4.02	3.36	0.0868	6.3	5.36
0.695	0.918	0.118	10	2.17	0.105	10.2	2.09	0.102	6.93	2.72	0.0568	5.03	4.04	0.0495	4.77	4.25	0.0436	9.16	6.41
0.918	1.15	0.0637	6.64	2.98	0.0657	7.22	2.62	0.0547	6.69	3.64	0.0267	5.55	5.57	0.0256	5.78	5.63	0.0245	9.96	8.78
1.15	1.5	0.0378	7.46	3.25	0.0349	10.2	3.1	0.0321	7.6	4.2	0.0162	6.55	5.78	0.0115	7.25	7.08	0.00856	10.5	12.1
1.5	1.95	0.0188	8.3	4.1	0.0178	9.9	3.84	0.0141	12.3	5.68	0.00581	7.34	9.17	0.007	6.9	7.89	0.00268	16	18.6
1.95	2.52	0.011	9.21	4.73	0.0095	16	4.43	0.00644	14.4	7.03	0.00347	8.7	9.49	0.00409	10.6	8.9	0.00109	32.6	23.4
2.52	3.28	0.00466	9.94	6.05	0.0049	12	5.4	0.00354	19.5	8.84	0.00269	11.4	9.36	0.00114	20.8	15.2	0.000112	80.4	116
3.28	5	0.00245	11.3	5.74	0.00225	11.8	5.49	0.00126	24.7	9.77	0.000631	14.1	15.4	0.000561	11.4	14.7	7.7e-05	39.9	65.3
5	10	0.000686	23.6	6.43	0.000574	17.6	6.42	0.000644	61.5	10.4	0.000226	13.4	14.4	0.000159	11.9	15.8	7.13e-05	39.9	37

Azimuthal decorrelation between leptons in the Drell-Yan process as a probe of infrared QCD:

Phenomenology, predictions and measurement of a novel collider observable using perturbative resummation techniques

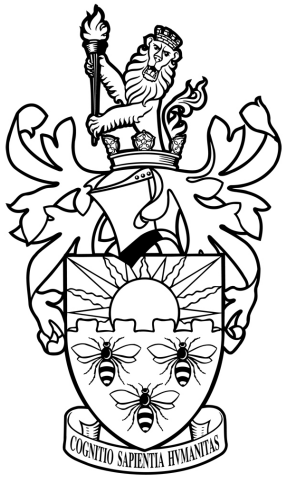

A thesis submitted to the University of Manchester for the degree of Doctor of Philosophy in the Faculty of Engineering and Physical Sciences

2014

Lee Tomlinson
Particle Physics Group
School of Physics and Astronomy

Contents

List of figures 7

List of tables 13

Abstract 15

Declaration 17

Copyright statement 17

Preface 19

List of publications and analysis notes 23

Part 1. Phenomenology of a novel collider observable: ϕ^* 25

Chapter 1. Introduction 27

Chapter 2. Fundamentals of QCD 29
2.1. The classical Lagrangian 29
2.2. Gauge invariance, colour and quantization 29
2.3. The Feynman rules 31
2.4. Renormalization in the Lagrangian 33
2.5. The renormalization group equation 34

Chapter 3. QCD in the infrared régime 39
3.1. Factorization of gluons in the soft limit 39
3.2. Soft gluon emission and coherence 42
3.3. Collinear gluon emission to all orders 49
3.4. Parton evolution and the DGLAP equation 51

Chapter 4. The Drell–Yan process and the ϕ^* observable 55
4.1. The hadronic cross-section 56
4.2. The full Q_{T} distribution 61
4.3. The origin of large logarithms 63
4.4. Kinematics of ϕ^* 68
4.5. The low ϕ^* distribution 69
4.6. Logarithmic structure of observables 71
4.7. Summation to all orders 72
4.8. The final resummed result 81

Chapter 5. Phenomenology of ϕ^* at Tevatron and the LHC 85
5.1. Scale dependence in the radiator 87
5.2. The fully scale-dependent radiator 90
5.3. Comparison of results to DØ data 92
5.4. Predictions for the ATLAS experiment 98
5.5. Probing the small-x régime 103
5.6. Predictions for the CMS experiment 104
5.7. Non-perturbative prescriptions in the b-space formalism 105
5.8. A non-perturbative study 106
5.9. Comparison with ResBos 110

Chapter 6. Conclusions 113

Part 2. Experimental analysis of ϕ^* in Drell–Yan events at ATLAS 115

Chapter 7. Introduction 117

Chapter 8. The ATLAS experiment 119
8.1. Detector components 119
8.2. Muons and electrons 121

Chapter 9. Measurement definition and strategy 123
9.1. Binning 123
9.2. Observable definition 127
9.3. Monte Carlo input, collision data and luminosity 128

Chapter 10. Monte Carlo corrections 131
10.1. Pileup re-weighting 131
10.2. Efficiencies 132
10.3. Muon momenta corrections 133
10.4. Z line-shape re-weighting 133

Chapter 11. Object and event selection 135
11.1. Muon selection 135
11.2. Electron selection 136
11.3. Event selection 137

Chapter 12. Backgrounds 139
12.1. Electroweak and top backgrounds 139
12.2. W+jets backgrounds 150
12.3. Multi-jet background 160
12.4. Total background contamination 168
12.5. Control distributions 172

Chapter 13. Final results 183
13.1. Bin-by-bin corrections 183
13.2. Systematic uncertainties 186

13.3. Results 193
13.4. Conclusions and future prospects 201

Part 3. Luminosity studies within ATLAS 203

Chapter 14. Introduction 205

Chapter 15. Long- and short-term detector stabilities 207
15.1. Introduction 207
15.2. The Beam Conditions Monitor (BCM) 207
15.3. The van der Meer calibration method 209
15.4. A study of drifts in BCM-reported luminosities 211
15.5. Recalibration of the visible cross-section for the AND algorithm 215
15.6. Conclusions 220

Chapter 16. Transverse beam coupling part 1 221
16.1. Introduction 221
16.2. The single-Gaussian model 227
16.3. Method 228
16.4. Fitted slopes and errors 230
16.5. Constraints on individual beam widths and correlation 231
16.6. The effect of beam crossing angles 235
16.7. Error on luminosity 237
16.8. Concluding remarks 238

Chapter 17. Transverse beam coupling part 2 241
17.1. Introduction 241
17.2. Analysis method and formalism with beam crossing angles 241
17.3. Application to in-plane vdM scan data 244
17.4. Compilation of all vdM scan results 268
17.5. Discussion of results and conclusions 269

Chapter 18. Concluding remarks 273

Appendix A. Explicit calculations 277
A.1. Drell–Yan in the Born approximation 277
A.2. Real corrections to Drell–Yan 282
A.3. Virtual corrections to Drell–Yan 288
A.4. The collinear splitting function 294

Appendix B. Mathematical appendix 297
B.1. Integral representations of Heaviside step functions 297
B.2. Special functions 298
B.3. Azimuthal integration of radiation function 299
B.4. NNLL approximation 301

Appendix C. Control plots for resummed predictions 305

C.1. Cancellation of logs for DØ predictions 305
C.2. Cancellation of logs for ATLAS predictions 326
C.3. Cancellation of logs for CMS predictions 332

Appendix D. Azimuthal distribution of muons 339

Appendix E. Luminosity 347
E.1. Optimized $\sigma_{\text{vis}}^{\text{AND}}$ plots 347
E.2. Systematics due to non-zero α_{xz} 349
E.3. Luminous centroid movements with non-zero beam crossing angle 350
E.4. When does crossing angle become negligible? 351

Bibliography 353

Word count: 57,409

List of figures

2.1 The conventions for the Feynman rules used throughout this thesis 32

3.1 Single gluon radiation in the final state 40
3.2 Factorization of a soft gluon from a general hard process 42
3.3 The eight diagrams contributing to the two-gluon emission from a $q\bar{q}$ pair 43
3.4 A 'ladder' diagram for an arbitrary number of gluon emissions 51

4.1 The Drell-Yan process in the Born approximation and the naïve Parton Model 56
4.2 Kinematics of the ϕ^* observable in the transverse plane 68

5.1 DØ ϕ^* data in comparison with ResBos predictions 86
5.2 DØ Q_{T} data in comparison with ResBos predictions 87
5.3 Remainder plots for the muon and electron channels in DØ data 94
5.4 Our matched calculation for DØ data in the electrons channel 95
5.5 Our matched calculation for DØ data in the muons channel 96
5.6 The contribution of various scale variations to the total uncertainty 96
5.7 A comparison of theoretical uncertainties for a NLL and a NNLL calculation 97
5.8 Predictions for the low-mass ϕ^* distributions at DØ 97
5.9 Remainder plots for the predicted low-mass ϕ^* distributions at DØ 98
5.10 The remainder plots for our ATLAS ϕ^* and Q_{T} (p_{T}) predictions 99
5.11 Our NNLL+NLO predictions for ϕ^* and Q_{T} for ATLAS 100
5.12 Our NNLL+NLO prediction for ϕ^* in comparison with ATLAS data 101
5.13 Our ϕ^* predictions for ATLAS kinematics in three rapidity regions 102
5.14 Ratios of different rapidity bins for our ATLAS ϕ^* predictions 103
5.15 Our NNLL+NLO prediction for the ϕ^* observable for CMS 105
5.16 A Gaussian non-perturbative model vs. DØ muon data 107
5.17 A Gaussian non-perturbative model vs. DØ electron data 108
5.18 A comparison between our NNLL+NLO prediction and that of ResBos 110

8.1 A cutaway drawing of the ATLAS detector 119
8.2 The ATLAS inner detector 120

9.1 Migration of events from the peak mass region 125

9.2 The purities of the ϕ^* bins (on peak) 126
9.3 The purities of the ϕ^* bins (off peak) 127
9.4 The total integrated luminosity delivered by the LHC 129

10.1 Pileup distributions in simulated and collision data 131

12.1 Electroweak backgrounds to Drell–Yan signal selection 140
12.2 Missing transverse energy distributions in $e\,\mu$ events 142
12.3 Invariant mass distributions in $e\,\mu$ events 143
12.4 Transverse momentum and rapidity distributions in $e^+\mu^-/\mu^+e^-$ events 144
12.5 Lepton kinematics distributions in $e^+\mu^-/\mu^+e^-$ events 145
12.6 ϕ^* distributions of $e^+\,\mu^-/e^-\,\mu^+$ events (on-peak) 146
12.7 ϕ^* distributions of $e^+\,\mu^-/e^-\,\mu^+$ events (on-peak) 147
12.8 ϕ^* distributions of $e^+\,\mu^-/e^-\,\mu^+$ events (low-mass) 148
12.9 ϕ^* distributions of $e^+\,\mu^-/e^-\,\mu^+$ events (high-mass) 149
12.10 Missing transverse energy distributions in the 'W+jets' selection 152
12.11 Invariant mass distributions in the 'W+jets' selection 153
12.12 Transverse momentum and rapidity distributions in the 'W+jets' selection 154
12.13 Lepton kinematics distributions in the 'W+jets' selection 155
12.14 ϕ^* distributions for the 'W+jets' selection (on-peak) 156
12.15 ϕ^* distributions for the 'W+jets' selection (on-peak) 157
12.16 ϕ^* distributions for the 'W+jets' selection (low-mass) 158
12.17 ϕ^* distributions for the 'W+jets' selection (high-mass) 159
12.18 The fitted values of A and B, and the binning used to perform the fit 161
12.19 ϕ^* distributions for *anti*-isolated muons (off peak) 164
12.20 ϕ^* distributions for *anti*-isolated muons (on peak) 165
12.21 Opposite-sign event selection efficiencies, ϵ and f 167
12.22 Anti-isolated ϕ^* distributions, opposite- and like-sign 167
12.23 Background contamination with alternative and default multi-jet estimate 168
12.24 Percentage background contamination for ϕ^* (on-peak) 170
12.25 Percentage background contamination for ϕ^* (off-peak) 171
12.26 ϕ^* and Q_{T} correlation in Powheg+Pythia8 and Sherpa 173
12.27 Missing transverse energy distributions for signal selection 175
12.28 Invariant mass distributions for signal selection 176
12.29 Boson transverse momentum and rapidity distributions for signal selection 177
12.30 Muon transverse momentum and rapidity distributions for signal selection 178
12.31 Data–MC comparison for ϕ^* (on-peak) 179

12.32 Data–MC comparison for ϕ^* (on-peak) 180
12.33 Data–MC comparison for ϕ^* (low-mass) 181
12.34 Data–MC comparison for ϕ^* (high-mass) 182

13.1 On-peak Bin-by-bin correction factors for ϕ^* 184
13.2 Off-peak Bin-by-bin correction factors for ϕ^* 185
13.3 Systematic uncertainties on the final on-peak ϕ^* distributions 189
13.4 Systematic uncertainties on the final on-peak ϕ^* distributions 190
13.5 Systematic uncertainties on the final low-mass ϕ^* distributions 191
13.6 Systematic uncertainties on the final high-mass ϕ^* distributions 192
13.7 Final ϕ^* distributions for ATLAS at 8 TeV (on peak) 194
13.8 Final ϕ^* distributions for ATLAS at 8 TeV (off peak) 195
13.9 ATLAS data with NNLL+NLO at 8 TeV 196
13.10 ATLAS data with NNLL+NLO at 8 TeV 197
13.11 ATLAS data with NNLL+NLO at 8 TeV 198

15.1 The so-called '.7% problem' 211
15.2 Average μ values for each detector, in ratio to BCMH_EventOR (2011) 213
15.3 Ratio of luminosity reported by BCMH_ and BCMV_EventOR to TileCal 213
15.4 Ratio of luminosity reported by BCMH_ and BCMV_EventAND to TileCal 214
15.5 Variations of $\sigma_{\text{vis}}^{\text{AND}}$ for May 2011 vdM scan data 216
15.6 The corresponding parabolae to determine the best χ^2 for May 2011 data 217
15.7 Variations of $\sigma_{\text{vis}}^{\text{AND}}$ for May 2011 vdM scan data (background-subtracted) 219

16.1 Position of the luminous centroid during Scan IV 223
16.2 Position of the luminous centroid during Scan V 224
16.3 Position of the luminous centroid during Scan VII 225
16.4 Position of the luminous centroid during Scan VIII 226
16.5 Beam width constraints from October 2010 scans 231
16.6 Beam width constraints from May 2011 scans 232
16.7 Correlation coefficient of each beam (October 2010 and May 2011) 234

17.1 Luminous centroid movements during Scan I in (March) 2011 246
17.2 Luminous centroid movements during Scan II in (March) 2011 247
17.3 Beam width constraints for Scan I of March 2011 248
17.4 Beam width constraints for Scan II of March 2011 248
17.5 Beam correlation constraints for scans I and II of March 2011 249
17.6 April 2012 Scan I data 252

17.7 April 2012 Scan II data 253
17.8 April 2012 Scan III data 254
17.9 Individual beam widths for April 2012 scan I 255
17.10 Individual beam widths for April 2012 scan II 255
17.11 Individual beam widths for April 2012 scan III 256
17.12 Correlation coefficient constraints for April 2012 scans I, II and III 257
17.13 July 2012 Scan IV data 259
17.14 July 2012 Scan V data 260
17.15 July 2012 Scan VI data 261
17.16 July 2012 Scan VII data 262
17.17 July 2012 Scan VIII data 263
17.18 July 2012 Scan IX data 264
17.19 Constrained beam widths for scans IV – VI, performed in July 2012 265
17.20 Constrained beam widths for scans VII – IX, performed in July 2012 266
17.21 Constrained x-y correlation for scans IV – IX, performed in July 2012 267

18.1 An example of non-linear tails in beamspot data 273
18.2 Data calling for a model beyond Gaussians 274

A.1 Drell-Yan in the Born approximation 277
A.2 2-to-2 scattering angle 280
A.3 2-to-3 scattering kinematics 282
A.4 Drell–Yan: real diagrams 282
A.5 Drell–Yan: virtual diagrams 288
A.6 Initial-state collinear gluon radiation 294

B.1 Definition of complex contour 302

C.1 Remainder plots for DØ Z $\to ee$ on peak with $|y| < 1$ and $\mu_{\mathrm{Q}} = M/2$ 305
C.2 Remainder plots for DØ Z $\to ee$ on peak with $|y| < 1$ and $\mu_{\mathrm{Q}} = M$ 306
C.3 Remainder plots for DØ Z $\to ee$ on peak with $|y| < 1$ and $\mu_{\mathrm{Q}} = 2M$ 307
C.4 Remainder plots for DØ Z $\to ee$ on peak with $1 < |y| < 2$ and $\mu_{\mathrm{Q}} = M/2$ 308
C.5 Remainder plots for DØ Z $\to ee$ on peak with $1 < |y| < 2$ and $\mu_{\mathrm{Q}} = M$ 309
C.6 Remainder plots for DØ Z $\to ee$ on peak with $1 < |y| < 2$ and $\mu_{\mathrm{Q}} = 2M$ 310
C.7 Remainder plots for DØ Z $\to ee$ on peak with $|y| > 2$ and $\mu_{\mathrm{Q}} = M/2$ 311
C.8 Remainder plots for DØ Z $\to ee$ on peak with $|y| > 2$ and $\mu_{\mathrm{Q}} = M$ 312
C.9 Remainder plots for DØ Z $\to ee$ on peak with $|y| > 2$ and $\mu_{\mathrm{Q}} = 2M$ 313
C.10 Remainder plots for DØ Z $\to \mu\mu$ on peak with $|y| < 1$ and $\mu_{\mathrm{Q}} = M/2$ 314

C.11 Remainder plots for DØ Z $\to \mu\mu$ on peak with $|y| < 1$ and $\mu_{\rm Q} = M$ 315
C.12 Remainder plots for DØ Z $\to \mu\mu$ on peak with $|y| < 1$ and $\mu_{\rm Q} = 2M$ 316
C.13 Remainder plots for DØ Z $\to \mu\mu$ on peak with $1 < |y| < 2$ and $\mu_{\rm Q} = M/2$ 317
C.14 Remainder plots for DØ Z $\to \mu\mu$ on peak with $1 < |y| < 2$ and $\mu_{\rm Q} = M$ 318
C.15 Remainder plots for DØ Z $\to \mu\mu$ on peak with $1 < |y| < 2$ and $\mu_{\rm Q} = 2M$ 319
C.16 Remainder plots for DØ at low mass with $|y| < 1$ and $\mu_{\rm Q} = M/2$ 320
C.17 Remainder plots for DØ at low mass with $|y| < 1$ and $\mu_{\rm Q} = M$ 321
C.18 Remainder plots for DØ at low mass with $|y| < 1$ and $\mu_{\rm Q} = 2M$ 322
C.19 Remainder plots for DØ at low mass with $1 < |y| < 2$ and $\mu_{\rm Q} = M/2$ 323
C.20 Remainder plots for DØ at low mass with $1 < |y| < 2$ and $\mu_{\rm Q} = M$ 324
C.21 Remainder plots for DØ at low mass with $1 < |y| < 2$ and $\mu_{\rm Q} = 2M$ 325
C.22 Remainder plots for ATLAS ϕ^*, with $\mu_{\rm Q} = M/2$ 326
C.23 Remainder plots for ATLAS ϕ^*, with $\mu_{\rm Q} = M$ 327
C.24 Remainder plots for ATLAS ϕ^*, with $\mu_{\rm Q} = 2M$ 328
C.25 Remainder plots for ATLAS $Q_{\rm T}$, with $\mu_{\rm Q} = M/2$ 329
C.26 Remainder plots for ATLAS $Q_{\rm T}$, with $\mu_{\rm Q} = M$ 330
C.27 Remainder plots for ATLAS $Q_{\rm T}$, with $\mu_{\rm Q} = 2M$ 331
C.28 Remainder plots for CMS ϕ^* and $Q_{\rm T}$ (central) 332
C.29 Remainder plots for CMS ϕ^*, with $\mu_{\rm Q} = M/2$ 333
C.30 Remainder plots for CMS ϕ^*, with $\mu_{\rm Q} = M$ 334
C.31 Remainder plots for CMS ϕ^*, with $\mu_{\rm Q} = 2M$ 335
C.32 Remainder plots for CMS $Q_{\rm T}$, with $\mu_{\rm Q} = M/2$ 336
C.33 Remainder plots for CMS $Q_{\rm T}$, with $\mu_{\rm Q} = M$ 337
C.34 Remainder plots for CMS $Q_{\rm T}$, with $\mu_{\rm Q} = 2M$ 338

D.1 Azimuthal distribution of leading muons ($-\pi < \theta < -\pi/2$) 339
D.2 Azimuthal distribution of leading muons ($-\pi/2 < \theta < 0$) 340
D.3 Azimuthal distribution of leading muons ($0 < \theta < \pi/2$) 341
D.4 Azimuthal distribution of leading muons ($\pi/2 < \theta < \pi$) 342
D.5 Azimuthal distribution of sub-leading muons ($-\pi < \theta < -\pi/2$) 343
D.6 Azimuthal distribution of sub-leading muons ($-\pi/2 < \theta < 0$) 344
D.7 Azimuthal distribution of sub-leading muons ($0 < \theta < \pi/2$) 345
D.8 Azimuthal distribution of sub-leading muons ($\pi/2 < \theta < \pi$) 346

E.1 Effect of optimizing $\sigma_{\rm vis}^{\rm AND}$ on the AND-over-OR luminosity ratios (μ bins) 347
E.2 Effect of optimizing $\sigma_{\rm vis}^{\rm AND}$ on the AND-over-OR luminosity ratios (PLB bins) 348

List of tables

9.1 The Monte Carlo samples used in the Z $\rightarrow \mu\mu$ channel ϕ^* analysis. 130

12.1 Results of the multi-jet background fits 162

13.1 On-peak ϕ^* distributions with systematic and statistical uncertainties 199
13.2 Off-peak ϕ^* distributions with systematic and statistical uncertainties 200

15.1 Percentages by which the nominal values of $\sigma_{\text{vis}}^{\text{AND}}$ should be multiplied 218
15.2 Values of $\sigma_{\text{vis}}^{\text{AND}}$ determined for BCMH and BCMV using $\mu_{\text{OR}}^{\text{Corrected}}$ 220

16.1 Luminous centroid movements in single-Gaussian model 222
16.2 Fitted $d\langle\{x,y,z\}\rangle/dh_{\{x,y\}}$ values for October 2010 data 230
16.3 Fitted $d\langle\{x,y,z\}\rangle/dh_{\{x,y\}}$ values for May 2011 data 230
16.4 Constraints on individual beam widths (October 2010 and May 2011) 233
16.5 Bunch-averaged convolved beam widths (October 2010 and May 2011) 233
16.6 Constraints on the x-y correlation coefficient (October 2010 and May 2011) 235

17.1 Convolved widths used as input in the March 2011 analyses 245
17.2 Luminous region x-y correlation coefficients 245
17.3 Table of input parameters for the April 2012 analysis 251
17.4 Table of input parameters for the July 2012 analysis 258
17.5 October 2010 widths (μm) 268
17.6 March 2011 widths (μm) and correlation coefficients 268
17.7 May 2011 widths (μm) 268
17.8 April 2012 widths (μm) 268
17.9 July 2012 widths (μm) and correlation coefficients 269
17.10 Approximate individual beam widths determined from the LHC design emittance and nominal beta functions. 269

E.1 Changes in MC observables w.r.t. discrete changes in α_{xz} 349

Abstract

Azimuthal decorrelation between leptons in the Drell-Yan process as a probe of infrared QCD: Phenomenology, predictions and measurement of a novel collider observable using perturbative resummation techniques

A thesis submitted to the University of Manchester for the degree of Doctor of Philosophy in the Faculty of Engineering and Physical Sciences

This thesis presents phenomenological studies of a state-of-the-art NNLL+NLO theoretical calculation of a novel collider observable known as ϕ^*. In these studies the ϕ^* observable, a measure of azimuthal decorrelation, is applied directly to the leptons in the production of massive lepton pairs in hadron collisions (the *Drell–Yan* process). This provides an alternate measure of the recoil of the massive vector boson (Z/γ^*) against initial state QCD radiation, but with distinct experimental advantages over the traditional boson transverse momentum. Attention is focused on the small-ϕ^* régime (the quasi-back-to-back régime) where the infrared dynamics of soft/collinear gluon emissions become important. These phenomenological studies are followed up with the presentation of a measurement of ϕ^* in $\mathrm{Z} \to \mu\mu$ events using $20.3\,\mathrm{fb}^{-1}$ of collision data collected by the ATLAS experiment in 2012. Finally, studies directly related to the ATLAS absolute luminosity calibration by the van der Meer (vdM) method are presented, with the objective of elucidating the rôle of transverse linear beam correlation. In particular, I present studies using an analytical method I have developed in order to precisely extract individual beam information by way of studying phenomena pertaining to the luminous region during vdM scans. In addition, a dedicated study of the long- and short-term stabilities of the principal detectors for luminosity monitoring is also presented, along with an appropriate recalibration of these detectors.

Lee Tomlinson
The University of Manchester
December 24, 2014

Declaration

No portion of the work referred to in the thesis has been submitted in support of an application for another degree or qualification of this or any other university or other institute of learning.

Copyright statement

Preface

I became a PhD student in the particle physics group at Manchester in 2010, and have since worked on both high-energy particle physics theory and experiment, under the joint supervision of Dr. Mrinal Dasgupta and Prof. Terry Wyatt FRS. My primary PhD research has been in precision QCD and electroweak physics, focusing in particular on a novel collider observable called 'ϕ^*'. The theoretical aspects of this work have centred on a state-of-the-art calculation of ϕ^* along with several associated phenomenological studies. I now work within the ATLAS collaboration at CERN where I have been a qualified author since November 2012 and where, most recently, I have also been performing a measurement of ϕ^* using the 2012 data set. I performed my service work for authorship qualification within the luminosity measurement task force, becoming a primary author on the 2011 luminosity measurement paper. During my PhD I have also become a primary author of software which automates our theoretical calculation of ϕ^* for and end-user, and which has now been used by ATLAS and DØ, with whom I have enjoyed very fruitful collaboration. The following thesis is divided into three parts, covering the work I have done on ϕ^* in association with the Drell–Yan process (the production of massive lepton pairs in hadronic collisions) and the luminosity studies I performed within the ATLAS collaboration.

The first part of this thesis is dedicated to theoretical and phenomenological work I have done with the ϕ^* observable. It is my intention that this part will form a pedagogical introduction to QCD and calculational techniques within, finally culminating in explicit calculations for ϕ^* and the results of my phenomenological work as applied to experiments at Tevatron and the LHC. I had more than my thesis defence examiner in mind when writing this part: In fact, I was writing to a student very much like myself, who might decide to pursue a PhD in QCD research, or who might simply want to become familiar with some of the calculational techniques therein for his or her own needs. However, for the purpose of this remaining a thesis *to be examined*, I opted to remove quite a significant amount of material that I had brought together as pedagogy but which may, nonetheless, be discovered in the literature following the references I have retained. The reader will still find explicit calculations, in some cases relegated to appropriate appendices, which are directly relevant to my work herein.

A reader who is already familiar with the foundations of perturbative QCD might wish to skip Chapter 2. The remaining chapters however, even for a familiar reader, are very relevant to my work on ϕ^* and should still provide crucial insight. Chapter 3 discusses relevant aspects of the dynamics of soft and collinear gluon emission by way of explicit calculation, followed by a discussion of the interpretation of the final results. Chapter 4 ultimately describes our 'resummed' calculation of ϕ^*, after first addressing theoretical

aspects of the Drell–Yan process and the origin of logarithmically enhanced terms. In addition, this chapter provides the reader with the connection to the more familiar Q_{T} observable: the transverse momentum of the lepton pair. Finally, Chapter 5 presents my phenomenological work in detail. This work includes comparisons to data available at the time, and also *predictions* for data that would become available later.

The second part of this thesis describes the experimental measurement of ϕ^* I performed in the $\mathrm{Z} \to \mu\mu$ channel at $\sqrt{s} = 8$ TeV using data from the ATLAS experiment. It had always been foreseen that I would perform an experimental measurement of ϕ^* in order to complement the theoretical calculations I worked on. A measurement of ϕ^* within ATLAS had already been performed at $\sqrt{s} = 7$ TeV by the time I had made the transition to dedicating my research efforts to experiment (i.e. after becoming a qualified ATLAS author). The results of my earlier phenomenological work strongly indicated that a measurement performed at 8 TeV, with approximately four times the data as used in the 7 TeV measurement, could be very complementary to the former analysis if it included additional measurements performed away from the Z peak. Put concretely, the rôle of non-perturbative effects in comparisons to DØ data, and the remarkable agreement of our prediction with low-mass DØ data, suggested that additional off-peak measurements at 8 TeV should form an essential aspect of this experimental analysis.

The third and final part of this thesis details the service work I contributed to the ATLAS collaboration within the luminosity measurement task force, in the form of three dedicated internal analysis notes. It is within this group that I worked closely with the *Beam Conditions Monitor*—the principal luminosity monitor within ATLAS. Chapter 15 introduces the concept of a *van der Meer* beam separation scan as a method for determining the absolute luminosity calibration, and then presents a study I performed with the aim of addressing the short- and long-term stability of the BCM detector. Chapters 16 and 17 then present my worked aimed at quantifying the transverse beam correlation within ATLAS, and the uncertainty this induced in the determination of the absolute luminosity calibration.

I owe huge thanks to my supervisors Dr. Mrinal Dasgupta and Prof. Terry Wyatt FRS, not only for the opportunity to pursue such exciting research topics and the commitment they've had towards my career, but also for the pleasure of having them as mentors. I also owe special thanks to Dr. Andrea Banfi, Prof. Witold Kozanecki and Dr. Simone Marzani for the enormous dedication and devotion they have given to my work and to my learning of physics—I am truly grateful to have had the opportunity to work with, and learn from, these kind and committed people. It has been a privilege to collaborate with Samuel Webb, whom I would like to acknowledge and thank for innumerable insightful discussions. I also gratefully acknowledge the financial support of the UK Science & Technology Facilities Council (STFC), and wish to thanks the Particle Physics Group at Manchester for being such a warm and pleasant place in which to carry out my research.

I dedicate this thesis to Mum, Dad and my sister Lisa, for their love, understanding and unwavering support throughout my physics career, particularly during the years it has taken me far from home. I would like to thank those who are both colleagues and dear friends, for all the wonderful times and adventures we've shared together. It has been my

pleasure to meet my friend Aidan whilst on LTA at CERN, and to be permitted to ask the most naïve questions without judgement! I finally owe my warmest thanks to Mandy for always being there, despite the $\sim 5,300$ miles between us.

In loving memory of Roo.

Lee Tomlinson
Manchester, September 2014

List of publications and analysis notes

Papers:

(1) G. Aad *et al.* [ATLAS Collaboration], "Improved luminosity determination in pp collisions at $\sqrt{s} = 7$ TeV using the ATLAS detector at the LHC," Eur. Phys. J. C **73** (2013) 2518 [arXiv:1302.4393 [hep-ex]].

(2) A. Banfi, M. Dasgupta, S. Marzani and L. Tomlinson, "Predictions for Drell-Yan ϕ^* and Q_T observables at the LHC," Phys. Lett. B **715** (2012) 152 [arXiv:1205.4760 [hep-ph]].

(3) A. Banfi, M. Dasgupta, S. Marzani and L. Tomlinson, "Probing the low transverse momentum domain of Z production with novel variables," JHEP **1201** (2012) 044 [arXiv:1110.4009 [hep-ph]].

Internal notes:

(4) M. Karnevskiy, T.-H. Lin, M. Schott, L. Tomlinson, S. Webb, C. Zimmermann, "Measurement of the transverse momentum and azimuthal decorrelation of leptons in Drell-Yan events at $\sqrt{s} = 8$ TeV with ATLAS," ATL-COM-PHYS-2014-281.

(5) L. Tomlinson, "A study on the drift in the BCM-reported luminosity and the recalibration of the visible cross-section," ATL-COM-LUM-2013-019.

(6) L. Tomlinson, "An analytical determination of the parameters of the single-Gaussian model of bunch densities and their impact on the luminosity calibration by the van der Meer method," ATL-COM-LUM-2013-009.

(7) L. Tomlinson, "The effect of linear transverse coupling on the luminosity calibration by the van der Meer method," ATL-COM-LUM-2012-011.

Conference proceedings:

(8) L. Tomlinson, "The resummation of the low-phistar domain of Z production," PoS DIS **2013** (2013) 130 [arXiv:1306.0919 [hep-ph]].

Part 1

Phenomenology of a novel collider observable: ϕ^*

CHAPTER 1

Introduction

Part 1 of this thesis details the theoretical calculations and phenomenological work that have formed a significant part of my PhD research. The theory presented herein centres on the production of massive lepton pairs in high-energy hadron-hadron collisions [**1**] (the *Drell–Yan* process) which has earned a great deal of attention since its conception, in both collider physics theory and experiment. In particular, I present and discuss the calculation of several observables, starting with the classic transverse momentum of the lepton pair, Q_{T}, which has remained central to phenomenology over the decades [**2, 3, 4, 5, 6, 7, 8**], since the pioneering work of Dokshitzer, Diakonov & Troian (DDT) [**9**], Altarelli, Parisi & Petronzio [**10, 11**], Davies, Stirling & Webber [**12, 13**] and Collins, Soper & Sterman (CSS) [**14**], taking place between the late '70s and mid '80s.

Much more recently, the closely related but completely angular ϕ^* observable [**15**] was introduced, which has distinct experimental advantages over its Q_{T} cousin, making it suitable for precision electroweak phenomenology. For this reason, it has been the focus of detailed theoretical [**16, 17, 18**] and experimental [**19, 20**] studies in recent years. It is the theoretical study, predictions and a recent experimental measurement of ϕ^* (Part 2) with which I have been involved, and which form the main topic of my thesis.

In our research, the calculational efforts have been in computing the perturbative quantum chromodynamical (pQCD) corrections to the underlying electroweak process. As I will show, this involves invoking the technology of *resummation* to produce a calculation to all orders in perturbation theory. The reason for doing so is that a calculation of the simplest process capable of generating a non-zero Q_{T} of the lepton pair is mathematically divergent as Q_{T} becomes small. In this limit, and at each order of the perturbative expansion in α_{s}, one finds the effective expansion parameter in the differential distribution to be of the form $\alpha_{\mathrm{s}}^n \log^m(M^2/Q_{\mathrm{T}}^2)$, where M is the invariant mass of the lepton pair and $m \leq 2n-1$, with $m, n \in \mathbb{N}$. The disparity between M and Q_{T} means each term can be numerically large, and the formal validity of a truncated (or 'fixed-order') perturbation series breaks down. One must be careful to treat these logarithmic enhancements appropriately, and in practice this amounts to the aforementioned all-orders approach.

The physical content of such a calculation is that one is forced to consider the emission of up to an infinite number of collinear and/or soft gluons, which themselves dominate the dynamics in the kinematic region where fixed-order fails. In the non-divergent regions of phase space where $Q_{\mathrm{T}} \approx M$—the mass of the lepton pair or, equivalently, the intermediate γ^*/Z boson—a fixed-order calculation provides a good description of the physics. Given one's aim of obtaining a differential distribution that is free of divergences across all values of the observable, it is necessary to use a consistent scheme for *matching* the two main

elements of the calculation: both fixed-order and resummed. The scheme we adopt is a smooth one in which

$$\left(\frac{d\sigma}{d\mathcal{O}}\right)_{\text{matched}} = \left(\frac{d\sigma}{d\mathcal{O}}\right)_{\text{resummed}} + \left(\frac{d\sigma}{d\mathcal{O}}\right)_{\text{fixed-order}} - \left(\frac{d\sigma}{d\mathcal{O}}\right)_{\text{expanded}}, \tag{1.1}$$

where $\mathcal{O} = \{Q_{\text{T}}, \phi^*\}$ is the observable under consideration and 'expanded' denotes the expansion of the resummed calculation. The expansion is performed to the same order in α_{s} with which the fixed-order piece is calculated, in order to remove double counting of emissions. One is at liberty to do this because all logs are properly accounted for. Using this method we obtain a calculation that is, in principle, well-suited to describe the physics over a broad range of $\mathcal{O}$.

With reference to the method of resummation, one is in principle regrouping the calculable terms of an all-orders perturbation expansion into an *exponentiated* form, such that one recovers a series (in the exponent) in which each successive term is formally suppressed relative to the previous one, and which may be truncated. Schematically, for an observable whose leading enhancement is double-logarithmic and provided the observable fulfils certain requirements, as are both the case for the cumulative Q_{T} and ϕ^* distributions, this may be written [**21**]

$$\sum_{m=0}^{\infty}\sum_{n=0}^{2m} C_{mn}\,\alpha_{\text{s}}^m\,L^n = (1+\text{consts})\,\exp\big[\underbrace{L\,g_1(\alpha_{\text{s}}\,L)}_{\text{LL}} + \underbrace{g_2(\alpha_{\text{s}}\,L)}_{\text{NLL}} + \underbrace{\alpha_{\text{s}}\,g_3(\alpha_{\text{s}}\,L)/\pi}_{\text{NNLL}} + \ldots\big], \tag{1.2}$$

where C_{nm} are the coefficients at each order in the expansion and L is the large logarithm. This is the origin of the associated adjectives LL (leading log), NLL (next-to-leading log), NNLL (next-to-next-to-leading log), *etc.* when one speaks of such calculations. The work presented herein makes use of a full NNLL+NLO[1] calculation, which at the time of writing is the state of the art, building on former pioneering work at NNLL (e.g. [**12**]) and mirroring the state of the art at NNLL accuracy in more recent pioneering work [**22, 23, 24, 25, 26**].

The remainder of Part 1 is set out as follows: First, in Chapter 2, I review the foundations of QCD as a quantum gauge field theory. In Chapter 3 I discuss the elements of soft and collinear QCD that are relevant to the process and observables under consideration, by way of explicit calculations. In Chapter 4 I present and discuss the ϕ^* observable and its resummed calculation as applied to the Drell–Yan process, with details consigned to the appendices. In particular, Appendix A contains a fully worked NLO calculation of $q\,\bar{q} \to \gamma^* + X$. Finally, I present my phenomenological work, as applied to various collider experiments, in Chapter 5. This work, in addition to comparisons with data, also includes the predictions for certain experiments when data were not present at the time.

[1]Here NLO refers to the calculation of the Z+jets process; i.e. meaning $\mathcal{O}(\alpha_{\text{s}}^2)$

CHAPTER 2

Fundamentals of QCD

Quantum chromodynamics[1], or QCD, is a non-Abelian gauge field theory, which exhibits exact symmetry under the SU(3) group (of 'colour'). It is a theory of quarks and gluons, being the elementary fields, which transform under the group's fundamental and adjoint representations respectively. Since the gauge group of QCD is the (non-Abelian) SU(3) group—as opposed to the U(1) group in the case of electrodynamics—there exist three distinct charges, also known as *colour*.

2.1. The classical Lagrangian

The classical QCD Lagrangian, up to gauge-fixing terms, is given by

$$\mathcal{L}_{\text{classical}} = -\frac{1}{4} F^a_{\mu\nu} F^{a\,\mu\nu} + \sum_f \bar{\psi}^i_f \left(i\gamma^\mu D^{ij}_\mu - \delta^{ij}\, m_f \right) \psi^j_f, \tag{2.1}$$

where $\bar{\psi} = \psi^\dagger \gamma^0$,

$$F^a_{\mu\nu} = \partial_\mu G^a_\nu - \partial_\nu G^a_\mu + g_{\text{s}} f^{abc} G^b_\mu G^c_\nu \tag{2.2}$$

is the field strength tensor for the Yang-Mills (gluon) field $G^a_\mu(x)$, and

$$D^{ij}_\mu = \partial_\mu \delta^{ij} - i g_{\text{s}} \left(T^a\right)^{ij} G^a_\mu(x) \tag{2.3}$$

is the covariant derivative. The gluon colour index $a \in \{1, \ldots, 8\}$ is implicitly summed over in the first term of Eq. 2.1. Furthermore, $i \in \{1, 2, 3\}$ indexes the quark colour, and $f \in \{u, d, c, s, t, b\}$ indexes the flavour of the quark. The SU(3) generator T^a is explained in the following section. The spinor indices have been suppressed on the Dirac spinors, $\psi^i_f(x)$, and matrices, γ^μ, the latter of which satisfy the Clifford algebra: $\{\gamma^\mu, \gamma^\nu\} = 2g^{\mu\nu}\, I$, where $\{,\}$ denotes anticommutation, $g^{\mu\nu}$ is the Minkowski metric tensor and I is the identity matrix, whose dimension is that of γ. The numbers $f^{abc} \in \mathbb{R}$ are the structure constants of the SU(3) algebra. The final term in Eq. 2.2 is a non-Abelian term, whose consequence is to give rise to triple and quadruple self-couplings of the gluon. Finally, g_{s} is the gauge field coupling strength and will be discussed at length throughout this thesis.

2.2. Gauge invariance, colour and quantization

The SU(N) group is the group of $N \times N$ unitary matrices with unit determinant. For an element $U \in \text{SU}(N)$, these properties are summarized as:

$$\text{SU}(N) = \left\{ U \in \text{GL}(N, \mathbb{C}) : U^\dagger U = U U^\dagger = 1 \wedge \det U = 1 \right\}, \tag{2.4}$$

where GL is the general linear group, the set of $N \times N$ invertible matrices with complex entries. Elements of the defining representation of the SU(3) group follow immediately,

[1]Examples of excellent and accessible texts on QCD and gauge theories are given in [**27, 28**].

and may be generated by exponentiation of the group generators, T^a :

$$U\left(\theta^1,\ldots,\theta^8\right)=\exp\left(i\theta^a\frac{T^a}{2}\right), \tag{2.5}$$

where $a\in\{1,\ldots,8\}$ since the number of generators of the SU(N) group is N^2-1, θ^a are elements of the group parameter space, and T^a satisfy

$$\left[T^a,T^b\right]=i\,f^{abc}\,T^c\,. \tag{2.6}$$

The structure constants themselves, when interpreted as the 8×8 matrices $(T^a)_{bc}=-if^{abc}$, satisfy the same algebra and generate the adjoint representation.

Elements of the SU(N) group can be regarded as linear transformations on an N-dimensional complex vector space, effecting the mapping $U\in\mathrm{SU}(N):\mathbb{C}^N\to\mathbb{C}^N$. As such, we may write

$$\psi_i\to\psi_i'=U_i{}^j\psi_j, \tag{2.7}$$

for $\psi\in\mathbb{C}^N$, which may be written as a column vector, with implicit summation over repeated indices. The placement of indices here is deliberate, and affords a compact notation for the transformation of its complex conjugate, $\psi^i\equiv\psi_i^*$:

$$\psi^i\to\psi'^i=U^i{}_j\psi^j, \tag{2.8}$$

where the identification $U_i^{*j}\equiv U^i{}_j$ is made. The SU(N) invariant mapping $(\psi,\phi):\mathbb{C}^N\times\mathbb{C}^N\to\mathbb{R}$ may now be written, contracting up and down indices, as $\psi^i\phi_i$.

If we insist that the theory of QCD is *locally* gauge invariant, then its Lagrangian should remain invariant—up to divergence terms, which do not affect the derived Euler-Lagrange equations of motion—if we allow elements of the SU(3) parameter space to become space-time dependent, i.e. $\theta^a\to\theta^a(x)$. Acting from the left with ∂_μ on Eq. 2.7, the x-dependence of U would generate an additional term, *vis-à-vis* the global case, demonstrating that the partial derivative is not gauge-invariant. Demanding that a so-called *covariant derivative*, however, should transform in the same manner as the fields themselves—preserving the invariant nature of the Lagrangian—one can derive the appropriate transformation of the Yang-Mills field G_μ^a, which must be performed simultaneously with any gauge transformation of the Dirac fields ψ_i. This transformation is

$$T^aG_\mu^a(x)\to T^aG_\mu'^a(x)=U(x)T^aG_\mu^a(x)U^\dagger(x)-ig_{\mathrm{s}}^{-1}\left[\partial_\mu U(x)\right]U^\dagger(x), \tag{2.9}$$

with a summation over the colour index a, which in infinitesimal form becomes

$$G_\mu^a(x)\to G_\mu^a(x)-f^{abc}\theta^b(x)G_\mu^c(x)+g_{\mathrm{s}}^{-1}\partial_\mu\theta^a(x). \tag{2.10}$$

Furthermore, the gauge-invariant Yang-Mills term $-\frac{1}{4}F_{\mu\nu}^aF^{a\mu\nu}$ is built from the field strength tensor, which may be defined via the commutator

$$F_{\mu\nu}:=-\frac{i}{g_{\mathrm{s}}}\left[D_\mu,D_\nu\right], \tag{2.11}$$

in which the non-Abelian term of Eq. 2.2 has its origin. In order to remove the arbitrariness of the gauge freedom permitted by Eq. 2.10, one has to fix the gauge. At the level of the

Lagrangian, this can be achieved by adding a Lagrange multiplier of the form

$$\mathcal{L}_{\text{gauge}} = \lambda \left[\partial^\mu G^a_\mu(x)\right]^2 . \tag{2.12}$$

This introduces the Lorentz covariant constraint that the gauge be fixed according to $\partial^\mu G^a_\mu(x) = 0$, the Lorenz[2] gauge, obtained by extremizing $\mathcal{L}_{\text{gauge}}$ with respect to λ. The gauge parameter η is introduced, and is related by $\lambda = -1/(2\eta)$. The QCD Lagrangian, before passing to the quantized theory, now stands as

$$\mathcal{L} = \mathcal{L}_{\text{classical}} + \mathcal{L}_{\text{gauge}}. \tag{2.13}$$

Other forms of gauge fixing may be used, e.g. the axial (physical) gauge in which $n \cdot G = 0$, introducing the gauge vector n.

In order to practically quantize the theory using the method of path integrals, the classical Lagrangian is supplemented with a Faddeev–Popov contribution [**29**], which gives rise to ghosts:

$$\mathcal{L}_{\text{F–P}} = (\partial^\mu \chi^{a*})\, D^{ab}_\mu \chi^b \tag{2.14}$$

Here, χ is the ghost field (χ^* being the complex conjugate ghost field), and D^{ab}_μ is the covariant derivative in the adjoint representation,

$$D^{ab}_\mu = \delta^{ab}\, \partial_\mu - g\, f^{abc}\, G^c_\mu . \tag{2.15}$$

Taking all contributions collectively, the quantum Lagrangian for QCD is

$$\mathcal{L} = \mathcal{L}_{\text{classical}} + \mathcal{L}_{\text{gauge}} + \mathcal{L}_{\text{F–P}} . \tag{2.16}$$

2.3. The Feynman rules

Many of the calculations in this thesis necessarily take place in d dimensions, with $d \neq 4$, in order to regulate the divergences that occur for integrals over unconstrained loop momenta. Nonetheless, one would like to preserve the dimensionlessness of the physical couplings involved. The following short exercise shows how this may be done in practice. The concept of mass dimension is introduced, such that a quantity of mass has mass dimension $[m] = 1$. We work with natural units in which $\hbar = c = 1$, thus the action has mass dimension $[S] = 0$. Since

$$S = \int d^d x\, \mathcal{L}, \tag{2.17}$$

and $[x] = -1$, one infers the mass dimension of the Lagrange density to be $[\mathcal{L}] = d$. In the case of QCD, whose classical Lagrangian is given by Eq. 2.1, one is able to systematically infer that $[\psi] = \frac{d-1}{2}$, $[G] = \frac{d}{2} - 1$ and $[g_{\text{s}}] = \frac{4-d}{2}$. In four space-time dimensions ($d = 4$) the coupling is dimensionless. This dimensionlessness may be preserved in $d \neq 4$ dimensions by introducing a new (arbitrary) mass parameter μ, making the replacement $g_{\text{s}} \to g_{\text{s}}\, \mu^{(4-d)/2}$ in the Feynman rules. Indeed this is what has been done in many of the calculations throughout this thesis, hence the appearance of μ^ϵ in several places, where d is taken to be $4 - 2\epsilon$ in order to dimensionally regulate divergent integrals [**30**]. In order to avoid

[2]The Danish mathematician and physicist Ludvig Valentin Lorenz, not to be confused with the Dutch physicist Hendrik Antoon Lorentz

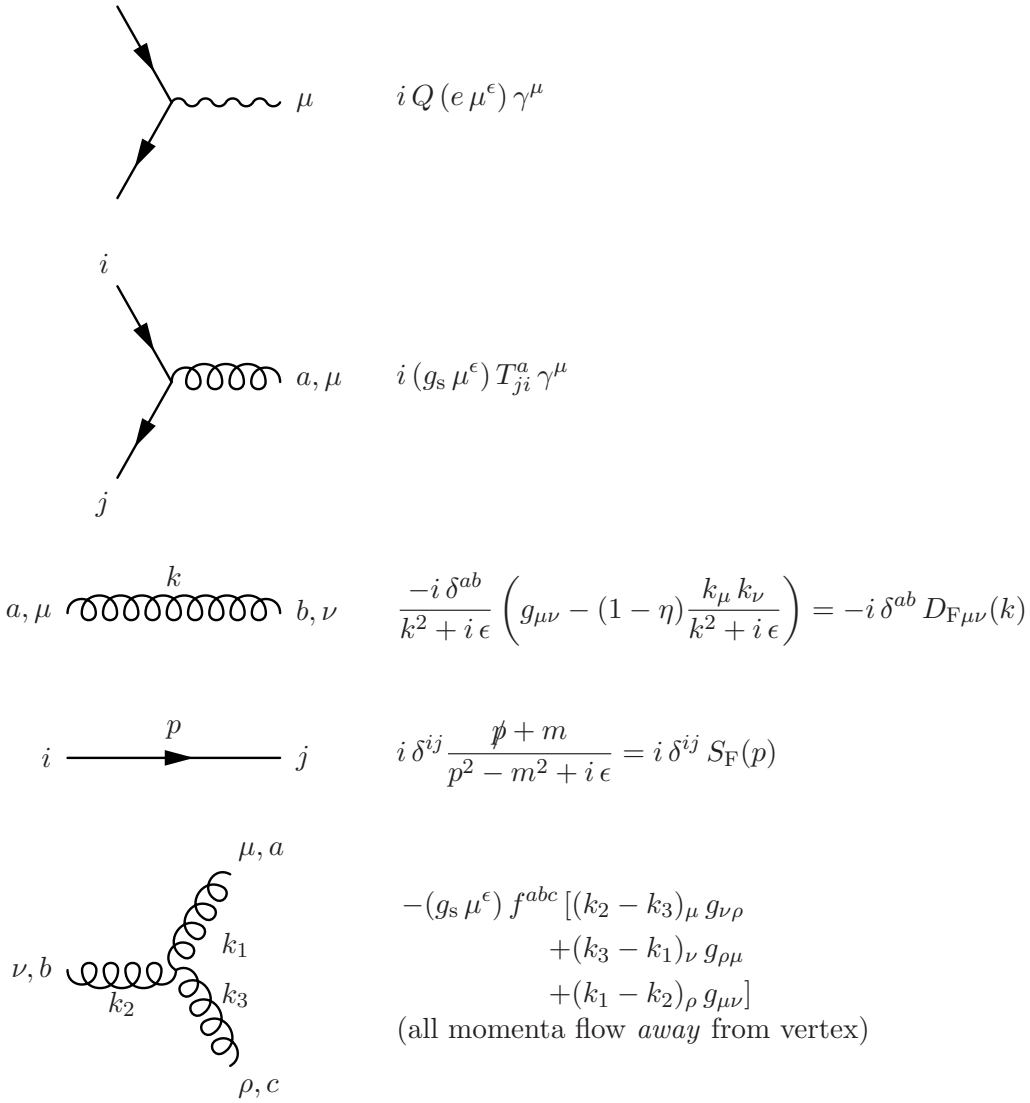

FIGURE 2.1. The conventions for the Feynman rules used throughout this thesis. The corresponding propagator rules for the photon and colourless fermion are given by those for the gluon and coloured fermion above, but removing the δ^{ab} or δ^{ij} as appropriate.

any ambiguity, the conventions for the Feynman rules used throughout this thesis are summarized in Figure 2.1.

2.4. Renormalization in the Lagrangian

The quantities appearing in the original Lagrangian, Eq. 2.16, are not necessarily observable (i.e. are *bare*) and may therefore be suitably infinite in such a way as to cancel the divergences arising from loop integrations in calculations of observable quantities (S-matrix elements, *etc.*). To this end, we introduce renormalized quantities which are related to the bare quantities, denoted[3] by a '0', as follows:

$$\begin{aligned} \psi_0^i &= \sqrt{Z_\psi}\,\psi^i & g_0\,\mu_0^\epsilon &= Z_g\,g\,\mu^\epsilon \\ G_{0\,\mu}^a &= \sqrt{Z_G}\,G_\mu^a & m_0 &= Z_m\,m \\ \chi_0^a &= \sqrt{Z_\chi}\,\chi^a & \eta_0 &= Z_\eta\,\eta \end{aligned} \tag{2.18}$$

Writing the bare Lagrangian in terms of renormalized quantities, using Eq. 2.18, one obtains in $d = 4 - 2\epsilon$ dimensions:

$$\begin{aligned} \mathcal{L} = &-\frac{1}{4}\,Z_G\,(\partial_\mu G_\nu^a - \partial_\nu G_\mu^a)\,(\partial^\mu G^{a\,\nu} - \partial^\nu G^{a\,\mu}) \\ &+ i\,Z_\psi\,\bar\psi^i\gamma^\mu\partial_\mu\psi^i - Z_\psi Z_m\,m\,\bar\psi^i\psi^i \\ &+ Z_\chi\,(\partial^\mu\chi^{a*})\,\partial_\mu\chi^a \\ &- \frac{1}{2\eta}\,Z_G Z_\eta^{-1}\,(\partial^\mu G_\mu^a)^2 \\ &+ Z_\psi Z_g Z_G^{1/2}\,g\mu^\epsilon\,\bar\psi^i\gamma^\mu\,G_\mu^a(T^a)^{ij}\psi^j \\ &- \frac{1}{2}\,Z_g Z_G^{3/2}\,g\mu^\epsilon\,f^{abc}\,(\partial_\mu G_\nu^a - \partial_\nu G_\mu^a)\,G^{b\,\mu}\,G^{c\,\nu} \\ &- \frac{1}{4}\,Z_G^2 Z_g^2\,(g\mu^\epsilon)^2\,f^{abc}f^{ade}\,G_\mu^b\,G_\nu^c\,G^{d\,\mu}\,G^{e\,\nu} \\ &- Z_\chi Z_g Z_G^{1/2}\,g\mu^\epsilon\,f^{abc}\,(\partial^\mu\chi^{a*})\,G_\mu^c\,\chi^b. \end{aligned} \tag{2.19}$$

The free parts (lines 1 – 4) are written separately from the interaction parts (lines 5 – 8) for clarity. The renormalization procedure is now briefly summarized.

In this section I outline the formulation of renormalization due to Bogoliubov, Parasiuk, Hepp & Zimmermann (BPHZ) [**31, 32, 33, 34**]. One uses the Lagrangian above, $\mathcal{L}$, to compute amplitudes for physical processes. For a tree-level computation, all the renormalization constants $\{Z_i\}$, where $i \in \{G, g, \psi, m, \chi, \eta\}$, may be set to unity, since no UV divergences will occur. For a one-loop calculation, however, one anticipates the appearance of UV divergences and thus writes $Z_i = 1 + (\delta Z)_i$. In doing so, one obtains

$$\mathcal{L} = \mathcal{L}_\mathrm{R} + \mathcal{L}_\mathrm{counter}, \tag{2.20}$$

where $\mathcal{L}_\mathrm{R}$ is the *renormalized* Lagrangian, which has precisely the same form as the original Lagrangian but is written simply by replacing the bare quantities with their renormalized counterparts; i.e. $m_0 \to m$, *etc.* Thus the same set of Feynman rules, but with renormalized quantities, may be established. The remaining terms, collectively $\mathcal{L}_\mathrm{counter}$ and which contain the '$(\delta Z)_i$'s, are known as *counter terms* and give rise to new Feynman rules.

One must supplement the calculation with the remaining necessary tree-level diagrams generated from the counter-term Feynman rules. The '$(\delta Z)_i$'s which enter the amplitude

[3]The subscript 's' for the strong coupling is dropped here to accommodate the new notation.

are then chosen specifically to cancel the UV divergences arising due to integrations over unconstrained loop momenta.

The principle that allows this seemingly arbitrary cancellation to be made is that neither the bare quantities nor the 'Z_i's can be physically measured, and may simultaneously be infinite in such a way as to yield finite measurable quantities—i.e. the renormalized ones. This procedure extends to all orders in a renormalizable theory without introducing new interactions at each successive order and, as such, one is led to write

$$Z_i = 1 + (\delta Z)_i^1 + (\delta Z)_i^2 + (\delta Z)_i^3 + \ldots , \tag{2.21}$$

where the '$(\delta Z)_i$'s are carefully chosen at each loop order.

Associating a renormalization constant, $Z_{G\psi\psi}$, with the entire interaction term $g\mu^\epsilon\, \bar{\psi}^i \gamma^\mu\, G_\mu^a (T^a)^{ij} \psi^j$ in Eq. 2.19 allows us to identify

$$Z_g = \frac{Z_{G\psi\psi}}{Z_\psi \sqrt{Z_G}} \, . \tag{2.22}$$

The ultraviolet-divergent parts of Z_ψ and Z_G, at one-loop order, are [**35**]

$$Z_\psi = 1 - \frac{\alpha_{\rm s}}{4\pi}\, C_{\rm F}\, \eta\, \Delta \, , \tag{2.23}$$

$$Z_G = 1 - \frac{\alpha_{\rm s}}{4\pi} \left(\frac{2N_{\rm F}}{3} - \frac{13 - 3\eta}{6}\, C_{\rm A} \right) \Delta \, , \tag{2.24}$$

and the renormalization constant, $Z_{G\psi\psi}$, for this quark-quark-gluon interaction is, in the $\overline{\rm MS}$ scheme to $\mathcal{O}(\alpha_{\rm s})$,

$$Z_{G\psi\psi} = 1 - \frac{\alpha_{\rm s}}{4\pi} \left(\eta\, C_{\rm F} + \frac{3 + \eta}{4}\, C_{\rm A} \right) \Delta \, , \tag{2.25}$$

with

$$\Delta := \left(\frac{1}{\epsilon} - \gamma_{\rm E} + \ln 4\pi \right) . \tag{2.26}$$

This allows us to deduce

$$Z_g = 1 - \frac{\alpha_{\rm s}}{4\pi} \left(\frac{11 C_{\rm A}}{6} - \frac{N_{\rm F}}{3} \right) \Delta \tag{2.27}$$

which, referring to Eq. 2.18, is the multiplicative relationship between $g_0\, \mu_0^\epsilon$ and $g\, \mu^\epsilon$.

2.5. The renormalization group equation

The definition of a renormalized quantity is not unique, for one may choose which finite parts to simultaneously absorb *ad libitum*, provided that the Slavnov-Taylor identities [**36, 37**] are respected. Consider the renormalized coupling, defined as

$$g(\mu) = \mu^{-\epsilon}\, Z_g(\mu)\, g_0\, \mu_0 \, , \tag{2.28}$$

for instance. One could just as well have defined a different renormalized coupling as

$$g(\mu') = (\mu')^{-\epsilon}\, Z_g(\mu')\, g_0\, \mu_0 \, . \tag{2.29}$$

Since the bare coupling is unique, the two renormalized couplings are related via a finite renormalization, namely

$$g(\mu') = Z_g(\mu', \mu)\, g(\mu) \, , \tag{2.30}$$

with

$$Z_g(\mu', \mu) = \frac{\mu^\epsilon}{(\mu')^\epsilon} \frac{Z_g(\mu)}{Z_g(\mu')}. \tag{2.31}$$

The set of finite renormalization constants, $\{Z_g(\mu', \mu)\}$, are endowed with group structure under multiplication, and hence form the *renormalization group*. Exploiting the independence of certain quantities on a given renormalization scale leads to powerful differential equations known as the *renormalization group equations* (RGEs), of which we will be interested in those that are associated with the *minimal subtraction scheme* [**38, 39**].

Defining the dimensionless β-function

$$\beta\big(g(\mu)\big) := \mu \frac{dg(\mu)}{d\mu} \tag{2.32}$$

and using Eq. 2.30 with Eq. 2.31, it can be deduced that

$$\begin{aligned} \beta\big(g(\mu)\big) &= -\epsilon\, g(\mu) - g(\mu)\, \frac{\mu}{Z_g(\mu)} \frac{dZ_g(\mu)}{d\mu} \\ &= -\epsilon\, g(\mu) - g(\mu)\, \beta\big(g(\mu)\big) \frac{\partial \ln Z_g}{\partial g}, \end{aligned} \tag{2.33}$$

where the second equality holds if we may assume that the μ-dependence of $Z_g(\mu)$ is only implicit via $g(\mu)$, permitting one to use

$$\frac{dZ_g(\mu)}{d\mu} = \frac{dg(\mu)}{d\mu} \frac{\partial Z_g}{\partial g}. \tag{2.34}$$

A remarkable property of working in a minimal subtraction (e.g. $\overline{\text{MS}}$) scheme is that the renormalization constants, the 'Z_i's, *are* indeed independent of any mass scale by construction: save for a factor $(4\pi)^\epsilon$, only the divergent ϵ^{-1} pole terms are subtracted. These pole terms are of ultraviolet origin, and are thus associated with a régime in which masses are negligible. The MS schemes are therefore mass-independent schemes. Furthermore, since the β-function is dimensionless, it can only depend upon μ implicitly via $g(\mu)$, since a dimensionless ratio μ/m does not exist, hence the minimally indicated functional dependence in Eq. 2.32.

It can also be shown that β is finite in the limit $\epsilon \to 0$, and that it is independent of the gauge parameter η. Here we take these properties as given, and deduce that β must have the expansion

$$\beta = \sum_{n=0}^{\infty} a_n\, \epsilon^n, \tag{2.35}$$

i.e. including only positive powers of ϵ. It's easily shown by direct substitution into Eq. 2.33, given the Laurent expansion of Z_g in general as

$$Z_g = 1 + \sum_{n=1}^{\infty} \frac{Z_g^{(n)}(g)}{\epsilon^n}, \tag{2.36}$$

that the expansion of β terminates after $\mathcal{O}(\epsilon)$. Substituting Eq. 2.36 into Eq. 2.33, i.e.

$$Z_g\, \beta + \epsilon\, g\, Z_g + g\, \beta\, \frac{\partial Z_g}{\partial g} = 0 \qquad \text{with } \beta = a_0 + \epsilon\, a_1, \tag{2.37}$$

one obtains

$$\left(1+\frac{Z_g^{(1)}}{\epsilon}+\sum_{n=2}^{\infty}\frac{Z_g^{(n)}(g)}{\epsilon^n}\right)[a_0+(a_1+g)\,\epsilon] + g\,(a_0+\epsilon\,a_1)\left(\frac{1}{\epsilon}\,\frac{dZ_g^{(1)}}{dg}+\frac{d}{dg}\sum_{n=2}^{\infty}\frac{Z_g^{(n)}(g)}{\epsilon^n}\right)=0\,. \tag{2.38}$$

Comparing coefficients of ϵ and 1, one obtains

$$a_1=-g \tag{2.39}$$

$$\text{and}\qquad a_0=g^2\,\frac{dZ_g^{(1)}}{dg}. \tag{2.40}$$

Finally, taking the limit $\epsilon\to 0$, one obtains a simple expression for the β-function:

$$\beta\big(g(\mu)\big)=g^2\,\frac{dZ_g^{(1)}}{dg}. \tag{2.41}$$

From Eq. 2.27 it is easily deduced that

$$\beta(g)=-\frac{2g^3}{(4\pi)^2}\left(\frac{11\,C_{\rm A}}{6}-\frac{N_{\rm F}}{3}\right). \tag{2.42}$$

It is also useful to define the β-function alternatively, using $g^2=4\pi\alpha_{\rm s}$, as

$$\beta\big(\alpha_{\rm s}(\mu)\big):=\mu^2\,\frac{d\alpha_{\rm s}(\mu)}{d\mu^2}=-\alpha_{\rm s}^2\sum_{n=0}^{\infty}\beta_n\,\alpha_{\rm s}^n\,, \tag{2.43}$$

where an expansion in $\alpha_{\rm s}$ has been assumed. With this definition, the expansion coefficients for SU(N) are [**40**]

$$\beta_0=\frac{11C_{\rm A}-2N_{\rm F}}{12\pi}\,, \tag{2.44}$$

$$\beta_1=\frac{17C_{\rm A}^2-5C_{\rm A}N_{\rm F}-3C_{\rm F}N_{\rm F}}{24\pi^2} \tag{2.45}$$

and

$$\beta_2=\frac{\frac{2857}{54}C_{\rm A}^3-\frac{1415}{54}C_{\rm A}^2N_{\rm F}-\frac{205}{18}C_{\rm A}C_{\rm F}N_{\rm F}+C_{\rm F}^2N_{\rm F}+\frac{79}{54}C_{\rm A}N_{\rm F}^2+\frac{11}{9}C_{\rm F}N_{\rm F}^2}{64\pi^3}\,. \tag{2.46}$$

We now consider the renormalization of a general truncated connected Green's function with N_ψ external quarks and N_G external gluons, which is given as

$$\Gamma_0(\alpha_0,m_0,\eta_0,\{p_i\})=Z_\psi^{N_\psi/2}\,Z_G^{N_G/2}\,\Gamma(\mu,\alpha_{\rm s},m,\eta,\{p_i\}), \tag{2.47}$$

where $\{p_i\}$ represents the external momenta. Since Γ_0 is independent of the renormalization scale μ, we have

$$\mu^2\,\frac{d}{d\mu^2}\left\{Z_\psi^{N_\psi/2}\,Z_G^{N_G/2}\,\Gamma(\mu,\alpha_{\rm s},m,\eta,\{p_i\})\right\}=0 \tag{2.48}$$

and so

$$\left\{\mu^2\,\frac{\partial}{\partial\mu^2}+\beta\,\frac{\partial}{\partial\alpha_{\rm s}}+\mu^2\,\frac{dm}{d\mu^2}\,\frac{\partial}{\partial m}+\mu^2\,\frac{d\eta}{d\mu^2}\,\frac{\partial}{\partial\eta} +\mu^2\,\frac{N_\psi}{2}\,\frac{d\ln Z_\psi}{d\mu^2}+\mu^2\,\frac{N_G}{2}\,\frac{d\ln Z_G}{d\mu^2}\right\}\Gamma(\mu,\alpha_{\rm s},m,\eta,\{p_i\})=0\,, \tag{2.49}$$

which is the RGE for a general truncated connected Green's function, with β given in Eq. 2.43.

The renormalization group equation, Eq. 2.49, may be solved by the method of characteristics. First, the renormalized parameters and the mass scale μ are assumed to be functions of a parameter t, and as such they become $\mu(t)$, $\alpha_{\rm s}(t)$, $m(t)$ and $\eta(t)$. We thus have $\Gamma = \Gamma(\mu(t), \alpha_{\rm s}(t), m(t), \eta(t), \{p_i\})$ and so its total derivative with respect to t may be written as

$$\frac{d\Gamma}{dt} = \left(\frac{d\mu^2(t)}{dt} \frac{\partial}{\partial \mu^2} + \frac{d\alpha_{\rm s}(t)}{dt} \frac{\partial}{\partial \alpha_{\rm s}} + \frac{dm(t)}{dt} \frac{\partial}{\partial m} + \frac{d\eta(t)}{dt} \frac{\partial}{\partial \eta} \right) \Gamma \,. \tag{2.50}$$

Upon making identifications between the coefficients of the partial derivatives in Eq. 2.50 and Eq. 2.49, particularly

$$\frac{d\mu^2(t)}{dt} = \mu^2(t) \tag{2.51}$$

$$\text{and} \qquad \frac{d\alpha_{\rm s}(t)}{dt} = \beta(\alpha_{\rm s}) \,, \tag{2.52}$$

we recover the RGE in the form

$$\left\{ \frac{d}{dt} + \mu^2 \frac{N_\psi}{2} \frac{d \ln Z_\psi}{d\mu^2} + \mu^2 \frac{N_G}{2} \frac{d \ln Z_G}{d\mu^2} \right\} \Gamma(\mu(t), \alpha_{\rm s}(t), m(t), \eta(t), \{p_i\}) = 0. \tag{2.53}$$

Therefore, the solution of the RGE by the method of characteristics necessarily gives rise to parameters that run with t, and the relevant equations that govern these evolutions for μ and $\alpha_{\rm s}$ are Eqs. 2.51 and 2.52. Solving the first of these, Eq. 2.51, gives

$$\int_{\mu(0)}^{\mu(t)} \frac{d\mu^2(t)}{\mu^2(t)} = \int_0^t dt' \Rightarrow t = \ln \left(\frac{\mu'^2}{\mu^2} \right) , \tag{2.54}$$

where the definitions $\mu := \mu(0)$ and $\mu' := \mu(t)$ have been made. Eq. 2.52 is then solved using this expression for t, as in

$$\int_{\alpha_{\rm s}(0)}^{\alpha_{\rm s}(t)} \frac{d\alpha_{\rm s}}{\beta} = \int_0^t dt' = t = \ln \left(\frac{\mu'^2}{\mu^2} \right) . \tag{2.55}$$

In order to continue one must take the expression for β as a power series in $\alpha_{\rm s}$ (Eq. 2.43), whose coefficients were presented previously, and perform the integration over $\alpha_{\rm s}$. To begin with, we work to leading order and truncate β after the $\alpha_{\rm s}^2$ term, i.e. taking $\beta = -\beta_0 \, \alpha_{\rm s}^2$. Thus

$$\begin{aligned} \int_{\alpha_{\rm s}(0)}^{\alpha_{\rm s}(t)} \frac{d\alpha_{\rm s}}{\beta} &= -\frac{1}{\beta_0} \int_{\alpha_{\rm s}(0)}^{\alpha_{\rm s}(t)} \frac{d\alpha_{\rm s}}{\alpha_{\rm s}^2} \\ &= \frac{1}{\beta_0} \left(\frac{1}{\alpha_{\rm s}(\mu)} - \frac{1}{\alpha_{\rm s}(\mu')} \right) , \end{aligned} \tag{2.56}$$

and, taken with Eq. 2.55, implies

$$\alpha_{\rm s}(\mu') = \frac{\alpha_{\rm s}(\mu)}{1 + \alpha_{\rm s}(\mu) \, \beta_0 \, \ln \left(\frac{\mu'^2}{\mu^2} \right)} . \tag{2.57}$$

Working to next-to-leading order and taking $\beta = -\alpha_{\rm s}^2(\beta_0+\alpha_{\rm s}\,\beta_1)$, one obtains the two-loop running coupling implicitly as

$$\beta_0\,\ln\left(\frac{\mu'^2}{\mu^2}\right) = \left[\frac{1}{\alpha_{\rm s}} + \frac{\beta_1}{\beta_0}\,\ln\left(\frac{\alpha_{\rm s}}{\beta_0+\beta_1\,\alpha_{\rm s}}\right)\right]_{\alpha_{\rm s}(\mu)}^{\alpha_{\rm s}(\mu')}, \tag{2.58}$$

for which an approximate solution, accurate to next-to-leading order, is given by [**41**]

$$\alpha_{\rm s}(\mu') = \frac{\alpha_{\rm s}(\mu)}{\rho}\,\left(1 - \frac{\beta_1}{\beta_0}\,\alpha_{\rm s}(\mu)\,\frac{\ln\rho}{\rho}\right), \tag{2.59}$$

where $\rho = 1 + 2\,\beta_0\,\alpha_{\rm s}(\mu)\,\ln(\mu'/\mu)$.

CHAPTER 3

QCD in the infrared régime

In this chapter I address the dynamics of soft and collinear QCD, where *soft* is used to describe emission in the case where the energy carried away is significantly smaller than any of the *harder* characteristic energy scales in the picture. One of the profound properties of calculations performed in this 'infrared' régime is that of factorization, whereby the squared emission amplitude amounts to only a multiplicative factor on the squared amplitude for the original process in absence of the emission. This property is vital when one considers calculations to all orders, on account of the dramatic simplifications it provides. The physical principle at work with the emission of soft gluons is that the relatively long wavelengths of the emitted gluons become incapable of resolving the details of the short-distance-scale hard scattering process and, as such, they respond only to the overall charge of the system: a phenomenon known as *coherence*. We begin by computing the amplitude for one soft gluon emission from a $q\,\bar{q}$ 'dipole'. Afterwards we move on to computing the two-soft-gluon amplitude where I will make some assumptions about the relative ordering of gluon energies. This will allow us to witness coherence at work and deduce certain features that persist to an arbitrary number of emissions.

3.1. Factorization of gluons in the soft limit

Consider the production of a quark and anti-quark pair, from the decay of a virtual photon, γ^*, supplemented by an additional single gluon radiation in the final state: $\gamma^* \to q\,\bar{q}\,g$. The two distinct mechanisms by which this process can occur are show in Fig. 3.1. The momenta of the quark and anti-quark are labelled p_1 and p_2, respectively, and k is the gluon momentum. We consider this process to occur in the limit where the emitted gluon is soft; i.e. $k \ll p_1, p_2$.

The amplitude for this process, in reference to Fig. 3.1, is

$$\mathcal{M} = -i\,Q\,e\,g_{\rm s}\,T^a_{ij}\,\bar{u}_1\left[\frac{\not\epsilon^*_g\,(\not p_1 + \not k + m)\,\not\epsilon_\gamma}{(p_1+k)^2 - m^2} - \frac{\not\epsilon_\gamma\,(\not p_2 + \not k - m)\,\not\epsilon^*_g}{(p_2+k)^2 - m^2}\right] v_2 \tag{3.1}$$

where the following shorthand notation has been used: For the quark and anti-quark spinors $\bar{u}_1 \equiv \bar{u}^i(p_1, s_1)$ and $v_2 \equiv v^j(p_2, s_2)$, where i and j are colour indices and s_1, s_2 label their spins, respectively. For the polarization vectors, $(\epsilon_\gamma)_\mu \equiv \epsilon_\mu(q, \sigma)$ denotes that of the photon, of momentum $q \approx p_1 + p_2$ and polarization labelled σ, and $(\epsilon^*_g)_\alpha \equiv \epsilon^{a\,*}_\alpha(k, \lambda)$ denotes that for the gluon, of momentum k and polarization labelled λ. In general, these vectors are complex. Finally, Feynman slash notation is used, e.g. $\not p \equiv \gamma^\mu p_\mu$.

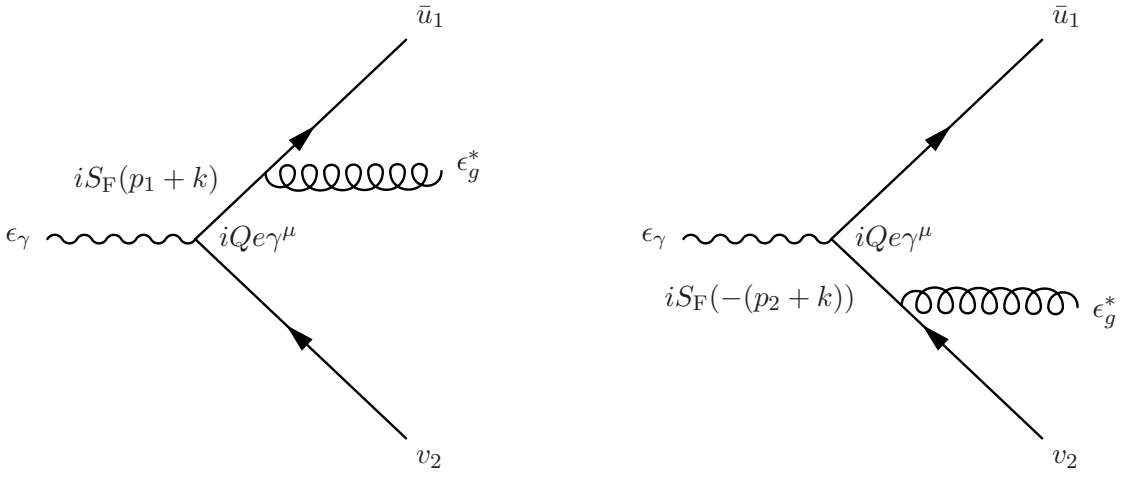

FIGURE 3.1. The production of a quark and anti-quark pair, from the decay of a virtual photon, supplemented by an additional single gluon radiation in the final state: $\gamma^* \to q\,\bar{q}\,g$. $iS_{\rm F}(p)$ is the Feynman fermion propagator.

Invoking the 'eikonal' approximation, whereby we neglect k terms in the numerators of the propagators, one obtains, for the two terms in square brackets in Eq. 3.1,

$$\frac{\not\epsilon_g^*\,(\not p_1+\not k+m)\,\not\epsilon_\gamma}{(p_1+k)^2-m^2} \to \frac{\not\epsilon_g^*\,(\not p_1+m)\,\not\epsilon_\gamma}{2p_1\cdot k} = \frac{[2\,p_1\cdot\epsilon_g^* - (\not p_1-m)\,\not\epsilon_g^*]\,\not\epsilon_\gamma}{2p_1\cdot k} \tag{3.2}$$

and

$$\frac{\not\epsilon_\gamma\,(\not p_2+\not k-m)\,\not\epsilon_g^*}{(p_2+k)^2-m^2} \to \frac{\not\epsilon_\gamma\,(\not p_2-m)\,\not\epsilon_g^*}{2p_2\cdot k} = \frac{\not\epsilon_\gamma\,[2\,p_2\cdot\epsilon_g^* - \not\epsilon_g^*\,(\not p_2+m)]}{2p_2\cdot k}, \tag{3.3}$$

where the Clifford algebra for γ matrices has been used in the form $\not p\not\epsilon = 2\,p\cdot\epsilon - \not\epsilon\not p$, and only the gluon is assumed massless: $k^2=0$ but $p_1^2=p_2^2=m^2$. Finally, using the Dirac equation for the quark and anti-quark spinors, namely $\bar{u}_1(\not p_1 - m)=0$ and $(\not p_2+m)v_2=0$, we obtain the amplitude in the eikonal approximation,

$$\mathcal{M} = -i\,Q\,e\,g_{\rm s}\,\bar{u}_1\,T^a_{ij}\,\not\epsilon_\gamma\,v_2\left(\frac{p_1\cdot\epsilon_g^*}{p_1\cdot k} - \frac{p_2\cdot\epsilon_g^*}{p_2\cdot k}\right), \tag{3.4}$$

where the soft gluon emission has factorized from the amplitude for $\gamma^* \to q\bar{q}$. We seek the squared amplitude where the factorization, when inclusive over all the quantum numbers of the gluon, takes a particularly simple expression. The complex conjugate of the amplitude is

$$\mathcal{M}^* = i\,Q\,e\,g_{\rm s}\,\bar{v}_2\not\epsilon_\gamma^* T^b_{ji} u_1\left(\frac{p_1\cdot\epsilon_g}{p_1\cdot k} - \frac{p_2\cdot\epsilon_g}{p_2\cdot k}\right), \tag{3.5}$$

where a distinct gluon colour dummy index has been introduced, and the Hermiticity of the fundamental generators has been used: $(T^b_{ij})^* = T^b_{ji}$. The squared matrix element is

then

$$|\mathcal{M}|^2 = Q^2 e^2 g_{\rm s}^2\, T^a_{ij}\, T^b_{ji}\ {\rm Tr}\left[u_1\,\bar{u}_1\,\gamma^\mu\,v_2\,\bar{v}_2\,\gamma^\nu\right]\epsilon_\mu\,\epsilon^*_\nu \\ \times\,\epsilon^{*a}_\rho\,\epsilon^b_\sigma\,\left(\frac{p_1^\rho}{p_1\cdot k}-\frac{p_2^\rho}{p_2\cdot k}\right)\left(\frac{p_1^\sigma}{p_1\cdot k}-\frac{p_2^\sigma}{p_2\cdot k}\right), \tag{3.6}$$

where a trace over Dirac matrices has been introduce to permit their permutation as shown, in the case that one would like to sum over spins of the quark and anti-quark. We now perform the sum over the gluon's quantum numbers. In addition, it is useful to also sum over the colours of the quark and anti-quark, since these quantum numbers 'talk' to the gluon. First, we obtain the summation over gluon polarization states via the replacement (in the physical gauge; cf. Eq. 3.16)

$$\sum_\lambda \epsilon^b_\sigma(k,\lambda)\,\epsilon^{*a}_\rho(k,\lambda) \to -\left(g_{\rho\sigma}-\frac{k_\rho\,n_\sigma+n_\rho\,k_\sigma}{n\cdot k}+\frac{(n^2+\lambda\,k^2)\,k_\rho\,k_\sigma}{(n\cdot k)^2}\right)\delta^{ab}. \tag{3.7}$$

Note that the final two terms give zero upon contraction with the eikonal currents in Eq. 3.6. One then obtains

$$\begin{aligned}\overline{|\mathcal{M}|^2} &= \sum_{i,j,a}|\mathcal{M}|^2 \\ &= |\mathcal{M}_0|^2 g_{\rm s}^2 C_{\rm F}\frac{2p_1\cdot p_2}{p_1\cdot k\,p_2\cdot k}\end{aligned} \tag{3.8}$$

where $C_{\rm F} = {\rm Tr}\left[T^a\,T^a\right]$, and $|\mathcal{M}_0|^2$ is the squared amplitude for the process $\gamma^* \to q\bar{q}$, with a summation over colours of the final state quark and anti-quark.

We thus see that, in the eikonal approximation, the soft gluon emission factorizes. The gluon has in some sense become dissociated from any particular emitter, and is rather associated with the hard process (the QED vertex) as a whole. The physical interpretation, as mentioned in the introduction to this chapter, is that the gluon's wavelength is too long to resolve any detailed structure of the hard process, although this picture breaks down when one considers emission that is simultaneously collinear to a given emitter. It is a straightforward exercise to show that this factorization property extends to *any* hard process, as shown for example in Sec. 3.7 of [**35**]. The softness of the gluon means we ought only to consider it attached to an external leg of a general hard process, as in Fig. 3.2, if we wish to extract the leading soft enhancement, since highly virtual internal propagators cannot be put on shell.

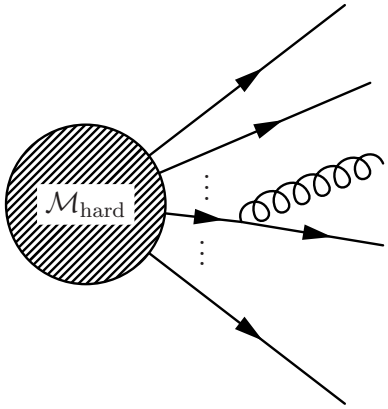

FIGURE 3.2. A soft gluon factorizes completely from any general hard process, labelled $\mathcal{M}_{\rm hard}$ in the diagram. It only gives rise to a soft enhancement when attached to external legs, since highly virtual internal propagators cannot be put on shell.

3.2. Soft gluon emission and coherence

The emission of two soft gluons from a $q\bar{q}$ pair in QCD is complicated somewhat by the presence of two extra diagrams as compared with the equivalent case in QED, namely those involving the triple-gluon vertex. Furthermore, the non-Abelian nature of the theory gives rise to a complicated colour structure. Notwithstanding, the situation may be simplified by making some underlying assumptions that one need not invoke in the case of soft *photon* emission. For a more general survey, the reader might wish to consult [**42**]. The following calculation I present is one I computed independently, as an exercise to offer insight regarding the angular properties of soft emissions and their connection with the *coherence* phenomenon in QCD [**43, 44, 45, 46, 47**].

To begin with, Fig. 3.3 shows the eight diagrams that contribute to the process under present consideration. In order to be explicit, I do not write down the amplitudes for these diagrams using the eikonal Feynman rules, but rather write down the full amplitude and subsequently take limits. This way the reader can observe the subtleties involved, particularly where the triple-gluon vertices are concerned. The explicit amplitude for the first diagram, Fig. 3.3(a), is given by

$$\begin{aligned}\mathcal{M}_{\rm a} = \bar{u}(p_1,s_1)\, i\, g_{\rm s}\, \not{\epsilon}^*(k_1,\lambda_1)\, T^a_{ik}\, i\, \frac{\not{p}_1 + \not{k}_1}{(p_1+k_1)^2 + i\epsilon} \\ \times\, i\, g_{\rm s}\, \not{\epsilon}^*(k_2,\lambda_2)\, T^b_{kj}\, i\, \frac{\not{p}_1 + \not{k}_1 + \not{k}_2}{(p_1+k_1+k_2)^2 + i\epsilon}\, i\, Q_f\, e\, \gamma^\alpha\, v(p_2).\end{aligned} \tag{3.9}$$

Taking the limit $k_1, k_2 \ll p_1, p_2$ allows this to be written as

$$\mathcal{M}_{\rm a} = i\, Q_f\, e\, \bar{u}_1\, \gamma^\alpha\, v_2\, g_{\rm s}^2\, T^a_{ik}\, T^b_{kj}\, \frac{p_1\cdot\epsilon_1^*}{p_1\cdot k_1}\, \frac{p_1\cdot\epsilon_2^*}{p_1\cdot(k_1+k_2)}, \tag{3.10}$$

where $\bar{u}_1 \equiv \bar{u}(p_1,s_1)$, $\epsilon_1^* \equiv \epsilon^*(k_1,\lambda_1)$, etc. In the same way as before, the Clifford algebra of the γ matrices, and the Dirac equation for spinors have been used. The following diagrams (b)–(f) proceed straightforwardly in the same manner. However, the final two diagrams (g) and (h) are complicated due to the presence of the triple-gluon vertex, and further

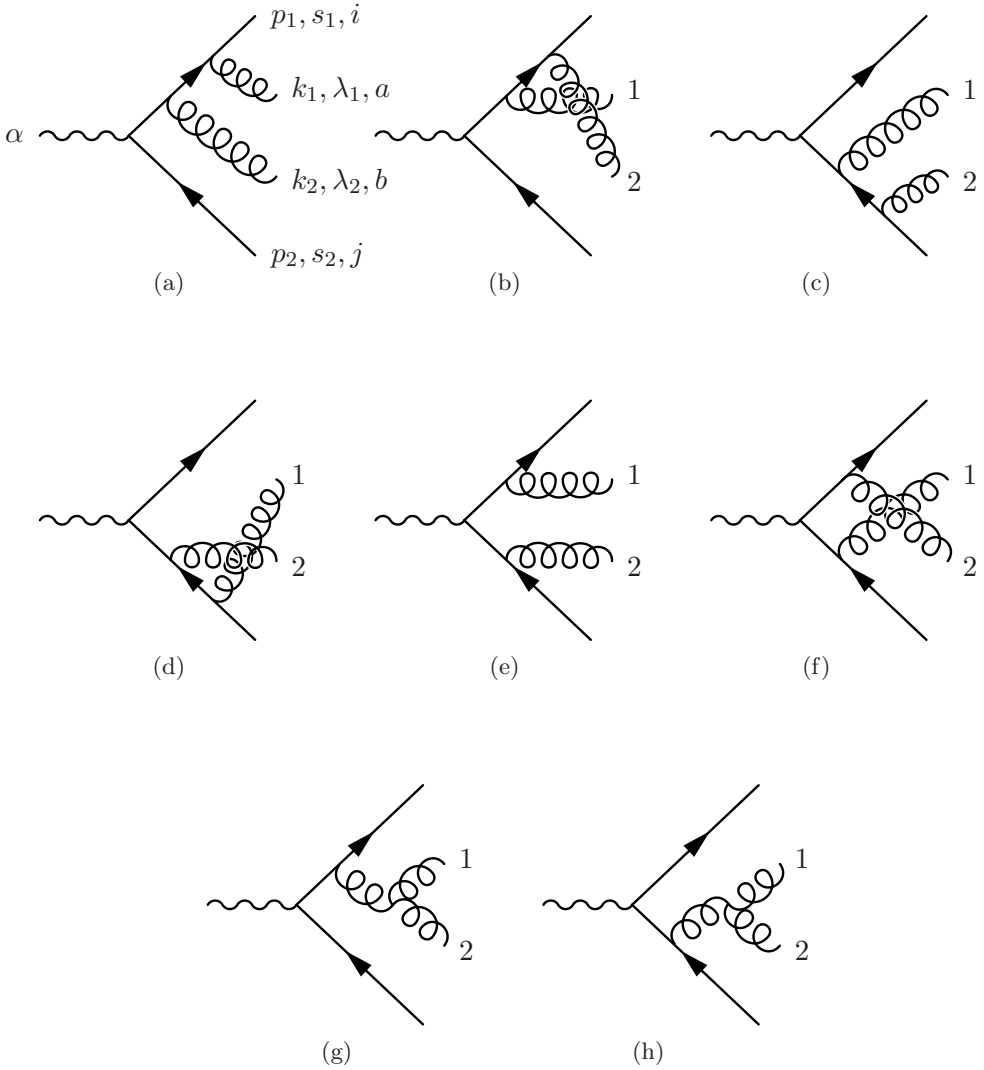

FIGURE 3.3. The eight diagrams contributing to the two-gluon emission from a $q\bar{q}$ pair. Gluon 1 (2) has colour a (b), spin $\lambda_{1(2)}$ and momentum $k_{1(2)}$. The outgoing (anti-) fermion has colour i (j), spin $s_{1(2)}$ and momentum $p_{1(2)}$.

assumption about the nature of the emissions k_1 and k_2 must be made. First, recall the triple-gluon vertex is given by the Feynman rule

$$-g_{\rm s}\, f^{abc}\big[(-2k_1-k_2)_\nu\, g_{\sigma\mu} + (k_1-k_2)_\sigma\, g_{\mu\nu} + (k_1+2k_2)_\mu\, g_{\nu\sigma}\big], \tag{3.11}$$

as shown in Fig. 2.1.

We thus obtain, for diagram (g),

$$\begin{aligned}\mathcal{M}_{\rm g} = {}& \bar{u}_1\, i\, g_{\rm s}\, \gamma_\rho\, T^c_{ij}\, \frac{-i\, d^{\rho\sigma}(k_1+k_2)}{(k_1+k_2)^2+i\epsilon} \\ & \times (-g_{\rm s}) f^{abc}\big[(-2k_1-k_2)_\nu\, g_{\sigma\mu} + (k_1-k_2)_\sigma\, g_{\mu\nu} + (k_1+2k_2)_\mu\, g_{\nu\sigma}\big] \\ & \times i\, \frac{\not{p}_1 + \not{k}_1 + \not{k}_2}{(p_1+k_1+k_2)^2+i\epsilon}\, i\, Q_f\, e\, \gamma^\alpha\, v_2\, \epsilon_1^{*\mu}\, \epsilon_2^{*\nu},\end{aligned} \tag{3.12}$$

which again may be simplified by taking the limit $k_1, k_2 \ll p_1, p_2$, then using the Clifford algebra and Dirac equation for spinors, thus obtaining

$$\begin{aligned}\mathcal{M}_{\rm g} = i\,Q_f\,e\,\bar{u}_1\,\gamma^\alpha\,v_2\,g_{\rm s}^2\,(-i\,T^c_{ij}\,f^{abc})\,\frac{p_{1\rho}}{p_1\cdot(k_1+k_2)}\,\frac{d^{\rho\sigma}(k_1+k_2)}{2\,k_1\cdot k_2} \\ \times\left[(-2k_1-k_2)_\nu\,g_{\sigma\mu}+(k_1-k_2)_\sigma\,g_{\mu\nu}+(k_1+2k_2)_\mu\,g_{\nu\sigma}\right]\epsilon_1^{*\mu}\,\epsilon_2^{*\nu}.\end{aligned} \tag{3.13}$$

Computing all eight diagrams, the final expression for the amplitude for $\gamma^* \to q\,\bar{q}\,g\,g$ in the limit where the two gluons are soft, $k_1, k_2 \ll p_1, p_2$, may be written

$$\begin{aligned}\mathcal{M} = i\,Q_f\,e\,\bar{u}_1\,\gamma^\alpha\,v_2\,g_{\rm s}^2 \\ \times\Bigg\{T^a_{ik}\,T^b_{kj}\left[\overbrace{\frac{p_1\cdot\epsilon_1^*}{p_1\cdot k_1}\,\frac{p_1\cdot\epsilon_2^*}{p_1\cdot(k_1+k_2)}}^{\rm (a)}-\overbrace{\frac{p_1\cdot\epsilon_1^*}{p_1\cdot k_1}\,\frac{p_2\cdot\epsilon_2^*}{p_2\cdot k_2}}^{\rm (e)}+\overbrace{\frac{p_2\cdot\epsilon_1^*}{p_2\cdot(k_1+k_2)}\,\frac{p_2\cdot\epsilon_2^*}{p_2\cdot k_2}}^{\rm (c)}\right] \\ +T^b_{ik}\,T^a_{kj}\left[\overbrace{\frac{p_1\cdot\epsilon_1^*}{p_1\cdot(k_1+k_2)}\,\frac{p_1\cdot\epsilon_2^*}{p_1\cdot k_2}}^{\rm (b)}-\overbrace{\frac{p_2\cdot\epsilon_1^*}{p_2\cdot k_1}\,\frac{p_1\cdot\epsilon_2^*}{p_1\cdot k_2}}^{\rm (f)}+\overbrace{\frac{p_2\cdot\epsilon_1^*}{p_2\cdot k_1}\,\frac{p_2\cdot\epsilon_2^*}{p_2\cdot(k_1+k_2)}}^{\rm (d)}\right] \\ -i\,T^c_{ij}\,f^{abc}\left[\overbrace{\frac{p_{1\rho}}{p_1\cdot(k_1+k_2)}}^{\rm (g)}-\overbrace{\frac{p_{2\rho}}{p_2\cdot(k_1+k_2)}}^{\rm (h)}\right]\frac{d^{\rho\sigma}(k_1+k_2)}{2\,k_1\cdot k_2} \\ \times\left[(-2k_1-k_2)_\nu\,g_{\sigma\mu}+(k_1-k_2)_\sigma\,g_{\mu\nu}+(2k_2+k_1)_\mu\,g_{\nu\sigma}\right]\epsilon_1^{*\mu}\,\epsilon_2^{*\nu}\Bigg\},\end{aligned} \tag{3.14}$$

where the aforementioned shorthand has been used. Extracting the polarization vectors, we have

$$\mathcal{M} = \mathcal{M}_{\mu\nu}\,\epsilon_1^{*\mu}\,\epsilon_2^{*\nu}. \tag{3.15}$$

Before continuing, it is instructive to consider what happens when ϵ_i^* in Eq. 3.15 is replaced with the corresponding momentum k_i, with $i \in \{1, 2\}$. First we turn to $d^{\rho\sigma}(k_1 + k_2)$ for two specific gauge choices:

$$\begin{aligned} d^{\rho\sigma}(k) &= g^{\rho\sigma} - (1-\eta)\,\frac{k^\rho\,k^\sigma}{k^2} && \text{covariant} \\ d^{\rho\sigma}(k) &= g^{\rho\sigma} - \frac{k^\rho\,n^\sigma + n^\rho\,k^\sigma}{n\cdot k} + \frac{(n^2+\lambda\,k^2)\,k^\rho\,k^\sigma}{(n\cdot k)^2} && \text{axial (physical)}\end{aligned} \tag{3.16}$$

In these two expressions, $k = k_1 + k_2$, and η parameterizes the covariant gauge freedom, while λ and the vector n parameterize the axial (physical) gauge freedom.

By a direct computation, making the replacements $\epsilon_1^* \to k_1$ and/or $\epsilon_2^* \to k_2$ as necessary, it can be shown that

$$\mathcal{M}_{\mu\nu}\,k_1^\mu\,k_2^\nu = 0 \tag{3.17}$$

and

$$\mathcal{M}_{\mu\nu}\,k_1^\mu\,\epsilon_2^{*\nu} \propto \frac{1}{2\,k_1\cdot k_2}\left[\frac{p_1\cdot k_1}{p_1\cdot(k_1+k_2)} - \frac{p_2\cdot k_1}{p_2\cdot(k_1+k_2)}\right]k_2\cdot\epsilon_2^*\,, \tag{3.18}$$

along with a similar expression for $\mathcal{M}_{\mu\nu}\,\epsilon_1^{*\mu}\,k_2^\nu$. In the limit $k_2 \ll k_1$, one may make the replacement $k_1 \to k_1 + k_2$ in the numerators with impunity, and the resulting expression for Eq. 3.18 is identically zero. Thus, a useful Ward identity holds in the limit of soft

gluons strongly ordered in energy. Writing this second expression more explicitly as

$$\begin{aligned}\mathcal{M}_{\mu\nu}\, k_1^\mu\, \epsilon_2^{*\nu} \propto \frac{1}{2\, k_1 \cdot k_2}\Bigg[&\frac{p_1^0\, k_1^0(1-\cos\theta_{11})}{p_1^0\, k_1^0(1-\cos\theta_{11}) + p_1^0\, k_2^0(1-\cos\theta_{12})} \\ &- \frac{p_2^0\, k_1^0(1-\cos\theta_{21})}{p_2^0\, k_1^0(1-\cos\theta_{21}) + p_2^0\, k_2^0(1-\cos\theta_{22})}\Bigg] k_2 \cdot \epsilon_2^*\,,\end{aligned} \tag{3.19}$$

and then parameterizing the energy of the first gluon as $k_1^0 = \alpha\, k_2^0$, one can make a Taylor expansion about $\alpha = 0$ to find that this expression also vanishes in the limit $\alpha \ll 1$, showing that the Ward identity also holds when the gluons are strongly ordered in energy as $k_1 \ll k_2$. The same results would hold if one were to make the replacement $\epsilon_2^* \to k_2$. To summarize,

$$\begin{aligned}\mathcal{M}_{\mu\nu}\, k_1^\mu\, k_2^\nu = 0 \quad &\text{when} \quad k_1, k_2 \ll p_1, p_2 \quad \text{and} \\ \mathcal{M}_{\mu\nu}\, \epsilon_1^{*\mu}\, k_2^\nu = \mathcal{M}_{\mu\nu}\, k_1^\mu\, \epsilon_2^{*\nu} = 0 \quad &\text{when} \quad k_1, k_2 \ll p_1, p_2 \quad \text{with} \quad k_1 \ll k_2 \quad \text{or} \quad k_1 \gg k_2.\end{aligned} \tag{3.20}$$

These Ward identities have very important consequences, particularly for the triple-gluon vertex and the sum over gluon polarisations in the squared amplitude. I will address the latter here first. The squared amplitude, inclusive over all gluon polarisations, may be written

$$\begin{aligned}\sum_{\lambda_1,\lambda_2} |\mathcal{M}|^2 &= \sum_{\lambda_1,\lambda_2} (\mathcal{M}^{\mu\nu}\, \epsilon_{1\mu}^*\, \epsilon_{2\nu}^*)(\mathcal{M}^{*\mu'\nu'}\, \epsilon_{1\mu'}\, \epsilon_{2\nu'}) \\ &= \mathcal{M}^{\mu\nu}\, \mathcal{M}^{*\mu'\nu'}\, \left(-g_{\mu\mu'} + \text{gauge terms}\right)\, \left(-g_{\nu\nu'} + \text{gauge terms}\right),\end{aligned} \tag{3.21}$$

where the usual completeness relation for spinors has been used. Upon multiplying out the terms in parentheses, one finds that the only term to survive is the one proportional to $g_{\mu\mu'}\, g_{\nu\nu'}$ on account of the Ward identities derived above, assuming the strong ordering of gluon energies. Thus, in this limit, the sum over gluon polarization states is accomplished simply as

$$\sum_{\lambda_1,\lambda_2} |\mathcal{M}|^2 = \mathcal{M}^{\mu\nu}\, \mathcal{M}^*_{\mu\nu}. \tag{3.22}$$

The second manner in which the Ward identities help us is in simplifying the triple gluon vertex. Assuming strong ordering of the gluons' energies, taken here with complete generality to mean $k_2 \ll k_1$, the part of the expression in Eq. 3.14 due to the triple-gluon vertex becomes

$$\begin{aligned}(-2k_1 - k_2)_\nu\, g_{\sigma\mu} + (k_1 - k_2)_\sigma\, g_{\mu\nu} + (2k_2 + k_1)_\mu\, g_{\nu\sigma} \\ \to -2k_{1\nu}\, g_{\sigma\mu} + k_{1\sigma}\, g_{\mu\nu} + k_{1\mu}\, g_{\nu\sigma}\,,\end{aligned} \tag{3.23}$$

of which the final two terms in the second line may be discarded for the following reasons: The third term in this expression, $k_{1\mu}\, g_{\nu\sigma}$, will appear multiplying the complex conjugate amplitude in the polarization-inclusive squared amplitude, yielding zero by the Ward identity. In the same manner as before, the second term in this expression, $k_{1\sigma}\, g_{\mu\nu}$, may be replaced with $(k_1 + k_2)_\sigma\, g_{\mu\nu}$, which gives zero identically in the broader context of the

expression:

$$\begin{aligned}\left[\frac{p_{1\rho}}{p_1\cdot(k_1+k_2)}-\frac{p_{2\rho}}{p_2\cdot(k_1+k_2)}\right] d^{\rho\sigma}(k_1+k_2)\,(k_1+k_2)_\sigma\, g_{\mu\nu}&\\ =\left[\frac{p_1\cdot(k_1+k_2)}{p_1\cdot(k_1+k_2)}-\frac{p_2\cdot(k_1+k_2)}{p_2\cdot(k_1+k_2)}\right] g_{\mu\nu}&\\ =0,&\end{aligned} \tag{3.24}$$

since $d^{\rho\sigma}(k_1+k_2)$ may be shown to be effectively $g^{\rho\sigma}$.

Our starting point for the remainder of the calculation, is Eq. 3.14 in the limit $k_2 \ll k_1$, using the simplified triple gluon vertex and taking $d^{\rho\sigma}(k_1+k_2)=g^{\rho\sigma}$, namely

$$d^{\rho\sigma}(k_1+k_2)\,[(-2k_1-k_2)_\nu\, g_{\sigma\mu}+(k_1-k_2)_\sigma\, g_{\mu\nu}+(2k_2+k_1)_\mu\, g_{\nu\sigma}]\to -2\,k_{1\nu}\,g^\rho_\mu\,, \tag{3.25}$$

on account of the derived Ward identities in this limit. Thus we start with

$$\begin{aligned}\mathcal{M}=i\,Q_f\,e\,\bar u_1\,\gamma^\alpha\,v_2\,g_{\rm s}^2&\\ \times\Bigg\{T^a_{ik}\,T^b_{kj}\left[\frac{p_1\cdot\epsilon_1^*}{p_1\cdot k_1}\,\frac{p_1\cdot\epsilon_2^*}{p_1\cdot(k_1+k_2)}-\frac{p_1\cdot\epsilon_1^*}{p_1\cdot k_1}\,\frac{p_2\cdot\epsilon_2^*}{p_2\cdot k_2}+\frac{p_2\cdot\epsilon_1^*}{p_2\cdot(k_1+k_2)}\,\frac{p_2\cdot\epsilon_2^*}{p_2\cdot k_2}\right]&\\ +T^b_{ik}\,T^a_{kj}\left[\frac{p_1\cdot\epsilon_1^*}{p_1\cdot(k_1+k_2)}\,\frac{p_1\cdot\epsilon_2^*}{p_1\cdot k_2}-\frac{p_2\cdot\epsilon_1^*}{p_2\cdot k_1}\,\frac{p_1\cdot\epsilon_2^*}{p_1\cdot k_2}+\frac{p_2\cdot\epsilon_1^*}{p_2\cdot k_1}\,\frac{p_2\cdot\epsilon_2^*}{p_2\cdot(k_1+k_2)}\right]&\\ +i\,T^c_{ij}\,f^{abc}\,\frac{k_1\cdot\epsilon_2^*}{k_1\cdot k_2}\left[\frac{p_1\cdot\epsilon_1^*}{p_1\cdot(k_1+k_2)}-\frac{p_2\cdot\epsilon_1^*}{p_2\cdot(k_1+k_2)}\right]\Bigg\},&\end{aligned} \tag{3.26}$$

which, after using the Lie algebra $i\,T^c_{ij}\,f^{abc}=[T^a,T^b]_{ij}$ to write $T^a_{ik}\,T^b_{kj}\to T^b_{ik}\,T^a_{kj}+i\,T^c_{ij}\,f^{abc}$, becomes

$$\begin{aligned}\mathcal{M}=i\,Q_f\,e\,\bar u_1\,\gamma^\alpha\,v_2\,g_{\rm s}^2\Bigg\{T^b_{ik}\,T^a_{kj}\times\text{eikonal}&\\ +i\,T^c_{ij}\,f^{abc}\Bigg[\frac{p_1\cdot\epsilon_1^*}{p_1\cdot k_1}\,\frac{p_1\cdot\epsilon_2^*}{p_1\cdot(k_1+k_2)}-\frac{p_1\cdot\epsilon_1^*}{p_1\cdot k_1}\,\frac{p_2\cdot\epsilon_2^*}{p_2\cdot k_2}&\\ +\frac{p_2\cdot\epsilon_1^*}{p_2\cdot(k_1+k_2)}\,\frac{p_2\cdot\epsilon_2^*}{p_2\cdot k_2}&\\ +\frac{k_1\cdot\epsilon_2^*}{k_1\cdot k_2}\left(\frac{p_1\cdot\epsilon_1^*}{p_1\cdot(k_1+k_2)}-\frac{p_2\cdot\epsilon_1^*}{p_2\cdot(k_1+k_2)}\right)\Bigg]\Bigg\},&\end{aligned} \tag{3.27}$$

where 'eikonal' indicates the usual product of eikonal currents:

$$\text{eikonal}=\left(\frac{p_1\cdot\epsilon_1^*}{p_1\cdot k_1}-\frac{p_2\cdot\epsilon_1^*}{p_2\cdot k_1}\right)\left(\frac{p_1\cdot\epsilon_2^*}{p_1\cdot k_2}-\frac{p_2\cdot\epsilon_2^*}{p_2\cdot k_2}\right) \tag{3.28}$$

The final part is very subtle, as we now analyse the angular ordering of the two gluons. Using p_i as a reference, I will now define three angles according to $p_i\cdot k_1=E_i\,\omega_1\,(1-\cos\theta_{i1})$, $p_i\cdot k_2=E_i\,\omega_2\,(1-\cos\theta_{i2})$ and $k_1\cdot k_2=\omega_1\,\omega_2\,(1-\cos\tilde\theta_{12})$, where E_i is the energy of the fermion and $\omega_{1(2)}$ is the energy of gluon 1 (2). If we now take the expression

$$p_i\cdot(k_1+k_2)=E_i\,\omega_1\left[(1-\cos\theta_{i1})+\frac{\omega_2}{\omega_1}(1-\cos\theta_{i2})\right] \tag{3.29}$$

we identify a problem. On account of the condition $\omega_2 \ll \omega_1$, we would like to drop the second term and conclude $p_i \cdot (k_1 + k_2) \approx p_i \cdot k_1$, however we may only[1] do this as long as $\theta_{i1} \not\approx 0$. Our interest begins with the region for which k_1 *is* collinear, without loss of generality, to p_1.

In the collinear limit of k_1 we may approximately replace $k_1 \to (\omega_1/E_1)\, p_1$ in the numerator. Therefore,

$$\frac{k_1 \cdot \epsilon_2^*}{k_1 \cdot k_2} \to \frac{\omega_1}{E_1} \frac{p_1 \cdot \epsilon_2^*}{\omega_1\, \omega_2\, (1 - \cos\tilde{\theta}_{12})} \approx \frac{p_1 \cdot \epsilon_2^*}{E_1\, \omega_2\, (1 - \cos\theta_{12})} = \frac{p_1 \cdot \epsilon_2^*}{p_1 \cdot k_2} \tag{3.30}$$

where $\tilde{\theta}_{12} \approx \theta_{12}$ has been used, which requires $\theta_{11} \ll \theta_{12}$, i.e. the softer gluon is emitted at a much wider angle. Using this result, and the fact that $p_2 \cdot (k_1 + k_2)$ may be replaced with $p_2 \cdot k_1$ (k_1 is already assumed collinear to p_1, and so this approximation is safe according to the above arguments) one finds upon direct computation that

$$\begin{aligned} i\, T^c_{ij}\, f^{abc} \Bigg[& \frac{p_1 \cdot \epsilon_1^*}{p_1 \cdot k_1} \frac{p_1 \cdot \epsilon_2^*}{p_1 \cdot (k_1 + k_2)} - \frac{p_1 \cdot \epsilon_1^*}{p_1 \cdot k_1} \frac{p_2 \cdot \epsilon_2^*}{p_2 \cdot k_2} + \frac{p_2 \cdot \epsilon_1^*}{p_2 \cdot (k_1 + k_2)} \frac{p_2 \cdot \epsilon_2^*}{p_2 \cdot k_2} \\ & + \frac{k_1 \cdot \epsilon_2^*}{k_1 \cdot k_2} \left(\frac{p_1 \cdot \epsilon_1^*}{p_1 \cdot (k_1 + k_2)} - \frac{p_2 \cdot \epsilon_1^*}{p_2 \cdot (k_1 + k_2)} \right) \Bigg] \\ & \to i\, T^c_{ij}\, f^{abc} \times \text{eikonal}, \end{aligned} \tag{3.31}$$

and so

$$\mathcal{M} = i\, Q_f\, e\, \bar{u}_1\, \gamma^\alpha\, v_2\, g_\mathrm{s}^2\, T^a_{ik}\, T^b_{kj} \times \text{eikonal}. \tag{3.32}$$

The same result may have been achieved by taking k_1 collinear to p_2 instead. The physical content of this result is that, if the softer gluon is emitted at a wider angle it resolves only the total colour charge of the system, and this emission is independent and eikonal. This is *coherence*.

The remaining scenario to consider is where $\theta_{12} \lesssim \theta_{11}$; i.e. the softer gluon is emitted at a similar or lesser angle than the harder gluon. If the harder gluon is not collinear to either p_1 or p_2, this condition applies no constraint on what the angle of the softer gluon may be. In this case, one may always replace $p_i \cdot (k_1 + k_2) \to p_i \cdot k_1$ with impunity in the denominators. Upon making this simplification in Eq. 3.26, one finds

$$\begin{aligned} \mathcal{M} = i\, Q_f\, e\, \bar{u}_1\, \gamma^\alpha\, v_2\, g_\mathrm{s}^2 \Bigg\{ & T^a_{ik}\, T^b_{kj} \Bigg[\text{eikonal} + \frac{p_1 \cdot \epsilon_1^*}{p_1 \cdot k_1} \left(\frac{p_1 \cdot \epsilon_2^*}{p_1 \cdot k_1} - \frac{p_1 \cdot \epsilon_2^*}{p_1 \cdot k_2} \right) \\ & + \frac{p_2 \cdot \epsilon_1^*}{p_2 \cdot k_1} \frac{p_1 \cdot \epsilon_2^*}{p_1 \cdot k_2} + \frac{k_1 \cdot \epsilon_2^*}{k_1 \cdot k_2} \left(\frac{p_1 \cdot \epsilon_1^*}{p_1 \cdot k_1} - \frac{p_2 \cdot \epsilon_1^*}{p_2 \cdot k_1} \right) \Bigg] \\ & + T^b_{ik}\, T^a_{kj} \Bigg[\text{eikonal} + \frac{p_2 \cdot \epsilon_1^*}{p_2 \cdot k_1} \left(\frac{p_2 \cdot \epsilon_2^*}{p_2 \cdot k_1} - \frac{p_2 \cdot \epsilon_2^*}{p_2 \cdot k_2} \right) \\ & + \frac{p_1 \cdot \epsilon_1^*}{p_1 \cdot k_1} \frac{p_2 \cdot \epsilon_2^*}{p_2 \cdot k_2} + \frac{k_1 \cdot \epsilon_2^*}{k_1 \cdot k_2} \left(\frac{p_2 \cdot \epsilon_1^*}{p_2 \cdot k_1} - \frac{p_1 \cdot \epsilon_1^*}{p_1 \cdot k_1} \right) \Bigg] \Bigg\}. \end{aligned} \tag{3.33}$$

Within the first and third sets of parentheses, the term proportional to $(p_1 \cdot k_1)^{-1}$ may be dropped since it is small relative to the term proportional to $(p_1 \cdot k_2)^{-1}$, because of the strongly ordered gluon energies $\omega_2 \ll \omega_1$ and the fact that we are considering the case

[1] In fact, all we require is that $\theta_{i1} \not\ll \theta_{i2}$, i.e. the harder of the two gluons is not significantly *more* collinear than the softer one.

where $\theta_{12} \lesssim \theta_{11}$. That is,

$$\left(\frac{p_1\cdot\epsilon_2^*}{p_1\cdot k_1}-\frac{p_1\cdot\epsilon_2^*}{p_1\cdot k_2}\right)\to-\frac{p_1\cdot\epsilon_2^*}{p_1\cdot k_2},\qquad\text{etc.}\tag{3.34}$$

Finally, this expression may be cast in the form

$$\begin{aligned}\mathcal{M}=i\,Q_f\,e\,\bar u_1\,\gamma^\alpha\,v_2\,g_{\rm s}^2\,&\left(\frac{p_1\cdot\epsilon_1^*}{p_1\cdot k_1}-\frac{p_2\cdot\epsilon_1^*}{p_2\cdot k_1}\right)\\&\times\left[T^a_{ik}\,T^b_{kj}\left(\frac{k_1\cdot\epsilon_2^*}{k_1\cdot k_2}-\frac{p_2\cdot\epsilon_2^*}{p_2\cdot k_2}\right)-T^b_{ik}\,T^a_{kj}\left(\frac{k_1\cdot\epsilon_2^*}{k_1\cdot k_2}-\frac{p_1\cdot\epsilon_2^*}{p_1\cdot k_2}\right)\right],\end{aligned}\tag{3.35}$$

where the eikonal current for gluon 1, the harder of the two, is an overall factor in the expression.

Squaring this result and summing over gluon polarization states and quark colours gives, considering only the terms in the square brackets,

$$\begin{aligned}&\sum_{i,j}\sum_{\lambda_1,\lambda_2}|\mathcal{M}|^2\propto\\&2\,i\,{\rm Tr}\left[T^aT^bT^c\right]f^{abc}\frac{1}{\omega_2^2}\left[\frac{(k_1,p_1)}{(k_1,k_2)\,(k_2,p_1)}+\frac{(k_1,p_2)}{(k_1,k_2)\,(k_2,p_2)}-\frac{(p_1,p_2)}{(p_1,k_2)\,(k_2,p_2)}\right]\\&\qquad-2\,{\rm Tr}\left[T^aT^bT^bT^a\right]\frac{p_1\cdot p_2}{p_1\cdot k_2\,p_2\cdot k_2}\,,\end{aligned}\tag{3.36}$$

where the gluon's energy ω_2 has been factored out in the non-Abelian piece and

$$(a,b):=1-\cos\theta_{ab}\tag{3.37}$$

is defined for the vectors a and b, with $\cos\theta_{ab}$ the angle between them. Independent emission essentially means that the non-Abelian term—in the large square brackets, which does not appear in QED—must vanish. We have already seen that this term disappears when the softer of the two gluons is emitted at a significantly wider angle than the less soft gluon. We now demonstrate that this term also vanishes in the case that the softer of the two gluons is emitted significantly *more* collinearly to either the quark or anti-quark.

Adopting the method used in [**48, 49**], the non-Abelian term, proportional to

$${\rm NA}=\frac{(k_1,p_1)}{(k_1,k_2)\,(k_2,p_1)}+\frac{(k_1,p_2)}{(k_1,k_2)\,(k_2,p_2)}-\frac{(p_1,p_2)}{(p_1,k_2)\,(k_2,p_2)}\,,\tag{3.38}$$

may be written in terms of

$$\tilde W^k_{[i]j}:=\frac{(i,j)}{(i,k)\,(k,j)}+\frac{1}{(i,k)}-\frac{1}{(j,k)}\tag{3.39}$$

as

$${\rm NA}=\tilde W^{k_2}_{[p_1]k_1}-\tilde W^{k_2}_{[p_1]p_2}+\tilde W^{k_2}_{[k_1]p_2}\,.\tag{3.40}$$

A remarkable property of the function $\tilde W^k_{[i]j}$ is that, if we integrate over the azimuth of the vector k, with the azimuth defined to be about the direction of the vector i in square brackets, one obtains

$$\int\frac{d\phi}{2\pi}\,\tilde W^k_{[i]j}=\frac{1}{(i,k)}\,\Theta[(i,j)-(i,k)]=\frac{1}{(i,k)}\,\Theta(\cos\theta_{ik}-\cos\theta_{ij})\,,\tag{3.41}$$

as shown in Appendix B.3. Since the $\tilde{W}^k_{[i]j}$ functions are scalars, we are free to choose our coordinate system in each case over which to perform the phase space integration. With that in mind, we pick the azimuth of k to be the angle *about* the direction of the vector i (in square brackets to remind us). We therefore obtain the expression

$$\int \frac{d\phi}{2\pi}\,\mathrm{NA} = \frac{1}{(p_1,k_2)}\Big\{\Theta\big[(p_1,k_2)-(p_1,p_2)\big]-\Theta\big[(p_1,k_2)-(p_1,k_1)\big]\Big\} + \frac{1}{(k_1,k_2)}\,\Theta\big[(k_1,p_2)-(k_1,k_2)\big]\,. \tag{3.42}$$

The collinear enhancement as k_2 becomes parallel to p_1 is in the first term, but this goes to zero as $(p_1,k_2)\to 0$ because of the Heaviside step functions. The general result may be stated [**50**] as follows: soft gluons emitted at *widely disparate* angular scales are emitted independently *because of QCD coherence*, whereby the gluon emitted at a wider angle 'feels' only the total colour charge of the $(q\,g)$ system from which it's being emitted—which, in this case, is just that of the original quark. This result is crucial to the consideration of soft gluon resummation to all orders.

As a final remark for the interested reader, I will point out that this thesis deals principally with the resummation of continuous global observables. For a discussion of the resummation of so called 'non-global' QCD observables, see [**51**]. In particular, [**52**] presents a discussion of coherence in the context of such an observable.

3.3. Collinear gluon emission to all orders

In Appendix A.4 I have computed the (azimuthally averaged, d-dimensional) differential cross-section for a general process involving the splitting $q\to q\,g$, in the limit where the emitted gluon (g) is *collinear* to the quark (q). This demonstrates the universality of the factor one obtains in association with such emissions which, in $d=4$ dimensions, is

$$\frac{\alpha_\mathrm{s}}{2\pi}\,\frac{dk_\mathrm{T}^2}{k_\mathrm{T}^2}\,dz\,P_{qq}(z)\,, \tag{3.43}$$

where $P_{qq}(z)$ is the *Altarelli–Parisi* splitting function [**53**], z is the momentum fraction carried forth by the quark, and k_T is transverse momentum of the gluon with respect to the direction of the *quark*[2].

To understand how we might obtain a result to all orders, we follow [**54**]. Let us therefore consider a quark of momentum $p=(E,\underline{0},E)$ emitting a gluon of momentum k, as shown in Fig. A.6. We parameterize the gluon momentum as

$$k=(z\,E,\underline{k}_\mathrm{T},\beta\,E) \tag{3.44}$$

and, requiring the gluon to be massless—i.e. $k^2=0$, one can deduce that

$$\beta = z\sqrt{1-\frac{k_\mathrm{T}^2}{z^2\,E^2}} \approx z-\frac{k_\mathrm{T}^2}{2\,z\,E^2} \tag{3.45}$$

[2]There is a singularity associated with soft gluon emission, i.e. when $1-z\to 0$.

in the limit where $k_{\rm T} \ll z\,E$, the collinear limit. The momentum carried by the quark after the emission is therefore

$$q = (p-k) = \left(E', -\underline{k}_{\rm T}, E' + \frac{k_{\rm T}^2}{2\,z\,E}\right), \tag{3.46}$$

where $E' = (1-z)\,E$, and so

$$q^2 = -\frac{k_{\rm T}^2}{z} + \mathcal{O}(k_{\rm T}^4)\,. \tag{3.47}$$

Upon integration over the gluon's transverse momentum $k_{\rm T}^2$ we obtain a logarithm associated with the collinear emission.

Consider, the subsequent emission of a gluon carrying momentum $k' = (z'\,E', \underline{k}'_{\rm T}, \beta'\,E')$. Similarly, in order that this gluon be massless, we have

$$\beta' \approx z' - \frac{k_{\rm T}'^2}{2\,z'\,E'^2}\,. \tag{3.48}$$

We therefore find the momentum carried by the quark after the second emission to be

$$q' = q - k' = \left(E'', -(\underline{k}_{\rm T} + \underline{k}'_{\rm T}), E'' + \frac{k_{\rm T}'^2}{2\,z'\,E'} + \frac{k_{\rm T}^2}{2\,z\,E}\right), \tag{3.49}$$

where $E'' = (1-z')\,E'$. This implies that

$$q'^2 = -(\underline{k}_{\rm T} + \underline{k}'_{\rm T})^2 - E''\left(\frac{k_{\rm T}'^2}{z'\,E'} + \frac{k_{\rm T}^2}{z\,E}\right) + \ldots\,, \tag{3.50}$$

where $\ldots$ represents terms $\mathcal{O}(k_{\rm T}^4)$, $\mathcal{O}(k_{\rm T}'^4)$ and $\mathcal{O}(k_{\rm T}^2\,k_{\rm T}'^2)$. Only in the limit $k_{\rm T} \ll k'_{\rm T}$ does q'^2 vary as $k_{\rm T}'^2$, giving us a double logarithm upon integration of the propagators over the second gluon's transverse momentum $k_{\rm T}'^2$, followed by integration over that of the first gluon, namely $k_{\rm T}^2$:

$$\int_{k_{\rm T}^{\rm min}}^{k_{\rm T}^{\rm max}} \frac{dk_{\rm T}^2}{k_{\rm T}^2} \int_{k_{\rm T}^{\rm min}}^{k_{\rm T}} \frac{dk_{\rm T}'^2}{k_{\rm T}'^2} = \frac{1}{2}\,\ln^2\left(\frac{k_{\rm T}^{\rm max\,2}}{k_{\rm T}^{\rm min\,2}}\right). \tag{3.51}$$

In performing the integration over $k_{\rm T}'^2$, we may set the upper limit to $k_{\rm T}^2$, which is sufficient to obtain the double-logarithm.

Since two gluon emissions gives a term formally $\mathcal{O}(\alpha_{\rm s}^2)$, only the circumstance in which we obtain this double logarithm do we find a correction that may be as large as that associated with single collinear gluon emission at $\mathcal{O}(\alpha_{\rm s})$. This necessarily implies the ordering of emissions as $k_{\rm T} \ll k'_{\rm T}$. This argument extends to an arbitrary number of collinear gluon emissions straightforwardly.

The argument for strong ordering in transverse momenta of successive gluon emissions has been based entirely on kinematical considerations for the propagators. It actually gives rise to a simplification in the calculation of the dynamics for multiple collinear gluon emission, for it implies that quantum mechanical interference between processes where the gluons are ordered differently is suppressed. Pictorially, this interference may be represented by ladder diagrams in which gluon 'rungs' cross, as shown in Fig. 3.4 (left). Only those diagrams in which no rungs cross give the leading collinear contribution (of a single log) at each order in $\alpha_{\rm s}$, as shown in Fig. 3.4 (right).

Since interference may be neglected at this accuracy, this gives rise to the notion of independent emission, where the probability for n successive collinear gluon emissions is

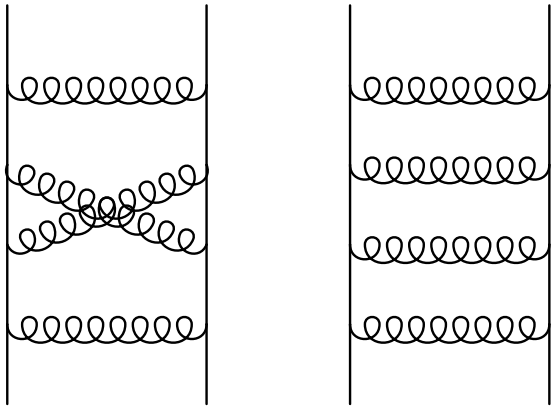

(a) A ladder diagram with some crossed rungs.

(b) A ladder diagram in which no rungs cross.

FIGURE 3.4. A 'ladder' diagram representation of $|\mathcal{M}|^2$ for an arbitrary number of gluon emissions. In the collinear limit, the leading terms come from the diagram in which no rungs cross, which gives rise to the concept of independent emission probabilities. Diagrams in which rungs cross give sub-leading contributions.

simply proportional to the probability of one collinear gluon emission to the nth power. It should be borne in mind that this picture is correct only if one is concerned with the leading collinear enhancements at each order. In fact, the so called DGLAP equations presented in the following section (due to Dokshitzer, Gribov, Lipatov, Altarelli & Parisi [**53, 55, 56**]) provide a *resummation* of these enhancements to all orders.

For processes in which the leading logarithmic enhancement at each order is a double log, arising from soft *and* collinear emissions, then the approximation discussed above contributes at NLL (next-to-leading logarithmic) accuracy, and it guarantees the single collinear logs at each order.[3]

3.4. Parton evolution and the DGLAP equation

The DIS structure function F_2 [**35, 48**]—the DIS equivalent of Eq. 4.22 for Drell–Yan, to be introduced later—is

$$F_2(x,Q^2) = x\sum_{q,\bar{q}} Q_q^2 \int_x^1 \frac{dz}{z}\,\phi_q^{\overline{\rm MS}}\left(\frac{x}{z},\mu\right)\left\{\delta(1-z)+\frac{\alpha_{\rm s}}{2\pi}\left[P_{qq}^{(0)}(z)\,\ln\frac{Q^2}{\mu^2}+R_{qq}^{\rm DIS}(z)\right]\right\}. \tag{3.52}$$

Here, $\phi_i(x,\mu)$ is a parton density function (PDF)—the probability that a parton of flavour i carries a momentum fraction x of the parent hadron, discussed further in Chapter 4. We take this, for example, as our starting point for obtaining the DGLAP [**53, 55, 56**] evolution equations. First, it should be noted that we consider all quantities defined in the $\overline{\rm MS}$ scheme, i.e. only the modified collinear pole $(4\pi e^{\gamma_{\rm E}})^{\epsilon}/\epsilon$ is absorbed into the definition of the renormalized PDFs. In the 'DIS' scheme, the entire function $R_{qq}^{\rm DIS}(z)$

[3]This is only true if we consider 'global' observables. Observables with non-global logarithms are different, and such arguments may not hold. For a discussion of such observables the reader is referred to [**51**].

would have been absorbed but, for our purposes, it remains present in the expression for $F_2(x,Q^2)$. Furthermore, the non-perturbative PDFs $\phi^{\overline{\rm MS}}$ must be determined from an initial experiment 'A' before they can be used to make a prediction of the outcome for experiment 'B'. In order to extract $\phi^{\overline{\rm MS}}$ from the measurement performed in experiment 'A', one necessarily chooses a particular value of μ, since this will change the value of $\phi^{\overline{\rm MS}}$ determined. A natural choice may be the characteristic hard scale $\mu^2 = Q^2$, for then the logarithm is zero. However, this means $\phi^{\overline{\rm MS}}$ acquires a dependence on μ. When used to make predictions for the outcome of experiment 'B', which may be performed at a different characteristic energy scale, we need some way of 'evolving' the PDFs to this new scale. It is precisely the observation that the physical quantity $F_2(x,Q^2)$ cannot depend on this mathematical construction μ^2 that gives us the relevant evolution equation. One starts with

$$\begin{aligned}
&\mu^2\,\frac{dF_2(x,\mu^2)}{d\mu^2} = 0 \\
&\Rightarrow \qquad \mu^2\,\frac{d}{d\mu^2}\int_x^1 \frac{dz}{z}\,\phi^{\overline{\rm MS}}\left(\frac{x}{z},\mu\right)\left\{\delta(1-z)+\frac{\alpha_{\rm s}}{2\pi}\left[P_{qq}^{(0)}(z)\,\ln\frac{Q^2}{\mu^2}+R_{qq}^{\rm DIS}(z)\right]\right\} = 0
\end{aligned} \tag{3.53}$$

Collecting terms of $\mathcal{O}(\alpha_{\rm s})$, noting that $\mu^2\,\partial\phi(x,\mu)/\partial\mu^2$ is itself an $\mathcal{O}(\alpha_{\rm s})$ quantity, one finds

$$\begin{aligned}
\mu^2\,\frac{\partial\phi(x,\mu)}{\partial\mu^2} &= \int_x^1 \frac{dz}{z}\,\frac{\alpha_{\rm s}}{2\pi}\,P_{qq}^{(0)}(z)\,\phi\left(\frac{x}{z},\mu\right) \\
&= \frac{\alpha_{\rm s}}{2\pi}\,P_{qq}^{(0)}(x)\otimes\phi(x,\mu)
\end{aligned} \tag{3.54}$$

after performing the trivial integration over the δ-function. This integro-differential equation for $\phi(x,\mu)$ is the DGLAP equation, which allows one to determine the PDFs at a physical scale μ', upon integration, from those known at a physical scale μ.

In fact, the full DGLAP equations are $(2\,N_{\rm F}+1)$-dimensional matrix equations for the matrix of PDFs $(\phi_q,\phi_{\bar q},\phi_g)$

$$\mu^2\,\frac{\partial}{\partial\mu^2}\begin{pmatrix}\phi_q(x,\mu)\\ \phi_g(x,\mu)\end{pmatrix} = \frac{\alpha_{\rm s}}{2\pi}\begin{pmatrix}P_{qq}(x,\alpha_{\rm s}(\mu)) & P_{qg}(x,\alpha_{\rm s}(\mu))\\ P_{gq}(x,\alpha_{\rm s}(\mu)) & P_{gg}(x,\alpha_{\rm s}(\mu))\end{pmatrix}\otimes\begin{pmatrix}\phi_q(x,\mu)\\ \phi_g(x,\mu)\end{pmatrix} \tag{3.55}$$

Focusing simply on Eq. 3.54, we can solve it by taking Mellin moments with respect to x, i.e.

$$\tilde\phi(N,\mu^2) = \int_0^1 dx\,x^{N-1}\,\phi(x,\mu^2)\,. \tag{3.56}$$

In Mellin space the convolution becomes a simple product, and one has simply

$$\mu^2\,\frac{d\tilde\phi(N,\mu^2)}{d\mu^2} = \frac{\alpha_{\rm s}(\mu^2)}{2\pi}\,\tilde\phi(N,\mu^2)\,\gamma_{qq}(N,\alpha_{\rm s}(\mu^2))\,. \tag{3.57}$$

In this expression, $\gamma_{qq}(N)$ is the anomalous dimension (see Eq. 4.48 later) namely the Nth Mellin moment of the regularized splitting function. We may integrate this expression, for a given N, to find

$$\int_{Q_0^2}^{Q^2}\frac{1}{\tilde\phi(N,\mu^2)}\,\frac{d\tilde\phi(N,\mu^2)}{d\mu^2}\,d\mu^2 = \int_{Q_0^2}^{Q^2}\frac{d\mu^2}{\mu^2}\,\frac{\alpha_{\rm s}(\mu^2)}{2\pi}\,\gamma_{qq}(N,\alpha_{\rm s}(\mu^2)) \tag{3.58}$$

and so

$$\tilde{\phi}(N,Q^2) = \tilde{\phi}(N,Q_0^2)\,\exp\left[\int_{Q_0^2}^{Q^2}\frac{d\mu^2}{\mu^2}\,\frac{\alpha_{\rm s}(\mu^2)}{2\pi}\,\gamma_{qq}(N,\alpha_{\rm s}(\mu^2))\right]. \tag{3.59}$$

The right-hand side may be solved exactly, for instance, if one assumes $\alpha_{\rm s}$ fixed, to give

$$\tilde{\phi}(N,Q^2) = \tilde{\phi}(N,Q_0^2)\left(\frac{Q^2}{Q_0^2}\right)^{\frac{\alpha_{\rm s}(\mu^2)}{2\pi}\,\gamma_{qq}(N,\alpha_{\rm s}(\mu^2))}. \tag{3.60}$$

We have the desired expression: given the PDF determined for some starting scale Q_0, the PDF at the new scale Q. With this result, the term *anomalous dimension* may be elucidated: it quantifies the deviation from naïve scaling of the PDFs.

CHAPTER 4

The Drell–Yan process and the ϕ^* observable

The Drell-Yan process [**1**] may be described as: $h_1(p_1)+h_2(p_2) \to \ell^-(p_3)+\ell^+(p_4)+X$, namely the processes whereby two hadrons collide to produce two leptons of opposite charge and same flavour, and anything else, X. This process, in the naïve Parton Model[1], is shown in the Born approximation, $\mathcal{O}(\alpha^2)$ in the electroweak coupling parameter, in Fig. 4.1. The factorization theorem for Drell-Yan production [**57**] permits us to write the hadronic cross-section as a convolution of (possibly scale-dependent) parton distribution functions (PDFs) for each hadron h_1 and h_2, with the partonic cross-section for an allowed sub-process, up to terms formally suppressed by powers of $\Lambda^2_{\rm QCD}/M^6$, the inverse hard scale. Thus

$$\frac{d\sigma}{dM^2} \sim \sum_{i,j} \int_0^1 d\xi_1 \int_0^1 d\xi_2 \, \phi_{i/1}(\xi_1;\mu) \, \frac{d\hat{\sigma}_{ij}}{dM^2}(\xi_1\,\xi_2\,s;\mu) \, \phi_{j/2}(\xi_2;\mu) + \mathcal{O}\left(\frac{\Lambda^2_{\rm QCD}}{M^6}\right). \quad (4.1)$$

Here, ξ_1 and ξ_2 are the momentum fractions of partons 1 and 2 that enter the sub-process, denoted by a hat, and $\phi_{i/k}(\xi;\mu)$ is a scale-dependent PDF for a parton of type i in hadron k, namely the probability that this parton is found to have a momentum between $\xi\, p_k$ and $(\xi + d\xi)\, p_k$, where p_k is the momentum of the parent hadron, labelled $k \in \{1,2\}$. A sum over parton types is included. Eq. 4.1 is usually the starting point for the calculation of hadronic cross-sections in perturbative QCD (pQCD).

In this chapter I will present in detail the calculation of the cross-section for the Drell-Yan process in a hadron-hadron collider, including $\mathcal{O}(\alpha_{\rm s})$ perturbative corrections to the Born result, which is itself $\mathcal{O}(\alpha^2)$, in the electroweak coupling. The aim is to introduce the reader to a full next-to-leading order (NLO) calculation, demonstrating various results along the way that will be invoked later. I have computed the differential partonic cross-sections explicitly in Appendix A, for the Born process and also the real and virtual corrections, for the benefit of the interested reader.

In this chapter I also finally introduce the ϕ^* observable [**15**] that has essentially formed the topic of my PhD. The ϕ^* observable was originally introduced as a result of experimental considerations. It has an entirely angular construction, which means it is largely immune to experimental momenta mismeasurements, in contrary to its $Q_{\rm T}$ cousin. Throughout this thesis, the ϕ^* observable (along with $Q_{\rm T}$) is directly applied to the Drell-Yan process. It is important to note, however, that the observable itself is a kinematic definition and could equally apply to other suitable processes, as a measure of the azimuthal decorrelation between two objects. That said, we are for the present interested in this observable in the context of Drell-Yan for its ability to probe the effects of gluon

[1]The model in which hadronic constituents, known as *partons*, are assumed to instantaneously and incoherently undergo the actual scattering.

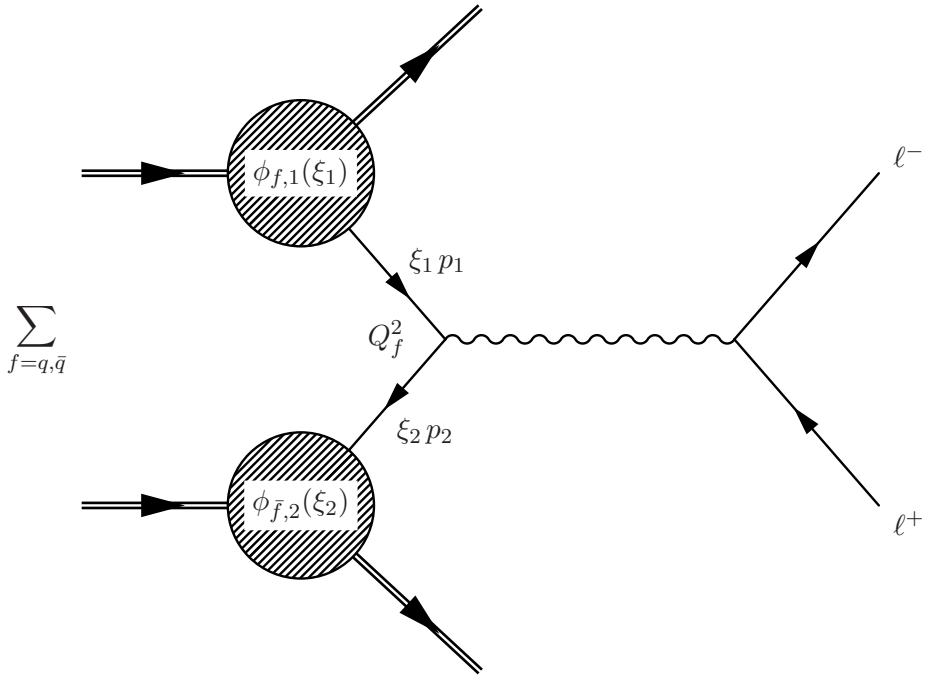

FIGURE 4.1. The Drell-Yan process in the Born approximation and the naïve Parton Model

emission from the process-initiating partons. In Section 4.4 I will present the kinematic construction of ϕ^* and relate it to other observables, before presenting its resummed calculation *vis-à-vis* that of $a_{\rm T}$ and $Q_{\rm T}$ for easy comparison in the sections that follow. First, I will address the Drell–Yan cross-section and logarithmic enhancements that arise in certain regions of phase space.

4.1. The hadronic cross-section

In this section I will address the full hadronic cross-section for the Drell–Yan process and the rôle of PDFs, focusing on the *annihilation* mechanism with photonic exchange: $h_1\, h_2 \to q\,\bar{q} + X \to \gamma^*(+g) + X$ to serve as a concrete example[2]. The reader will find detailed calculations of the relevant individual partonic processes in Appendix A, where dimensional regularization has been used in $d = 4 - 2\epsilon$ dimensions. Adding together the contributions at $\mathcal{O}(\alpha_{\rm s})$ to the Drell-Yan process under consideration, namely the real and virtual contributions to the *annihilation* sub-process in Eqs. A.74, A.75 and A.104, one obtains (see, for example, [**35, 48, 60**])

$$d\hat{\sigma}^{\rm R}_{q\bar{q}} + d\hat{\sigma}^{\rm V} = \hat{\sigma}_0\, \frac{\alpha_{\rm s}}{2\pi}\, \frac{dM^2}{M^2}\, D(\epsilon) \left[-\frac{2}{\epsilon} P^{(0)}_{qq}(z) + R_{q\bar{q}}(z) \right], \tag{4.2}$$

with $D(\epsilon)$ defined in Eq. A.66, and where $P^{(0)}_{qq}(z)$ is one of the *Altarelli–Parisi* splitting functions [**53**], given by

$$P^{(0)}_{qq}(z) = C_{\rm F} \left[\frac{1+z^2}{(1-z)_+} + \frac{3}{2}\delta(1-z) \right], \tag{4.3}$$

[2]A calculation of Drell–Yan production via Z exchange may be found in [**58**]. Furthermore, the total $\mathcal{O}(\alpha_{\rm s})$ result may be found by consulting [**59**].

and $R_{q\bar{q}}(z)$, given by

$$R_{q\bar{q}}(z) = C_{\rm F}\left\{\delta(1-z)\left(\frac{2\pi^2}{3}-8\right)+4(1+z^2)\left[\frac{\log(1-z)}{1-z}\right]_+ - 2\log(z)\frac{1+z^2}{1-z}\right\}, \quad (4.4)$$

is a function which is completely finite in the limit $\epsilon \to 0$.

The quantity $d\hat{\sigma}^{\rm R}_{q\bar{q}} + d\hat{\sigma}^{\rm V}$ above is not finite in the limit $\epsilon \to 0$, on account of the remaining pole in ϵ, and is therefore not infrared (IR) safe. The purpose of this section is to address this issue, and find how we can extract an IR safe quantity from it, by exploiting *factorization* [**57**]. The essential point is that, in Eq. 4.1 for the hadronic cross-section, we have introduced a new quantity, namely a PDF, which itself has an unrenormalized, yet unmeasurable form, along with a renormalized, finite and measurable form. The programme for obtaining the IR-safe version of the partonic cross-section will be via a redefinition, whereby the singular pieces are absorbed into the unmeasurable bare PDFs.

Following the method of [**60**], we begin by defining a quantity known as a *transition function*, Γ, which is to a parton what a bare PDF is to a hadron. The idea here is to absorb the singular pole in ϵ into the transition function, whose residue may be interpreted as the probability of finding a parton of a given type inside another parton—in this case a quark 'within' a quark—with a given momentum fraction z of the original parton. Thus, we define

$$\sigma^{\epsilon}_{ij}(s) = \int_0^1 dz_1 \int_0^1 dz_2\, \Gamma^{\epsilon}_{ik}(z_1)\, \sigma_{k\ell}(z_1 z_2 s)\, \Gamma^{\epsilon}_{j\ell}(z_2), \quad (4.5)$$

where the ϵ is there to remind the reader the quantity is *not* finite in the limit $\epsilon \to 0$. Assuming a perturbative expansion in $\alpha_{\rm s}$ for each of the quantities in Eq. 4.5, namely

$$\begin{aligned}
\sigma_{ij}(s) &= \sum_{n=0}^{\infty}\left(\frac{\alpha_{\rm s}}{2\pi}\right)^n \sigma_{n,ij}(s), \\
\sigma^{\epsilon}_{ij}(s) &= \sum_{n=0}^{\infty}\left(\frac{\alpha_{\rm s}}{2\pi}\right)^n \sigma^{\epsilon}_{n,ij}(s) \qquad (4.6)\\
\text{and} \qquad \Gamma^{\epsilon}_{ik}(z) &= \delta_{ik}\delta(1-z) + \sum_{n=1}^{\infty}\left(\frac{\alpha_{\rm s}}{2\pi}\right)^n \Gamma^{\epsilon}_{n,ik}(z)\,,
\end{aligned}$$

we may write the finite quantity σ order-by-order in terms of σ^{ϵ} and Γ^{ϵ}, by equating terms at the same perturbative order upon substitution of Eq. 4.6 into Eq. 4.5:

$$\begin{aligned}
&\sigma_{0,ij}(s) = \sigma^{\epsilon}_{0,ij}(s) \\
&\sigma_{1,ij}(s) = \sigma^{\epsilon}_{1,ij}(s) - \int_0^1 dz_1\, \Gamma^{\epsilon}_{1,ik}(z_1)\, \sigma^{\epsilon}_{0,kj}(z_1 s) - \int_0^1 dz_2\, \sigma^{\epsilon}_{0,i\ell}(z_2 s)\, \Gamma^{\epsilon}_{1,\ell j}(z_2) \qquad (4.7)\\
&\quad\vdots \qquad = \qquad \vdots
\end{aligned}$$

The method now is to pick suitable expressions for the 'Γ^{ϵ}'s in order that all the divergences (poles in ϵ) on the RHS of these expressions exactly cancel, leaving only finite quantities on the LHS.

First, the full hadronic cross-section is given, according to the factorization theorem, by

$$\begin{aligned}\frac{d\sigma}{dM^2}(s) = \int_0^1 d\xi_1 \int_0^1 d\xi_2 \\ \times\Bigg\{ \sum_q \left[\phi_{q/1}(\xi_1)\,\phi_{\bar{q}/2}(\xi_2) + (q \leftrightarrow \bar{q})\right] \left[\frac{d\hat{\sigma}_{0,q\bar{q}}}{dM^2}(\xi_1\xi_2 s) + \frac{d\hat{\sigma}_{1,q\bar{q}}}{dM^2}(\xi_1\xi_2 s)\right] \\ + \sum_{f=q,\bar{q}} \left[\phi_{g/1}(\xi_1)\,\phi_{f/2}(\xi_2) + (f \leftrightarrow g)\right] \frac{d\hat{\sigma}_{1,gq}(\xi_1\xi_2 s)}{dM^2}\Bigg\}.\end{aligned} \tag{4.8}$$

From Eq. A.25 we already know that

$$\frac{d\hat{\sigma}_{0,q\bar{q}}}{dM^2}(\hat{s}) = \frac{d\hat{\sigma}^{\epsilon}_{0,q\bar{q}}}{dM^2}(\hat{s}) = \frac{\hat{\sigma}_0(\hat{s})}{\hat{s}}\,\delta\left(1 - \frac{M^2}{\hat{s}}\right), \tag{4.9}$$

so we begin by finding the expression (using Eq. 4.7) for

$$\begin{aligned}\frac{d\hat{\sigma}_{1,q\bar{q}}}{dM^2}(\hat{s}) &= \frac{d\hat{\sigma}^{\epsilon}_{1,q\bar{q}}}{dM^2}(\hat{s}) - \int_0^1 dz_1\,\Gamma^{\epsilon}_{1,qq}(z_1)\,\frac{d\hat{\sigma}^{\epsilon}_{0,q\bar{q}}}{dM^2}(z_1\hat{s}) - \int_0^1 dz_2\,\frac{d\hat{\sigma}^{\epsilon}_{0,q\bar{q}}}{dM^2}(z_2\hat{s})\,\Gamma^{\epsilon}_{1,\bar{q}\bar{q}}(z_2) \\ &= \frac{d\hat{\sigma}^{\epsilon}_{1,q\bar{q}}}{dM^2}(\hat{s}) - \int_0^1 d\bar{z}\,[\Gamma^{\epsilon}_{1,qq}(\bar{z}) + \Gamma^{\epsilon}_{1,\bar{q}\bar{q}}(\bar{z})]\,\frac{\hat{\sigma}_0(\bar{z}\hat{s})}{\bar{z}\hat{s}}\,\delta\left(1 - \frac{M^2}{\bar{z}\hat{s}}\right),\end{aligned} \tag{4.10}$$

where I have introduced $\bar{z} = z_1 = z_2$ as the variable of integration. Performing the integral over $\bar{z}$, we obtain

$$\int_0^1 d\bar{z}\,[\Gamma^{\epsilon}_{1,qq}(\bar{z}) + \Gamma^{\epsilon}_{1,\bar{q}\bar{q}}(\bar{z})]\,\frac{\hat{\sigma}_0(\bar{z}\hat{s})}{\bar{z}\hat{s}}\,\delta\left(1 - \frac{M^2}{\bar{z}\hat{s}}\right) = [\Gamma^{\epsilon}_{1,qq}(z) + \Gamma^{\epsilon}_{1,\bar{q}\bar{q}}(z)]\,\frac{\hat{\sigma}_0(\hat{s})}{M^2} \tag{4.11}$$

where $\hat{\sigma}_0(M^2)/\hat{s} = \hat{\sigma}_0(\hat{s})/M^2$ and $z = M^2/\hat{s}$ has been used, as one may verify explicitly from the expression in Eq. A.25. Using the expansion for $D(\epsilon)$ given in Eq. A.72, one may now see that, defining

$$\Gamma^{\epsilon}_{1,qq}(z) = \Gamma^{\epsilon}_{1,\bar{q}\bar{q}}(z) = -\frac{1}{\epsilon}\,\left(4\pi e^{-\gamma_{\mathrm{E}}}\right)^{\epsilon}\,P^{(0)}_{qq}(z), \tag{4.12}$$

the poles in $\frac{d\hat{\sigma}^{\epsilon}_{1,q\bar{q}}}{dM^2}(\hat{s})$ of Eq. 4.10 are absorbed, yielding a finite expression for $\frac{d\hat{\sigma}_{1,q\bar{q}}}{dM^2}(\hat{s})$ in the limit $\epsilon \to 0$, namely

$$\frac{d\hat{\sigma}_{1,q\bar{q}}}{dM^2}(\hat{s}) = \frac{\hat{\sigma}_0(\hat{s})}{M^2}\left[2\,P^{(0)}_{qq}(z)\,\log\left(\frac{M^2}{\mu^2}\right) + R_{q\bar{q}}(z)\right] \tag{4.13}$$

with $\hat{\sigma}_0(\hat{s})$ given in Eq. A.28 ($d \to 4$). This particular choice results in additional finite terms being absorbed, along with the singular pole in ϵ. Such a choice is known as the $\overline{\mathrm{MS}}$ scheme.

Until now we have completely neglected the *Compton* sub-process: $h_1\,h_2 \to g\,q + X \to \gamma^* + q + X$, which is absent until $\mathcal{O}(\alpha_{\mathrm{s}})$ corrections are considered. Since the calculation of the annihilation sub-process to $\mathcal{O}(\alpha_{\mathrm{s}})$ has been worked in great detail, the result for the Compton piece is simply quoted here, but the reader is referred to the literature [**35, 48**], or the calculation may be used as an exercise. The result is

$$\frac{d\hat{\sigma}^{\epsilon}_{1,gq}}{dM^2} = \frac{\hat{\sigma}_0}{M^2}\,Q_f^2\,\frac{\alpha_{\mathrm{s}}}{2\pi}\,\left[-\frac{1}{\epsilon}P^{(0)}_{qg}(z) + R_{gq}(z)\right], \tag{4.14}$$

where

$$R_{gq}(z) = T_{\mathrm{F}} \left\{ 2\left[z^2 + (1-z)^2\right] \log\left[\frac{(1-z)^2}{z}\right] + 3 + 2z - 3z^2 \right\}, \tag{4.15}$$

and

$$P^{(0)}_{qg}(z) = T_{\mathrm{F}}\left[z^2 + (1-z)^2\right], \tag{4.16}$$

with $T_{\mathrm{F}} = \frac{1}{2}$. Using Eqs. 4.6 and A.25, we may now compute

$$\begin{aligned} \frac{d\hat{\sigma}_{1,gq}}{dM^2}(\hat{s}) &= \frac{d\hat{\sigma}^{\epsilon}_{1,gq}}{dM^2}(\hat{s}) - \int_0^1 d\bar{z}\, \Gamma^{\epsilon}_{1,g\bar{q}}(\bar{z})\, \frac{d\hat{\sigma}^{\epsilon}_{0,\bar{q}q}}{dM^2}(\bar{z}\hat{s}) \\ &= \frac{d\hat{\sigma}^{\epsilon}_{1,gq}}{dM^2}(\hat{s}) - \Gamma^{\epsilon}_{1,g\bar{q}}(z)\, \frac{\hat{\sigma}_0(\hat{s})}{M^2}, \end{aligned} \tag{4.17}$$

in a similar manner as before, and conclude that the definition

$$\Gamma^{\epsilon}_{1,g\bar{q}}(z) = -\frac{1}{\epsilon}\, \left(4\pi e^{-\gamma_{\mathrm{E}}}\right)^{\epsilon}\, P^{(0)}_{qg}(z) \tag{4.18}$$

renders $\frac{d\hat{\sigma}_{1,gq}}{dM^2}(\hat{s})$ finite.

So far we have computed the Drell-Yan partonic cross-section at NLO, necessarily in $d \neq 4$ space-time dimensions, finding there are poles in ϵ that remain when all pieces are summed together, and which are associated with collinear emission. We have thus far absorbed these poles into so-called *transition functions*, whose residues at the pole may be interpreted as the probability to find a parton of a given type inside another parton. It is now that we finally introduce the bare and renormalized PDFs, to absorb this pole once-and-for-all, in a consistent fashion. Finally, order-by-order, we will demand that the physical hadronic cross-section be independent of the mathematical construction μ, introduced to retain dimensionless coupling parameters, and thus insist that the renormalized PDFs are themselves functions of μ in such a way as to cancel the dependence due to the renormalized partonic cross-section for Drell–Yan. We thus see that PDFs are scale-dependent quantities which may be extracted from experiment and evolved according to a set of coupled integro-differential equations given the name DGLAP [**53, 55, 56**], for use in predicting the outcome of experiments performed at a *different* scale. In this context, μ becomes known as the *factorization scale*.

We begin by defining the renormalized PDF as the following convolution:

$$\phi_{i/k}(\xi) = \int_0^1 dx \int_0^1 dz\, \phi^{\epsilon}_{j/k}(x)\, \Gamma^{\epsilon}_{ij}(z)\, \delta(\xi - x\, z). \tag{4.19}$$

The physical interpretation is as follows: The probability of finding a parton of type i inside hadron k with a momentum fraction ξ to $\xi + d\xi$ of that of its parent, is the sum of probabilities to find a parton of type j inside k with momentum fraction x to $x + dx$, times the probability of finding a parton of type i inside the parton of type j, with momentum fraction z to $z + dz$, in such a way that $\xi = x\, z$ in each case. This definition permits us to compensate the singularity in Γ^{ϵ}_{ij} with an equivalent one in the unmeasurable (bare) PDF $\phi^{\epsilon}_{j/k}$, such that the measurable $\phi_{i/k}$ remains finite.

To obtain the the Drell-Yan cross-section in terms of renormalized quantities, we begin with the double convolution in terms of our calculated *unrenormalized* quantities which,

as it stands, is dangerous (on account of the presence of explicitly infinite quantities in the expression):

$$\begin{aligned}\frac{d\sigma}{dM^2}(s) &= \sum_{i,j}\int_0^1 dx_1\int_0^1 dx_2\,\phi^\epsilon_{k/1}(x_1)\,\frac{d\hat{\sigma}^\epsilon_{k\ell}}{dM^2}(x_1x_2s)\,\phi^\epsilon_{\ell/2}(x_2)\\ &= \sum_{i,j}\int_0^1 dx_1\int_0^1 dx_2 \\ &\qquad \phi^\epsilon_{k/1}(x_1)\int_0^1 dz_1\int_0^1 dz_2\,\Gamma^\epsilon_{ik}(z_1)\,\frac{d\hat{\sigma}_{ij}}{dM^2}(z_1z_2x_1x_2s)\,\Gamma^\epsilon_{j\ell}(z_2)\,\phi^\epsilon_{\ell/2}(x_2)\,.\end{aligned} \tag{4.20}$$

Introducing the identity in the form $\int_0^1 d\xi\,\delta(\xi - x\,z)$, given that $x_{1/2}\,z_{1/2}\in[0,1]$ always, then one may rewrite the argument of the partonic cross-section, as such:

$$\begin{aligned}\frac{d\sigma}{dM^2}(s) &= \sum_{i,j}\int_0^1 d\xi_1\int_0^1 dx_1\int_0^1 dz_1\,\phi^\epsilon_{k/1}(x_1)\,\Gamma^\epsilon_{ik}(z_1)\,\delta(\xi_1 - x_1z_1)\\ &\qquad\times\int_0^1 d\xi_2\int_0^1 dx_2\int_0^1 dz_2\,\phi^\epsilon_{\ell/2}(x_2)\,\Gamma^\epsilon_{j\ell}(z_2)\,\delta(\xi_2 - x_2z_2)\,\frac{d\hat{\sigma}_{ij}}{dM^2}(x_1z_1x_2z_2s)\\ &= \sum_{i,j}\int_0^1 d\xi_1\int_0^1 d\xi_2\,\phi_{i/1}(\xi_1)\,\frac{d\hat{\sigma}_{ij}}{dM^2}(\xi_1\xi_2s)\,\phi_{j/2}(\xi_2)\,,\end{aligned} \tag{4.21}$$

where in the final line the expression for the renormalized PDF in terms of the convolution in Eq. 4.19 has been used, hopefully elucidating the choice for its original definition. In summary we have, for inclusive Drell–Yan at NLO,

$$\begin{aligned}\frac{d\sigma}{dM^2} = \int_0^1 d\xi_1\int_0^1 d\xi_2\,\frac{\hat{\sigma}}{\hat{s}}\Bigg\{&\sum_q Q_g^2\,\left[\phi^{\overline{\rm MS}}_{q/1}(\xi_1;\mu_{\rm F})\,\phi^{\overline{\rm MS}}_{\bar{q}/2}(\xi_2;\mu_{\rm F}) + (q\leftrightarrow\bar{q})\right]\\ &\times\left\{\delta(1-\hat{z}) + \frac{\alpha_{\rm s}}{2\pi}\left[2P^{(0)}_{qq}(\hat{z})\,\ln\left(\frac{M^2}{\mu_{\rm F}^2}\right) + R_{q\bar{q}}(\hat{z})\right] + \mathcal{O}\left(\alpha_{\rm s}^2\right)\right\}\\ &+\sum_{f=q,\bar{q}} Q_f^2\,\left[\phi^{\overline{\rm MS}}_{g/1}(\xi_1;\mu_{\rm F})\,\phi^{\overline{\rm MS}}_{f/2}(\xi_2;\mu_{\rm F}) + (f\leftrightarrow g)\right]\\ &\times\left\{\frac{\alpha_{\rm s}}{2\pi}\,\left[2P^{(0)}_{qg}(\hat{z})\,\ln\left(\frac{M^2}{\mu_{\rm F}^2}\right) + R_{gq}(\hat{z})\right] + \mathcal{O}\left(\alpha_{\rm s}^2\right)\right\}\Bigg\}.\end{aligned} \tag{4.22}$$

In Appendix A.4 I discuss the universality of the initial-state collinear singularities associated with parton emissions. Now that we have an expression for the differential *hadronic* Drell–Yan cross-section, I will address the $Q_{\rm T}$ distribution of Drell–Yan pairs and the issue associated with the small-$Q_{\rm T}$ limit.

4.2. The full $Q_{\rm T}$ distribution

Taking Eq. A.49 (see also [**60**]), the differential partonic cross-section for real emission in the annihilation sub-process is

$$\frac{d\hat{\sigma}}{dM^2} = 4\,\hat{\sigma}_0\,\alpha_{\rm s}\,\mu^{2\epsilon}\,C_{\rm F}\,\frac{1}{M^2}\,d{\rm PS}_2\,\left[\frac{2M^2\hat{s}+\hat{t}^2+\hat{u}^2}{\hat{t}\,\hat{u}} - \epsilon\left(\frac{\hat{t}^2+\hat{u}^2+2\,\hat{t}\,\hat{u}}{\hat{t}\,\hat{u}}\right)\right]. \tag{4.23}$$

The Mandelstam variables in the centre-of-momentum frame are $\hat{t} = -\sqrt{\hat{s}}\,E_k\,(1-\cos\theta)$ and $\hat{u} = -\sqrt{\hat{s}}\,E_k\,(1+\cos\theta)$. We define $k_{\rm T} := |\vec{k}|\sin\theta = E_k\,\sin\theta$, since $E_k = |\vec{k}|$ for a massless particle, and deduce that

$$\hat{t}\,\hat{u} = \hat{s}\,k_{\rm T}^2 \tag{4.24}$$

$$\text{and} \qquad \hat{t}^2+\hat{u}^2 = 2\hat{s}\,(2E_k^2 - k_{\rm T}^2)\,. \tag{4.25}$$

We now have

$$\frac{2M^2\hat{s}+\hat{t}^2+\hat{u}^2}{\hat{t}\,\hat{u}} = \frac{2}{k_{\rm T}^2}\,(M^2+2E_k^2-k_{\rm T}^2) \tag{4.26}$$

and

$$\frac{\hat{t}^2+\hat{u}^2+2\,\hat{t}\,\hat{u}}{\hat{t}\,\hat{u}} = \frac{4E_k^2}{k_{\rm T}^2}\,. \tag{4.27}$$

The differential phase space element in $d = 4-2\epsilon$ dimensions is given in Eq. A.50:

$$d{\rm PS}_2 = \frac{E_k^{1-2\epsilon}\,dE_k\,d\theta\sin^{1-2\epsilon}\theta}{(4\pi)^{1-\epsilon}\,\Gamma(1-\epsilon)}\,\delta\left(\hat{s}-2E_k\sqrt{\hat{s}}-M^2\right)\,, \tag{4.28}$$

after using $d\Omega_{d-2}$ given by Eq. A.53. Using the definition of $k_{\rm T} = E_k\,\sin\theta$, along with $d\theta = d\sin\theta/\sqrt{1-\sin^2\theta}$, we have

$$E_k^{1-2\epsilon}\,d\theta\sin^{1-2\epsilon}\theta = 2\,\frac{k_{\rm T}^{1-2\epsilon}\,dk_{\rm T}}{\sqrt{E_k^2-k_{\rm T}^2}} = \frac{d^{1-\epsilon}k_{\rm T}^2}{\sqrt{E_k^2-k_{\rm T}^2}} \tag{4.29}$$

The extra factor of two has been included since, when it comes to integrating the expression for $d\hat{\sigma}/dk_{\rm T}^2\,dM^2$, we could just as well integrate from $\theta_{\rm min}$ to $\pi/2$ (instead of from $\theta_{\rm min}$ to $\pi-\theta_{\rm min}$) given that the expression in Eq. 4.23 is symmetric about $\theta=\pi/2$, provided we double the result. For an integration over $k_{\rm T}$, from $k_{\rm T}^{\rm min}$ to $k_{\rm T}^{\rm max}$, this change of limits is convenient.

The δ-function may be written

$$\delta\left(\hat{s}-2E_k\sqrt{\hat{s}}-M^2\right) = \frac{1}{2\sqrt{\hat{s}}}\,\delta\left(E_k - \frac{\hat{s}-M^2}{2\sqrt{\hat{s}}}\right) \tag{4.30}$$

and so, collecting results so far, one has

$$\begin{aligned}\frac{d\hat{\sigma}}{dM^2} = \hat{\sigma}_0\,\frac{\alpha_{\rm s}}{2\pi}\,\frac{(4\pi\mu^2)^\epsilon}{\Gamma(1-\epsilon)}\,C_{\rm F}\,\frac{1}{M^2}\,\frac{d^{1-\epsilon}k_{\rm T}^2}{k_{\rm T}^2} \\ 2\times\frac{1}{\sqrt{\hat{s}}}\,\frac{M^2+2E_k^2-k_{\rm T}^2-2\,\epsilon\,E_k^2}{\sqrt{E_k^2-k_{\rm T}^2}}\,dE_k\,\delta\left(E_k-\frac{\hat{s}-M^2}{2\sqrt{\hat{s}}}\right).\end{aligned} \tag{4.31}$$

Using the definitions $z := M^2/\hat{s}$ and $\Delta := k_\mathrm{T}^2/M^2$, the argument of the δ-function tells us $E_k = \sqrt{\hat{s}}\,(1-z)/2$ and calls for the replacement

$$\frac{1}{\sqrt{\hat{s}}}\,\frac{M^2 + 2E_k^2 - k_\mathrm{T}^2 - 2\,\epsilon\,E_k^2}{\sqrt{E_k^2 - k_\mathrm{T}^2}} \to \frac{1 + z^2 - 2\,\Delta\,z - \epsilon\,(1-z)^2}{\sqrt{(1-z)^2 - 4\,\Delta\,z}}\,. \tag{4.32}$$

Furthermore, $dE_k = -\sqrt{\hat{s}}\,dz/2$, so changing variables of integration gives us

$$\begin{aligned}\frac{d\hat{\sigma}}{dM^2} = \hat{\sigma}_0\,\frac{\alpha_\mathrm{s}}{2\pi}\,\frac{1}{\Gamma(1-\epsilon)}\left(\frac{4\pi\mu^2}{M^2}\right)^{\epsilon} C_\mathrm{F}\,\frac{1}{M^2}\,\frac{d^{1-\epsilon}\Delta}{\Delta} \\ \times\,2\int dz\,\frac{1 + z^2 - 2\,\Delta\,z - \epsilon\,(1-z)^2}{\sqrt{(1-z)^2 - 4\,\Delta\,z}}\,\delta\left(z - \frac{M^2}{\hat{s}}\right),\end{aligned} \tag{4.33}$$

including the integration over z. It is important to note the limits of the z integration are constrained by demanding a non-zero k_T. The minimum energy carried away by the gluon is k_T. As such, we have the relation

$$\begin{aligned}E_k^{\min} = \sqrt{\hat{s}}\,(1 - z^{\max})/2 = k_\mathrm{T} \\ \Rightarrow z^{\max} = 1 + 2\Delta - 2\sqrt{\Delta(1+\Delta)} \approx 1 - 2\sqrt{\Delta} \qquad \text{for } \Delta \ll 1\,.\end{aligned} \tag{4.34}$$

The lower limit of z is zero.

Finally, the differential hadronic cross-section is, according to the previous analysis of Sec. 4.1, the convolution of the bare PDFs with the partonic cross-section derived above:

$$\frac{d\sigma}{dk_\mathrm{T}^2\,dM^2} = \int_0^1 dx_1 \int_0^1 dx_2\,[\phi_{q/1}(x_1)\,\phi_{\bar{q}/2}(x_2) + q \leftrightarrow \bar{q}]\,\frac{d\hat{\sigma}}{dk_\mathrm{T}^2\,dM^2}\,. \tag{4.35}$$

4.3. The origin of large logarithms

In this section, I adopt certain methods employed in [**61, 62**] in order to determine the low-$Q_{\rm T}$ behaviour in Drell–Yan. Here I work with the integrated distribution, defined by

$$\Sigma(Q_{\rm T}) := \int_0^{Q_{\rm T}^2} \frac{d^2\sigma}{dk_{\rm T}^2\, dM^2}\, dk_{\rm T}^2, \tag{4.36}$$

which is proportional to the number of events with $k_{\rm T} \leq Q_{\rm T}$. Explicitly, taking the results of the previous section, we have

$$\begin{aligned}\Sigma(Q_{\rm T}) = \frac{4\pi\,\alpha^2\,Q_f^2}{3\,N_{\rm c}\,M^2} \int_0^1 dx_1 \int_0^1 dx_2\, [\phi_{q/1}(x_1)\,\phi_{\bar{q}/2}(x_2) + q \leftrightarrow \bar{q}]\, \frac{\alpha_{\rm s}}{2\pi}\, C_{\rm F}\, \frac{1}{\Gamma(1-\epsilon)} \left(\frac{4\pi\mu^2}{M^2}\right)^{\epsilon} \\ \times 2 \int \frac{d^{1-\epsilon}\Delta}{\Delta} \int dz\, \frac{1 + z^2 - 2\,\Delta\,z - \epsilon\,(1-z)^2}{\sqrt{(1-z)^2 - 4\,\Delta\,z}}\, \delta(x_1\,x_2\,s\,z - M^2)\,.\end{aligned} \tag{4.37}$$

Taking moments of Eq. 4.92 with respect to the so-called *Drell–Yan variable* $\tau := M^2/s = x_1\,x_2\,z$—the hadronic equivalent of z—as in

$$\tilde{\Sigma}(N, Q_{\rm T}) := \int_0^1 d\tau\, \tau^{N-1}\, \Sigma(Q_{\rm T})\,, \tag{4.38}$$

decouples the convolution integrals yielding the simple product

$$\begin{aligned}\tilde{\Sigma}(N, Q_{\rm T}) = \tilde{\Sigma}^{(0)}(N)\, \frac{1}{M^2}\, \frac{\alpha_{\rm s}}{2\pi}\, C_{\rm F}\, \frac{1}{\Gamma(1-\epsilon)} \left(\frac{4\pi\mu^2}{M^2}\right)^{\epsilon} \int \frac{d^{1-\epsilon}\Delta}{\Delta} \\ \times 2 \int dz\, z^N \left\{ \frac{1 + z^2 - 2\,\Delta\,z}{\sqrt{(1-z)^2 - 4\,\Delta\,z}} - \frac{\epsilon\,(1-z)^2}{\sqrt{(1-z)^2 - 4\,\Delta\,z}} \right\},\end{aligned} \tag{4.39}$$

where

$$\tilde{\Sigma}^{(0)}(N) = \frac{4\pi\,\alpha^2\,Q_f^2}{3\,N_{\rm c}\,M^2} \left[\tilde{\phi}_{q/1}(N)\,\tilde{\phi}_{\bar{q}/2}(N) + q \leftrightarrow \bar{q}\right] \tag{4.40}$$

and

$$\tilde{\phi}(N) := \int_0^1 dx\, x^N\, \phi(x)\,. \tag{4.41}$$

It is convenient to treat the 'ϵ' part of the integrand separately. Since for this term there is no divergence as $z \to 1$, we may take the upper limit of the integral to be 1 without losing any terms which don't already vanish in the limit $\Delta \to 0$. Furthermore, we can take the limit $\Delta \to 0$ in the denominator, thus

$$\int_0^{z^{\rm max}} dz\, z^N\, \frac{\epsilon\,(1-z)^2}{\sqrt{(1-z)^2 - 4\,\Delta\,z}} \to \epsilon \int_0^1 dz\, z^N\,(1-z)\,. \tag{4.42}$$

The remaining Δ-integral for this term is simply

$$\int_0^{\Delta_{\rm max}} \frac{d^{1-\epsilon}\Delta}{\Delta} = -\frac{\Delta_{\rm max}^{-\epsilon}}{\epsilon} = -\frac{1}{\epsilon} + \log\Delta_{\rm max} + \mathcal{O}(\epsilon) \tag{4.43}$$

and so, in the limit $\epsilon \to 0$, we simply obtain

$$-\int \frac{d^{1-\epsilon}\Delta}{\Delta} \int dz\, z^N \frac{\epsilon\,(1-z)^2}{\sqrt{(1-z)^2 - 4\,\Delta\,z}} \to \int dz\, z^N (1-z)\,. \tag{4.44}$$

Writing z^N as $(z^N-1)+1$ in the first term of the integrand in Eq. 4.39—hence splitting this term into two parts, the first of which contains no divergence as $z \to 1$—results in

$$\begin{aligned}\int \frac{d^{1-\epsilon}\Delta}{\Delta} \int dz\, z^N \, \frac{1+z^2-2\,\Delta\, z}{\sqrt{(1-z)^2-4\,\Delta\, z}} &= \int \frac{d^{1-\epsilon}\Delta}{\Delta} \frac{\gamma_{qq}(N)}{C_{\rm F}} + I \\ &= \frac{\gamma_{qq}(N)}{C_{\rm F}} \left(-\frac{1}{\epsilon} + \log \Delta_{\rm max} \right) + I\end{aligned} \tag{4.45}$$

again using Eq. 4.43, where

$$\gamma_{qq}(N) := C_{\rm F} \int_0^1 dz\, (z^N - 1)\, \frac{1+z^2}{1-z}\,, \tag{4.46}$$

and

$$I = \int \frac{d^{1-\epsilon}\Delta}{\Delta} \int dz\, \frac{1+z^2-2\,\Delta\, z}{\sqrt{(1-z)^2-4\,\Delta\, z}}\,. \tag{4.47}$$

In obtaining $\gamma_{qq}(N)$, the limit $\Delta \to 0$ was taken in the denominator of the z integral and the upper limit on z was taken to 1, again on account of the absence of a divergence as $z \to 1$. In fact, this may be written in terms of the 'plus' prescription as

$$\gamma_{qq}(N) := C_{\rm F} \int_0^1 dz\, z^N \left(\frac{1+z^2}{1-z} \right)_+ \tag{4.48}$$

and, on account of the equivalence

$$\left(\frac{1+z^2}{1-z} \right)_+ \equiv \frac{1+z^2}{(1-z)_+} + \frac{3}{2}\,\delta(1-z) = \frac{P_{qq}(z)}{C_{\rm F}}\,, \tag{4.49}$$

we see that $\gamma_{qq}(N)$ is nothing more than the Nth moment of the regularized quark splitting function.

Finally, the z integral in Eq. 4.47, evaluated between the proper limits, is

$$\begin{aligned}\int_0^{z^{\rm max}} dz\, \frac{1+z^2-2\,\Delta\, z}{\sqrt{(1-z)^2-4\,\Delta\, z}} &= -\frac{3}{2} - \Delta - 2\,(1+\Delta)^2\, \ln\Delta + (1+\Delta)^2\, \ln[\Delta\,(1+\Delta)] \\ &= -\frac{3}{2} - \ln\Delta\,, \qquad \text{in the limit } \Delta \to 0.\end{aligned} \tag{4.50}$$

The limit $\Delta \to 0$ here is sufficient to obtain the logarithmic and constant terms in $\Sigma(Q_{\rm T})$ at small $Q_{\rm T}$. (For that reason the $2\,\Delta\, z$ term might have been ignored in the numerator of the integrand and the effective upper limit $1-2\sqrt{\Delta}$ for the z integral might have been used.) Finally performing the Δ integral over this result gives

$$I = \int_0^{\Delta^{\rm max}} \frac{d^{1-\epsilon}\Delta}{\Delta} \left(-\frac{3}{2} - \ln\Delta \right) = \frac{1}{\epsilon^2} + \frac{3}{2\,\epsilon} - \frac{3}{2} \ln\Delta^{\rm max} - \frac{1}{2} \ln^2 \Delta^{\rm max} \tag{4.51}$$

in the $\epsilon \to 0$ limit.

Since $\Sigma(Q_{\rm T})$ contains contributions from the virtual corrections at $Q_{\rm T} = 0$, we expect the poles in ϵ to cancel between the real and virtual contributions. The (partonic) virtual contribution in Eq. A.104 is proportional to $D(\epsilon)$, given by Eq. A.66. In order to conveniently add in these virtual contributions we first rewrite, in the real part,

$$\frac{1}{\Gamma(1-\epsilon)} = \frac{\Gamma(1-\epsilon)}{\Gamma(1-2\epsilon)} \times \frac{\Gamma(1-2\epsilon)}{\Gamma^2(1-\epsilon)} = \frac{\Gamma(1-\epsilon)}{\Gamma(1-2\epsilon)} \times \left[1 + \epsilon^2 \frac{\pi^2}{6} + \mathcal{O}(\epsilon^3) \right]. \tag{4.52}$$

With this in mind, the real contribution to $\Sigma(Q_{\rm T})$ is

$$\begin{aligned}\tilde{\Sigma}(N,Q_{\rm T}) = \tilde{\Sigma}^{(0)}(N)\,\frac{1}{M^2}\,\frac{\alpha_{\rm s}}{2\pi}\,C_{\rm F}\,D(\epsilon)\\ \times 2\left\{\int_0^1 dz\,z^N\,(1-z) + \frac{\gamma_{qq}(N)}{C_{\rm F}}\left[-\frac{1}{\epsilon}+\ln\left(\frac{Q_{\rm T}^2}{M^2}\right)\right] + \frac{\pi^2}{6}\right.\\ \left. + \frac{1}{\epsilon^2} + \frac{3}{2\,\epsilon} - \frac{3}{2}\ln\left(\frac{Q_{\rm T}^2}{M^2}\right) - \frac{1}{2}\,\ln^2\left(\frac{Q_{\rm T}^2}{M^2}\right)\right\}.\end{aligned} \tag{4.53}$$

Since $\int_0^1 dz\,z^N\,\delta(1-z)=1$, the Mellin transform is trivial to invert[3] and, adding in the virtual piece from Eq. A.104, gives ($\hat{\sigma}_0 = 4\,\pi\,Q_f^2\,\alpha^2/3\,N_{\rm c}\,s$)

$$\begin{aligned}\Sigma(Q_{\rm T}) = \int_0^1 dx_1\int_0^1 dx_2\,[\phi_{q/1}(x_1;\mu)\,\phi_{\bar{q}/2}(x_2;\mu)+q\leftrightarrow\bar{q}]\,\hat{\sigma}_0\,\frac{\alpha_{\rm s}}{2\pi}\,\frac{1}{M^2}\\ \times\,2\int_0^1 dz\left[\ln\left(\frac{M^2}{\mu^2}\right)P_{qq}(z)+R^{\Delta}_{q\bar{q}}(z)\right]\,\delta\left(\frac{M^2}{s}-x_1\,x_2\,z\right)\end{aligned} \tag{4.54}$$

in the limit $\epsilon\to 0$, where

$$\begin{aligned}R^{\Delta}_{q\bar{q}}(z) = C_{\rm F}\left\{\delta(1-z)\left[\left(\frac{\pi^2}{2}-4\right)-\frac{3}{2}\ln\left(\frac{Q_{\rm T}^2}{M^2}\right)-\frac{1}{2}\,\ln^2\left(\frac{Q_{\rm T}^2}{M^2}\right)\right]\right.\\ \left.+\,(1-z)+\frac{P_{qq}(z)}{C_{\rm F}}\,\ln\left(\frac{Q_{\rm T}^2}{M^2}\right)\right\}.\end{aligned} \tag{4.55}$$

The expansion of $D(\epsilon)$, Eq. A.72, has also been used, and the remaining pole term $-(1/\epsilon)\,(4\pi e^{-\gamma_{\rm E}})^{\epsilon}\,\gamma_{qq}(N)$ has been absorbed into the transition function $\tilde{\Gamma}^{\epsilon}_{1,qq}(N)$, rendering the PDFs formally scale-dependent. The single-logarithmic Compton result is [**62**]

$$R^{\Delta}_{qq}(z) = T_{\rm F}\left\{2\,z\,(1-z)+\frac{P_{qg}(z)}{T_{\rm F}}\,\ln\left(\frac{Q_{\rm T}^2}{M^2}\right)\right\}, \tag{4.56}$$

and may be included in $\Sigma(Q_{\rm T})$ above, in a way analogous to Eq. 4.22.

Here I shall comment on the origin of the logarithmic terms. The double log in Eq. 4.54 comes from emission that is both soft *and* collinear. The single log, however, comes solely from hard–collinear emission. In the case of the $Q_{\rm T}$ distribution of Drell-Yan lepton pairs at leading-order—i.e. $\mathcal{O}(\alpha_{\rm s})$—there are no single soft logs, which would be due to soft–'wide-angle' emission. To see that this is the case, one can either show that the single log which appears in Eq. 4.54 comes entirely from hard–collinear emission or, more transparently, one can borrow the result of Eq. 3.8 and (using crossing symmetry) write the *partonic* Drell-Yan cross-section as

$$\begin{aligned}d\hat{\sigma} &= \hat{\sigma}_0\,4\,\pi\,\alpha_{\rm s}\,C_{\rm F}\,\frac{2\,p_1\cdot p_2}{p_1\cdot k\,p_2\cdot k}\,\frac{d^3k}{(2\pi)^3\,2\,\omega}\\ &= 4\,\hat{\sigma}_0\,\frac{\alpha_{\rm s}}{2\pi}\,C_{\rm F}\,\frac{d\omega}{\omega}\,\frac{d\theta}{\sin\theta}\,\frac{d\phi}{2\pi}\,.\end{aligned} \tag{4.57}$$

[3] Using $\int_0^1 d\tau\,\tau^{N-1}\,\delta(z\,x_1\,x_2\,s-M^2) = \frac{1}{M^2}\,x_1^N\,x_2^N\,z^N$

In the second line it has been assumed that the incoming parton momenta p_1 and p_2 are back-to-back, with $\hat{s} = (p_1 + p_2)^2$. In this expression $k = (\omega, \vec{k})$ is the gluon's four-momentum. Introducing the rapidity of the gluon,

$$\eta := \frac{1}{2} \ln \left(\frac{\omega + k_z}{\omega - k_z} \right) = \frac{1}{2} \ln \left(\frac{1 + \cos\theta}{1 - \cos\theta} \right) , \tag{4.58}$$

and its transverse momentum $k_\mathrm{T} = \omega \sin\theta$, we see that $d\omega/\omega = dk_\mathrm{T}/k_\mathrm{T}$ and $d\theta/\sin\theta = d\eta$. We may thus write

$$d\hat{\sigma} = \hat{\sigma}_0 \frac{\alpha_\mathrm{s}}{\pi} C_\mathrm{F} \frac{dk_\mathrm{T}^2}{k_\mathrm{T}^2} d\eta \frac{d\phi}{2\pi} . \tag{4.59}$$

The cross-section for a single soft gluon emission from the back-to-back dipole is therefore uniform in rapidity and azimuth.

If we consider the integrated cross-section $\Sigma(Q_\mathrm{T}) = \int_{Q_\mathrm{T}^2} (d\hat{\sigma}/dk_\mathrm{T}^2)\, dk_\mathrm{T}^2$, the kinematic limits on η are

$$|\eta| \leq \frac{1}{2} \ln \left(\frac{\omega^\mathrm{max} + k_z^\mathrm{max}}{\omega^\mathrm{max} - k_z^\mathrm{max}} \right) . \tag{4.60}$$

Using $\omega^2 = k_\mathrm{T}^2 + k_z^2$, along with $k_\mathrm{T}^\mathrm{min} = Q_\mathrm{T}$ and $\omega^\mathrm{max} = \sqrt{\hat{s}}/2$, one finds in the limit $Q_\mathrm{T} \ll \sqrt{\hat{s}}$ that

$$\eta^\mathrm{max} = \frac{1}{2} \ln \frac{\hat{s}}{k_\mathrm{T}^2} \tag{4.61}$$

Performing the integration over η followed by k_T^2 gives simply

$$\begin{aligned} \Sigma(Q_\mathrm{T}) &= \hat{\sigma}_0 \frac{\alpha_\mathrm{s}}{\pi} C_\mathrm{F} \int_{Q_\mathrm{T}^2} \frac{dk_\mathrm{T}^2}{k_\mathrm{T}^2} \ln \frac{\hat{s}}{k_\mathrm{T}^2} \\ &= \hat{\sigma}_0 \frac{\alpha_\mathrm{s}}{\pi} C_\mathrm{F} \left[\frac{1}{2} \ln^2 \left(\frac{Q_\mathrm{T}^2}{\hat{s}} \right) \right] . \end{aligned} \tag{4.62}$$

We only need to consider the lower limit of k_T^2 to recover the logarithmic enhancement at small Q_T. The upper limit of k_T^2 corresponds to the configuration in which $\eta \to 0$ for the gluon, and so does not give a logarithmically enhanced term.

From this exercise we see that, in the soft limit, we necessarily obtain a double logarithm since the limits on η corresponding to small Q_T are in the collinear region. Hence, our observable is not sensitive to soft-'wide-angle' emission. Conversely, an observable which places a restriction on η, for example gaps-between-jets observables, may result in single soft logarithms associated with wide-angle emission. Introducing an artificial cut-off on η results in

$$\begin{aligned} \hat{\sigma} &= \hat{\sigma}_0 \frac{\alpha_\mathrm{s}}{\pi} C_\mathrm{F} \int_{Q_\mathrm{T}^2} \frac{dk_\mathrm{T}^2}{k_\mathrm{T}^2} \int_{-y}^{y} d\eta \\ &= \hat{\sigma}_0 \frac{\alpha_\mathrm{s}}{\pi} C_\mathrm{F} \left[-2\, y \, \ln Q_\mathrm{T}^2 \right] , \end{aligned} \tag{4.63}$$

which has an enhancement of the form $\alpha_\mathrm{s}\, L$, and the gluon is necessarily emitted into the ('wide-angle') angular region corresponding to $|\eta| < y$. Once again, for the interested reader, non-global observables (of which those involving rapidity gaps between jets are examples) are discussed at length in [**51, 52**].

As a final remark, if one were to have replaced

$$\int dz\,\frac{1+z^2-2\,\Delta\,z}{\sqrt{(1-z)^2-4\,\Delta\,z}} \qquad \text{with} \qquad \int dz\,\frac{\hat{P}(z)}{C_{\rm F}} \tag{4.64}$$

—i.e. the unregularized Altarelli-Parisi splitting function—simultaneously changing the upper limit of z integration from $z_{\rm max}$, defined in Eq. 4.34, to $1-\sqrt{\Delta}$, then one could show that the same *logarithmic* terms are obtained for $\Sigma(Q_{\rm T})$:

$$\int_0^{1-\sqrt{\Delta}} dz\,\frac{1+z^2}{1-z} = -\frac{3}{2} - \ln\Delta\,, \qquad \text{in the limit } \Delta\to 0\,; \tag{4.65}$$

(cf. Eq. 4.50). This is what is done in [**61**].

4.4. Kinematics of ϕ^*

The ϕ^* observable was first introduced in [**15**] and is defined according to

$$\phi^* := \tan\left(\frac{\phi_{\text{acop}}}{2}\right) \sin\theta^* \,. \tag{4.66}$$

The kinematics in the transverse plane are shown in Fig. 4.2. The angle ϕ_{acop} is the *acoplanarity* angle, and is a measure of the deviation from 'back-to-backness' of the two leptons in the transverse plane. The star indicates the frame in which the two leptons were produced back-to-back *longitudinally*, which defines a unique boost from the lab frame. In this frame, θ^* is the angle made by the lepton(s) with respect to the beam axis.

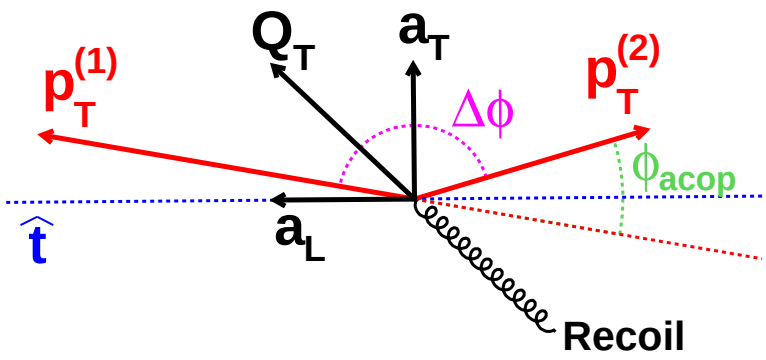

FIGURE 4.2. Kinematics of the ϕ^* observable in the transverse plane [**15**]

The ϕ^* observable clearly probes physics similar to the familiar Q_{T} observable, in that they both measure the recoil of the vector boson (photon and/or Z boson). In the case of Q_{T}, the net transverse momentum of the leptons will become non-zero under recoil, and in the case of ϕ^* the leptons are no longer back-to-back, on account of the recoil. The net transverse momentum $\vec{Q}_{\text{T}} = \vec{p}_{\text{T}}^{(1)} + \vec{p}_{\text{T}}^{(2)}$ may be decomposed into transverse and longitudinal components, labelled a_{T} and a_{L} respectively, relative to the so-called lepton *thrust* axis, which is defined to be the direction

$$\hat{t} = \frac{\vec{p}_{\text{T}}^{(1)} - \vec{p}_{\text{T}}^{(2)}}{\left|\vec{p}_{\text{T}}^{(1)} - \vec{p}_{\text{T}}^{(2)}\right|} \,. \tag{4.67}$$

Thus we have

$$a_{\text{L}} := \vec{Q}_{\text{T}} \cdot \hat{t} = \frac{p_{\text{T}}^{(1)^2} + p_{\text{T}}^{(2)^2}}{\left|\vec{p}_{\text{T}}^{(1)} - \vec{p}_{\text{T}}^{(2)}\right|} \tag{4.68}$$

and

$$a_{\text{T}} := \left|\vec{Q}_{\text{T}} \times \hat{t}\right| = \frac{2\, p_{\text{T}}^{(1)}\, p_{\text{T}}^{(2)}\, \sin\phi_{\text{acop}}}{\left|\vec{p}_{\text{T}}^{(1)} - \vec{p}_{\text{T}}^{(2)}\right|} \tag{4.69}$$

using $\sin(\Delta\phi) = \sin\phi_{\text{acop}}$. The a_{T} observable was originally proposed as a novel way to study the transverse momentum of the Z boson in [**63**]. Indeed, this observable was studied phenomenologically in [**61**].

In the small-$Q_{\rm T}$ limit, both components of the transverse vector $\vec{Q}_{\rm T}$ are small and therefore $\vec{p}_{\rm T}^{(2)} \to -\vec{p}_{\rm T}^{(1)}$. Therefore, in this limit,

$$a_{\rm T} \to p_{\rm T}^{(1)} \sin\phi_{\rm acop}\,. \tag{4.70}$$

In the frame in which the two leptons make the same angle θ^* with respect to the beam line, this angle may be given as

$$\sin\theta^* = \frac{p_{\rm T}^{(1)}}{\left|\vec{p}^{(1)}\right|} = \frac{p_{\rm T}^{(2)}}{\left|\vec{p}^{(2)}\right|}\,. \tag{4.71}$$

Since we have already established $\vec{p}_{\rm T}^{(2)} \approx -\vec{p}_{\rm T}^{(1)}$ in the $Q_{\rm T} \to 0$ limit, we can now also conclude that $\left|\vec{p}^{(2)}\right| = \left|\vec{p}^{(1)}\right|$ in this frame. Finally, for massless $p^{(1)}$ and $p^{(2)}$,

$$\begin{aligned} (p^{(1)}+p^{(2)})^2 &= (|\vec{p}^{(1)}|+|\vec{p}^{(2)}|)^2 - (\vec{p}^{(1)}+\vec{p}^{(2)})^2 = M^2 \\ &\Rightarrow 4\,|\vec{p}^{(1)}|^2 = M^2, \qquad \text{in the limit } Q_{\rm T}\to 0\,. \end{aligned} \tag{4.72}$$

We finally conclude that

$$\sin\theta^* = \frac{2\,p_{\rm T}^{(1)}}{M} \qquad \text{in the limit } Q_{\rm T}\to 0\,. \tag{4.73}$$

As $\phi \to 0$, we have $\tan(\phi/2) \approx \frac{1}{2}\sin\phi$. Therefore

$$\phi^* \approx \frac{p_{\rm T}^{(1)}\,\sin\phi_{\rm acop}}{M} = \frac{a_{\rm T}}{M}\,, \tag{4.74}$$

having used Eqs. 4.73 and 4.70.

By conservation of momentum, $\vec{Q}_{\rm T}$ is balanced by the sum of all recoil emissions:

$$\vec{Q}_{\rm T} = \vec{p}_{\rm T}^{(1)} + \vec{p}_{\rm T}^{(2)} = -\sum_i \vec{k}_{{\rm T}i} \tag{4.75}$$

Picking the origin of the azimuthal angle to be in the direction of $\vec{p}_{\rm T}^{(1)}$, we define the parameterization

$$\vec{p}_{\rm T}^{(1)} = p_{\rm T}^{(1)}(1,0,0) \tag{4.76}$$

$$\text{and} \qquad \vec{k}_{{\rm T}i} = k_{{\rm T}i}\,(\cos\phi_i, \sin\phi_i, 0)\,. \tag{4.77}$$

In the small-$Q_{\rm T}$ limit, $\hat{t} \to \vec{p}_{\rm T}^{(1)}/\left|\vec{p}_{\rm T}^{(1)}\right|$ and so

$$a_{\rm T} = \left|\sum_i k_{{\rm T}i}\,\sin\phi_i\right|\,. \tag{4.78}$$

We have thus derived the kinematical dependence of $a_{\rm T}$ on multiple $k_{\rm T}$ emissions whose vector sum $\vec{Q}_{\rm T}$ remains small.

4.5. The low ϕ^* distribution

In this section we derive the integrated ϕ^* distribution in the low-ϕ^* limit. Since we have already done this in the case of $Q_{\rm T}$, Eqs. 4.54 and 4.55, it turns out we will require only a minimal modification to this result to obtain that for ϕ^*. We already derived an

expression for ϕ^* in the small limit in the previous section, namely

$$\phi^* \approx \frac{a_{\mathrm{T}}}{M} \,. \tag{4.79}$$

We could therefore derive $\Sigma(a_{\mathrm{T}})$, obtaining the equivalent ϕ^* distribution automatically with the replacement $a_{\mathrm{T}}/M \to \phi^*$, but I will proceed directly with $\Sigma(\phi^*)$. The only differences from the calculation for $\Sigma(Q_{\mathrm{T}})$ are that the Δ integration range will change, and the azimuthal integration for the phase space is no longer trivial, on account of the ϕ dependence of ϕ^*.

In fact, the only part of the expression for $\Sigma(Q_{\mathrm{T}})$ that changes is the integral given in Eq. 4.45, since this is the only integral to depend on the Q_{T} kinematics, via the upper limit of integration over Δ—i.e. $\Delta^{\max} = Q_{\mathrm{T}}^2/M^2$. Our attention is initially focused on the integral I (Eq. 4.47). Furthermore, in order to recover the logarithmic terms generated by this integral—which are independent of the other limit of integration—we may equivalently integrate from $\Delta^{\max} = Q_{\mathrm{T}}^2/M^2$ to 1 (introducing an overall minus sign), thus avoiding the singularity at $Q_{\mathrm{T}} = 0$ and allowing us to work in $d = 4$ dimensions.

With one low-k_{T} emission, we have

$$\phi^* = k_{\mathrm{T}} \, \sin\phi / M \,. \tag{4.80}$$

To obtain the logarithms in the $\Sigma(\phi^*)$ distribution, we may therefore perform the Δ integral over the interval $[0, 1]$ and introduce the Heaviside step function $\Theta\big(\sqrt{\Delta}\,|\sin\phi| - \phi^*\big)$ to enforce the lower limit. Restoring the azimuthal phase-space integration and taking the limit $\epsilon \to 0$, we are thus left with the integral (cf. Eq. 4.47)

$$I_{\phi^*} = -\int_0^{2\pi} \frac{d\phi}{2\pi} \int_0^1 \frac{d\Delta}{\Delta} \int_0^{z^{\max}} dz \, \frac{1 + z^2 - 2\,\Delta\, z}{\sqrt{(1-z)^2 - 4\,\Delta\, z}} \, \Theta\big(\sqrt{\Delta}\,|\sin\phi| - \phi^*\big) \,. \tag{4.81}$$

Performing the integration over z as before, with the upper limit $z^{\max} = 1 + 2\Delta - 2\sqrt{\Delta\,(1+\Delta)}$, followed by the integration over Δ—with the Heaviside step-function enforcing a lower limit of $(\phi^*)^2\,|\sin\phi|^2$—one obtains

$$I_{\phi^*} = -\int_0^{2\pi} \frac{d\phi}{2\pi} \left[\frac{3}{2} \ln\left(\frac{(\phi^*)^2}{|\sin\phi|^2} \right) + \frac{1}{2} \ln^2\left(\frac{(\phi^*)^2}{|\sin\phi|^2} \right) \right] . \tag{4.82}$$

Using [**61**]

$$\int_0^{2\pi} \frac{d\phi}{2\pi} \, \ln^2 |\sin\phi| = \ln^2 2 + \frac{\pi^2}{12} \tag{4.83}$$

$$\text{and} \qquad \int_0^{2\pi} \frac{d\phi}{2\pi} \, \ln |\sin\phi| = -\ln 2 \,, \tag{4.84}$$

this becomes

$$I_{\phi^*} = -3 \, \ln(2\,\phi^*) - 2 \, \ln^2(2\,\phi^*) - \frac{\pi^2}{6} \,. \tag{4.85}$$

Therefore, the low-ϕ^* limit of the integrated ϕ^* distribution differs from that of the Q_{T} distribution via the replacement $Q_{\mathrm{T}} \to 2\,M\,\phi^*$ and the addition of a single constant term. Equivalently, we also have the low-a_{T} integrated distribution $\Sigma(a_{\mathrm{T}})$, since $a_{\mathrm{T}} \approx M\,\phi^*$ in this limit. This result should be compared with the finite part of Eq. 4.51 in the $\epsilon \to 0$ limit.

In addition, the integral containing the anomalous dimension $\gamma_{qq}(N)$ in Eq. 4.45 becomes

$$\int \frac{d\phi}{2\,\pi}\,\frac{\gamma_{qq}(N)}{C_{\rm F}}\left(-\frac{1}{\epsilon}+\log\Delta_{\rm max}\right)=\frac{\gamma_{qq}(N)}{C_{\rm F}}\left(-\frac{1}{\epsilon}+2\,\log(2\,\phi^*)\right)\,. \tag{4.86}$$

The final result, cf. Eqs. 4.54 and 4.55, is then

$$\begin{aligned}\Sigma(\phi^*)=\int_0^1 dx_1\int_0^1 dx_2\,\left[\phi_{q/1}(x_1;\mu)\,\phi_{\bar{q}/2}(x_2;\mu)+q\leftrightarrow\bar{q}\right]\hat{\sigma}_0\,\frac{\alpha_{\rm s}}{2\pi}\,\frac{1}{M^2}\\ \times\,2\int_0^1 dz\left[\ln\left(\frac{M^2}{\mu^2}\right)P_{qq}(z)+R^{\Delta}_{q\bar{q}}(z)\right]\,\delta\left(\frac{M^2}{s}-x_1\,x_2\,z\right)\end{aligned} \tag{4.87}$$

where

$$\begin{aligned}R^{\Delta}_{q\bar{q}}(z)=C_{\rm F}\Bigg\{&\delta(1-z)\left[\left(\frac{\pi^2}{3}-4\right)-3\ln\left(2\,\phi^*\right)-2\,\ln^2\left(2\,\phi^*\right)\right]\\ &+(1-z)+2\,\frac{P_{qq}(z)}{C_{\rm F}}\,\ln\left(2\,\phi^*\right)\Bigg\}\,.\end{aligned} \tag{4.88}$$

4.6. Logarithmic structure of observables

For observables that are sensitive to both soft and collinear emissions, one expects that double large logarithms will appear for each emission. Since each emission is associated with a single power of the coupling, such observables will have, at maximum, terms of the form $(\alpha_{\rm s}\,L^2)^n$ appearing at the nth order in perturbation theory. The effective coupling is no longer the relatively small $\alpha_{\rm s}$, but rather $\alpha_{\rm s}\,L^2$, where L is the large logarithm, which may be in the ratio of two disparate mass scales, e.g. $Q_{\rm T}/M$, or in a small dimensionless quantity, e.g. ϕ^*.

The general partonic structure for such *double log* observables is

$$\begin{aligned}\hat{\Sigma}(\phi^*)=C_{00}&+\alpha_{\rm s}\left(C_{12}\,L^2+C_{11}\,L+C_{10}\right)\\ &+\alpha_{\rm s}^2\left(C_{24}\,L^4+C_{23}\,L^3+C_{22}\,L^2+C_{21}\,L+C_{20}\right)\\ &+\alpha_{\rm s}^3\left(C_{36}\,L^6+C_{35}\,L^5+C_{34}\,L^4+C_{33}\,L^3+\ldots\right)\\ &+\ldots\,,\end{aligned} \tag{4.89}$$

where the 'C_{ij}'s are perturbative coefficients with the potentially large logarithms factored out, and are assumed not to spoil the perturbative expansion by themselves. Here, $C_{00}\propto\delta(\phi^*)$. It is clear that, on account of the large logarithm L negating the smallness of $\alpha_{\rm s}$ at each order, a truncation of this perturbation series is rendered invalid.

The ϕ^* observable we have resummed, as is the case for all recursively infrared-safe (rIRC-safe) observables [**21**], satisfies a property known as *exponentiation*, which means one can define a resummed exponent R such that e^R essentially encapsulates the effect of resumming the logarithmic enhancements due to soft–collinear emissions to all orders; of course, that these terms may be expressed in the compact form of e^R is highly non-trivial, and requires stringent relationships between the 'C_{ij}'s. Supplemented with appropriate constant terms to the desired accuracy, the ϕ^* integrated cross-section may be written

schematically as

$$\Sigma(\phi^*) \propto \big(1 + C(\alpha_{\rm s})\big)\, e^{R(L;\alpha_{\rm s})} \tag{4.90}$$

with the resummed exponent given by

$$R(L;\alpha_{\rm s}) = L\, g_1(\alpha_{\rm s}\, L) + g_2(\alpha_{\rm s}\, L) + \frac{\alpha_{\rm s}}{\pi}\, g_3(\alpha_{\rm s}\, L) + \ldots \tag{4.91}$$

The leading logarithmic (LL) terms are generated from $L\, g_1(\alpha_{\rm s}\, L)$, the next-to-leading logarithmic (NLL) terms from $g_2(\alpha_{\rm s}\, L)$, the next-to-next-to-leading logarithmic (NNLL) terms from $\alpha_{\rm s}\, g_3(\alpha_{\rm s}\, L)/\pi$, etc. Reorganizing the sum in Eq. 4.89 into this form, by exploiting various factorization properties of gluonic emissions in certain kinematical régimes, is what we call *resummation*.

4.7. Summation to all orders

The resummation of ϕ^* presented in this section follows closely that of $a_{\rm T}$, owing to their simple relation in the small ϕ^* limit, namely Eq. 4.79. I have reproduced much of the discussion originally given in [**61**] here for the purposes of pedagogy. However, in this section—and related appendices—I provide some additional discussion for the reader, along with certain proofs concerning the derivation. The resummed calculation of ϕ^* was originally presented in [**16**].

In order to perform the all-orders resummation of the logarithmically divergent terms, we consider the integrated cross-section defined by

$$\Sigma(v) := \int_0^v \frac{d^2\sigma}{dv'\, dM^2}\, dv', \tag{4.92}$$

where v is the observable under consideration: the transverse momentum of the lepton pair ($Q_{\rm T}$), the component of $\vec{Q}_{\rm T}$ perpendicular to the lepton thrust axis ($a_{\rm T}$), or ϕ^*. The case of ϕ^* will be discussed specifically, making reference to the cases of $Q_{\rm T}$ and/or $a_{\rm T}$ along the way, to compare the similarities and contrast the differences.

In the Born approximation, one has the equality

$$M^2 = \hat{s} = s\, x_1\, x_2, \tag{4.93}$$

with M^2 the invariant mass of the lepton pair, s the scattering energy in the centre-of-momentum system ($\hat{s}$ being that of the partonic system) and $x_{1,2}$ the momentum fractions of partons 1 and 2 that initiated the process. The first equality no longer holds when additional radiation is associated with the process. For this reason the energy fraction z_i is introduced, which is the fractional energy carried forth by an initial parton after the ith emission, with respect to its energy immediately before this emission. After n emissions, one therefore has

$$z = \prod_{i=1}^{n} z_i\,, \tag{4.94}$$

the fraction of energy remaining in the initial partons after all emissions occurred, and so $M^2/\hat{s} = z$.

As before, we work with Mellin moments of the integrated distribution, with respect to $\tau := M^2/s$ (see Eq. 4.38). Our concern here is with the logarithmically enhanced terms

in the low-ϕ^* limit, so we take as our starting point (cf. Eq. 4.39 in the limit $d = 4$):

$$\begin{aligned}\tilde{\Sigma}(\phi^*, N) = \tilde{\Sigma}^{(0)}(N)\frac{1}{M^2}\int \frac{dk_{\mathrm{T}}^2}{k_{\mathrm{T}}^2}\int \frac{d\phi}{2\pi}\int dz\, z^N \\ \times \frac{\alpha_{\mathrm{s}}(k_{\mathrm{T}}^2)}{2\pi}\, 2\,\hat{P}_{qq}(z)\,\Theta\left(\phi^* - \left|\frac{k_{\mathrm{T}}\,\sin\phi}{M}\right|\right).\end{aligned} \tag{4.95}$$

for a single real emission in the annihilation sub-process. In this expression, $\hat{P}_{qq}(z)$ is the unregularized *Altarelli–Parisi* splitting function [**53**], i.e.

$$\hat{P}_{qq}(z) = C_{\mathrm{F}}\,\frac{1+z^2}{1-z}\,. \tag{4.96}$$

Furthermore, a Heaviside step-function has been introduced in order to limit the integral over k_{T} to only those values which contribute to the integrated distribution up to the value of ϕ^* we are considering. This greatly simplifies the extension to multiple real gluon emissions. The upper limit on z is still $z^{\max} = 1 - k_{\mathrm{T}}/M$, as in Eq. 4.65. The factor of two that multiplies $\hat{P}_{qq}(z)$ is to account for the fact that both incoming partons radiate. The running coupling, evaluated at the scale of k_{T}^2 for the emission, has also been used. Finally, the azimuthal integration has been retained since our observable depends upon it.

The integral over k_{T}^2 in Eq. 4.95 diverges in the limit $k_{\mathrm{T}}^2 \to 0$, and so we may introduce a lower limit of Q_0^2 as a cutoff. We can therefore introduce scale-dependent PDFs in $\Sigma^{(0)}(N)$ and consider all emissions with $k_{\mathrm{T}} < Q_0$ to be included in the PDFs. We therefore write explicitly

$$\tilde{\Sigma}^{(0)}(N, Q_0^2) = \frac{4\,\pi\,\alpha^2\,Q_f^2}{3\,N_{\mathrm{c}}\,M^2}\left[\tilde{\phi}_{q/1}(N, Q_0^2)\,\tilde{\phi}_{\bar{q}/2}(N, Q_0^2) + q \leftrightarrow \bar{q}\right], \tag{4.97}$$

which replaces $\tilde{\Sigma}^{(0)}(N)$ used in Eq. 4.95 (i.e. that given in Eq. 4.40) in the case where we regulate the k_{T}^2 integral. Using the DGLAP evolution equation for the PDFs (Eq. 3.59) we can now evolve $\tilde{\Sigma}^{(0)}(N, Q_0^2)$ from Q_0^2 to the hard scale of the process under consideration, namely M^2—the invariant mass of the lepton pair. Thus we have

$$\tilde{\Sigma}^{(0)}(N, Q_0^2) = \tilde{\Sigma}^{(0)}(N, M^2)\,\exp\left[-2\int_{Q_0^2}^{M^2}\frac{dk_{\mathrm{T}}^2}{k_{\mathrm{T}}^2}\,\frac{\alpha_{\mathrm{s}}(k_{\mathrm{T}}^2)}{2\pi}\,\gamma_{qq}\big(N, \alpha_{\mathrm{s}}(k_{\mathrm{T}}^2)\big)\right]. \tag{4.98}$$

This expression will prove useful later, since its exponential form will work seamlessly with the exponentiated form of the all-order resummation. Eventually we will take the limit $Q_0^2 \to 0$, such that all emissions are taken account of by our resummation. Just for now, we proceed using the scale-independent $\tilde{\Sigma}^{(0)}(N)$.

Eq. 4.95 generalizes, under the approximation of multiple independent *real* gluon emissions, to

$$\tilde{\Sigma}(\phi^*, N) = \tilde{\Sigma}^{(0)}(N)\,\frac{1}{M^2}\,W_N^{\mathrm{real}}(\phi^*), \tag{4.99}$$

where

$$\begin{aligned}W_N^{\mathrm{real}}(\phi^*) = \sum_{n=0}^{\infty}\frac{1}{n!}\prod_{i=1}^{n}\int\frac{dk_{\mathrm{T}i}^2}{k_{\mathrm{T}i}^2}\int\frac{d\phi_i}{2\pi}\int dz_i\, z_i^N \\ \times\frac{\alpha_{\mathrm{s}}(k_{\mathrm{T}i}^2)}{2\pi}\,2\,\hat{P}_{qq}(z_i)\,\Theta\left(\phi^* - \left|\sum_i\frac{k_{\mathrm{T}i}\,\sin\phi_i}{M}\right|\right).\end{aligned} \tag{4.100}$$

In this expression, the probability for n gluons to be emitted is approximated by the probability of one gluon to be emitted to the nth power. The probability for an arbitrary number of gluons to be emitted then becomes a sum over all probabilities from $n = 0$ to ∞ gluons to be emitted. The $n!$ factor in the denominator serves to remove multiple-counting of final states which are degenerate under the exchange of identical gluons. What we observe as a result is the exponential series and, for this reason, the gluon emissions are said to *exponentiate*.

At this point, the reader will no doubt want further explanation as to why we may treat the successive emission of gluons, fundamentally quantum in nature, as simply probabilistic in this multiplicative manner. We can consider the *leading logarithmic* behaviour to motivate this argument: We have seen in Sec. 3.2 that soft gluons emitted at widely disparate angular scales are emitted effectively *independently* (i.e. one recovers factorization of the emissions at the level of the *squared amplitude*). This phenomenon owes itself to *coherence*, and amounts to the vanishing of the second *correlated* (non-Abelian) term in

$$|\mathcal{M}_2(k_1, k_2)|^2 = |\mathcal{M}_1(k_1)|^2 \, |\mathcal{M}_1(k_2)|^2 + |\overline{\mathcal{M}_2}(k_1, k_2)|^2 \tag{4.101}$$

where $\mathcal{M}_1$ and $\mathcal{M}_2$ are the matrix elements for one- and two-gluon production respectively, and $\overline{\mathcal{M}_2}$ denotes the correlation.

The leading logarithmic behaviour associated with a given emission is double logarithmic: one logarithm if the emission is soft, and another if the emission is collinear. The leading behaviour is recovered when each emission becomes successively 'much more collinear' (to the emitter) than the previous one, for then we obtain the collinear logarithmic enhancement at each order. This is emphasized in Sec. 3.3 by way of explicit calculation. For emissions that were equal in energy, this would immediately translate into a disparity between the angular scales at which the gluons were successively emitted. In the soft limit, which is also necessary to obtain the *leading* behaviour at each order, this subsequently results in the relative independence of emissions, by the vanishing of $|\overline{\mathcal{M}_2}|^2$. Thus we have motivated Eq. 4.100 to extract the leading logarithmic enhancements to all orders.

For the case of strictly *hard* collinear gluons, Sec. 3.3 demonstrates the k_{T}-ordering required in order to recover the leading logarithmic enhancements to all orders: this time *single* logarithms. Interference (or squared) terms involving amplitudes in which the strict k_{T}-ordering is violated, even for a single emission, are suppressed relative to the leading terms. One essentially 'drops' a logarithm each time this should occur, but such considerations become important for a correct treatment of sub-leading logs. The single collinear logarithms, in our framework, are identified as formally NLL. We have already noted that our continuously global observables Q_{T} and ϕ^* are not sensitive to the dynamics of soft gluons emitted at wide angles (see end of Sec. 4.3).

If we work to NLL accuracy, a subtlety arises. At $\mathcal{O}(\alpha_{\mathrm{s}})$ the double (soft and collinear) log is $\alpha_{\mathrm{s}} L^2$, and the single log is $\alpha_{\mathrm{s}} L$. When we consider two emissions, however, the single logs at $\mathcal{O}(\alpha_{\mathrm{s}}^2)$ are $\alpha_{\mathrm{s}}^2 L^2$. This means that, to NLL accuracy, we need to include also the $\mathcal{O}(\alpha_{\mathrm{s}}^2)$ correction to the double-log term for single gluon emission—a term which is formally

NLL. The NLO splitting function [**64**], retaining only the soft ($z \to 1$) contribution to the NLO correction, is

$$\hat{P}_{qq}(z) = C_{\mathrm{F}} \frac{1+z^2}{1-z} \left(1 + \frac{\alpha_{\mathrm{s}}}{2\pi} K\right) , \tag{4.102}$$

with

$$K = C_{\mathrm{A}} \left(\frac{67}{18} - \frac{\pi^2}{6}\right) - \frac{5}{9} N_{\mathrm{F}} . \tag{4.103}$$

Alternatively, one may use the LO splitting function, but in the so-called *Bremsstrahlung* scheme [**65**] for the running coupling, given as

$$\alpha_{\mathrm{s}}^{\mathrm{CMW}}(k_{\mathrm{T}}^2) = \alpha_{\mathrm{s}} \left(1 + \frac{\alpha_{\mathrm{s}}(k_{\mathrm{T}}^2)}{2\pi} K\right) , \tag{4.104}$$

where $\alpha_{\mathrm{s}}(k_{\mathrm{T}}^2)$ is defined in the $\overline{\mathrm{MS}}$ scheme. With all these considerations, we have an expression for the emission of up to an infinite number of gluons correct to NLL. For the interested reader, this final subtlety, which has its origins in correlated two-gluon emissions and which is intimately linked to the running coupling, is explained in greater detail in [**50**] (Sec. 2.2). The reader may also find [**42**] useful for explicit calculations involving soft gluon emissions. The extension of the above arguments to NNLL accuracy is, in terms of explaining the esoteric details, beyond the scope of this thesis. The NNLL results we use in our phenomenology are taken from the literature, and are documented with appropriate references in Chap. 5.2. However, for a discussion of the considerations that must be made in order to extend the picture of independent emission to NNLL accuracy, the reader is again referred to [**50**].

So far the factorization is not yet complete, for we also require factorization of the phase space. All that is required is to factorize the Heaviside step-function, which may be achieved using an integral representation in *impact parameter* space (the Fourier conjugate of transverse momentum) as in

$$\Theta\left(\phi^* - \left|\sum_i \frac{k_{\mathrm{T}i} \sin\phi_i}{M}\right|\right) = \frac{2}{\pi} \int_0^\infty \frac{db}{b} \sin\left(b\, M\, \phi^*\right) \prod_{i=1}^{n} e^{i\, b\, k_{\mathrm{T}i} \sin\phi_i / M} , \tag{4.105}$$

where the real part of the RHS is implicitly assumed. To see why this is true, the reader is referred to Appendix B.1. We pause at this point to consider the Q_{T} distribution.

So far every consideration has been identical to the case of Q_{T} *except* the kinematics which are encapsulated, for the integrated distribution, in the Θ-function. It pays however to consider the *differential* Q_{T} distribution: $d\sigma/dQ_{\mathrm{T}}$. The kinematics are fixed by a momentum conserving δ function, which balances the boson Q_{T} against an arbitrary number of recoil emissions, and which may be written in terms of an integral representation:

$$\begin{aligned}
\delta\left(\mathbf{Q}_{\mathrm{T}} - \sum_i \mathbf{k}_{\mathrm{T}i}\right) &= \frac{1}{(2\pi)^2} \int_{-\infty}^{\infty} d^2\mathbf{b} \exp\left[i\, \mathbf{b} \cdot \left(\mathbf{Q}_{\mathrm{T}} - \sum_i \mathbf{k}_{\mathrm{T}i}\right)\right] \\
&= \frac{1}{(2\pi)^2} \int_0^\infty b\, db \int_0^{2\pi} d\phi\, e^{i\, b\, Q_{\mathrm{T}} \cos\phi} \prod_i e^{-i\, b\, k_{\mathrm{T}i} \cos\phi_i} \\
&= \frac{1}{2\pi} \int_0^\infty b\, db\, J_0(b\, Q_{\mathrm{T}}) \prod_i e^{-i\, b\, k_{\mathrm{T}i} \cos\phi_i} .
\end{aligned} \tag{4.106}$$

In the last line,

$$\int_0^{2\pi} e^{i\,a\,\cos\phi}\,d\phi = 2\pi\,J_0(|a|)\,, \tag{4.107}$$

for $a \in \mathbb{R}$, has been used, where J_0 is a Bessel function of the first kind. Furthermore, $\mathbf{Q}_{\rm T}$, $\mathbf{k}_{{\rm T}i}$ and $\mathbf{b}$ are the *two-dimensional* vectors whose moduli are $Q_{\rm T}$, $k_{{\rm T}i}$ and b respectively. To employ the equivalent kinematic constraint in the integrated distribution $\Sigma(Q_{\rm T}) = \int_0^{Q_{\rm T}} (d\sigma/dQ_{\rm T}'^{\,2})\,dQ_{\rm T}'^{\,2}$, we may use the result

$$\int_0^{Q_{\rm T}} Q_{\rm T}'\,J_0(b\,Q_{\rm T}')\,dQ_{\rm T}' = \frac{Q_{\rm T}\,J_1(b\,Q_{\rm T})}{b}\,. \tag{4.108}$$

In either case, we find the crucial difference between the two distributions to be the presence of either a Bessel function or a trigonometric function. For the differential distributions, this difference results in a plateau for ϕ^* where one would observe a Sudakov peak in the case of $Q_{\rm T}$.

Returning now to ϕ^*, with the additional factorization of the phase space, we have for Eq. 4.100,

$$\begin{aligned} W_N^{\rm real}(\phi^*) &= \frac{2}{\pi}\int_0^\infty \frac{db}{b}\,\sin(b\,M\,\phi^*) \\ &\qquad \times \left\{ \sum_{n=0}^{\infty} \frac{1}{n!} \prod_{i=1}^{n} \int \frac{dk_{{\rm T}i}^2}{k_{{\rm T}i}^2} \int \frac{d\phi_i}{2\pi} \int dz_i\, z_i^N \right. \\ &\qquad\qquad \left. \times\, \frac{\alpha_{\rm s}(k_{{\rm T}i}^2)}{2\pi}\,2\,\hat{P}_{qq}(z_i)\,e^{i\,b\,k_{{\rm T}i}\,\sin\phi_i/M} \right\} \\ &= \frac{2}{\pi}\int_0^\infty \frac{db}{b}\,\sin(b\,M\,\phi^*)\,e^{\bar{R}(b)}\,. \end{aligned} \tag{4.109}$$

In the final equality the infinite sum has been evaluated, yielding simply the exponential function.

The next step is to include the appropriate virtual corrections to all orders since, until now, we have only considered independent *real* emission. These contributions do not change the kinematics, and so are independent of both the Mellin moments with respect to the kinematic variable z_i, and also of the impact parameter b. Unitarity arguments [**50**] may be invoked to see that the virtual corrections have the same form as the real corrections in the infrared limit (up to a minus sign). The resummed exponent, often known as the *radiator*, becomes, with real and virtual corrections to all orders at NLL accuracy,

$$\bar{R}(b) \to -R(b) = \int \frac{dk_{\rm T}^2}{k_{\rm T}^2} \int \frac{d\phi}{2\pi} \int dz\,\frac{\alpha_{\rm s}(k_{\rm T}^2)}{2\pi}\,2\,\hat{P}_{qq}(z)\,\left(z^N\,e^{i\,b\,k_{\rm T}\,\sin\phi/M} - 1\right) \tag{4.110}$$

Note the convention of the minus sign.

We now briefly discuss the upper limit on the z integration. Since we consider the integrated distribution $\Sigma(\phi^*)$ in the small-ϕ^* limit, we may set our upper limit of the $k_{\rm T}^2$ integral to be M^2, since the Θ-function introduced in Eq. 4.95 has already effected the upper cutoff at the relevant value of $Q_{\rm T}^2$. Furthermore, if we set the lower limit of the $k_{\rm T}^2$ integral to be Q_0^2 and use $\tilde{\Sigma}^{(0)}(N, Q_0^2)$ in place of $\tilde{\Sigma}^{(0)}(N)$—thereby relegating all emissions

with $k_{\rm T}^2 < Q_0^2$ to be included in *scale dependent* PDFs—we may use Eq. 4.98 to write

$$\tilde{\Sigma}(\phi^*, N) = \tilde{\Sigma}^{(0)}(N, M^2)\,\frac{1}{M^2}\,\frac{2}{\pi}\int_0^\infty \frac{db}{b}\,\sin(b\,M\,\phi^*)\,e^{-R(b)} \tag{4.111}$$

where

$$\begin{aligned} -R(b) = 2\int_{Q_0^2}^{M^2}\frac{dk_{\rm T}^2}{k_{\rm T}^2}\,\frac{\alpha_{\rm s}(k_{\rm T}^2)}{2\pi}\int\frac{d\phi}{2\pi}\Bigg\{\int dz\,\hat{P}_{qq}(z)\left(z^N\,e^{i\,b\,k_{\rm T}\,\sin\phi/M}-1\right) \\ -\gamma_{qq}\left(N,\alpha_{\rm s}(k_{\rm T}^2)\right)\Bigg\} \end{aligned} \tag{4.112}$$

is a modified form of the radiator. This expression henceforth replaces the expression for $\tilde{\Sigma}(\phi^*, N)$ originally presented in Eq. 4.99, having now taken into consideration the above analysis.

The explicit z integral in this expression has an upper limit $z_{\rm max}$, however the implicit z integration in the definition of the anomalous dimension, Eq. 4.48, has an upper limit of 1. Notwithstanding, the entire expression may be simplified as

$$\begin{aligned} &\int_0^{z_{\rm max}} dz\,\hat{P}_{qq}(z)\left(z^N\,e^{i\,b\,k_{\rm T}\,\sin\phi/M}-1\right)-\gamma_{qq}(N) \\ &\qquad = \int_0^{z_{\rm max}} dz\,z^N\,\hat{P}_{qq}(z)\left(e^{i\,b\,k_{\rm T}\,\sin\phi/M}-1\right)+\mathcal{O}\left(\frac{k_{\rm T}}{M}\right), \end{aligned} \tag{4.113}$$

where the $\mathcal{O}(k_{\rm T}/M)$ terms may be neglected in our approximation.

We now make the approximation, valid to NNLL accuracy [**66**],

$$1-e^{i\,b\,k_{\rm T}\,\sin\phi/M} \approx \Theta\left(\left|\frac{k_{\rm T}\,\sin\phi}{M}\right|-\frac{1}{\bar{b}}\right), \tag{4.114}$$

derived[4] in Appendix B.4, where $\bar{b} = b\,e^{\gamma_{\rm E}}$ and $\gamma_{\rm E}$ is the Euler–Mascheroni constant. Again, the real part of the LHS is assumed. Since this sets a lower limit on the $k_{\rm T}$ integration, we may now safely take $Q_0 \to 0$. Thus, we have truly started with PDFs with no prior emission, and we are providing the full evolution with our resummation. The radiator now stands at

$$R(b) = 2\int_0^{M^2}\frac{dk_{\rm T}^2}{k_{\rm T}^2}\,\frac{\alpha_{\rm s}(k_{\rm T}^2)}{2\,\pi}\int\frac{d\phi}{2\,\pi}\int_0^{z_{\rm max}} dz\,z^N\,\hat{P}_{qq}(z)\,\Theta\left(k_{\rm T}-\frac{M}{\bar{b}\,|\sin\phi|}\right). \tag{4.115}$$

As in Section 4.3, we split the z integration into two parts as

$$\begin{aligned} \int_0^{z_{\rm max}} dz\,z^N\,\hat{P}_{qq}(z) &= \int_0^{z_{\rm max}} dz\,\hat{P}_{qq}(z)+\int_0^{z_{\rm max}} dz\,(z^N-1)\,\hat{P}_{qq}(z) \\ &\approx C_{\rm F}\left(-\frac{3}{2}-\ln\Delta\right)+\gamma_{qq}(N) \end{aligned} \tag{4.116}$$

where the upper limit $z_{\rm max} \to 1$ on the second z integral has been taken, yielding $\gamma_{qq}(N)$, and the final expression has been expanded about $\Delta = 0$. The reader is encouraged to consult the text surrounding Eqs. 4.50 and 4.65 for evaluating the first integral of the

[4] I offer a simplified derivation where I demonstrate it to be formally accurate to NLL.

splitting function between the appropriate limits. The radiator therefore becomes

$$\begin{aligned} R(b) &= 2C_{\rm F} \int \frac{d\phi}{2\,\pi} \int_0^{M^2} \frac{dk_{\rm T}^2}{k_{\rm T}^2} \, \frac{\alpha_{\rm s}(k_{\rm T}^2)}{2\,\pi} \left(-\frac{3}{2} - \ln \Delta + \frac{\gamma_{qq}(N)}{C_{\rm F}} \right) \Theta \left(k_{\rm T} - \frac{M}{\bar{b}\,|\sin\phi|} \right) \\ &= \int \frac{d\phi}{2\,\pi} \, \tilde{R}(b) \end{aligned} \tag{4.117}$$

with

$$\tilde{R}(b) = \int_0^M dk_{\rm T} \, I(k_{\rm T}) \, \Theta \left(k_{\rm T} - \frac{M}{\bar{b}\,|\sin\phi|} \right) , \tag{4.118}$$

thus defining $I(k_{\rm T})$. I now make a short digression regarding the logarithmic expansion of $R(b)$, which will serve to facilitate the evaluation of terms of a specific logarithmic accuracy, and also help us deal with the residual azimuthal dependence. Performing a series expansion in powers of $\ln|\sin\phi|$ about $|\sin\phi| = 1$ for the integrand, as in [**61**], using

$$\Theta \left(k_{\rm T} - \frac{M}{\bar{b}\,|\sin\phi|} \right) = \Theta \left(k_{\rm T} - \frac{M}{\bar{b}} \right) + \frac{M}{\bar{b}} \, \delta \left(k_{\rm T} - \frac{M}{\bar{b}} \right) \ln|\sin\phi| \, , \tag{4.119}$$

one obtains

$$\begin{aligned} R(b) &= \tilde{R}(b; |\sin\phi| = 1) + \frac{M}{\bar{b}} \int \frac{d\phi}{2\,\pi} \int_0^M dk_{\rm T} \, I(k_{\rm T}) \, \delta \left(k_{\rm T} - \frac{M}{\bar{b}} \right) \ln|\sin\phi| \\ &= \tilde{R}(b; |\sin\phi| = 1) + \frac{M}{\bar{b}} \, I \left(\frac{M}{\bar{b}} \right) \int \frac{d\phi}{2\,\pi} \, \ln|\sin\phi| \, . \end{aligned} \tag{4.120}$$

However, changing the variable of integration in $\tilde{R}(b; |\sin\phi| = 1)$ to $x = M\,k_{\rm T}$, such that

$$\tilde{R}(b; |\sin\phi| = 1) = \int_{M/\bar{b}}^M dk_{\rm T} \, I(k_{\rm T}) = M \int_1^{\bar{b}} \frac{dx}{x^2} \, I \left(\frac{M}{x} \right) , \tag{4.121}$$

one sees that, upon differentiating with respect to $\ln\bar{b}$,

$$\bar{b} \, \frac{\partial}{\partial \bar{b}} \tilde{R}(b; |\sin\phi| = 1) = \frac{M}{\bar{b}} \, I \left(\frac{M}{\bar{b}} \right) . \tag{4.122}$$

One may rather therefore write Eq. 4.120 as

$$R(b) = \tilde{R}(b; |\sin\phi| = 1) + \frac{\partial}{\partial \ln \bar{b}} \tilde{R}(b; |\sin\phi| = 1) \int \frac{d\phi}{2\,\pi} \, \ln|\sin\phi| \, . \tag{4.123}$$

Since the second term contains a logarithmic derivative, each logarithm in $\tilde{R}(b; |\sin\phi| = 1)$ becomes further suppressed by one power relative to $\alpha_{\rm s}$. Thus, in this second term, $\tilde{R}(b; |\sin\phi| = 1)$ may be replaced by its super-leading form; i.e. if $\tilde{R}(b; |\sin\phi| = 1)$ is already accurate to NLL, one may simply use the LL version.

The anomalous dimension may be dropped from the radiator if one simultaneously uses PDFs at the relevant scale, this time $1/\bar{b}$. Performing the final integration over $k_{\rm T}$ in the expression for $R(b)$, using the running coupling appropriately converted into the $\overline{\rm MS}$ scheme, one obtains

$$R(b) = L \, g_1(\alpha_{\rm s} \, L) + g_2(\alpha_{\rm s} \, L) + \ldots \tag{4.124}$$

where $L = \ln\left(\bar{b}^2 \, M^2\right)$. The explicit calculation for g_1 follows: Working to LL accuracy, we start with

$$R_{\rm LL}(b) = 2\,C_{\rm F} \int_{1/\bar{b}^2}^{M^2} \frac{dk_{\rm T}^2}{k_{\rm T}^2} \, \frac{\alpha_{\rm s}(k_{\rm T}^2)}{2\,\pi} \, \ln \frac{M^2}{k_{\rm T}^2} \, . \tag{4.125}$$

Here we are considering simply $R(b;|\sin\phi|=1)$ of Eq. 4.117 (the azimuthal dependence is sub-leading) and only the terms in its integrand that would give leading logs according to our definition; i.e. we only require the $\log\Delta$ term. Using the one-loop expression for the running coupling in Eq. 2.59—the difference between the $\overline{\rm MS}$ and CMW schemes does not play a rôle here—and writing $\Delta = k_{\rm T}^2/M^2$, we have

$$R_{\rm LL}(b) = -\frac{C_{\rm F}}{\pi\,\beta_0}\int_{1/(M\bar{b})^2}^{1}\frac{d\Delta}{\Delta}\,\frac{\bar{\alpha_{\rm s}}\,\beta_0\,\ln\Delta}{1+\bar{\alpha_{\rm s}}\,\beta_0\,\ln\Delta} \tag{4.126}$$

where $\bar{\alpha_{\rm s}} = \alpha_{\rm s}(M^2)$. Performing the integration and defining $\lambda = \bar{\alpha_{\rm s}}\,\beta_0\,L$ and $L = \ln\left(\bar{b}^2\,M^2\right)$, we have

$$L\,g_1 = R_{\rm LL}(b) = L\,\frac{C_{\rm F}}{\pi\,\beta_0}\,\frac{-\lambda-\ln(1-\lambda)}{\lambda}\,. \tag{4.127}$$

A similar exercise, considering terms in the radiator which give rise to single logarithmic terms $(\alpha_{\rm s}\,L)^n$ upon integration, yields $g_2(\alpha_{\rm s}\,L)$. The new terms, formally NLL, that arise in g_2 have their origins in:

- the hard-collinear term $-\frac{3}{2}$ in Eq. 4.117,
- the change from the CMW (Bremsstrahlung) scheme to the $\overline{\rm MS}$ scheme; i.e. K,
- the two-loop running coupling (approximation),
- the azimuthal dependence; i.e. $|\sin\phi|$, and
- the anomalous dimension $\gamma_{qq}(N)$.

The difference with respect to the $Q_{\rm T}$ distribution, at this order, comes from this additional ϕ-dependent piece in Eq. 4.123.

Since we have already developed a convenient way to handle the azimuthal dependence by taking logarithmic derivatives, we again consider as our starting point Eq. 4.117 with $R(b;|\sin\phi|=1)$:

$$R(b) = 2\,C_{\rm F}\int_{1/(M\bar{b})^2}^{1}\frac{d\Delta}{\Delta}\,\frac{\alpha_{\rm s}}{2\pi\rho}\left(1-\frac{\beta_1}{\beta_0}\,\alpha_{\rm s}\,\frac{\log\rho}{\rho}\right)\left(1+K\,\frac{\alpha_{\rm s}}{2\pi\rho}\right)\left(-\frac{3}{2}-\log\Delta\right). \tag{4.128}$$

I have explicitly used the two-loop running coupling approximation where necessary, and the one-loop running coupling elsewhere, all in terms of $\rho = 1+\alpha_{\rm s}\,\beta_0\,\log\Delta$. I have also explicitly included the conversion for the scheme dependence. The one-loop running coupling, without scheme dependence, and considering only the logarithmic term $-\log\Delta$ was enough to compute the LL function $L\,g_1$. We now explicitly compute *new* NLL terms (following, in order, the first four items in the list above):

$$R_{\rm NLL} = R_{\text{hard-coll.}} + R_{\rm CMW} + R_{\text{2-loop}} + R_{\text{azimuthal}} \tag{4.129}$$

The integrals in these terms may be directly evaluated to give

$$R_{\text{hard-coll.}} = 2\,C_{\rm F}\int_{1/(M\bar{b})^2}^{1}\frac{d\Delta}{\Delta}\,\frac{\alpha_{\rm s}}{2\pi\rho}\left(-\frac{3}{2}\right) = \frac{3C_{\rm F}}{2\pi\beta_0}\,\log(1-\lambda)\,, \tag{4.130}$$

$$\begin{aligned} R_{\rm CMW} &= 2\,C_{\rm F}\int_{1/(M\bar{b})^2}^{1}\frac{d\Delta}{\Delta}\,\frac{\alpha_{\rm s}}{2\pi\rho}\,K\,\frac{\alpha_{\rm s}}{2\pi\rho}\,(-\log\Delta) \\ &= \frac{K\,C_{\rm F}\,[\lambda+(1-\lambda)\,\log(1-\lambda)]}{2\pi^2\beta_0^2(1-\lambda)}\,, \end{aligned} \tag{4.131}$$

$$\begin{aligned} R_{\text{2-loop}} &= 2\,C_{\rm F}\int_{1/(M\bar{b})^2}^1 \frac{d\Delta}{\Delta}\,\frac{\alpha_{\rm s}}{2\pi\rho}\left(-\frac{\beta_1}{\beta_0}\,\alpha_{\rm s}\,\frac{\log\rho}{\rho}\right)(-\log\Delta) \\ &= -\frac{C_{\rm F}\beta_1}{\pi\beta_0^3}\left[\frac{\lambda+\log(1-\lambda)}{1-\lambda}+\frac{1}{2}\log^2(1-\lambda)\right] \end{aligned} \tag{4.132}$$

and

$$R_{\text{azimuthal}} = \frac{d}{d\log\bar{b}}\,R_{\rm LL}\,(-\log 2) = \frac{2C_{\rm F}}{\pi\beta_0}\,\frac{\lambda}{1-\lambda}\,(-\log 2)\,. \tag{4.133}$$

In the cases of the two-loop running coupling and the CMW scheme change, we are computing only those $\mathcal{O}(\alpha_{\rm s})$ corrections to the soft-collinear term $\alpha_{\rm s}\,\log\Delta$ in $R(b)$, which would have become double-logarithmic upon integration. Thus we are controlling the terms containing $\alpha_{\rm s}^2\,L^2$, and which are therefore formally NLL. We have thus derived the NLL function g_2, written explicitly in full in Eq. 5.32. The expression for the remaining NNLL function g_3, with explicit dependence on the perturbative scales $\mu_{\rm Q}$ and $\mu_{\rm R}$, will be presented in Sec. 5.2. Prior to this, in Sec. 5.1, I explicitly compute this scale dependence for g_1 and g_2.

As already mentioned, in our formalism the anomalous dimension is used to evolve the PDFs via DGLAP evolution. We thus neglect this term in the radiator and choose to evaluate our PDFs at the correct scale $\sim 1/\bar{b}$ instead. Inverting the Mellin transform[5] in Eq. 4.111 and adopting $\sim 1/\bar{b}$ as the relevant scale, we have

$$\begin{aligned} \Sigma(\phi^*) = \frac{4\,\pi\,\alpha^2\,Q_f^2}{3\,N_{\rm c}\,M^2}\int_0^1 dx_1\int_0^1 dx_2\left[\phi_{q/1}\left(x_1,\frac{1}{\bar{b}^2}\right)\phi_{\bar{q}/2}\left(x_2,\frac{1}{\bar{b}^2}\right)+(q\leftrightarrow\bar{q})\right] \\ \times\,\frac{2}{\pi}\int_0^\infty\frac{db}{b}\,\sin(b\,M\,\phi^*)\,e^{-R(b)}\,\frac{1}{s}\,\delta\left(x_1\,x_2-\frac{M^2}{s}\right). \end{aligned} \tag{4.134}$$

As a final remark, by making the replacement $\delta(x_1\,x_2-M^2/s)\to\int_0^1 dz\,\delta(1-z)\,\delta(x_1\,x_2\,z-M^2/s)$ in the above expression, it is easy to incorporate the non-logarithmic $\mathcal{O}(\alpha_{\rm s})$ corrections to the small-ϕ^* integrated cross-section. Such terms are formally NNLL, since they are *of the same form* as terms arising from the expansion of $\exp(\alpha_{\rm s}\,g_3(\alpha_{\rm s}\,L)/\pi)$, albeit non-logarithmic. The $\mathcal{O}(\alpha_{\rm s})$ small-ϕ^* integrated cross-section is presented in Eqs. 4.87 and 4.88. The terms in $R^{\Delta}_{q\bar{q}}(z)$ arising from the integration of the logarithmic terms in I^*_ϕ (see Eq. 4.85) are of course already included in our resummation via the resummed exponent, and we can adopt the remaining constant terms in our resummed expression for $\Sigma(\phi^*)$ above. It is also instructive to consider the integral

$$\frac{2}{\pi}\int_0^\infty\frac{db}{b}\,\sin(b\,M\,\phi^*)\,\log\left(\frac{1}{\bar{b}\,M}\right)=\log(2\,\phi^*) \tag{4.135}$$

which shows that, in our b-space formalism, the correspondence between the logarithms is $\log(2\,\phi^*)\leftrightarrow\log\big(1/(\bar{b}\,M)\big)$. We observe yet again that choosing $\mu=1/\bar{b}$ as the scale at which to evaluate the PDFs, the logarithmic terms multiplying the splitting functions in Eqs. 4.87 and 4.88 cancel, suggesting this is the appropriate scale. The full expression for the resummed cross-section in presented in the following section, where the PDFs have been convolved with constant functions to effect this incorporation of these non-logarithmic terms.

[5] As before but with $z=1$; i.e. using $\frac{1}{s}\int_0^1 d\tau\,\tau^{N-1}\delta(x_1\,x_2-\tau)=\frac{1}{M^2}\,x_1^N\,x_2^N$

4.8. The final resummed result

So far I have discussed the Drell–Yan differential cross-sections in Q_{T} and ϕ^*, and the logarithmic enhancements that arise for small values of these observables, all in the context of photon-only exchange, solely to serve as a simplified paradigm in which to lay the theoretical foundations. The unabridged calculation that I have worked with, and which I have used in my phenomenological studies, is presented in this section.

The result for the resummed form of the differential ϕ^* distribution, for a Drell–Yan lepton pair of invariant mass M at a hadronic scattering energy of $\sqrt{s}$, is

$$\begin{aligned}\frac{d\sigma}{d\phi^*}(\phi^*, M, \cos\theta^*, y) = \frac{\pi\,\alpha^2}{s\,N_{\mathrm{c}}} \int_0^\infty db\, M\, \cos(b\,M\,\phi^*)\, e^{-R(\bar{b},M,\mu_{\mathrm{Q}},\mu_{\mathrm{R}})} \\ \times\, \Sigma(x_1, x_2, \cos\theta^*, b, M, \mu_{\mathrm{Q}}, \mu_{\mathrm{R}}, \mu_{\mathrm{F}})\,,\end{aligned} \tag{4.136}$$

where $x_{1,2} = \frac{M}{\sqrt{s}}\, e^{\pm y}$, y is the rapidity of the boson, $\bar{b} = \frac{b\, e^{\gamma_{\mathrm{E}}}}{2}$, $\gamma_{\mathrm{E}} = 0.5772\ldots$ being the Euler-Mascheroni constant, and full scale dependence (to be discussed in detail in Sec. 5.1) is explicitly indicated in terms of μ_{Q}, μ_{R} and μ_{F}: the resummation, renormalization and factorization scales, respectively. The function Σ is essentially the Born calculation, supplemented with additional coefficients and correction factors appropriate for the resummation, and is given by

$$\begin{aligned}\Sigma(x_1, x_2, \cos\theta^*, b, M, \mu_{\mathrm{Q}}, \mu_{\mathrm{R}}, \mu_{\mathrm{F}}) = \\ \exp\left[-\frac{\alpha_{\mathrm{s}}(\mu_{\mathrm{R}})}{\pi} g^{\mathrm{corr}}\left(\frac{M}{\mu_{\mathrm{Q}}}\right)\right] \bar{\Sigma}(x_1, x_2, \cos\theta^*, b, M, \mu_{\mathrm{Q}}, \mu_{\mathrm{R}}, \mu_{\mathrm{F}})\end{aligned} \tag{4.137}$$

where

$$\begin{aligned}\bar{\Sigma}(x_1, x_2, \cos\theta^*, b, M, \mu_{\mathrm{Q}}, \mu_{\mathrm{R}}, \mu_{\mathrm{F}}) = \\ (1 + \cos^2\theta^*)\, \left[Q_q^2 - 2\,Q_q\,V_\ell\,V_q\,\chi_1(M^2) + (A_\ell^2 + V_\ell^2)\,(A_q^2 + V_q^2)\,\chi_2(M^2)\right] \mathcal{F}_q^+ \\ + \cos\theta^*\, \left[-4\,Q_q\,A_\ell\,A_q\,\chi_1(M^2) + 8\,A_\ell\,V_\ell\,A_q\,V_q\,\chi_2(M^2)\right] \mathcal{F}_q^-\,.\end{aligned} \tag{4.138}$$

The factor containing g^{corr} will be explained in detail in Sec. 5.1, but it suffices to say this factor acts as a counter-term to absorb spurious scale dependence arising in the resummed exponent. The axial and vector electroweak couplings are

$$A_f = T_f^3 \tag{4.139}$$

$$\text{and} \quad V_f = T_f^3 - 2\,Q_f\,\sin^2\theta_{\mathrm{W}}\,, \tag{4.140}$$

respectively, with $f = \ell, q$ (for a lepton or quark), T_f^3 is the third component of weak isospin ($T_f^3 = +\frac{1}{2}$ for $f = \nu, u, \ldots$ and $T_f^3 = -\frac{1}{2}$ for $f = e, d, \ldots$), and θ_{W} is the electroweak mixing, or 'Weinberg', angle. The functions $\chi_1(M^2)$ and $\chi_2(M^2)$ model the γ^*/Z interference and the Z resonance respectively, and may be found in [**48**]. They are

$$\chi_1(M^2) = \kappa\, \frac{M^2\,(M^2 - M_{\mathrm{Z}}^2)}{(M^2 - M_{\mathrm{Z}}^2)^2 + \Gamma_{\mathrm{Z}}^2\,M_{\mathrm{Z}}^2} \tag{4.141}$$

and

$$\chi_2(M^2) = \kappa^2\, \frac{M^4}{(M^2 - M_{\mathrm{Z}}^2)^2 + \Gamma_{\mathrm{Z}}^2\,M_{\mathrm{Z}}^2}\,, \tag{4.142}$$

where $M_{\rm Z}$ is the Z mass and $\Gamma_{\rm Z}$ is the Z width. In these expressions,

$$\kappa = \frac{\sqrt{2}\, G_{\rm F}\, M_{\rm Z}^2}{4\,\pi\,\alpha}\,, \tag{4.143}$$

$G_{\rm F}$ being the Fermi constant.

The functions $\mathcal{F}^{\pm}$,

$$\begin{aligned}\mathcal{F}^{\pm} = {} & [C_{q\alpha}\otimes\phi_{\alpha/1}](x_1,\bar{b},\mu_{\rm Q},\mu_{\rm R},\mu_{\rm F})\,[C_{\bar{q}\alpha'}\otimes\phi_{\alpha'/2}](x_2,\bar{b},\mu_{\rm Q},\mu_{\rm R},\mu_{\rm F}) \\ & \pm[C_{\bar{q}\beta}\otimes\phi_{\beta/1}](x_1,\bar{b},\mu_{\rm Q},\mu_{\rm R},\mu_{\rm F})\,[C_{q\beta'}\otimes\phi_{\beta'/2}](x_2,\bar{b},\mu_{\rm Q},\mu_{\rm R},\mu_{\rm F})\,,\end{aligned} \tag{4.144}$$

are convolutions of the parton density functions (PDFs) with the relevant coefficient functions (with an implicit sum over incoming parton flavours, e.g. $\alpha\in\{q,\bar{q},g\}$) as in

$$[C_{q\alpha}\otimes\phi_{\alpha/i}](x_i,\bar{b},\mu_{\rm Q},\mu_{\rm R},\mu_{\rm F}) = \int_{x_i}^1 \frac{dz}{z}\, C_{q\alpha}\left(\alpha_{\rm s}\left(\frac{\mu_{\rm R}}{\bar{b}\,\mu_{\rm Q}}\right), \frac{x_i}{z}\,, \frac{\mu_{\rm F}}{\mu_{\rm Q}}\right)\phi_{\alpha/i}\left(z, \frac{\mu_{\rm F}}{\bar{b}\,\mu_{\rm Q}}\right). \tag{4.145}$$

Here $i=1,2$ labels the incoming hadron. The coefficient functions themselves are the perturbative expansions

$$C_{q\alpha}\left(\alpha_{\rm s}\left(\frac{\mu_{\rm R}}{\bar{b}\,\mu_{\rm Q}}\right), x\,, \frac{\mu_{\rm F}}{\mu_{\rm Q}}\right) = \delta_{q\alpha}\,\delta(1-x) + \frac{\alpha_{\rm s}\big(\mu_{\rm R}/(\bar{b}\,\mu_{\rm Q})\big)}{2\pi}\, C_{q\alpha}^{(1)}\left(x, \frac{\mu_{\rm F}}{\mu_{\rm Q}}\right) + \mathcal{O}(\alpha_{\rm s}^2) \tag{4.146}$$

and the $\mathcal{O}(\alpha_{\rm s})$ terms for $q\,\bar{q}$ and $q\,g$ are, respectively,

$$C_{q\bar{q}}^{(1)}\left(x, \frac{\mu_{\rm F}}{\mu_{\rm Q}}\right) = C_{\rm F}\left(\frac{\pi^2}{2}-4\right)\delta(1-x) + C_{\rm F}(1-x) + \ln\left(\frac{\mu_{\rm Q}^2}{\mu_{\rm F}^2}\right) P_{qq}^{(0)}(x) \tag{4.147}$$

and

$$C_{qg}^{(1)}\left(x, \frac{\mu_{\rm F}}{\mu_{\rm Q}}\right) = x\,(1-x) + \ln\left(\frac{\mu_{\rm Q}^2}{\mu_{\rm F}^2}\right) P_{qg}^{(0)}(x)\,. \tag{4.148}$$

The purpose of these coefficient functions is to incorporate the non-logarithmic (i.e. constant) terms that appear in the fixed-order calculation of the small-ϕ^* differential cross-section for Drell–Yan; they represent the perturbative corrections to the collinear branching of the incoming partons. Our computer software package, which provides an automated implementation of the resummed calculation for an end-user, interfaces with both HOPPET [**67**] and LHAPDF [**68**] to obtain information pertaining directly to the PDF sets we use, and also to effect their DGLAP evolution and provide other manipulations.

All scale-dependence has been explicitly written in the above equations. I will postpone the discussion of the scale dependence of R, which will be elucidated in Sec. 5.1 after which I will also present the full NNLL form in Sec. 5.2. At this point I would like to address the scale dependence appearing in the coefficient terms, i.e. the choices for the arguments of the running coupling and the PDFs. I will start with the running coupling, whose argument in Eq. 4.146 is $\mu_{\rm R}/(\bar{b}\,\mu_{\rm Q})$. Setting all perturbative scales, for now, such that $\mu_{\rm R}=\mu_{\rm Q}=M$, we find the argument to be $1/\bar{b}$. To see why this should be so, consider (to truncated NLL accuracy) the exponentiated radiator supplemented with our coefficient terms, as in

$$\big[1+\alpha_{\rm s}(1/\bar{b})\,\text{consts}\big]\exp\left[-\left(L\,g_1+g_2^*\right)\right]. \tag{4.149}$$

Here, $L\,g_1$ is given in Eq. 4.127, and we consider a truncated g_2 term (g_2^*) given simply by $R_{\text{hard-coll.}}$ in Eq. 4.130. Changing the argument of the running coupling from $1/\bar{b}$ to M, using the one-loop approximation in Eq. 2.57 with $\mu = M$ and $\mu' = 1/\bar{b}$, i.e.

$$\alpha_{\rm s}(1/\bar{b}) = \frac{\bar{\alpha_{\rm s}}}{1-\bar{\alpha_{\rm s}}\,\beta_0\,L} = \frac{\bar{\alpha_{\rm s}}}{1-\lambda}\,, \tag{4.150}$$

we recover

$$\begin{aligned}\big[1+\alpha_{\rm s}(1/\bar{b})\,\text{consts}\big]\,&\exp\left[-\left(L\,g_1+g_2^*\right)\right]\\ &= \left(1+\frac{\bar{\alpha_{\rm s}}\,\text{consts}}{1-\bar{\alpha_{\rm s}}\,\beta_0\,L}\right)\exp\left\{\frac{C_{\rm F}\left[2\,L\,\lambda+(2\,L-3\,\lambda)\,\log(1-\lambda)\right]}{2\,\pi\,\beta_0\,\lambda}\right\}\\ &= 1+\frac{\bar{\alpha_{\rm s}}}{2\pi}\left(\text{consts}+3\,C_{\rm F}\,L-C_{\rm F}\,L^2\right)\end{aligned} \tag{4.151}$$

after using a series expansion in $\bar{\alpha_{\rm s}}$ on the RHS. Once again I have adopted the notation $L = \ln(\bar{b}^2\,M^2)$ and $\bar{\alpha_{\rm s}} = \alpha_{\rm s}(M)$, and used $\lambda = \bar{\alpha_{\rm s}}\,\beta_0\,L$. This expression, which includes the soft-collinear double log, and the single log from hard collinear emission, is precisely in accordance with the $\mathcal{O}(\alpha_{\rm s})$ terms we derived for the small-ϕ^* differential cross-section[6]; i.e. $2\times R^{\Delta}_{q\bar{q}}(z)$ in Eq. 4.88. Thus we have demonstrated the correct scale of the running coupling to be $1/\bar{b}$.

Repeating this analysis with the scale-dependent radiator (i.e. $\mu_{\rm R}$ and $\mu_{\rm Q}$ left free) the appropriate scale of the running coupling, required to reproduce the correct logarithms when we combine with constant terms to get $R^{\Delta}_{q\bar{q}}(z)$, is $\mu_{\rm R}/(\bar{b}\,\mu_{\rm Q})$. In this case our resummed exponent is in terms of $\lambda = \alpha_{\rm s}(\mu_{\rm R})\,\beta_0\,L$, with $L = \ln(\bar{b}^2\,\mu_{\rm Q}^2)$, and we change the argument of the coupling from $\mu_{\rm R}/(\bar{b}\,\mu_{\rm Q})$ to $\mu_{\rm R}$. After truncating a series expansion in $\alpha_{\rm s}(\mu_{\rm R})$, we recover the correct terms in $R^{\Delta}_{q\bar{q}}(z)$.

More succinctly, one may simply consider the absence of any explicit resummation, for which then the *resummed exponent* $R(b) = 0$. This is the case when $\bar{b} = \mu_{\rm Q}^{-1}$, since then the resummed logarithms L are absent. In this limit we should recover simply the small-ϕ^* differential cross-section at fixed-order, with the running coupling and the PDFs evaluated at the relevant scales $\mu_{\rm R}$ and $\mu_{\rm F}$, respectively. This is ensured if the scale choices in Eq. 4.146 are chosen as they presently stand.

[6]Recall the correspondence $L \equiv \log(\bar{b}^2\,M^2) \leftrightarrow -2\,\log(2\,\phi^*)$

CHAPTER 5

Phenomenology of ϕ^* at Tevatron and the LHC

In this chapter I present my phenomenological work on the ϕ^* observable. The structure of the presentation is as follows: First I discuss the various aspects of my phenomenological study of ϕ^*, starting with a survey of the scale dependence in the resummed component, and then I will present comparisons and predictions for the DØ, ATLAS and CMS experiments, before moving to a technical discussion regarding the rôle of non-perturbative effects I have studied.

In order to obtain theoretical predictions over a broad range of ϕ^*, it is necessary to match fixed-order and resummed predictions. The fixed-order approach describes the high-ϕ^* physics well, where one is not sensitive to soft or collinear gluon emission, and the resummed approach (as we have seen) is necessary to obtain a theoretically sound description of the low-ϕ^* physics. In our work we take both descriptions and combine them according to

$$\left(\frac{d\sigma}{d\phi^*}\right)_{\text{matched}} = \left(\frac{d\sigma}{d\phi^*}\right)_{\text{resummed}} + \left(\frac{d\sigma}{d\phi^*}\right)_{\text{fixed-order}} - \left(\frac{d\sigma}{d\phi^*}\right)_{\text{expansion}}, \qquad (5.1)$$

where 'expansion' denotes the series expansion of the resummed component in α_{s}, truncated at the same perturbative order to which the fixed-order component is calculated. For example, NLL+LO matching would involve subtracting the expansion of the resummed component to $\mathcal{O}(\alpha_{\text{s}})$, NNLL+NLO matching would involve subtracting the expansion of the resummed component to $\mathcal{O}(\alpha_{\text{s}}^2)$, etc. A NNLL+NLO matching is what we employ in particular, yielding a smooth description of the physics of azimuthal decorrelation over a broad range.

In order to obtain the fixed-order component we use the calculation in MCFM [**69**]. In addition, the Born weights used in the resummation are also taken from MCFM, however the structure of our code is adapted to use other fixed-order calculations, e.g. DYNNLO [**70**]. Our calculation is also fully differential in all of the relevant kinematic variables, allowing experimental cuts to be placed on the final-state (leptons). In principle, our code may be extended to the study of azimuthal decorrelation in other processes whose final state is a colour-singlet system, e.g. ϕ^* in $\text{H} \to \gamma\gamma$. The Q_{T} distribution for this process has already been studied at NNLL accuracy, and the interested reader is referred to [**25**]. Furthermore, one could in principle use any NLO calculation for the fixed-order component, e.g. FEWZ [**71, 72**], provided the cancellation between the large logarithms inherent in the fixed-order and expanded components could be numerically demonstrated as one approached smaller values of ϕ^*.

One of the remarkable properties of ϕ^* is that is has been able to unambiguously discriminate against a certain non-perturbative (NP) model, which was unprecedented,

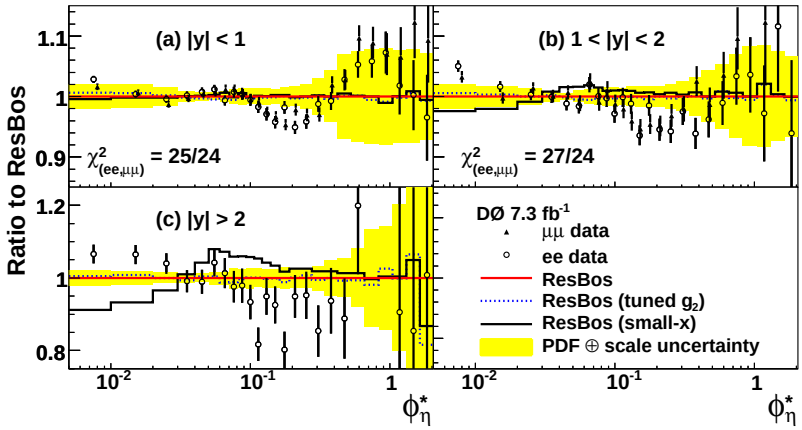

FIGURE 5.1. ϕ^* data from DØ corresponding to 7.3 fb^{-1}, showing both the Z $\to$ *ee* and Z $\to$ $\mu\mu$ channels for Drell–Yan [**19**]. These data are in comparison with ResBos predictions, although the perturbative scale uncertainty does *not* include the resummation scale, μ_Q.

even after many years of Drell–Yan study with the Q_T observable. The small-x broadening model implemented in ResBos [**73, 74, 75**] is a non-perturbative prescription, which contributes principally when the Bjorken x variable for either parton is small—i.e. at higher $\sqrt{s}$ or at higher boson rapidities—and which gives rise to a broader spectrum of the transverse momentum of the boson. In particular, Fig. 5.1 shows how this small-x broadening model is disfavoured by ϕ^* data from DØ [**19**]. Figure 5.2 shows the equivalent comparison for the Q_T observable in the $|y| > 2$ region, albeit for only 0.98 fb^{-1} of integrated luminosity, where a similar conclusion this time cannot be made on account of the larger measurement uncertainties. It is important to note that the uncertainties which set a limitation on the overall achievable measurement uncertainty for Q_T here are *systematic* in nature.

The experimental precision of ϕ^*, owing to its immunity to momentum resolution inefficiencies, provides an exciting opportunity to attempt to determine what NP physics (if any) are required to supplement a purely perturbative prediction, in order to gain good agreement with data. The phenomenological study presented here attempts to address this issue, but also draws attention to the need for a good understanding of the perturbative component. To this end, full consideration of the theoretical uncertainty, estimated by varying the perturbative scales, is made.

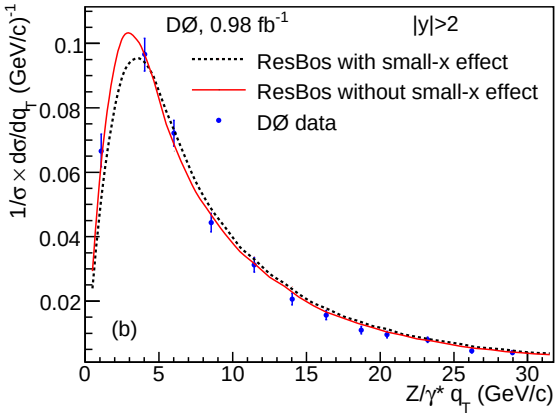

FIGURE 5.2. DØ Q_{T} data, corresponding to 0.98 fb^{-1}, in comparison with ResBos both with and without the small-x broadening effect [**76**].

5.1. Scale dependence in the radiator

In this section I will derive the dependence of the radiator R on the perturbative scales μ_{R} and μ_{Q}, the renormalization and resummation scales respectively. Note that I have independently computed this here in a very explicit manner, which differs from the way it was originally computed in our work. I hope the level of detail here offers a certain insight for the reader. We begin by recalling the NLL expression for $R(\bar{b}\,M)$ in the absence of these scales:

$$\bar{R}_{\mathrm{NLL}}(\bar{b}\,M) = \bar{L}\,g_1(\bar{\alpha}_{\mathrm{s}}\,\bar{L}) + g_2(\bar{\alpha}_{\mathrm{s}}\,\bar{L}) \tag{5.2}$$

where $\bar{L} = \ln(\bar{b}^2\,M^2)$ and $\bar{\alpha}_{\mathrm{s}} = \alpha_{\mathrm{s}}(M^2)$. The overline in $\bar{L}$ and $\bar{\alpha}_{\mathrm{s}}$ denotes that the scale at which these quantities are evaluated is M, the invariant mass of the lepton pair.

We consider, just for the moment, the LL scale dependence. The resummation scale, μ_{Q}, is introduced in order to generalize the argument of the logarithms we resum. As such, we replace

$$\bar{L} \to L = \ln(\bar{b}^2\,\mu_{\mathrm{Q}}^2)\,. \tag{5.3}$$

In principle, the value of μ_{Q} should be set to $\sim M$, but is otherwise arbitrary. Defining $x_{\mathrm{Q}} := \mu_{\mathrm{Q}}/M$ we see, for instance, that a general LL term

$$\begin{aligned}\alpha_{\mathrm{s}}\,L^2 &= \alpha_{\mathrm{s}}\,\left[\ln(\bar{b}^2\,M^2) + \ln x_{\mathrm{Q}}^2\right]^2 \\ &= \alpha_{\mathrm{s}}\,\bar{L}^2 + 2\,\ln x_{\mathrm{Q}}^2\,\alpha_{\mathrm{s}}\,\bar{L} + \alpha_{\mathrm{s}}\,\ln^2 x_{\mathrm{Q}}^2\,.\end{aligned} \tag{5.4}$$

The first term in the final line is of the form $(\alpha_{\mathrm{s}}\,\bar{L}^2)^n$—of course, with $n = 1$—and is therefore a genuine LL term. However, the second term in the final line is of the form $(\alpha_{\mathrm{s}}\,\bar{L})^n$ and is therefore formally a NLL term. The final term is even more sub-leading. Thus, to LL accuracy, $\bar{L} = L$. The arbitrariness in the choice of μ_{Q} here is a NLL correction, and the variation of μ_{Q} about its nominal value of M may therefore be used to estimate the size of genuine NLL terms.

If we perform a calculation to NLL logarithmic accuracy, however, then any NLL terms introduced by the arbitrariness of μ_{Q} in g_1 are spurious, and must be cancelled by

introducing appropriate counter-terms in g_2. This is the programme we adopt for deriving the scale dependence of R.

We begin with

$$g_1(\bar{\alpha_s}\,\bar{L}) = -\frac{A^{(1)}}{\pi\,\beta_0}\,\frac{\bar{\lambda}+\ln(1-\bar{\lambda})}{\bar{\lambda}}\,, \tag{5.5}$$

where $\bar{\lambda} = \alpha_s(M^2)\,\beta_0\,\ln(\bar{b}^2\,M^2)$. Now, the LL radiator evaluated with $\mu_R = \mu_Q = M$ is

$$\begin{aligned}\bar{R}_{LL}(\bar{b}\,M) &= \bar{L}\,g_1(\bar{\alpha_s}\,\bar{L}) \\ &= -\frac{A^{(1)}}{\pi\,\beta_0}\left[L + \ln\frac{M^2}{\mu_Q^2} + \frac{\ln(1-\bar{\lambda})}{\bar{\alpha_s}\,\beta_0}\right]\,.\end{aligned} \tag{5.6}$$

The one-loop running coupling in our notation is

$$\bar{\alpha_s} = \frac{\alpha_s}{1-\alpha_s\,\beta_0\,\ln\frac{\mu_R^2}{M^2}}\,, \tag{5.7}$$

and so we may also write $\bar{\lambda}$ in terms of λ, as

$$\bar{\lambda} = \bar{\alpha_s}\,\beta_0\,\bar{L} = \frac{\lambda + \alpha_s\,\beta_0\,\ln\frac{M^2}{\mu_Q^2}}{1-\alpha_s\,\beta_0\,\ln\frac{\mu_R^2}{M^2}}\,. \tag{5.8}$$

This further implies that

$$1-\bar{\lambda} = (1-\lambda)\,\frac{G}{H}\,, \tag{5.9}$$

where I have introduced, as shorthand, the quantities

$$G := 1 - \frac{\alpha_s\,\beta_0\,\ln\frac{\mu_R^2}{\mu_Q^2}}{1-\lambda} \tag{5.10}$$

$$\text{and} \qquad H := 1 - \alpha_s\,\beta_0\,\ln\frac{\mu_R^2}{M^2}\,. \tag{5.11}$$

Using Eq. 5.9 for $1-\bar{\lambda}$ and Eq. 5.7 for the running coupling, we may write the $\ln(1-\bar{\lambda})/\bar{\alpha_s}\,\beta_0$ term in Eq. 5.6 as

$$\frac{\ln(1-\bar{\lambda})}{\bar{\alpha_s}\,\beta_0} = \frac{\ln(1-\lambda)}{\alpha_s\,\beta_0} - \ln(1-\lambda)\,\ln\frac{\mu_R^2}{M^2} + \frac{\ln G}{\alpha_s\,\beta_0} - \frac{\ln H}{\alpha_s\,\beta_0} - \ln\frac{G}{H}\,\ln\frac{\mu_R^2}{M^2}\,. \tag{5.12}$$

Given that

$$R_{LL} = -\frac{A^{(1)}}{\pi\,\beta_0}\left[L + \frac{\ln(1-\lambda)}{\alpha_s\,\beta_0}\right]\,, \tag{5.13}$$

i.e. the LL radiator with full dependence on μ_Q and μ_R, we are now in a position to isolate the counter-terms, which are given by

$$\bar{R}_{LL} - R_{LL} = -\frac{A^{(1)}}{\pi\,\beta_0}\left[\ln\frac{M^2}{\mu_Q^2} - \ln(1-\lambda)\,\ln\frac{\mu_R^2}{M^2} + \frac{\ln G}{\alpha_s\,\beta_0} - \frac{\ln H}{\alpha_s\,\beta_0} - \ln\frac{G}{H}\,\ln\frac{\mu_R^2}{M^2}\right]\,. \tag{5.14}$$

The counter-terms appropriate for g_2, however, are those which are NLL. We now proceed to isolate these NLL pieces.

First we write, using series expansions (since $0 < \lambda < 1$),

$$G = 1 - \alpha_s\,\beta_0\,\ln\frac{\mu_R^2}{\mu_Q^2}\sum_{n=0}^{\infty}\lambda^n \tag{5.15}$$

$$\Rightarrow \quad \frac{\ln G}{\alpha_{\rm s}\,\beta_0} = -\frac{1}{\alpha_{\rm s}\beta_0}\sum_{m=1}^{\infty}\frac{\left(\alpha_{\rm s}\,\beta_0\,\ln\frac{\mu_{\rm R}^2}{\mu_{\rm Q}^2}\sum_{n=0}^{\infty}\lambda^n\right)^m}{m} \\ = -\ln\frac{\mu_{\rm R}^2}{\mu_{\rm Q}^2}\sum_{n=0}^{\infty}\lambda^n - \sum_{m=2}^{\infty}\frac{(\alpha_{\rm s}\,\beta_0)^{m-1}}{m}\left(\ln\frac{\mu_{\rm R}^2}{\mu_{\rm Q}^2}\sum_{n=0}^{\infty}\lambda^n\right)^m . \tag{5.16}$$

The terms in the sum from $m = 2$ to ∞ in the second line are beyond NLL accuracy, leaving only the $m = 1$ contribution which *is* NLL and which has been isolated. Thus, to NLL accuracy,

$$\frac{\ln G}{\alpha_{\rm s}\,\beta_0} \approx \ln\frac{\mu_{\rm Q}^2}{\mu_{\rm R}^2}\frac{1}{1-\lambda}\,, \tag{5.17}$$

reverting to the $1/(1-\lambda)$ form. For the case of $\ln G$, i.e. *without* the division by $\alpha_{\rm s}\,\beta_0$, we may take G to be simply $1-\alpha_{\rm s}\,\beta_0\,\ln(\mu_{\rm R}^2/\mu_{\rm Q}^2)$ (to NLL accuracy with an $\mathcal{O}(\alpha_{\rm s})$ correction, i.e. retaining only the $n = 0$ term of the sum in Eq. 5.15) and so we may approximate

$$\ln G \approx -\alpha_{\rm s}\,\beta_0\,\ln\frac{\mu_{\rm R}^2}{\mu_{\rm Q}^2}\,, \tag{5.18}$$

having used $\ln(1+x) \approx x$, owing to the fact that

$$\alpha_{\rm s}\,\beta_0\,\ln\frac{\mu_{\rm R}^2}{\mu_{\rm Q}^2} \ll 1 \tag{5.19}$$

since the scales are chosen such that $\mu_{\rm Q} \sim \mu_{\rm R} \sim M$. Similarly, we may approximate

$$\ln H \approx -\alpha_{\rm s}\,\beta_0\,\ln\frac{\mu_{\rm R}^2}{M^2}\,. \tag{5.20}$$

These expressions will be useful later when we determine constant NNLL counter-terms. For now, to NLL accuracy, the $\ln G/H$ term in Eq. 5.14 does not contribute.

We are now in a position to extract the NLL counter-terms from Eq. 5.14. Using the NLL expressions for the various terms derived above, namely Eqs. 5.17 and 5.20, we may finally write

$$R_{\rm NLL}^{\text{counter-term}} = -\frac{A^{(1)}}{\pi\,\beta_0}\left\{\left[\frac{\lambda}{1-\lambda}+\ln(1-\lambda)\right]\ln\frac{\mu_{\rm Q}^2}{\mu_{\rm R}^2} + \ln(1-\lambda)\,\ln\frac{M^2}{\mu_{\rm Q}^2}\right\} \tag{5.21}$$

where the logarithm multiplying $\ln(1-\lambda)$ has been split as $\ln(M^2/\mu_{\rm R}^2) = \ln(\mu_{\rm Q}^2/\mu_{\rm R}^2) + \ln(M^2/\mu_{\rm Q}^2)$. Note that we only consider NLL terms in this expression, i.e. terms in the single-logarithmic variable λ.

If one works to NNLL accuracy, a new possibility arises. In addition to spurious scale-dependent *logarithmic* terms appearing in g_3—owing to the arbitrariness of $\mu_{\rm R}$ and $\mu_{\rm Q}$ in g_1 and g_2—one should also consider spurious *constant* terms at $\mathcal{O}(\alpha_{\rm s})$, since these are also of the NNLL form $\alpha_{\rm s}\,(\alpha_{\rm s}\,L)^n$ (just with $n = 0$) and appropriate counter-terms must be introduced. Here, for example, we focus just on deriving these constant terms.

We first begin by including the $\mathcal{O}(\alpha_{\rm s})$ constant term in Eq. 5.16, to obtain

$$\frac{\ln G}{\alpha_{\rm s}\,\beta_0} = -\ln\frac{\mu_{\rm R}^2}{\mu_{\rm Q}^2}\,\frac{1}{1-\lambda} - \frac{\alpha_{\rm s}\,\beta_0}{2}\,\ln^2\frac{\mu_{\rm R}^2}{\mu_{\rm Q}^2}\,. \tag{5.22}$$

The second term here is new, and corresponds to the $m = 2$ ($\mathcal{O}(\alpha_s)$) with $n = 0$ (non-logarithmic, i.e. λ^0) term of the sum in Eq. 5.16. Furthermore, we retain the $\mathcal{O}(\alpha_s)$ term in the series expansion for $\ln H/\alpha_s\,\beta_0$, giving

$$\frac{\ln H}{\alpha_s\,\beta_0} = -\ln\frac{\mu_R^2}{M^2} - \frac{\alpha_s\,\beta_0}{2}\,\ln^2\frac{\mu_R^2}{M^2}\,. \tag{5.23}$$

We now use the $\mathcal{O}(\alpha_s)$ expressions for $\ln G$ and $\ln H$, given in Eqs. 5.18 and 5.20 respectively, to write the $\mathcal{O}(\alpha_s)$ expression for the final term in Eq. 5.14 which we did not previously consider:

$$\ln\frac{G}{H}\,\ln\frac{\mu_R^2}{M^2} = -\alpha_s\,\beta_0\,\ln\frac{M^2}{\mu_Q^2}\,\ln\frac{\mu_R^2}{M^2}\,. \tag{5.24}$$

Including all the constant $\mathcal{O}(\alpha_s)$ corrections considered above (Eqs. 5.22, 5.23 and 5.24) in the expression for $\bar{R}_{LL} - R_{LL}$ in Eq. 5.14, the *additional* counter-terms (from g_1) are

$$\begin{aligned} -\frac{A^{(1)}}{\pi\,\beta_0}\Bigg\{&-\frac{\alpha_s\,\beta_0}{2}\,\ln^2\frac{\mu_R^2}{\mu_Q^2} + \frac{\alpha_s\,\beta_0}{2}\,\ln^2\frac{\mu_R^2}{M^2} \\ &+\alpha_s\,\beta_0\,\ln\frac{\mu_R^2}{\mu_Q^2}\,\ln\frac{\mu_R^2}{M^2} - \alpha_s\,\beta_0\,\ln^2\frac{\mu_R^2}{M^2}\Bigg\} \\ &= -\frac{\alpha_s}{\pi}\,\frac{A^{(1)}}{2}\,\ln^2\frac{M^2}{\mu_Q^2} \end{aligned} \tag{5.25}$$

In fact, the only other $\mathcal{O}(\alpha_s)$ non-logarithmic NNLL counter-term is required for the $-B^{(1)}\,\ln(1-\lambda)/\pi\,\beta_0$ term in g_2. Using results derived above, we have

$$\ln(1-\bar{\lambda}) = \ln(1-\lambda) - \ln\frac{G}{H} \approx \ln(1-\lambda) + \alpha_s\,\beta_0\,\ln\frac{M^2}{\mu_Q^2}\,. \tag{5.26}$$

Therefore, the only counter-term required for g_2 is

$$\frac{B^{(1)}}{\pi\,\beta_0}\,\alpha_s\,\beta_0\,\ln\frac{M^2}{\mu_Q^2}\,. \tag{5.27}$$

Finally, taking all $\mathcal{O}(\alpha_s)$ non-logarithmic NNLL counter-terms together, we introduce

$$g^{\rm corr}\left(\frac{M}{\mu_Q}\right) := \frac{C_F}{2}\,\ln^2\frac{M^2}{\mu_Q^2} - \frac{3}{2}\,C_F\,\ln\frac{M^2}{\mu_Q^2}\,. \tag{5.28}$$

Since these counter-terms are of a constant nature, we rather choose to associate them with the Born weight in our formalism, rather than with the resummed exponent, although this is just a convention. Constant terms at $\mathcal{O}(\alpha_s)$ that arise in $R_{NLL} - \bar{R}_{NLL}$ (LL and NLL inclusive) are factored out, and written

$$\exp\big[-\big(R_{NLL} - \bar{R}_{NLL}\big)\big] = \exp\big[-\big(R^{\log}_{NLL} - \bar{R}^{\log}_{NLL}\big)\big]\,\exp\left[-\frac{\alpha_s(\mu_R)}{\pi}\,g^{\rm corr}\left(\frac{M}{\mu_Q}\right)\right]\,. \tag{5.29}$$

5.2. The fully scale-dependent radiator

Using the methods of the previous section we were able to derive the scale dependence of the radiator along with appropriate NLL counter-terms which should be added to g_2 when one considers a resummed calculation to NLL accuracy. If one wishes to work to

NNLL accuracy, then appropriate counter-terms must also be added to g_3 in order to absorb the spurious scale-dependence which materializes at this order due to the arbitrariness of choosing $\mu_{\rm R}$ and $\mu_{\rm Q}$ in g_1 and g_2. In this section I simply summarize the full NNLL radiator, with all scale dependence included.

The radiator is given by

$$\begin{aligned} R\left(\bar{b}\,\mu_{\rm Q}, \frac{M}{\mu_{\rm Q}}, \frac{\mu_{\rm Q}}{\mu_{\rm R}}; \alpha_{\rm s}(\mu_{\rm R})\right) = L\, g_1(\alpha_{\rm s}\, L) + g_2\left(\alpha_{\rm s}\, L, \frac{M}{\mu_{\rm Q}}, \frac{\mu_{\rm Q}}{\mu_{\rm R}}\right) \\ + \frac{\alpha_{\rm s}}{\pi}\, g_3\left(\alpha_{\rm s}\, L, \frac{M}{\mu_{\rm Q}}, \frac{\mu_{\rm Q}}{\mu_{\rm R}}\right), \end{aligned} \tag{5.30}$$

where $L = \ln(\bar{b}^2\,\mu_{\rm Q}^2)$ and $\alpha_{\rm s}$ is shorthand for the scale-dependent running coupling in the $\overline{\rm MS}$ scheme, $\alpha_{\rm s}(\mu_{\rm R})$. The functions $g^{(i)}$, $i \in \{1,2,3\}$, are given by

$$g_1(\lambda) = -\frac{A^{(1)}}{\pi\,\beta_0}\,\frac{\lambda + \ln(1-\lambda)}{\lambda}\,, \tag{5.31}$$

$$\begin{aligned} g_2(\lambda) = &-\frac{B^{(1)}}{\pi\,\beta_0}\,\ln(1-\lambda) + \frac{A^{(2)}}{\pi^2\,\beta_0^2}\left(\frac{\lambda}{1-\lambda} + \ln(1-\lambda)\right) \\ &- \frac{A^{(1)}\,\beta_1}{\pi\,\beta_0^3}\left[\frac{\lambda + \ln(1-\lambda)}{1-\lambda} + \frac{1}{2}\ln^2(1-\lambda)\right] \\ &- \frac{A^{(1)}}{\pi\,\beta_0}\left(\frac{\lambda}{1-\lambda} + \ln(1-\lambda)\right)\ln\frac{\mu_{\rm Q}^2}{\mu_{\rm R}^2}\,, \end{aligned} \tag{5.32}$$

and

$$\begin{aligned} g_3(\lambda) = &\frac{A^{(3)}}{2\,\pi^2\,\beta_0^2}\,\frac{\lambda^2}{(1-\lambda)^2} + \frac{B^{(2)}}{\pi\,\beta_0}\,\frac{\lambda}{1-\lambda} \\ &- \frac{A^{(2)}\,\beta_1}{\pi\,\beta_0^3}\left(\frac{\lambda\,(3\,\lambda-2)}{2\,(1-\lambda)^2} - \frac{(1-2\,\lambda)\,\ln(1-\lambda)}{(1-\lambda)^2}\right) \\ &- \frac{A^{(1)}}{\beta_0^4}\left(\frac{\beta_1^2}{2}\,\frac{1-2\,\lambda}{(1-\lambda)^2}\,\ln^2(1-\lambda) + \frac{\ln(1-\lambda)}{1-\lambda}\,(\beta_0\,\beta_2\,(1-\lambda) + \beta_1^2\,\lambda)\right. \\ &\left. + \frac{\lambda}{2\,(1-\lambda)^2}\,(\beta_0\,\beta_2\,(2-3\,\lambda) + \beta_1^2\,\lambda)\right) \\ &- \frac{B^{(1)}\,\beta_1}{\beta_0^2}\left(\frac{\lambda}{1-\lambda} + \ln(1-\lambda)\right) + \frac{A^{(1)}}{2}\,\frac{\lambda^2}{(1-\lambda)^2}\,\ln^2\frac{\mu_{\rm Q}^2}{\mu_{\rm R}^2} \\ &- \left[B^{(1)}\,\frac{\lambda}{1-\lambda} + \frac{A^{(2)}}{\pi\,\beta_0}\,\frac{\lambda^2}{(1-\lambda)^2}\right. \\ &\left. + A^{(1)}\,\frac{\beta_1}{\beta_0^2}\left(\frac{\lambda}{1-\lambda} + \frac{1-2\,\lambda}{(1-\lambda)^2}\,\ln(1-\lambda)\right)\right]\ln\frac{\mu_{\rm Q}^2}{\mu_{\rm R}^2}\,, \end{aligned} \tag{5.33}$$

where

$$\lambda = \alpha_{\rm s}(\mu_{\rm R})\,\beta_0\,\ln(\bar{b}^2\,\mu_{\rm Q}^2)\,. \tag{5.34}$$

The coefficients appearing in these expressions are given by

$$A^{(1)} = C_{\rm F}\,, \tag{5.35}$$

$$A^{(2)} = \frac{C_{\rm F}}{2}\left[C_{\rm A}\left(\frac{67}{18} - \frac{\pi^2}{6}\right) - \frac{5}{9}\,N_{\rm F}\right], \tag{5.36}$$

$$A^{(3)} = \frac{C_{\rm F}}{16}\left[C_{\rm A}^2\left(\frac{245}{6} - \frac{134}{27}\pi^2 + \frac{11}{45}\pi^4 + \frac{22}{3}\zeta(3)\right)\right.$$
$$+\frac{1}{2}C_{\rm A}N_{\rm F}\left(-\frac{418}{27} + \frac{40}{27}\pi^2 - \frac{56}{3}\zeta(3)\right) \qquad (5.37)$$
$$\left.+\frac{1}{2}C_{\rm F}N_{\rm F}\left(-\frac{55}{3} + 16\,\zeta(3)\right) - \frac{4}{27}N_{\rm F}^2\right] + \frac{1}{8}\pi\beta_0 d_2\,,$$

(for which, see [**26**])

$$B^{(1)} = -\frac{3}{2}\,C_{\rm F} + A^{(1)}\,\ln\frac{M^2}{\mu_{\rm Q}^2}\,, \qquad (5.38)$$

and [**12**]

$$B^{(2)} = \frac{1}{4}\left[C_{\rm F}^2\left(\pi^2 - \frac{3}{4} - 12\zeta(3)\right) + C_{\rm F}C_{\rm A}\left(\frac{11}{9}\pi^2 - \frac{193}{12} + 6\zeta(3)\right)\right.$$
$$\left.+\frac{1}{2}C_{\rm F}N_{\rm F}\left(-\frac{4}{9}\pi^2 + \frac{17}{3}\right)\right] + A^{(2)}\ln\frac{M^2}{\mu_{\rm Q}^2}\,. \qquad (5.39)$$

The coefficient d_2 is given by [**26**]

$$d_2 = C_{\rm F}\,C_{\rm A}\left(\frac{808}{27} - 28\,\zeta(3)\right) - \frac{112}{27}\,C_{\rm F}\,N_{\rm F}\,. \qquad (5.40)$$

Finally, the coefficients of the β-function for QCD, in the convention we use, are given in Eqs. 2.44, 2.45 and 2.46.

5.3. Comparison of results to DØ data

In this section I present the results of our resummed calculation with DØ kinematic cuts in place, and comparisons to DØ data. The DØ data are from proton–antiproton collisions at an energy $\sqrt{s} = 1.96\,\text{TeV}$, and correspond to an integrated luminosity of $7.3\,\text{fb}^{-1}$. The data are divided into two channels, corresponding to final states consisting of either e^+e^- pairs or $\mu^+\mu^-$ pairs, known as the electron and muon channels respectively. In the electron channel, the data are divided into three boson rapidity (y) bins: $|y| < 1$, $1 < |y| < 2$ and $|y| > 2$. The muon-channel data are binned in $|y| < 1$ and $1 < |y| < 2$ only. The invariant mass of the lepton pair is restricted to the range $70\,\text{GeV} < M < 110\,\text{GeV}$ for both channels. However, cuts on lepton transverse momenta ($p_{\rm T}^i$) and pseudorapidity (η^i) of the ith lepton differ between the two channels. For the muon channel, one has $p_{\rm T}^{1,2} > 15\,\text{GeV}$ and $|\eta^{1,2}| < 2$. For the electron channel, one has $p_{\rm T}^{1,2} > 20\,\text{GeV}$. The pseudorapidity cut is more complicated in the electron channel, and allows leptons with either $|\eta^{1,2}| < 1.1$ or $1.5 < |\eta^{1,2}| < 3$. The resummed calculations presented in this section reflect these experimental cuts. In addition, the CTEQ6M [**77**] PDFs are used, where the value of the strong coupling (evaluated at the Z boson mass) is $\alpha_{\rm s}(M_{\rm Z}) = 0.1179$.

Additionally, it is important to test the numerical cancellation of the large logarithms that appear in the fixed-order component of Eq. 5.1 at low ϕ^* against the large logarithms that appear in the expansion of the resummed component. For small values of ϕ^*, the resummation of soft and collinear gluon emission in this quasi-back-to-back region of the two leptons should dominate. The additional contribution from the fixed-order component in this region should be exactly cancelled by the expansion of the resummed component

to the same perturbative order. We therefore want to check that, indeed,

$$\lim_{\phi^* \to 0} \left[\left(\frac{d\sigma}{d\phi^*} \right)_{\text{fixed-order}} - \left(\frac{d\sigma}{d\phi^*} \right)_{\text{expansion}} \right] \to 0, \tag{5.41}$$

a quantity which we call the *remainder*. Figures 5.3 demonstrate this cancellation across the five rapidity bins for $\mathrm{Z} \to e\,e$ and $\mathrm{Z} \to \mu\,\mu$, for the scale choice $\mu_\mathrm{Q} = \mu_\mathrm{R} = \mu_\mathrm{F} = M$. The rapidity range $|y| > 2$ for the electron channel remains the only exception, where will employ a LO matching and therefore only the cancellation at $\mathcal{O}(\alpha_\mathrm{s})$ is shown. The equivalent plots for other scale choices considered are summarized in Appendix C.1, in Figs. C.1 to C.15.

The results of our calculations in comparison with DØ data are shown in Figs. 5.4 and 5.5 for electrons and muons, respectively. The yellow band represents the estimate of the theoretical uncertainty. It is determined by varying the three perturbative scales (μ_Q, μ_R and μ_F) about their nominal value of M. The actual variations are discrete and are subject to the constraint $M/2 \leq \mu_\mathrm{Q}, \mu_\mathrm{R}, \mu_\mathrm{F} \leq 2M$. Furthermore, the ratio between any two scales may not exceed the range $\frac{1}{2}$ to 2; i.e. $1/2 \leq \mu_i/\mu_j \leq 2 \;\forall\, i, j \in \{\mathrm{R}, \mathrm{F}, \mathrm{Q}\}$. The data show good agreement with our NNLL+NLO matched calculation for the ϕ^* distribution in Drell–Yan events at $\sqrt{s} = 1.96\,\mathrm{GeV}$, taking into account experimental errors and the theoretical uncertainty due to the arbitrariness in perturbative scale choices.

It is crucial to consider a variety of combinations of the scale choice, as opposed to varying only one at a time whilst keeping the remaining scales fixed at their nominal values. This is exemplified in Fig. 5.6 which shows, for the muon channel in the $|y| < 1$ rapidity bin, the theoretical uncertainty band produced by varying

- only the resummation scale (μ_Q),
- only the factorization and renormalization scales (μ_F and μ_R) and
- all scales.

One observes that indeed the band widens and becomes more symmetric about the *central* scale choice ($\mu_\mathrm{Q} = \mu_\mathrm{R} = \mu_\mathrm{F} = M$) when all variations are considered. A comparison of the estimated size of these bands for a NLL and a NNLL calculation is shown in Fig. 5.7.

Uncertainties associated with the PDF set used have been omitted in the evaluation of the theoretical uncertainties quoted here, owing to their relative insignificance. I have studied the propagation of PDF uncertainties onto the resummed component of the normalized ϕ^* distribution, demonstrating them to be at the level of $\sim 1\%$ for values of $\phi^* \lesssim 0.1$. Moreover, differences between two distributions evaluated using CTEQ6M [**77**] and MSTW 2008 [**78**] PDF sets is significantly smaller than the per mill level across most of the ϕ^* range.

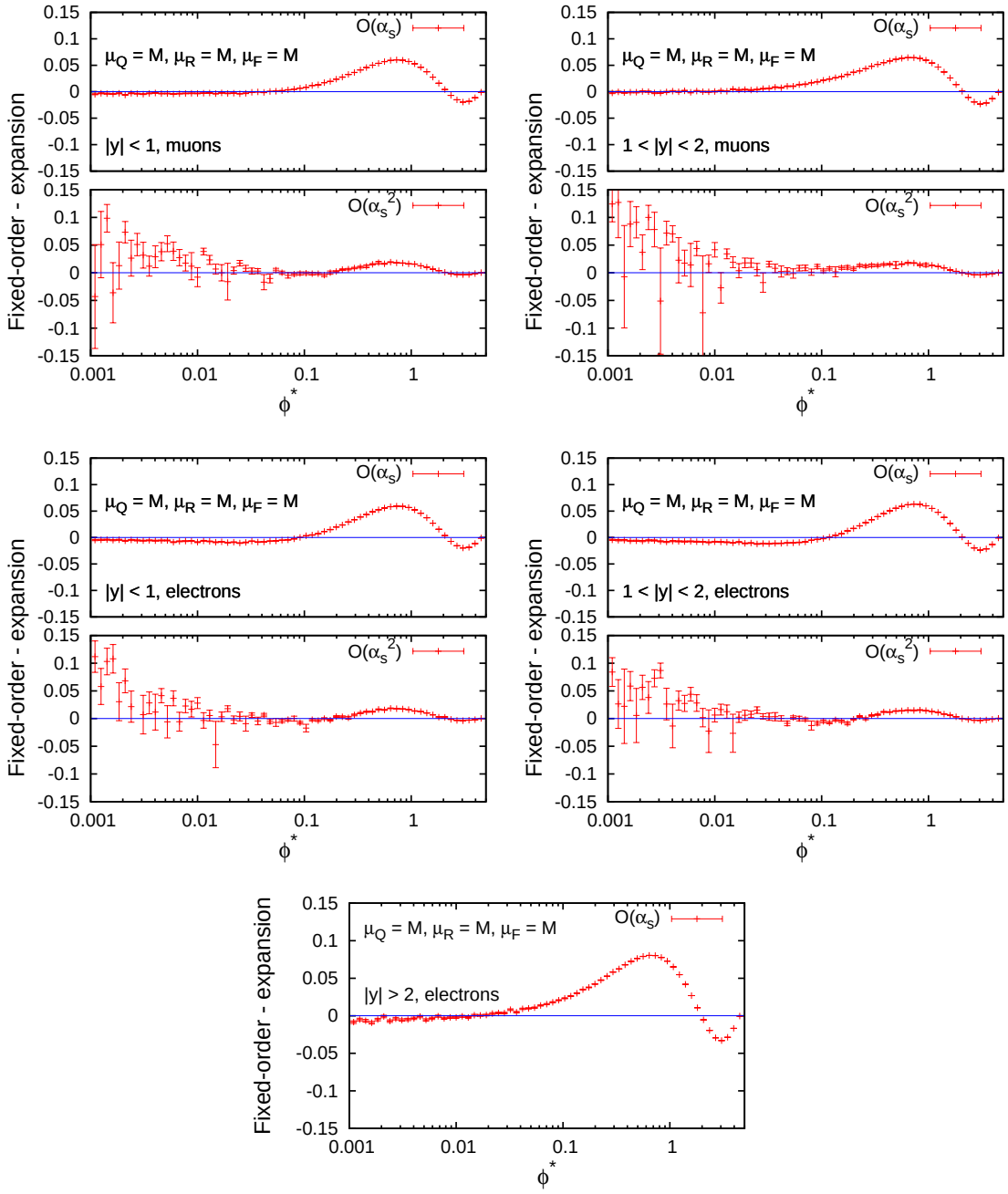

FIGURE 5.3. Remainder plots showing the cancellation of large logarithms between the fixed-order component and the expansion of the resummed component, order by order, for small values of ϕ^*. The plots show the various rapidity ranges for the muon and electron channels in DØ data.

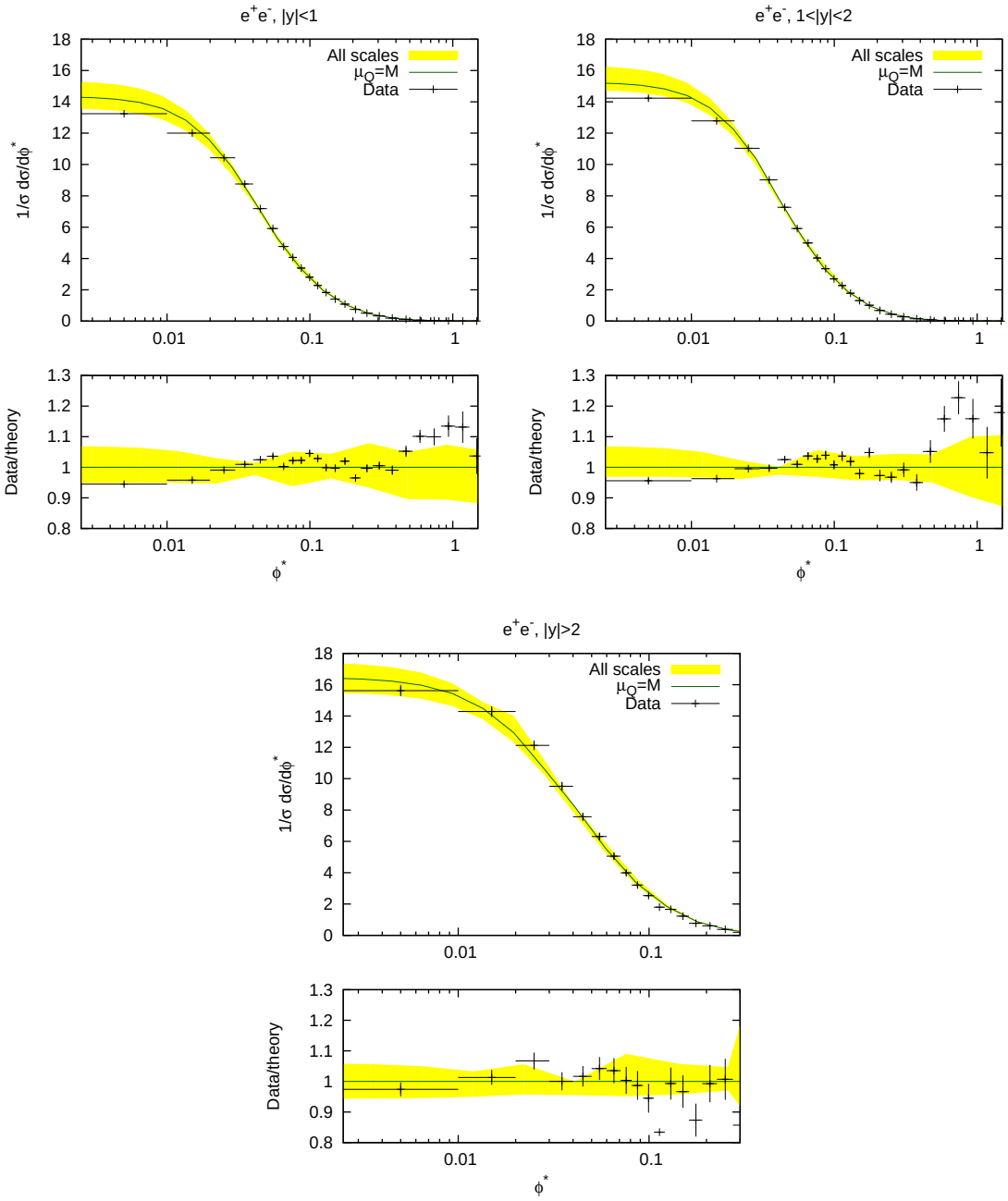

FIGURE 5.4. Our matched calculation for DØ data in the electrons channel, for the three boson rapidity regions $|y| < 1$, $1 < |y| < 2$ and $|y| > 2$.

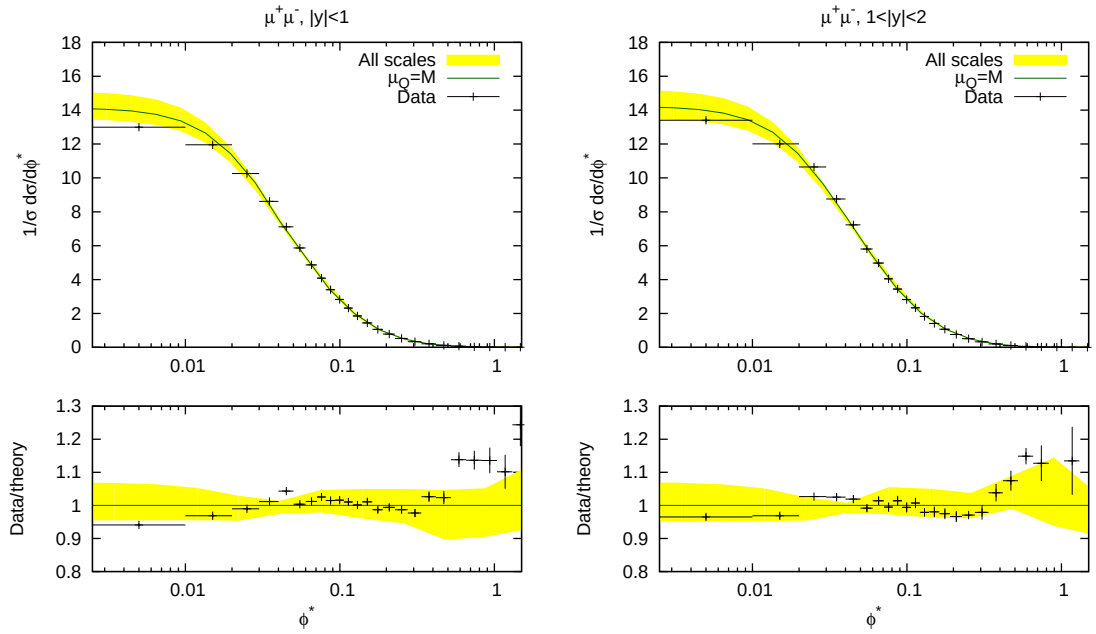

FIGURE 5.5. Our matched calculation for DØ data in the muons channel, for the two boson rapidity regions $|y| < 1$ and $1 < |y| < 2$.

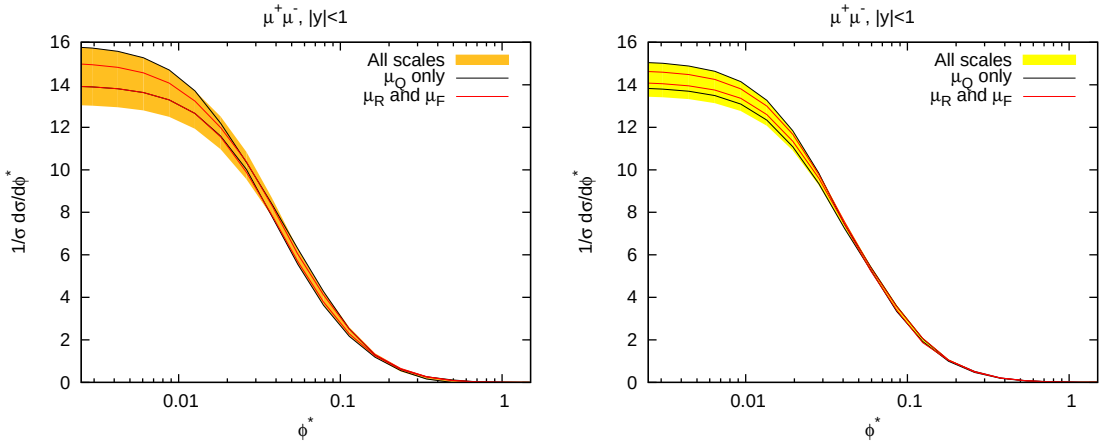

FIGURE 5.6. The contribution of the various scale variations to the total uncertainty band for a NLL (left) and NNLL (right) calculation.

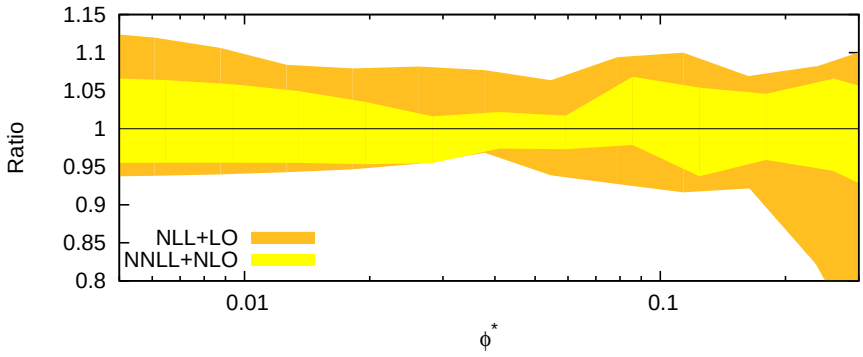

FIGURE 5.7. A direct comparison of the estimated theoretical uncertainties for a NLL and a NNLL calculation.

I have additionally used our resummed calculation to produce *predictions* for *low-mass* Drell–Yan data from DØ. At the time of writing, data are not yet publicly available. The predictions for the ϕ^* distribution with the kinematic selection

- $p_{\mathrm{T}}^{(1)} \geq 15$ GeV (transverse momentum of leading lepton)
- $p_{\mathrm{T}}^{(2)} \geq 10$ GeV (transverse momentum of second lepton)
- 30 GeV $< M <$ 60 GeV (invariant mass)
- $|\eta| \leq 2$ (pseudorapidities of both leptons)

in the two rapidity regions $|y| < 1$ and $1 < |y| < 2$, are show in Fig. 5.8. The corresponding remainder plots for the scale choice $\mu_{\mathrm{Q}} = \mu_{\mathrm{R}} = \mu_{\mathrm{F}} = M$ are shown, for illustration, in Fig 5.9. Due to large statistical uncertainties in the fixed-order component at $\mathcal{O}(\alpha_{\mathrm{s}}^2)$, the numerical cancellation of large logarithms is only guaranteed at $\mathcal{O}(\alpha_{\mathrm{s}})$. Remainder plots corresponding to other scale choices considered are summarized in Appendix C.1, in Figs. C.16 to C.21.

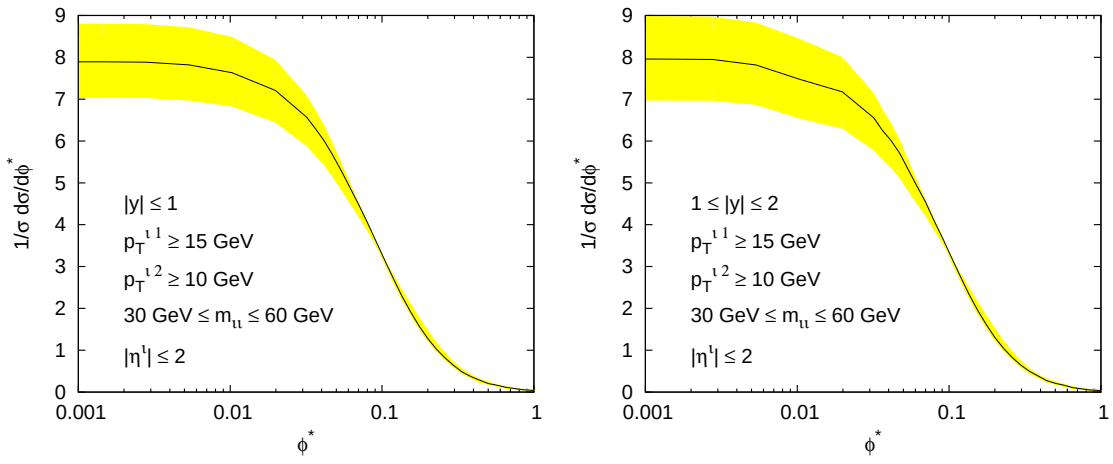

FIGURE 5.8. Predictions for the low-mass ϕ^* distributions at DØ, in the two rapidity regions $|y| < 1$ and $1 < |y| < 2$.

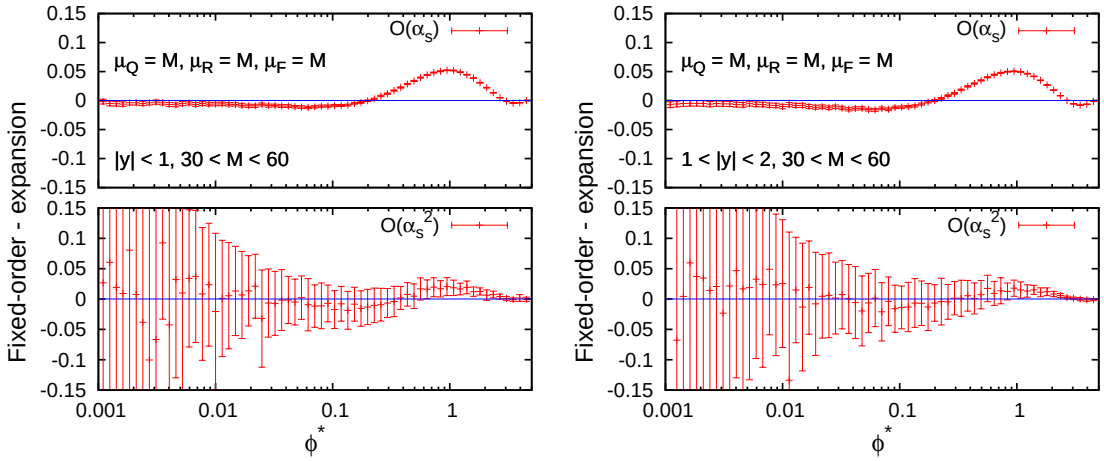

FIGURE 5.9. Remainder plots for the predicted low-mass ϕ^* distributions at DØ. in the two rapidity regions $|y| < 1$ and $1 < |y| < 2$. The scales correspond to $\mu_{\rm Q} = \mu_{\rm R} = \mu_{\rm F} = M$.

5.4. Predictions for the ATLAS experiment

In this section I present *predictions* for the ϕ^* distribution with the kinematics appropriate for the ATLAS experiment. At the time these predictions were made, ATLAS data on ϕ^* were not available. However, at the end of this section I will present a comparison to ATLAS data that were subsequently made public in 2012 [**20**]. In addition to ϕ^* predictions, the $Q_{\rm T}$ observable is also shown in comparison to ATLAS data as a way of validating our resummed calculation.

The following predictions are for proton–proton collisions at an energy of $\sqrt{s} = 7\,\text{TeV}$. For each lepton $i = 1, 2$, a cut is placed on its transverse momentum and pseudorapidity, of $p_{\rm T}^{1,2} > 20\,\text{GeV}$ and $|\eta^{1,2}| < 2.4$ respectively. The invariant mass of the lepton pair is also constrained to be within the range $66\,\text{GeV} < M_{\ell\ell} < 116\,\text{GeV}$. Initially, results are presented across the entire range of boson rapidities, i.e. $|y| < 2.4$. At the end of this section, however, I present our results binned in the three rapidity regions $|y| < 0.8$, $0.8 < |y| < 1.6$ and $1.6 < |y| < 2.4$.

Our predictions were also generated for a variety of scale choices. We allowed each scale, $\mu_{\rm R}$, $\mu_{\rm F}$ and $\mu_{\rm Q}$, to vary independently between $M/2$ and $2M$, with the additional constraint that the ratio of any two scales must be between $1/2$ and 2. To summarize, we allow $M/2 \leq \mu_i \leq 2M$ provided that $1/2 \leq \mu_i/\mu_j \leq 2\,\forall\, i, j$, where $i, j \in \{\text{R}, \text{F}, \text{Q}\}$. Figures C.22–C.27 in Appendix C.2 show the remainders $(d\sigma/d\phi^*_{\text{fixed-order}} - d\sigma/d\phi^*_{\text{expansion}}$, and similarly for $Q_{\rm T})$ for our ATLAS predictions in the full rapidity region $|y| < 2.4$, for all discrete scale choices we considered. Below, the corresponding plots for the case of $\mu_{\rm Q} = \mu_{\rm R} = \mu_{\rm F} = M$ are shown (Fig. 5.10). The left plot shows the case of ϕ^* and the right plot shows the case of $Q_{\rm T}$. The top plots show the cancellation of the remainder at $\mathcal{O}(\alpha_{\rm s})$, while the bottom plots show this cancellation at $\mathcal{O}(\alpha_{\rm s}^2)$. The objective here is to determine if the large logs cancel numerically between the fixed-order component and the expansion of the resummed component, as they should. In practice, one becomes statistically limited

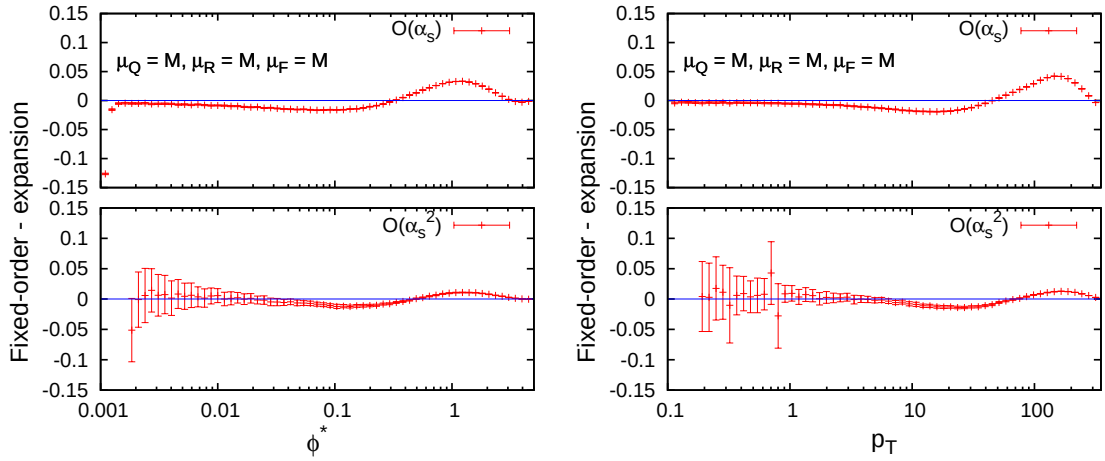

FIGURE 5.10. The *remainder* plots for our ATLAS ϕ^* and Q_{T} (p_{T}) predictions, where $\mu_{\mathrm{R}} = \mu_{\mathrm{F}} = \mu_{\mathrm{Q}} = M$. These plots show the numerical cancellation of the large logarithms between the fixed-order calculation and the expansion of the resummation.

for small values of either ϕ^* or Q_{T}, particularly for the $\mathcal{O}(\alpha_{\mathrm{s}}^2)$ contribution. For this reason, one attempts to determine if the logs show a trend towards cancellation for small values of the observable. If this is the case, one can neglect the contribution from the fixed-order (which is statistically limited in this region, along with the remainder) below a certain value of the observable. Thus, below this *cut* value, the only contribution to the distribution is from the resummed component. Since the Born weights which enter the resummed component are just $\mathcal{O}(\alpha)$—i.e. not even an $\mathcal{O}(\alpha_{\mathrm{s}})$ contribution—one is not statistically limited.

There is no reason to use the same cut value for both the $\mathcal{O}(\alpha)$ and $\mathcal{O}(\alpha^2)$ contributions. In the case of ϕ^* we choose $\phi^* = 0.0035$ for the $\mathcal{O}(\alpha)$ cut and $\phi^* = 0.03$ for the $\mathcal{O}(\alpha^2)$ cut. In reference to Fig. 5.10, this is the point at which one is confident about the numerical large-logarithmic cancellation, yet at which one does not experience large statistical errors. In this light, the cut parameter is tuned.

There is also a cut which we apply for higher values of ϕ^*. This time, however, we observe that the resummation becomes unnecessary and the fixed-order component describes the data well. For this reason we adopt a cut in ϕ^* beyond which the resummation (and its expansion) is manually set to zero. This is in effort to suppress spurious $\mathcal{O}(\alpha^3)$ terms (and beyond) for high values of ϕ^*, which lie beyond the jurisdiction of resummation. The position we choose for this cut is at $\phi^* = 0.5$. Thus, for values of $\phi^* > 0.5$ only the fixed-order component is used.

The corresponding low-Q_{T} cuts, below which only the resummed component is used, are set to $Q_{\mathrm{T}} = 0.2\,\mathrm{GeV}$ and $Q_{\mathrm{T}} = 4.5\,\mathrm{GeV}$ for the $\mathcal{O}(\alpha)$ and $\mathcal{O}(\alpha^2)$ contributions, respectively. For values of $Q_{\mathrm{T}} > 50\,\mathrm{GeV}$, only the fixed-order component is used. As in the case of ϕ^*, this high-Q_{T} cut is at a point where the resummation is deemed unnecessary, since the argument of the resummed logarithms is $50\,\mathrm{GeV}/M$, with $M \sim M_{\mathrm{Z}}$. Not only is resummation unnecessary in this region, where the logs in Q_{T}/M are not large, but we

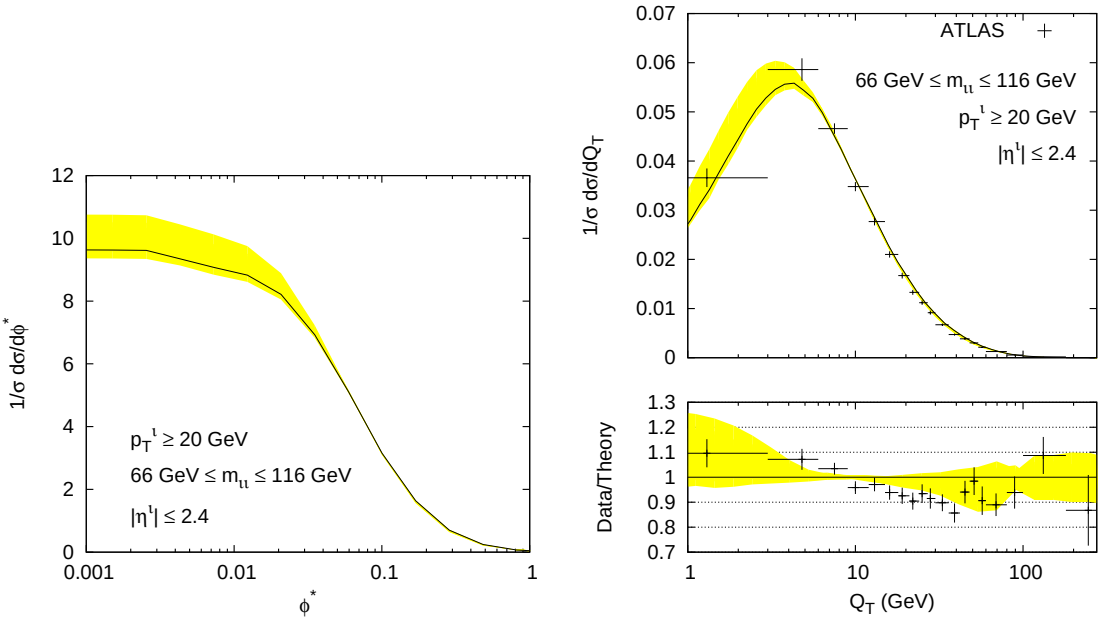

FIGURE 5.11. Our NNLL+NLO prediction for the ϕ^* observable (left) for ATLAS at $\sqrt{s} = 7$ TeV. On the right, our corresponding calculation for Q_{T} is shown in comparison to existing ATLAS data [**79**], for the purpose of validating our calculation.

again want to suppress spurious $\mathcal{O}(\alpha^3)$ contributions (and beyond) where the resummation has no jurisdiction.

With these considerations in place, the ϕ^* prediction and Q_{T} comparison to existing ATLAS data [**79**] are shown in Fig. 5.11. The plot on the left shows our ϕ^* prediction while the plot on the right shows our calculation of Q_{T} in comparison with existing ATLAS data. The black line is the curve determined by setting all scales equal to the invariant mass of the lepton pair, i.e. $\mu_{\mathrm{Q}} = \mu_{\mathrm{R}} = \mu_{\mathrm{F}} = M$. The yellow band extends to the extreme points on any curve, each of which comes from considering the scale variations already discussed. For each value of ϕ^*, the yellow band extends from the minimum value of $d\sigma/d\phi^*$ to the maximum value, generated by any of the scale choices under consideration.

In March 2013, the ATLAS measurement of the differential ϕ^* cross-section measurement at $\sqrt{s} = 7\,\mathrm{TeV}$ was published [**20**]. Figure 5.12, below, shows a comparison between our resummed prediction and the ATLAS data. These data correspond to an integrated luminosity of $4.6\,\mathrm{fb}^{-1}$, and have the same kinematic cuts applied to the final-state leptons as described above.

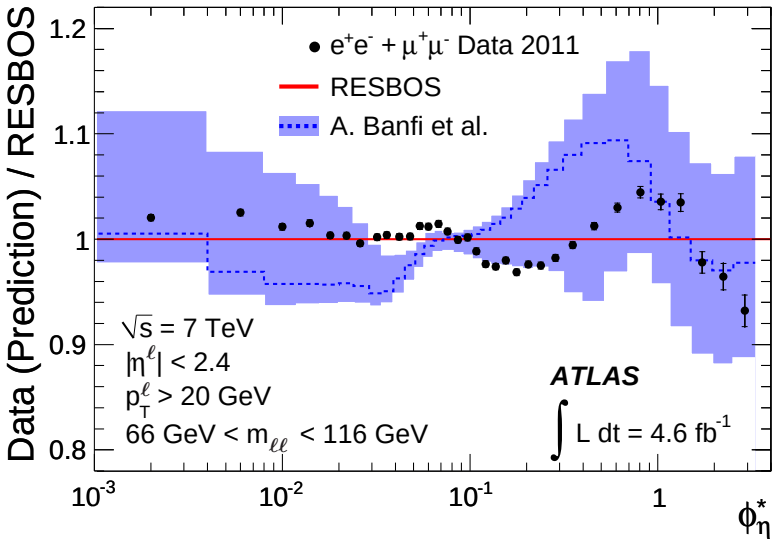

FIGURE 5.12. Our NNLL+NLO prediction for the ϕ^* observable in comparison with 4.6 fb^{-1} of ATLAS data at $\sqrt{s} = 7$ TeV, published in March 2013 [**20**], but which became publicly available in 2012.

Finally, I present our ϕ^* predictions for ATLAS in the three rapidity ranges $|y| < 0.8$, $0.8 < |y| < 1.6$ and $1.6 < |y| < 2.4$, as shown in Fig. 5.13. Figure 5.14 shows a ratio of these distributions for easy comparison, in which a significant amount of theoretical perturbative uncertainty cancels.

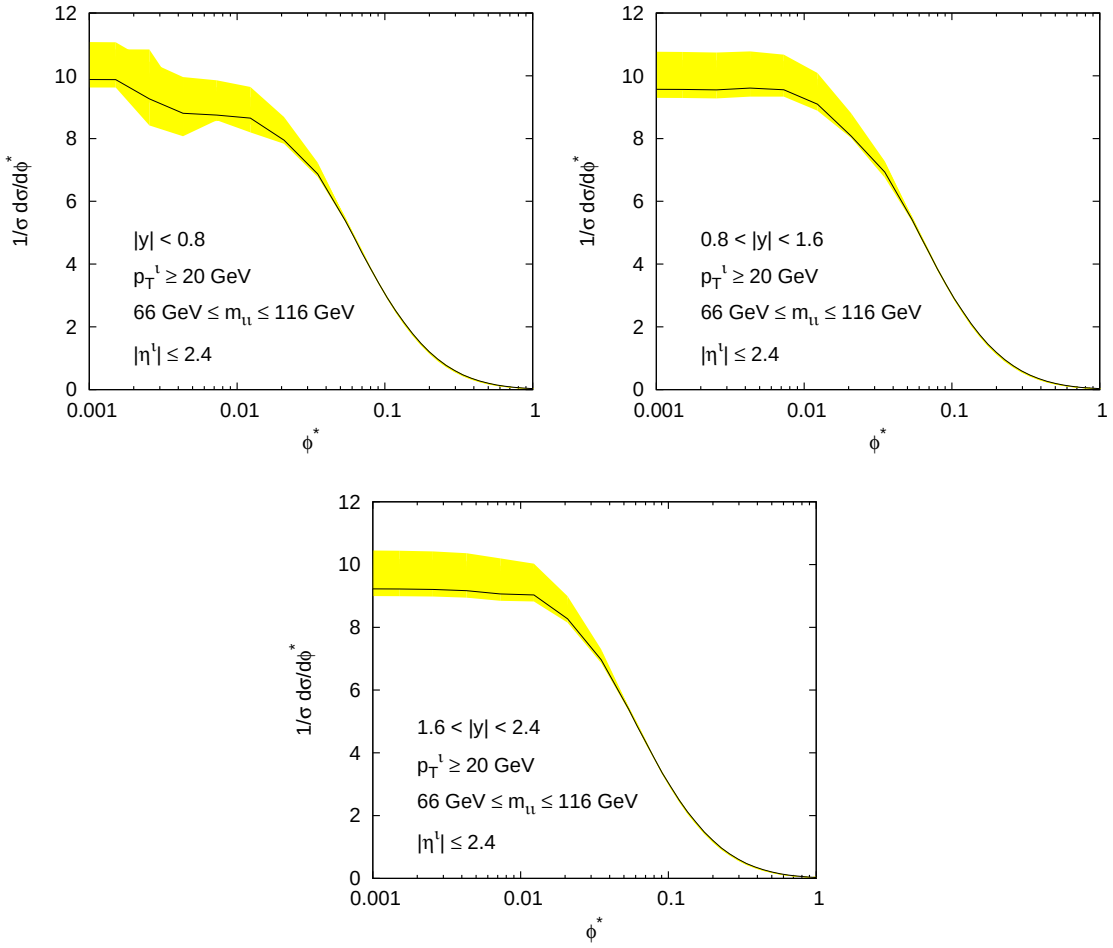

FIGURE 5.13. Our ϕ^* predictions for ATLAS kinematics at $\sqrt{s} = 7$ TeV, in the three rapidity regions $|y| < 0.8$, $0.8 < |y| < 1.6$ and $1.6 < |y| < 2.4$, top left, top right and bottom centre, respectively.

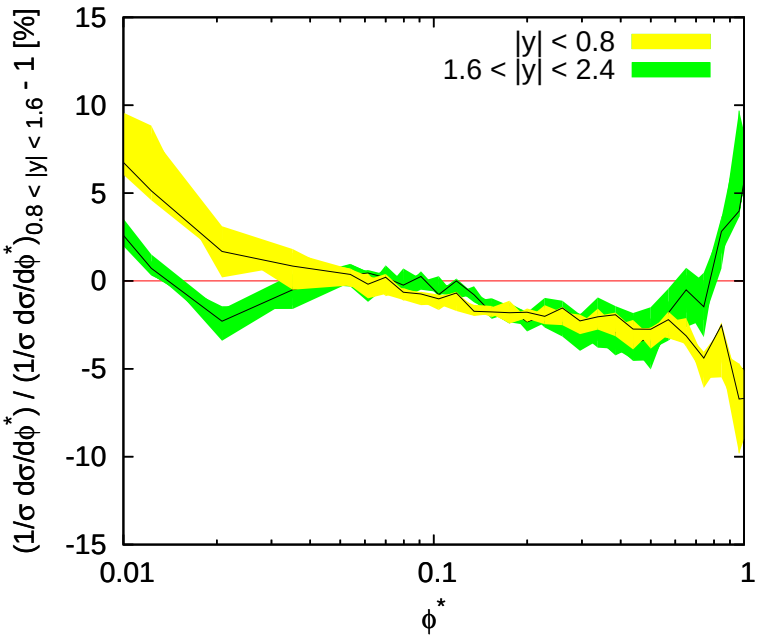

FIGURE 5.14. Here I show the ratios of different rapidity bins for our ATLAS ϕ^* predictions, to supplement Fig. 5.13.

5.5. Probing the small-x régime

In our DØ studies corresponding to Tevatron energies of $\sqrt{s} = 1.96\,\text{GeV}$, we chose to freeze the PDF evolution below values of $Q = Q_0$, i.e.

$$\phi_i(x,Q) \to \bar{\phi}_i(x,Q) = \begin{cases} \phi_i(x,Q) & \text{for} \quad Q > Q_0 \\ \phi_i(x,Q_0) & \text{for} \quad Q \leq Q_0 \end{cases} \tag{5.42}$$

In this case, the freezing point was chosen at $Q_0 = 1\,\text{GeV}$. Since the PDFs are evaluated using DGLAP evolution at $Q = \mu_\text{F}/(\mu_\text{Q}\,\bar{b})$, low values of Q correspond to high values of b in the argument, and *vice versa*. I have varied the value of Q_0 about this nominal value to ensure that this non-perturbative prescription results in an uncertainty much less than our perturbative uncertainty.

Owing to the increase in $\sqrt{s}$ at the LHC relative to Tevatron, the momentum fractions x_1 and x_2 of the partons at the LHC entering the hard scattering process are conversely typically much smaller than those at Tevatron. The Q-dependence of $\phi_i(x,Q)$ in this small-x régime is steeper and a fixed cutoff in the PDF evolution below $Q = Q_0$ is not appropriate. In fact, in the b-space formalism (in which one works in the space Fourier conjugate to Q_T) the discontinuity that arises because of the piecewise construction of the PDFs, Eq. 5.42, results in oscillatory behaviour of the ϕ^* and Q_T spectra. We thus employ an exponential extrapolation of $\phi_i(x,Q)$ below $Q = Q_0$, mitigating this behaviour.

The extrapolation in fact rather concerns the actual Drell–Yan weight $\bar{\Sigma}$ given in Eq. 4.138, which itself contains the PDFs. We consider the piecewise construction

$$\bar{\Sigma}(Q) = \begin{cases} \bar{\Sigma}(Q) & \text{for} \quad Q > Q_0 \\ A\, e^{-B\,Q} & \text{for} \quad Q \leq Q_0 \end{cases} \tag{5.43}$$

where

$$\begin{aligned} A &= \bar{\Sigma}(Q_1)\, e^{-B\,Q_1} \\ \text{and} \qquad B &= \frac{\log\left(\bar{\Sigma}(Q_1)/\bar{\Sigma}(Q_2)\right)}{Q_2 - Q_1}\,. \end{aligned} \tag{5.44}$$

The transition scale Q_0 is now taken to be 1.5 GeV. While still not a mathematically continuous construction, the extrapolation is sufficiently continuous *numerically* in its first derivative so as to mitigate former modulations in the resummed distribution, owing to a local deficiency of Fourier modes around $Q = Q_0$, without introducing new ones. The two scales Q_1 and Q_2 are taken to be 1.4 and 2.0 GeV respectively[1], and the weight $\bar{\Sigma}$ is evaluated at these two scales in order to deduce the constants A and B used in the extrapolation.

Certain combinations of perturbative scale choices which result in lower values of $\mu_{\mathrm{F}}/\mu_{\mathrm{Q}}$, however, serve to enhance the inversely proportional relationship between Q and b in the argument of the PDFs. Whilst the oscillations are no longer present after employing the exponential extrapolation of the PDFs, these combinations of scale choices still result in significantly outlying curves for the ϕ^* and Q_{T} spectra. Considering that PDF evolution based on the DGLAP framework of collinear factorization may become invalid for $Q < 1\,\mathrm{GeV}$, we simply choose to ignore these scale choices in our uncertainty band. Thus, we impose the additional restriction that scale combinations which enter our theoretical uncertainty band must also yield $\mu_{\mathrm{F}}/\mu_{\mathrm{Q}} \geq 1$. Such manifestations may be indicative of the need of transverse-momentum-dependent PDFs (or 'TMDs'). For further information regarding TMDs, collinear factorization and the small-x régime, the reader is encouraged to consult [**80, 81, 82**].

5.6. Predictions for the CMS experiment

At the time of writing, CMS public results for the differential Drell-Yan cross-section in ϕ^* are not available for $\sqrt{s} = 7\,\mathrm{TeV}$. Notwithstanding, adopting the same kinematic cuts as applied in the CMS measurement of the Q_{T} observable for Drell-Yan, we have generated a prediction for ϕ^*. This prediction is shown in Fig. 5.15, along with our computed Q_{T} observable compared with existing CMS data [**83**]. The kinematic cuts applied in each case are as follows: For each lepton $i = 1, 2$, a minimum transverse momentum $p_{\mathrm{T}}^{1,2} > 20\,\mathrm{GeV}$ is required, along with a constraint on its pseudorapidity $|\eta^{1,2}| < 2.1$. Finally, the invariant mass of the lepton pair is required to fall within the window $60\,\mathrm{GeV} < M_{\ell\ell} < 120\,\mathrm{GeV}$. In comparison with the event selection performed by ATLAS, this corresponds to a slightly tighter η cut and a slightly looser M cut. The corresponding remainder plots for all scale variations may be found in Appendix C.3.

[1] In principle, Q_1 should equal Q_0 to ensure the continuity of the construction.

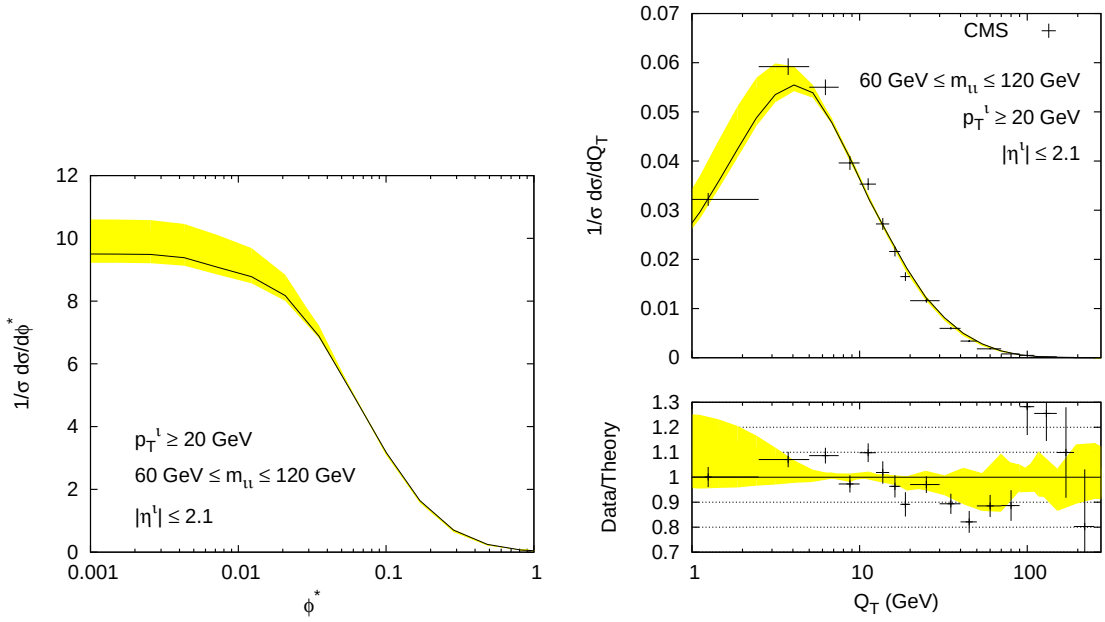

FIGURE 5.15. Our NNLL+NLO prediction for the ϕ^* observable (left) for CMS at $\sqrt{s} = 7$ TeV. On the right, our corresponding calculation for $Q_{\rm T}$ is shown in comparison to existing CMS data [**83**], for the purpose of validating our calculation.

5.7. Non-perturbative prescriptions in the b-space formalism

The coefficients g_i in the resummed exponent $R(\bar{b}\,\mu_{\rm Q})$, Eq. 5.30, depend on the dimensionless parameter

$$\lambda = \beta_0\,\alpha_{\rm s}(\mu_{\rm R})\,\ln(\bar{b}^2\,\mu_{\rm Q}^2)\,, \tag{5.45}$$

with $\alpha_{\rm s}(\mu_{\rm R})$ defined in the $\overline{\rm MS}$ scheme. Substituting the one-loop expression for $\alpha_{\rm s}(\mu_{\rm R})$, written in terms of the dimensionful quantity $\Lambda_{\rm QCD}$, i.e.

$$\alpha_{\rm s}(\mu_{\rm R}) = \frac{1}{\beta_0\,\ln(\mu_{\rm R}^2/\Lambda_{\rm QCD}^2)}\,, \tag{5.46}$$

one obtains

$$\lambda = \frac{\ln(\bar{b}\,\mu_{\rm Q})}{\ln(\mu_{\rm R}/\Lambda_{\rm QCD})} \tag{5.47}$$

As $\lambda \to 1$, this implies $\bar{b} \to (\mu_{\rm R}/\mu_{\rm Q})\,\Lambda_{\rm QCD}^{-1}$. In this limit one approaches the Landau pole of QCD, where the notion of a perturbative expansion breaks down. In order to safeguard against this, we introduce an upper limit of $b_{\rm max}$ on the b integration such that $\bar{b}_{\rm max} < \Lambda_{\rm QCD}^{-1}$. In principle, the upper limit on the b-space integration (set by $\lambda_{\rm max} = 1$) is

$$b_{\rm max} = 2\,\mu_{\rm Q}^{-1}\,e^{-\gamma_{\rm E}}\,\exp[1/(2\,\beta_0\,\alpha_{\rm s}(\mu_{\rm R}))]\,, \tag{5.48}$$

having used $\bar{b} \equiv b\,e^{\gamma_{\rm E}}/2$.

The cutoff at $b_{\rm max}$ is an intrinsically non-perturbative prescription which is arbitrary, along with the actual choice of $b_{\rm max}$. For this reason we have varied $b_{\rm max}$ about the value we choose (which is typically $\sim (3\,\Lambda_{\rm QCD})^{-1}$) in order to verify that it has negligible impact on the theoretical prediction, which is indeed the case. From a practical point of view,

setting $b_{\max}$ no higher than necessary to achieve our desired accuracy also increases the performance of the numerical integration over b.

There is also a lower limit of λ at $\lambda_{\min} = 0$. This limit requires $\ln(\bar{b}^2\,\mu_{\rm Q}^2) \to 0$, and so $\bar{b} \to \mu_{\rm Q}^{-1}$. As such, we have a lower limit on the b integration, set by

$$b_{\min} = 2\,\mu_{\rm Q}^{-1}\,e^{-\gamma_{\rm E}}\,, \tag{5.49}$$

beneath which one is outside the jurisdiction of the resummation. At precisely $b = b_{\min}$, the resummed exponent $R(\bar{b}_{\min}\,\mu_{\rm Q}) = 0$. At values of $b < b_{\min}$, we adopt the prescription of *freezing* the radiator $R(\bar{b}\,\mu_{\rm Q})$ at zero. The b-integral is thus separated into two contributions, as in

$$\begin{aligned}
&\int_0^\infty db\,M\,\cos(b\,M\,\phi^*)\,e^{-R(\bar{b},M,\mu_{\rm Q},\mu_{\rm R})} \\
&\qquad\to \int_0^{b_{\min}} db\,M\,\cos(b\,M\,\phi^*) + \int_{b_{\min}}^{b_{\max}} db\,M\,\cos(b\,M\,\phi^*)\,e^{-R(\bar{b},M,\mu_{\rm Q},\mu_{\rm R})} \\
&\qquad\quad = \frac{\sin(b_{\min}\,M\,\phi^*)}{\phi^*} + \int_{b_{\min}}^{b_{\max}} db\,M\,\cos(b\,M\,\phi^*)\,e^{-R(\bar{b},M,\mu_{\rm Q},\mu_{\rm R})}\,,
\end{aligned} \tag{5.50}$$

of which the remaining integral from $b_{\min}$ to $b_{\max}$ is performed numerically. In the case of the $Q_{\rm T}$ observable, the separation is

$$\begin{aligned}
&\int_0^\infty db\,b\,J_0(b\,Q_{\rm T})\,e^{-R(\bar{b},M,\mu_{\rm Q},\mu_{\rm R})} \\
&\qquad\to \int_0^{b_{\min}} db\,b\,J_0(b\,Q_{\rm T}) + \int_{b_{\min}}^{b_{\max}} db\,b\,J_0(b\,Q_{\rm T})\,e^{-R(\bar{b},M,\mu_{\rm Q},\mu_{\rm R})} \\
&\qquad\quad = \frac{b_{\min}\,J_1(b_{\min}\,Q_{\rm T})}{Q_{\rm T}} + \int_{b_{\min}}^{b_{\max}} db\,b\,J_0(b\,Q_{\rm T})\,e^{-R(\bar{b},M,\mu_{\rm Q},\mu_{\rm R})}\,.
\end{aligned} \tag{5.51}$$

The numerical evaluation of the remaining integrals in b-space is performed for both observables using a lightweight implementation of a 32-point Gaussian quadrature rule. A fast numerical implementation of b-space integration is of course critical for our purposes of obtaining precise resummed predictions which require high statistics. This bespoke implementation is very competitive in terms of performance, with computation times similar to other free implementations, owing to its lightweight nature.

5.8. A non-perturbative study

In addition to the purely perturbative computations which were compared to DØ data, with the caveat of the aforementioned prescriptions in b-space, I also studied a non-perturbative (NP) model designed to mimic the effect of intrinsic parton transverse momenta within the hadrons. NP models have previously been studied in the context of Drell–Yan $Q_{\rm T}$ [**84**] and also the *energy-energy correlation* in e^+e^- annihilation [**85**]. The model we utilize in our phenomenological approach adds a Gaussian smearing term to the radiator, such that

$$R(\bar{b}\,M) \to R_{\rm NP}(\bar{b}\,M) = R(\bar{b}\,M) + g_{\rm NP}\,b^2\,, \tag{5.52}$$

where the parameter $g_{\rm NP}$ characterizes the smearing and has units $(\text{GeV})^2$. In the context of the resummed expression, this amounts to an overall multiplication by a Gaussian in b

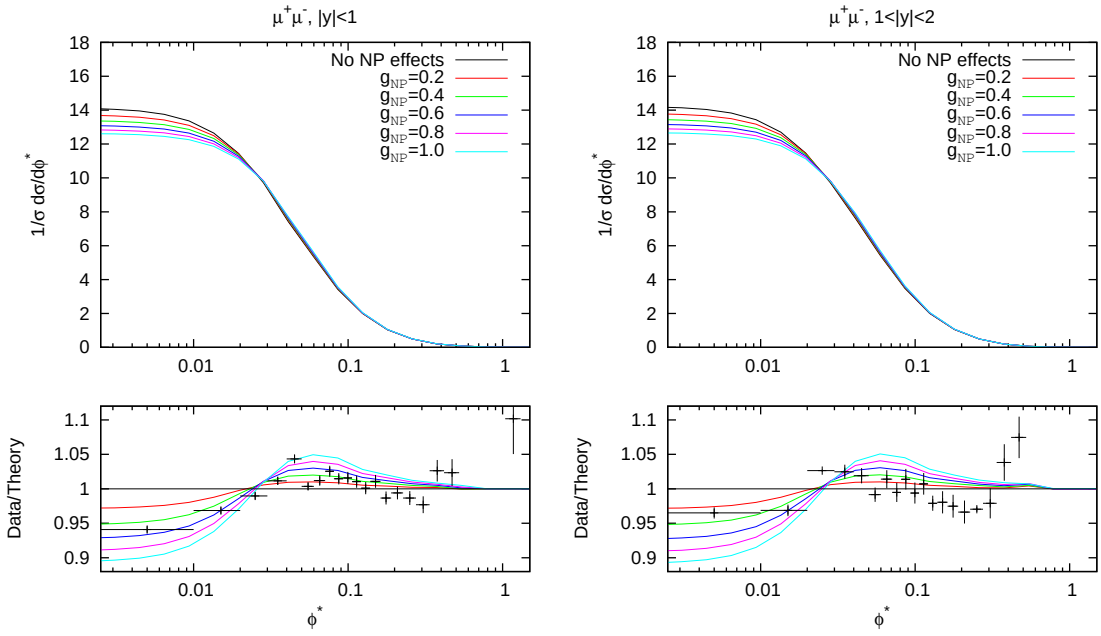

FIGURE 5.16. The inclusion of a non-perturbative Gaussian form factor in our NNLL+NLO calculations for DØ at $\sqrt{s} = 1.96$ TeV. The curves shown correspond to different values of the associated parameter, g_{NP}. The two rapidity bins for the muons channel are shown.

with a width $\sigma = 1/\sqrt{2\, g_{\mathrm{NP}}}$. Since b is the Fourier conjugate to Q_{T}, this translates into a Gaussian smearing of Q_{T} by $\sqrt{2\, g_{\mathrm{NP}}}$.

Indeed, the Gaussian *ansatz* of our model is consistent with the exponentiation of the model employed in [**84**] (which is quadratic in b near $b = 0$) where further discussion of its motivation may be found. Further parameterizations of a NP form factor on the Drell–Yan Q_{T} spectrum may be found in the literature, including the BLNY parameterization of Brock, Landry, Nadolsky & Yuan [**86**], which is also of the Gaussian form.

Figures 5.16 and 5.17 show the impact of this NP model on the calculation corresponding to the 'central' scale choice (i.e. with $\mu_{\mathrm{Q}} = \mu_{\mathrm{R}} = \mu_{\mathrm{F}} = M$) for different values of the NP parameter g_{NP}.

Ostensibly, given the size of the theoretical uncertainties on the perturbative calculations for DØ kinematics, estimated by varying the perturbative scales about their nominal values, one cannot make a conclusive statement regarding the need for NP effects to successfully describe the data. The essential point is that one should be careful not to falsely ascribe any discrepancy between data and theory to the need for NP input, which may be mitigated using purely perturbative techniques. To this end it is of crucial importance that one has a sound perturbative prediction and understanding of theoretical uncertainty. Recent work has shown, however, that even in light of a theoretical uncertainty band seemingly concluding an agreement with data in the absence of explicit NP input, the data do indeed prefer a non-zero value of g_{NP} [**87**]. This conclusion is reached by treating scales related to μ_{Q}, μ_{R} and μ_{F} as nuisance parameters in a χ^2 minimization attempting to fit g_{NP}.

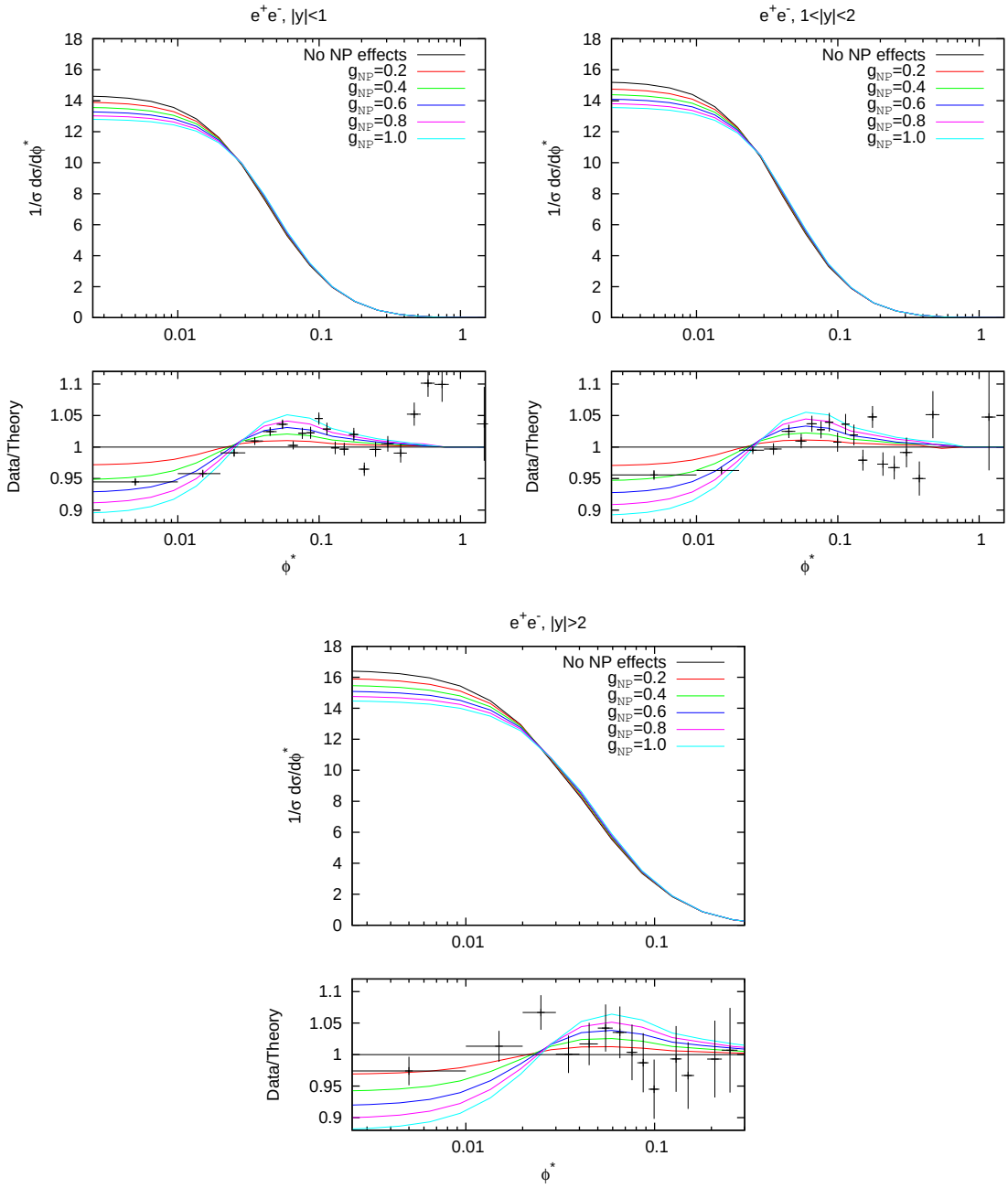

FIGURE 5.17. The inclusion of a non-perturbative Gaussian form factor in our NNLL+NLO calculations for DØ at $\sqrt{s} = 1.96$ TeV. The curves shown correspond to different values of the associated parameter, $g_{\rm NP}$. The three rapidity bins for the electrons channel are shown.

In this work, M. Guzzi, P. M. Nadolsky and B. Wang (GNW) pursue two approaches in the determination of a parameter labelled $a_{\rm Z}$ (equivalent to $g_{\rm NP}$; i.e. the coefficient of b^2 in an exponentiated NP form factor) associated with the NP model in ResBos. It is important to note that the studies therein are carried out in the CSS formalism [**14**], and so a different and non-trivially related set of perturbative scales are considered, namely C_1, C_2, C_3 and C_4. The first approach assumes these scales to be fixed at some values,

while the χ^2 is minimized by discretely varying the parameter a_Z to find the best fit. The χ^2 definition adopted for this specific case is given by

$$\chi^2(a_Z) = \sum_{i=1}^{N} \left(\frac{D_i - \bar{T}_i(a_Z)}{s_i} \right)^2 , \tag{5.53}$$

which is minimized with respect to a_Z, yielding the preferred value. In this definition, N data points $\{D_i\}$ are considered, with corresponding uncorrelated uncertainties $\{s_i\}$. Theoretical predictions are computed for each data point i using fixed scales and distinct values of a_Z, and are denoted $\bar{T}_i(a_Z)$.

The second approach extends this method by allowing the scales to effectively float in the fit. The scales themselves are treated by defining corresponding nuisance parameters $\lambda_\alpha \equiv \log_2(C_\alpha/\bar{C}_\alpha)$, where the bar denotes a specific nominal configuration for these values. It is assumed that the scale variations should be small. As such, the theoretical prediction for the ith point is written as a Taylor expansion

$$T_i(a_Z, \{\lambda_\alpha\}) = T_i(a_Z, \{\bar{\lambda}_\alpha\}) + \sum_{\alpha=1}^{3} \left[\frac{\partial}{\partial \lambda_\alpha} T_i(a_Z, \{\lambda_\alpha\}) \right]_{\{\lambda_\alpha\}=\{\bar{\lambda}_\alpha\}} (\lambda_\alpha - \bar{\lambda}_\alpha) , \tag{5.54}$$

where the expansion is truncated beyond the first derivative. Here, $\{\lambda_\alpha\}$ is shorthand for $\lambda_1, \lambda_2, \lambda_3$, and the bar denotes those nuisance parameters corresponding to the nominal values of the scales. By definition of the nuisance parameter, however, $\bar{\lambda}_\alpha = 0$. The partial derivative is then estimated by a finite-difference derivative:

$$\frac{\partial}{\partial \lambda_\alpha} T_i(a_Z, \{\lambda_\alpha\}) \approx \frac{T_i(a_Z, \lambda_\alpha^+, \{\bar{\lambda}_{\beta\neq\alpha}\}) - T_i(a_Z, \lambda_\alpha^-, \{\bar{\lambda}_{\beta\neq\alpha}\})}{\Delta\lambda_\alpha} \equiv \beta_{i\alpha}(a_Z, \{\bar{\lambda}_\alpha\}) \tag{5.55}$$

Here, $\Delta\lambda_\alpha = \lambda_\alpha^+ - \lambda_\alpha^-$, the difference between positive and negative variations of the nuisance parameter λ_α. The variations actually used are $\lambda_\alpha^\pm = \pm 1$, corresponding to scale variations ranging from $\frac{1}{2}$ to 2 times their nominal values. The theoretical prediction for the ith point is now written simply

$$T_i(a_Z, \{\lambda_\alpha\}) = T_i(a_Z, \{\bar{\lambda}_\alpha\}) + \sum_{\alpha=1}^{3} \beta_{i\alpha}\, \lambda_\alpha , \tag{5.56}$$

incorporating this linearized model of scale variations.

As in the first approach, the goodness of fit is measured using a χ^2 expression which accounts for the nuisance parameters:

$$\chi^2(a_Z) = \sum_{i=1}^{N} \left(\frac{D_i - \bar{T}_i(a_Z) - \sum_{\alpha=1}^{3} \beta_{i\alpha}\, \lambda_\alpha}{s_i} \right)^2 + \sum_{\alpha=1}^{3} \frac{\lambda_\alpha^2}{\sigma_\lambda^2} . \tag{5.57}$$

The final term effectively restricts scale variations by penalizing those which are considered beyond reasonable. This second method considers the fit without this additional term, but also with the value $\sigma_\lambda^{-1} = 1$. The reader is encouraged to consult [**87**] for the values of a_Z determined in specific cases. However, I note here the value $a_Z = 0.82^{+0.22}_{-0.11}\,\mathrm{GeV}^2$ determined from the fit to 60 DØ data points, covering all rapidity bins with $\phi^* \leq 0.1$. The reduced χ^2 for this fit is 1.31.

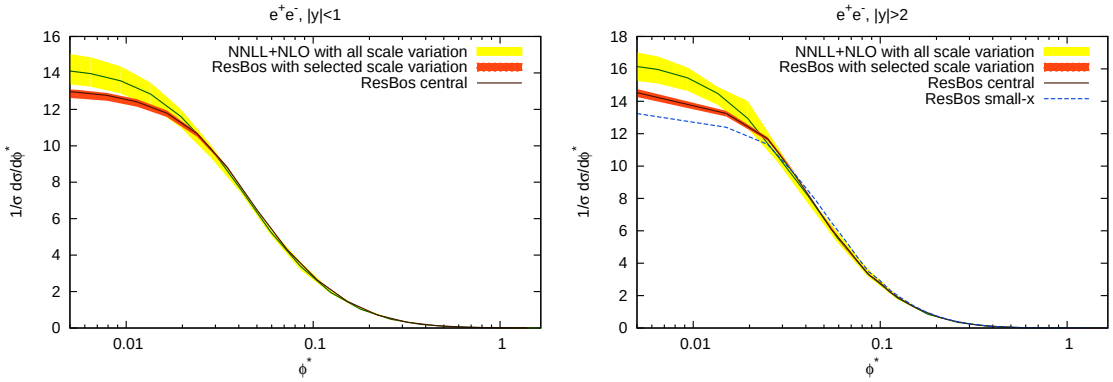

FIGURE 5.18. A comparison between our NNLL+NLO prediction and that of ResBos is shown, for the DØ electrons channel in the two rapidity bins $|y| < 1$ (central) and $|y| > 2$ (forward).

5.9. Comparison with ResBos

In this section I present the comparison of our calculations for the DØ experiment with those computed using ResBos [**73**], another program widely used within the community to performed resummed calculations of processes involving vector bosons. The comparisons for both a central and forward boson rapidity are shown in Fig. 5.18. In this comparison, the ResBos calculation also includes a non-perturbative model, very similar to the one studied in Sec. 5.8, with an associated parameter $g_2 = 0.6$, which essentially plays the rôle of g_{NP} in our calculation. More specifically, the ResBos program employs a non-perturbative model using the BLNY (Brock–Landry–Nadolsky–Yuan) parameterization [**86**].

In addition to this non-perturbative contribution, there exist other differences between ResBos (or rather the back-end software named 'Legacy' [**73, 86, 88**]) and our prediction. The formal accuracy of the two calculations is essentially the same, namely a NNLL resummation matched to a fixed-order calculation at $\mathcal{O}(\alpha_{\text{s}}^2)$. ResBos, however, is an implementation of the CSS formalism [**14**] while our formalism is more closely related to that of G. Bozzi, S. Catani, D. de Florian, M. Grazzini (e.g. [**25**]). A notable consequence of employing the two different formalisms is that the perturbative scales defined in each are not in a simple one-to-one correspondence.

A further difference between our predictions and those of ResBos is that we use coefficient functions (Wilson coefficients) computed exactly to $\mathcal{O}(\alpha_{\text{s}})$, as in Eq. 4.146, while ResBos uses approximate Wilson coefficients which extend this accuracy to $\mathcal{O}(\alpha_{\text{s}}^2)$, employing a mixture of K-factors and exact computation, such that the scale dependence is indeed exact at $\mathcal{O}(\alpha_{\text{s}}^2)$.

Furthermore, the prescription for curtailing the b integral as one approaches the non-perturbative régime is also different. Our calculation simply employs a hard upper limit of b_{max} while ResBos rather defines the quantity [**14**]

$$b_*(b, b_{\text{max}}) := \frac{b}{\sqrt{1 + (b/b_{\text{max}})^2}}\,. \tag{5.58}$$

This is then used to redefine the perturbative scales in the Sudakov exponential, and to avoid evaluating PDFs below some minimum scale ~ 1 GeV [**87**].

The final major difference concerns the fixed-order component used in the matching of our formalism, which is computed to $\mathcal{O}(\alpha_s^2)$ accuracy by MCFM. The ResBos formalism prefers to consider as a single entity the the non-singular remainder ('fixed-order minus expansion') labelled Y. The fixed-order component of Y is computed exactly to $\mathcal{O}(\alpha_s^2)$ in the large-Q_T limit according to [**89**].

The figure on the left in Fig. 5.18 compares the ResBos prediction for the $|y| < 1$ rapidity bin of the electrons channel to our prediction. The yellow theory band on our prediction includes the full perturbative scale dependence (i.e. μ_Q, μ_R and μ_F) whilst the red theory band on the ResBos prediction only includes the factorization and renormalization scale dependence and is hence narrower. The figure on the right makes the same comparison but for the $|y| > 2$ bin, again in the electrons channel. This time, the ResBos result which also includes a non-perturbative small-x broadening model is also shown, as the blue dashed curve.

CHAPTER 6

Conclusions

The technology of all-orders resummation, in the context of the transverse momentum distribution of massive lepton pairs produced in hadron collisions, has existed since the late '70s [**9**]: the DDT formula in the LLA (leading-logarithmic approximation). Resummation is based on factorization principles that persist to the level of the squared amplitude. These were first demonstrated in the case of Abelian theories and were subsequently borrowed for QCD [**11**]. The logarithmic accuracy of resummation has increased since its conception, such that NNLL accuracy is now the state of the art in the cases of the ϕ^* and Q_{T} distributions for Drell–Yan, but also for the Higgs Q_{T} spectrum [**25**]. This has important implications for phenomenology, but it seems that experimental results are ahead of theory in terms of uncertainty [**20**], as we will soon see first-hand in Part 2.

From a technical point of view, we have seen that resummation presents the issue of b-space integration. The utility of b-space rests in the convenient factorization of phase space it provides, but we find that we must introduce various *prescriptions* for handling the integration. First we consider prescriptions which are intimately related to the non-perturbative domain. In our case, for example, we use a cutoff for the upper limit of integration, b_{max}. Other authors use a prescription in which the contour of integration is modified so as to *skirt* the Landau pole, examples of which are given by [**90, 91**]. At the other end of the spectrum, we consider the lower limit of integration, b_{min}. In our formalism we freeze the radiator at $R(b) = 0$ for values of $b < b_{\mathrm{min}}$; the high-ϕ^* region in which resummation has no jurisdiction, and which is controlled by fixed-order calculations. The Florence group (e.g. [**25**]) adopt an alternative prescription, in which the b-space logarithm is replaced as follows: $L \equiv \log(\bar{b}^2\, M^2) \to \log(1 + \bar{b}^2\, M^2)$. For values of $\bar{b}^2\, M^2 < 1$, the logarithm and, hence, the resummed exponent go smoothly to zero. For $\bar{b}\, M \gg 1$, the logarithm may be written $\log(1 + \bar{b}^2\, M^2) = \log(\bar{b}^2\, M^2) + \mathcal{O}\big(1/(\bar{b}\, M)^2\big)$ and thus the formal perturbative accuracy is preserved in the kinematic region where resummation is important.

Non-perturbative (NP) effects have played a particularly important rôle in the studies presented herein. The mantra we have followed is to ensure we have a sound perturbative calculation of the ϕ^* observable, using a resummation formalism based on collinear factorization. We then allow ourselves, within our established perturbative uncertainties, to ascribe any discrepancies with collision data to the apparent need for NP physics. I have therefore presented studies of a phenomenologically driven NP model, based on a simple Gaussian form factor, driven by a single parameter g_{NP}. Ostensibly, within our well-established perturbative uncertainties, it is not possible to make absolute claims regarding the rôle of NP physics on the ϕ^* distribution. However, more recent work by

M. Guzzi, P. M. Nadolsky and B. Wang [**87**], in which perturbative scales are treated as nuisance parameters, has shown that data unambiguously favour a NP contribution. It is noteworthy that the work presented in this thesis, culminating in [**17**] and [**18**] for ϕ^*, has been a driving factor in the importance placed on precisely understanding perturbative scale uncertainties and their rôle in the precise determination of NP contributions. It is also noteworthy that an *experimentally* driven definition of a collider observable has paved the way in making such studies possible. Even after decades of study using the classic Q_{T} observable for the Drell–Yan process, this was unprecedented; experimental insight and theoretical collaboration have provided a unique opportunity to pin down a long-standing issue.

It could now be said that the focus of future theoretical work should be to match the unprecedented experimental precision, which now resides around the $\sim 1\%$ level or better, of Drell–Yan ϕ^* data. The state of the art from the theoretical side, depending on the $\sqrt{s}$ energy, remains at the 5-10% level. This does have implications for future work, which might involve extending the formal accuracy of theoretical calculations to $\mathrm{N^3LL}$.

During the course of this thesis there has been a revolution in our understanding of the Standard Model: the discovery, in 2012, of a new particle consistent with the Higgs boson, proposed nearly fifty years earlier [**92**]. Presumably, with the estimated $3,000\,\mathrm{fb}^{-1}$ of collision data that the LHC will have delivered by the end of its third run, we will be endowed with a high number of Higgs events sufficient for precision phenomenology. An important mechanism for Higgs production at the LHC is via *gluon fusion*, for which the QCD transverse-momentum resummation is carried out in [**93**]. High-statistics data samples of $\mathrm{H} \to \gamma\gamma$ would then permit a precise phenomenological study of soft-collinear gluon radiation (employing a ϕ^* definition applied to the photons) from a gluon-gluon-initiated process. One would expect in this case to observe a broader spectrum, and this would provide an ideal paradigm in which to test the predictions of a richer structure inherent in such a resummation. Indeed such studies are already underway within ATLAS [**94**].

Until this point I have not begun to mention a wealth on literature dedicated to effective theories in which the infrared divergences inherent in soft/collinear QCD amplitudes are consistently treated in a reformulation of QCD theory, which provides an alternative to traditional resummation techniques. One such theory, known as soft-collinear effective theory (or 'SCET') has itself received significant attention (as applied to Drell–Yan Q_{T} [**95, 96**], for example) although an in-depth discussion would be far beyond the scope of this thesis.

The phenomenological study of NP effects motivates a new experimental measurement of ϕ^* using high-statistics Run I LHC data: we have witnessed a mild rapidity dependence of the g_{NP} parameter in our rudimentary NP model *vis-á-vis* DØ data. In particular, it is desirable to have high-statistics experimental data, both in narrow $|y|$ (absolute boson rapidity) bins and in mass bins away from the Z resonance peak, with which to make precise comparisons, in order to elucidate the functional dependence of NP physics. Part 2 of this thesis is concerned with an experimental measurement of ϕ^* in $\mathrm{Z} \to \mu\mu$ events that I performed at $\sqrt{s} = 8\,\mathrm{TeV}$, using $20.1\,\mathrm{fb}^{-1}$ of ATLAS collision data.

Part 2

Experimental analysis of ϕ^* in Drell–Yan events at ATLAS

CHAPTER 7

Introduction

The present part of this thesis details and discusses an analysis of the ϕ^* observable I have performed, as applied to Drell–Yan events at $\sqrt{s} = 8$ TeV, using the ATLAS detector. It is an analysis that is currently in progress, and a fully corrected measurement of this observable in $\mathrm{Z} \to \mu\mu$ events is presented herein. This analysis has formed the latter stage of my PhD research topic, but forms Part 2 of this thesis for continuity with Part 1, which discusses the relevant theory in detail.

We begin with an overview of the ATLAS experiment in Chapter 8, emphasizing the detector systems that are relevant to the current analysis. (A discussion of the principal detectors relevant to my luminosity studies is postponed until Part 3.) Chapter 9 then discusses precisely the measurement definition and the strategy I follow, along with the collision and simulated data samples used as input. A discussion of the various corrections applied to simulated data samples then follows in Chapter 10. In Chapter 11 I document the criteria used to select candidate muon objects and Drell–Yan signal events from data. Chapter 12 then presents various studies which are aimed at estimating the background contamination of data events selected in this manner. The final results of this analysis, namely the normalized, detector-corrected and background-subtracted distributions for the ϕ^* observable, are presented along with their corresponding uncertainties in Chapter 13, in comparison with theoretical predictions. I close this part with a discussion of future prospects for this measurement.

CHAPTER 8

The ATLAS experiment

8.1. Detector components

The ATLAS experiment, Fig. 8.1, derives its name from the highly descriptive[1] acronym **A T**oroidal **L**HC **A**pparatu**S**. Measuring 25 m in diameter and 44 m in length, and weighing 7 kilotons, its constituent detectors and systems can be roughly categorized into four essential components: the inner detector, the calorimeters, the muon spectrometer and the magnet systems. For the analysis presented in this thesis, the muon spectrometer and other detectors and systems related to muon tracking, identification and reconstruction are the most important and, as such, emphasis will be placed on these. A recent and comprehensive survey of the ATLAS detector may be found in [**97**].

The inner detector, shown in Fig. 8.2, is surrounded by a solenoidal magnet producing a magnetic field of ~ 2 T. Extending from a radius of several centimetres from the beam line to 1.15 m, and covering a longitudinal distance of ~ 7 m in total, the primary purpose of the inner detector is to track charged particles that interact with material in its constituent components: the *pixel detector*, the SCT (*semiconductor tracker*) and the TRT (*transition radiation tracker*). The pixel detector comprises silicon (Si) pixel sensors in three concentric layers and three discs on each end, and its proximity to the interaction point (IP) affords precise tracking in this region. The minimum size of a pixel, expressed

[1]The magnet systems employed in the ATLAS detector significantly dictated the R&D of other constituent parts of ATLAS.

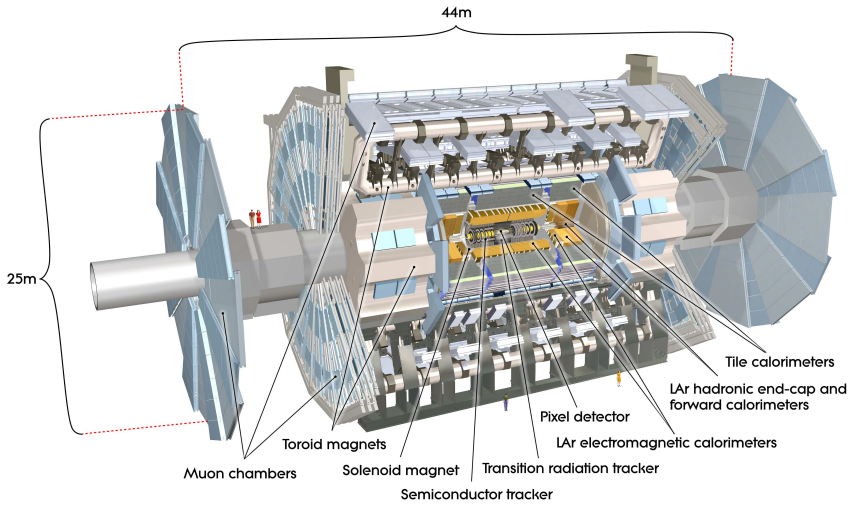

FIGURE 8.1. A cutaway drawing of the ATLAS detector, revealing all its detector systems [**97**].

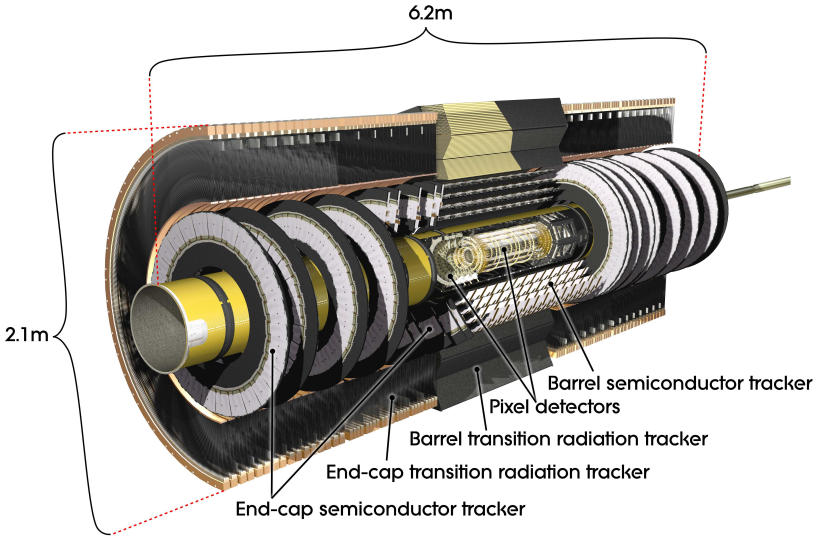

FIGURE 8.2. The ATLAS inner detector, often shortened to 'ID' [**97**].

as $(r\,\phi) \times z$, is $50\,\mu\text{m} \times 400\,\mu\text{m}$. The SCT further provides tracking beyond the radial extent of the pixel detector. The SCT is comprised of silicon detectors arranged in a configuration of four concentric *double* layers in the central ('barrel') region and nine discs on each side. In the barrel region, each detector contains 780 6.4 cm-long readout strips with an $80\,\mu$m pitch. The barrel SCT is used to provide tracking in the transverse plane, although a relative rotation between pairs of corresponding strips by 40 mrad in a *stereo* configuration also provides longitudinal tracking capabilities. Finally, the outermost TRT is composed of drift tubes known as 'straws', which are 4 mm in diameter. Each straw in the barrel region contains a 114 cm-long, 30 μm-diameter gold-plated tungsten-rhenium (W-Re) wire held at a potential of -1.5 kV and is filled with Xe (xenon), CO_2 and O_2 gases in the ratio 70:27:3, respectively. The passage of charged particles causes ionization of the gaseous mixture, the ions of which are collected by the wires and manifest as pulses of current which can be measured. In terms of pseudorapidity, the geometrical acceptances of the components of the ID are: $|\eta| < 2.5$ for the pixel detector and the SCT, and $|\eta| < 2$ for the TRT.

The purpose of the calorimeters is to capture all the energy of a particle in order to measure it. Components of the calorimeter system are categorized according to their specialization in terms of electromagnetic (EM) or hadronic calorimetry. For present purposes, we are most concerned with the EM part of the calorimetry system sharing a common geometrical acceptance with the ID—approximately the region $|\eta| < 2.5$, which is well-suited for precision physics. The EM calorimeter is made from lead (Pb) absorber plates, corrugated in the fashion of an accordion, with liquid argon (LAr) as the sensing element. It has a greater precision in its localization of particles than its hadronic cousin, with an $|\eta|$-dependent granularity, ranging from 0.025 to 0.1 in both $|\eta|$ and ϕ.

The muon spectrometer subjects particles to a local magnetic field of up to ~ 4 T depending on their location within the field produced by the superconducting toroids, of which there are three sets, each arranged in an octant structure. The two smaller

sets supply the magnetic field in the end-cap regions, while the largest set supplies the barrel region. The purpose of the muon spectrometer is to measure the curvatures of the tracks of muons in this field, and hence deduce their momenta. This part of the ATLAS detector occupies the region radially outward from 4.25 m. The muon spectrometer itself has triggering chambers (consisting of *resistive plate chambers* and *thin gap chambers*) effective in the range $|\eta| < 2.4$. This is permitted since the time-of-flight of muons from their typical interaction vertices out to these distances is comparable to the time scale of bunch crossings (10s of ns), and not significantly greater. Muon data is also recorded on a separate data *stream*, as compared with electrons and photons which are detected by the EM calorimeter. The tracking of muons is provided largely by drift tubes known as the MDT (*monitored drift tubes*). In addition, multi-wire proportional chambers known as the CSC (*cathode strip chambers*) provide tracking at large pseudo-rapidity ($1 < |\eta| < 2.7$).

Various aspects of the candidate muon and electron selection criteria (to be presented in Chap. 11), both in terms of kinematic selection and quality control cuts, will follow as direct consequences of the nature of the components of the ATLAS detector described in this section.

8.2. Muons and electrons

ATLAS defines several types of reconstructed muon candidates (or 'muons') according to the detector system(s) in which they were identified. The three muons with which we are concerned are known as 'ID' muons, which are reconstructed from tracks in the inner detector, 'MS' muons, which are reconstructed from tracks in the muons spectrometer, and 'combined' muons, which are reconstructed from tracks in both the inner detector and the muon spectrometer. There are also 'calo' muons, which are identified using energy depositions in the calorimeters, but these are of no real concern in this analysis—they are typically only employed to recover efficiency losses in the $|\eta| \lesssim 0.1$ region, but this measurement of the *normalized* differential cross-section will not be affected. We actually need not consider stand-alone MS muons, since they extend muon acceptance from $|\eta| = 2.5$ up to $|\eta| = 2.7$, which is outside the kinematic acceptance chosen for this analysis. Using ϕ^* as a precision observable necessarily demands good azimuthal angular resolution, which the ID is very effective at providing given its precision tracking capabilities. Since the geometrical acceptance of the ID is curtailed for $|\eta| > 2.5$ and we demand ID tracking information as part of our muon reconstruction, we therefore restrict our kinematic selection criteria accordingly.

Corresponding to the sub-detector in which a track may be reconstructed and identified as a muon candidate, is an algorithm for performing the reconstruction. For ID and MS muons, there are dedicated algorithms. The choice of algorithm used for combining information in the inner detector and the muon spectrometer performs a full refit to all track data, as opposed to a statistical combination, and is known as the *third chain* algorithm. Reconstructed muon candidates are therefore known as third-chain muons.

This thesis presents a measurement of ϕ^* in *muonic* Drell–Yan events. However, I have used various data-driven techniques in order to validate simulated data, one in particular which performs an $e\,\mu$ selection. I will therefore briefly describe here the measurement of

electrons in ATLAS. There is presently only one algorithm for reconstructing the kinematics of an electron, which straightforwardly makes use of information regarding energy depositions in the EM calorimeter and tracking information taken from the ID. In certain cases, more loosely defined electrons may use tracking information made available directly by the EM calorimeter, although this will be of a diminished precision. It is the properties of the manner in which the particle undergoes a showering of electromagnetic *bremsstrahlung*, as it relinquishes its energy in the EM calorimeter, which enables one to discern an electron from a photon.

CHAPTER 9

Measurement definition and strategy

9.1. Binning

The quantity we would like to determine is the normalized differential cross-section

$$\frac{1}{\sigma}\,\frac{d^3\sigma}{d\phi^*\,dM\,dy}\,. \tag{9.1}$$

To estimate this quantity, we measure a discrete distribution in the number of Drell–Yan events that yield a value of ϕ^*, M (invariant mass of lepton pair) and y (boson rapidity) within the specified ranges respectively: ϕ_i^* to $(\phi_i^* + \Delta\phi_i^*)$, M_i to $(M_i + \Delta M_i)$ and y_i to $(y_i + \Delta y_i)$, with $\Delta\phi_i^*\,\Delta M_i\,\Delta y_i$ being the volume of the bin labelled i. Thus, the integrated cross-section over this 'ith' bin is

$$\sigma_i = \frac{N_{i\,\mathrm{cand}} - \tau\,N_{i\,\mathrm{reco\ back}}}{A_i\,L}\,. \tag{9.2}$$

Here, $N_{i\,\mathrm{cand}}$ is the number of candidate events in data, $\tau\,N_{i\,\mathrm{reco\ back}}$ is the estimated number of background events in data, $L = \int dt\,\mathcal{L}$ is the integrated luminosity of the data sample and A_i is the acceptance efficiency of this ith bin. The latter is determined using a simulated model of the detector, as

$$A_i = \frac{N_{i\,\mathrm{reco}}}{N_{i\,\mathrm{gen}}}\,, \tag{9.3}$$

where $N_{i\,\mathrm{gen}}$ is the number of events generated in bin i and $N_{i\,\mathrm{reco}}$ is the number of Drell–Yan dimuon signal events reconstructed in bin i. The measurement further takes place within a fiducial volume, defined by kinematic cuts on the final state: $p_{\mathrm{T}}^{(1)} > 20$ GeV, $p_{\mathrm{T}}^{(2)} > 20$ GeV, $|\eta^{(1)}| < 2.4$ and $|\eta^{(2)}| < 2.4$, where the superscript in parentheses indexes the lepton. The bins of M are 46 GeV $< M <$ 66 GeV, 66 GeV $< M <$ 116 GeV and 116 GeV $< M <$ 150 GeV. The binning in $|y|$ will depend on the mass region under consideration. The binning $|y| < 0.8$, $0.8 < |y| < 1.6$ and $1.6 < |y| < 2.4$ is employed for the low- and high-mass regions, while a finer binning of $|y| < 0.4$, $0.4 < |y| < 0.8$, $0.8 < |y| < 1.2$, $1.2 < |y| < 1.6$, $1.6 < |y| < 2.0$ and $2.0 < |y| < 2.4$ is chosen for the central mass region, exploiting the availability of a high-statistics data set.

In fact, it is actually rather the *shape* of the ϕ^* distribution that provides the phenomenological handle to the soft–collinear QCD we are most interested in. The overall normalization $1/\sigma$, in Eq. 9.1, ostensibly refers to the *fiducial* cross-section integrated over all ϕ^*, M and y bins. This would seem to be a natural choice. It is experimentally advantageous, however, to consider the one-dimensional ϕ^* distribution $(1/\sigma)\,d\sigma/d\phi^*$, in *individually*-normalized bins of M and y. In this way, each kinematic region in M and y is experimentally independent and, e.g., the resonant ('on-peak') analysis remains immune to systematic uncertainties and large backgrounds that would otherwise arise from the

'off-peak' regions via a global normalization. For this reason, each of the (twelve) distributions in ϕ^*—corresponding to the different coarse bins in M and y—will be individually normalized.

Let us return now to the bin-by-bin detector correction factor. Since $N_{i\,\mathrm{reco}}$ may be decomposed as

$$N_{i\,\mathrm{reco}} = N_{i\,\mathrm{gen}} + N_{i\,\mathrm{faked}} - N_{i\,\mathrm{missed}} + N_{i\,\mathrm{mig.\ in}} - N_{i\,\mathrm{mig.\ out}}\,, \tag{9.4}$$

which may be verified by considering the sets of events

- generated in the ith bin,
- reconstructed in the ith bin from a lepton pair which does *not* correspond to the two *prompt* leptons from Drell–Yan (faked),
- not reconstructed but generated in the ith bin (missed),
- reconstructed in the ith bin but generated in another bin (migrated in), and
- generated in the ith bin but reconstructed in another bin (migrated out),

we see that the definition of A_i in Eq. 9.3 not only accounts for the reconstruction efficiency but also implicitly treats faked events and any bin-to-bin migration of events upon reconstruction, owing to the limited resolution of the detector. If the bin *purities* are sufficiently high, then bin-to-bin migration is significantly reduced in any case. The purity (P_i) is defined, respectively along with *stability* (S_i), using a simulated detector model, for a given bin labelled i, as

$$P_i = \frac{N_{i\,\mathrm{reco\ \&\ gen}}}{N_{i\,\mathrm{reco}}} \quad \text{and} \quad S_i = \frac{N_{i\,\mathrm{reco\ \&\ gen}}}{N_{i\,\mathrm{gen}}}\,, \tag{9.5}$$

where $N_{i\,\mathrm{reco\ \&\ gen}}$ is the number of events both generated and reconstructed in the same bin i. The bin purities are indeed high, as shown in Fig. 9.2 for the on-peak analysis, and Fig. 9.3 for the off-peak analysis.

The terminology of *generated* muon in the definition of purity remains ambiguous, and several generation levels exist. Two notable definitions of a level relevant herein are called *Born* and *bare*, corresponding to generator-level muons before and after the effects of FSR (final-state radiation) respectively. In principle, it is the *bare* muon which is most representative of the nature of an actual muon before the indelible effects of particle detection have been imprinted on its kinematics. The Born muon hence differs from the bare muon by a theory-dependent model of FSR. For this reason, it is crucial to keep in mind that no additional physics content is introduced to the measurement by such a correction, which is purely to facilitate the comparison with theoretical predictions that do not inherent model FSR.

The ϕ^* bin purities for all twelve kinematic regions of interest are shown in Figs. 9.2 and 9.3, where the definition of purity both in terms of Born and bare generator-level muons is considered. As expected, the bin purity in terms of *bare* muons is significantly higher than that for Born muons on account of the absence of any correction for FSR, which would clearly otherwise result in an enhanced degree of bin-to-bin migration of events due to the resulting changes to the momenta of the muons upon radiative emission. Furthermore, Fig. 9.1 shows the extent to which mass bins become impure, owing to the

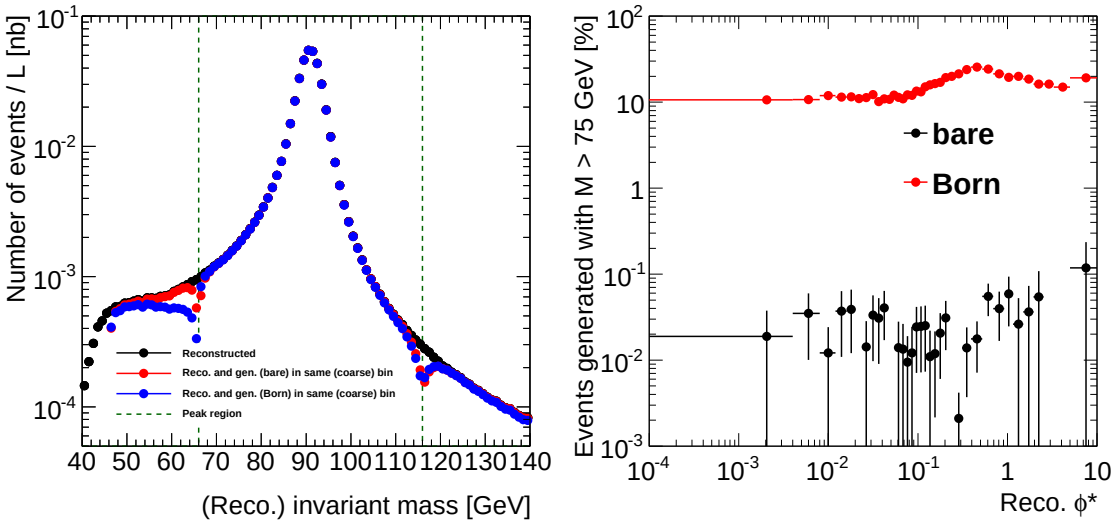

FIGURE 9.1. The left plot probes the simulated mass resolution of the detector, along with that of the combined FSR model and detector. The reconstructed invariant mass is plotted for signal events in which: no event vetoes are applied (black), vetoes are applied to impure events whose generator reference is bare level (red), and vetoes are applied to impure events whose generator reference is Born level (blue). The right plot shows, in bins of the reconstructed ϕ^*, the percentage of events reconstructed in the mass range $46\,\text{GeV} < M < 66\,\text{GeV}$, given they have a generated mass (bare or Born) of $> 75\,\text{GeV}$.

migration of events due to FSR and particle reconstruction. In particular, the right pane shows the percentage of events *reconstructed* in the mass range $46\ \text{GeV} < M < 66\ \text{GeV}$, given they were *generated* with a mass > 75 GeV, quantifying event migration into the low-mass region. The two orders of magnitude between event yields of Born and bare muons is not surprising, since for Born muons we must correct for FSR which is the principal cause of this migration, while the migration is largely absent for bare muons. Given the established bin purities in ϕ^* and M, and the philosophical implications of making theory-dependent corrections, the measurement presented in this thesis is corrected for detector effects only—i.e. back to *bare*-level muons.

The cross-section and number of events summed over all bins are respectively given as $\sigma = \sum_i \sigma_i$ and $N = \sum_i N_i$. Thus, the definition of my measurement to *estimate* $(1/\sigma)\, d\sigma/d\phi^*$ is

$$\frac{1}{\sigma}\left(\frac{d\sigma}{d\phi^*}\right)_i \approx \frac{\sigma_i}{\sigma\,(\Delta\phi^*)_i} = \mathcal{N}\,\frac{N_{i\,\text{cand}} - \tau\, N_{i\,\text{reco back}}}{(\Delta\phi^*)_i\, A_i}\,, \tag{9.6}$$

where $\mathcal{N}$ remains a normalization constant (for the corresponding kinematic region) to be determined.

The number of background events is typically estimated using simulated data, with $N_{i\,\text{reco back}}$ being the determined number of background events reconstructed in the ith bin. τ corrects for the difference between the true luminosity of the data sample, L, and

the *effective* luminosity of the simulated data sample:

$$\tau = \frac{\sigma_{\text{sim}}\, L}{N_{\text{gen back}}}\,, \tag{9.7}$$

where σ_{sim} is the simulated cross-section and $N_{\text{gen back}}$ is the total number of generated (simulated) background events.

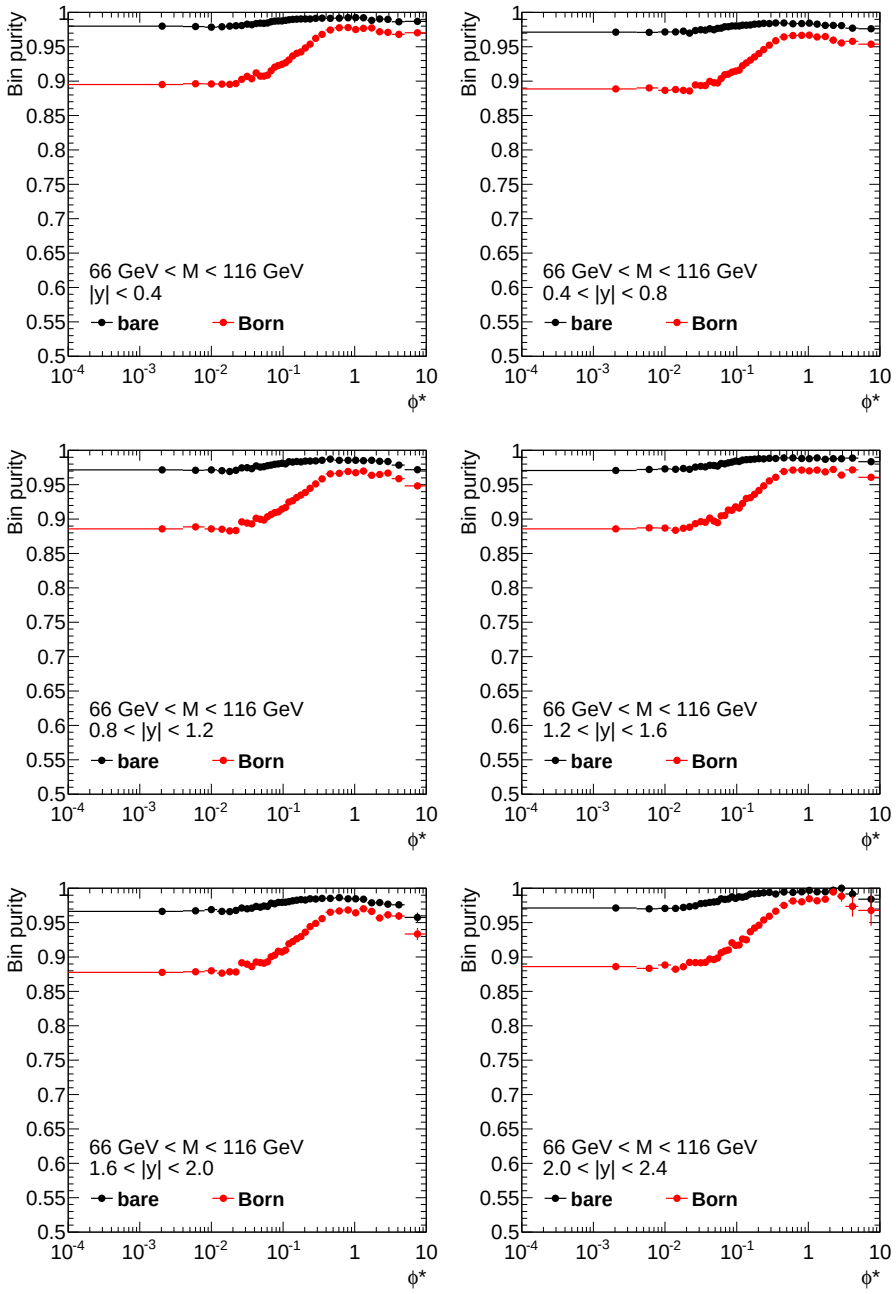

FIGURE 9.2. The purities of the ϕ^* bins proposed for the on-peak measurement.

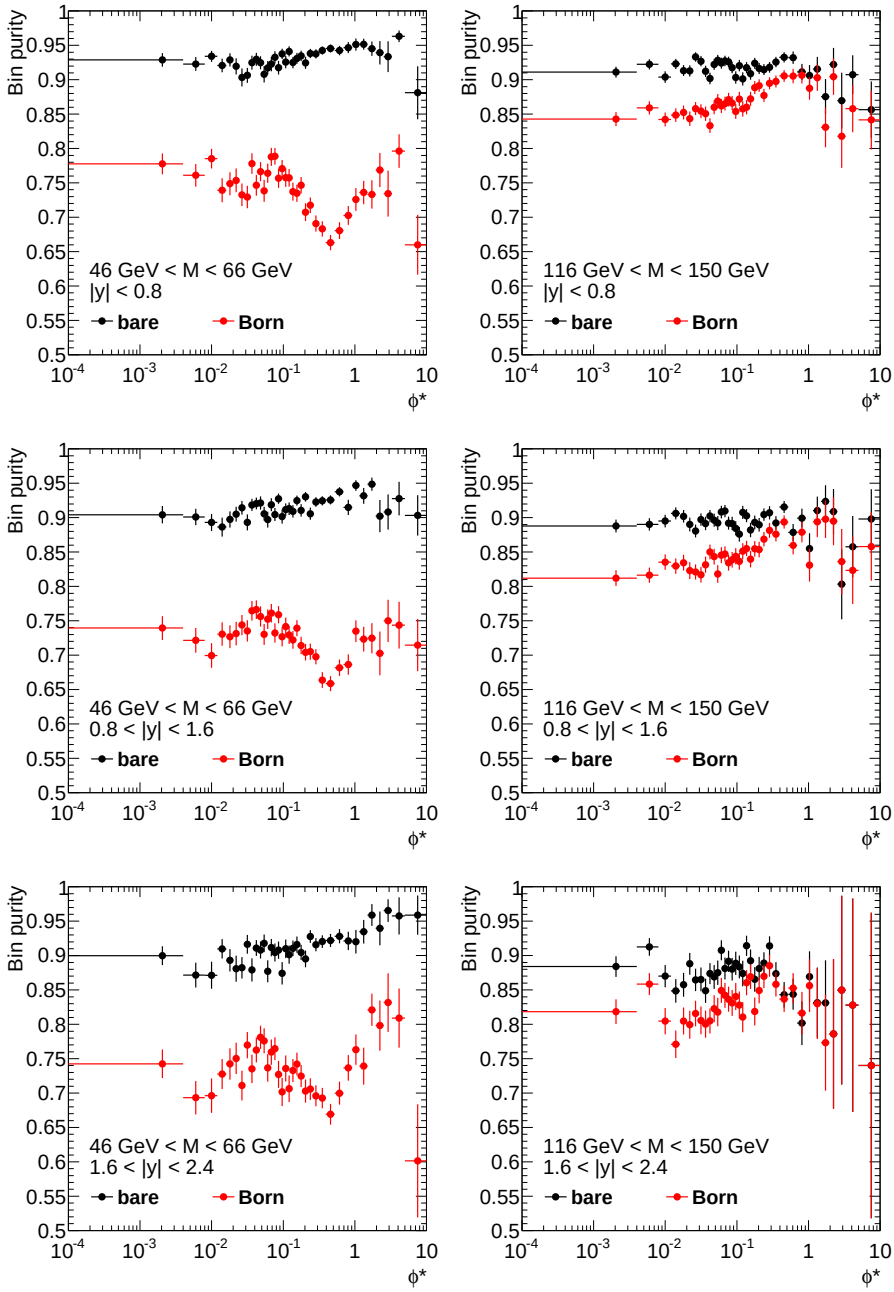

FIGURE 9.3. The purities of the ϕ^* bins proposed for the off-peak measurement.

9.2. Observable definition

As already mentioned, the ϕ^* observable provides a measure of the azimuthal decorrelation between two objects (see Part 1 for a detailed theoretical discussion). In this analysis it is applied to the two leptons produced in Drell–Yan events in proton–proton collisions at a centre-of-momentum energy of $\sqrt{s} = 8\,\text{TeV}$, and is measured using the ATLAS detector using $\sim 20\,\text{fb}^{-1}$ of integrated luminosity. The formal definition of ϕ^* used in this analysis is [**15**]

$$\phi^*_\eta = \tan\left(\frac{\phi_{\text{acop}}}{2}\right)\sin\theta^*_\eta\,, \tag{9.8}$$

with θ^*_η given using

$$\cos\theta^*_\eta = \tanh\left(\frac{\eta^- - \eta^+}{2}\right). \tag{9.9}$$

The purpose and advantage of this definition of θ^*—as opposed to, for example, that defined in the Collins–Soper frame—is that it does not rely on measurements of lepton momenta, rendering θ^*_η immune from lepton momenta mismeasurements due to limitations imposed by detector resolutions and inefficiencies. The ability to precisely track muons with the ATLAS detector makes a high-precision determination of ϕ^* very feasible, particularly for the $\mathrm{Z} \to \mu\mu$ channel. My work on non-perturbative effects immediately suggests phenomenological utility of a cross-section differential in $|y|$, and also in M.

In studying the quasi-back-to-back region of massive lepton pair production via the Drell–Yan mechanism, one is in a position to probe the dynamics of gluon emission in the soft–collinear régime, providing a test of perturbative calculations to adequately describe these dynamics. Owing to the presence of large logarithms which appear in calculations truncated at finite order in perturbation theory in the kinematical region of low ϕ^*, theoretical predictions must generally make use of resummation techniques, for example in [**16, 17, 18, 73, 86, 88**]. For a detailed account of these techniques, the reader is referred to Part 1 of this thesis.

9.3. Monte Carlo input, collision data and luminosity

In this analysis, extensive use is made of simulated data generated using Monte Carlo methods. The simulated data-sets (or 'Monte Carlo samples') are generated using a variety of computer tools—namely POWHEG [**98, 99, 100, 101**], PYTHIA 8 [**102, 103**], MC@NLO [**104**], JIMMY [**105**], SHERPA [**106**] and HERWIG [**107**]—in order to simulate the physical processes, before being further processed in a GEANT 4-based simulation [**108, 109**] in order to model the effects of the ATLAS detector. The principal purposes of these Monte Carlo samples are to model the contamination of the 'signal' process with other 'background' processes, and also to understand the detector and its potential effects on the measured observable distribution. Such modelling of signal and background processes is invaluable, as it allows us to better understand and discern differences in their experimental signatures, and to optimize discrimination between them where such signatures may potentially be very similar. With the exception of HERWIG-generated processes, which uses CTEQ6L1 PDFs [**77**], all physics simulations make use of the newer CT10 PDF sets [**110**].

In addition to containing simulated data after the effects of the ATLAS detector have been modelled (the 'detector-level' simulation), the Monte Carlo samples also retain the corresponding simulation of the underlying physical processes *only* (the 'generator-' or 'truth-level' simulation). This is how the Monte Carlo samples are used to correct the measured data for the effects of the detector, such that as-close-as-possible a comparison may be made with theoretical predictions.

The Monte Carlo samples used in this analysis for the various signal and background contributions are listed in Table 9.1. The total numbers of events in each sample, along with the corresponding cross-sections of these samples, are also shown. The 2012 data

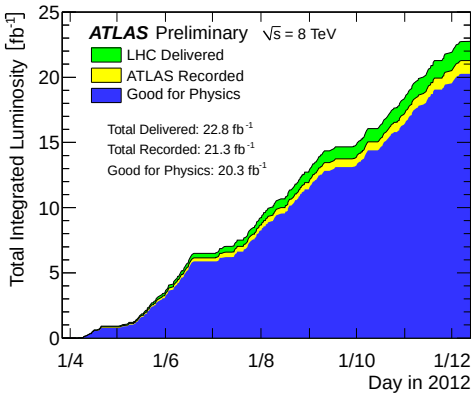

FIGURE 9.4. The total integrated luminosity delivered by the LHC, recorded by ATLAS and good for physics during the year 2012 [**112**].

used in this analysis are spread over 10 'periods'. Within these periods, only those runs during which all the relevant detectors within ATLAS were fully operational and performing properly, corresponding to an integrated luminosity $\int \mathcal{L}\, dt = (20.3 \pm 0.6)\,\text{fb}^{-1}$ [**111**], are included. Figure 9.4 shows the relevant integrated luminosities throughout the year. The luminosity for 2012 data is determined using the same method outlined in the 2011 luminosity measurement paper [**113**], which is described in Part 3 of this thesis.

TABLE 9.1. The Monte Carlo samples used in the $Z \to \mu\mu$ channel ϕ^* analysis.

Nomenclature	Description	Number of events (before selection)	Theoretical cross-section [fb]
PowhegPythia8_AU2CT10_Zmumu	$Z \to \mu\mu$ ($M > 60$ GeV)	21,108,857	$6.28 \cdot 10^5$
PowhegPythia8_AU2CT10_DYmumu_20M60	$Z \to \mu\mu$ (20 GeV $< M <$ 60 GeV)	4,998,191	$7.89 \cdot 10^5$
PowhegPythia8_AU2CT10_Ztautau	$Z \to \tau\tau$	4,999,692	$1.15 \cdot 10^6$
McAtNloJimmy_CT10_ttbar_LeptonFilter	$t\bar{t}$	14,993,322	$1.29 \cdot 10^5$
Sherpa_CT10_Wmunu	$W \to \mu\nu$	39,996,634	$1.22 \cdot 10^7$
Sherpa_CT10_Wtaunu	$W \to \tau\nu$	6,998,385	$1.22 \cdot 10^7$
Herwig_AUET2CTEQ6L1_WW	WW	2,494,694	$1.24 \cdot 10^4$
Herwig_AUET2CTEQ6L1_ZZ	ZZ	249,999	$9.93 \cdot 10^2$
Herwig_AUET2CTEQ6L1_WZ	WZ	999,797	$3.67 \cdot 10^3$

CHAPTER 10

Monte Carlo corrections

10.1. Pileup re-weighting

The average number of interactions per bunch crossing—aka the average *pileup*—is defined over a short interval of collision data-taking (typically 60 secs) known as a *lumiblock*, and is labelled $\langle\mu\rangle$. The pileup distributions in collision and simulated data differ somewhat and may be corrected for by re-weighting each simulated event such that the distributions *before event cuts* agree by construction. This is known as *pileup re-weighting*. Pileup re-weighting has been applied to all simulated data in this analysis, and the final comparison between simulated and collision data is shown in Fig. 10.1. There remain some very severe discrepancies outside the bulk of events, although discrepancies of any kind are taken into account in the study of systematic uncertainties and are demonstrated to be inconsequential with respect to the final measurement.

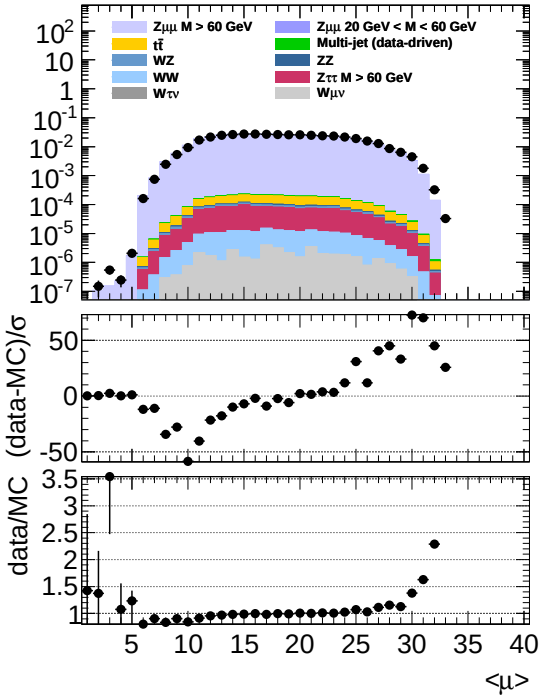

FIGURE 10.1. A comparison of the distributions of the average number of interactions per bunch crossing in simulated and collision data

10.2. Efficiencies

Muons are not reconstructed with 100% efficiency by the ATLAS detector. Similarly, the triggering, e.g. of events containing muons, is also not 100% efficient. Instead of correcting data for such inefficiencies, the simulated (Monte Carlo) data are rather corrected such that the simulated efficiencies are representative of real data. Small corrections to event weights (known as *scale factors*) are therefore applied to Monte Carlo events such that various efficiencies are well-modelled. It is important to note that Monte Carlo samples are already generated with such simulated inefficiencies, and the purpose of these corrections is fine-tuning *a posteriori*. The precise corrections are typically determined using so-called *tag and probe* methods. In this analysis, corrections are applied to improve simulated reconstruction and trigger efficiencies for muons.

The *tag and probe* method is a data-driven technique by which one determines the efficiency of an algorithm or selection criterion (e.g. object triggering and reconstruction, object isolation, etc.) by means of exploiting a 'standard candle'[1] process. This process should result in two objects being correlated, in the sense of being directly entangled via the process dynamics, and a kinematic selection on the two objects can be used to ensure this—e.g. as a suitably restrictive mass window cut might be applied to a pair of particles in order to ensure they are the decay products of a common unstable particle. One of the objects will have been known *a priori*, and is identified (or 'tagged') as such. The other object is then 'probed', using the selection for the standard candle process, to determine its correlation with the tagged object. Once this correlation has been established and the probe is thus identified, one can compute the efficiency of the algorithm (e.g. to identify a high-p_{T} track as a muon) by observing if this identification had been made in reality.

To flesh out this description, its instructive to follow with the example of muon identification efficiency. One begins, for instance, by confidently tagging a high-p_{T} isolated muon. One then identifies tracks compatible with a second high-p_{T} muon, and determines the invariant mass of the two-particle system formed by this putative muon and the former tagged muon. If this invariant mass is sufficiently close to M_{Z}, one can reasonably conclude the high-p_{T} track under consideration is indeed that of a muon, resulting from the standard candle process $\mathrm{Z} \to \mu^+\mu^-$. One might also ensure the curvature of the probed high-p_{T} track is also compatible with a muon of opposite charge to the tagged muon. In reality, the probed track either will or will not have been reconstructed as a muon candidate, and so for many tag and probe 'experiments' a statistical efficiency can be ascertained. As mentioned, the modelling of such efficiencies is already present, to an extent, in simulated data. The tag and probe method is applied to both data and Monte Carlo, and the relevant factors by which the weights of Monte Carlo events must be scaled can thus be determined.

[1] An adjective I have appropriated from astronomy.

10.3. Muon momenta corrections

Muon momenta are of course not measured in data without some degree of uncertainty. The detector simulation itself attempts to model this uncertainty to an extent, although this alone is insufficient for our needs. The simulated muon momenta are therefore appropriately smeared *a posteriori* to better model this imprecision. In order to determine the amount by which muon momenta should be smeared, the Z and Υ resonance peaks in the invariant mass distribution of the lepton pair for Drell–Yan events are used, while the J/Ψ resonance provides a low-mass cross-check. The level of random momenta smearing is optimized in order to maximize the agreement between data and simulation in this distribution. Muon momenta in simulated data are accordingly smeared in this analysis, using the results of dedicated studies.

10.4. Z line-shape re-weighting

The comparison of two distributions is particularly troublesome if the distributions contain strong peaks, since a misalignment in the position of the peaks will dominate the discrepancies observed and mask any finer details of discrepancy that one might try to deduce. This is particularly true of the invariant mass distribution of lepton pairs in Drell–Yan events, should the Z mass be insufficiently modelled when comparing simulation with data. In order to mitigate such a gross discrepancy, events generated using the POWHEG generator have been re-weighted, since an insufficiency in the modelling of the Z propagator and electroweak coupling is well-identified and understood.

CHAPTER 11

Object and event selection

11.1. Muon selection

The ϕ^* analysis described in this thesis employs various criteria to identify and select candidate muon signatures ('muons') in the detector to be treated as genuine physical objects. The algorithm used for identifying muons uses the following components of the ATLAS detector:

- The muon spectrometer (MS)
- The inner detector (ID)
- The electromagnetic calorimeter

Muon momenta are determined by performing a full fit to all tracking information made available by these components. The muons must first pass selection criteria which ensure a good-quality track, i.e. the reconstruction of an actual trajectory, is correspondingly recorded in the inner detector. Before reviewing these criteria, I shall expound some terminology. Given the properties of a track in the ID (e.g. direction) one expects *a priori* a certain number of hits in each of the constituent parts of the ID, based on the number of sensory layers the particle would necessarily traverse. The absence of a hit when one would otherwise be expected is termed a 'hole'. A muon in the barrel region would be expected to leave three hits in the pixel detector along its trajectory, for example, owing to the three concentric sensory layers of which the pixel detector is comprised. A sensor along a track which is known not to be operational is termed 'dead', and a certain clemency is granted to a track which is devoid (to varying degrees depending on the actual detector part) of the expected number of hits, should the culpability lie with a dead sensor. In the case of the TRT, the term 'outlier' refers to a hit whose fit to the track yields a χ^2 above a given threshold, and which is therefore excluded in the determination of track parameters. The following requirements are then made (where $n_{\text{something}}$ indicates 'number of something'):

- Require $n_{\text{pixel hits}} + n_{\text{dead pixel sensors}} > 0$
- Require $n_{\text{SCT hits}} + n_{\text{dead SCT sensors}} > 4$
- Require $n_{\text{pixel holes}} + n_{\text{SCT holes}} < 3$
- Defining $n = n_{\text{TRT hits}} + n_{\text{TRT outliers}}$, if $0.1 < |\eta| < 1.9$ then require $n > 5$ and $n_{\text{TRT outliers}} < 0.9n$

The muon candidate is then required to satisfy the criterion of being *combined*, having good-quality tracks established in both the ID and the MS, with a *momentum imbalance* (MI) significance $\text{MI}/\sigma_{\text{MI}} < 4$. A large discrepancy between the track momenta of a candidate muon in the ID and the MS (i.e. an 'imbalance', of which MI is a quantitative measure) is indicative of a muon produced during the in-flight decay of a pion or kaon,

where the ID track is actually that of the heavier meson. Requirements on the ID track fit quality and the momentum imbalance significance therefore strongly favour the acceptance of direct muons, whilst simultaneously rejecting the partially irreducible backgrounds due to in-flight decays of mesons.

Finally the muon candidate is required to satisfy certain kinematical conditions and isolation requirements, namely:

- $|\eta| < 2.4$
- $I < 0.1$
- $p_{\mathrm{T}} > 20\,\mathrm{GeV}$
- $|z_0 \sin\theta| < 0.5\,\mathrm{mm}$
- $|d_0/\sigma_{d_0}| < 3$

Here, the isolation, I, is defined to be the scalar sum over the transverse momenta of tracks within a 'cone' of radius $\Delta R = \sqrt{\Delta\eta^2 + \Delta\phi^2} = 0.2$, divided by the transverse momentum (magnitude) of the muon itself:

$$I = \frac{\sum_i p_{\mathrm{T}i}}{p_{\mathrm{T}}}\,, \tag{11.1}$$

where the sum runs over all objects (indexed i) within the cone.

In a single bunch-crossing, there is an average of $\langle\mu\rangle$ proton–proton ($p\,p$) interactions, each of which may result in detector tracks corresponding to the detected particulate products of the reaction. Algorithmic methods are then used to deduce the approximate locations, known as *vertices*, of each $p\,p$ interaction based on this track information. The vertex corresponding to the largest scalar sum of associated track transverse momenta is labelled the primary vertex. Respectively, z_0 and d_0 are the longitudinal and transverse displacements of the reconstructed track of the muon under consideration with respect to the primary vertex, at the point of closest approach to the z axis, and θ is the angle between this track and the z axis at the same point. Such cuts reject, for example, cosmic ray muons and muons produced in other $p\,p$ collisions within the same bunch crossing. If all the aforementioned conditions are met, then the muon candidate is considered to be a 'good' muon.

11.2. Electron selection

A putative electron object, whose identity is to be confirmed according to a standard clustering algorithm, must be found within the electromagnetic calorimeter. This may additionally be accompanied by a corresponding track in the ID. In the case of electron selection, we consider a quantity called the *transverse energy* defined as

$$E_{\mathrm{T}} = \begin{cases} E\,\cosh\eta_{\mathrm{track}} & \text{if } n_{\text{pixel hits}} + n_{\text{SCT hits}} \geq 4\,, \text{ or} \\ E\,\cosh\eta_{\mathrm{calo}} & \text{otherwise.} \end{cases} \tag{11.2}$$

Again, $n_{\text{pixel hits}}$ and $_{\text{SCT hits}}$ are the numbers of hits in the pixel detector and SCT respectively. This definition ensures that tracking information from these components of the ID is used if and only if the track quality exceeds a certain threshold defined in terms of these numbers of hits, in order to provide a measure of the pseudorapidity as η_{track}. In the absence of a track quality established according to this criterion, calorimetry information

is used to establish the pseudorapidity instead, i.e. as η_{calo}. The electron energy itself, E, is of course taken from clusters in the electromagnetic calorimeter.

In order to select electrons, for use in the data-driven $t\bar{t}$, WW and $Z \to \tau\tau$ event selections, I define a 'good' electron to be one for which

- $|\eta| < 1.37$ or $1.52 < |\eta| < 2.47$
- $E_T > 20$ GeV, where $E_T = E/\cosh\eta$ is its transverse energy
- $|z_0 \sin\theta| < 0.5$ mm
- $|d_0/\sigma_{d_0}| < 3$
- $I < 0.1$

where η here is obtained from ID tracking information, and I is defined in precisely the same way as for the corresponding criterion in the muon selection.

11.3. Event selection

For an event to be considered a genuine Drell-Yan candidate event, it must also fulfil various selection criteria:

- The number of tracks, n_{tracks}, associated with the primary vertex must be > 2
- The `EF_mu18_tight_mu8_EFFS` trigger must have fired ($Z \to \mu\mu$ selection)
  - This *dimuon* trigger requires at least two muons with transverse momenta > 8 GeV and > 18 GeV. This trigger is *unprescaled*; i.e. all triggered events are retained.
- The `EF_mu18_tight_e7_medium1` trigger must have fired ($e\,\mu$ selection)
  - This *dilepton* trigger requires at least one electron and one muon with transverse momenta > 8 GeV and > 18 GeV respectively. This trigger is also *unprescaled*.
- The event must contain exactly two 'good' muons (events with more are vetoed)
  - The $e\,\mu$ selection requires exactly one 'good' electron and one 'good' muon (events with more of either are vetoed)
- The two 'good' leptons must be oppositely charged
- The two 'good' leptons together must have an invariant mass M that lies within a prescribed range, depending on the bin under consideration:
  - 46 GeV $< M <$ 66 GeV ('low mass') or
  - 66 GeV $< M <$ 116 GeV ('on peak') or
  - 116 GeV $< M <$ 150 GeV ('high mass')

Control plots and the multi-jet background fits include events with 20 GeV$< M <$600 GeV, unless otherwise specified.

CHAPTER 12

Backgrounds

In this chapter I analyse and discuss the backgrounds which contaminate the Drell–Yan signal selection. In the majority of cases, such backgrounds are modelled using Monte Carlo methods, and appropriate data-driven methods have been used to ensure these models produce reliable predictions, which are explained in Secs. 12.1 and 12.2. For the estimation of the contamination due to events which predominantly contain jets (the 'multi-jet' events) I make exclusive use of data-driven methods, which are presented in Sec. 12.3. A compendium of the relative background fractions expected for the various ϕ^* distributions is presented in Sec. 12.4, after which I conclude this chapter by presenting a discussion of control distributions in which all such backgrounds are explicitly considered, in Sec. 12.5.

12.1. Electroweak and top backgrounds

Particularly in the *low* and *high* mass bins of the lepton pair, common electroweak backgrounds include $t\bar{t}$, WW and $Z \to \tau\tau$ events, which pass the selection criteria for the signal Drell–Yan events. The principal reason for this contamination is the presence of two W bosons in each of these three processes which decay leptonically, yielding two muons which mimic the signature of genuine (muonic) Drell–Yan. Examples of such processes are shown in Fig. 12.1, below.

In addition to the $t\bar{t}$ production mechanism shown, there also exist two other tree-level processes: that induced by quark annihilation ($q\bar{q} \to g \to t\bar{t}$) which is relatively suppressed in pp collisions, and the gluon-induced 't-channel' process without the triple-gluon coupling (i.e. two gluons coupling to the top quark current). Furthermore, WW production may also occur via sequential emission of two oppositely charged bosons during the scattering of quarks, again in a t-channel process. Other possibilities for these processes become available at higher orders. In all cases, since the muons are produced in W decays, there is missing *transverse energy* ($E_{\mathrm{T}}^{\mathrm{miss}}$) associated with the event, due to the absence of any interaction between neutrinos and the detector. Unfortunately, the requirement of $E_{\mathrm{T}}^{\mathrm{miss}} \approx 0$ is not an efficient discriminator between these background events and the signal Drell–Yan events, because it is often the case that missing transverse energy will be recorded in the case of genuine Drell–Yan, should a physics object not be properly reconstructed within the geometrical acceptance of ATLAS.

A feature of these processes which may be exploited is that such events may be efficiently selected by requiring the presence of two isolated and oppositely charged high-p_{T} leptons in the final state, where the leptons are of different flavour; i.e. $e^+\mu^-$ or μ^+e^-.

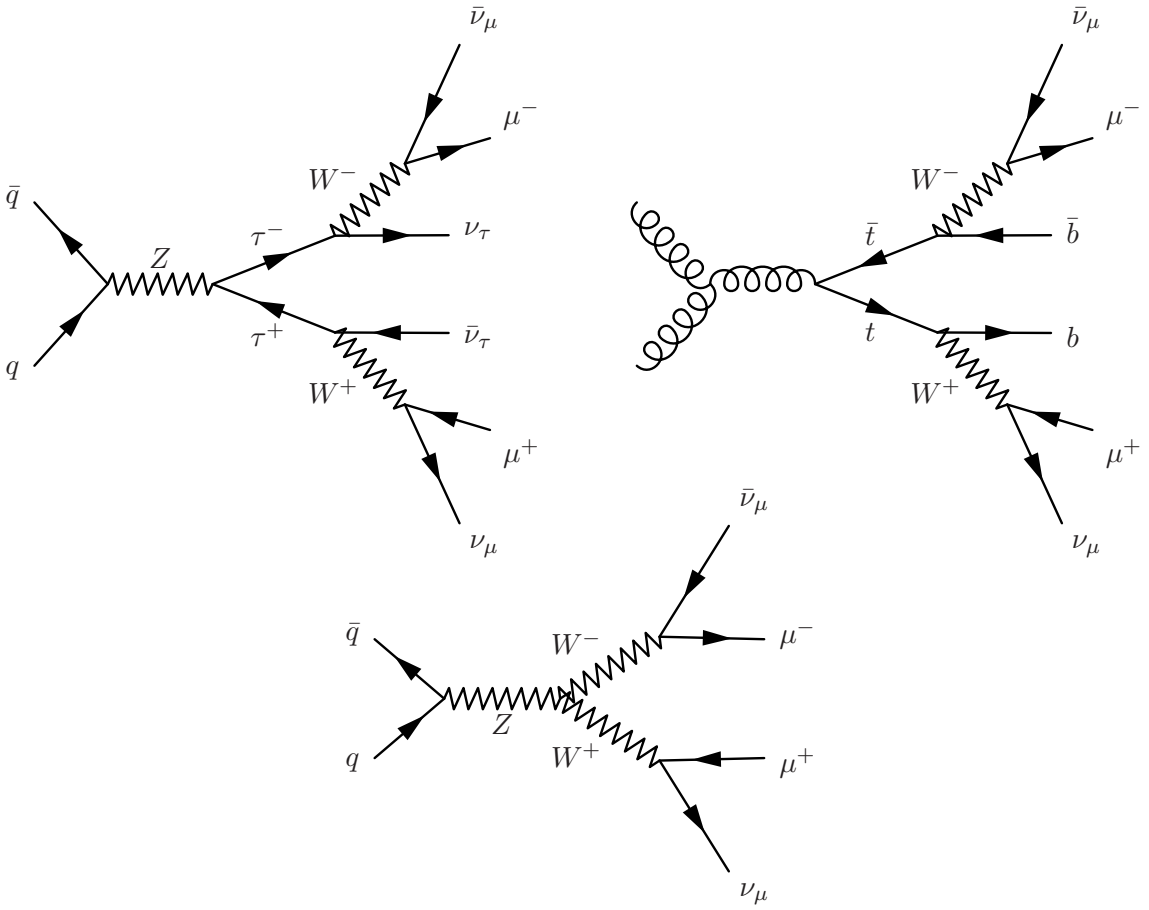

FIGURE 12.1. Examples of the most common types of electroweak processes that form a background to the Drell–Yan signal selection. Top-left, top-right and bottom, respectively, show examples of the $Z \to \tau\tau$, $t\bar{t}$ and WW background processes that are encountered in this analysis. In addition to the processes shown here, other tree-level mechanisms for $t\bar{t}$ and WW processes also exist, as explained in the text.

Lepton universality in weak decays implies the probability for these two final states to occur is precisely twice that for the $\mu^+\mu^-$ final state, which may contaminate the Drell–Yan signal. Thus, a reasonable data-driven estimate of the $t\bar{t}$, WW and $Z \to \tau\tau$ background event numbers may be obtained by simply replacing the lepton flavour requirements in the signal event selection, and dividing by two (while accounting for the difference between electron and muon acceptance efficiencies).

An $e^\pm\mu^\mp$ selection has indeed been performed, and the level of agreement with simulated Monte Carlo events is shown, for various control distributions, in Figs. 12.2—12.9. The purpose of this data-driven estimate is to validate the simulated $t\bar{t}$ and electroweak backgrounds, particularly in the low and high mass bins, where these backgrounds can represent as many as half of the collision events in high-ϕ^* bins. It should be noted that in all cases the kinematic selection is 20 GeV $< M <$ 600 GeV and $|y| < 2.4$, unless otherwise specified on the plot. At this point, corrections to the modelled electron efficiencies have *not* been applied, although corrections to the modelled muon efficiencies *are* applied, as

described in Chap. 10. Furthermore, all control distributions for this $e^{\pm}\,\mu^{\mp}$ selection include the multi-jet backgrounds, as estimated according to the principal method explained in Sec. 12.3.1. The normalization of the simulated events in Figs. 12.2—12.9 is intimately linked to that of data, on account of the fit used in this multi-jet background estimate.

Figure 12.2 shows the $E_{\mathrm{T}}^{\mathrm{miss}}$ distribution in different mass bins, for the $e\,\mu$ event selection. This is a particularly important distribution in which to validate the Monte Carlo estimates for $t\,\bar{t}$, WW and $Z \to \tau\tau$, since all involve leptonic weak decays in this analysis, nominally resulting in two undetected neutrinos. The agreement between simulated and collision data is particularly good for $E_{\mathrm{T}}^{\mathrm{miss}} > 40$ GeV. The agreement is also fair in the invariant mass distributions for $M > 66$ GeV, shown in Fig. 12.3. Troublesome distributions, include the invariant mass distribution of the boson in the low-mass region (Fig. 12.3, left) along with the transverse momentum distributions of both the boson itself (Fig. 12.4) and the leptons (Fig. 12.5, bottom). It appears as though the Monte Carlo predictions consistently overestimate the number of $\mathrm{Z} \to \tau\tau$ events.

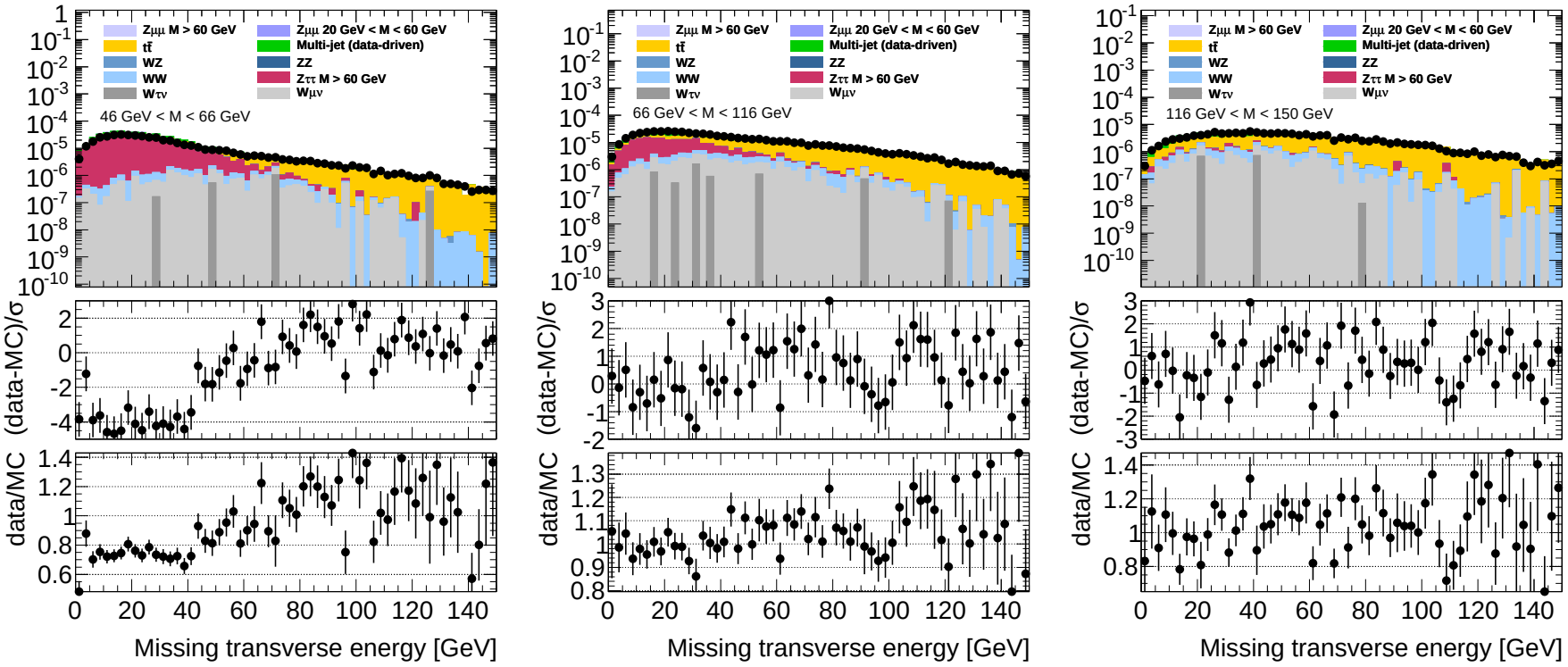

FIGURE 12.2. Missing transverse energy distributions of $e^+\mu^-/\mu^+e^-$ events for the mass bins 46 GeV $< M <$ 66 GeV, 66 GeV $< M <$ 116 GeV and 116 GeV $< M <$ 150 GeV, from left to right respectively.

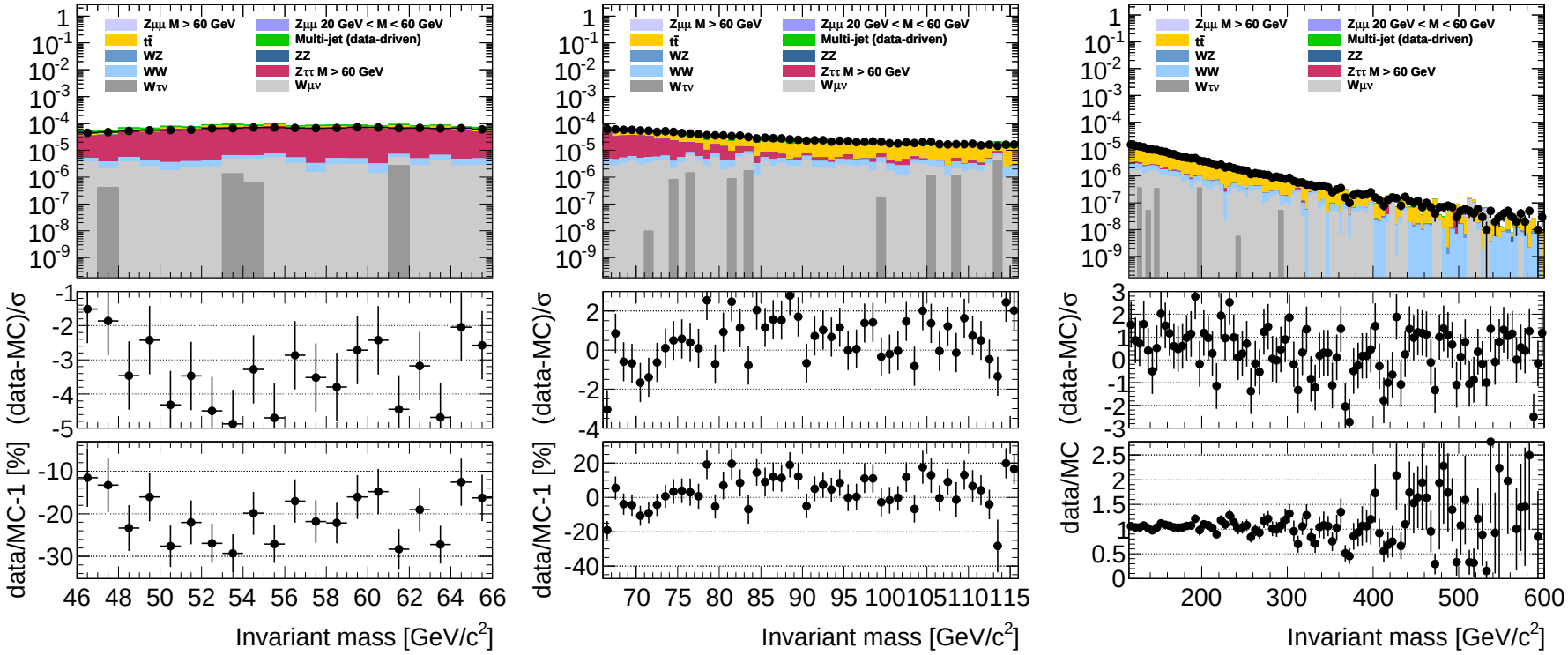

FIGURE 12.3. Invariant mass distributions of lepton pairs in $e^+\mu^-/\mu^+e^-$ events for the mass bins 46 GeV $< M <$ 66 GeV, 66 GeV $< M <$ 116 GeV and 116 GeV $< M <$ 600 GeV, from left to right respectively.

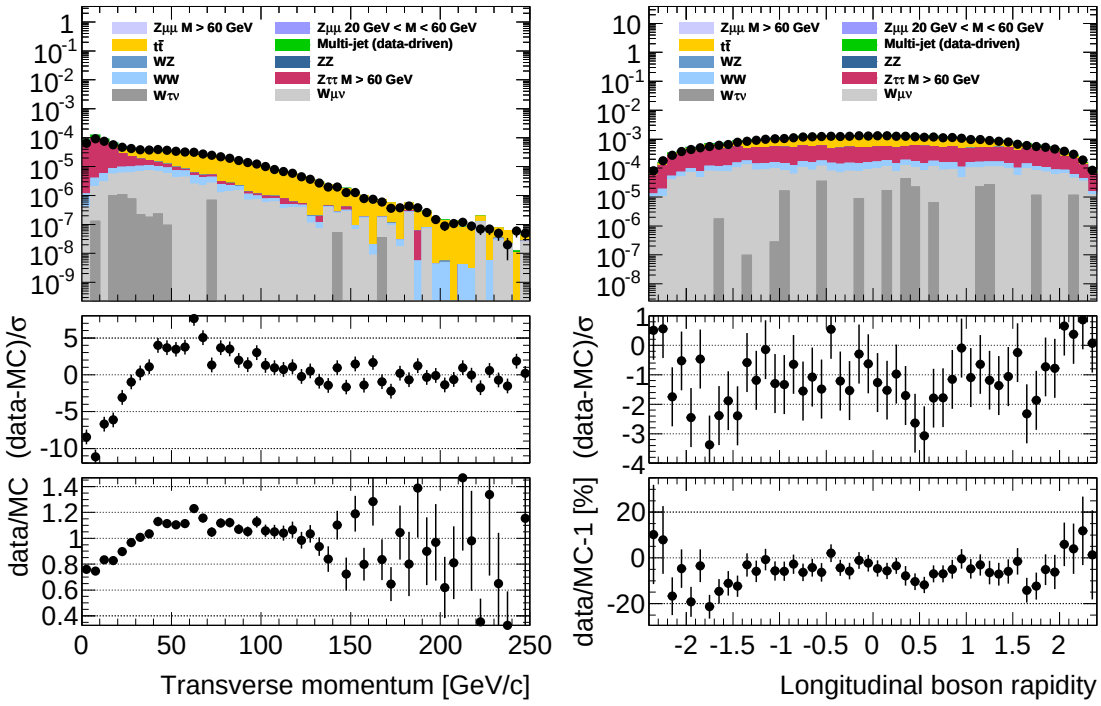

FIGURE 12.4. Transverse momentum and rapidity distributions of the lepton pairs in $e^+\mu^-/\mu^+e^-$ events.

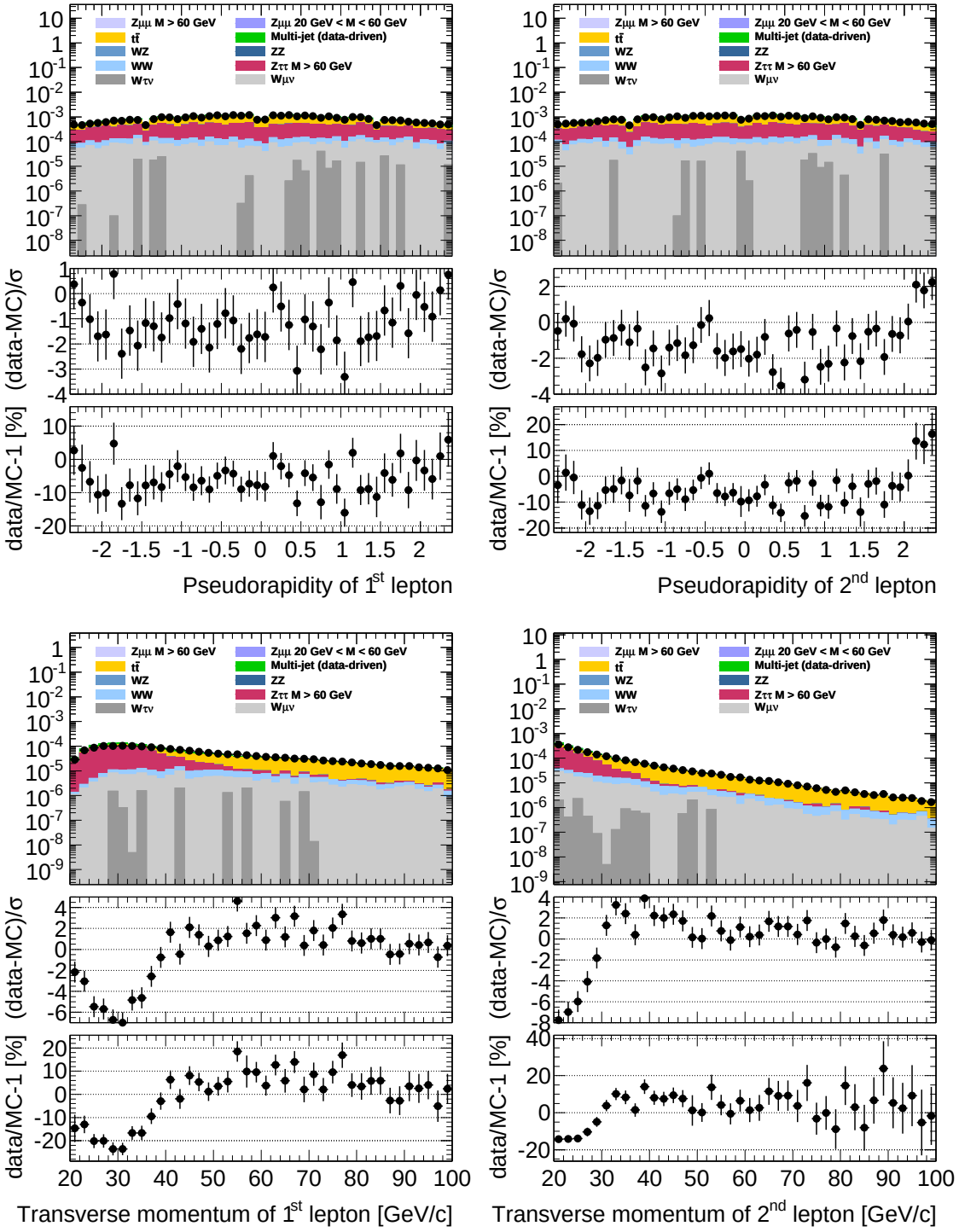

FIGURE 12.5. Pseudorapidity (top) and transverse momentum (bottom) distributions of the highest-p_{T} (left) and next-highest-p_{T} (right) leptons in events passing the $e\,\mu$ selection criteria.

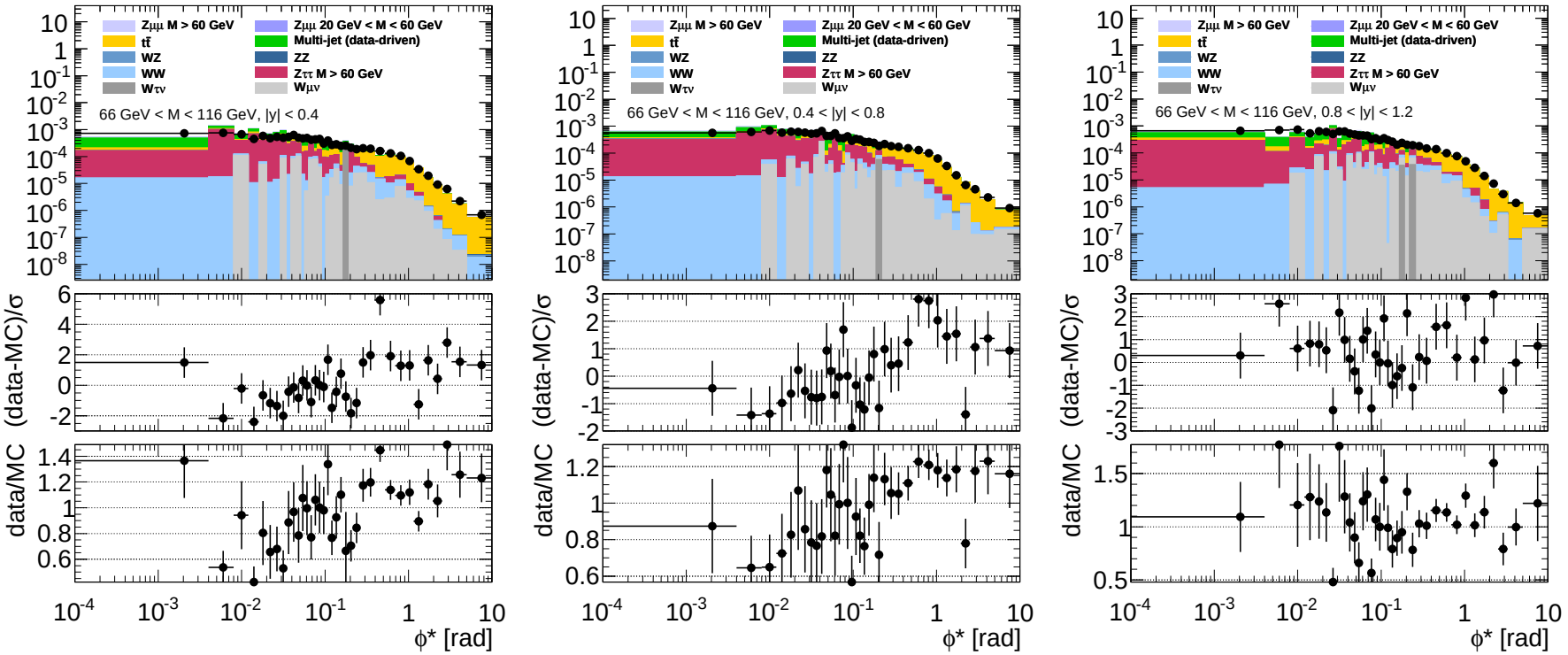

FIGURE 12.6. The ϕ^* distributions of events passing the $e^+\,\mu^-/e^-\,\mu^+$ final-state selection criteria. Left to right, respectively, show the $|y| < 0.4$, $0.4 < |y| < 0.8$ and $0.8 < |y| < 1.2$ rapidity bins in the $66\,\text{GeV} < M < 116\,\text{GeV}$ region.

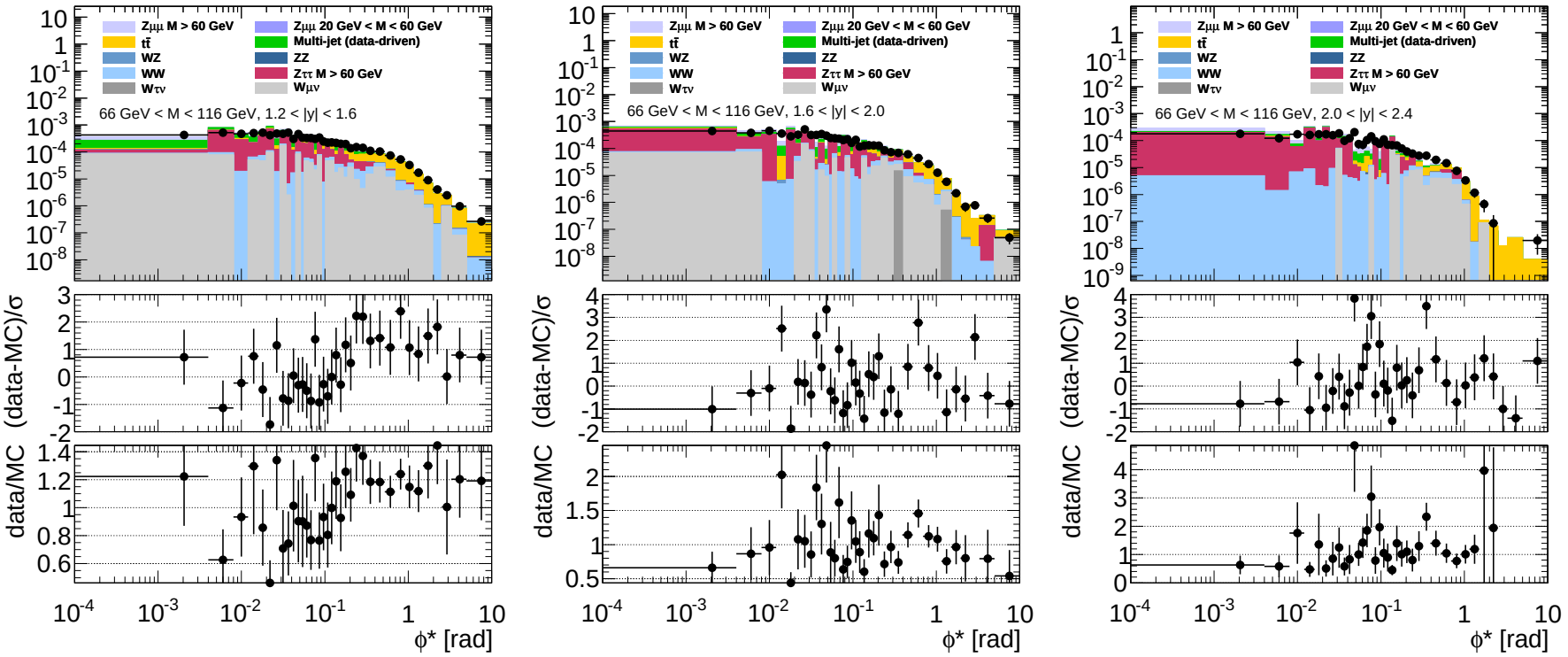

FIGURE 12.7. The ϕ^* distributions of events passing the $e^+\,\mu^-/e^-\,\mu^+$ final-state selection criteria. Left to right, respectively, show the $1.2 < |y| < 1.6$, $1.6 < |y| < 2.0$ and $2.0 < |y| < 2.4$ rapidity bins in the $66\,\text{GeV} < M < 116\,\text{GeV}$ region.

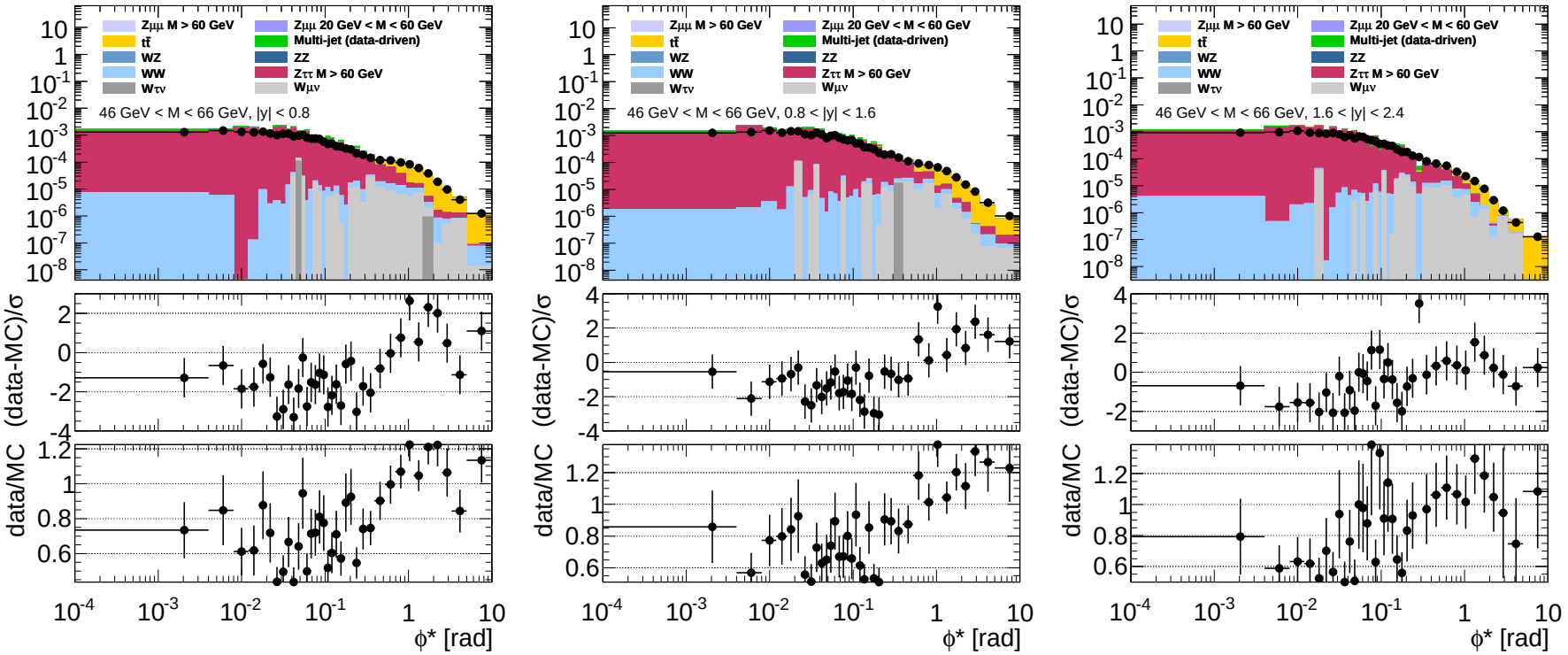

FIGURE 12.8. The ϕ^* distributions of events passing the $e^+\,\mu^-/e^-\,\mu^+$ final-state selection criteria. Left to right, respectively, show the $|y| < 0.8$, $0.8 < |y| < 1.6$ and $1.6 < |y| < 2.4$ rapidity bins in the $46\,\text{GeV} < M < 66\,\text{GeV}$ region.

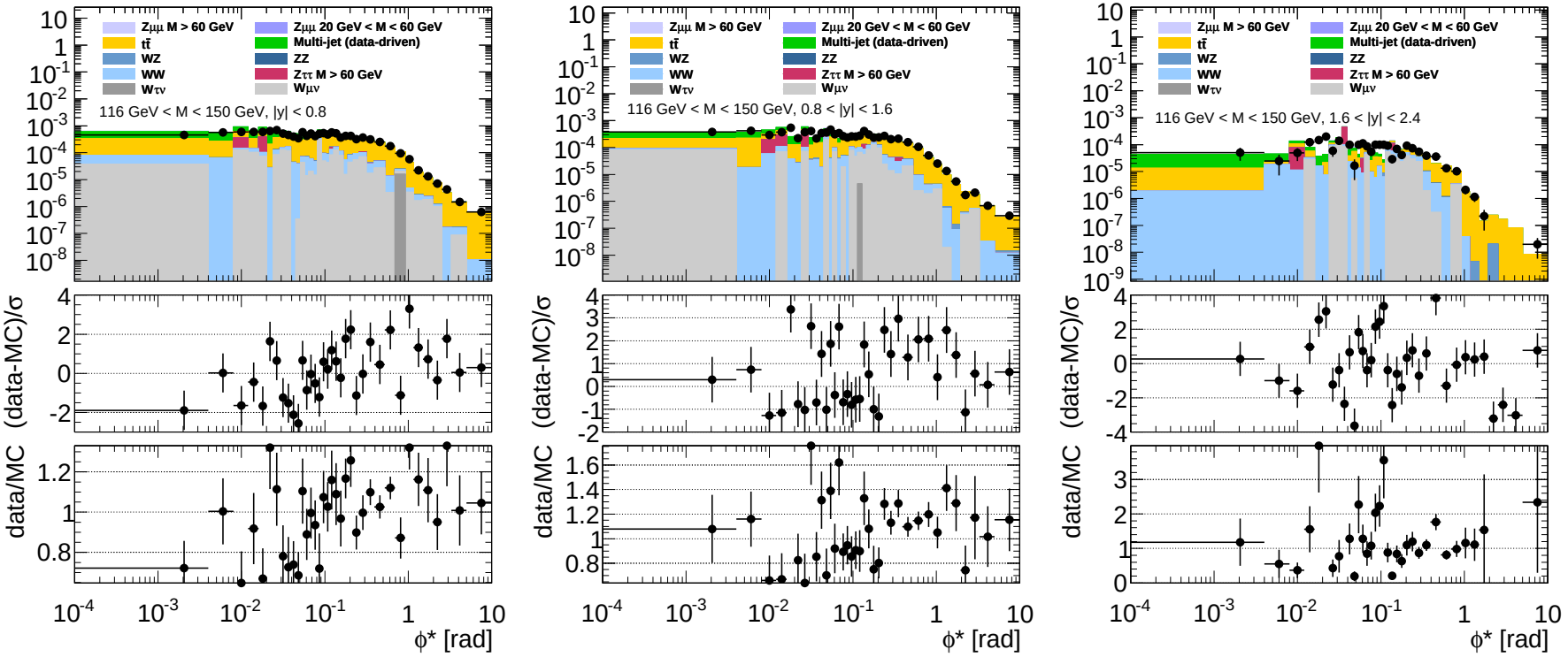

FIGURE 12.9. The ϕ^* distributions of events passing the $e^+\,\mu^-/e^-\,\mu^+$ final-state selection criteria. Left to right, respectively, show the $|y| < 0.8$, $0.8 < |y| < 1.6$ and $1.6 < |y| < 2.4$ rapidity bins in the $116\,\text{GeV} < M < 150\,\text{GeV}$ region.

12.2. W+jets backgrounds

In addition to the multi-jet background (to be discussed in Sec. 12.3) and the three main electroweak backgrounds discussed in Sec. 12.1, there are also potential backgrounds from events containing W bosons and other hadronic activity ('W+jets') which are not classifiable as strictly multi-jet or electroweak. Such events are expected to contain one high-p_{T} muon which arises directly in the leptonic decay of the W boson, along with other possible muon candidates. These other muons, however, are expected to originate 'within' jets (perhaps via the decay of a charged 'pion', $\pi^{\pm}$, buried within the hadronic jet).

A simple discriminator which should distinguish such events from genuine Drell–Yan signal and the aforementioned electroweak backgrounds is the isolation of the muons. One expects, in principle, one isolated muon and other possible muons which are not isolated—i.e. they are accompanied by substantial hadronic activity. Since the signal selection criteria stipulates exactly two muons, we consider W+jets events with precisely one isolated and one 'anti-isolated' muon. Specifically, the relatively small W+jets backgrounds, as estimated using Monte Carlo methods, are therefore validated by considering data–MC comparisons for distributions of events which pass the signal event selection, but with one of the muons failing the isolation cut—i.e. simultaneously having $I^{1(2)} < 0.1$ and $I^{2(1)} > 0.1$, where $1, 2$ labels the muon candidate.

Figures 12.10 to 12.17 show the main control distributions of events passing these selection criteria, where the estimation of the multi-jet background component is obtained using the data-driven method to be explained in Sec. 12.3. Once again, since these W+jets events involve leptonic decays of W bosons, the distributions of events according to the missing transverse energy $E_{\mathrm{T}}^{\mathrm{miss}}$ are of immediate interest, and are shown in Fig. 12.10. The agreement is generally rather good, as is the case for most other distributions, although there is a noticeable discrepancy associated with events around the Z peak in the signal $\mathrm{Z} \to \mu\mu$ process, as is evident from the invariant mass distribution in the peak region (Fig. 12.11). This discrepancy is also observed in the two lepton transverse momentum distributions (Fig. 12.13, bottom) around $M_{\mathrm{Z}}/2 \approx 46$ GeV. Since these discrepancies are associated with the signal process, they are taken into account with the inclusion of a general systematic uncertainty associated with the correction factor A_i; the modelling of the signal process is also used in the determination of A_i, and a re-weighting of events to account for such physics modelling insufficiencies is employed, as explained in detail in Sec. 13.2.

There are also discrepancies at the very low end (~ 20 GeV) of the lepton transverse momentum distributions (Fig. 12.13, bottom) along with the $Q_{\mathrm{T}} < 10$ GeV bins of the boson transverse momentum distribution (Fig. 12.12). These discrepancies are due to a very general difficulty associated with the modelling of low-Q_{T} Drell–Yan pairs.

The W+jets selection we consider here does indeed enhance the acceptance of W+jets events. This can be seen in absolute terms by comparing the event yields for W+jets in this selection with those of the Drell–Yan signal selection, for instance by studying the relatively flat invariant mass distributions for 46 GeV $< M <$ 116 GeV in Fig. 12.11 and Fig. 12.28 (of Sec. 12.5). Even with the enhanced W+jets acceptance however, the absolute

numbers of these events remain small in most of our control distributions. The W+jets selection we consider here in fact simultaneously enhances the acceptance of multi-jet background events, owing to the allowance of a single muon which is strictly not isolated. An overall conclusion we may deduce is that, away from those regions associated with the Z resonance and low-Q_{T} objects, both the W+jets *and* multi-jet backgrounds appear to be well-modelled in our control distributions. Moreover, this study then demonstrates we can be confident regarding the predicted very low W+jets background event yields across all ϕ^* bins.

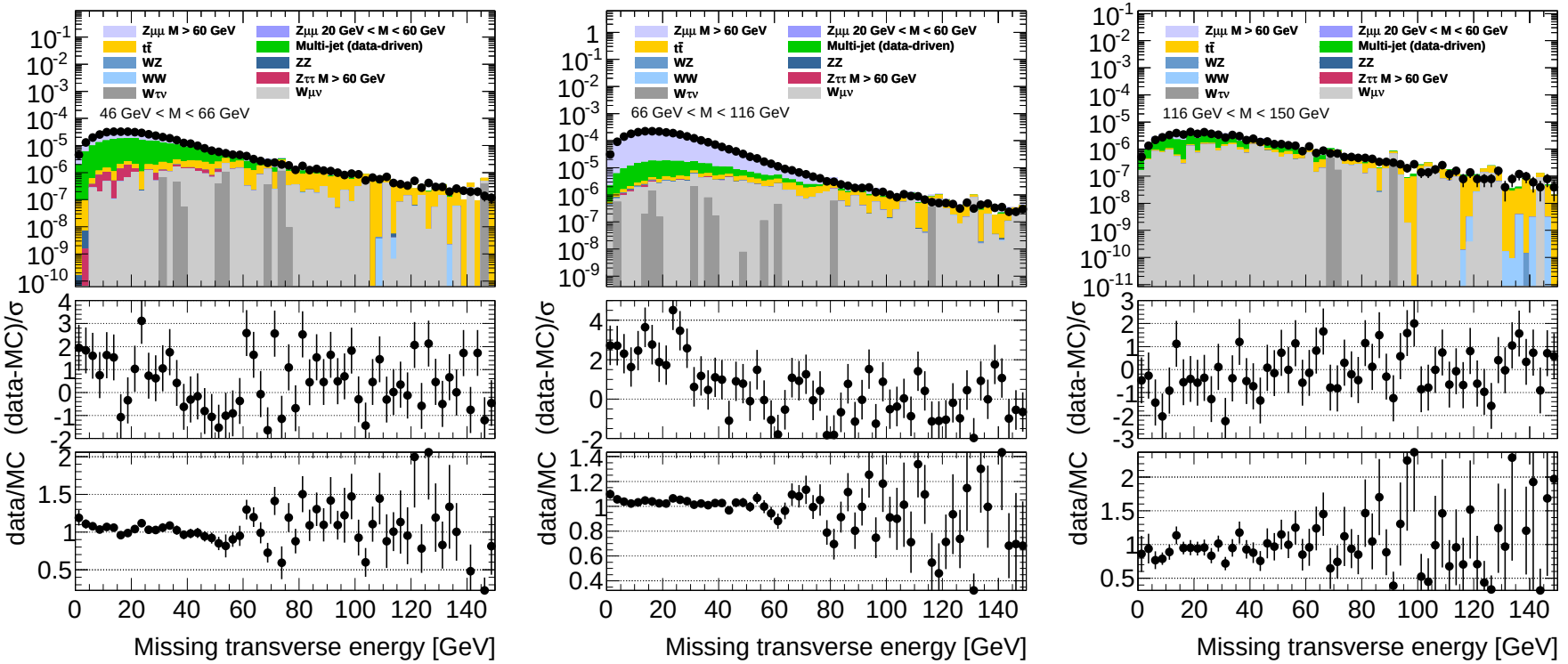

FIGURE 12.10. Missing transverse energy distributions of events selected in which one muon is isolated and the other is *anti*-isolated, for the mass bins 46 GeV $< M <$ 66 GeV, 66 GeV $< M <$ 116 GeV and 116 GeV $< M <$ 150 GeV, from left to right respectively.

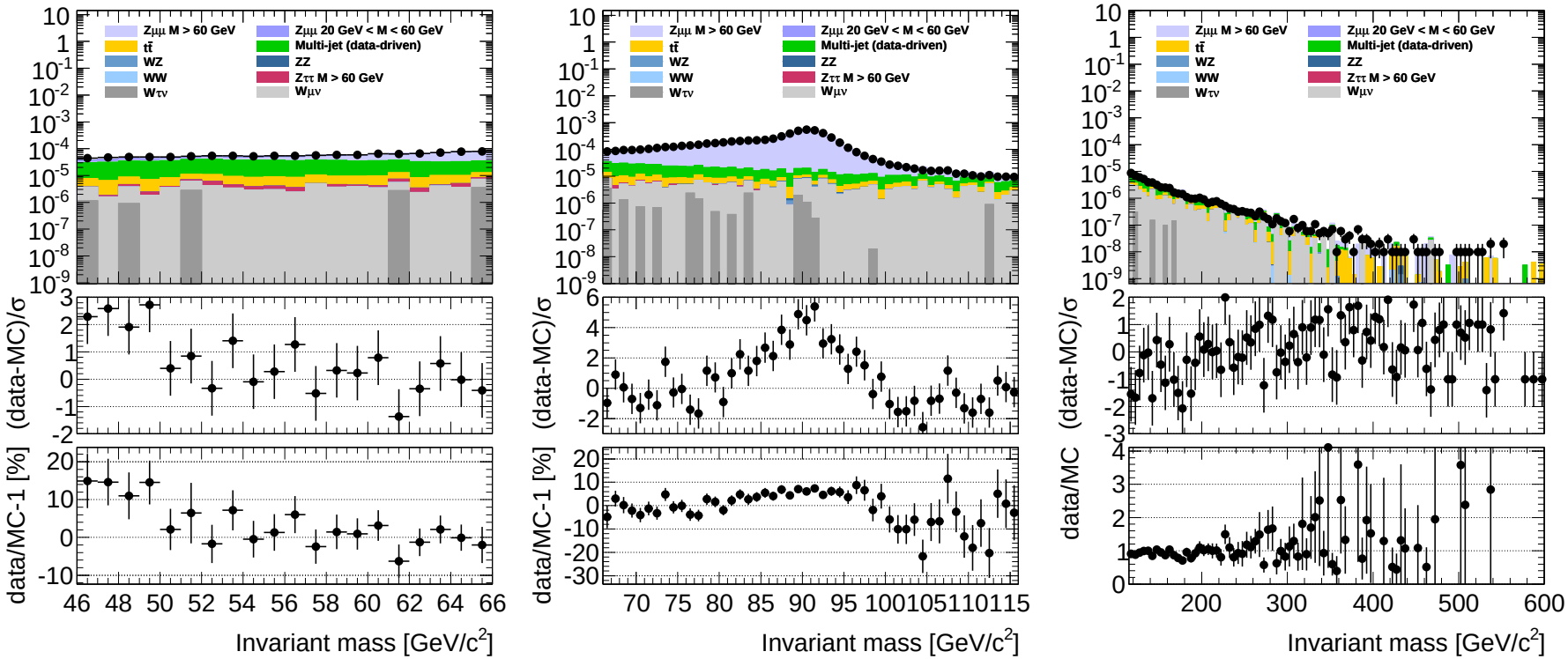

FIGURE 12.11. Invariant mass distributions of lepton pairs for events selected in which one muon is isolated and the other is *anti*-isolated, for the mass bins 46 GeV $< M <$ 66 GeV, 66 GeV $< M <$ 116 GeV and 116 GeV $< M <$ 600 GeV, from left to right respectively.

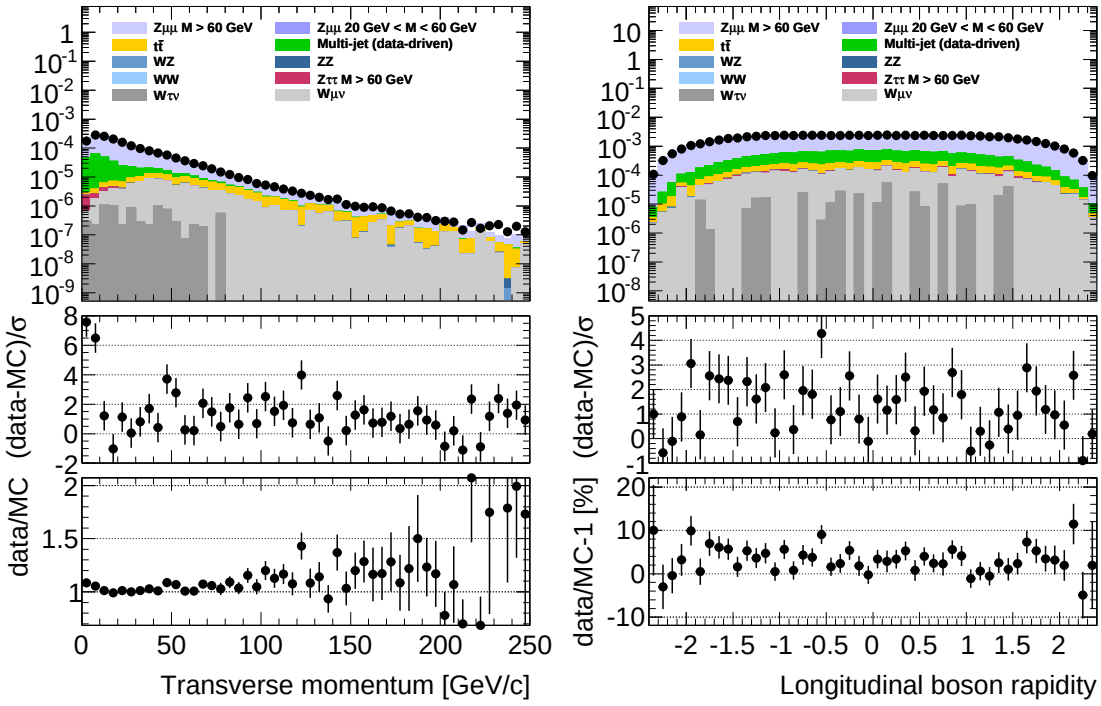

FIGURE 12.12. Transverse momentum and rapidity distributions of the lepton pairs for events selected in which one muon is isolated and the other is *anti*-isolated.

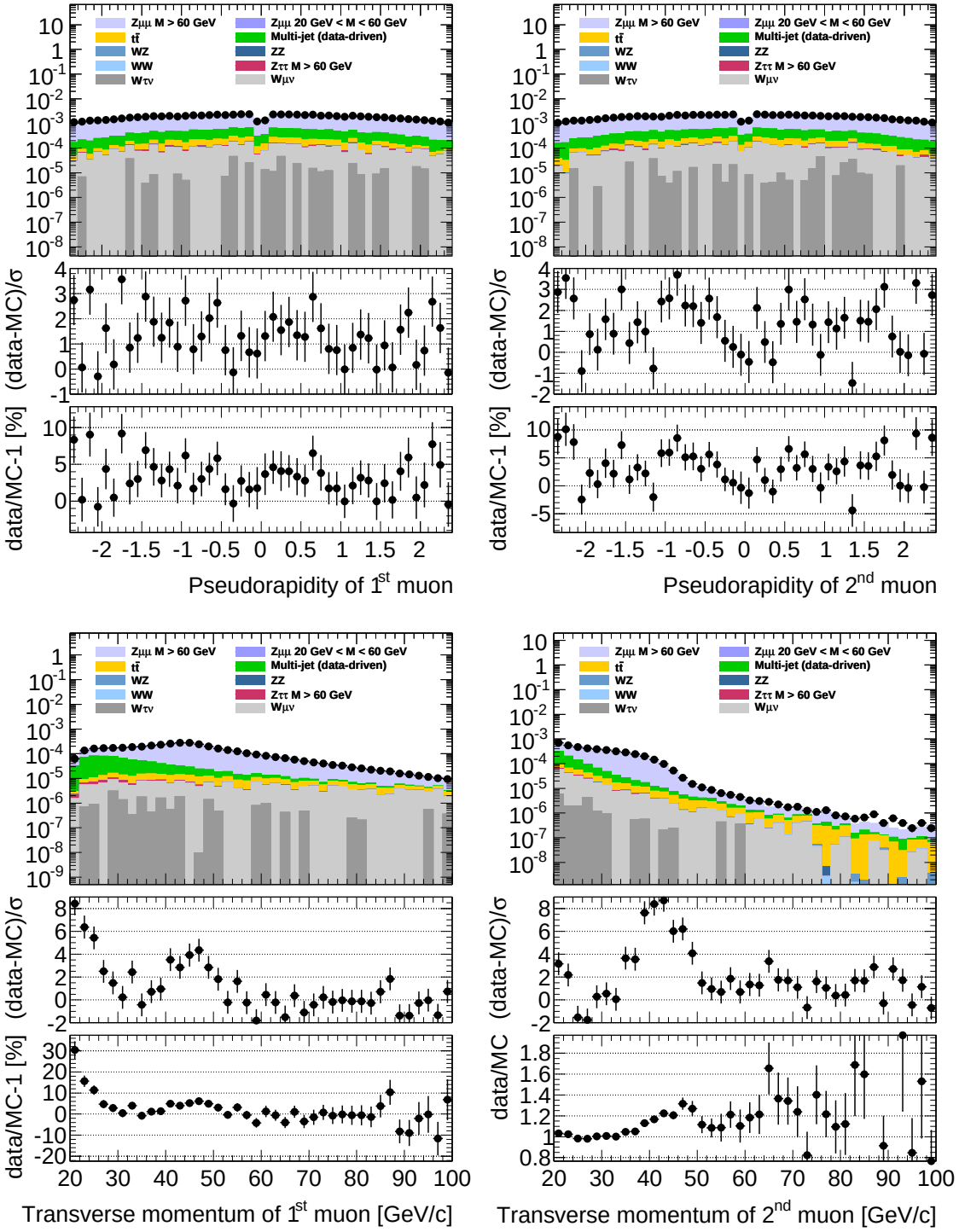

FIGURE 12.13. Pseudorapidity (top) and transverse momentum (bottom) distributions of the highest-p_{T} (left) and next-highest-p_{T} (right) leptons, for events selected in which one muon is isolated and the other is *anti*-isolated.

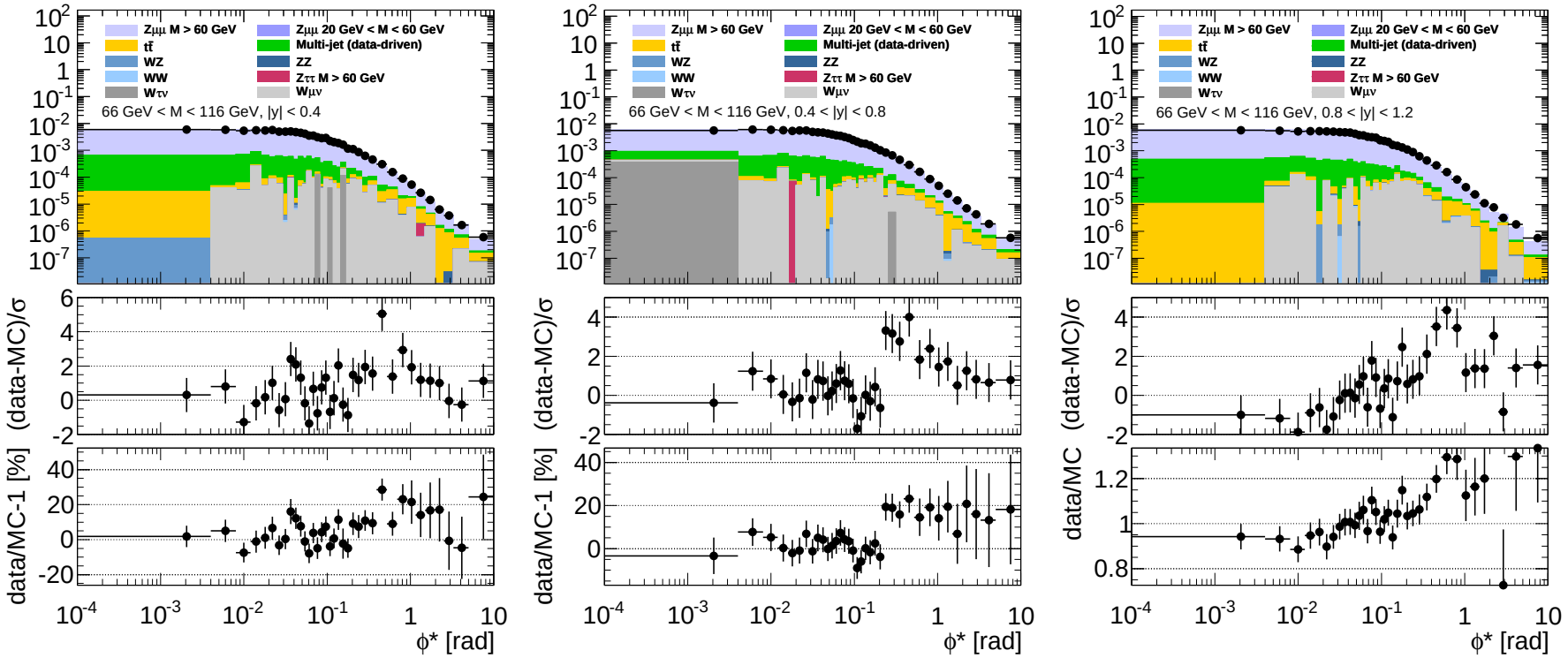

FIGURE 12.14. The ϕ^* distributions of events selected in which one muon is isolated and the other is *anti*-isolated. Left to right, respectively, show the $|y| < 0.4$, $0.4 < |y| < 0.8$ and $0.8 < |y| < 1.2$ rapidity bins in the $66\,\text{GeV} < M < 116\,\text{GeV}$ region.

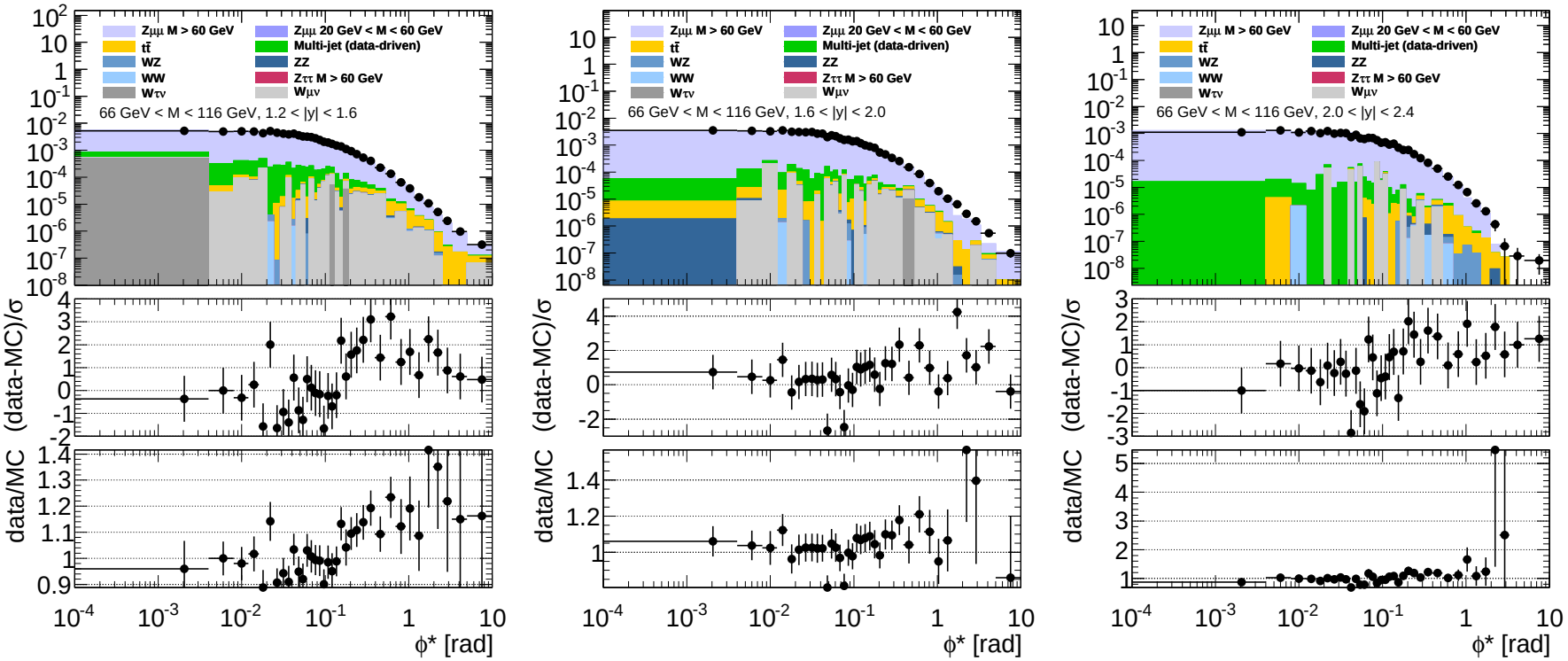

FIGURE 12.15. The ϕ^* distributions of events selected in which one muon is isolated and the other is *anti*-isolated. Left to right, respectively, show the $1.2 < |y| < 1.6$, $1.6 < |y| < 2.0$ and $2.0 < |y| < 2.4$ rapidity bins in the $66\,\text{GeV} < M < 116\,\text{GeV}$ region.

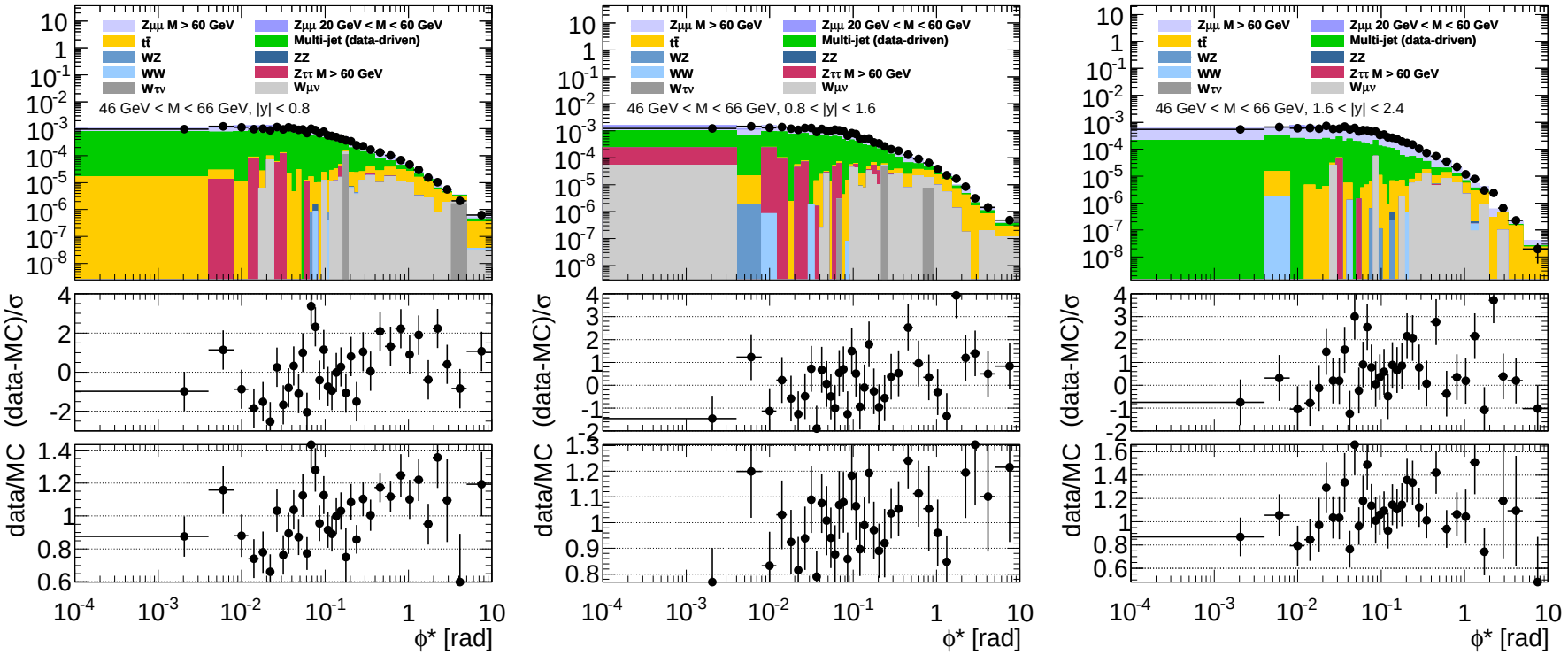

FIGURE 12.16. The ϕ^* distributions of events selected in which one muon is isolated and the other is *anti*-isolated. Left to right, respectively, show the $|y| < 0.8$, $0.8 < |y| < 1.6$ and $1.6 < |y| < 2.4$ rapidity bins in the $46\,\text{GeV} < M < 66\,\text{GeV}$ region.

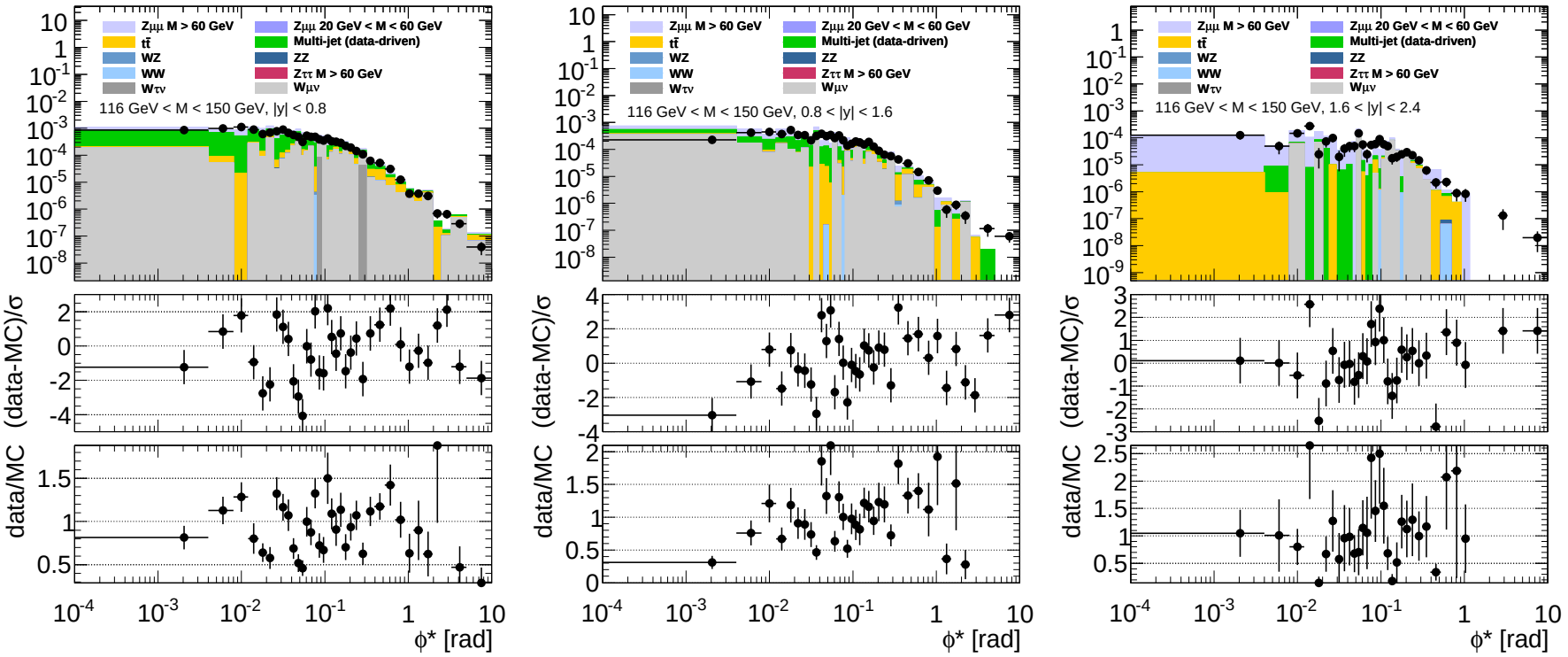

FIGURE 12.17. The ϕ^* distributions of events selected in which one muon is isolated and the other is *anti*-isolated. Left to right, respectively, show the $|y| < 0.8$, $0.8 < |y| < 1.6$ and $1.6 < |y| < 2.4$ rapidity bins in the $116\,\text{GeV} < M < 150\,\text{GeV}$ region.

12.3. Multi-jet background

In principle, multi-jet events are those events which produce multiple instances of collimated hadronic activity, owing to the showering and hadronization of partons produced in hard scatterings. The decay of short-lived hadrons via the weak interaction can give rise to the production of secondary leptons in this picture. Particularly troublesome is the case in which two secondary muons are produced via such decays, which might mimic the signature of a genuine Drell–Yan event. The event selection attempts to safeguard against this largely by applying isolation cuts to the muons, which severely restrict the amount of hadronic activity by which these muons may be accompanied, in an attempt to ensure they are themselves produced as a direct result of the hard scattering. In practice, the multi-jet events are defined by exclusion, according to this isolation parameter: multi-jet events are those events in which muons are typically not isolated, but which are also not the diboson, $t\bar{t}$, W+jets, etc. events already explicitly considered using Monte Carlo methods. The fact that a small fraction of multi-jet events will nonetheless pass the isolation criterion is what gives rise to a background, the data-driven estimation of which is presented in this section.

12.3.1. Principal multi-jet background estimate. The multi-jet background is estimated using a data-driven method, in which the isolation requirement on the muons in the event is inverted; i.e. the only change in the event selection becomes $I > 0.1$ for both muons. The reason for this is that such an 'anti-isolation' cut strongly suppresses genuine Drell–Yan signal processes, whose muons are produced in absence of accompanying hadronic activity in the geometrical vicinity. Contrarily, muons as a result of mesonic decays, for instance $b\bar{b}$ and $c\bar{c}$ would, by expectation, be accompanied by substantial hadronic activity within the detector. Whilst strongly suppressing signal, the anti-isolation cut therefore enhances the multi-jet background contribution. The anti-isolation cut is applied directly to events in collision data. Further subtracting Drell–Yan signal and non-multi-jet backgrounds according to the same selection (modelled using Monte Carlo simulated data) from this result then yields an estimation of the *shape* of the multi-jet background in the distribution of a given observable.

The overall *scale* of the multi-jet background contribution is then estimated by performing a χ^2 fit in the invariant mass distribution of collision events in the *signal* region. The χ^2 function is defined as

$$\chi^2 = \sum_i \left(\frac{N_i^{\text{cand}} - A\, N_i^{\text{EW}} - B\, N_i^{\text{QCD}}}{\sigma_i} \right)^2 , \tag{12.1}$$

where N_i^{cand} is the number of candidate events in data in the ith bin, N_i^{EW} is the estimated number of 'physics' (signal and non-multi-jet background) events (established using Monte Carlo) in the ith bin, $B\, N_i^{\text{QCD}}$ is the estimated number of multi-jet background events in the ith bin, determined from the aforementioned procedure—with A and B left as constants to be fitted—and σ_i is the appropriate statistical error for the ith bin. The values chosen for A and B are those which minimize χ^2. Since χ^2 is quadratic and bilinear in A and B, this minimization is trivially performed to yield A_{min} and B_{min}. This overall

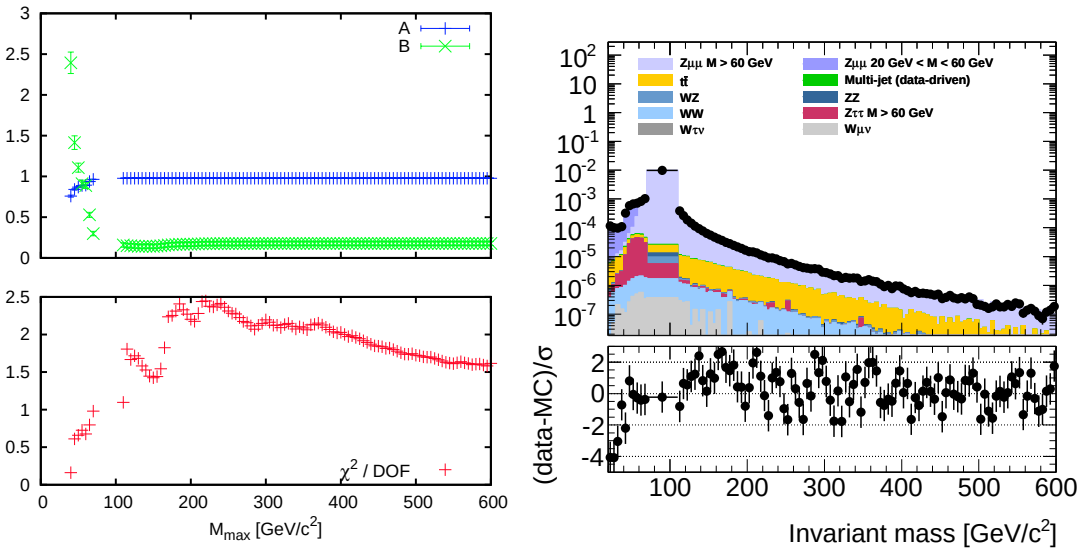

FIGURE 12.18. The plots on the left show the fitted values of A and B, along with the reduced χ^2 for the fit, as a function of $M_{\max}$ where the fit is performed over the range 20 GeV $< M < M_{\max}$. The plot on the right shows the binning of the invariant mass distribution used to perform the fit.

scale factor is then applied to the multi-jet background event shape determined for the distribution of a given observable, in order to provide the estimate of the number of multi-jet events. The overall scale factor for the signal and non-multi-jet backgrounds (A in Eq. 12.1) is allowed to float, since such freedom would be permitted by the theoretical cross-section uncertainty in any case, provided a value of $A \approx 1$ is preferred by the fit. This is indeed the case, and the fit results show $A_{\min} = 1.00044 \pm 0.00045$ (stat) and $B_{\min} = 0.068 \pm 0.026$ (stat). In order to mitigate the effects of small discrepancies between the precise shape and position of the Z peak in data and Monte Carlo, which would otherwise have a devastatingly adverse effect on the quality of the fit, the invariant mass distribution used not only has wider 5 GeV bins, but also a single 40 GeV bin which spans the entire Z resonance.

The determination of $A_{\min}$ and $B_{\min}$ is performed over the bins of the invariant mass distribution, from 20 GeV $< M <$ 600 GeV, and the fit results in a reduced $\chi^2 = 181/109$. Other ranges have been considered, specifically 20 GeV $< M <$ $M_{\max}$ where $M_{\max}$ varies between 40 GeV and 600 GeV. Figure 12.18 shows the quality of these fits and the scale factors determined. The purpose of including lower values of M in this fit is because it is expected that more multi-jet background events will contribute at this low end of the spectrum, owing to the soft spectrum in p_{T} of muons from b and c decay. It should be noted that, since the scale of the non-multi-jet event weights A is also allowed to float, the correction factor for the effective luminosity is effectively replaced according to $\tau \to A\tau$, thus rendering this formerly absolute normalization now relative to data.

The various ϕ^* distributions of collision and simulated events selected using anti-isolation cuts on both muons are shown in Figs. 12.19 and 12.20. The discrepancy between

TABLE 12.1. Results of the multi-jet background fits

Selection	A_{min}	B_{min}	χ^2/DOF
Signal	1.00044 ± 0.00045 (stat)	0.068 ± 0.026 (stat)	181/109
W+jets	1.0368 ± 0.0039 (stat)	0.3203 ± 0.0057 (stat)	237/93
$e\,\mu$ ($t\,\bar{t}$, WW & Z $\to \tau\tau$)	0.9852 ± 0.0075 (stat)	0.0449 ± 0.0022 (stat)	436/115

data and simulation is then ascribed to the multi-jet background not included in Monte Carlo simulations. Directly adopting this discrepancy as our data-driven multi-jet estimate in each of the distributions for this event selection, these data–MC comparisons therefore agree by construction. The fundamental assumption of this prescription is that the multi-jet distributions are the same in both the anti-isolated and signal regions. The reason for employing a data-driven method instead of Monte Carlo is simply that one cannot guarantee a dedicated simulation would faithfully model the multi-jet processes.

Since an event-selection in which one muon is isolated and the other is *anti*-isolated is also statistically independent of the events in which the multi-jet shape is determined, one can also use this method to estimate the multi-jet background for such a selection, where the overall normalization is again fitted in the corresponding invariant mass distribution. This has indeed been done, and is used in the validation of W+jets events in Sec. 12.2. Moreover, a similar anti-isolation requirement has *additionally* been employed for the *electron* when estimating the multi-jet backgrounds in $e\,\mu$ events. These fits for these estimates are again performed over the range 20 GeV $< M <$ 600 GeV, and all fit results for the scales of the multi-jet backgrounds (B_{min}) and the non-multi-jet processes (A_{min}) are collected in Table 12.1. The interpretation of B_{min} is essentially the number of multi-jet events which pass a given selection, expressed as a fraction of the number of events which pass the same selection but with an anti-isolation requirement on both leptons. Since the W+jets selection requires one isolated lepton, where both the signal and $e\,\mu$ selections require two, $B_{\text{min}}^{\text{signal}} \approx B_{\text{min}}^{e\,\mu} \approx \left(B_{\text{min}}^{\text{W+jets}}\right)^2$.

The fit results we have considered for the signal region and the selections designed to enhance the acceptance of W+jets, $t\,\bar{t}$ and electroweak events are inconsistent with one another if we consider statistical uncertainties alone. The discrepancies between the various fitted values are accounted for by the inclusion of appropriate systematic uncertainties. For the multi-jet background, a systematic uncertainty is included on the final result, which is presently taken to be 100% of the event yields determined in the signal region. The discrepancies between values of A_{min} determined for the different selections is well within the systematic uncertainties associated with the theoretically computed cross-sections for the non-multi-jet processes. These cross-sections are known approximately to within 5% for the Drell–Yan and electroweak processes, and within 7% for the $t\,\bar{t}$ and W+jets processes.

The overall determinations of the multi-jet backgrounds for the ϕ^* distributions, expressed as a fraction of the total event yields along with all other backgrounds considered, are presented in Sec. 12.4. It will be clear from Figs. 12.24 and 12.25 that the multi-jet background contribution determined using this method is small. Consequently, in light of

other systematic uncertainties that will be considered in Sec. 13.2, a precise determination of that due to the multi-jet background estimation will be far from paramount. The following subsection explores an alternative data-driven technique to determine the multi-jet background contribution in the hope of corroborating this principal estimate.

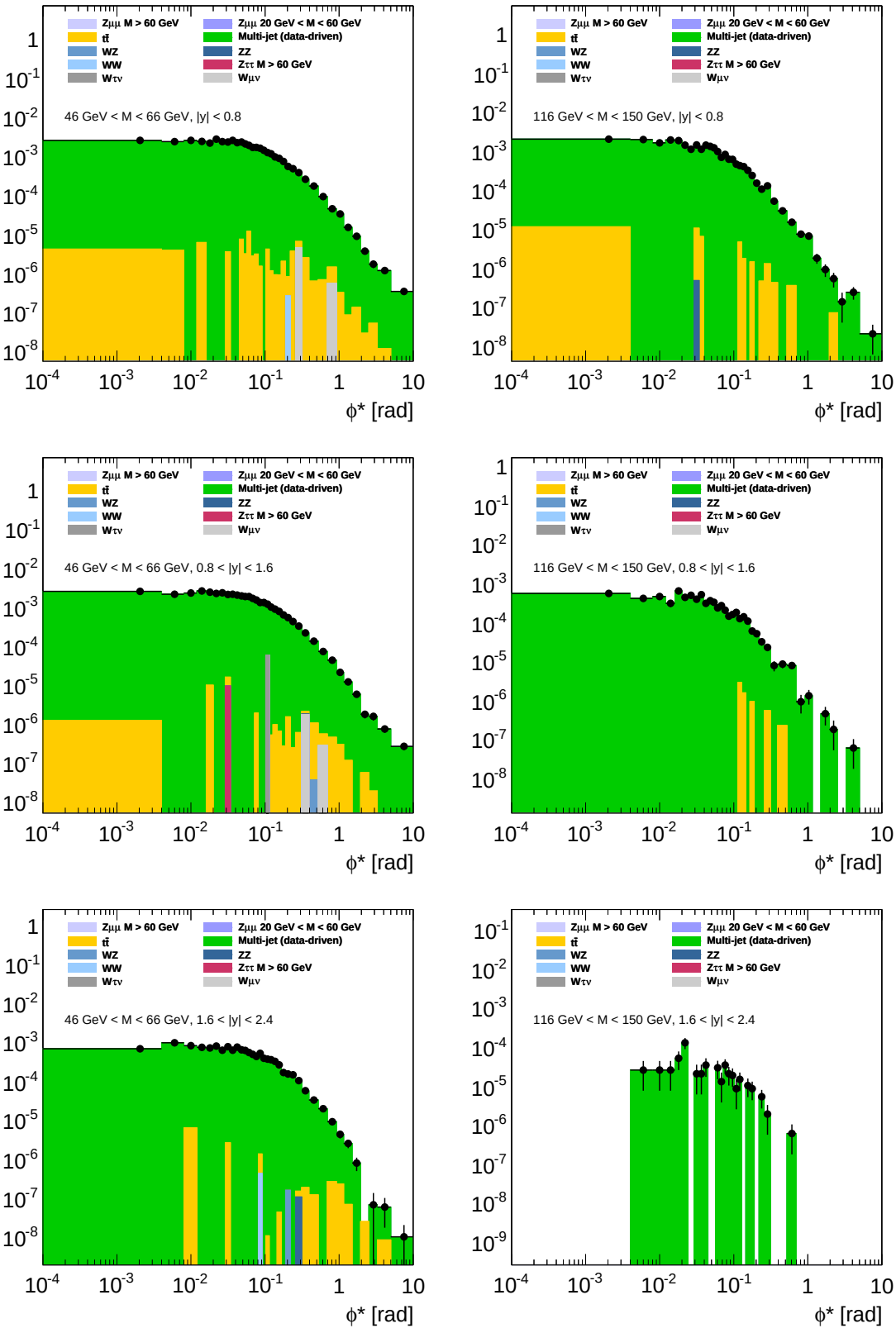

FIGURE 12.19. Plots showing the ϕ^* distributions of events in which both muons are *anti*-isolated. Upon subtraction of the Drell–Yan signal and non-multi-jet background events which contaminate in this selection, and following appropriate scaling, these distributions become the multi-jet background estimates. The plots here correspond to off-peak regions: 46 GeV $< M <$ 66 GeV (left) and 116 GeV $< M <$ 150 GeV (right).

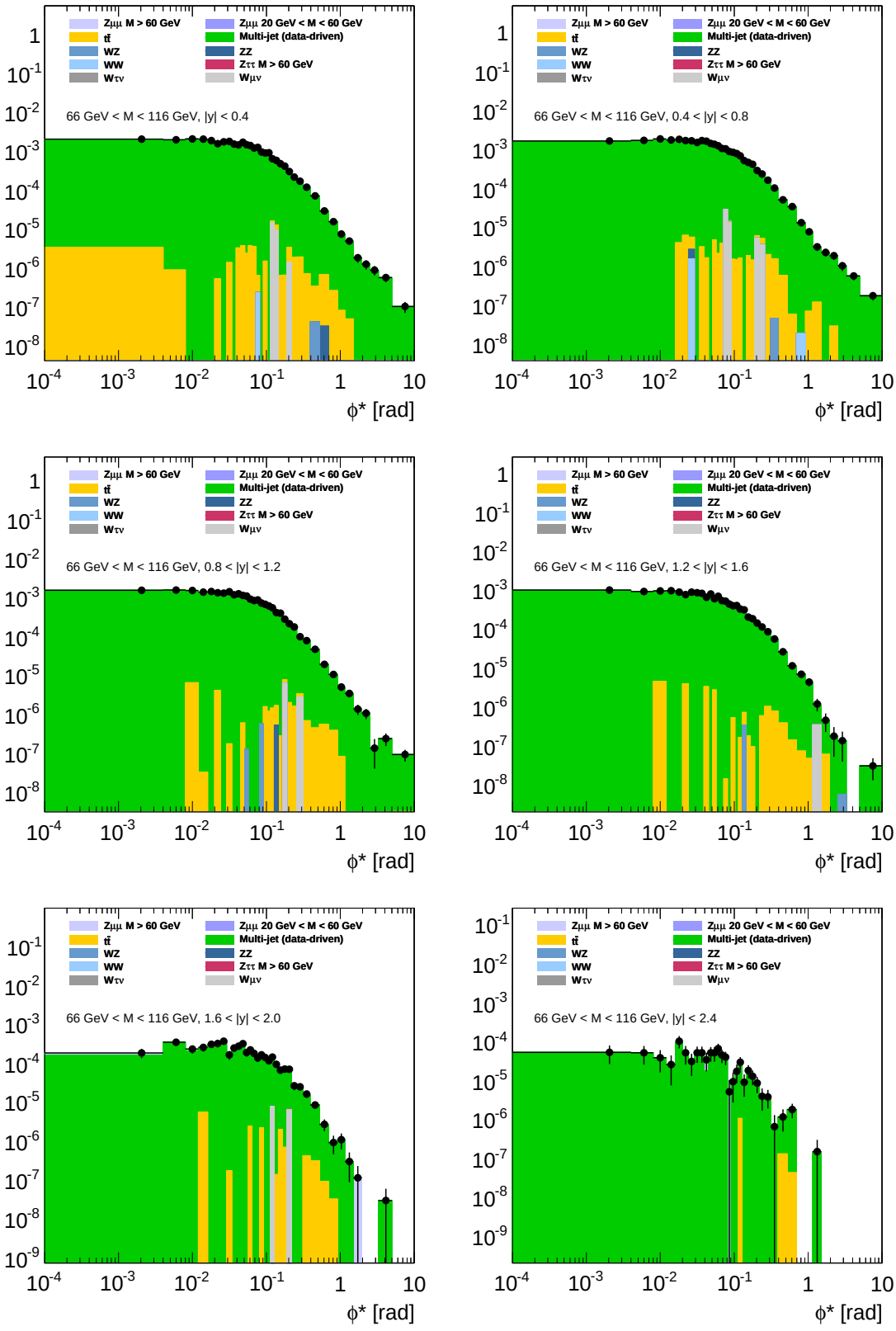

FIGURE 12.20. Plots showing the ϕ^* distributions of events in which both muons are *anti*-isolated. Upon subtraction of the Drell–Yan signal and non-multi-jet background events which contaminate in this selection, and following appropriate scaling, these distributions become the multi-jet background estimates. The plots here correspond to the on-peak region: 66 GeV $< M <$ 116 GeV.

12.3.2. Alternative multi-jet background estimate. In order to provide an alternative estimate of the multi-jet background, I have used a second technique. This involves dividing the data into statistically independent samples, based on the likeness of the muon charges and a combined measure of their isolations. Put concretely, I consider an *event* to be isolated if and only if $I < 0.1$ for *both* muons. Similarly, an event is considered to be anti-isolated if and only if $I > 0.1$ again for *both* muons. Once again, this method is data-driven.

Consider the candidate signal event selection criteria, lifting the restriction of the opposite charge requirement on the two muons. Denoting the number of events by $N = N_{\rm os} + N_{\rm ls}$, where 'os' and 'ls' denote opposite-sign and like-sign categories respectively, one can further categorize these events as 'physics' and 'QCD'. For our purposes, the 'physics' category encompasses all events which are not strictly multi-jet events, which we call 'QCD' for convenience. Thus one can write

$$N_{\rm os} = N_{\rm os}^{\rm phys} + N_{\rm os}^{\rm QCD} = \epsilon\, N^{\rm phys} + f\, N^{\rm QCD} \tag{12.2}$$

$$\text{and} \qquad N = N^{\rm phys} + N^{\rm QCD}\,. \tag{12.3}$$

Here, $\epsilon = N_{\rm os}^{\rm phys}/N^{\rm phys}$ is the efficiency with which the charge-relaxed event selection yields an opposite-sign event (given that the event is physics in nature), and $f = N_{\rm os}^{\rm QCD}/N^{\rm QCD}$ is the corresponding efficiency for multi-jet events. One can solve these four equations to obtain four new equations, the subjects of which are the quantities $N_{\rm os}^{\rm phys}$, $N_{\rm os}^{\rm QCD}$, $N^{\rm phys}$ and $N^{\rm QCD}$. The relevant quantity we seek is, expressed in terms of directly accessible quantities,

$$N_{\rm os}^{\rm QCD} = \frac{f\,(N_{\rm os} - \epsilon\, N)}{f - \epsilon}\,. \tag{12.4}$$

The object now is to determine ϵ and f independently, such that one may use the event yields $N_{\rm os}$ and N in collision data (the latter according to the charge-relaxed candidate signal selection) to obtain a data-driven estimate of the multi-jet background contamination, $N_{\rm os}^{\rm QCD}$, in the signal region.

The efficiency ϵ may be determined directly from simulated events generated using Monte Carlo techniques. The efficiency f, however, may in fact be obtained using collision data, in a statistically independent manner. As already discussed, the candidate event selection may be reasonably optimized for multi-jet event acceptance and physics event rejection, simply by reversing the isolation requirement on both muons, thus defining a 'loose' event selection. Further subtracting physics events from the resulting samples, using simulated data events, one can determine f: the ratio of opposite-sign to any-sign multi-jet events.

Unlike the template-fit method, which determines the overall normalization of the multi-jet background by appealing to the invariant mass distribution, this alternative method is performed individually for each distribution of interest. The efficiencies determined for the ϕ^* distribution, in the kinematic region $66\,{\rm GeV} < M < 116\,{\rm GeV}$ and $|y| < 2.4$, are shown in Fig. 12.21 to provide an example. The loosely isolated event distributions (with $I > 0.1$ for both muons, selected in order to determine the efficiency f in this example) in the cases of opposite-sign and like-sign, are shown in Fig. 12.22.

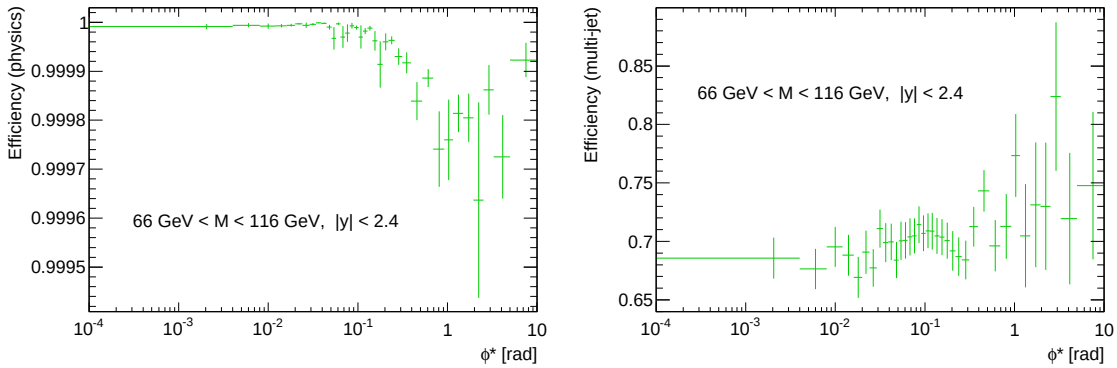

FIGURE 12.21. The efficiencies for selecting opposite-sign events from any-sign samples, for physics (left) and multi-jet (right) events.

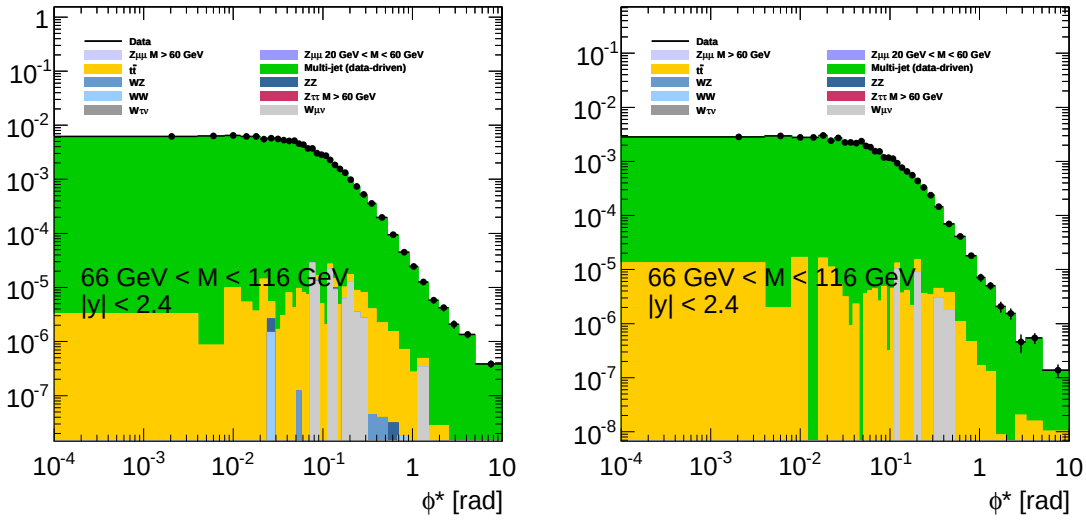

FIGURE 12.22. The ϕ^* distributions, in the on-peak region integrated over all boson rapidities, for events selected in which the isolation requirement on both muons is inverted. Furthermore, the events are separated into opposite-sign (left) and like-sign (right) categories. Simulated 'physics' events are subtracted from this collision data selection to yield the multi-jet estimate in each case. These estimates are then used to determine f.

An unfortunate shortcoming of this method is the instability of the expression in Eq. 12.4. The number of candidate signal events having suppressed the opposite-charge requirement, N, is surely greater than N_{os}, the number of candidate signal events according to the usual event selection criteria. The efficiency ϵ is approximately unity, while the efficiency for faked events f is much lower. The denominator is therefore negative and robustly determined, given available event statistics. The remaining problem exists owing to the fact that the numerator is not necessarily negative, on account of limited available event statistics across the distribution. While such a high-statistics sample of candidate Drell–Yan events exists in order to perform a precision measurement, the sample of like-sign events is small and Eq. 12.4 is unstable. In order to mitigate this issue, I have produced an estimate of the multi-jet background according to this method for the rapidity-inclusive

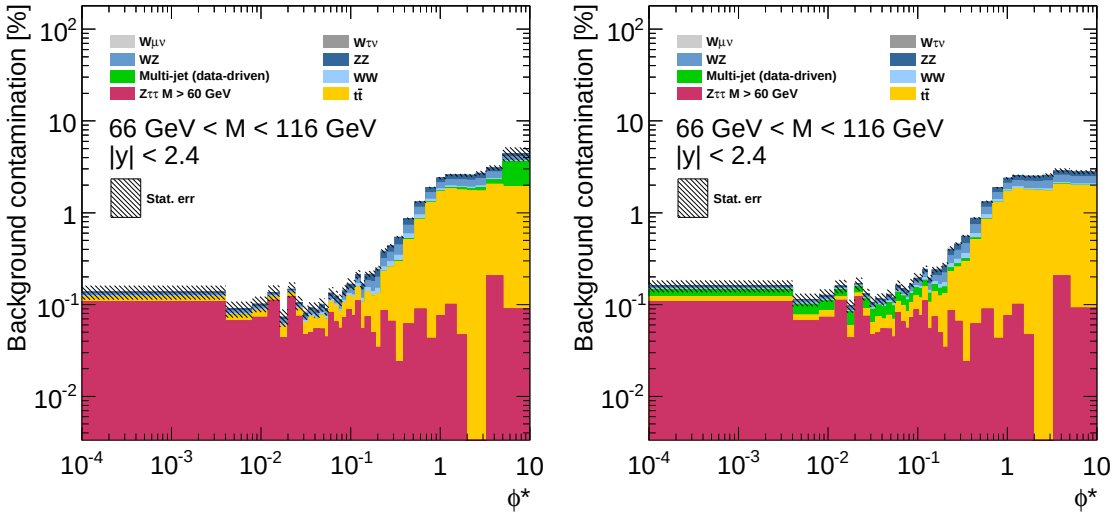

FIGURE 12.23. Estimated percentage background contamination of signal events as a function of ϕ^*, for the kinematic region 66 GeV $< M <$ 116 GeV and $|y| < 2.4$. The multi-jet background event distribution is computed for the left plot using the alternative method described in this section. The right plot uses the default template fit method.

peak mass bin, i.e. 66 GeV $< M <$ 116 GeV and $|y| < 2.4$. The final result is shown in Fig. 12.23 (left), in comparison to the corresponding result of the template fit method (right).

It is clear that this method furthermore yields a strikingly different conclusion regarding the azimuthal correlation of muons produced in multi-jet events, compared with the default method (Fig. 12.23, right). According to this alternative estimate there are fewer events populating the low-ϕ^* bins, and a large degree of decorrelation causes a peak in the high-ϕ^* region. The prediction at low-ϕ^* here is consistent with the former prediction of the template fit method, if one assumes the conservative 100% systematic uncertainty on the former result. The high-ϕ^* prediction here is apparently somewhat statistically significant in this rapidity-integrated distribution.

Notwithstanding, given the relative robustness of the principal method with respect to this alternative method, I have elected to take the result of the former estimate at face value. This is taken along with a conservative systematic uncertainty, which is nonetheless very small, given the smallness of the estimated fraction of multi-jet background events determined according to both methods (albeit with significant differences in the determined *shapes*).

12.4. Total background contamination

A compendium of all backgrounds to the ϕ^* distributions of events passing the Drell–Yan signal selection criteria are shown, expressed as percentages of the total event yields, in Figs. 12.24 and 12.25. These plots take the principal estimates for the multi-jet background contaminations, using the template fit method described in Sec. 12.3.1. The salient feature of all these plots is that many of the backgrounds are peaked around the high-ϕ^* region.

Interpreting ϕ^* as the degree to which the two final-state muons become azimuthally uncorrelated with one another (i.e. high-ϕ^* implies low correlation) we see this is the result we would have expected. The notable exceptions include the multi-jet background events, which are roughly uniformly distributed in ϕ^*, and the $\mathrm{Z} \to \tau\tau$ events, which are distributed favouring the low-ϕ^* region.

To better understand these differences, take for example the $\mathrm{Z} \to \tau\tau$ and $t\,\bar{t}$ processes. We note the high mass of the top quark in comparison to that of the tau lepton will result in different kinematics and therefore different distributions of momenta among the final-state particles. For the $\mathrm{Z} \to \tau\tau$ process, the tau leptons with masses of ~ 1.8 GeV are produced highly boosted with respect to Z rest frame. The subsequent weak decays produce muons which are therefore also boosted in the same directions, and thus the directions of the muons are representative of the directions of the tau leptons, which are themselves azimuthally correlated in the lab frame in the absence of recoil against the emission of one or more hard jets in the initial state. In contrast, the much heavier top quarks will likely not be produced with any significant boost at 'moderate' partonic collision energies. The subsequent weak decays produce muons, missing energy and bottom quarks which recoil strongly against *one another*, but any correlation between the directions of the muons becomes washed out. It has here been tacitly assumed that effects due to spin correlations do not play a significant rôle.

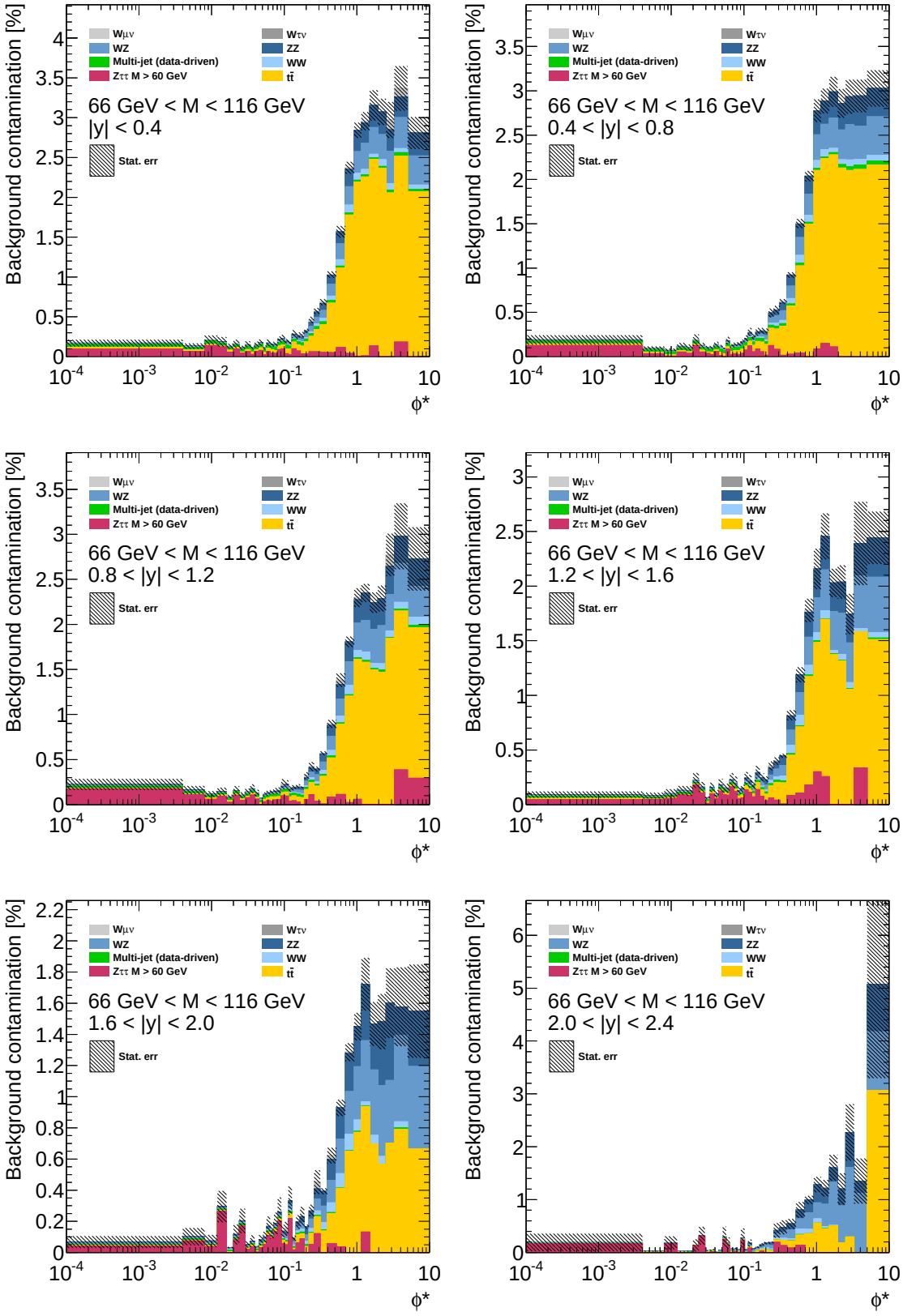

FIGURE 12.24. Distributions of background events, expressed as a percentage of the total event yield, for ϕ^*. The *template fit* method is used here to estimate the multi-jet background contribution. Statistical uncertainties are shown. These plots correspond to measurements made on peak: 66 GeV $< M <$ 116 GeV.

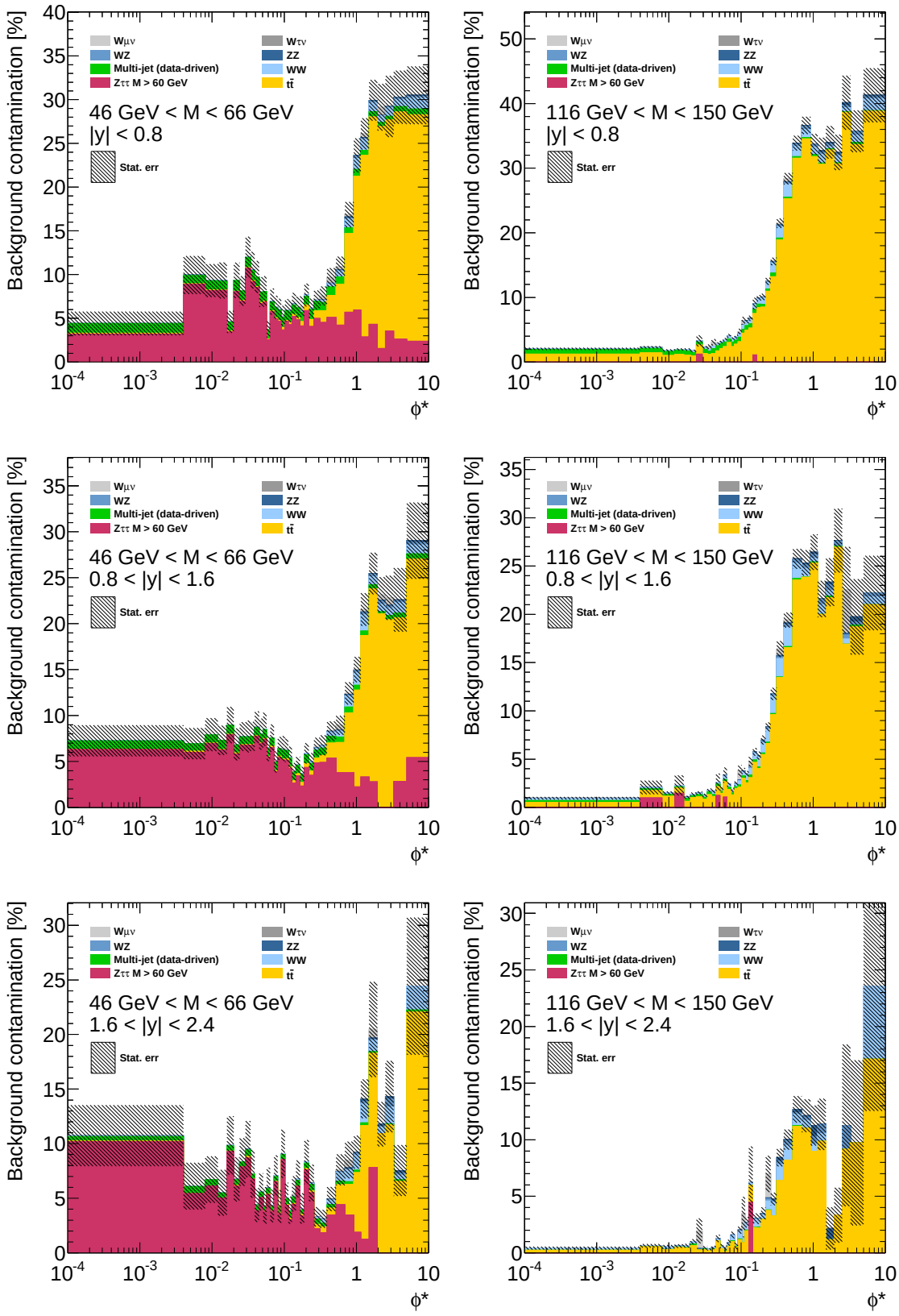

FIGURE 12.25. Distributions of background events, expressed as a percentage of the total event yield, for ϕ^*. The *template fit* method is used here to estimate the multi-jet background contribution. Statistical uncertainties are shown. These plots correspond to measurements made off peak: 46 GeV $< M <$ 66 GeV (left) and 116 GeV $< M <$ 150 GeV (right).

12.5. Control distributions

This section is a compilation of plots showing comparisons between collision data and simulated data events in various control distributions. In summary, the agreement is impressive in the majority of cases, which is a testament to the quality of physics modelling in the various Monte Carlo generators available today. Certainly in all aspects consequential to this particular analysis, the agreement is highly satisfactory, and one is inclined to trust the background event yields are faithfully estimated. Appropriate systematic errors, assigned to various inadequacies of the simulations in terms of either their physics or detector modelling, are considered in Sec. 13.2.

The reader will nonetheless observe that for certain observables, in which good agreement between collision and simulated data would presumably be critical, there are some striking discrepancies. I will take this opportunity to indicate such instances, and explain how they are mitigated or indeed inconsequential. The first major discrepancy observed in a seemingly critical observable concerns the peak mass region of the invariant mass distribution, shown in Fig. 12.28. Small differences between the peak observed in the distribution of collision events and the peak modelled in simulated data are exacerbated in the comparison, which Z line shape re-weighting attempts to mitigate. While there are indeed many instances of statistically significant discrepancies in bins surrounding the peak mass region, the on-peak analysis is integrated over this entire region. It has already been demonstrated that, at least in the case of muons corrected back to the bare level, the migration of events between *coarse* mass bins is negligible, as demonstrated in Fig. 9.1. Precisely the same phenomenon is observed in the transverse momentum distributions of the individual muons (Fig. 12.30, bottom) where the discrepancies are observed around ~ 46 GeV.

Another critical concern is the transverse momentum distribution of the lepton pairs, as shown in Fig. 12.29. There is a high degree of correlation between Q_{T} and ϕ^* in the low-Q_{T} region in particular, as shown in Fig. 12.26. It is this low-Q^*_{T} region where another striking discrepancy is observed. Therefore, let us also consider the actual ϕ^* distributions shown in Figs. 12.31 to 12.34, where again there are many instances of statistically significant discrepancies at the level of many standard deviations in the low-ϕ^* region. In order to account for these discrepancies in the final result, I have introduced a corresponding systematic uncertainty. The discrepancies are typically at the level of no more than 10% in relative terms, so for the background subtraction this should introduce a negligible uncertainty in the peak region, for the backgrounds themselves are typically $< 3\%$ at most, and indeed $\ll 1\%$ across several orders of magnitude of ϕ^*. The issue is instead pertinent to the computed bin-by-bin correction factors, which themselves make use of simulated signal events. The method used to obtain an appropriate systematic uncertainty is described in Sec. 13.2. Given the high degree of correlation between ϕ^* and Q_{T}, we thus consider the discrepancies observed in both distributions as being one and the same, and moreover accounted for by the same systematic.

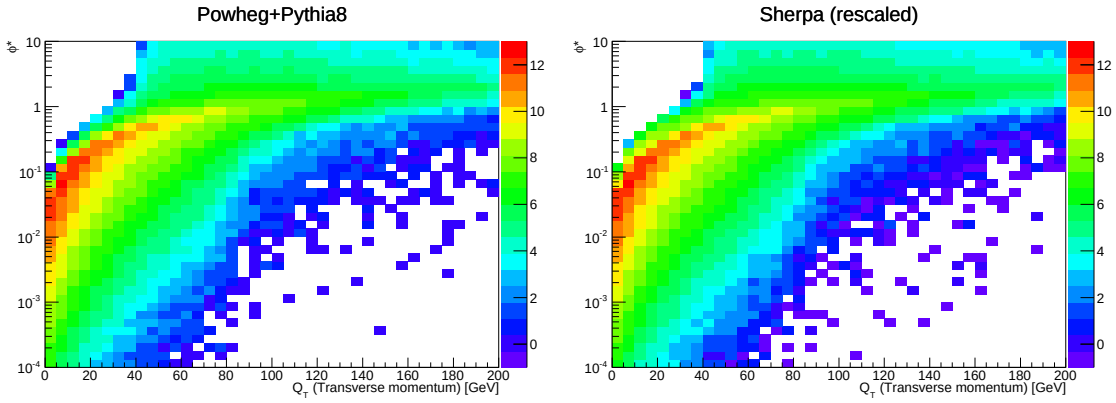

FIGURE 12.26. The correlation between ϕ^* and Q_{T} in Powheg+Pythia8 (left) and Sherpa (right). Sherpa events are re-weighted such that the invariant mass distribution is the same as that of Powheg+Pythia8 events by construction.

Ultimately, the principal use of simulated signal data here is to model detector effects, and thus implement appropriate corrections of distributions in collision data. The modelling of the strongly peaked $E_{\mathrm{T}}^{\mathrm{miss}}$ distributions (shown in Fig. 12.27 for the three mass regions) of simulated signal events is not precisely representative of the distributions in collision data. The culpability again lies with the signal process, and the discrepancies are likely due to mismodelling of the muon momentum resolution in simulation, since nominally of course there is no missing energy in muonic Drell–Yan signal events, lest an object fall outside the geometrical acceptance of ATLAS or be improperly measured. The discrepancy is inconsequential for this measurement of ϕ^* however, whose advantage over Q_{T} lies in its immunity to such momenta mismeasurements.

Given the ostensible eight-fold symmetry of the ATLAS detector about the central axis, owing itself to the structure of the toroidal magnet system and muon detection system, *a priori* one would expect a regular modulation in the muon reconstruction efficiency. This has important implications for ϕ^*, which is driven by the so-called *acoplanarity angle* between the leptons, since this could introduce a potential bias if not properly corrected for.

To elucidate this point a little more, consider an ensemble of events in which the first muon so happens to have been reconstructed in a particularly efficient region of the detector. Given the known symmetry of the detector about the central axis, the supposition that a second muon produced back-to-back with respect to the first muon would therefore be reconstructed more efficiently, yields concern over the potential for lower values of ϕ^* to be favoured. A similar but reverse argument may be applied to cases in which the first muon is reconstructed in an *inefficient* region of the detector. Now the reconstruction of the back-to-back configuration is *disfavoured*, owing to the supposed similar inefficiency with which a second muon would be reconstructed to yield such a configuration.

Plots in Figs. D.1—D.8 of Appendix D show the finely binned distributions of events in the azimuthal angle for the leading and sub-leading muons, in data and Monte Carlo. This

confirms that, within statistical uncertainties, any modulations in efficiency, or indeed any isolated regions of inefficiency, are correctly modelled by the detector simulation. Thus one expects to be able to reliably correct for detector effects, in order to recover the *physics* ϕ^* distribution. This is what is done in Sec. 13.1.

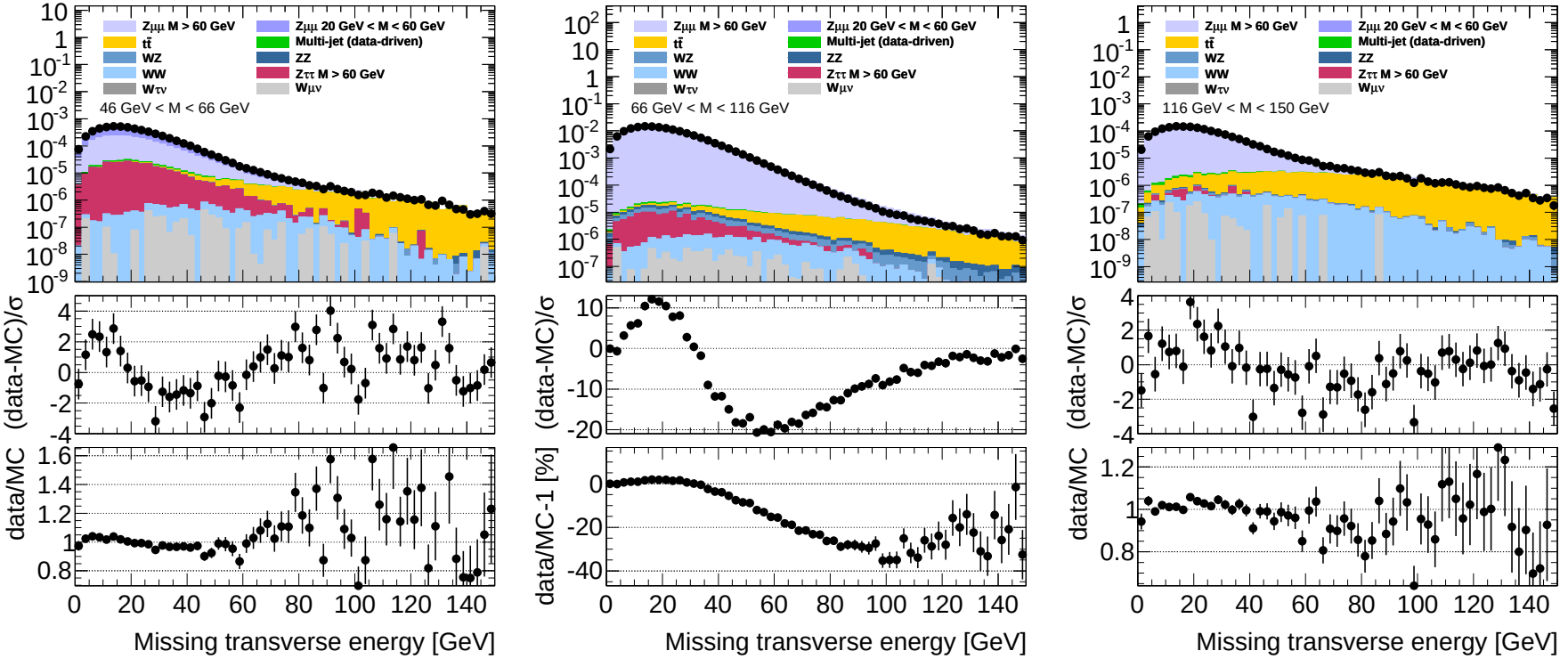

FIGURE 12.27. The missing transverse energy ($E_{\mathrm{T}}^{\mathrm{miss}}$) distributions of candidate events, with estimated backgrounds shown, for the mass regions 46 GeV $< M <$ 66 GeV, 66 GeV $< M <$ 116 GeV and 116 GeV $< M <$ 150 GeV and the inclusive rapidity region $|y| < 2.4$.

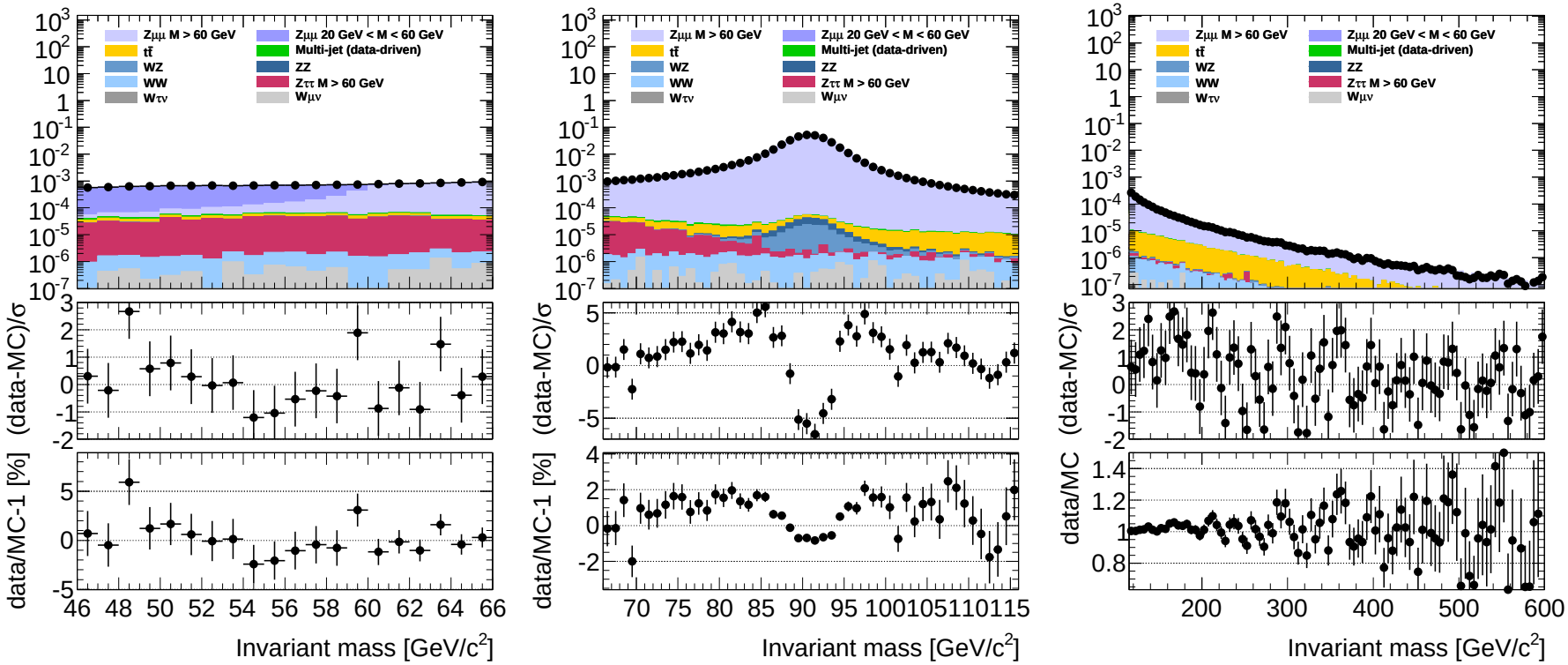

FIGURE 12.28. The invariant mass (M) distributions of candidate events, with estimated backgrounds shown, for the inclusive rapidity region $|y| < 2.4$.

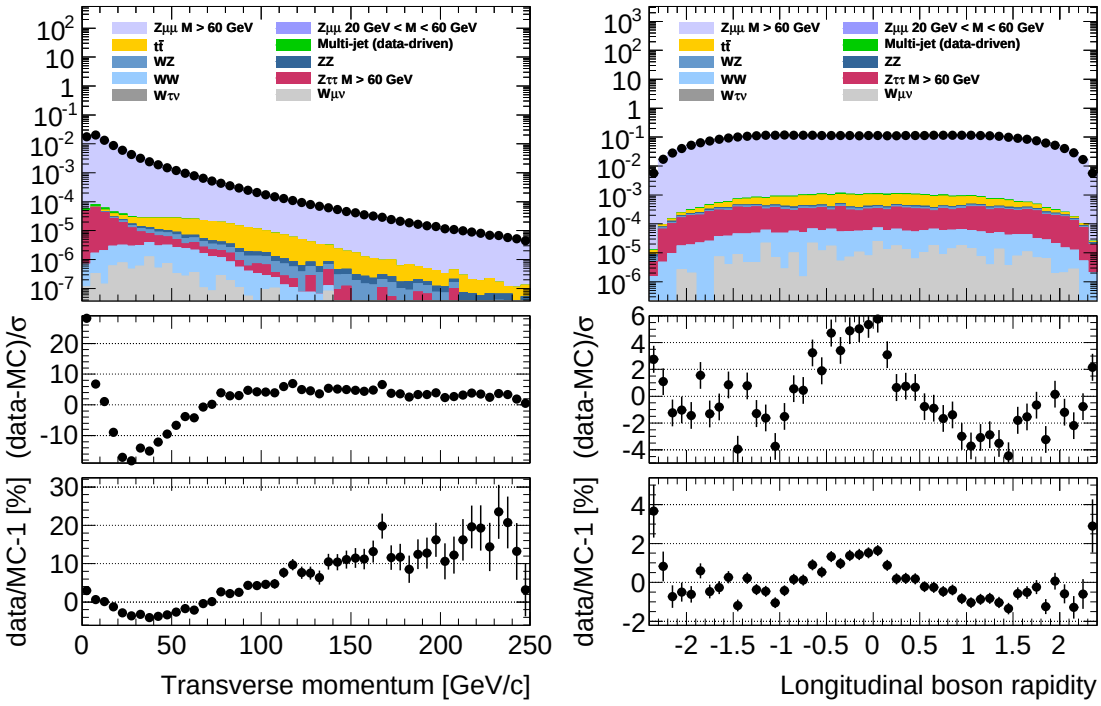

FIGURE 12.29. The boson transverse momentum (Q_{T}) and boson rapidity (y) distributions of candidate events, with estimated backgrounds shown.

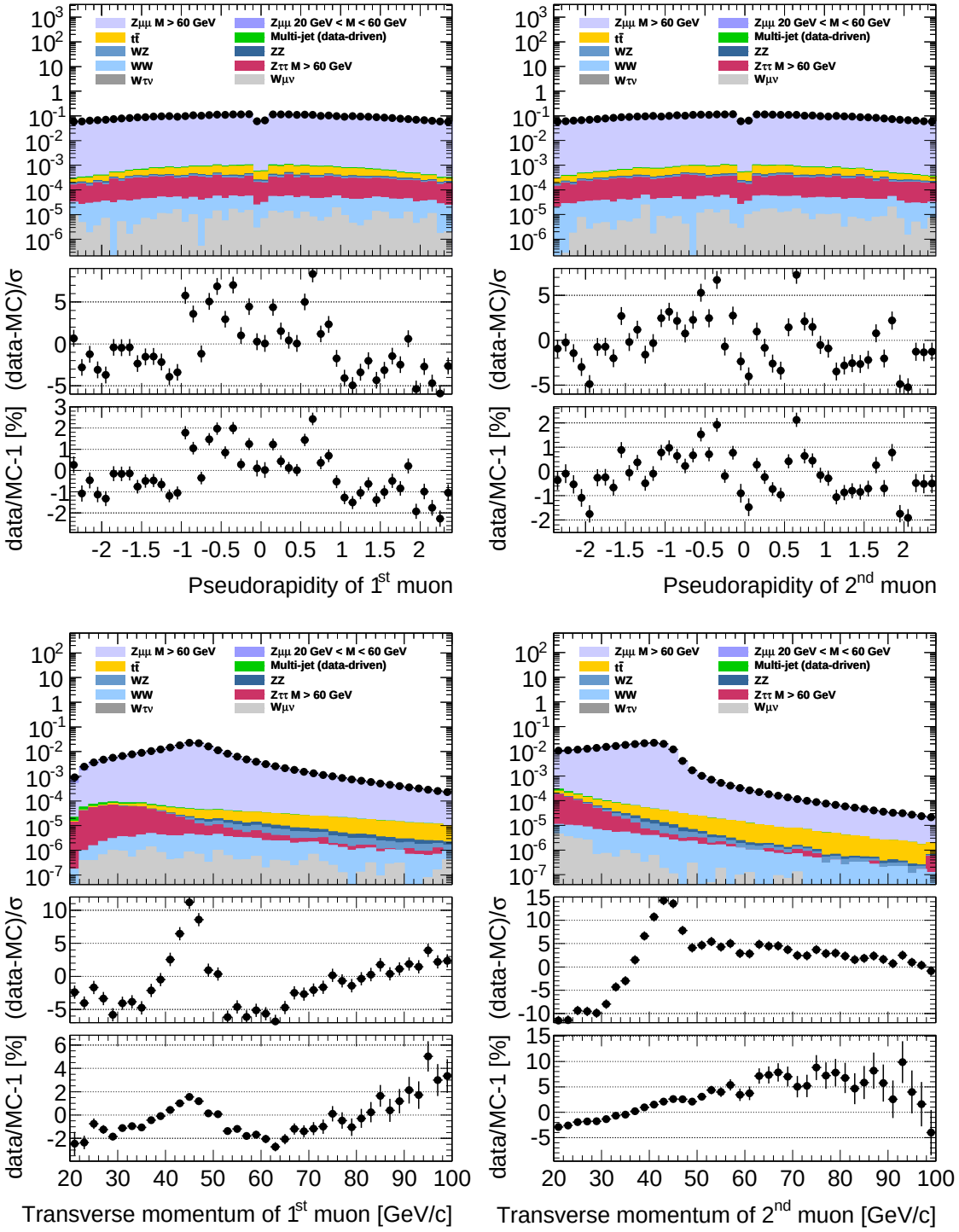

FIGURE 12.30. The transverse momenta (p_{T}) and pseudorapidity (η) distributions of candidate events for leading and sub-leading muons, with estimated backgrounds shown.

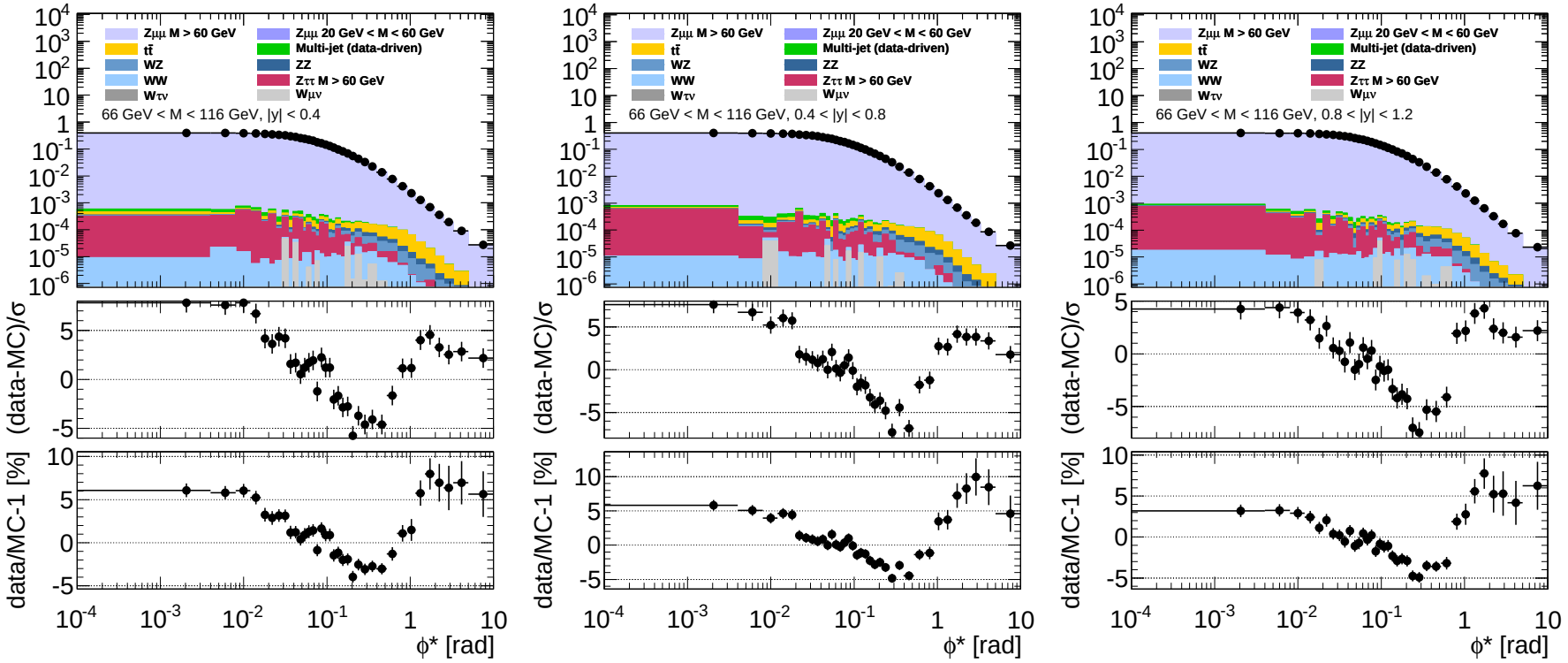

FIGURE 12.31. The ϕ^* distributions of collision and simulated events selected in the signal region, for the mass range 66 GeV $< M <$ 116 GeV. Rapidity ranges $|y| < 0.4$, $0.4 < |y| < 0.8$ and $0.8 < |y| < 1.2$ are shown.

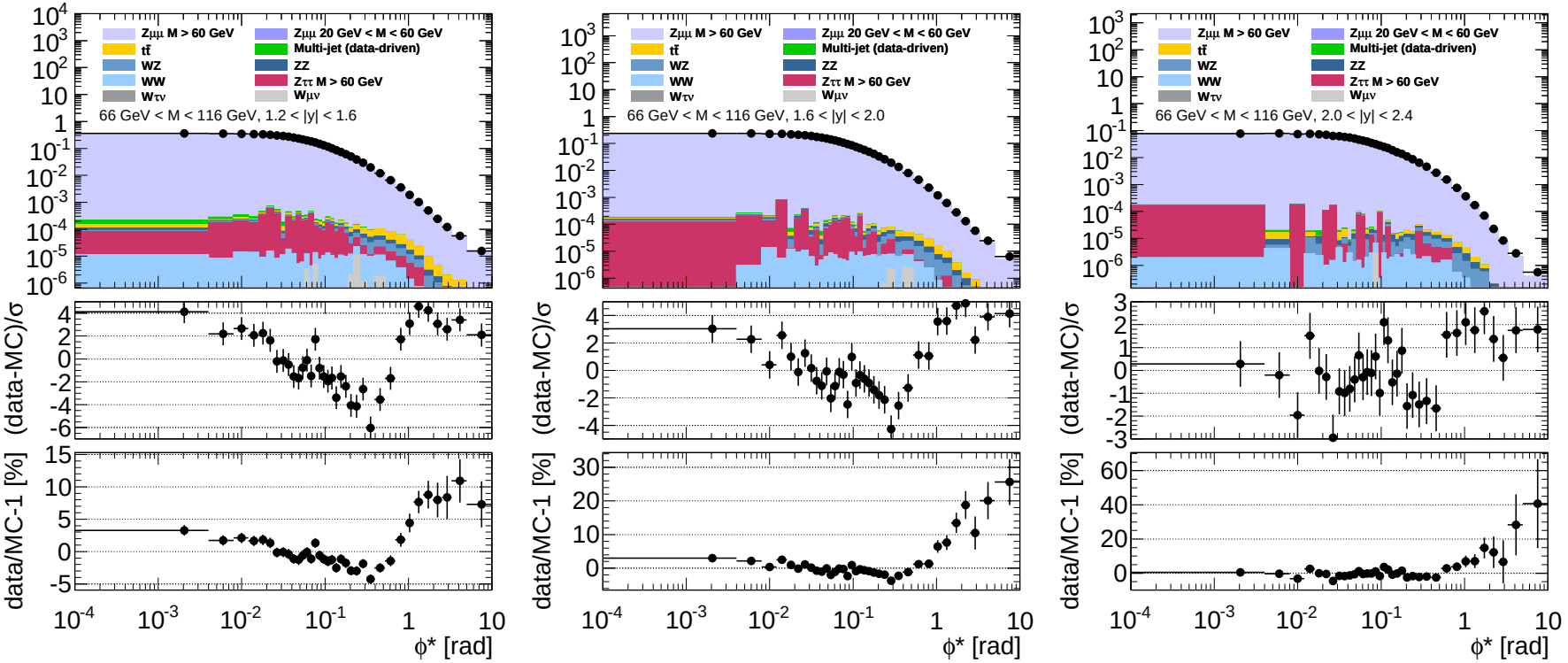

FIGURE 12.32. The ϕ^* distributions of collision and simulated events selected in the signal region, for the mass range 66 GeV $< M <$ 116 GeV. Rapidity ranges $1.2 < |y| < 1.6$, $1.6 < |y| < 2.0$ and $2.0 < |y| < 2.4$ are shown.

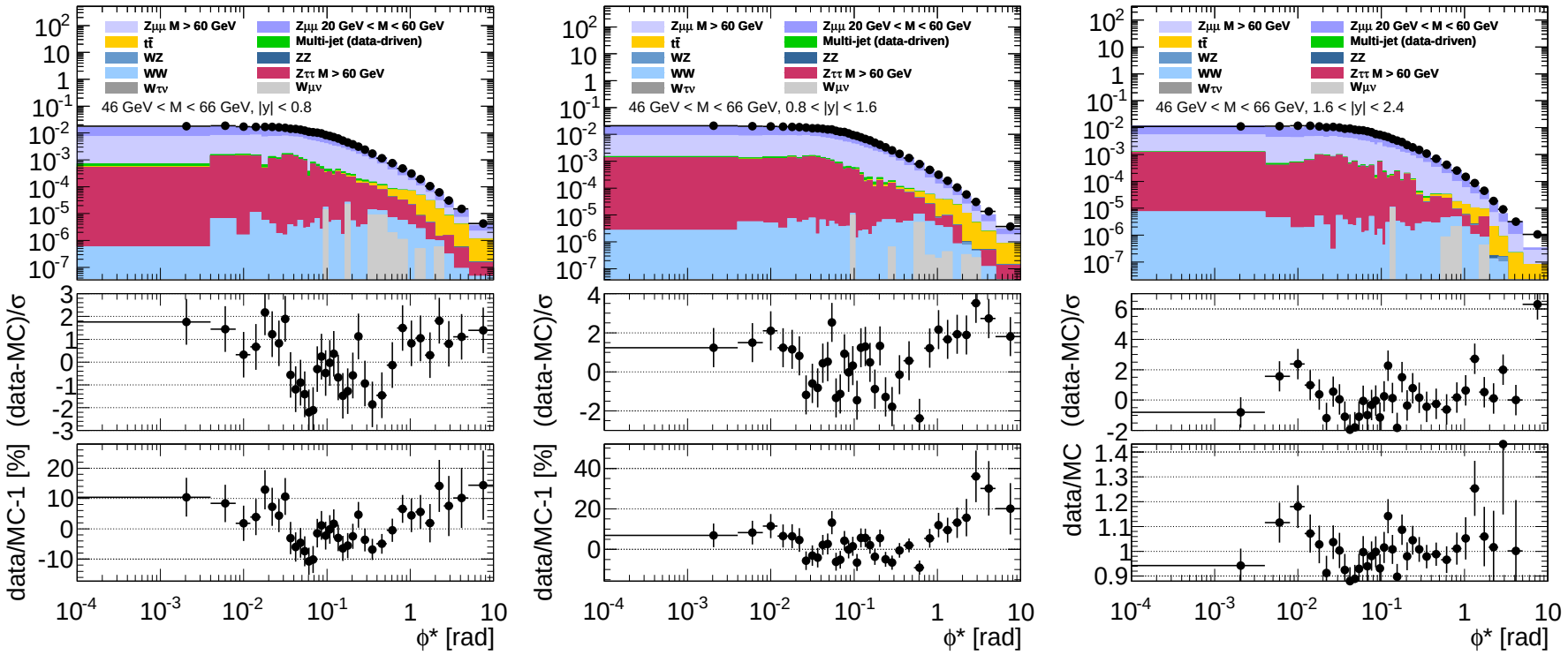

FIGURE 12.33. The ϕ^* distributions of collision and simulated events selected in the signal region, for the mass range 46 GeV $< M <$ 66 GeV. Rapidity ranges $|y| < 0.8$, $0.8 < |y| < 1.6$ and $1.6 < |y| < 2.4$ are shown.

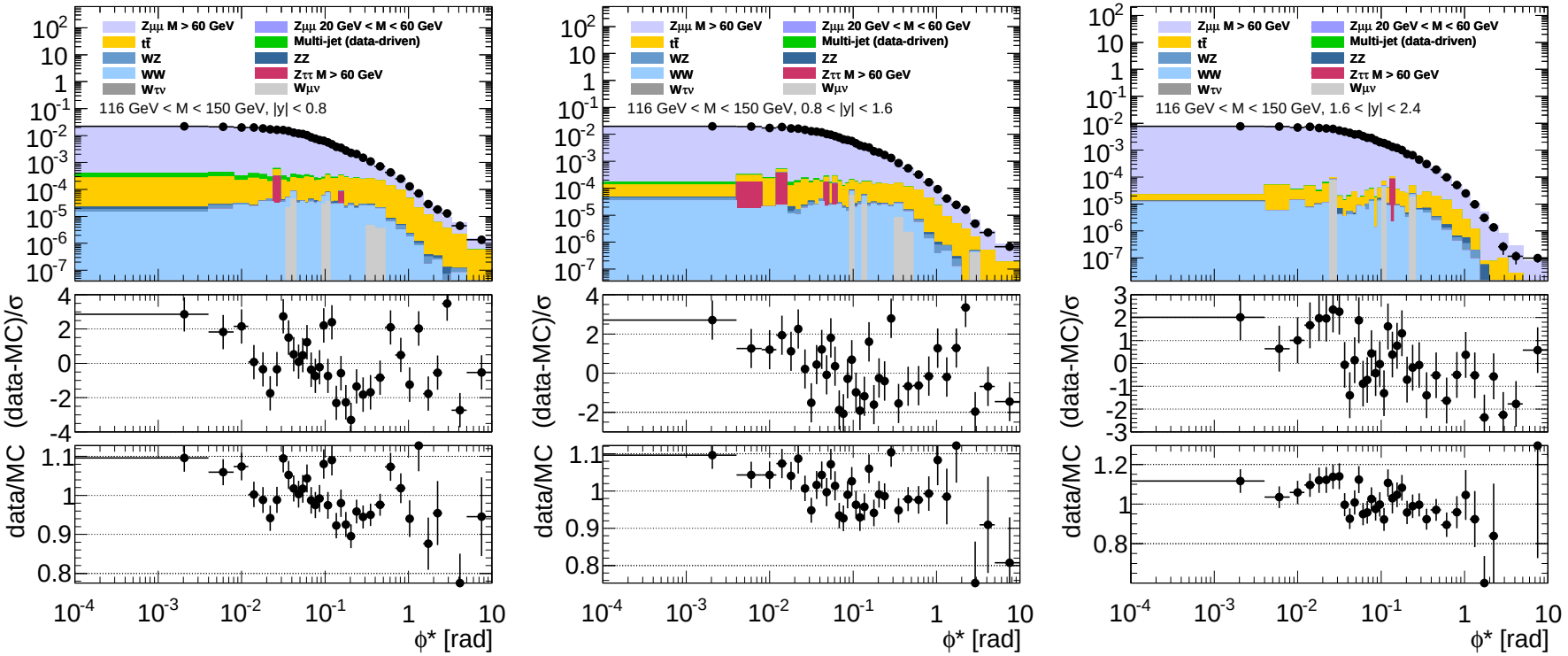

FIGURE 12.34. The ϕ^* distributions of collision and simulated events selected in the signal region, for the mass range 116 GeV $< M <$ 150 GeV. Rapidity ranges $|y| < 0.8$, $0.8 < |y| < 1.6$ and $1.6 < |y| < 2.4$ are shown.

CHAPTER 13

Final results

13.1. Bin-by-bin corrections

Bin-by-bin correction factors (see Eq. 9.3 in the context of Eq. 9.6) are applied to background-subtracted ϕ^* distributions populated by collision data events, before normalizing to obtain the final results. The purpose of these correction factors, plotted in Figs. 13.1 and 13.2, is to account for the effect of particle detection and reconstruction, which are peculiar to the experiment, thus recovering the underlying *physics* distributions in ϕ^*.

In principle, since generator-level particle information is available, contingent on the nature of the given Monte Carlo generator, one can also correct to various physics generator levels beyond a simple detector correction. One can correct, for instance, to the bare level distribution but equally to the Born level distribution. This certainly raises some philosophical issues however, and it is my opinion that an experimental measurement should minimally depend on any specific theoretical assumptions. For that reason, I present the ϕ^* distribution correction factors applicable to obtain the *bare level* distributions, and so the content of the measurement is experimentally driven. A theoretical prediction should therefore include the effects of, e.g., final-state radiation (FSR) before a comparison is made to these results. Any residual theoretical dependence is accounted for by the inclusion of an appropriate systematic uncertainty on the final measurement, as in Sec. 13.2.

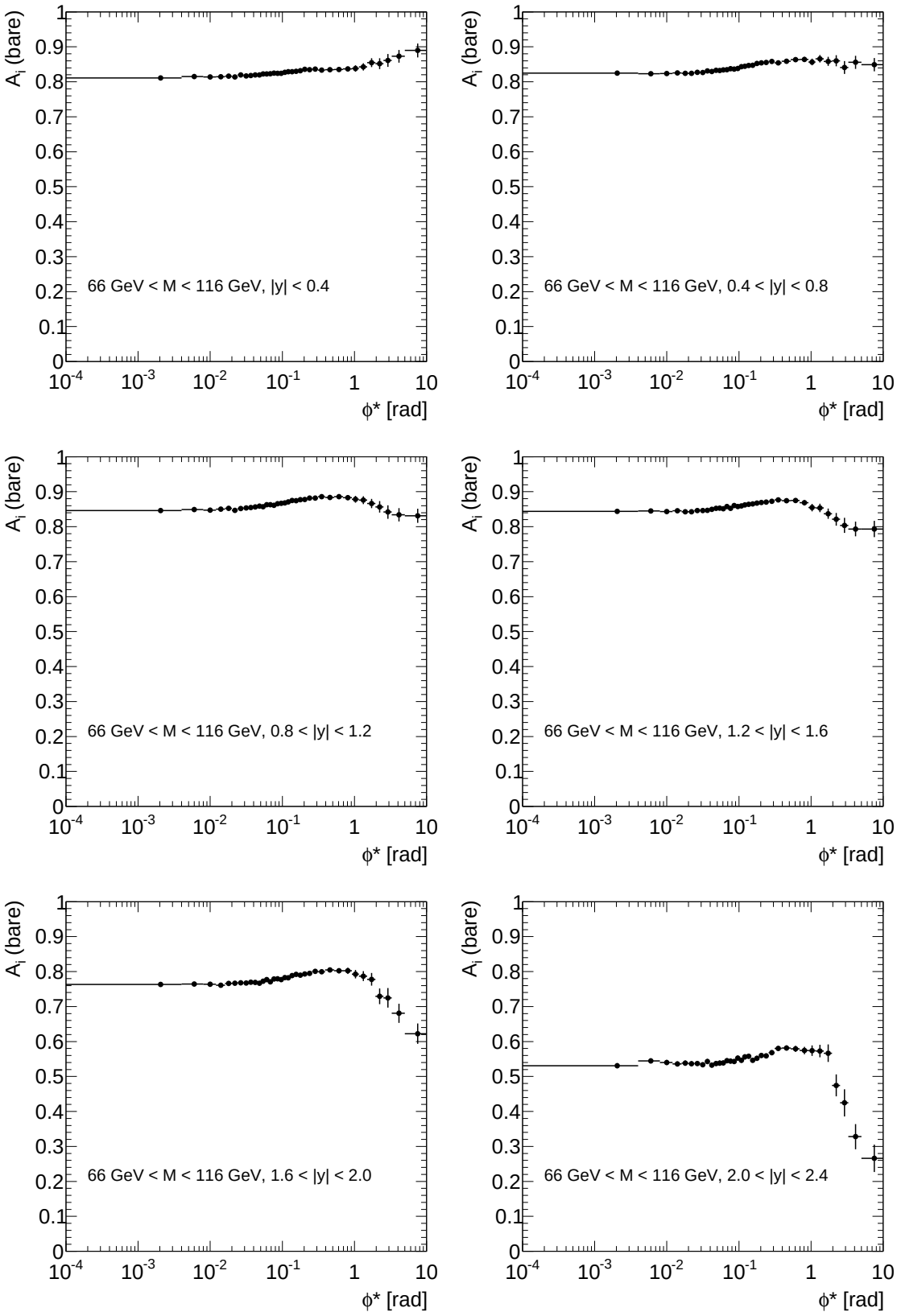

FIGURE 13.1. Bin-by-bin correction factors for the ϕ^* distributions in the 66 GeV $< M <$ 116 GeV region, in different $|y|$ bins. These factors are to be applied to the background-subtracted distributions of the number of candidate events in data.

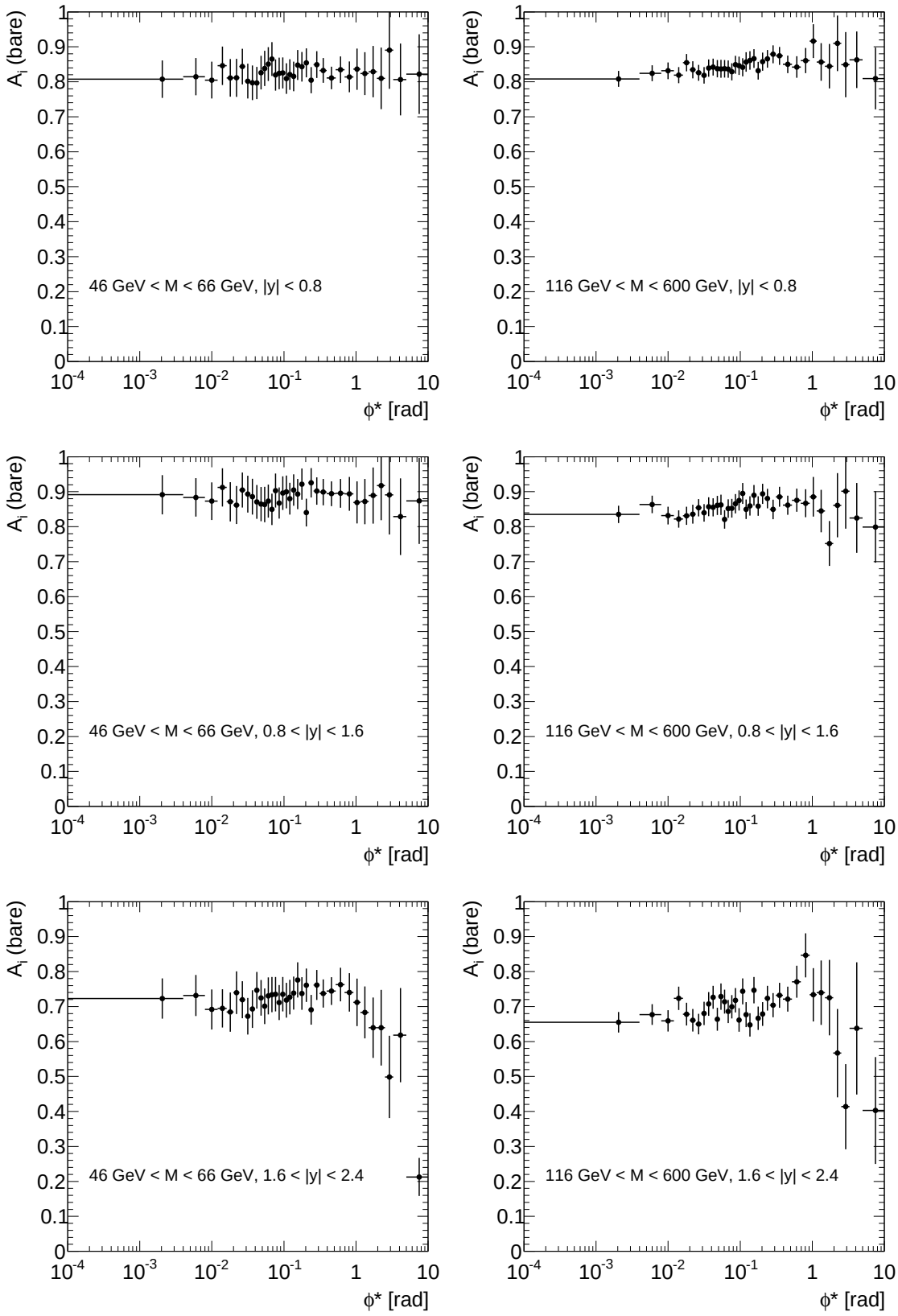

FIGURE 13.2. Bin-by-bin correction factors for the ϕ^* distributions in the 46 GeV $< M <$ 66 GeV (left) and 116 GeV $< M <$ 150 GeV (right) regions, in different $|y|$ bins. These factors are to be applied to the background-subtracted distributions of the number of candidate events in data.

13.2. Systematic uncertainties

The final background-subtracted and normalized distributions of events in bins of ϕ^*, corrected for detector effects, are to be presented in Sec. 13.3 for the on-peak and off-peak analyses. A compendium of established uncertainties on these distributions, expressed in terms of percentages of the event yields in each bin, are shown in Figs. 13.3 to 13.6. The bin uncertainties that are considered here on $1/\sigma\,(d\sigma/d\phi^*)_i$ (for which, see Eq. 9.6) arise from the uncertainties on $N_{i\,\mathrm{cand}}$, $N_{i\,\mathrm{reco\ back}}$ and A_i. The normalization factor $\mathcal{N}$ then introduces a bin-to-bin correlation on these uncertainties. In principle the factor τ is also a source of uncertainty. The multi-jet background estimation employed in this analysis, however, allows the overall scale of simulated signal and non-multi-jet background data to float in the fit. This therefore inhibits the propagation of the luminosity uncertainty into our final distribution, since the effective luminosity of the simulated data sample is now tethered to that of collision data. The uncertainty on $N_{i\,\mathrm{cand}}$ is purely statistical in nature. It is therefore the quantities $N_{i\,\mathrm{reco\ back}}$ and A_i which contribute to the systematic uncertainties. In this section I will describe the methodology behind ascertaining these uncertainties.

A significant systematic uncertainty on the distributions owes itself to the modelling of final-state QED radiation. This uncertainty, labelled 'FSR', is currently estimated in a very conservative fashion, by simply correcting background-subtracted distributions of candidate signal events to both the bare and Born levels, and examining the difference between the resulting distributions. The percentage difference between corresponding bins in the two distributions is taken to be the uncertainty on that bin in the final distribution, which is corrected to the bare level. It may be argued that this is indeed too conservative. The typical fashion in which such uncertainties are computed is to take two models of FSR and examine the differences between the resulting final distributions.

As mentioned in Sec. 12.5, our estimate of the normalized differential cross-section in ϕ^* (Eq. 9.6) relies heavily on simulated data via the correction factor A_i. For a correction back to the bare level, this dependence is rather more largely via the modelling of the detector in simulated data than on the modelling of physics. Ideally, this correction factor should indeed depend as minimally as possible on the modelling of the actual physical process, and any residual dependence on this modelling must be accounted for via the inclusion of an appropriate systematic uncertainty. Here I demonstrate how this uncertainty is computed.

If we keep under consideration the measured distribution corrected for detector effects—so precisely our estimate according to Eq. 9.6—then the appropriate comparison to theory is made at the level of *generated* signal event distributions. We can therefore define an event weight which depends on the ϕ^* bin in which the event was *generated*, as

$$w_i \equiv \frac{M_i}{T_i}\,, \tag{13.1}$$

where $M_i = (d\sigma/d\phi^*)_i$ as estimated in Eq. 9.6 and

$$T_i = \tilde{\mathcal{N}}\,\frac{N_{i\,\mathrm{gen}}}{(\Delta\phi^*)_i} \tag{13.2}$$

is simply our theoretical physics distribution. Here $N_{i\,\mathrm{gen}}$ is the number of generated events in the ith ϕ^* bin and $\tilde{\mathcal{N}}$ is an independent normalization factor for the generated distribution. We thus have a set of weights which may be applied directly to generated events such that the generated and estimated distributions agree by construction. Adopting the notation $N_{i\,\mathrm{reco},j\,\mathrm{gen}}$ for the number of events reconstructed in the ith ϕ^* bin having been generated in the jth bin, and assuming a negligible number of faked events, we may explicitly write

$$N_{i\,\mathrm{reco}} = \sum_j N_{i\,\mathrm{reco},j\,\mathrm{gen}}\,. \tag{13.3}$$

Now we define a new correction factor

$$A'_i = \frac{\sum_j w_j N_{i\,\mathrm{reco},j\,\mathrm{gen}}}{w_i N_{i\,\mathrm{gen}}}\,, \tag{13.4}$$

which differs from A_i simply by the inclusion of the weights, which themselves depend on the bin in which the event was generated. We see of course that, in the absence of bin-to-bin migration of events, we simply obtain the same weight A_i as computed initially, since then $N_{i\,\mathrm{reco},j\,\mathrm{gen}} \approx N_{i\,\mathrm{reco},j\,\mathrm{gen}}\,\delta_{ij} = N_{i\,\mathrm{reco\,\&\,gen}}$ and the weight w_i cancels in the numerator and the denominator. This is as we would expect, for then the underlying physics would have no impact on a correction factor contrived to solely correct for *detector* effects. Using the new correction factor A'_i instead, we now re-evaluate our estimation of the differential cross-section as

$$\frac{1}{\sigma'}\left(\frac{d\sigma}{d\phi^*}\right)'_i \approx \frac{\sigma'_i}{\sigma'\,(\Delta\phi^*)_i} = \mathcal{N}'\,\frac{N_{i\,\mathrm{cand}} - \tau\,N_{i\,\mathrm{reco\ back}}}{(\Delta\phi^*)_i\,A'_i}\,. \tag{13.5}$$

In principle we have re-weighted the generated event distribution, in order that the physics modelling is as perfectly representative of that in nature as possible, and assessed the extent to which our detector correction depends upon this change in underlying physics. The systematic we have computed here is labelled 'correction factor'.

A far-less-significant source of systematic uncertainty is the multi-jet background estimation, labelled 'QCD'. The uncertainty on the final distributions associated with the determination of the multi-jet background event yields is conservatively ascertained by simply computing the final distributions both with and without multi-jet background subtraction, and examining the differences.

Additional sources of systematic uncertainty that are similarly far less significant include those due to muon momenta modelling in simulated data ('muon momenta'), the theoretical cross-sections computed for all physical processes considered ('cross-section'), the average number of interactions per bunch crossing ('pileup'), the 'Z line shape', the modelling of the efficiencies with which muons are reconstructed in simulated data ('muon reco. efficiency') and the modelling of the trigger efficiency in simulated data ('trigger efficiency'). For all sources, the final distributions have again been recomputed assuming the appropriate variations in the applied event weights, or simply in the absence of such corrections, and comparing to the final distribution with all appropriate corrections in place, to yield a percentage uncertainty. Such variations have been applied independently to obtain each uncertainty.

For these uncertainties, I have considered a total weight for each simulated event j, expressed as the product of *component* weights:

$$W_j = W_{\text{MC}} \cdot W_{\text{line}} \cdot W_{\text{pileup}} \cdot W_{\text{trig.}} \cdot W_{\text{mu 1}} \cdot W_{\text{mu 2}} \cdot W_{\text{xsct}} \tag{13.6}$$

It is important to note here that there is one such weight for *each* event, although for notational simplicity I have dropped the event index j on the RHS. The remaining weights, read from left to right respectively, account for the Z line shape (mass distribution), the average number of interactions per bunch crossing (pileup), the trigger efficiency, the reconstruction efficiencies of the two muons, and finally the theoretical cross-section of the process considered.

Systematic uncertainties corresponding to the Z line shape and the event pileup are obtained simply by independently setting $W_{\text{line}} = 1$ and $W_{\text{pileup}} = 1$, and examining the differences with respect to the final distribution computed using the nominal weights. Systematic uncertainties corresponding to the simulated trigger efficiency and muon reconstruction efficiencies are obtained by independently setting

$$\begin{aligned} &W_{\text{trig.}} \to W_{\text{trig.}} + \delta W_{\text{trig.}} \\ \text{and} \quad &W_{\text{mu 1}} \cdot W_{\text{mu 2}} \to W_{\text{mu 1}} \cdot W_{\text{mu 2}} + \sqrt{W_{\text{mu 1}}^2 + (\delta W_{\text{mu 1}})^2} + \sqrt{W_{\text{mu 2}}^2 + (\delta W_{\text{mu 2}})^2}\,, \end{aligned} \tag{13.7}$$

where δW is the uncertainty computed for a particular weight W, and again examining the differences with respect to the final distribution computed using the nominal weights. An uncertainty on the theoretically computed cross-section for background processes in simulated data is obtained by varying W_{xsct} for all events simultaneously. For $t\bar{t}$ and diboson (WW, WZ and ZZ) processes, the variation is 7%. For W+jets (W+$\tau\nu$ and W+$\mu\nu$) and Z $\to \tau\tau$ processes, the variation is 5%. Finally, the systematic associated with the modelling of muon momenta in simulated data is obtained simply by examining the differences between the final distributions in which muon momenta smearing is either applied or absent.

The total systematic uncertainty, on a given bin in a distribution, is taken to be the quadrature sum of all systematic uncertainties considered, along with the Monte Carlo statistical uncertainty (labelled 'MC stat.') due to the bin-by-bin correction factor. Indeed, all sources of systematic uncertainty are assumed to be uncorrelated with respect to one another in this analysis. Uncertainties due to FSR tend to dominate, typically across most of the ϕ^* range. The total statistical uncertainties (for collision data) are also shown in Figs. 13.3 to 13.6, and afford a direct comparison with the total systematic uncertainties. For the on-peak analysis, the statistical and systematic uncertainties are of a similar magnitude. This is also true for the high-mass analysis, while for the low-mass analysis the systematic uncertainties dominate.

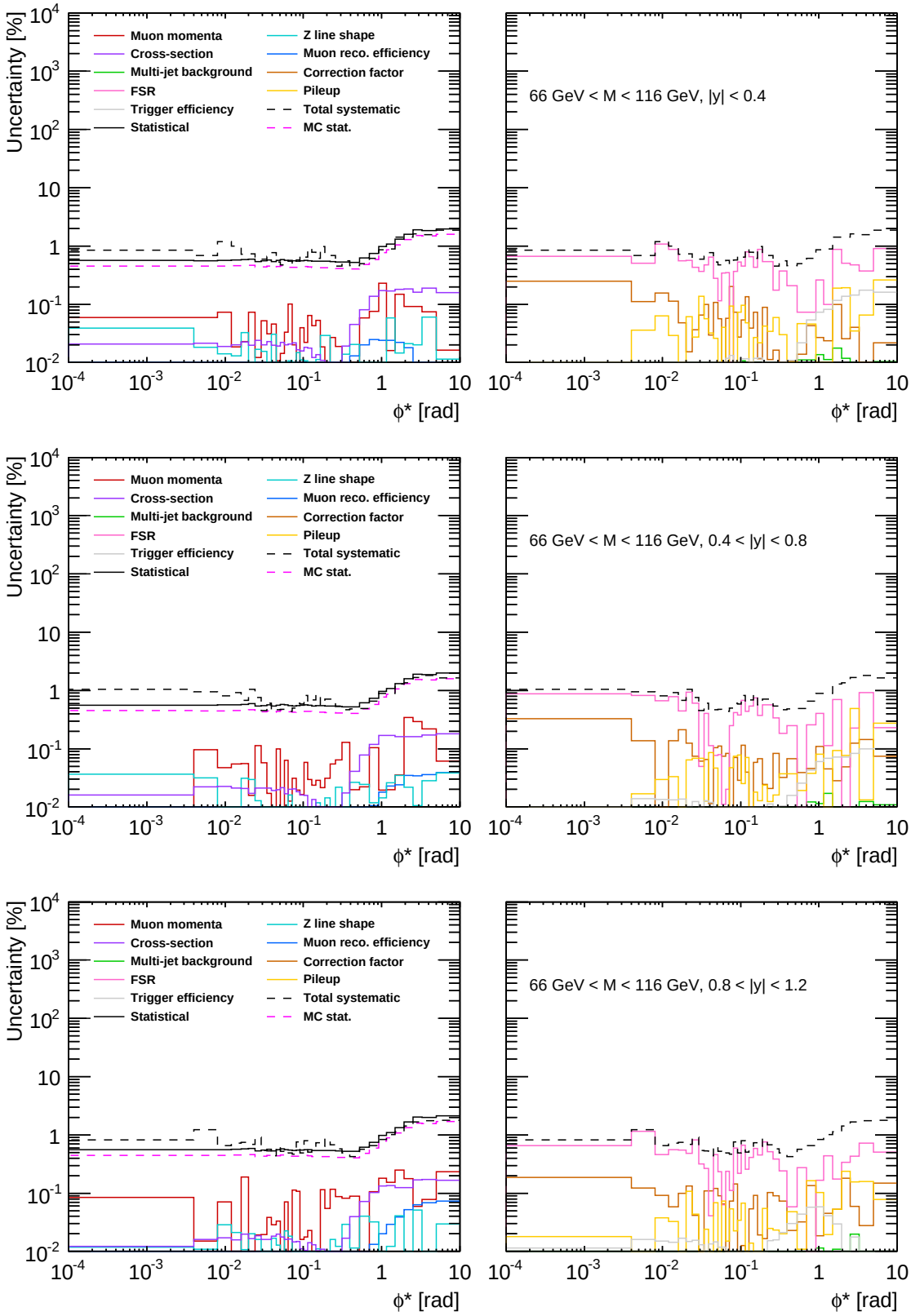

FIGURE 13.3. Systematic uncertainties on the final on-peak ϕ^* distributions (66 GeV $< M <$ 116 GeV)

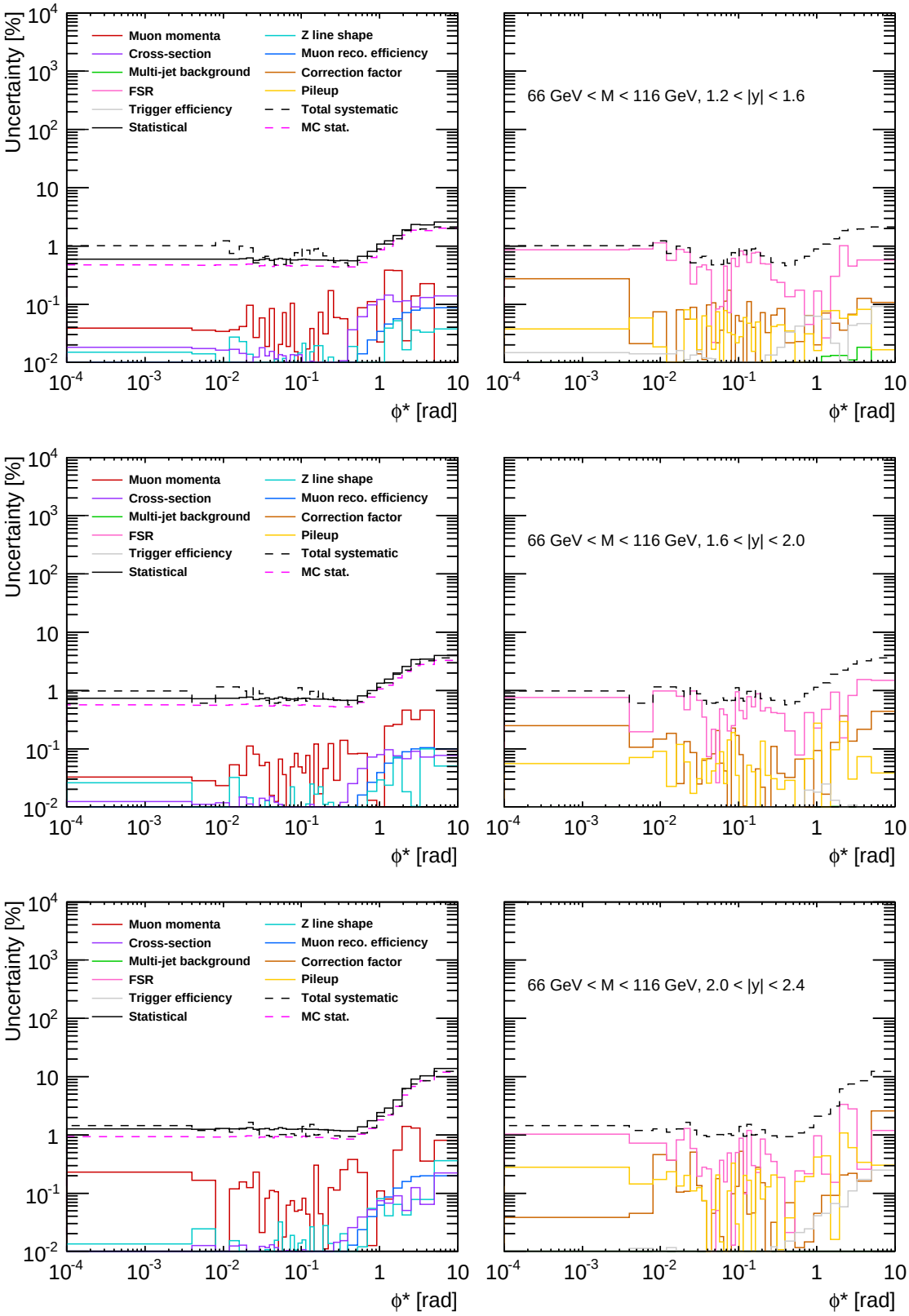

FIGURE 13.4. Systematic uncertainties on the final on-peak ϕ^* distributions (66 GeV $< M <$ 116 GeV)

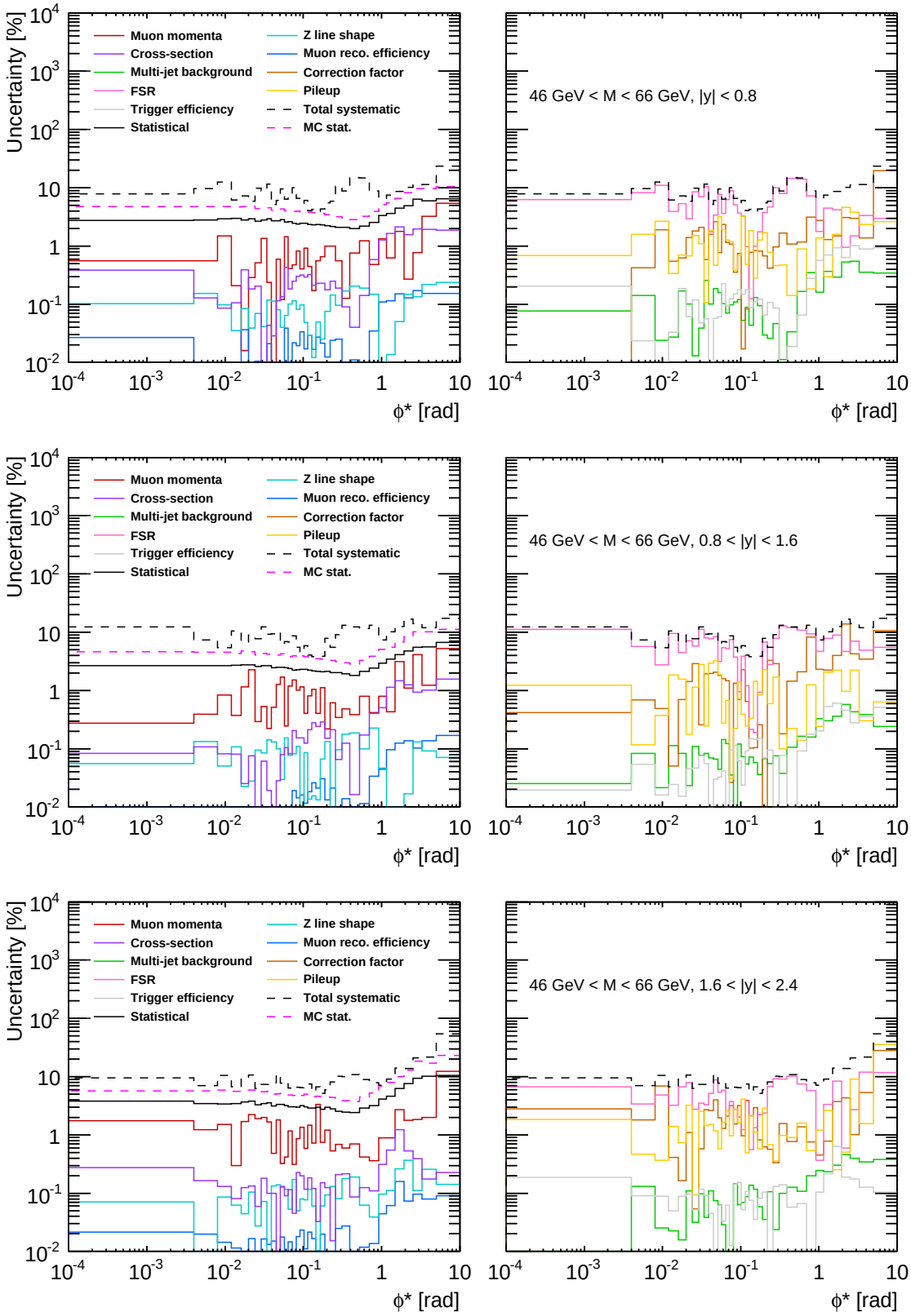

FIGURE 13.5. Systematic uncertainties on the final low-mass ϕ^* distributions (46 GeV $< M <$ 66 GeV)

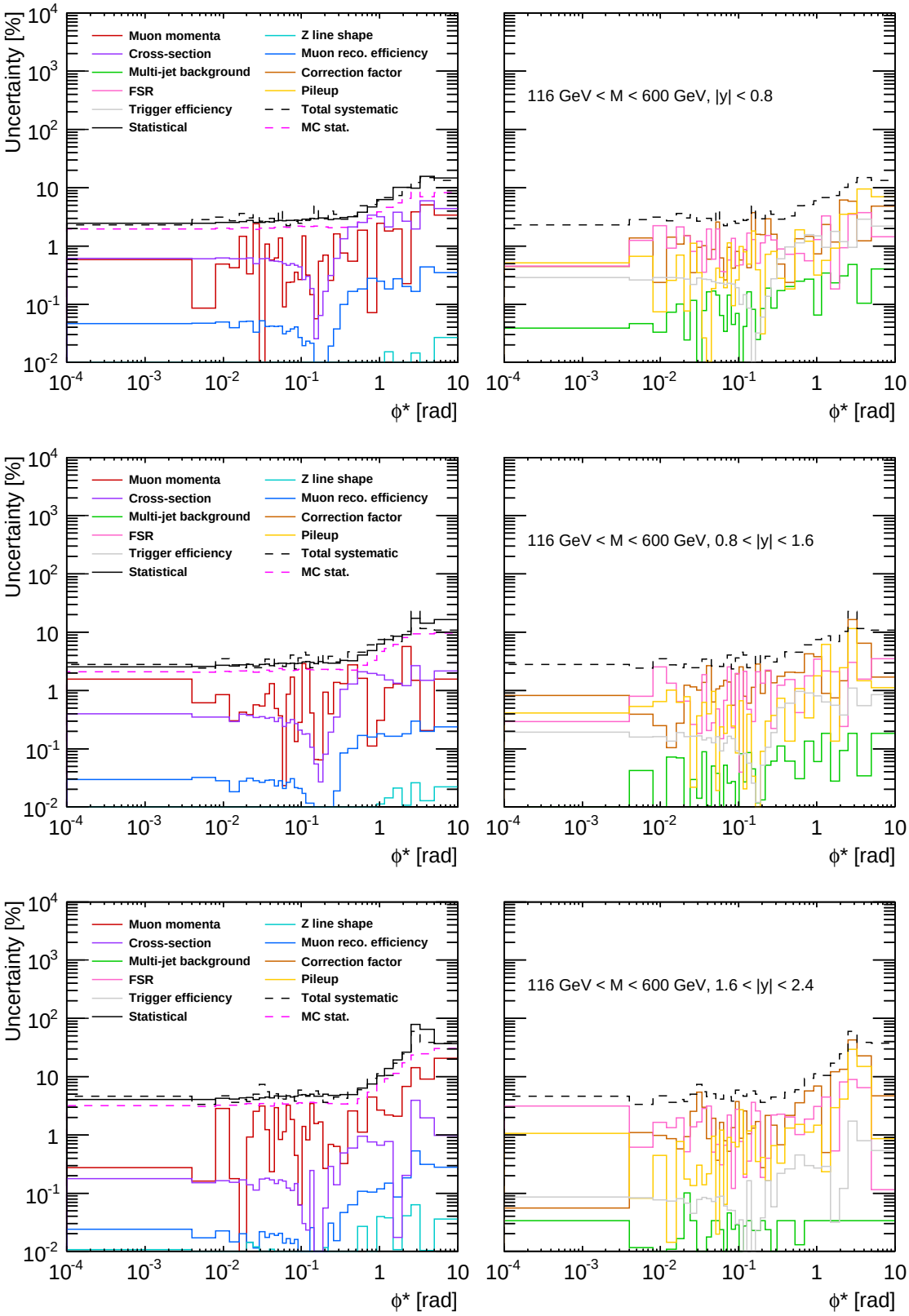

FIGURE 13.6. Systematic uncertainties on the final high-mass ϕ^* distributions (116 GeV $< M <$ 150 GeV)

13.3. Results

The results of this analysis are presented in this section. Figures 13.7 and 13.8 show the normalized ϕ^* distributions determined for this analysis, in the twelve kinematic regions of interest; i.e. the twelve bins of boson invariant mass and rapidity. The normalized distributions presented are of background-subtracted candidate data events, and these distributions have then been corrected for the various detector effects, in order to present a result that is representative of the underlying physical process, defined in terms of bare-level muons. The figures include systematic and statistical uncertainties on each bin, the computation of the former of which is presented in Sec. 13.2. These results are tabulated in Tables 13.1 and 13.2. Figures 13.7 and 13.8 additionally present a comparison to corresponding data simulated using Powheg and Pythia8.

The same collision data are reproduced in Figs. 13.9 to 13.11 for masses in the range 66 GeV $< M <$ 150 GeV, this time in comparison to results of the NNLL+NLO calculation presented in Part 1 of the thesis, evaluated at $\sqrt{s} = 8$ TeV and with the appropriate experimental cuts. The yellow bands represent the perturbative theoretical uncertainties on these results, determined as usual by discretely varying the three perturbative scales μ_{Q}, μ_{R} and μ_{F}—the resummation, renormalization and factorization scales—within the range $M/2$ to $2M$. PDF uncertainties are not included in these uncertainty estimates, since they have previously been shown to be small. The green lines indicate the predictions corresponding to the particular configuration in which all scales are set to the nominal value M.

The NNLL+NLO results presented in this section do not account for final-state radiation (FSR). In principle, any comparisons to data should therefore be made at the Born level, wherein collision data are corrected for this radiation instead. However, given the conservative uncertainty assigned to FSR in this analysis (which is determined from the differences between distributions corrected back to the bare and Born levels in any case) the absence of explicit inclusion of FSR modelling in the NNLL+NLO results is essentially already covered in the comparisons.

The reader will note that a comparison is only made for masses in the range 66 GeV $< M <$ 150 GeV, thereby excluding the low-mass region. Presumed idiosyncrasies have presented themselves in this low-mass region at $\sqrt{s} = 8$ TeV, as compared with our similar Tevatron study at $\sqrt{s} = 1.96$ TeV (Section 5.3), apparently owing to unprecedented low values of $M/\sqrt{\hat{s}}$ being sampled. At the time of writing, an effort continues to understand these newly presented features, which are inherent in the theoretical result itself. Specifically, the cancellation of large logarithms between the fixed-order component and the expansion of the resummed component is postponed to the significantly lower value of $\phi^* \approx 10^{-4}$, as compared with other studies presented in this thesis. To a far lesser degree, this effect is also present in some of the NNLL+NLO results in the range 66 GeV $< M <$ 116 GeV, although the size of this effect is smaller than the quoted theoretical uncertainties. It is important for the reader to bear in mind that, for the fixed-order component, we are using MCFM in a kinematic region beyond that intended, i.e at very low ϕ^*, and there may be inherent features that are not understood in this extreme region.

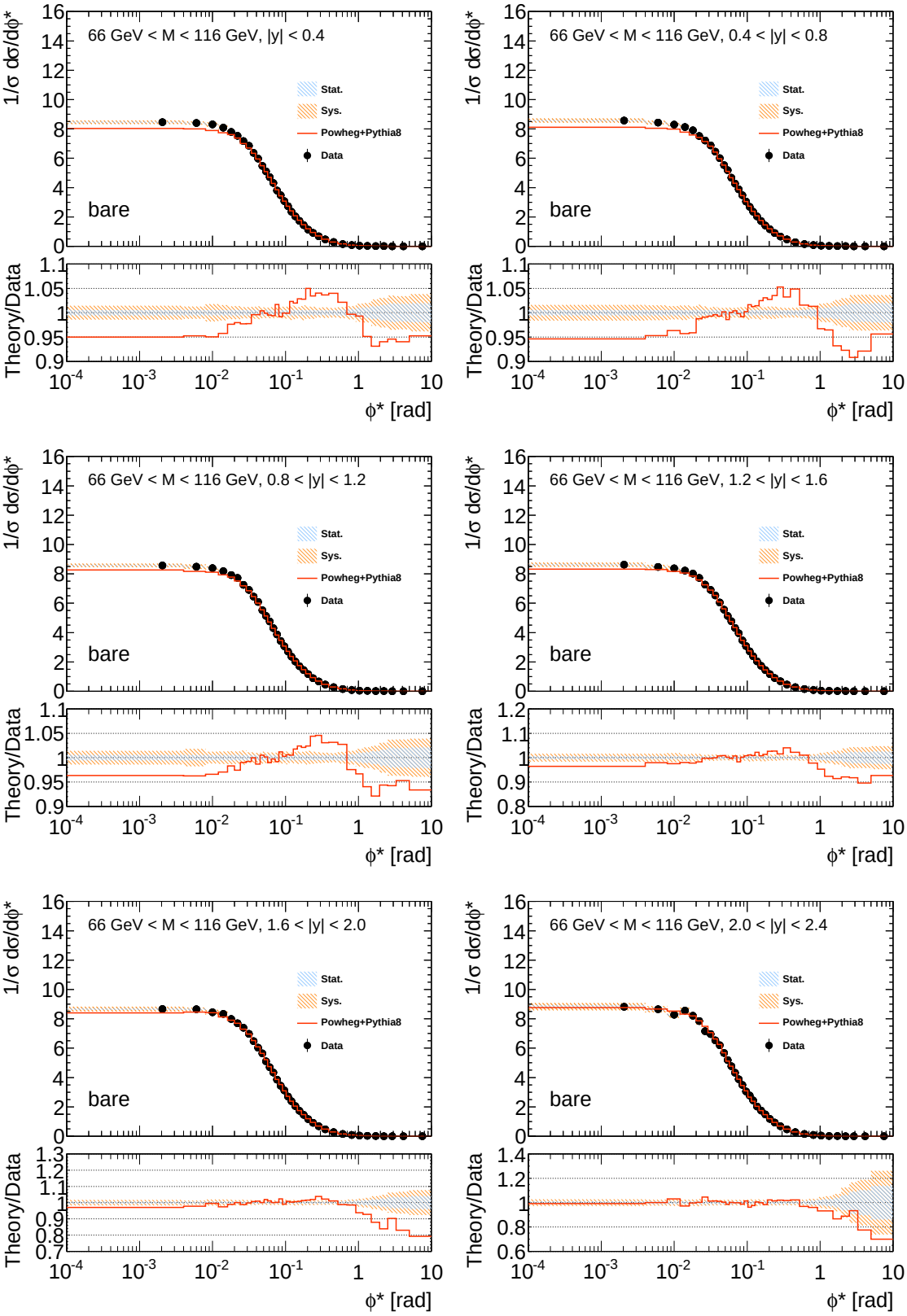

FIGURE 13.7. The results of the ATLAS ϕ^* analysis in the $Z \to \mu\mu$ channel. These distributions are background-subtracted and corrected for detector effects to the *bare-level* distribution, before being individually normalized. The mass region shown is 66 GeV $< M <$ 116 GeV, and each distribution corresponds to one of the six equally-sized rapidity bins across the total range $|y| < 2.4$.

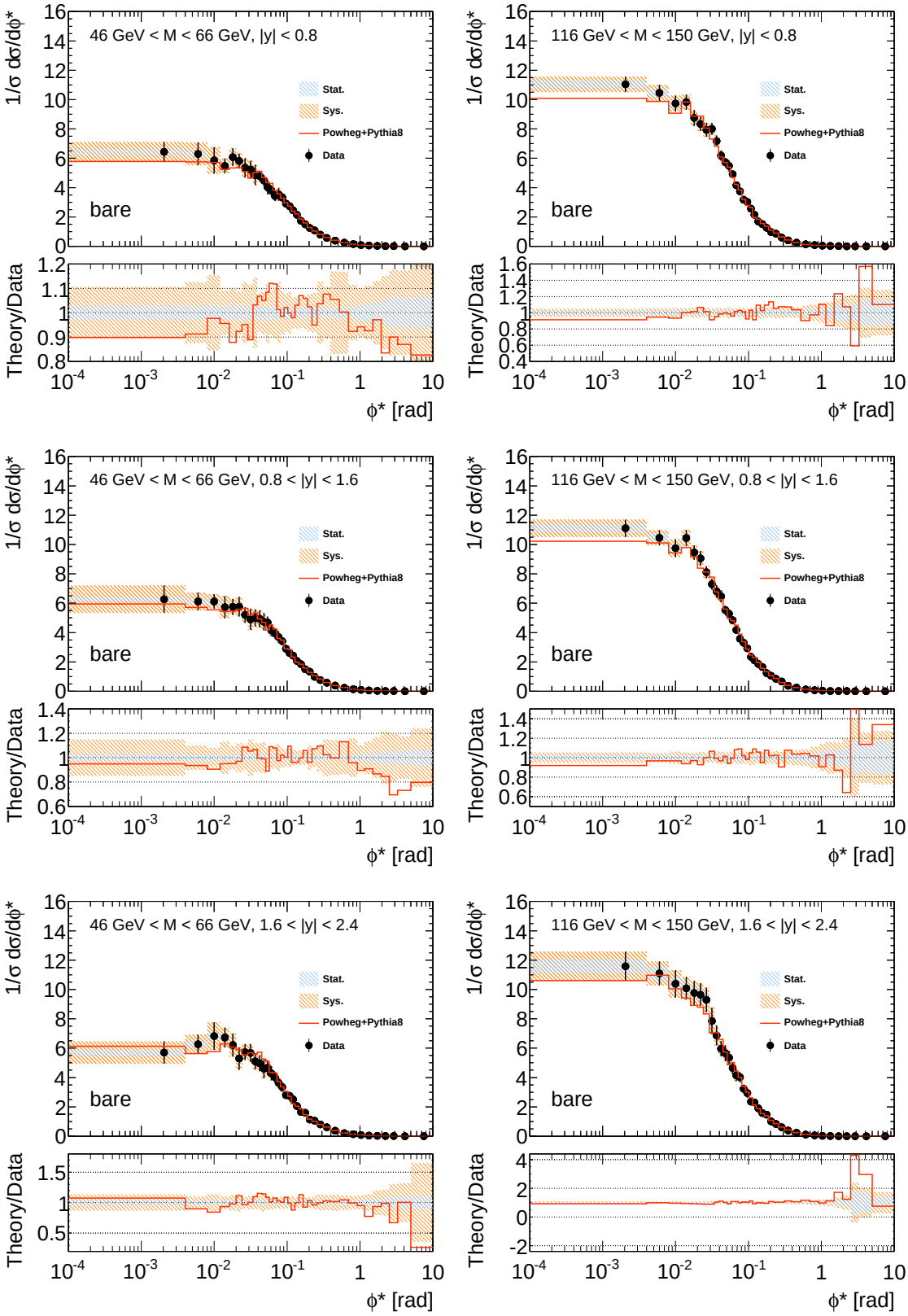

FIGURE 13.8. The results of the ATLAS ϕ^* analysis in the $Z \to \mu\mu$ channel. These distributions are background-subtracted and corrected for detector effects to the *bare-level* distribution, before being individually normalized. The mass regions shown are 46 GeV $< M <$ 66 GeV (left) and 116 GeV $< M <$ 150 GeV (right), and each left-right pair of distributions corresponds to one of the three equally-sized rapidity bins across the total range $|y| < 2.4$.

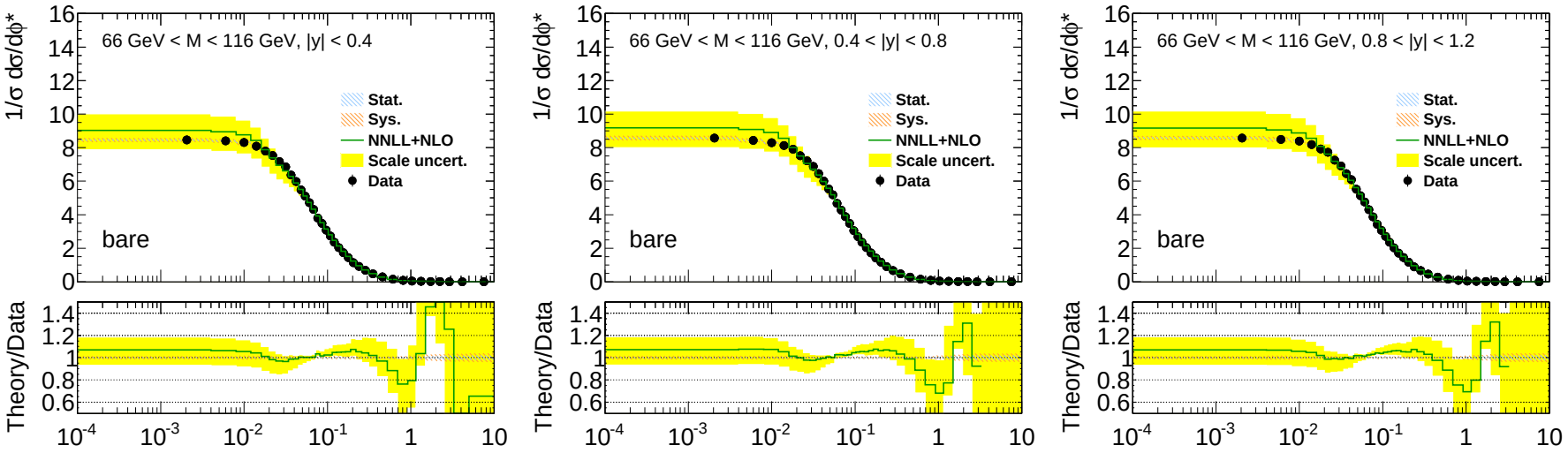

FIGURE 13.9. ATLAS data compared with NNLL+NLO prediction at 8 TeV (66 GeV $< M <$ 116 GeV, $|y| < 1.2$)

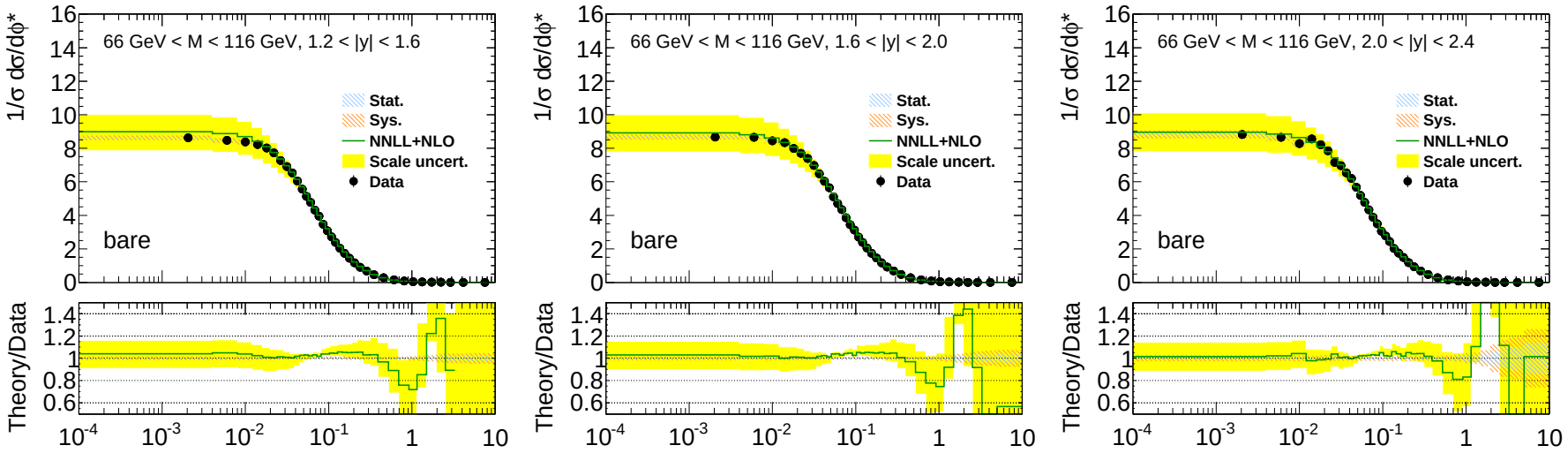

FIGURE 13.10. ATLAS data compared with NNLL+NLO prediction at 8 TeV (66 GeV $< M <$ 116 GeV, $1.2 < |y| < 2.4$)

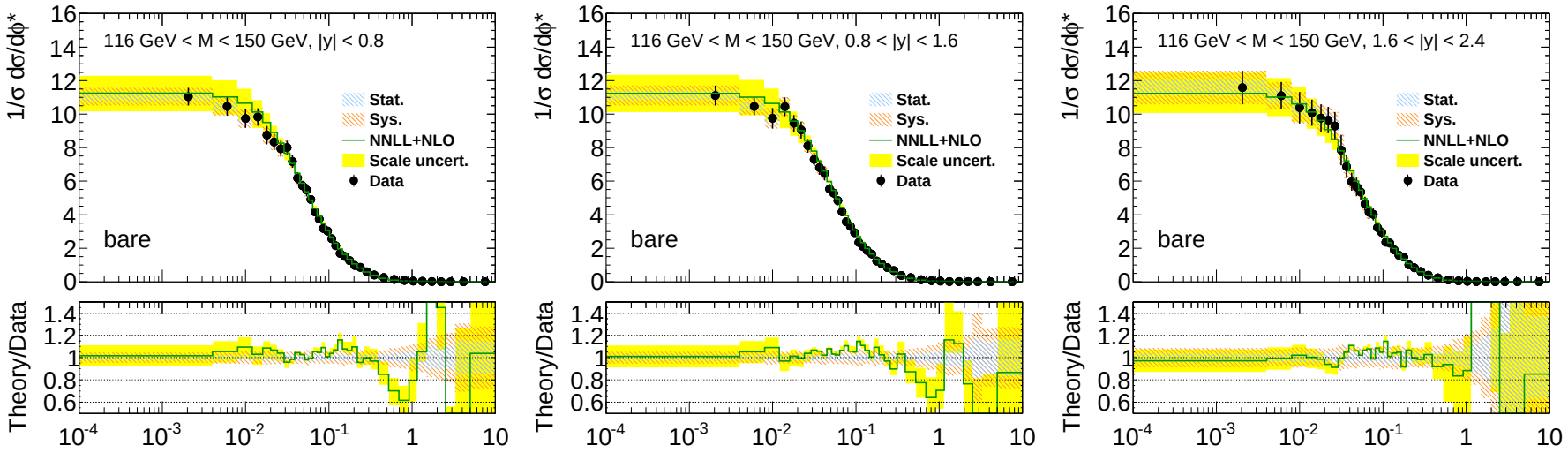

FIGURE 13.11. ATLAS data compared with NNLL+NLO prediction at 8 TeV (116 GeV $< M <$ 150 GeV)

TABLE 13.1. Tabulation of ϕ^* distributions, along with corresponding systematic and statistical uncertainties, for the on-peak analysis: $66\,\text{GeV} < M < 116\,\text{GeV}$. The relative dominance of the uncertainties for each bin are indicated using a red-blue spectrum: red = more dominant, blue = less dominant.

		$\lvert y\rvert < 0.4$			$0.4 < \lvert y\rvert < 0.8$			$0.8 < \lvert y\rvert < 1.2$			$1.2 < \lvert y\rvert < 1.6$			$1.6 < \lvert y\rvert < 2.0$			$2.0 < \lvert y\rvert < 2.4$		
low	high	$(1/\sigma)\,d\sigma/d\phi^*$	$\delta\phi^*_{\text{sys}}$[%]	$\delta\phi^*_{\text{stat}}$[%]	$(1/\sigma)\,d\sigma/d\phi^*$	$\delta\phi^*_{\text{sys}}$[%]	$\delta\phi^*_{\text{stat}}$[%]	$(1/\sigma)\,d\sigma/d\phi^*$	$\delta\phi^*_{\text{sys}}$[%]	$\delta\phi^*_{\text{stat}}$[%]	$(1/\sigma)\,d\sigma/d\phi^*$	$\delta\phi^*_{\text{sys}}$[%]	$\delta\phi^*_{\text{stat}}$[%]	$(1/\sigma)\,d\sigma/d\phi^*$	$\delta\phi^*_{\text{sys}}$[%]	$\delta\phi^*_{\text{stat}}$[%]	$(1/\sigma)\,d\sigma/d\phi^*$	$\delta\phi^*_{\text{sys}}$[%]	$\delta\phi^*_{\text{stat}}$[%]
0.0001	0.004	8.45	0.846	0.569	8.57	1.04	0.561	8.57	0.824	0.56	8.63	1.02	0.593	8.67	0.985	0.733	8.83	1.44	1.28
0.004	0.008	8.4	0.693	0.562	8.44	0.953	0.559	8.48	1.24	0.555	8.47	1.02	0.591	8.65	0.607	0.724	8.66	1.19	1.26
0.008	0.012	8.31	1.19	0.566	8.29	0.809	0.563	8.4	0.655	0.558	8.37	1.24	0.595	8.45	1.15	0.733	8.28	1.27	1.29
0.012	0.016	8.09	0.99	0.574	8.13	0.922	0.569	8.18	0.722	0.565	8.22	0.744	0.6	8.34	1.16	0.74	8.56	1.11	1.27
0.016	0.02	7.8	0.726	0.583	7.9	0.677	0.577	7.92	0.746	0.573	8.02	1	0.608	7.98	0.988	0.753	8.21	1.28	1.3
0.02	0.024	7.53	0.74	0.595	7.51	1.05	0.592	7.72	0.694	0.582	7.72	0.937	0.62	7.7	0.773	0.767	7.85	1.64	1.33
0.024	0.029	7.17	0.609	0.543	7.21	0.757	0.539	7.25	0.927	0.536	7.27	0.512	0.571	7.39	1.12	0.7	7.16	1.21	1.24
0.029	0.034	6.85	0.594	0.557	6.87	0.45	0.553	6.9	0.537	0.549	6.91	0.64	0.585	6.98	0.879	0.72	6.97	0.956	1.26
0.034	0.039	6.37	0.669	0.577	6.45	0.606	0.569	6.44	0.534	0.567	6.54	0.672	0.601	6.47	0.678	0.746	6.53	0.989	1.29
0.039	0.045	5.97	0.776	0.543	6.01	0.447	0.539	6.09	0.44	0.532	6.05	0.609	0.57	6.03	0.548	0.706	6.19	0.935	1.23
0.045	0.051	5.48	0.535	0.567	5.53	0.471	0.56	5.52	0.651	0.558	5.56	0.478	0.593	5.65	0.607	0.731	5.67	0.939	1.28
0.051	0.057	5.1	0.478	0.587	5.18	0.478	0.579	5.13	0.522	0.58	5.14	0.5	0.617	5.11	0.622	0.766	5.19	1.02	1.33
0.057	0.064	4.72	0.562	0.565	4.67	0.453	0.564	4.76	0.462	0.555	4.77	0.484	0.594	4.7	0.751	0.737	4.77	1.01	1.29
0.064	0.072	4.31	0.569	0.552	4.27	0.441	0.551	4.3	0.493	0.547	4.32	0.658	0.582	4.33	0.674	0.721	4.33	0.933	1.25
0.072	0.081	3.8	0.486	0.554	3.88	0.498	0.544	3.86	0.468	0.544	3.95	0.506	0.575	3.86	0.604	0.717	3.88	1.05	1.25
0.081	0.091	3.47	0.572	0.55	3.48	0.608	0.546	3.43	0.758	0.547	3.46	0.769	0.58	3.44	0.674	0.72	3.5	0.982	1.25
0.091	0.102	3.08	0.692	0.558	3.05	0.582	0.556	3.07	0.489	0.551	3.08	0.644	0.587	3.13	1.12	0.721	3.04	1.06	1.27
0.102	0.114	2.73	0.646	0.565	2.69	0.822	0.565	2.7	0.8	0.562	2.71	0.948	0.599	2.7	0.732	0.74	2.77	1.4	1.28
0.114	0.128	2.36	0.924	0.563	2.36	0.622	0.559	2.36	0.51	0.555	2.38	0.853	0.59	2.38	0.653	0.73	2.44	0.958	1.25
0.128	0.145	2.03	0.785	0.55	2.04	0.691	0.543	2.02	0.595	0.543	2.03	0.702	0.579	2.05	0.961	0.711	2.03	1.51	1.24
0.145	0.165	1.73	0.613	0.55	1.72	0.863	0.546	1.71	0.732	0.545	1.73	0.891	0.579	1.74	0.768	0.711	1.75	1.01	1.25
0.165	0.189	1.43	0.979	0.55	1.41	0.57	0.548	1.44	0.631	0.541	1.44	0.914	0.579	1.45	1.03	0.711	1.49	1.01	1.23
0.189	0.219	1.14	0.697	0.551	1.16	0.709	0.541	1.17	0.87	0.538	1.16	0.679	0.575	1.17	0.718	0.707	1.17	1.24	1.23
0.219	0.258	0.912	0.686	0.541	0.903	0.709	0.538	0.891	0.683	0.539	0.903	0.687	0.572	0.92	0.746	0.698	0.926	1.01	1.21
0.258	0.312	0.678	0.451	0.533	0.668	0.54	0.531	0.668	0.579	0.529	0.679	0.523	0.56	0.673	0.679	0.691	0.682	0.96	1.19
0.312	0.391	0.469	0.556	0.531	0.465	0.469	0.527	0.461	0.491	0.526	0.456	0.512	0.564	0.473	0.677	0.683	0.472	0.907	1.18
0.391	0.524	0.285	0.458	0.526	0.28	0.483	0.523	0.28	0.427	0.522	0.279	0.462	0.558	0.282	0.568	0.68	0.282	0.929	1.17
0.524	0.695	0.157	0.502	0.626	0.157	0.492	0.616	0.154	0.565	0.62	0.152	0.565	0.667	0.156	0.642	0.808	0.158	1.09	1.38
0.695	0.918	0.085	0.613	0.747	0.0839	0.657	0.74	0.083	0.652	0.743	0.0812	0.665	0.804	0.0791	0.885	0.996	0.0772	1.33	1.74
0.918	1.15	0.0463	0.866	0.988	0.0468	0.898	0.972	0.0456	0.842	0.98	0.0439	0.888	1.08	0.0419	1.13	1.34	0.0383	2.11	2.41
1.15	1.5	0.026	0.896	1.09	0.0259	0.888	1.08	0.0251	1.01	1.1	0.0235	1.08	1.22	0.0216	1.35	1.56	0.018	2.26	2.92
1.5	1.95	0.0136	1.41	1.3	0.0135	1.28	1.31	0.0132	1.13	1.32	0.0118	1.33	1.51	0.00998	1.91	2	0.00739	3.16	4
1.95	2.52	0.00709	1.42	1.6	0.00702	1.36	1.6	0.00667	1.42	1.66	0.0059	1.85	1.91	0.00494	2.24	2.6	0.00283	6.14	6.24
2.52	3.28	0.00382	1.62	1.89	0.00383	1.68	1.91	0.00353	1.68	2.01	0.00303	1.94	2.35	0.00222	2.83	3.4	0.00115	7.54	9.05
3.28	5	0.00176	1.56	1.84	0.00173	1.81	1.87	0.00159	1.75	2	0.00142	1.96	2.29	0.00101	3.25	3.45	0.000504	8.58	10.3
5	10	0.000524	1.86	1.95	0.000533	1.64	1.99	0.000488	1.79	2.12	0.000389	2.12	2.57	0.000282	3.65	4	0.000121	12.4	13.8

TABLE 13.2. Tabulation of ϕ^* distributions, along with corresponding systematic and statistical uncertainties, for the off-peak analyses: $46\,\text{GeV} < M < 66\,\text{GeV}$ and $116\,\text{GeV} < M < 150\,\text{GeV}$. The relative dominance of the uncertainties for each bin are indicated using a red-blue spectrum: red = more dominant, blue = less dominant.

		$46\,\text{GeV} < M < 66\,\text{GeV}$									$116\,\text{GeV} < M < 150\,\text{GeV}$								
		$\lvert y\rvert < 0.8$			$0.8 < \lvert y\rvert < 1.6$			$1.6 < \lvert y\rvert < 2.4$			$\lvert y\rvert < 0.8$			$0.8 < \lvert y\rvert < 1.6$			$1.6 < \lvert y\rvert < 2.4$		
low	high	$(1/\sigma)\,d\sigma/d\phi^*$	$\delta\phi^*_{\text{sys}}[\%]$	$\delta\phi^*_{\text{stat}}[\%]$	$(1/\sigma)\,d\sigma/d\phi^*$	$\delta\phi^*_{\text{sys}}[\%]$	$\delta\phi^*_{\text{stat}}[\%]$	$(1/\sigma)\,d\sigma/d\phi^*$	$\delta\phi^*_{\text{sys}}[\%]$	$\delta\phi^*_{\text{stat}}[\%]$	$(1/\sigma)\,d\sigma/d\phi^*$	$\delta\phi^*_{\text{sys}}[\%]$	$\delta\phi^*_{\text{stat}}[\%]$	$(1/\sigma)\,d\sigma/d\phi^*$	$\delta\phi^*_{\text{sys}}[\%]$	$\delta\phi^*_{\text{stat}}[\%]$	$(1/\sigma)\,d\sigma/d\phi^*$	$\delta\phi^*_{\text{sys}}[\%]$	$\delta\phi^*_{\text{stat}}[\%]$
0.0001	0.004	6.43	7.91	2.77	6.27	12.3	2.65	5.7	9.57	3.82	11	2.32	2.45	11.1	2.81	2.55	11.6	4.58	4.08
0.004	0.008	6.3	9.67	2.82	6.11	7.34	2.65	6.27	7.02	3.44	10.5	2.85	2.46	10.5	2.42	2.57	11.1	3.33	4.06
0.008	0.012	5.85	12.5	2.95	6.12	5.39	2.68	6.82	10.4	3.4	9.73	3.15	2.54	9.75	3.51	2.7	10.4	4.73	4.25
0.012	0.016	5.48	6.17	2.97	5.72	10.6	2.71	6.72	6.65	3.43	9.83	2.73	2.55	10.4	2.74	2.65	10.1	3.62	4.12
0.016	0.02	6.07	7.27	2.8	5.75	6.82	2.78	6.21	9.11	3.67	8.75	3.61	2.64	9.45	2.45	2.74	9.77	4.03	4.32
0.02	0.024	5.81	5.9	2.93	5.76	8.95	2.78	5.29	10.7	3.83	8.33	3.06	2.74	9.05	2.83	2.8	9.64	3.74	4.41
0.024	0.029	5.35	9.85	2.67	5.2	7.7	2.57	5.73	6.28	3.31	7.94	3.46	2.55	8.11	2.46	2.62	9.29	5.01	4.07
0.029	0.034	5.23	8.75	2.82	4.9	12.3	2.68	5.67	7.35	3.48	8	2.65	2.53	7.3	2.46	2.78	7.86	7.33	4.3
0.034	0.039	4.86	11.5	2.95	5	9.21	2.65	5.1	7.36	3.59	7.17	2.68	2.63	6.81	3.43	2.86	6.87	5.47	4.5
0.039	0.045	4.78	5.14	2.69	4.94	9.38	2.45	4.97	7.8	3.14	6.18	3	2.6	6.46	3.72	2.68	5.97	4.53	4.36
0.045	0.051	4.47	6.05	2.72	4.73	10.2	2.51	4.6	11.1	3.34	5.72	2.51	2.71	5.54	2.61	2.9	5.66	5.06	4.69
0.051	0.057	4.02	9.5	2.84	4.68	6.16	2.51	4.66	7.77	3.34	5.47	4.2	2.77	5.29	2.72	2.95	5.35	3.82	4.59
0.057	0.064	3.82	6.42	2.6	4.14	6.89	2.45	4.29	8.12	3.17	4.91	2.34	2.72	4.83	2.6	2.95	4.65	4.12	4.61
0.064	0.072	3.43	7.68	2.61	3.94	6.77	2.39	4.01	6.38	3.05	4.15	2.23	2.77	4.17	2.89	2.91	4.14	4.82	4.67
0.072	0.081	3.54	9.98	2.47	3.69	8.62	2.23	3.63	6.91	3.04	3.74	2.69	2.76	3.57	4.07	2.95	4.02	4.52	4.43
0.081	0.091	3.33	6.57	2.4	3.41	5.51	2.26	3.34	6.6	3.01	3.17	2.65	2.81	3.31	2.36	2.89	3.23	3.79	4.62
0.091	0.102	2.91	5.44	2.44	2.89	4.46	2.3	2.81	6.45	3.2	3.02	2.48	2.76	2.93	3.63	2.93	2.94	5.91	4.84
0.102	0.114	2.73	6.12	2.44	2.6	5.89	2.33	2.75	6.66	3.04	2.57	2.93	2.91	2.35	4.58	3.11	2.35	4.8	4.93
0.114	0.128	2.45	4.03	2.36	2.42	4.08	2.24	2.5	7.49	2.91	2.15	2.77	2.91	2.1	4.04	3.12	2.3	4.6	4.8
0.128	0.145	2.14	4.24	2.32	2.06	3.8	2.16	2.05	5.54	2.91	1.69	2.83	2.99	1.86	2.46	3.01	1.9	5.27	5.03
0.145	0.165	1.73	3.92	2.33	1.85	3.83	2.12	1.65	6.65	2.97	1.52	4.85	2.94	1.65	2.61	2.9	1.58	5.66	4.63
0.165	0.189	1.5	4.35	2.29	1.5	3.87	2.11	1.59	5.21	2.77	1.26	2.8	3.02	1.24	4.23	3.12	1.47	5.02	4.63
0.189	0.219	1.25	5.51	2.24	1.34	7.91	2.12	1.14	5.97	2.97	0.972	2.96	3.04	1.05	2.97	2.99	1.01	3.61	4.97
0.219	0.258	1.09	5.89	2.16	0.987	5.49	2.04	1.05	8.14	2.81	0.854	4	2.86	0.849	3.89	2.96	0.826	4.16	4.77
0.258	0.312	0.793	10.6	2.1	0.758	9.06	2.04	0.798	10.1	2.56	0.589	3.49	2.96	0.659	3.08	2.94	0.604	4.46	4.74
0.312	0.391	0.571	8.73	2.08	0.575	13.2	1.92	0.603	10	2.47	0.398	2.87	3.11	0.377	3.67	3.28	0.38	4.23	4.95
0.391	0.524	0.388	14.9	1.99	0.391	12.4	1.82	0.376	10.9	2.42	0.25	3.29	3.2	0.245	4.6	3.23	0.236	5.43	4.91
0.524	0.695	0.246	14.6	2.18	0.229	11.6	2.12	0.21	8.94	2.87	0.144	4.91	3.8	0.129	4.55	4.06	0.108	6	6.33
0.695	0.918	0.151	8.83	2.54	0.136	13.2	2.44	0.133	7.85	3.19	0.076	5.2	4.72	0.0685	6.09	4.86	0.0531	9.33	7.46
0.918	1.15	0.0871	6.54	3.35	0.0912	7.35	2.95	0.0799	7.14	4.15	0.0381	5.99	6.24	0.0373	7.47	6.32	0.0299	11.1	10.3
1.15	1.5	0.0528	7.45	3.64	0.05	10.1	3.43	0.0469	9.15	4.64	0.0246	6.82	6.31	0.0182	8.69	7.54	0.0116	10.6	13.8
1.5	1.95	0.0277	8.59	4.49	0.0268	12.6	4.12	0.0233	14	6.25	0.0086	7.37	10.1	0.0121	6.88	8.46	0.0041	17	19.4
1.95	2.52	0.0174	10.2	4.92	0.0148	16.9	4.75	0.011	13.7	7.6	0.0056	10.2	10.2	0.0071	10.4	9.07	0.00228	24.7	26.4
2.52	3.28	0.00755	11.2	6.36	0.00834	14	5.51	0.00701	20.9	9.34	0.00454	12.3	9.87	0.00172	22.8	17.2	0.000397	59.8	79.3
3.28	5	0.00406	11.3	6.02	0.00385	11.9	5.61	0.002	21.6	10.3	0.0011	15.1	15.6	0.00103	11.7	14.3	0.000137	38.5	65.3
5	10	0.00116	23.5	6.51	0.000952	17.4	6.67	0.00194	54	10.5	0.000405	13.4	14.7	0.00029	10.9	16.6	0.000209	37.3	37

13.4. Conclusions and future prospects

I have presented a measurement of the normalized differential ϕ^* distribution, corrected for detector effects back to the bare level, using $20.3\,\mathrm{fb}^{-1}$ of ATLAS collision data at $\sqrt{s} = 8$ TeV. Backgrounds which potentially contaminate the signal event selection have been modelled using both Monte Carlo and data-driven techniques, as appropriate, and have been subtracted from the distributions of candidate events in data in order to account for this contamination. Systematic uncertainties applicable to both the background subtraction and the detector correction have been ascertained for the final distributions.

It is worth recapitulating all these considerations in light of what a precision measurement of the ϕ^* distribution in different kinematic régimes aims to achieve. The ϕ^* observable, as it has been employed in this analysis, aims to quantify the azimuthal decorrelation between the muons in Drell–Yan events in order to probe the infrared régime of QCD, which amounts to studying the nature of the soft and collinear dynamics of gluon radiation for the purposes of testing the perturbative approach and also quantifying any discrepancies which might indicate the need for further non-perturbative treatment. It is therefore vital that our measured ϕ^* distribution of events remains unbiased, for such a precision measurement. Biases induced both by the simulation of physical processes used in this analysis and by the varying detector efficiencies have been taken into account by assigning appropriate systematic uncertainties. It is certainly a testament to the precision of the experimental apparatus and to the quality of simulated data in terms of physics and detector modelling that, across a broad kinematic range for on-peak data, these systematic uncertainties rival the statistical uncertainties.

The measurement has been performed in a variety of boson invariant mass and absolute rapidity ranges, not only in order to provide an opportunity to further elucidate the kinematical dependence of non-perturbative dynamics which was identified in earlier phenomenological work (Chap. 5), but also to test the validity of the resummed approached in the framework of collinear factorization to make theoretical predictions in a variety of kinematic régimes. The off-peak analyses presented in this thesis have posed new challenges not present in the on-peak analysis. Most notable is the migration of events between mass bins when one considers corrections back to the Born level. A measurement of the ϕ^* distribution corrected back to the Born level muons, particularly in the low-mass region, is the subject of continuing work. A possible avenue to be pursued might involve the vetoing of additional photonic radiation in the final state, since it is such radiation which distinguishes the two levels and which is also responsible for the aforementioned migration. In particular, defining a fiducial measurement volume which included such a veto will serve to increase the physical correspondence between the two levels.

Since $t\,\bar{t}$ events form a significant background at high-ϕ^*, particularly in the high-mass region, one might envisage applying a cut on the number of b-tagged jets. These are jets nominally arising on account of the b-quarks produced in top decays, which may be tagged with a fairly high efficiency owing to their peculiar properties. These properties include namely the appreciable distances the b-quarks may travel ($\sim$ 1mm) before hadronization

effects take place, which typically result in a secondary vertices displaced somewhat with respect to the primary vertex of the $t\bar{t}$ interaction.

The final comparisons of the measured ϕ^* distributions in all kinematic regions of interest show agreement with the distribution of events simulated using the Powheg+Pythia8 Monte Carlo event generator at approximately the level of 10% we might have expected from previous studies performed at $\sqrt{s} = 7$ TeV. Theoretical uncertainties are not shown for the distributions predicted by Powheg+Pythia8 however. Comparisons to the results of the calculation presented in Part 1 of this thesis have also been presented for masses in the range 66 GeV $< M <$ 116 GeV. The results of this calculation are in agreement with corresponding collision data, within the both the quoted experimental and theoretical uncertainties, across most of the ϕ^* range, which itself spans five orders of magnitude.

Part 3

Luminosity studies within ATLAS

CHAPTER 14

Introduction

The following and final part of this thesis describes my luminosity work within the ATLAS collaboration. This part is comprised of three single-authored notes [**114, 115, 116**] which I contributed to the collaboration. Chapter 15 describes my work with the *Beam Conditions Monitor* (BCM) where I performed studies on the short- and long-term drifts which were observed in the reported luminosity. I have then followed these studies with an appropriate recalibration of the *visible cross-section* for proton–proton collisions. This chapter also introduces the van der Meer (vdM) method for the absolute luminosity calibration, along with other terminology and principles that are necessary for the subsequent two chapters. The two chapters which follow—Chapters 16 and 17—address the issue of transverse beam correlation and establish its effect on the absolute luminosity calibration as determined using the vdM method. Specifically, Chapter 16 introduces the method I have developed to extract precise beam quantities by studying properties of the *luminous centroid* during a typical vdM scan, and Chapter 17 extends these studies to further vdM scans which occurred during Run I, this time explicitly taking into account the possibility of non-zero crossing angles between the two colliding beams. I present the combined results of these studies as applied to vdM scans in October 2010, May 2011, March 2011, April 2012 and July 2012. The analyses presented herein became an integral part of the 2011 ATLAS luminosity determination at $\sqrt{s} = 7$ TeV [**113**].

CHAPTER 15

Long- and short-term detector stabilities: A study on the drift in the BCM-reported luminosity and the recalibration of the visible cross-section

15.1. Introduction

During 2011, significant luminosity drifts over several periods were reported by the diamond-based *Beam Conditions Monitor* (BCM) in ATLAS. In this chapter the use of the BCM as a luminosity monitor is introduced, along with a review of the van der Meer (vdM) method for the absolute luminosity calibration. The observation of significant drifts in the reported luminosity over several periods is then presented, with an attempt to quantify the nature of these drifts in terms of stabilization and relaxation times of the BCM detector. It is found that, in order to achieve accurate luminosity reporting from the diamond BCM detectors, they should be subjected to a recent radiation dose corresponding to an integrated luminosity of $L \gtrsim 5 \cdot 10^{36}\,\mathrm{cm}^{-2}$. Thus, a vdM calibration scan immediately following a long technical stop is not advised. This chapter concludes with a recalibration of the BCM algorithm known as the 'AND' algorithm. New values for the visible cross-section, $\sigma_{\mathrm{vis}}^{\mathrm{AND}}$, are finally presented for the BCM detectors, updating the preliminary values reported in [**117**].

15.2. The Beam Conditions Monitor (BCM)

The BCM has been used as a event-counting luminosity monitor, with several algorithms defined for what a signal should correspond to. The BCM consists of eight small diamond detectors in total, four on each side, A and C, of the interaction point (IP) at a distance of 184 cm. Each set of four, arranged as a cross, has two detectors on the horizontal, or H, axis and two on the vertical, or V, axis. Collectively these pairs are known as BCMH and BCMV, and are treated independently.

The algorithms, defined separately for BCMH and BCMV, concern the presence of at least one recorded hit on each side, A and C. The (inclusive) OR algorithm is satisfied when at least one hit on either side (or indeed both sides) is recorded. The (coincidence) AND algorithm is satisfied when a coincidental hit is recorded by a detector pair of the same orientation, i.e. at least one hit on each side simultaneously, where $\delta t = 12.5$ ns is the interval defined for simultaneity. Finally, the inclusive single-sided algorithms ORA and ORC are satisfied when at least one hit on that side is recorded.

The BCM detectors, originally designed to issue beam abort requests in the event of a problem and whose electronics have a rise time of 2 ns, are capable of luminosity monitoring on a bunch-by-bunch basis (whose separation is a minimum of 25 ns). The

detectors themselves have limited acceptance at pseudo-rapidities of $|\eta| = 4.2$, where $\eta = -\log[\tan(\theta/2)]$, and θ is the angle made with the z (beam) axis at $z = 0$. This small acceptance means the algorithms at the luminosities encountered during 2011 worked particularly well without the problem of saturation—the situation in which a particular algorithm is satisfied on every bunch crossing.

In order to convert from a rate of a given algorithm being satisfied to a value for the instantaneous luminosity, one applies the principle of *zero counting*. One makes the assumption that the event rate, i.e. the expected fraction of bunch crossings satisfying the algorithm, should be governed by Poisson's law:

$$P(k;\lambda) = \frac{\lambda^k\, e^{-\lambda}}{k!} \tag{15.1}$$

gives the probability of k arrivals to occur, where λ is the expected number. For example, the probability for the OR algorithm to be satisfied in a given interval is

$$\begin{aligned} \frac{N_{\mathrm{OR}}}{N_{\mathrm{BC}}} =: P_{\mathrm{OR}}\left(\mu_{\mathrm{vis}}^{\mathrm{OR}}\right) &= 1 - \overline{P}_{\mathrm{OR}}\left(\mu_{\mathrm{vis}}^{\mathrm{OR}}\right) \\ &= 1 - \exp\left(-\mu_{\mathrm{vis}}^{\mathrm{OR}}\right), \end{aligned} \tag{15.2}$$

where the overline indicates the complement; i.e. $\overline{P}_{\mathrm{OR}}$ is the probability that the OR algorithm is *not* satisfied ($k = 0$). The parameter $\mu_{\mathrm{vis}}^{\mathrm{OR}}$ plays the rôle of λ in Eq. 15.1. The subscript 'vis' indicates this is the visible, or measured, interaction rate (events per bunch crossing) and not the total inelastic rate, simply written μ. Finally, N_{OR} and N_{BC} are the number of times the OR algorithm is satisfied and the number of bunch crossings, respectively, in a given time interval. Inverting this gives

$$\mu_{\mathrm{vis}}^{\mathrm{OR}} = -\log\left(1 - \frac{N_{\mathrm{OR}}}{N_{\mathrm{BC}}}\right). \tag{15.3}$$

A similar argument is applied for the case of the AND algorithm, to obtain

$$\begin{aligned} \frac{N_{\mathrm{AND}}}{N_{\mathrm{BC}}} &=: P_{\mathrm{AND}}\left(\mu_{\mathrm{vis}}^{\mathrm{AND}}\right) \\ &= 1 - 2\exp\left[-\left(1 + \frac{\sigma_{\mathrm{vis}}^{\mathrm{OR}}}{\sigma_{\mathrm{vis}}^{\mathrm{AND}}}\right)\frac{\mu_{\mathrm{vis}}^{\mathrm{AND}}}{2}\right] + \exp\left[-\left(\frac{\sigma_{\mathrm{vis}}^{\mathrm{OR}}}{\sigma_{\mathrm{vis}}^{\mathrm{AND}}}\right)\mu_{\mathrm{vis}}^{\mathrm{AND}}\right], \end{aligned} \tag{15.4}$$

where N_{AND} is the number of times the AND algorithm is satisfied in the same time interval (over which N_{BC} bunch crossings occur) and $\mu_{\mathrm{vis}}^{\mathrm{AND}}$ is the expected visible interaction rate, according to the AND algorithm. Unfortunately, this expression cannot be analytically inverted, so a numerically generated look-up table is used in practice. It should be noted here that the limit in which $\mu_{\mathrm{vis}} \gg 1$, the aforementioned saturation of the algorithms begins to occur.

The notion of a single-sided inclusive algorithm may also be introduced, observing that

$$P_{\mathrm{OR}} + P_{\mathrm{AND}} = P_A + P_C, \tag{15.5}$$

which follows directly from considering two non-mutually-exclusive events in probability theory, defining $P_{\mathrm{OR}} := P(A \cup C)$, $P_{\mathrm{AND}} := P(A \cap C)$, and $P_F := P(F)$. The event A (C) occurs when the algorithm ORA (ORC)—requiring at least one hit on side A (C), irrespective of what happens on side C (A)—is satisfied. The visible interaction rate for

these two algorithms are derived in a similar way, assuming Poisson statistics and applying the zero-counting principle, and one obtains

$$\mu_{\text{vis}}^{\text{ORA}} = -\log(1 - P_A) \qquad \text{and} \qquad A \to C. \tag{15.6}$$

The expression for the AND algorithm introduced two new quantities, known as the *visible cross-sections* for the two algorithms, written $\sigma_{\text{vis}}^{\text{AND}}$ and $\sigma_{\text{vis}}^{\text{OR}}$. To understand the meaning of these, and further elucidate the 'vis' notation, it is instructive to write the luminosity of the LHC (or indeed any storage ring) as

$$\mathcal{L} = \sum_b \mathcal{L}_b = \sum_b \frac{\mu_b\, f_{\text{r}}}{\sigma_{\text{inel}}} = \sum_b \frac{\mu_{b,\text{vis}}\, f_{\text{r}}}{\sigma_{\text{vis}}} \approx \frac{\mu_{\text{vis}}\, n_{\text{b}}\, f_{\text{r}}}{\sigma_{\text{vis}}}, \tag{15.7}$$

where b indexes the colliding bunch pair, $f_{\text{r}} = 11245.5$ Hz is the revolution frequency of the LHC and σ_{inel} is the total inelastic cross-section for a proton–proton collision. Since the independent detectors (along with a choice of algorithm defined on each detector) will operate with < 100 % efficiency, one defines

$$\mu_{\text{vis}} = \epsilon\, \mu \qquad \text{and} \qquad \sigma_{\text{vis}} = \epsilon\, \sigma_{\text{inel}}, \tag{15.8}$$

where ϵ is the efficiency of that *detector and algorithm combination*. The AND and OR algorithms for BCM may have different efficiencies. The visible cross-section ratios in Eq. 15.4 may then be understood as an efficiency conversion, allowing one to use $\mu_{\text{vis}}^{\text{AND}}$ in the expression, the variable for which one would like to solve. In the final equality of Eq. 15.7, the bunch-averaged values $\sigma_{\text{vis}} = \langle \sigma_{b,\text{vis}} \rangle_b$ and $\mu_{\text{vis}} = \langle \mu_{b,\text{vis}} \rangle_b$ have been used, introducing the number of bunches n_{b}, which is an approximation. In order to avoid excessive notation, the b index is dropped where no confusion would arise.

The final ingredient in the process for writing the instantaneous luminosity in terms of an event counting rate is the calibration of the detector and algorithm. This is typically done by performing a van der Meer (vdM) scan, which involves recording the event rates for each algorithm (simultaneously) as the beams are separated by a known distance, then varying this distance, as described in the following section.

15.3. The van der Meer calibration method

The vdM calibration method [**118**], for our purposes, is a way of determining σ_{vis} in the expression for the luminosity, Eq. 15.7, of a given detector and algorithm combination. It is assumed herein that bunches of each beam collide with zero crossing angle, and that the individual proton densities for each bunch may be factorized into a product of one-dimensional densities.[1] At no point, however, is any particular model for the beam profile invoked.

One can therefore write an alternative expression for the luminosity of a given colliding bunch pair b, as

$$\mathcal{L}_b = f_{\text{r}}\, n_1\, n_2 \int dx\, dy\, \hat{\rho}_1(x,y)\, \hat{\rho}_2(x,y), \tag{15.9}$$

[1] One is not concerned with the proton density distribution in z here, since this plays an irrelevant rôle because of the zero-crossing angle assumption.

where n_1 and n_2 are the populations of the colliding bunches of beam 1 and 2, and $\hat{\rho}_j(x,y)$ is a normalized proton density for the colliding bunch in the jth beam, with $j \in \{1,2\}$. One should keep in mind that proton densities here are also strictly for the bunch pair b under consideration, i.e. $\rho \equiv \rho_b$ and similarly in what follows, although not explicitly indicated. The assumption of factorization amounts to writing $\hat{\rho}_j(x,y) = \rho_j^x(x)\,\rho_j^y(y)$, for bunches of each beam. One writes the *beam overlap integral* as the functional

$$\Omega_{x_i}[\rho_1(x_i),\rho_2(x_i)] := \int dx_i\,\rho_1(x_i)\,\rho_2(x_i), \qquad (i \in \{1,2\}) \tag{15.10}$$

where $x_1 = x$ and $x_2 = y$, and $\rho_j(x_i) \equiv \rho_j^{x_i}(x_i)$ is understood. Then,

$$\mathcal{L}_b = f_{\rm r}\,n_1\,n_2\,\Omega_x[\rho_1(x),\rho_2(x)]\,\Omega_y[\rho_1(y),\rho_2(y)]. \tag{15.11}$$

Now consider the luminosity as a function of beam separation, such that

$$\frac{\mathcal{L}_b(h_x,h_y)}{\mathcal{L}_b(0,0)} = \frac{\Omega_x(h_x)\,\Omega_y(h_y)}{\Omega_x(0)\,\Omega_y(0)} =: \frac{R_x(h_x)}{R_x(0)}\,\frac{R_y(h_y)}{R_y(0)}, \tag{15.12}$$

where a separation h_{x_i}, in either direction x or y, is introduced into the overlap integral by writing

$$\Omega_{x_i}(h_{x_i}) := \Omega_{x_i}[\rho_1(x_i),\rho_2(x_i+h_{x_i})] = \int dx_i\,\rho_1(x_i)\,\rho_2(x_i+h_{x_i}). \tag{15.13}$$

The counting rates $R_{x_i}(h_{x_i})$, in arbitrary units, are introduced and are *proportional* to the luminosity.

Dropping the explicit directionality, such that $h_{x_i} \to h$ and $x_i \to x$ elsewhere, consider the integral

$$\begin{aligned}\frac{\int dh\,R(h)}{R(0)} &= \frac{\int dh\,\left[\int dx\,\rho_1(x)\,\rho_2(x+h)\right]}{\int dx\,\rho_1(x)\,\rho_2(x)}\\ &= \frac{\int dx\,\rho_1(x)\int dz\,\rho_2(z)}{\int dx\,\rho_1(x)\,\rho_2(x)}\\ &= \frac{1}{\int dx\,\rho_1(x)\,\rho_2(x)},\end{aligned} \tag{15.14}$$

where the change of variables $x+h \to z$, such that $dh \to dz$, has been made in the second line. Note, this requires the integration limits to be from $-\infty$ to ∞ in principle. The scan is assumed to be performed to a sufficiently high separation that the luminosity becomes negligibly small, and the limits may be effectively taken to infinity. Normalization of the proton densities is used in the final equality, and means we may write

$$\Omega_x[\rho_1(x),\rho_2(x)] = \frac{R(0)}{\int dh\,R(h)}. \tag{15.15}$$

This *is* the vdM calibration method: the separation scan provides the overlap integral in terms of a peak counting rate and the integrated rate over a sufficiently large range of beam separations, i.e. it gives the absolute luminosity when nothing of it, except the independently determined bunch populations and revolution frequency, is known *a priori*. It is precisely the validity of assuming factorization which my studies presented in Chapters 16 and 17 aim to quantify.

The *convolved beam width* is defined by

$$\Sigma_{x_i} = \frac{1}{\sqrt{2\pi}} \frac{\int dh\, R_{x_i}(h_{x_i})}{R(0)}, \tag{15.16}$$

which becomes the standard deviation in the case of Gaussian beams in x, y. The luminosity of the colliding bunch pair is then written

$$\mathcal{L}_b = \frac{f_{\mathrm{r}}\, n_1\, n_2}{2\pi\, \Sigma_x\, \Sigma_y}, \tag{15.17}$$

and, equating this with Eq. 15.7, the visible cross-section of the previous section is calibrated as the bunch-averaged value of

$$\sigma_{b,\mathrm{vis}} = \mu_{b,\mathrm{vis}}^{\mathrm{MAX}} \frac{2\pi\, \Sigma_x\, \Sigma_y}{n_1\, n_2}, \tag{15.18}$$

where 'MAX' indicates the peak value during the scan, which is in principle at zero nominal separation, for symmetric beam profiles.

15.4. A study of drifts in BCM-reported luminosities

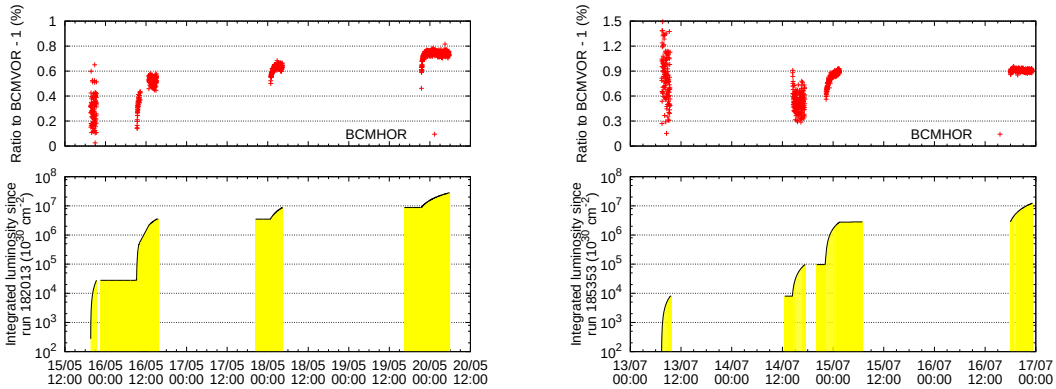

FIGURE 15.1. These plots show the so-called '.7% problem', namely a fairly rapid drift in the ratio of the H and V components of the BCM detector using the OR algorithm (BCMHOR and BCMVOR) since the detectors were calibrated in the May 2011 vdM scan (left). Similar behaviour is seen in the runs immediately following a technical stop (right) during which the detectors received no radiation. The bottom plots show the corresponding integrated luminosity since the most recent technical stop. The left plot shows runs 182013, 182032, 182034, 182161 and 182284, whilst the right plot shows runs 185353, 185518, 185536 and 185644.

15.4.1. BCM and the '.7% problem'. After having reviewed the vdM scan calibration method along with the BCM detector and its algorithms, the so-called '.7% problem' is now introduced. A manifestation of the essential problem may be stated as a relative excursion of approximately 0.7% of the BCM-reported luminosity ratio across two independent detectors (BCMH and BCMV) after a period of several hours following the vdM calibration scan of May 2011. Figure 15.1 shows this drift in the luminosity ratio, over four consecutive runs immediately following the initial scan (left plot) and then four

consecutive runs immediately following a technical stop that occurred in June/July 2011 (right plot).

To put these algorithms into a broader context, Fig. 15.2 shows the recorded $\langle\mu\rangle$ values of all the ATLAS luminosity monitors in ratio to that of BCMH_EventOR—the OR algorithm defined on BCMH (BCMHOR). The BCM detectors are calibrated simultaneously at the point of the vdM scan, which took place on 16 May 2011. It is therefore clear that a rapid *relative* drift between BCMH and BCMV occurred shortly after, as indicated by the blue points in Fig. 15.2, situated at -0.5 % to -0.8 %. This is consistent with Fig. 15.1 which shows the drift occurring in the four runs immediately following the May 2011 vdM scan and then in runs following the June/July technical stop. A further comparison is made with the luminosity reported by the tile calorimeter (Tile) in Fig. 15.3. The equivalent plot, but showing the Event_AND algorithms for BCM instead, is shown in Fig. 15.4.

Clearly the drifts appear to stabilize, so one would like to understand the time scale over which the stabilization takes place. It should also be noted in Fig. 15.2 that several technical stops occurred during the year of running during which the BCM detectors received no radiation: immediately prior to the vdM scan, then later in the year (as mentioned) in June/July, late August/early September and finally late September/early October. It was therefore suggested that the performances of the BCM diamond detectors may be sensitive to the amount of radiation they had recently received, and the technical stops provided 'dry' periods, during which the response would 'relax'.

With this in mind, the integrated luminosities since the previous technical stop are shown underneath the ratios in Fig. 15.1. It is clear that *stabilization* of the ratios appears to occur after an integrated luminosity of $L = \int dt\,\mathcal{L} \gtrsim 5 \cdot 10^{36}\,\mathrm{cm}^{-2}$, which is consistently established from both plots (left and right).

In conclusion, there are apparently two time scales in the problem: a time during which the BCM-reported luminosity stabilizes (τ_{stab}) whilst it is subject to ongoing radiation, and a relaxation time (τ_{relax}) during which there is no received radiation and the BCM-reported luminosity reverts. The limit of the time constant τ_{relax} associated with the effect of any radiation dose wearing off is set by the duration shortest technical stop after which an immediate drift was observed. The maximum value for this time constant is therefore around 21 days, the duration of the technical stop immediately before the vdM scan in May 2011. Since the BCM detectors should be accurately reporting luminosity during all runs with beam in collision, it is clear that the vdM calibration scan is best not performed immediately after a dry period, but rather after the BCM detectors have had a recent radiation dose corresponding to an integrated luminosity of at least $5 \cdot 10^{36}\,\mathrm{cm}^{-2}$. This way the detectors are calibrated in the same state as when they are required to give accurate luminosity monitoring during normal high-luminosity physics running.

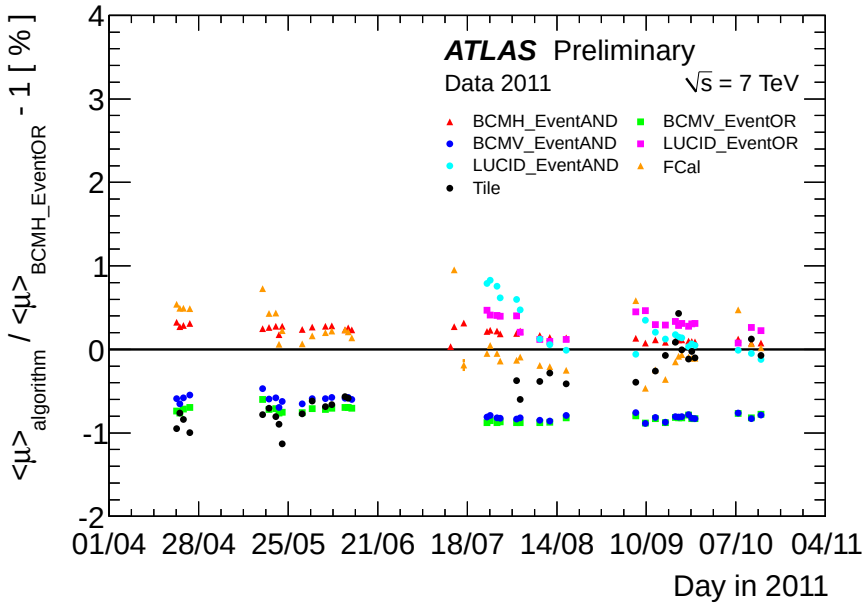

FIGURE 15.2. The average μ values (interactions per bunch crossing) are shown for each detector–algorithm combination, in ratio to BCMH_EventOR, throughout 2011 [**112, 113**]. It is clear there are several drifts in the reported luminosities of different detectors and at different levels, and that all ATLAS luminosity monitors agree on the level $\lesssim \pm 1\%$ overall. In particular our concern in this note is with BCM, whose horizontal (OR) component also appears here in the denominator.

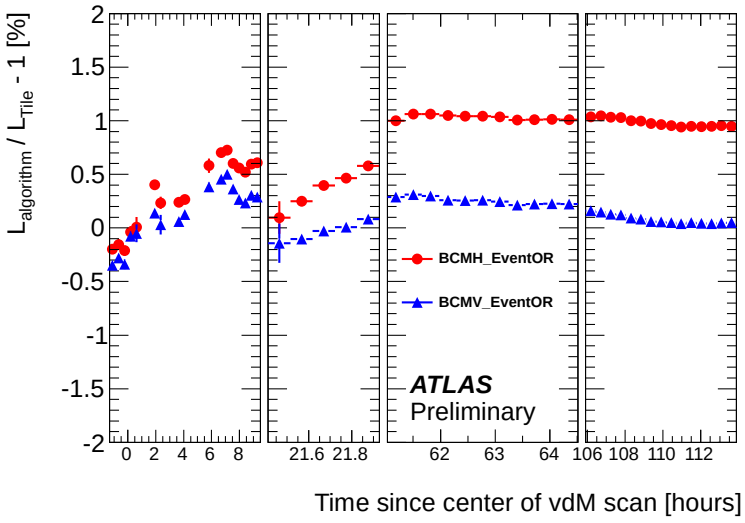

FIGURE 15.3. Here is shown the ratio of the luminosity reported by the BCMH_ and BCMV_EventOR detector-algorithms to that reported by the ATLAS tile calorimeter (Tile), following the May 2011 vdM scan (occurring at time $t \approx 0$ in the plot). A simple afterglow subtraction has been applied to the data. The Tile luminosity was calibrated such that it coincided with that of BCMV_EventOR during the vdM scan session, i.e. at time $t = 0$ in this figure.

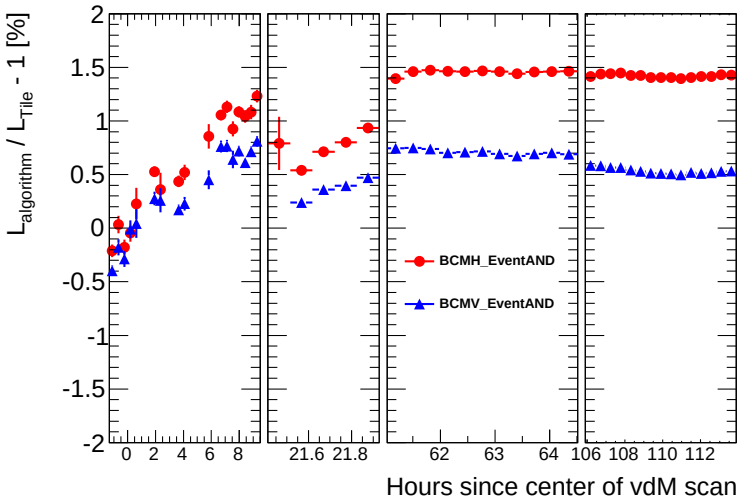

FIGURE 15.4. Here is shown the ratio of the luminosity reported by the BCMH_ and BCMV_EventAND detector-algorithms to that reported by the ATLAS tile calorimeter (Tile), following the May 2011 vdM scan (occurring at time $t \approx 0$ in the plot).

15.5. Recalibration of the visible cross-section for the AND algorithm

15.5.1. Introduction and method. The following study begins by considering the expressions for P_{OR} and P_{AND}, given by Eqs. 15.2 and 15.4, in the limits of large and small $\mu_{\mathrm{vis}} \in \{\mu_{\mathrm{vis}}^{\mathrm{OR}}, \mu_{\mathrm{vis}}^{\mathrm{AND}}\}$. In the limit of small μ_{vis}, one finds

$$P_{\mathrm{AND}} = \mu_{\mathrm{vis}}^{\mathrm{AND}} \qquad \text{and} \qquad P_{\mathrm{OR}} = \mu_{\mathrm{vis}}^{\mathrm{OR}}, \tag{15.19}$$

derived using $e^{-x} = 1 - x$ for $x \ll 1$. In the limit of large μ_{vis}, the expression for P_{OR} is the same as that in Eq. 15.2, but P_{AND} becomes, making a Taylor expansion about $\mu_{\mathrm{vis}}^{\mathrm{AND}} = \infty$,

$$\begin{aligned} P_{\mathrm{AND}} &= 1 + \exp\left(-\frac{\mu_{\mathrm{vis}}^{\mathrm{AND}}\,\sigma_{\mathrm{vis}}^{\mathrm{OR}}}{\sigma_{\mathrm{vis}}^{\mathrm{AND}}}\right) - 2\exp\left(-\frac{\mu_{\mathrm{vis}}^{\mathrm{AND}}\left(\sigma_{\mathrm{vis}}^{\mathrm{AND}} + \sigma_{\mathrm{vis}}^{\mathrm{OR}}\right)}{2\sigma_{\mathrm{vis}}^{\mathrm{AND}}}\right) \\ &= \left[1 - \exp\left(-\frac{\mu_{\mathrm{vis}}^{\mathrm{AND}}\,\sigma_{\mathrm{vis}}^{\mathrm{OR}}}{2\sigma_{\mathrm{vis}}^{\mathrm{AND}}}\right)\right]^2, \end{aligned} \tag{15.20}$$

where the factorization in the second line is permitted when one assumes that $\sigma_{\mathrm{vis}}^{\mathrm{AND}} \ll \sigma_{\mathrm{vis}}^{\mathrm{OR}}$ in the final exponential of the first line, which is valid for BCM. In the two limiting cases, the expressions for *both* P_{OR} *and* P_{AND} can now be analytically inverted, to obtain $\mu_{\mathrm{vis}}^{\mathrm{OR}}$ and $\mu_{\mathrm{vis}}^{\mathrm{AND}}$ in terms of P_{OR} and P_{AND}, respectively. This then allows us to write down an expression for the ratio of the luminosities determined according to each algorithm:

$$\frac{\mathcal{L}^{\mathrm{AND}}}{\mathcal{L}^{\mathrm{OR}}} = \frac{\mu_{\mathrm{vis}}^{\mathrm{AND}}}{\mu_{\mathrm{vis}}^{\mathrm{OR}}}\frac{\sigma_{\mathrm{vis}}^{\mathrm{OR}}}{\sigma_{\mathrm{vis}}^{\mathrm{AND}}} = \begin{cases} \dfrac{2\log\left(1-\sqrt{P_{\mathrm{AND}}}\right)}{\log\left(1-P_{\mathrm{OR}}\right)} & \text{for high } \mu_{\mathrm{vis}}, \text{ and} \\ \dfrac{P_{\mathrm{AND}}}{P_{\mathrm{OR}}}\dfrac{\sigma_{\mathrm{vis}}^{\mathrm{OR}}}{\sigma_{\mathrm{vis}}^{\mathrm{AND}}} & \text{for low } \mu_{\mathrm{vis}}. \end{cases} \tag{15.21}$$

It is clear from this expression that, in the limit of high μ_{vis}, the ratio is independent of $\sigma_{\mathrm{vis}}^{\mathrm{AND}}$. Moreover, in the low-$\mu_{\mathrm{vis}}$ domain, the ratio is directly proportional to $\mu_{\mathrm{vis}}^{\mathrm{AND}}$, and therefore any variation in the $\mu_{\mathrm{vis}}^{\mathrm{AND}}$ calibration would be expected to alter this luminosity ratio only for low μ_{vis} values.

The 'AND' algorithm may be satisfied in two distinct ways: by a *genuine* coincidence, whereby the 'A'- and 'C'-side detectors each record one or more hits from particles coming from *pp* interactions in the *same* bunch crossing, or by an *accidental* coincidence, whereby the algorithm is satisfied but not for the previous reason—e.g. particles from different proton–proton collisions in the same bunch crossing, afterglow, etc. The accidental coincidences thus form a background for the 'AND' algorithm. Given the relative unlikelihood of satisfying the 'AND' algorithm compared with that of the 'OR' algorithm, this background is very small in all but the very-low-μ régimes, specifically $\mu \lesssim 1$. Using the previously derived result that the luminosity ratio $(\mathcal{L}^{\mathrm{AND}}/\mathcal{L}^{\mathrm{OR}})$ is independent of $\sigma_{\mathrm{vis}}^{\mathrm{AND}}$ in the high-μ régime, one can recalibrate $\sigma_{\mathrm{vis}}^{\mathrm{AND}}$ to obtain better agreement for this ratio at low μ.

The initial calibration involved applying Eq. 15.4 directly in the vdM calibration method, i.e. fitting the luminosity scan curve[2] determined from this algorithm then extracting $\sigma_{\text{vis}}^{\text{AND}}$, as explained in Sec. 15.3. This recalibration differs from the way in which $\sigma_{\text{vis}}^{\text{AND}}$ was initially calibrated, since it does not rely on the Σ_x and Σ_y values determined during the vdM scan for this algorithm.

The recalibration procedure, for each detector, was to vary the value of $\sigma_{\text{vis}}^{\text{AND}}$ by some small amounts ($\pm 1\%$ and $\pm 2\%$) about its nominal value in order to minimize the discrepancy with the reported luminosity by the OR algorithm. The ratios of luminosities according to each algorithm (minus one) were binned in μ—determined according to the OR algorithm—and the minimization of the discrepancy precisely amounted to minimizing the χ^2 fit of these data with respect to the 'model' $\mathcal{L}^{\text{AND}}/\mathcal{L}^{\text{OR}} - 1 = 0\%$ over the entire μ range. The resulting χ^2 values, as a function of the variation in $\sigma_{\text{vis}}^{\text{AND}}$, are fitted with a parabola, whose minimum point is the precise value of $\sigma_{\text{vis}}^{\text{AND}}$ that minimizes the discrepancy, with errors given by the variation in $\sigma_{\text{vis}}^{\text{AND}}$ required in either direction to increase the χ^2 by one.

The effect of variations of $\sigma_{\text{vis}}^{\text{AND}}$ on the ratio for May 2011 vdM scan data are shown in Fig. 15.5. The corresponding parabolae to determine the best χ^2 fit are shown in Fig. 15.6.

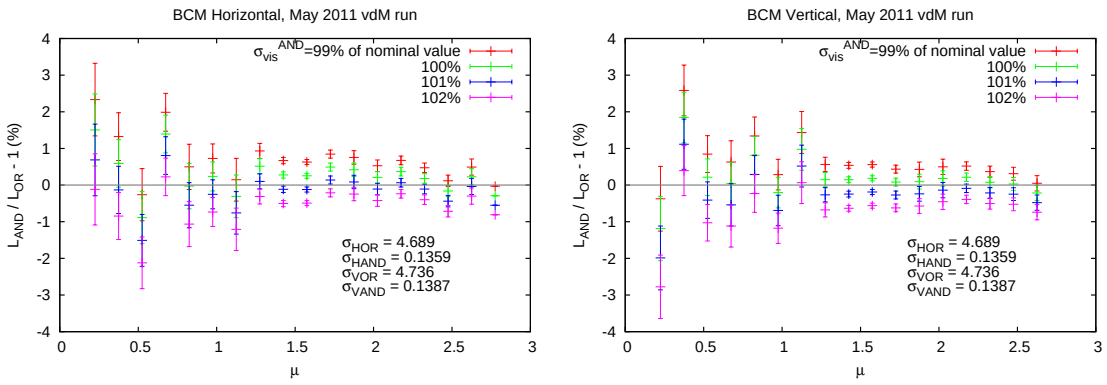

FIGURE 15.5. The effect of variations of $\sigma_{\text{vis}}^{\text{AND}}$ on the ratio for May 2011 vdM scan data. The *nominal* (starting) visible cross-sections are shown on the plot; i.e. the values *before* the optimization took place. Multiplying these nominal values by the determined percentage multipliers yields the new $\sigma_{\text{vis}}^{\text{AND}}$ values.

[2]The luminosity scan curve is obtained during the vdM scan by measuring a quantity proportional to the luminosity as a function of beam separation.

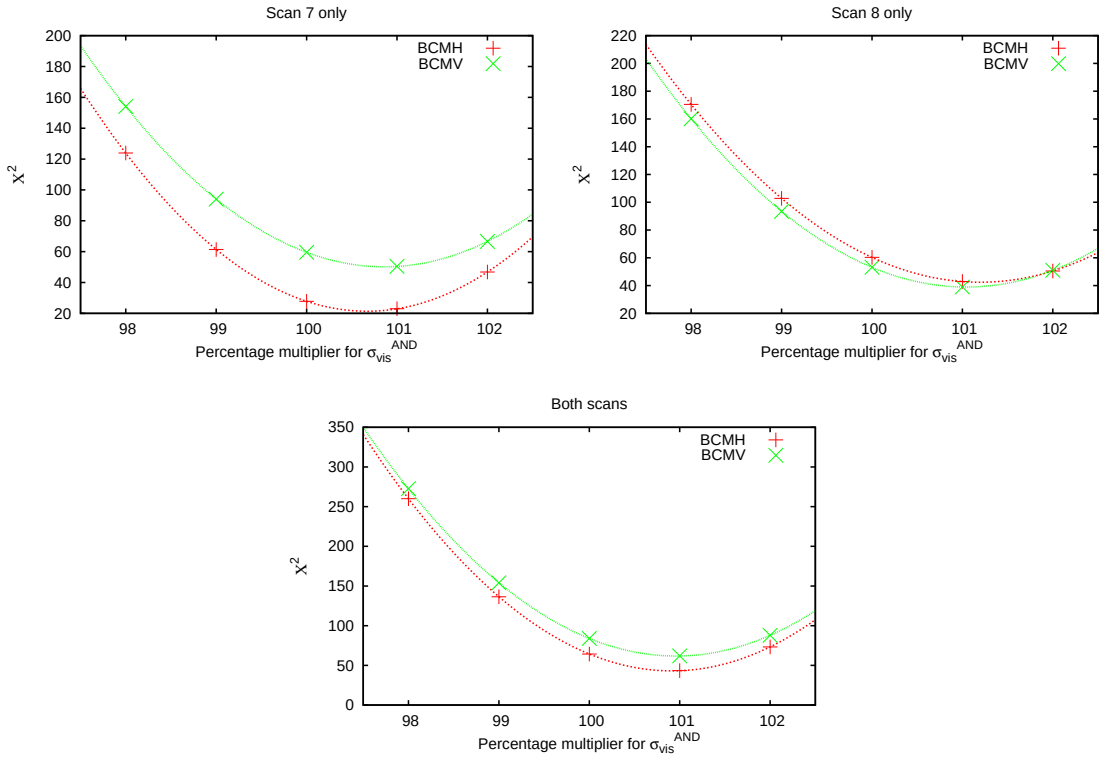

FIGURE 15.6. The corresponding parabolae to determine the best χ^2 for May 2011 data

TABLE 15.1. This table shows the appropriate percentages by which the nominal values of $\sigma_{\text{vis}}^{\text{AND}}$, i.e. those reported in [**117**], should be multiplied in order to minimize the luminosity discrepancy with respect to the OR algorithm, as determined for May 2011 vdM scans VII and VIII, both individually and together.

Scan	BCM	Percentage multiplier for ATLAS-CONF-2011-116 values	$\sigma_{\text{vis}}^{\text{AND}}$ after correction [mb] (from BCMH or BCMV as appropriate)
VII & VIII	H	(100.912 ± 0.198) %	0.1371 ± 0.0003
VII & VIII	V	(100.959 ± 0.204) %	0.1400 ± 0.0003
VII	H	(100.67 ± 0.264) %	0.1368 ± 0.0004
VII	V	(100.86 ± 0.281) %	0.1399 ± 0.0004
VIII	H	(101.195 ± 0.282) %	0.1375 ± 0.0004
VIII	V	(101.041 ± 0.276) %	0.1401 ± 0.0004

15.5.2. Background subtraction. In the lowest μ bins in Fig. 15.5, the background for the EventOR algorithm can be significant enough to have a $> 1\%$ effect on the luminosity, and so appropriate background corrections should be in place. The analysis above has been repeated but this time with background subtraction applied directly to μ values determined from the OR algorithms, given that

$$\mu = \mu_{\text{raw}} + \mu_{\text{bkg}}. \tag{15.22}$$

Once the background subtraction is applied to the luminosities computed according to the OR algorithm in the correct calibration scheme, the variation and fitting of the best value of $\sigma_{\text{vis}}^{\text{AND}}$ is repeated, now using background-subtracted OR data, as shown in Fig. 15.7 for the May 2011 vdM scan, for both BCMH and BCMV. The ratios are this time binned for background-subtracted μ values, namely $\mu_{\text{OR}}^{\text{Corrected}}$. The results, in addition to results where bins in beam separation were used in place of μ, are summarized in Table 15.2. Furthermore, plots may be found in Fig. E.1 as an appendix, which show the effect of these optimizations on the luminosity ratios.

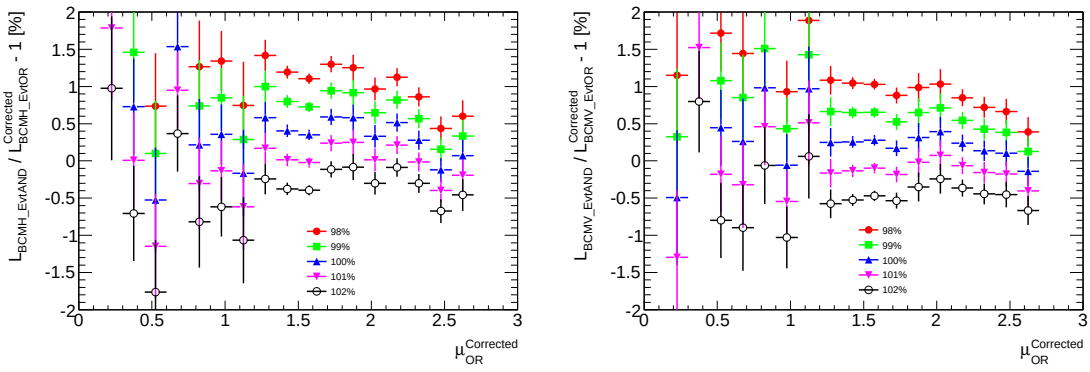

FIGURE 15.7. The effect of variations of $\sigma_{\text{vis}}^{\text{AND}}$ on the ratio for May 2011 vdM scan data. The *nominal* visible cross-sections are shown on the plot. This time background-subtracted μ-values for the OR algorithm are used, and all variations are with respect to the nominal visible-cross sections given in [**117**].

TABLE 15.2. The values of $\sigma_{\text{vis}}^{\text{AND}}$ determined for BCMH and BCMV using background-corrected OR data ($\mu_{\text{OR}}^{\text{Corrected}}$) in the analysis. The values have been determined for all scans both collectively and individually, and binned in either μ or beam separation as indicated. The corresponding plots for values determined using background-corrected μ bins are shown in Fig. E.1, and those corresponding to binning in nominal separation (or equivalently pseudo-lumiblocks) are shown in Fig. E.2.

Scan	$\sigma_{\text{vis}}^{\text{AND}}$ (BCMH) [mb]	$\sigma_{\text{vis}}^{\text{AND}}$ (BCMV) [mb]
VII & VIII (μ)	0.1372 ± 0.0003	0.1398 ± 0.0003
VII (μ)	0.1366 ± 0.0004	0.1394 ± 0.0004
VIII (μ)	0.1377 ± 0.0004	0.1402 ± 0.0004
VIIx (beam sep.)	0.1366 ± 0.0005	0.1401 ± 0.0005
VIIy (beam sep.)	0.1362 ± 0.0005	0.1393 ± 0.0005
VIIIx (beam sep.)	0.1372 ± 0.0005	0.1404 ± 0.0005
VIIIy (beam sep.)	0.1380 ± 0.0005	0.1403 ± 0.0005

15.6. Conclusions

The BCM detectors show a clear dependence on the recent integrated luminosity (radiation dose) they have received. It has been observed in all instances that the associated drifts in efficiency stabilize after some time. The recommendation is therefore that, before a vdM scan which is the crucial point at which all BCM detector calibrations are performed, these diamond detectors should have been recently subjected to the amount of radiation corresponding to $L = 5 \cdot 10^{36}\,\text{cm}^{-2}$ in order that the detectors have stabilized, to prevent drifting of up to $\sim 0.7\%$ after the calibration has already been performed, thus mitigating a fairly severe systematic uncertainty.

CHAPTER 16

Transverse beam coupling part 1: The effect of linear transverse coupling on the luminosity calibration by the van der Meer method

We return now to the question of the validity of the assumed factorization of the x and y components of the bunch densities in the vdM calibration method, which was raised towards the end of Sec. 15.3. In this chapter, an analysis of the effect of beam correlation on the measured luminosity is presented. A single-Gaussian model is used to parameterize the individual beam densities, which includes the possibility of having a non-zero x-y correlation within each beam. Using the approximation that any non-zero beam crossing angle may be ignored, the internal parameters of the model are systematically constrained using a set of analytically derived equations, in a method I have developed. The neglect of crossing angle is reintroduced as a systematic error on those constraints where it is deemed necessary. Finally, the implication of non-zero beam correlation on the measured luminosity is considered explicitly for the results of van der Meer scans performed during October 2010 and May 2011, namely scans IV, V, VII and VIII.

16.1. Introduction

The van der Meer (vdM) scan was first introduced in [**118**], and is summarized in Sec. 15.3. It involves the displacement of two colliding beams by some amount $\vec{h} = (h_x, h_y)$, in a direction transverse to the common[1] axis of their respective motions, in order to determine the *convolved beam widths*, $\Sigma_{x,y}$, which appear in the standard definition[2] of the luminosity:

$$L = \int d^3\vec{x}\, \mathcal{L}(\vec{x}) \propto \frac{1}{2\pi\, \Sigma_x\, \Sigma_y}, \tag{16.1}$$

where x and y are orthogonally chosen directions in the transverse plane. The vdM method also holds for arbitrary beam directions and scan plane, as explained in [**119**]. In addition, the beams may be centred or displaced in one direction whilst a scan takes place in the orthogonal direction, giving rise to in-plane (centred) and out-of-plane (offset) scans respectively.

The analysis presented here focuses on employing a single-Gaussian model for the individual beam densities, which may be used to predict a certain class of linear movements of the *luminous centroid*, to be soon defined formally, during a vdM scan. Confrontation of the predictions of this model with data from vdM scans performed during October 2010

[1] The two beams may be collided with a small crossing angle, as considered shortly.

[2] This definition is derived from the assumption that the individual beams have no internal correlation; i.e. no mixing of the x- and y-dependence

(scans IV and V) and May 2011 (scans VII and VIII)[3] enable relatively tight constraints to be placed on the internal parameters of such a model, of which there are six: the individual x and y beam widths, and an x-y correlation coefficient for each beam.

Under an approximation made here, namely that any beam crossing angles[4] are ignored, it should be noted that luminous centroid movements in the z direction will not arise but are, in any case, understood as a consequence of beam crossing at a non-zero angle. The focus of this analysis will be to extract information about x-y beam correlation using luminous centroid movements in the $z = 0$ plane, and to determine how the neglect of this correlation will impact the final luminosity result. It is instructive to summarize, for the single-Gaussian model, how certain observed phenomena should arise. If we use $\langle \vec{x} \rangle$, with $\vec{x} = (x, y, z)$, to label the position of the luminous centroid, we expect the measured quantities to be affected as summarized in Table 16.1.

TABLE 16.1. Observed phenomena related to the movement of the luminous centroid during vdM scans in the single-Gaussian model.

Observed phenomenon	Cause
$\dfrac{d\langle z \rangle}{dh_{x,y}}$	Beam crossing angle in x-z or y-z plane; α_{xz} and α_{yz}, respectively.
$\dfrac{d\langle x \rangle}{dh_x} \neq \dfrac{d\langle y \rangle}{dh_y} \neq 0$	Different beam sizes in transverse plane.
$\dfrac{d\langle y \rangle}{dh_x} \sim \dfrac{d\langle x \rangle}{dh_y} \neq 0$	x-y correlation within each beam.

[3]Note that out-of-plane (offset) scans have not been included here, for reasons addressed towards the end.
[4]This has been examined numerically [**120**] for all scans, and deviations from this approximation will be dealt with on a case-by-case basis.

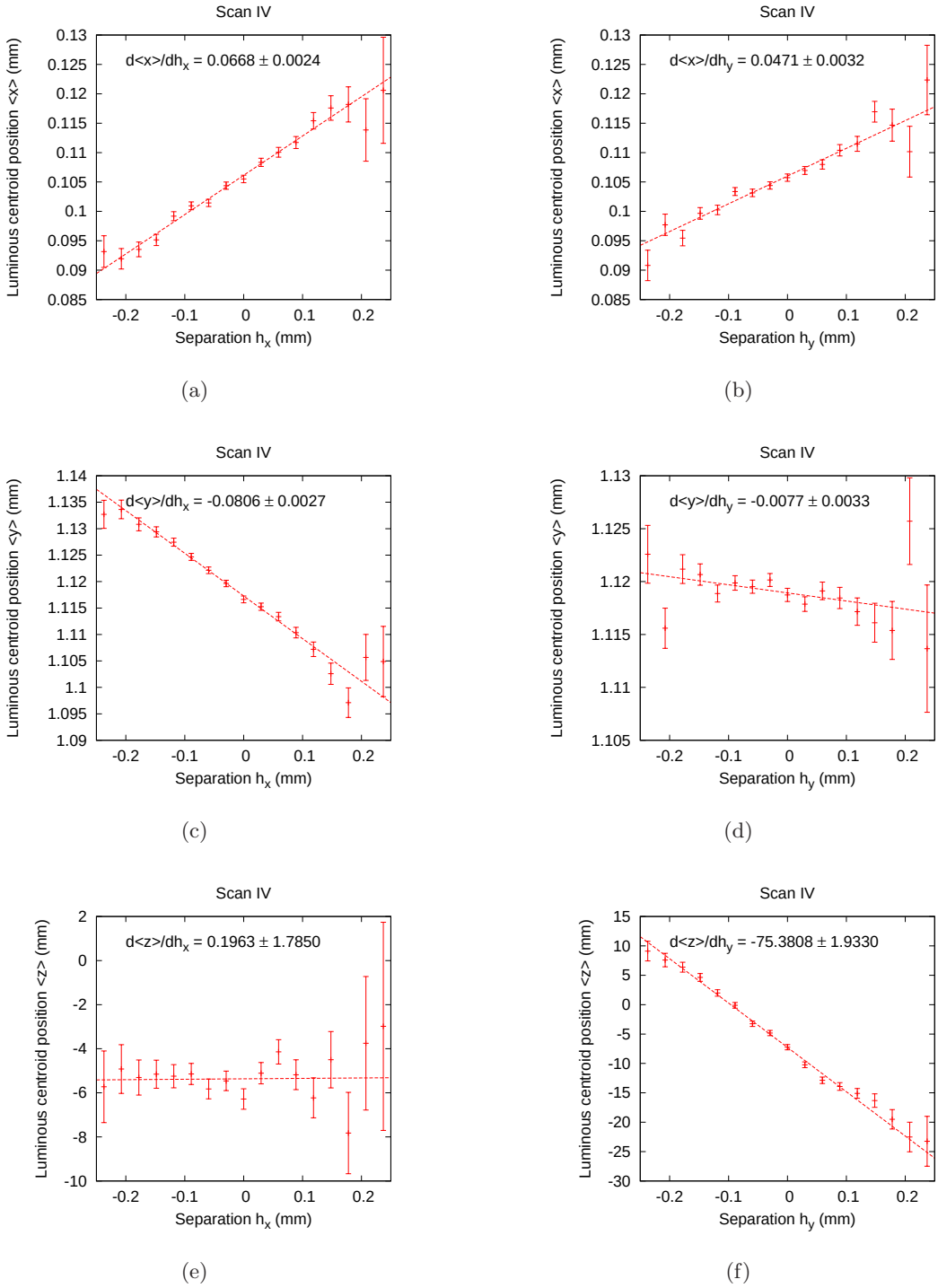

FIGURE 16.1. These plots show the position of the luminous centroid during the first set of x and y scans in October 2010, collectively labelled 'Scan IV'. A linear fit has been made to the central scan data, namely where the separation $|h| \leq 0.25\,\text{mm}$. The linear fit gives the gradient of the movement, and corresponds to the extraction of the observables $d\langle x\rangle/dh_x$, $d\langle y\rangle/dh_x$ and $d\langle z\rangle/dh_x$, as in Table 16.1.

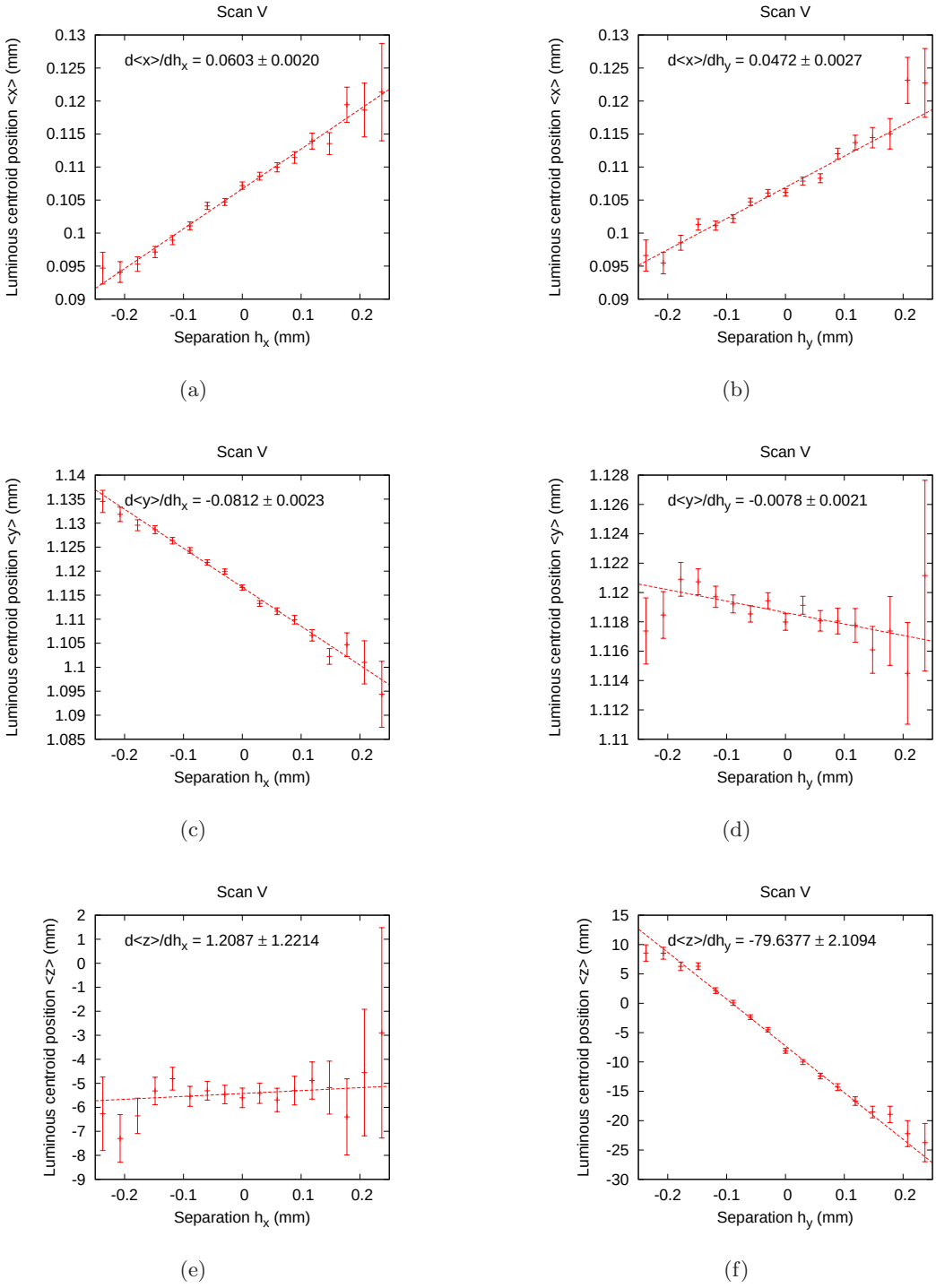

FIGURE 16.2. These plots show the position of the luminous centroid during the second set of x and y scans in October 2010, collectively labelled 'Scan V'. A linear fit has been made to the central scan data, namely where the separation $|h| \leq 0.25\,\text{mm}$. The linear fit gives the gradient of the movement, and corresponds to the extraction of the observables $d\langle x\rangle/dh_x$, $d\langle y\rangle/dh_x$ and $d\langle z\rangle/dh_x$, as in Table 16.1.

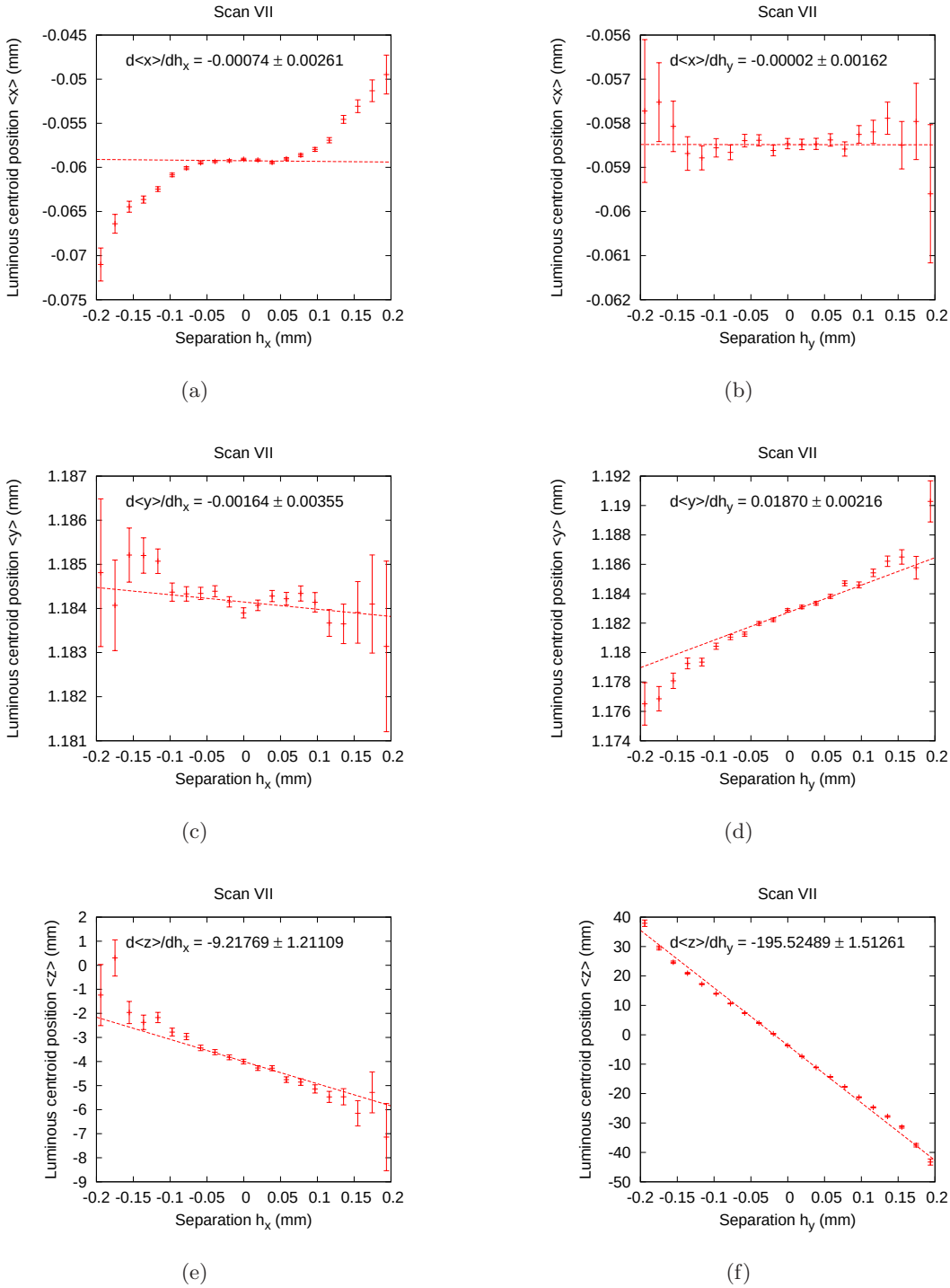

FIGURE 16.3. These plots show the position of the luminous centroid during the first set of x and y scans in May 2011, collectively labelled 'Scan VII'. A linear fit has been made to the central scan data, namely where the separation $|h| \leq 0.05\,\text{mm}$—these data show far greater non-linearity than scans IV and V. The linear fit gives the gradient of the movement, and corresponds to the extraction of the observables $d\langle x\rangle/dh_x$, $d\langle y\rangle/dh_x$ and $d\langle z\rangle/dh_x$, as in Table 16.1.

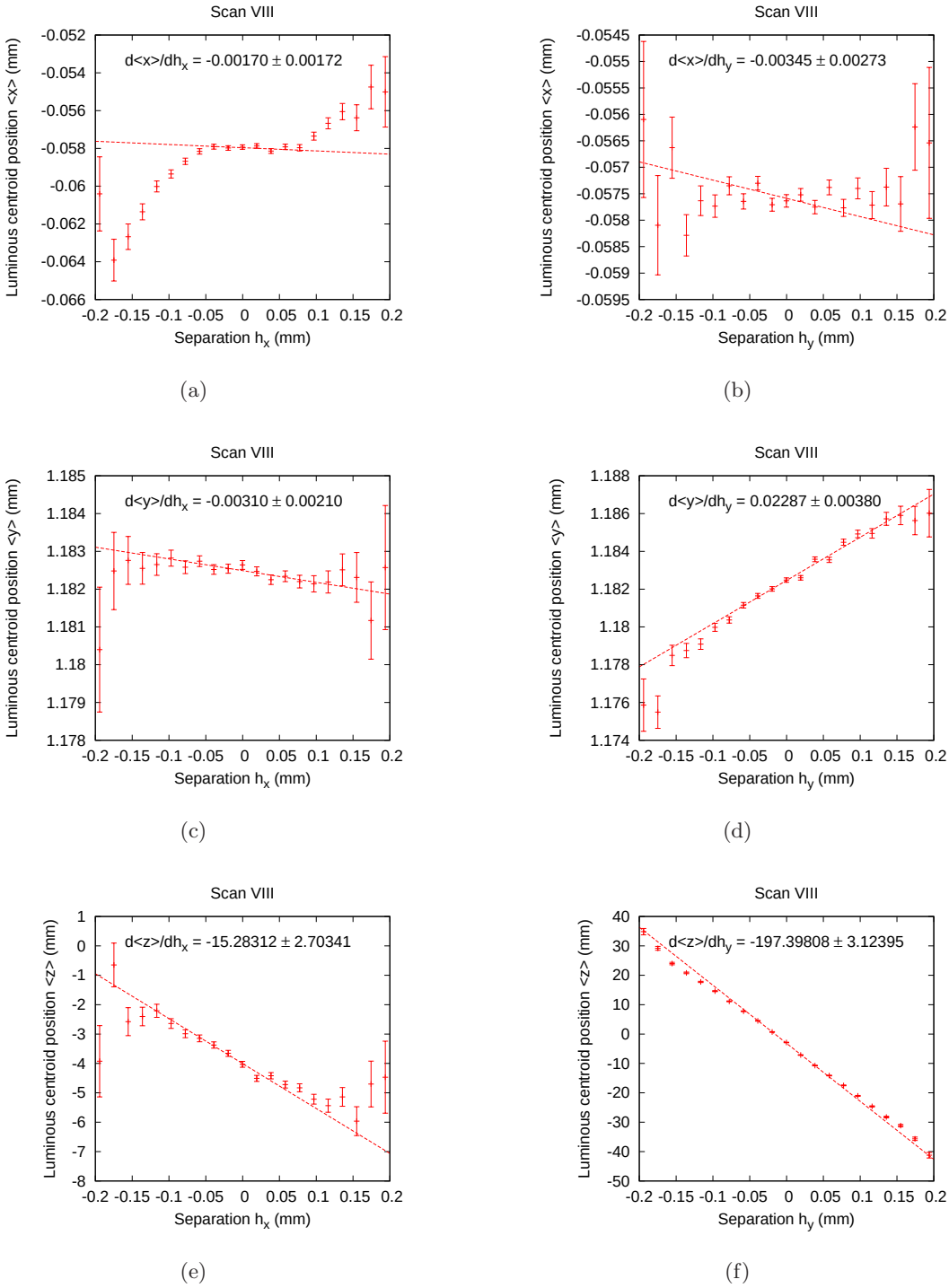

FIGURE 16.4. These plots show the position of the luminous centroid during the second set of x and y scans in May 2011, collectively labelled 'Scan VIII'. A linear fit has been made to the central scan data, namely where the separation $|h| \leq 0.05\,\text{mm}$—these data show far greater non-linearity than scans IV and V. The linear fit gives the gradient of the movement, and corresponds to the extraction of the observables $d\langle x\rangle/dh_x$, $d\langle y\rangle/dh_x$ and $d\langle z\rangle/dh_x$, as in Table 16.1.

16.2. The single-Gaussian model

In the single-Gaussian model, the density of each individual bunch is parameterized as a single Gaussian profile in three dimensions, as in Eq. 16.2,

$$\rho_i(x,y,z,t) = \frac{\exp\left(-\frac{1}{2}\vec{x}\cdot\underline{\sigma}_i^{-1}\cdot\vec{x}\right)}{\sqrt{(2\pi)^3|\underline{\sigma}_i|}}, \tag{16.2}$$

with the so-called *covariance matrix* given by

$$\underline{\sigma}_i = \begin{pmatrix} \sigma_{x,i}^2 & \kappa_i\,\sigma_{x,i}\,\sigma_{y,i} & 0 \\ \kappa_i\,\sigma_{x,i}\,\sigma_{y,i} & \sigma_{y,i}^2 & 0 \\ 0 & 0 & \sigma_{z,i}^2 \end{pmatrix} \text{ with } \vec{x} = \begin{pmatrix} x \\ y \\ z \pm z_0(t) \end{pmatrix} \tag{16.3}$$

and $i \in \{1,2\}$ labelling the beam. (See, for instance, [**121**].) This matrix describes the linear x-y correlation of the proton density within a bunch by introducing the *correlation coefficient* κ_i, in addition to specifying the overall individual beam widths $\sigma_{j,i}$ in each direction $j \in \{x,y\}$. The appropriate sign $\pm$ should be chosen for each beam according to convention.

At this point, an approximation is made in which the two beams collide with a zero crossing angle. A consequence of employing this approximation is the factorization of the x- and y-dependence from the z- and t-dependence in Eq. 16.2, owing to the block-diagonal form of the covariance matrix in Eq. 16.3. Up to factors of the collider revolution frequency (f_r) and the bunch populations ($n_{1,2}$) the luminosity density may be written

$$\begin{aligned} \mathcal{L}(x,y,z) &\propto \int \rho_1(x,y,z,t)\,\rho_2(x,y,z,t)\,dt \\ &= \rho_1(x,y)\,\rho_2(x,y)\int \rho_1(z,t)\,\rho_2(z,t)\,dt\,, \end{aligned} \tag{16.4}$$

where the factorization permitted by the zero-crossing-angle approximation is made explicit in the second line. The convolution integral may be evaluated in the $z = 0$ plane, reducing the problem to two dimensions. The luminous centroid, $\langle\vec{x}\rangle$, is then defined to be the vector $\vec{x}_\mathrm{max}$, such that the quantity $\mathcal{L}(\vec{x}_\mathrm{max})$ is maximized:

$$\langle\vec{x}\rangle := \vec{x} \quad \text{such that} \quad \mathcal{L}(\vec{x}) = \max(\mathcal{L}). \tag{16.5}$$

This statement can become ill-defined for more sophisticated parameterizations of the bunch densities that go beyond the single-Gaussian model (e.g. a double-Gaussian model), but here it is given by the simple condition

$$\left.\frac{d\mathcal{L}(\vec{x})}{d\vec{x}}\right|_{\vec{x}=\langle\vec{x}\rangle} := 0, \tag{16.6}$$

which holds for all three components of $\vec{x}$.

The remainder of this analysis will be concerned with the two-dimensional luminosity density

$$\mathcal{L}(x,y;h_x,h_y) = \rho_1(x-\overline{h}_x/2, y-\overline{h}_y/2)\,\rho_2(x+\overline{h}_x/2, y+\overline{h}_y/2), \tag{16.7}$$

where the possibility of a beam separation $\overline{h}_{x,y}$ has been explicitly introduced in the x- and y-directions respectively, which is symmetric about the origin. The bar is used to denote the beam separation defined with respect to the ATLAS co-ordinate system. Furthermore,

in the LHC coordinate system, the separation is defined to be the position of beam 2 minus that of beam 1. The separations in the LHC co-ordinate system (used in the remainder of this analysis) are given by

$$h_x = -\overline{h}_x \text{ and } h_y = \overline{h}_y \,. \tag{16.8}$$

It should be well-noted here that the model itself, along with all predicted and measured quantities, are defined with respect to the ATLAS coordinate system, where only the beam separations are given in the LHC coordinate system.

16.3. Method

The principal aim of the method I have developed here is to exploit the measurable movements of the luminous centroid during vdM scans in order to indirectly infer the properties of the *individual* beams as precisely as possible. Specifically, I appeal to the observable phenomena listed in Table 16.1 in order to attempt to extract the individual beam parameters under the assumption of the single-Gaussian model for the bunches within the two beams. The emphasis is on precisely quantifying the level of x-y correlation, in order to establish an appropriate systematic uncertainty for the absolute luminosity calibration by the vdM method, which assumes *factorization*.

It can be shown that the single-Gaussian model has the property that it predicts only *linear* movements of the luminous centroid with respect to scan separation. That is, one can write

$$\langle \vec{x} \rangle = h_x \, \frac{d\langle \vec{x} \rangle}{dh_x} + h_y \, \frac{d\langle \vec{x} \rangle}{dh_y}, \tag{16.9}$$

which is an *exact* expression for this model, and holds for both cases of an in-plane and an out-of-plane scan. It should be borne in mind that the single-Gaussian model is one of a limited set of models that actually possesses an analytical solution.

Adopting an analytical approach, my analysis of linear transverse correlation now follows by writing $d\langle \vec{x} \rangle / dh_j$, where $j \in \{x, y\}$, as a formal power series in $\kappa_{1,2}$, since it is assumed that this correlation coefficient should be small[5]. It is physically justified that any correlation coefficient as defined in Eq. 16.3 should indeed be small, i.e. $\kappa_{1,2} \ll 1$, since any larger coefficients would give rise to such highly deformed beams they are beyond reasonable consideration for LHC optics. One can therefore derive a set of four equations which govern the movement of the luminous centroid in the $z = 0$ plane, upon expanding the exact results in powers of the individual beam correlations, $\kappa_{1,2}$, and retaining only up to linear terms:

$$\frac{d\langle x \rangle}{dh_x} = \frac{\sigma_{x,1}^2 - \sigma_{x,2}^2}{2\big(\sigma_{x,1}^2 + \sigma_{x,2}^2\big)} + \ldots \tag{16.10}$$

$$\frac{d\langle y \rangle}{dh_x} = \frac{\sigma_{y,1}\,\sigma_{y,2}\big(\kappa_1\,\sigma_{x,1}\,\sigma_{y,2} - \kappa_2\,\sigma_{x,2}\,\sigma_{y,1}\big)}{\big(\sigma_{x,1}^2 + \sigma_{x,2}^2\big)\big(\sigma_{y,1}^2 + \sigma_{y,2}^2\big)} + \ldots \tag{16.11}$$

$$\frac{d\langle x \rangle}{dh_y} = \frac{\sigma_{x,1}\,\sigma_{x,2}\big(\kappa_2\,\sigma_{x,1}\,\sigma_{y,2} - \kappa_1\,\sigma_{x,2}\,\sigma_{y,1}\big)}{\big(\sigma_{x,1}^2 + \sigma_{x,2}^2\big)\big(\sigma_{y,1}^2 + \sigma_{y,2}^2\big)} + \ldots \tag{16.12}$$

[5]Mathematically speaking, it is defined only for the open interval $(-1, 1)$ anyway, but the smallness is required so that we may formally truncate the expansion after only one term in each expression.

$$\frac{d\langle y\rangle}{dh_y} = \frac{\sigma_{y,2}^2 - \sigma_{y,1}^2}{2\big(\sigma_{y,1}^2 + \sigma_{y,2}^2\big)} + \dots \tag{16.13}$$

Here ... refers to higher-order terms in $\kappa_{1,2}$.

It is instructive at this point to observe the dependence of these analytical expressions for the *gradients* of the (linear) luminous centroid movements on the individual beam parameters. The x (y) movement during an x (y) scan is independent of the beam parameters in the orthogonal, y (x), direction and is, moreover, independent to first order of the correlation coefficients $\kappa_{1,2}$. Therefore it is formally consistent for one to immediately use these gradients of the luminous centroid movements *in the scan direction* (Eqs. 16.10 and 16.13) in the extraction of the individual beam widths. The gradients themselves are determined, within some error, via a linear fit to data.

In the case of a vdM scan in which the residual beam crossing angles are negligible, the convolved beam widths can be shown to be

$$\Sigma_j = \sqrt{\sigma_{j,1}^2 + \sigma_{j,2}^2}\,. \tag{16.14}$$

We may supplement Eqs. 16.10–16.13 with this expression for the convolved beam widths in x and y, along with an expression for the correlation of the convolved *luminous region*,

$$\kappa^{\mathcal{L}} = \frac{\kappa_1\,\sigma_{x,2}\,\sigma_{y,2} + \kappa_2\,\sigma_{x,1}\,\sigma_{y,1}}{\Sigma_x\,\Sigma_y}, \tag{16.15}$$

which is also a measured quantity. This way one has enough equations to solve for the six 'unknowns': σ_{x1}, σ_{x2}, σ_{y1}, σ_{y2}, κ_1 and κ_2. A redundant second handle on the individual beam widths is provided by the width of the *luminous region*, which is related by

$$\big(\sigma_j^{\mathrm{L}}\big)^{-2} = \sigma_{j,1}^{-2} + \sigma_{j,2}^{-2}\,, \tag{16.16}$$

where again $j \in \{x, y\}$.

The inclusion of individual x-y beam correlation affects the individual beam widths, the *convolved* beam widths ($\Sigma_{x,y}$) and the width of the *luminous region* ($\sigma_{x,y}^{\mathrm{L}}$) only beyond terms linear in either $\kappa_{1,2}$—for proof in the case of $\Sigma_{x,y}$, the reader is referred to Section 16.7. It is therefore again formally consistent to extract the individual beam widths using the gradients of the luminous centroid movements *in the scan direction* (Eqs. 16.10 and 16.13) supplemented with the measured $\Sigma_{x,y}$ and $\sigma_{x,y}^{\mathrm{L}}$, while neglecting beam correlation. The analysis then proceeds by substituting the determined widths back into the expressions for the measured luminous centroid movements *orthogonal* to the scanning direction (i.e. Eqs. 16.11 and 16.12) and the measured correlation of the luminous region (Eq. 16.15) in order that we may then *extract* $\kappa_{1,2}$.

This summarizes the prescription followed in this analysis. Since the standard luminosity formula (Eq. 16.1) neglects beam correlation, this analysis concludes with a determination of how much the constrained beam correlation would impact a luminosity measurement that ignored this effect.

Eq. 16.9 has already demonstrated how the single-Gaussian model is insufficient to describe non-linear phenomena which, in some instances, is seen in the data (see Figs. 16.3(a) and 16.4(a), for examples of this more general feature). It should be noted that

the fits for the gradients are therefore often restricted somewhat to a limited range of beam separation where the data appear more linear.

As a final remark, one should note that the standard formula relating the convolved widths, the widths of the luminous region and the individual beam widths, i.e.

$$\sigma^2_{x,y;1,2} = \frac{\Sigma^2_{x,y}}{2} \pm \sqrt{\frac{\Sigma^4_{x,y}}{4} - \Sigma^2_{x,y}(\sigma^{\mathrm{L}}_{x,y})^2}\,, \tag{16.17}$$

remains valid, since no terms linear in $\kappa_{1,2}$ appear as corrections to this formula. Thus, it is demonstrated how the measured $\sigma^{\mathrm{L}}_{x,y}$ is used as a consistency check on the derived constraints but, as one will observe, these constraints from the luminous region widths are typically much less stringent. The solution of the widths for beams 1 and 2 corresponds to the choice of sign in Eq. 16.17. The ambiguity in this choice will be addressed in Sec. 16.5.

16.4. Fitted slopes and errors

The gradients for the linear fit of the various luminous centroid movements with respect to scan separation (h) are shown in Tables 16.2 and 16.3, below, and in Figs. 16.1 to 16.4.

TABLE 16.2. The fitted $d\langle\{x,y,z\}\rangle/dh_{\{x,y\}}$ values for October 2010 vdM scan data and fit errors.

Scan	Observable	Value	Percentage error
IV	$d\langle x\rangle/dh_x$	$(66.8 \pm 2.4)\cdot 10^{-3}$	4%
IV	$d\langle x\rangle/dh_y$	$(47.1 \pm 3.2)\cdot 10^{-3}$	7%
V	$d\langle x\rangle/dh_x$	$(60.3 \pm 2.0)\cdot 10^{-3}$	3%
V	$d\langle x\rangle/dh_y$	$(47.2 \pm 2.7)\cdot 10^{-3}$	6%
IV	$d\langle y\rangle/dh_x$	$(-80.6 \pm 2.7)\cdot 10^{-3}$	3%
IV	$d\langle y\rangle/dh_y$	$(-7.7 \pm 3.3)\cdot 10^{-3}$	43%
V	$d\langle y\rangle/dh_x$	$(-81.2 \pm 2.3)\cdot 10^{-3}$	3%
V	$d\langle y\rangle/dh_y$	$(-7.8 \pm 2.1)\cdot 10^{-3}$	27%

TABLE 16.3. The fitted $d\langle\{x,y,z\}\rangle/dh_{\{x,y\}}$ values for May 2011 vdM scan data and fit errors.

Scan	Observable	Value	Percentage error
VII	$d\langle x\rangle/dh_x$	$(-0.7 \pm 2.6)\cdot 10^{-3}$	370%
VII	$d\langle x\rangle/dh_y$	$(-2 \pm 162)\cdot 10^{-5}$	8100%
VIII	$d\langle x\rangle/dh_x$	$(-1.7 \pm 1.7)\cdot 10^{-3}$	100%
VIII	$d\langle x\rangle/dh_y$	$(-3.5 \pm 2.7)\cdot 10^{-3}$	77%
VII	$d\langle y\rangle/dh_x$	$(-1.6 \pm 3.6)\cdot 10^{-3}$	220%
VII	$d\langle y\rangle/dh_y$	$(18.7 \pm 2.2)\cdot 10^{-3}$	12%
VIII	$d\langle y\rangle/dh_x$	$(-3.1 \pm 2.1)\cdot 10^{-3}$	68%
VIII	$d\langle y\rangle/dh_y$	$(22.9 \pm 3.8)\cdot 10^{-3}$	17%

16.5. Constraints on individual beam widths and correlation

In this section, the constraints on the six single-Gaussian model parameters implied by the fitted quantities of Tables 16.2 and 16.3 are presented. The measured quantities used to constrain the model are, for Figs. 16.5(a) to 16.6(b), the convolved beam widths, $\Sigma_{x,y}$ (orange), and the movements of the luminous centroid in the direction of the scan, $d\langle\{x,y\}\rangle/dh_{\{x,y\}}$ (blue and red, sometimes overlapping). For the determination of the x widths ($\sigma_{x1,x2}$) the blue and red bands are due to $d\langle x\rangle/dh_x$, and for the determination of the y widths ($\sigma_{y1,y2}$) the blue and red bands are due to $d\langle y\rangle/dh_y$, with blue corresponding to scans IV and VII, and red corresponding to scans V and VIII. The widths of the luminous region (σ^{L}), as measured by the *beamspot fit*, are taken to be $\sigma_x^{\mathrm{L}} = 38.1\,\mu$m and $\sigma_y^{\mathrm{L}} = 37.8\,\mu$m for scans IV and V, and $\sigma_x^{\mathrm{L}} = 25\,\mu$m and $\sigma_y^{\mathrm{L}} = 27\,\mu$m for scans VII and VIII.

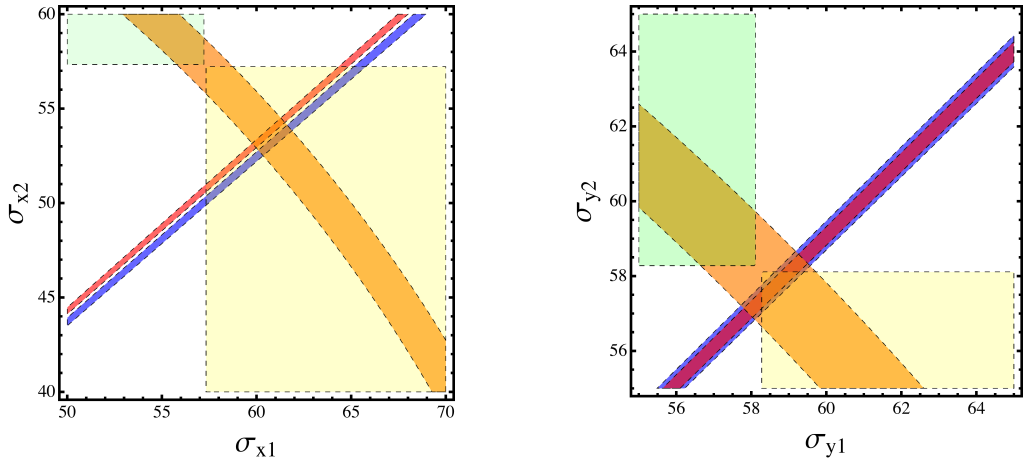

(a) Constraints on the individual x beam widths.

(b) Constraints on the individual y beam widths.

FIGURE 16.5. Constraints from October 2010 scans. Blue indicates scan IV and red indicates scan V. Orange is the constraint imposed by $\Sigma_{x,y}$, and yellow & green are the constraints imposed by $\sigma_{x,y}^{\mathrm{L}}$, of which only one must be satisfied, as explained in the text.

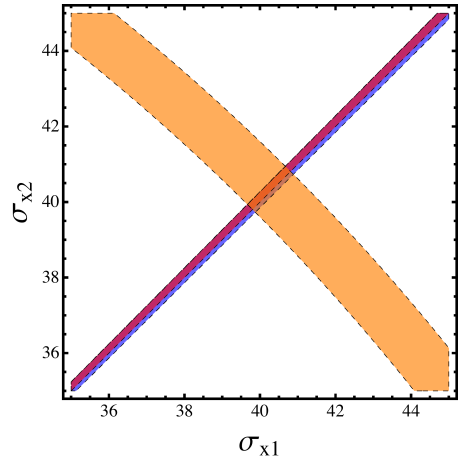

(a) Constraints on the individual x beam widths.

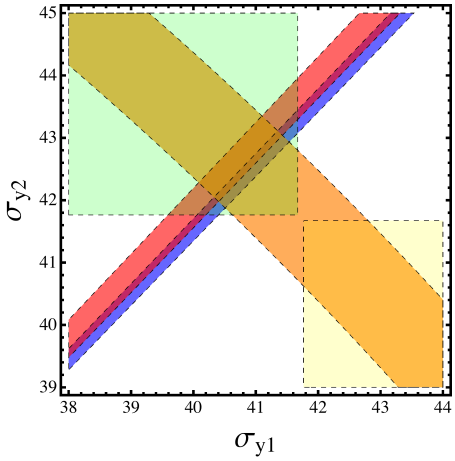

(b) Constraints on the individual y beam widths.

FIGURE 16.6. Constraints from May 2011 scans. Blue indicates scan VII and red indicates scan VIII. Orange is the constraint imposed by $\Sigma_{x,y}$, and yellow & green are the constraints imposed by $\sigma^{\mathrm{L}}_{x,y}$, of which only one must be satisfied, as explained in the text.

The consistency of the constraints is verified by overlaying a much weaker constraint implied by the measured width of the luminous region, $\sigma^{\mathrm{L}}_{x,y}$ (light yellow and green). In the latter case, because of the ambiguity in choosing the sign in Eq. 16.17, only *one* of the regions must overlap, not both.

The absence of a plotted region of constraint by $\sigma^{\mathrm{L}}_{x,y}$ in Fig. 16.6(a) is due to the lack of a consistent overlap of this constraint with the others that are shown. The overlap region from the remaining constraints is much more stringent in any case, so the assumption is made here that the individual beam widths may be determined from the plotted constraint regions alone.

In order to determine the widths of the constraining bands, which themselves correspond to 1σ uncertainties, errors from the corresponding measured quantities have been taken into account. These are, namely, an absolute error[6] of 1 μm on the determined convolved beam widths, $\Sigma_{x,y}$, and the errors on the fitted $d\langle\{x,y\}\rangle/dh_{\{x,y\}}$ values shown in Tables 16.2 and 16.3. The error on the constraining regions imposed by the measured $\sigma^{\mathrm{L}}_{x,y}$ values is taken to be $\sim 2.5\,\mu$m.

Figures 16.7(a)–16.7(e) show the constraints on the individual beam correlation, $\kappa_{1,2}$, implied by the measured quantities $d\langle\{x,y\}\rangle/dh_{\{y,x\}}$ (note the reversal of x and y) and the measured correlation of the luminous region, κ^{L}, which is related to beam parameters as in Eq. 16.15. It may be instructive at this point to refer back to Eqs. 16.11 and Eqs. 16.12, observing again that they have linear terms in $\kappa_{1,2}$.

The following colour correspondence is made for the constraining bands in Figs. 16.7(a)—16.7(e): blue and red are due to $d\langle x\rangle/dh_y$ and $d\langle y\rangle/dh_x$, respectively and green

[6]This is a very conservative error, which has since been reduced. Nonetheless, it is sufficiently small to provide a good constraint on the individual beam widths.

is due to κ^{L}. All the constraints made here are summarized in Tables 16.4 and 16.6. The convolved beam widths used in this analysis are tabulated in Table 16.5.

Figures. 16.7(a) and 16.7(b) certainly demonstrate an inconsistency with respect to the constrained values of κ_1 and κ_2 for the October 2010 scans (IV and V). The scans themselves are in fact rather scan *pairs*: an X scan and a Y scan. The red and blue slopes were respectively determined *individually* from the X and Y scans within the scan pair. One might therefore speculate as to the reproducibility of the results, since the X and Y scans are necessarily performed at slightly different times, or indeed a model limitation. Notwithstanding, the systematic uncertainty determined for the October 2010 scans is conservatively determined by considering both points of overlap with the $\kappa^{\mathcal{L}}$ constraint (green) and is still shown to be small (Sec. 16.7). In contrary, the consistency seen for scan (pair) VII for May 2011 (Fig. 16.7(c)) is very noteworthy, and both κ_1 and κ_2 are unambiguously determined to be very small.

The width of the blue band implied by the luminous centroid movement in Fig. 16.7(e) includes an approximate systematic of having neglected the beam crossing angle, cf. Fig. 16.7(d), an effect giving rise to $\sim 75\%$ error on the measured value, as determined numerically. Nonetheless, these bands still provide a good constraint on $\kappa_{1,2}$. The width of this band is now the quadrature sum of this systematic and the previously determined error neglecting beam crossing angles. (See Appendix E.2 for a description of the determination and the particular values used.)

The following section describes how a beam crossing angle can masquerade as an *effective x-y* beam correlation, and how these numerically determined systematics are given theoretical footing.

TABLE 16.4. Constraints on individual beam widths. Errors are determined by taking the approximate widths of the corresponding overlap regions in Figs. 16.5(a)–16.6(b).

Parameter	October scan IV	October scan V	May scan VII	May scan VIII
σ_{x1}	60.9±1.0 μm	60.6±1.0 μm	40.2±1.0 μm	40.2±1.0 μm
σ_{x2}	53.3±1.0 μm	53.8±1.0 μm	40.4±1.0 μm	40.4±1.0 μm
σ_{y1}	58.7±1.0 μm	58.7±1.0 μm	40.9±1.0 μm	40.9±1.0 μm
σ_{y2}	57.8±1.0 μm	57.8±1.0 μm	42.6±1.0 μm	42.6±1.0 μm

TABLE 16.5. Table of bunch-averaged convolved beam widths (Σ) measured during scans IV, V, VII and VIII.

Scan	Σ_x (μm)	Σ_y (μm)
Scan IV	81.0	82.3
Scan V	81.0	82.3
Scan VII	57	59
Scan VIII	57	59

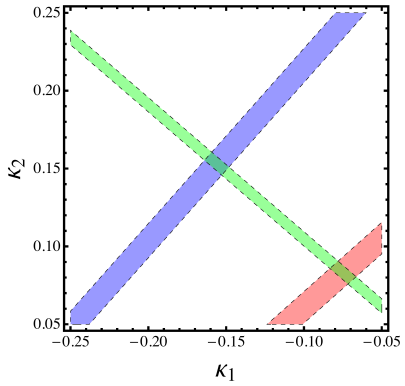

(a) Scans IV, with any non-zero crossing angle neglected.

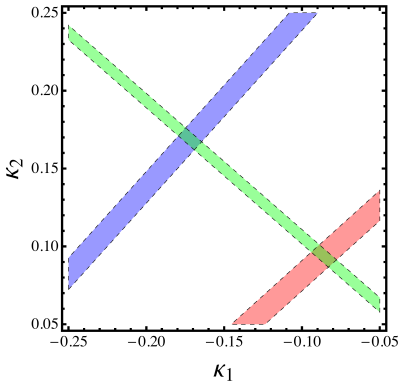

(b) Scans V, with any non-zero crossing angle neglected.

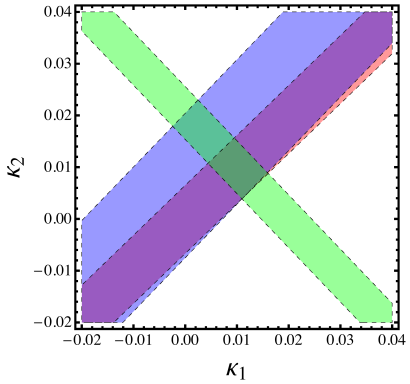

(c) Scans VII, any non-zero crossing angle neglected.

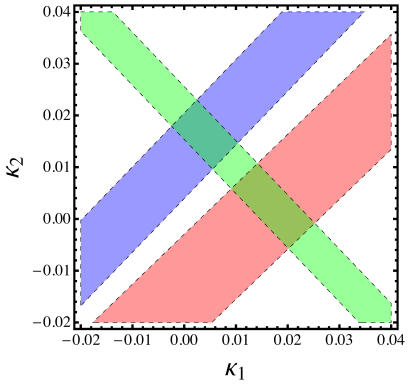

(d) Scans VIII, any non-zero crossing angle neglected.

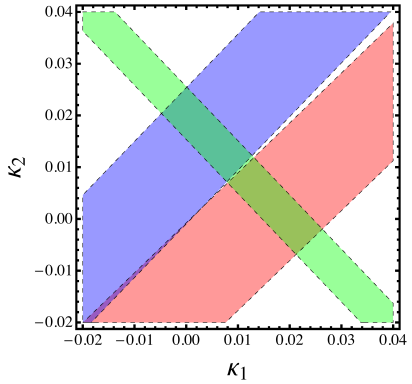

(e) Scans VIII, with crossing angle error determined numerically then summed in quadrature with the fit error, resulting in a more consistent constraint.

FIGURE 16.7. Constraints on the correlation coefficient of each beam. In the following cases, the beam crossing angle has been neglected: Figs. 16.7(a) and 16.7(b) show October 2010 scans IV and V respectively, where 16.7(c) and 16.7(d) show May 2011 scans VII and VIII respectively. Whilst a good approximation for scans IV and V it may not be a valid approximation to neglect beam crossing angles in VIII. The inclusion of the crossing angle is shown in Fig. 16.7(e), where the inclusion serves to widen one band. In all of the above, the green bands are constraints implied by the measured correlation of the luminous region, where the remaining bands are due to the measured quantities $d\langle\{x,y\}\rangle/dh_{\{y,x\}}$ of Eqs. 16.11 (blue) and 16.12 (red).

TABLE 16.6. Constraints on the x-y correlation coefficient, κ, for each beam. Again, errors are approximate widths of the corresponding overlap regions, this time in Figs. 16.7(a)—16.7(d).

Parameter	October IV	October V	May scan VII	May scan VIII
κ_1 from $d\langle y\rangle/dh_x$ (red)	-0.08 ± 0.01	-0.09 ± 0.01	0.010 ± 0.005	0.015 ± 0.010
κ_1 from $d\langle x\rangle/dh_y$ (blue)	-0.16 ± 0.01	-0.18 ± 0.01	0.005 ± 0.010	0 ± 0.005
κ_2 from $d\langle y\rangle/dh_x$ (red)	0.08 ± 0.01	0.09 ± 0.01	0.005 ± 0.005	0 ± 0.010
κ_2 from $d\langle x\rangle/dh_y$ (blue)	0.15 ± 0.01	0.17 ± 0.01	0.010 ± 0.010	0.015 ± 0.005

16.6. The effect of beam crossing angles

Realistically, the profile for each bunch should be transformed accordingly to mirror any small crossing angle in the collider. The numerical impact of such half-crossing angles of the order $\alpha_{yz}/2 \sim 100$–120 μrad in a *single* plane, e.g. with $\alpha_{xz}/2 \sim 0$ μrad, is safely negligible for observables of scans IV and V under consideration in this analysis. However, the introduction of a non-zero *second* crossing angle $\alpha_{xz}/2 \sim 20$ μrad (which may be determined by observing the z motion of the luminous centroid during a scan in the x direction) for scan VIII gives rise to certain observables for which it may be argued otherwise, and we will correspondingly introduce an appropriate systematic error, whose effect will be to relax the constraints on $\kappa_{1,2}$.

Generally it is seen that the aforementioned approximation of neglecting any beam crossing angles is sufficient for the determination of $\kappa_{1,2}$. It will be shown here, in addition, that the approximation is still valid insofar as determining the individual beam widths. The effect of having neglected crossing angles in the determination of $\kappa_{1,2}$ is then reintroduced as a systematic on the measured $d\langle\{x,y\}\rangle/dh_{\{y,x\}}$ values, which has the effect of relaxing one constraint and slightly improving the consistency of scan VIII, as in Fig. 16.7(e).

16.6.1. Including crossing angles in the covariance matrix. Consider the covariance matrix for a single-Gaussian model which includes beam correlation but does not account for any beam crossing angle, as in Eq. 16.3. In this special case, we have a neat factorization of the x- and y-dependence from the z- and t-dependence, which is the basis for the independent two-dimensional study of beam correlation.

Passively transforming the coordinate system (for the correlated model) in order to additionally model a small crossing angle in either the x-z or y-z plane (or both[7]) and retaining only linear, bilinear and quadratic terms in the corresponding rotation angles, α_{xz} and α_{yz} respectively, one obtains

$$\underline{\sigma} = \begin{pmatrix} \sigma_x^2 + \alpha_{xz}^2\,\sigma_z^2 & \kappa\,\sigma_x\,\sigma_y - \alpha_{xz}\,\alpha_{yz}\,\sigma_z^2 & \alpha_{xz}\,\sigma_z^2 \\ \kappa\,\sigma_x\,\sigma_y - \alpha_{xz}\,\alpha_{yz}\,\sigma_z^2 & \sigma_y^2 + \alpha_{yz}^2\sigma_z^2 & -\alpha_{yz}\,\sigma_z^2 \\ \alpha_{xz}\,\sigma_z^2 & -\alpha_{yz}\,\sigma_z^2 & \sigma_z^2 \end{pmatrix} \tag{16.18}$$

where the beam index i has been dropped.

[7]Commutation does not pose an issue here, since the angles in question are very small.

One is at liberty to restrict attention only to the features of the two-dimensional projection of the beam densities in the $z = 0$ plane, in which case is it not necessary to consider terms in the final row or column of Eq. 16.18; such elements would be important in the study of the z-movement of the luminous centroid, for instance. However, one may study, as before, just the terms directly affecting the x- and y-dependence of the beam profile.

It is now observed that beam crossing introduces corrections to the transverse beam widths (due to extra terms on the diagonal) and a new *effective* beam correlation in the off-diagonal terms $\kappa\,\sigma_x\,\sigma_y - \alpha_{xz}\,\alpha_{yz}\,\sigma_z^2$. Quadratic and bilinear terms in the crossing angles have been retained, since if they appear multiplying σ_z^2 they may still be numerically large. As usual, however, terms beyond the linear coupling, κ, have been ignored. Other conservative approximations have been invoked in deriving this rotated covariance matrix, such as $\sigma_{x,y} \ll \sigma_z$, etc.

16.6.2. Numerical impact and discussion. The beam crossing angle can indeed masquerade as x-y correlation, if the term $\alpha_{xz}\,\alpha_{yz}\,\sigma_z^2$ is of a comparable magnitude to $\kappa\,\sigma_x\,\sigma_y$. However, one requires at least a small crossing angle in both planes, which did not appear to be the case for scans IV–VI, for which the zero crossing angle was a good approximation. Scans VII–IX indicate a crossing angle in both planes, where it may be argued that this approximation *begins* to break down.

An approximate numerical evaluation reveals the extent to which this approximation fails for scans VII and VIII. Taking $\sigma_z \sim 70\,\text{mm}$, $\alpha_{xz} \sim 20\,\mu\text{rad}$, $\alpha_{yz} \sim 120\,\mu\text{rad}$ and $\sigma_x \approx \sigma_y \sim 40\,\mu\text{m}$ (which are very reasonable for the May 2011 data) along with κ which was found[8] to be of order 0.01 yields:

$$\alpha_{xz}\,\alpha_{yz}\,\sigma_z^2 \sim 10^{-5}\,\text{mm}^2$$

$$\kappa\,\sigma_x\,\sigma_y \sim 10^{-5}\,\text{mm}^2$$

This justifies the choice of assigning a $\sim 50\%$–80% systematic to the determined κ values for these scans. The specific uncertainties within this range may be determined by appealing to the actual values of $\alpha_{xz}\,\alpha_{yz}\,\sigma_z^2$ and $\kappa\,\sigma_x\,\sigma_y$ on a case-by-case basis, e.g. as in $\alpha_{xz}\,\alpha_{yz}\,\sigma_z^2/(\kappa\,\sigma_x\,\sigma_y)$.

Finally, the numerical impact on the determination of the beam widths is addressed. Taking the same order-of-magnitude values reveals:

$$\alpha_{xz}^2\,\sigma_z^2 \approx 2 \cdot 10^{-6}\,\text{mm}^2$$

$$\alpha_{yz}^2\sigma_z^2 \approx 7 \cdot 10^{-5}\,\text{mm}^2$$

These are to be compared with the original widths used: $\sigma_x^2 \approx \sigma_y^2 \approx 2 \cdot 10^{-3}\,\text{mm}^2$. In conclusion, the May 2011 scan analysis (scans VII and VIII) is still perfectly valid, since this error corresponds to $\sim 1.7\,\%$ on the measured value of σ_y and is negligible on σ_x—the estimated error on the current determination from luminous centroid movements and luminous width constraints was already $\sim 3\,\%$, so taking the error from crossing angle in quadrature means the error should be quoted slightly higher, at around $\sim 4\,\%$, but this

[8]See Tables 16.4 and 16.6 for details.

does not affect the aim of the study: a determination of κ and its impact on the measure luminosity.

Figure 16.7(e) shows how the inclusion of the systematic due to beam crossing somewhat improves the consistency of the overlap region for the extraction of $\kappa_{1,2}$.

16.7. Error on luminosity

The standard formula for luminosity, $L = \int \mathcal{L}\, d\vec{x}$ over all space, may be derived from the assumption of uncorrelated, single-Gaussian beams. It is given by Eq. 16.1, where $\Sigma_{x,y}$ are the so-called convolved beam widths,

$$\Sigma_{x,y}^2 = \sigma_{x,y;1}^2 + \sigma_{x,y;2}^2. \tag{16.19}$$

For a model that includes beam correlation, these definitions must change accordingly.

If we are blind to correlation, and therefore ignore it in a naïve computation of the luminosity, the ratio of the luminosity with the beams separated in the x-direction by some amount h and the luminosity measured at zero separation is

$$\frac{L(h)}{L(0)} = \exp\left[-\frac{h^2}{2\left(\sigma_{x1}^2 + \sigma_{x2}^2\right)}\right] \equiv \exp\left(-\frac{h^2}{2\Sigma_x^2}\right). \tag{16.20}$$

The vdM analysis gives us direct access to this value, since it is simply related to the width of the resulting Gaussian distribution. A similar equation holds for a y-scan, giving Σ_y.

Explicitly including beam correlation in our considerations, this becomes

$$\frac{\tilde{L}(h)}{\tilde{L}(0)} = \exp\left\{-\frac{h^2}{2\left[\Sigma_x^2 - (\kappa_1\sigma_{x1}\sigma_{y1} + \kappa_2\sigma_{x2}\sigma_{y2})^2/\Sigma_y^2\right]}\right\} \equiv \exp\left(-\frac{h^2}{2\overline{\Sigma}_x^2}\right) \tag{16.21}$$

and, of course, a similar equation holds for the y-scan. The tilde is used to distinguish this luminosity from that used in Eq. 16.20 above. Note: $\Sigma_{x,y}^2$ are the ones defined in Eq. 16.19. Here, one can then solve for the *measured* convolved beam widths in the *correlated* model (denoted by a bar), to obtain

$$\overline{\Sigma}_x^2 = \Sigma_x^2 - \frac{\left(\kappa_1\sigma_{x1}\sigma_{y1} + \kappa_2\sigma_{x2}\sigma_{y2}\right)^2}{\Sigma_y^2} \tag{16.22}$$

and similarly for $\overline{\Sigma}_y^2$.[9] A binomial expansion reveals that $\overline{\Sigma}_{x,y}$ are independent of linear terms in $\kappa_{1,2}$:

$$\overline{\Sigma}_{x,y} = \Sigma_{x,y} + \text{bilinears} + \text{quadratics} + \text{h.o.t.} \tag{16.23}$$

explicitly demonstrating the formal validity of its constraint on the individual beam widths (which were sought *before* attempting to constrain the correlation coefficients).

In the standard prescription, one would use the measured values of $\overline{\Sigma}_{x,y}$ to determine the luminosity using Eq. 16.1. However, the *actual* (κ-corrected) luminosity, distinguished with a tilde, in terms of the beam parameters is more complicated, and is given by $\tilde{L}(0)$. One may expand the two definitions of luminosity in powers of the correlation coefficients

[9] It should be noted here that, as always, the $\sigma_{x,y;1,2}$ quantities are the *projected* individual beam widths, as defined via the covariance matrix in Eq. 16.3, i.e. **not** the widths in the basis where this matrix would be diagonal.

$\kappa_{1,2}$:

$$\tilde{L}(0) \propto \frac{1}{2\pi\Sigma_x\Sigma_y} + \frac{\kappa_1^2\sigma_{x1}^2\sigma_{y1}^2}{4\pi\Sigma_x^3\Sigma_y^3} + \frac{\kappa_2^2\sigma_{x2}^2\sigma_{y2}^2}{4\pi\Sigma_x^3\Sigma_y^3} + \frac{\kappa_1\kappa_2\sigma_{x1}\sigma_{x2}\sigma_{y2}\sigma_{y2}}{2\pi\Sigma_x^3\Sigma_y^3} + \text{h.o.t.} \tag{16.24}$$

where 'h.o.t.' are higher-order terms, more than bilinear or quadratic in the $\kappa_{1,2}$. Expanding that one which would use in a naïve calculation of the luminosity that neglects potential correlation, one obtains

$$L(0) \propto \frac{1}{2\pi\overline{\Sigma}_x\overline{\Sigma}_y} = \frac{1}{2\pi\Sigma_x\Sigma_y} + \frac{\kappa_1^2\sigma_{x1}^2\sigma_{y1}^2}{2\pi\Sigma_x^3\Sigma_y^3} + \frac{\kappa_2^2\sigma_{x2}^2\sigma_{y2}^2}{2\pi\Sigma_x^3\Sigma_y^3} + \frac{\kappa_1\kappa_2\sigma_{x1}\sigma_{x2}\sigma_{y2}\sigma_{y2}}{\pi\Sigma_x^3\Sigma_y^3} + \text{h.o.t.} \tag{16.25}$$

The first term in each series is exactly that obtained from an uncorrelated model. The bilinear and quadratic terms in each series differ by a factor of 2. Taking the fractional difference between the two definitions of the luminosity therefore gives the error induced by beam correlation on the *measured* luminosity. Using the results of the preceding analysis, one obtains

$$\frac{L - \tilde{L}(0)}{\tilde{L}(0)} \lesssim 0.1\% \text{ and } \frac{L - \tilde{L}(0)}{\tilde{L}(0)} \lesssim 0.02\% \tag{16.26}$$

for the October 2010 scan and the May 2011 scan respectively.

16.8. Concluding remarks

In principle, the preceding analysis should be performed on a *per BCID* basis. The convolved beam widths are determined in this way, and only their average has been used in this analysis. In practice, however, statistics may become a problem. It has, nonetheless, been possible to constrain the model in a consistent fashion for scans VII and VIII, but October scans IV and V are indicative of a model limitation, due to the lack of consistent overlap for the $\kappa_{1,2}$ constraints. A discussion of extensions to the single-Gaussian model which have been considered is presented in Chap. 18. The preceding analytical analysis has been corroborated using a completely numerical tool, confirming the determination of the various parameters by reproducing the same movements with these parameters as input.

In summary, it has been possible to determine the parameters of the single-Gaussian model that give rise to the salient linear phenomena observed in distributions of the luminous centroid position with respect to beam separation, with the aforementioned October exception in mind. Even so, the results still indicate that one is dealing with a small correction to the luminosity via the neglect of beam correlation. A systematic method has been developed to constrain these parameters in a manner which is formally consistent, by studying the dependence of these phenomena analytically on parameters such as the beam correlation coefficient.

In addition, it would be interesting to see how one could make a minimal addition to the single-Gaussian model to mitigate the problem of inconsistency of the κ determination of scans IV and V.

The present study concerns October 2010 and May 2011 in-plane scan data. In addition, two out-of-plane scans were performed for each of the two months, namely scans VI and IX, in which beams were offset in the orthogonal-to-scan direction. These additional

scans should provide the ability to study the tails of the distributions of the luminous centroid movement with separation. In fact, the out-of-plane scans performed in May 2011 (scan IX) had a fixed orthogonal displacement of several times the nominal Gaussian width of the beams themselves, where the October scans (VI) were performed with a much smaller constant offset, closer to a single Gaussian width. This makes the scan IX data an ideal ground upon which to study non-linearities of the luminous centroid movement observed in these tails.

A foreseeable extension to the model presented herein would be to that of a double-Gaussian model, where each beam is modelled as the sum of two concentric Gaussians, each with different widths and peak heights. In particular, one would wish to recover the linear phenomena observed at small scan separations, so the model should consist of a tall and narrow 'primary' Gaussian with a 'secondary' flat and broad Gaussian which would begin to dominate the dynamics in the high-scan-separation régime. For sufficiently high scan separations (or, equivalently, an out-of-plane scan at large offset as in scan IX) the secondary Gaussian would dominate the dynamics of the luminous centroid movements, even to the extent that a carbon-copy of the single-Gaussian model presented here might be appropriate, neglecting the primary Gaussian, out of whose jurisdiction one becomes. In principle, one could then constrain the parameters of the secondary Gaussian in this régime, then proceed to construct the double-Gaussian model with all the parameters determined thus far, with the aim of reproducing the non-linear tail data observed for the *in-plane* scans.

One could further isolate the effect of the primary Gaussian by fitting only to high-separation scan data for out-of-plane scans, in a way analogous to how the linear fits have been made for in-plane scans neglecting the non-linear tail data in this analysis.

The following chapter aims to extend the analysis formalism presented here, in order to explicitly account for the possibility of non-zero beam crossing angles.

CHAPTER 17

Transverse beam coupling part 2: An analytical determination of the parameters of the single-Gaussian model of bunch densities and their impact on the luminosity calibration by the van der Meer method

17.1. Introduction

In this chapter, the effect of linear transverse coupling on the luminosity calibration by the van der Meer (vdM) method [**118**]—presented for the reader in Sec. 15.3—is studied for additional vdM scans which took place in March 2011, April 2012 and July 2012. The principal method is already described in Chap. 16 and [**115**], but this chapter presents an extension of the formalism to include explicit beam crossing angles in either plane. The new analysis is then followed with a compilation of all results obtained, for easy comparison. Finally, I conclude this chapter with a discussion of the results.

Upon repeating the analysis of October 2010 and May 2011 on data from more recent vdM scans, it has become unequivocally clear that the single-Gaussian model presented herein is insufficient to describe the high-separation scan data, since in this region one generally observes strong non-linear tails in the data. It was demonstrated in Eq. 16.9 the manner in which the single-Gaussian model may only describe linear movements of the luminous centroid during a vdM scan. It is clear that a more sophisticated model is required, but this necessarily requires the dimensionality of parameter space to more than double in most cases, e.g. a double-Gaussian model. Furthermore, the single-Gaussian model has the remarkable property that it is easily studied analytically, without recourse to numerical methods, even in the case of arbitrary x-y coupling and a beam crossing angle. For this reason, this analysis—as applied to central scan data which is usually very linear—has formed the starting point for analyses using more sophisticated models, since it may be used to provide a sensible starting point for a search within a large parameter space. Maintaining the single-Gaussian as the principal model for this analysis, I begin now by addressing the inclusion of explicit beam crossing angles.

17.2. Analysis method and formalism with beam crossing angles

An analysis of the characteristic length scales of this problem reveals a subtle inconsistency in the formalism of Chap. 16, when there exists a beam crossing angle in either (or both) direction(s). The problem, as analysed in Sec. 16.6 and [**115**], stems from the fact that, whilst the quantity α—the beam crossing angle in radians—may be the smallest dimensionless scale of the model (typically $\sim 10 - 100\,\mu$rad), if it appears multiplying the large z width, σ_z, of either beam then the numerical impact may be significant. In fact,

the numerical impact of such a term may be approximately that of the off-diagonal terms in the covariance matrix (Eq. 16.3) and will thus *manifest* as an effective correlation. In addition, a beam crossing angle gives rise to a new phenomenon: movement of the z position of the luminous centroid. Overall, it is identified to play a significant rôle in some of the vdM scans considered in this chapter.

One includes a non-zero crossing angle into the single-Gaussian model by simultaneously making the following passive transformations of the coordinate system for each of the two beams:

$$\vec{x}_1 \to \vec{x}_1 = R\left(\pm\frac{\alpha}{2}\right)\,\vec{x_1} \tag{17.1}$$

and

$$\vec{x}_2 \to \vec{x}_2 = R^{-1}\left(\pm\frac{\alpha}{2}\right)\,\vec{x_2}, \tag{17.2}$$

where the particular choice of $+$ and $-$ is chosen according to convention. Here, R is a rotation matrix by an angle $\alpha/2$ of the vector $\vec{x}_i$, given in Eq. 16.3, about the relevant axis. Indeed, the rotations may be compounded to include a crossing angle in both planes. This way,

$$\begin{aligned}\mathcal{L}(x,y,z,t) \;&\propto \rho_1(x,y,z,t)\,\rho_2(x,y,z,t)\\ &= \exp\left\{-\frac{1}{2}\left[\vec{x}_1\cdot\left(\underline{\sigma}_1^{-1}\right)\cdot\vec{x}_1+\vec{x}_2\cdot\left(\underline{\sigma}_2^{-1}\right)\cdot\vec{x}_2\right]\right\}\\ &\to \exp\left\{-\frac{1}{2}\left[\vec{x}_1\cdot R^{-1}\cdot\left(\underline{\sigma}_1^{-1}\right)\cdot R\cdot\vec{x}_1+\vec{x}_2\cdot R\cdot\left(\underline{\sigma}_2^{-1}\right)\cdot R^{-1}\cdot\vec{x}_2\right]\right\}.\end{aligned} \tag{17.3}$$

The transformation may actually be absorbed into the definition of the covariance matrix, which will result in at least some of the remaining zero elements in Eq. 16.3 becoming non-zero. In this sense, beam crossing angle is mathematically equivalent to x-z and y-z coupling. Revisiting the arguments presented at the start of this section, this coupling may be numerically as large as transverse (x-y) coupling.

The mathematical difficulty that one encounters when trying to include a beam crossing angle is that the expression in Eq. 16.4 for the luminosity no longer factorizes. However, as shown below, an analytical solution may still be obtained, and the corrections to the previous model appear explicitly as new terms in a set of equations similar to Eqs. 16.10 – 16.13.

The solution to this problem begins by identifying that the terms in the exponent of Eq. 17.3 are either bilinears or quadratics in the four space-time variables x, y, z and t. Thus, we may write the expression for the luminosity in matrix form, as

$$\mathcal{L}(x,y,z,t) = \mathcal{N}\,\exp\left(-\frac{1}{2}\sum_{i,j=1}^{4} x_i\,K_{ij}\,x_j + \sum_{i=1}^{4} J_i\,x_i\right) = \mathcal{N}\,\exp(\mathcal{E}), \tag{17.4}$$

where $\mathcal{N}$ is just a proportionality factor. In this expression, x_1, x_2 and x_3 are x, y and z, respectively, and x_4 is t. One can always determine the components of the vector J or the elements of the matrix K by differentiation of the exponent:

$$J_i = \left.\frac{d\mathcal{E}}{dx_i}\right|_{x_k\to 0} \qquad \forall k\in\{1,2,3,4\} \qquad \text{and} \qquad K_{ij} = -\frac{d^2\mathcal{E}}{dx_i x_j}. \tag{17.5}$$

One need not worry about any constant terms appearing, since these may be absorbed into the overall factor $\mathcal{N}$, which will remain unimportant in our analysis here.

In order to perform the temporal convolution that appears in the definition of the luminosity in Eq. 16.4 we integrate Eq. 17.4 over $x_4 = t$ to obtain

$$\mathcal{L}(x,y,z) = \int_{\infty}^{\infty} dt\, \mathcal{L}(x,y,z,t) = \mathcal{N}\, \frac{e^{\frac{J_t^2}{2K_{tt}}}\sqrt{2\pi}}{\sqrt{K_{tt}}}\, \exp\left(-\frac{1}{2}\sum_{i,j=1}^{3} x_i\, K'_{ij}\, x_j + \sum_{i=1}^{3} J'_i\, x_i \right), \tag{17.6}$$

where x_i are now components of the 3-tuple (x,y,z), since one variable has been integrated out. K' and J' are a 3×3 matrix and a 3-tuple respectively. Written in terms of the original components or elements of J and K, they are

$$K' = \begin{pmatrix} -\frac{K_{xt}^2}{K_{tt}} + K_{xx} & K_{xy} - \frac{K_{xt}K_{yt}}{K_{tt}} & K_{xz} - \frac{K_{xt}K_{zt}}{K_{tt}} \\ K_{xy} - \frac{K_{xt}K_{yt}}{K_{tt}} & -\frac{K_{yt}^2}{K_{tt}} + K_{yy} & K_{yz} - \frac{K_{yt}K_{zt}}{K_{tt}} \\ K_{xz} - \frac{K_{xt}K_{zt}}{K_{tt}} & K_{yz} - \frac{K_{yt}K_{zt}}{K_{tt}} & -\frac{K_{zt}^2}{K_{tt}} + K_{zz} \end{pmatrix} \tag{17.7}$$

and

$$J' = \begin{pmatrix} J_x - \frac{J_t K_{xt}}{K_{tt}} \\ J_y - \frac{J_t K_{yt}}{K_{tt}} \\ J_z - \frac{J_t K_{zt}}{K_{tt}} \end{pmatrix}. \tag{17.8}$$

As before, one obtains the luminous centroid (the position of the peak of the luminosity density) by maximizing $\mathcal{L}(\vec{x})$. Thus

$$\begin{aligned} \frac{\partial \mathcal{L}}{\partial x_k} &= \mathcal{N}'\, \frac{\partial}{\partial x_k}\, \exp\left(-\frac{1}{2}\sum_{i,j=1}^{3} x_i\, K'_{ij}\, x_j + \sum_{i=1}^{3} J'_i\, x_i \right) \\ &= \mathcal{N}'\left(-\sum_{i=1}^{3} K'_{ki}\, x_i + J'_k \right) \exp\left(-\frac{1}{2}\sum_{i,j=1}^{3} x_i\, K'_{ij}\, x_j + \sum_{i=1}^{3} J'_i\, x_i \right) := 0. \end{aligned} \tag{17.9}$$

The co-ordinates of the maximum, $\langle \vec{x} \rangle$, are then obtained by solving the three simultaneous equations

$$\sum_{i=1}^{3} K'_{ki}\, x_i = J'_k. \tag{17.10}$$

By differentiating the resulting expression for $\langle \vec{x} \rangle$ with respect to h_x or h_y (the beam separations) and expanding the (six) results in $\kappa_{1,2}$ and $\alpha_{x,y;z}$, one obtains a new set of equations, performing the rôle of Eqs. 16.10 – 16.13. The new equations are rather cumbersome, so only two particularly elucidating examples are included here, which have $\alpha_{xz} = 0$ and $\alpha = \alpha_{yz} \neq 0$:

$$\frac{d\langle y \rangle}{dh_y} = -\frac{\sigma_{y1}^2 - \sigma_{y2}^2}{2\Sigma_y^2} + \alpha^2 \frac{\sigma_{y1}^2\sigma_{z2}^2 - \sigma_{y2}^2\sigma_{z1}^2}{4\Sigma_y^4} + \ldots \tag{17.11}$$

$$\frac{d\langle z \rangle}{dh_y} = -\frac{\alpha\left(\Sigma_y^2 - \Sigma_z^2\right)}{4\Sigma_y^2} + \ldots \tag{17.12}$$

These are further simplified by setting $\sigma_{z1} = \sigma_{z2} = \sigma_z$, and noting that $\Sigma_y \ll \Sigma_z$. The reader is encouraged to compare Eq. 17.11 with Eq. 16.13, and note the fact that Eq.

17.12 is now no longer identically zero. Furthermore, the symbol Σ is being used with the same definition as Eq. 16.14, and it is stressed that this no longer corresponds to the definition of the convolved beam width in the case of non-zero beam crossing angle. For a compendium of all six equations, see Appendix E.3.

The actual convolved beam width one measures during a vdM scan, henceforth written $\tilde{\Sigma}$, is given in terms of Σ and a single crossing angle α by the expression [**122**]

$$\tilde{\Sigma} = \Sigma\, S^{-1} \qquad \text{where} \qquad S^{-1} = \sqrt{1 + \frac{2\sigma_z^2}{\Sigma^2} \tan^2\left(\frac{\alpha}{2}\right)}\,, \tag{17.13}$$

where σ_z is the z-width of the colliding bunches. Thus, when beam crossing angles are present and significant, the above definition will be used when considering the constraint implied on the individual beam widths.

17.3. Application to in-plane vdM scan data

In this section the fits of the luminous centroids, along with the constraints they imply on the individual beam parameters, are presented for the in-plane vdM scans in March 2011, April 2012 and July 2012. Finally, a summary of all scans (including October 2010 and May 2011) is presented.

17.3.1. March 2011. Figures 17.1 and 17.2 show scan data for Scans I and II of (March) 2011. Specifically, the position of the luminous centroid in (x, y, z) is shown, for each scan, as a function of beam separation, h, in either the x- or the y-plane. A linear fit to this data has been applied to the central scan data, since these data remain largely linear. The non-linear tails are a clear sign that one requires a model more sophisticated that the single-Gaussian model, which is incapable of reproducing such non-linear phenomena. Nonetheless, a linear analysis continues, in order to find the parameters of a single-Gaussian model that is expected to dominate the evolution of the luminous centroid at small beam separation.

Scans I and II did not call for a beam crossing angle to be introduced into the model. The justification for this can be seen by observing the final two plots in both Figs. 17.1 and 17.2, where the gradient of the luminous centroid movement in z with respect to scan separation is very small. One can quantify this by saying if $d\langle z\rangle/dh_{x_i} \ll \sigma_z/\sqrt{2}\,\Sigma_{x_i}$ then we may ignore the crossing angle in the (x_i, z) plane. The justification for this limit is given in Appendix E.4. This does indeed imply that a residual crossing angle was present in reality, but at this level it has been learnt to be negligible. Since it has been chosen to neglect beam crossing angle, no knowledge of the z profile of the proton densities is required, since the factorization of Eq. 16.4 still holds.

The errors on the constraint plots shown in Figs. 17.3 and 17.4 (i.e. the widths of the constraining bands) arise as follows: the bands of positive slope, which describe the constraints due to either $d\langle x\rangle/dh_x$ or $d\langle y\rangle/dh_y$, follow directly from the errors on the fitted gradients of Figs. 17.1 and 17.2. The width of the band of negative slope directly corresponds to the error on the convolved beam width for the given scan. Table 17.1 summarizes the convolved widths used. The quoted values are the BCID-averaged widths,

and the quoted errors are the standard deviations of the values that go into these averages. Table 17.2 shows the values used as input for the correlation of the luminous region.

Finally, Fig. 17.5 shows the constraint plots for the correlation coefficients κ_1 and κ_2. The red and blue bands come from the requirement that the expressions for $d\langle x\rangle/dh_y$ and $d\langle y\rangle/dh_x$ must satisfy the fitted quantities within the fit errors. In addition, the errors on the constrained individual beam widths have been propagated through into these plots, which is responsible for giving the bands their arched appearance. The orange bands are constructed according to the requirement that κ_1 and κ_2 satisfy Eq. 16.15 for the measured correlation of the luminous region, $\kappa^{\mathcal{L}}$ within errors. The value of $\kappa^{\mathcal{L}}$ is taken to be the X-Y scan pair BCID-average, with the error quoted as the standard deviation on the numbers that go into this average.

TABLE 17.1. Convolved widths used as input in the March 2011 analyses. The quoted values are the BCID-averaged widths, and the quoted errors are the standard deviations of the values that go into these averages.

Scan	Σ_x (μm)	Σ_y (μm)
I	229 ± 16	249 ± 19
II	200 ± 16	215 ± 18

TABLE 17.2. Luminous region x-y correlation coefficients. The quoted values are the scan-point-averaged values from X-Y scan pairs, and the quoted errors are the standard deviations of the values that go into these averages.

Scan	$\kappa^{\mathcal{L}}$
I	0.014 ± 0.001
II	0.013 ± 0.001

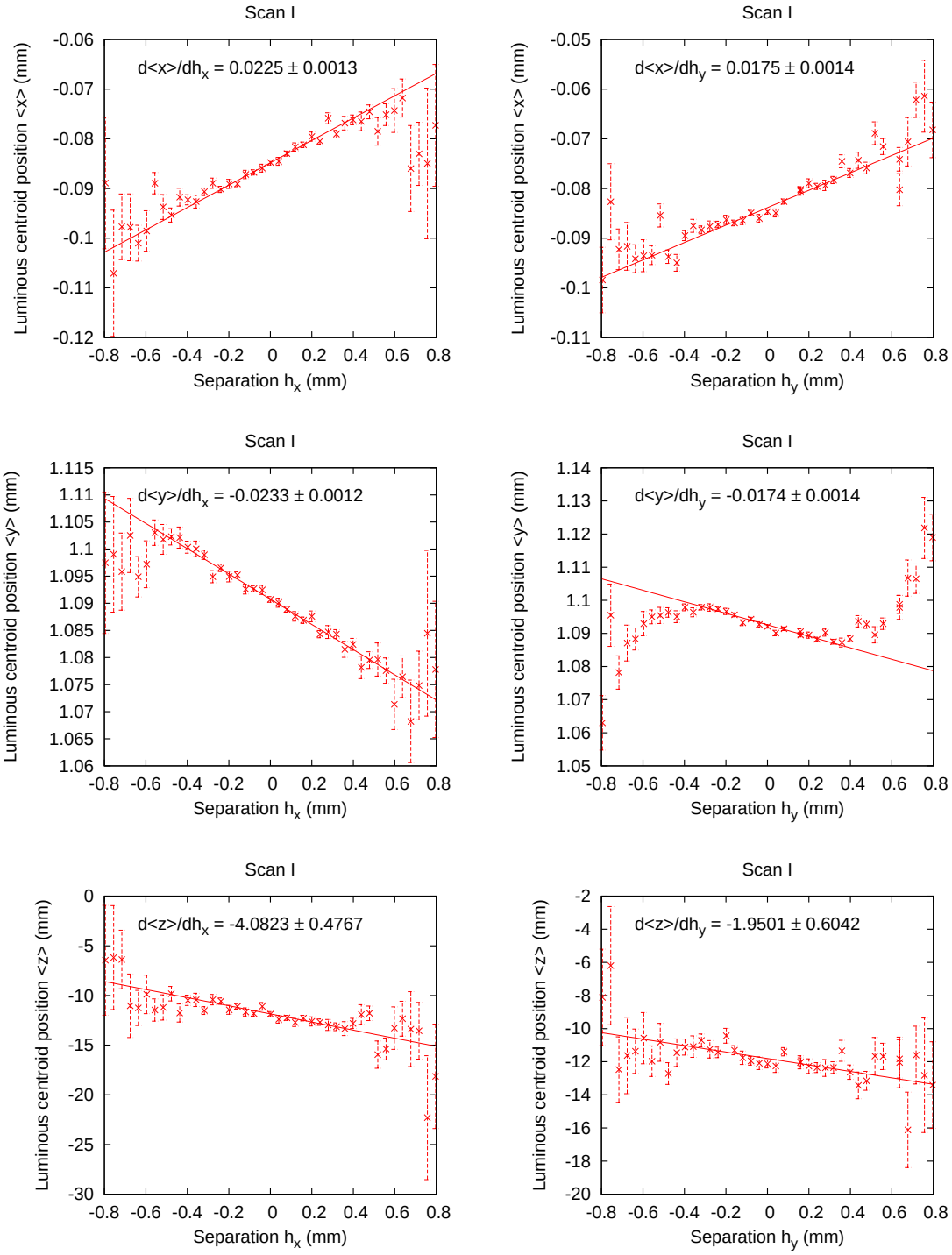

FIGURE 17.1. Luminous centroid movements during Scan I in (March) 2011. Given the appearance of clearly non-linear tails (which the single-Gaussian model is not sufficient to reproduce) the fits are to central scan data only, in the range $[-0.3, 0.3]$ mm. The errors on the luminous centroid positions are of statistical origin only.

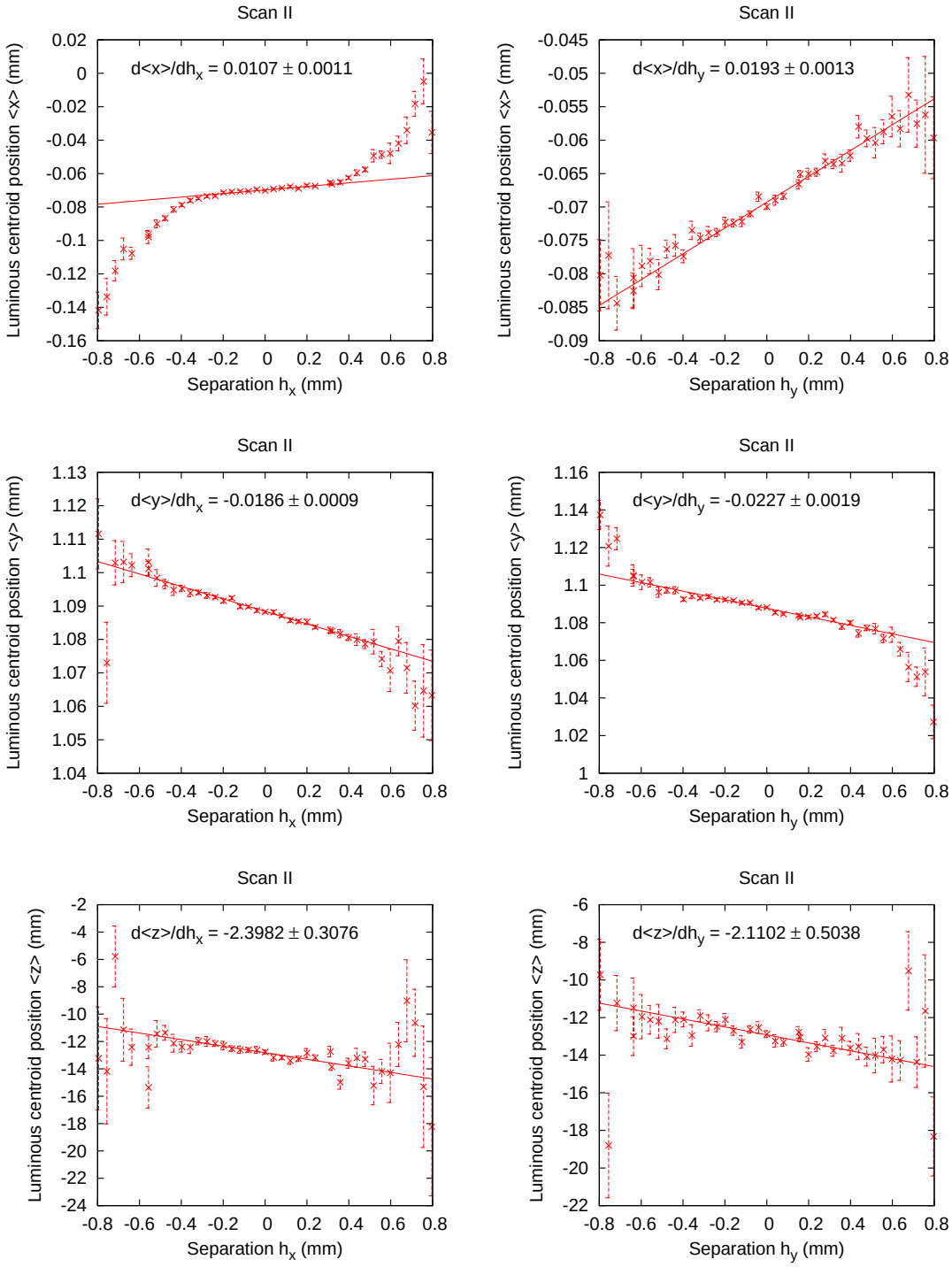

FIGURE 17.2. Luminous centroid movements during Scan II in (March) 2011. The continued presence of clearly non-linear tails again require that the fits are to central scan data only, in the range $[-0.3, 0.3]$ mm. The errors on the luminous centroid positions are of statistical origin only.

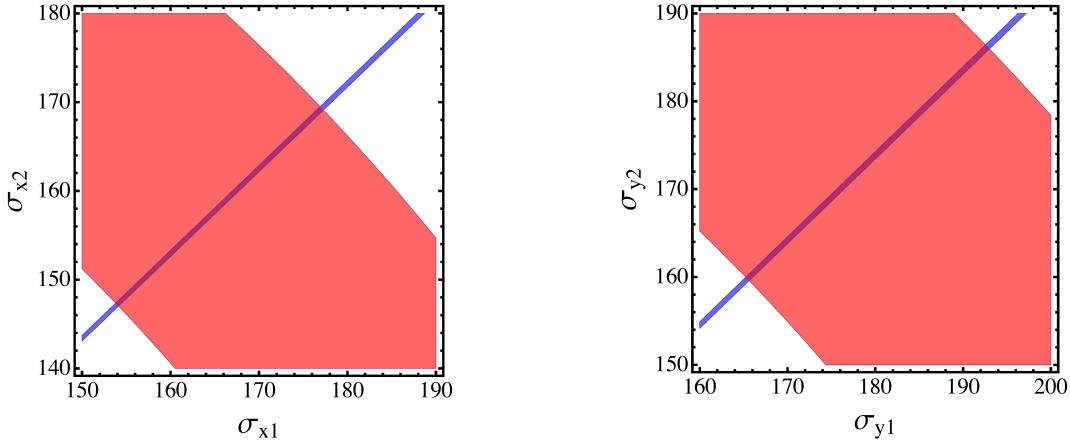

FIGURE 17.3. These plots show the constrained region of the $(\sigma_{x1}, \sigma_{x2})$ and $(\sigma_{y1}, \sigma_{y2})$ parameter spaces for Scan I of March 2011. The constraints are determined by a direct comparison between the fitted sloped of Figs. 17.1 and 17.2 with Eqs. 16.10 and 16.13 (producing the bands with positive slope) in addition to supplementary information given by the measured values of Σ_x and Σ_y, the convolved beam widths (bands with negative slope). The errors directly represent either the fit errors for the gradients, or the error on the convolved beam width, as explained in the text.

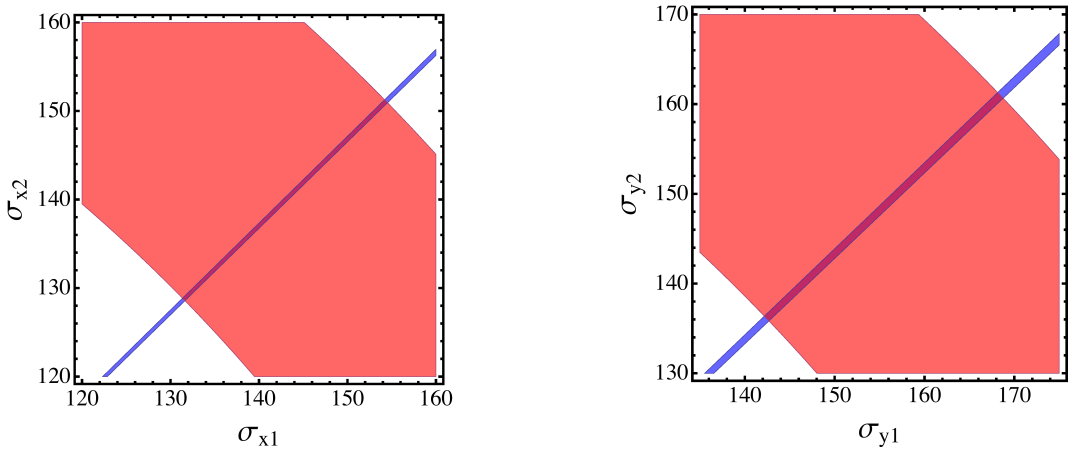

FIGURE 17.4. The results for Scan II of March 2011, shown here, are determined in the same manner described in the caption of Fig. 17.3, above.

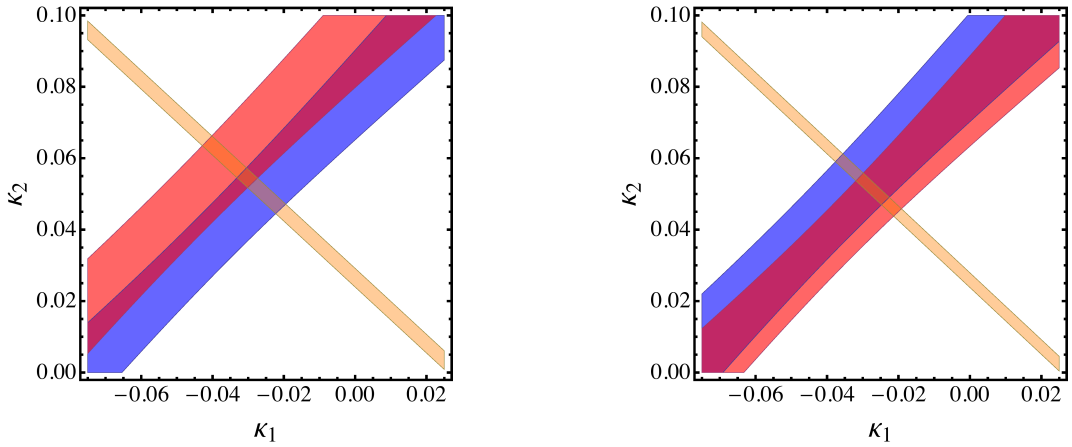

FIGURE 17.5. The constrained regions of (κ_1, κ_2) space, for scans I and II of March 2011. The constraints are generally very consistent, especially in scan II, and they are both strongly indicative of negligibly small correlation coefficients from the standpoint of the luminosity calibration error. The bands of negative slope come from a direct comparison of Eq. 16.15 with the values of $\kappa^{\mathcal{L}}$ measured for the luminous region. The widths of the bands directly reflect the errors on these measurements. The bands of positive slope come from comparing the analytical expressions for $d\langle x\rangle/dh_y$ (blue) and $d\langle y\rangle/dh_x$ (red) with the corresponding fitted slopes of Figs. 17.1 and 17.2. The widths come from the fit errors and the propagated errors from the constrained individual beam widths.

17.3.2. April 2012. It should be clear from Figs. 17.6 – 17.8 that much of the April 2012 vdM scan data is almost pathologically non-linear, from the standpoint of the single-Gaussian model. Whilst effort has been made to isolate a central, small-separation region of data for which one can approximately justify a linear fit, this remains close to impossible. The final extracted individual beam parameters should therefore be used with caution, but give ballpark figures with corresponding errors nonetheless.

The reader is encouraged to keep in mind that this analysis aims to determine the uncertainty induced by transverse beam correlation on the luminosity calibration by the van der Meer method, which itself assumes factorization of the transverse proton densities of the bunches in x and y. It does so by assuming a Gaussian form for these densities, on account of the analytic solubility it offers. While there will therefore in principle be a model uncertainty associated with this choice of Gaussian form *on the determined degree of correlation*, this study does *not* intend to provide an estimate of the *fit model* uncertainty associated with determining the luminosity calibration itself (by way of analysing the van der Meer scan curves). A separate study has shown this distinct uncertainty to be at the few percent level for these April 2012 scans [**123**].

Furthermore, the large gradients of the luminous centroid movement in z (with respect to beam separation in y) are highly indicative of the necessity to include a beam crossing angle into the model. Indeed, there is a nominal crossing angle in the y-z plane. For this reason, we begin using the extended analysis described in Sec. 17.2 from the beginning. As previously mentioned, the inclusion of a crossing angle necessarily introduces a correlation between the bunch profiles in z, with those in x and y. Therefore, information about the z profile will be required as input, and the *width* in z is taken from an independent source known as the *Beam Quality Monitor* (BQM). The profile of the proton distribution in z is relatively poorly known, compared with that of x or y. Nonetheless, the z width is used in the sense of being an approximate measure of the width over which 68% of the protons are contained, like a Gaussian width. Fundamentally in the analysis, this width sets the scale for the dimensional parameters α_{xz} and α_{yz}, the crossing angles.

Table 17.3 shows the parameters assumed *a priori*. The value of σ_z is assumed to be the same for all bunches of both beams. The crossing angles used are the nominal crossing angles. The values for the correlation of the luminous region, $\kappa^{\mathcal{L}}$, are determined by averaging over all colliding BCIDs.

Once again, constraint plots are generated from the fitted slopes of the movements of the luminous centroid, supplemented with the input data above, and the expressions for the convolved beam width (in the presence of a non-zero crossing angle) and the correlation of the luminous region.

It should be noted that modelling of the crossing angle is important here for a correct determination of the widths (in y). Since one crossing angle is still small, it has limited impact on the determination of $\kappa_{1,2}$, however, which would require a large crossing angle to be present in both planes. For more information, the reader is referred to the discussion in Sec. 16.6 (also [**115**]).

Figures 17.9 – 17.12 show the constrained parameters of the single-Gaussian model (in the small-scan-separation limit) for the April 2012 scans. The widths of the constraining bands are determined in exactly the same way as described for March 2011.

TABLE 17.3. Table of input parameters for the April 2012 analysis. Errors on Σ values are standard deviations across all BCIDs, whilst the actual value is taken to be the BCID-average. Errors on $\kappa^{\mathcal{L}}$ values are standard deviations across all scan points with the actual value given by the average across all scan points in a given X-Y scan *pair*.

Parameter	Value
$\alpha_{xz}/2$	0 μrad
$\alpha_{yz}/2$	145 μrad
Σ_x^{I}	$(24.9 \pm 0.4)\,\mu$m
Σ_y^{I}	$(32.5 \pm 0.3)\,\mu$m
Σ_x^{II}	$(25.2 \pm 0.3)\,\mu$m
Σ_y^{II}	$(32.5 \pm 0.3)\,\mu$m
Σ_x^{III}	$(26.3 \pm 0.3)\,\mu$m
Σ_y^{III}	$(33.1 \pm 0.3)\,\mu$m
σ_z	90 mm
$\kappa_{\mathrm{I}}^{\mathcal{L}}$	-0.02 ± 0.04
$\kappa_{\mathrm{II}}^{\mathcal{L}}$	-0.03 ± 0.04
$\kappa_{\mathrm{III}}^{\mathcal{L}}$	-0.03 ± 0.05

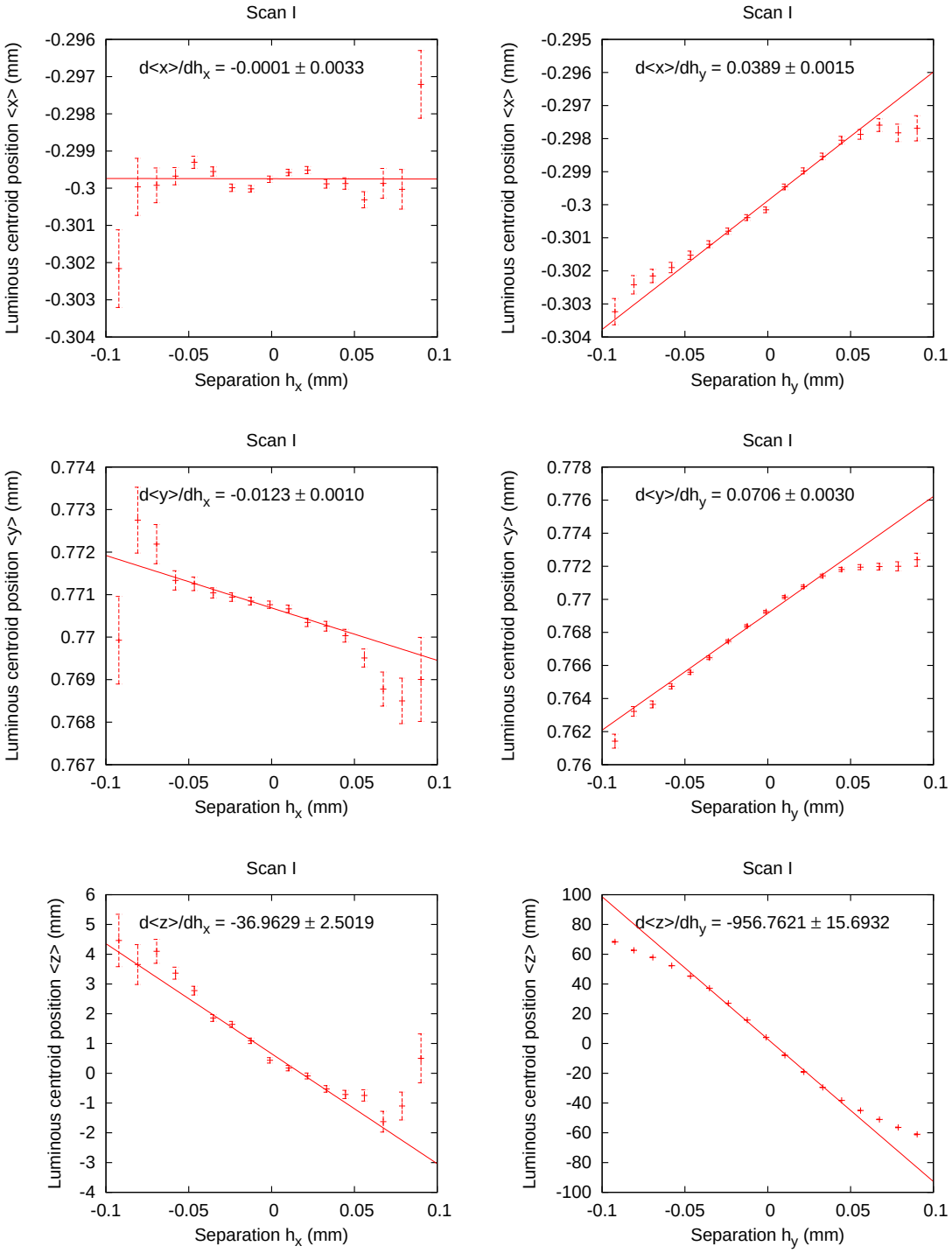

FIGURE 17.6. April 2012 Scan I data. The linear fit is to the central scan points corresponding to separations ≤ 0.05 mm. The errors on the luminous centroid positions are of statistical origin only.

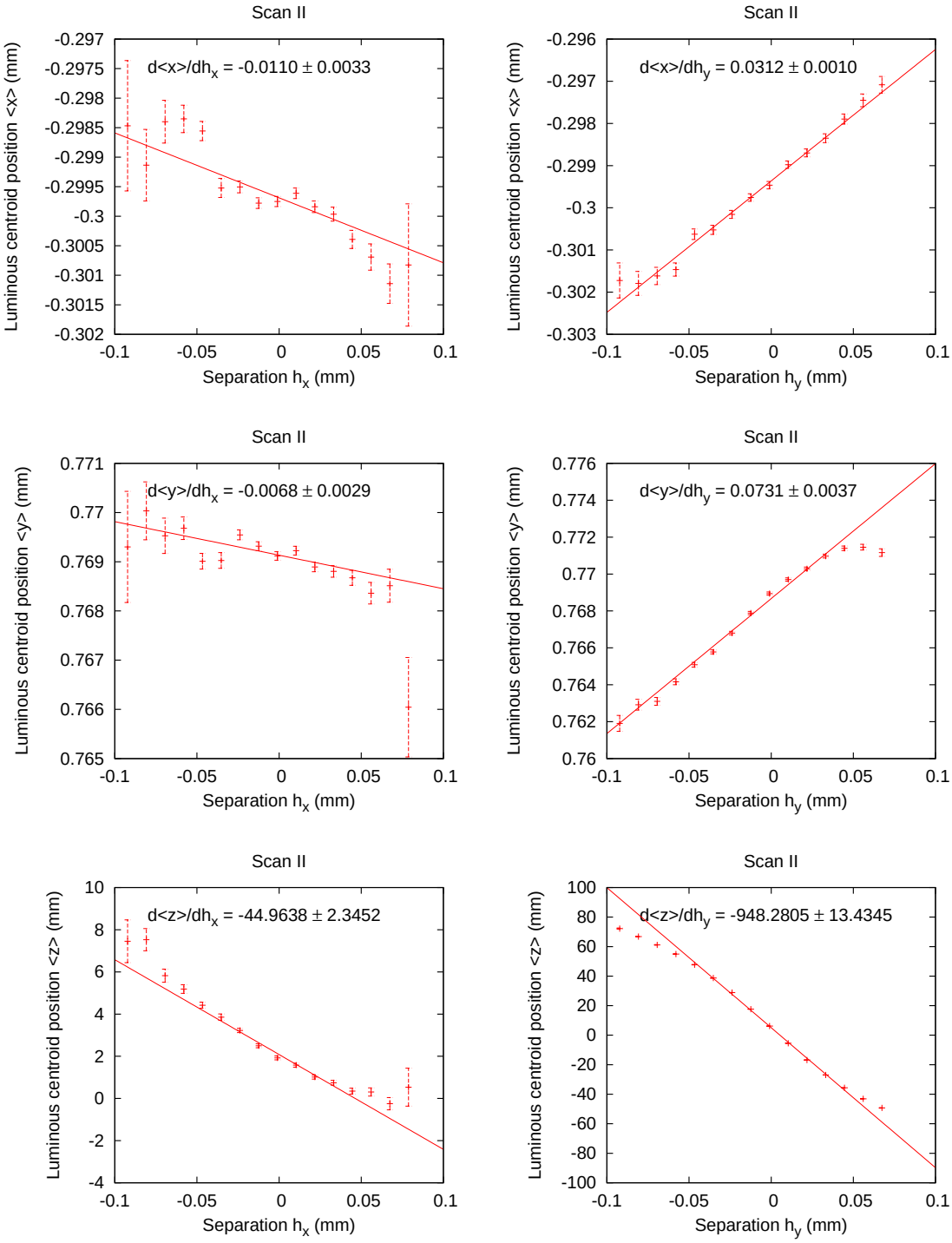

FIGURE 17.7. April 2012 Scan II data. The linear fit is to the central scan points corresponding to separations ≤ 0.05 mm. The errors on the luminous centroid positions are of statistical origin only.

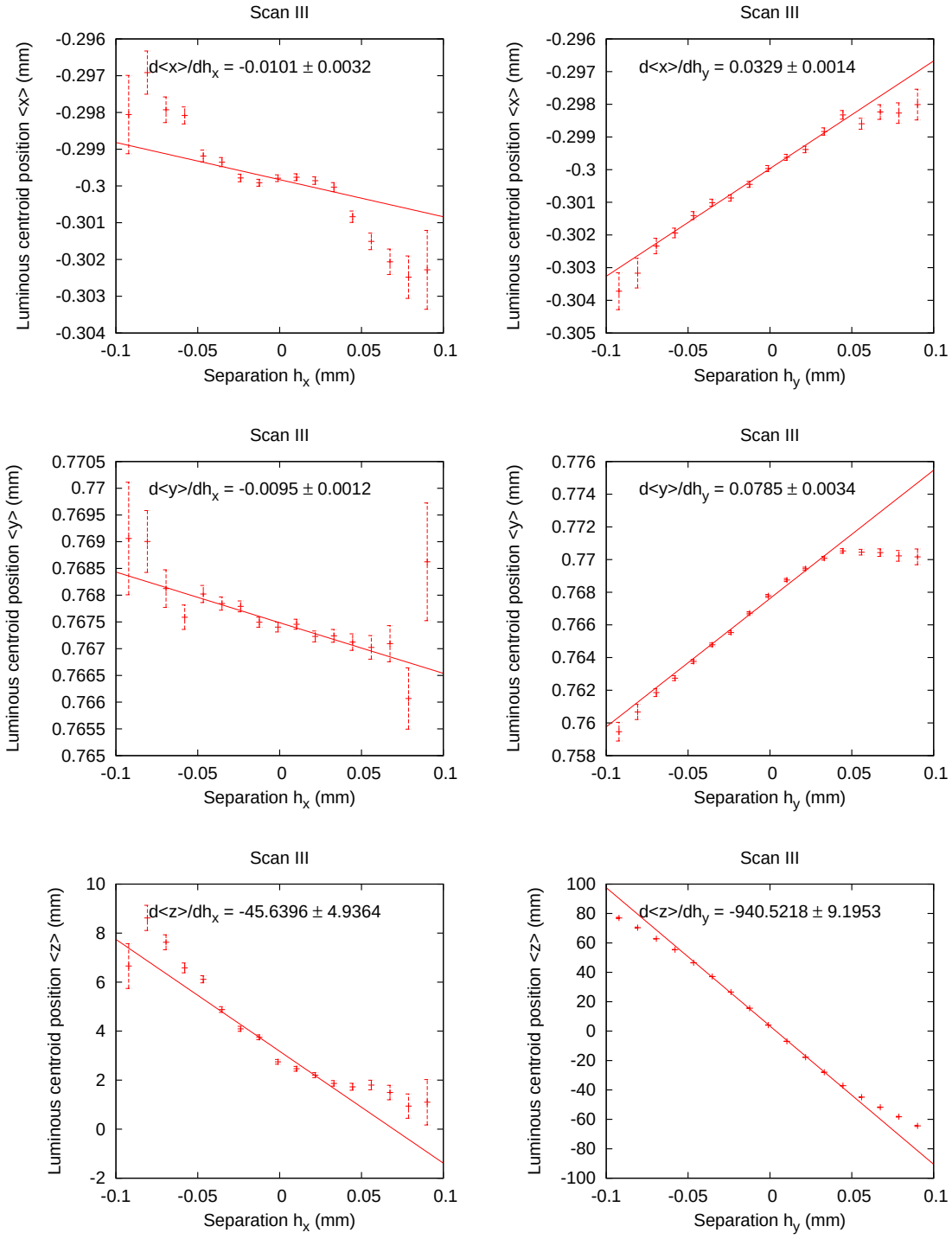

FIGURE 17.8. April 2012 Scan III data. The linear fit is to the central scan points corresponding to separations ≤ 0.05 mm. The errors on the luminous centroid positions are of statistical origin only.

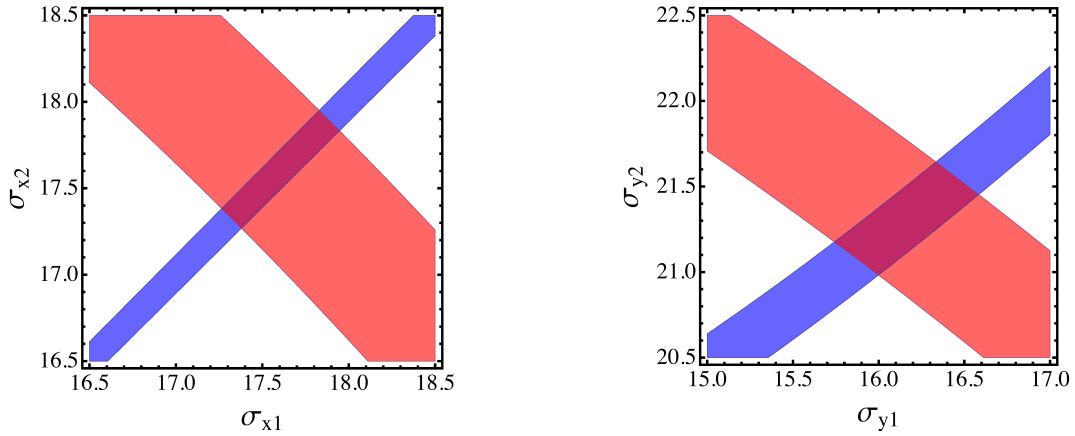

FIGURE 17.9. Individual beam widths for April 2012 scan I. The constraints are determined by a direct comparison between the fitted slopes of Fig. 17.6 with Eqs. E.3 and E.5 in the case of significant beam crossing angle (producing the bands with positive slope) in addition to supplementary information given by the measured values of Σ_x and Σ_y, the convolved beam widths (bands with negative slope). The errors directly represent either the fit errors for the gradients, or the error on the convolved beam width, as explained in the text.

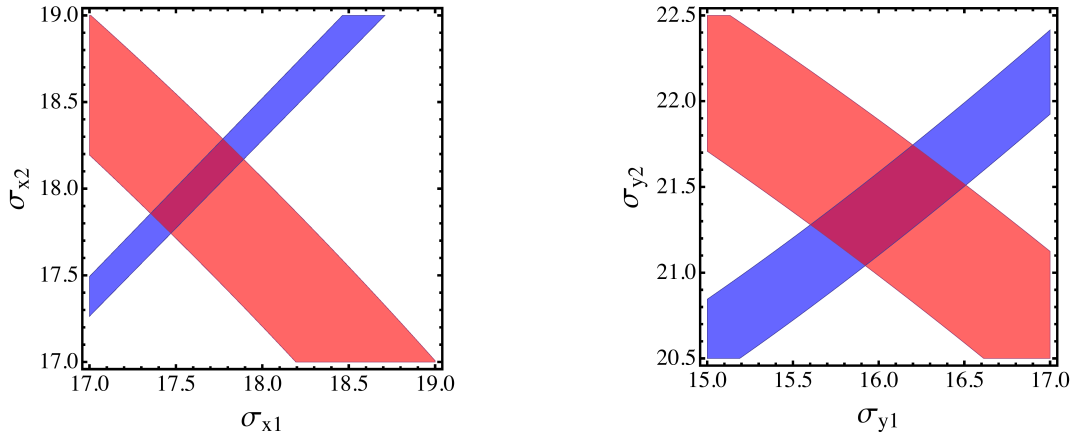

FIGURE 17.10. Individual beam widths for April 2012 scan II. The constraints are determined by a direct comparison between the fitted slopes of Fig. 17.7 with Eqs. E.3 and E.5 (producing the bands with positive slope) in the case of significant beam crossing angle in addition to supplementary information given by the measured values of Σ_x and Σ_y, the convolved beam widths (bands with negative slope). The errors directly represent either the fit errors for the gradients, or the error on the convolved beam width, as explained in the text.

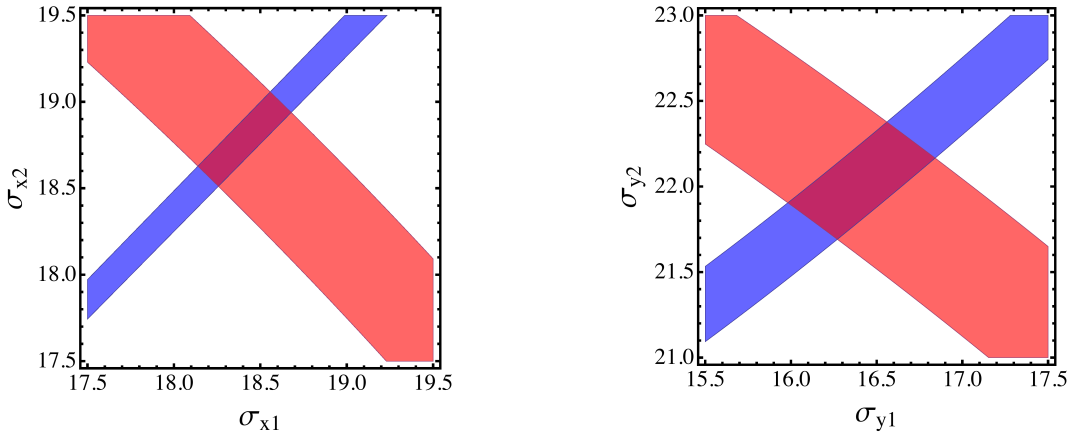

FIGURE 17.11. Individual beam widths for April 2012 scan III. The constraints are determined by a direct comparison between the fitted slopes of Fig. 17.8 with Eqs. E.3 and E.5 (producing the bands with positive slope) in the case of significant beam crossing angle in addition to supplementary information given by the measured values of Σ_x and Σ_y, the convolved beam widths (bands with negative slope). The errors directly represent either the fit errors for the gradients, or the error on the convolved beam width, as explained in the text.

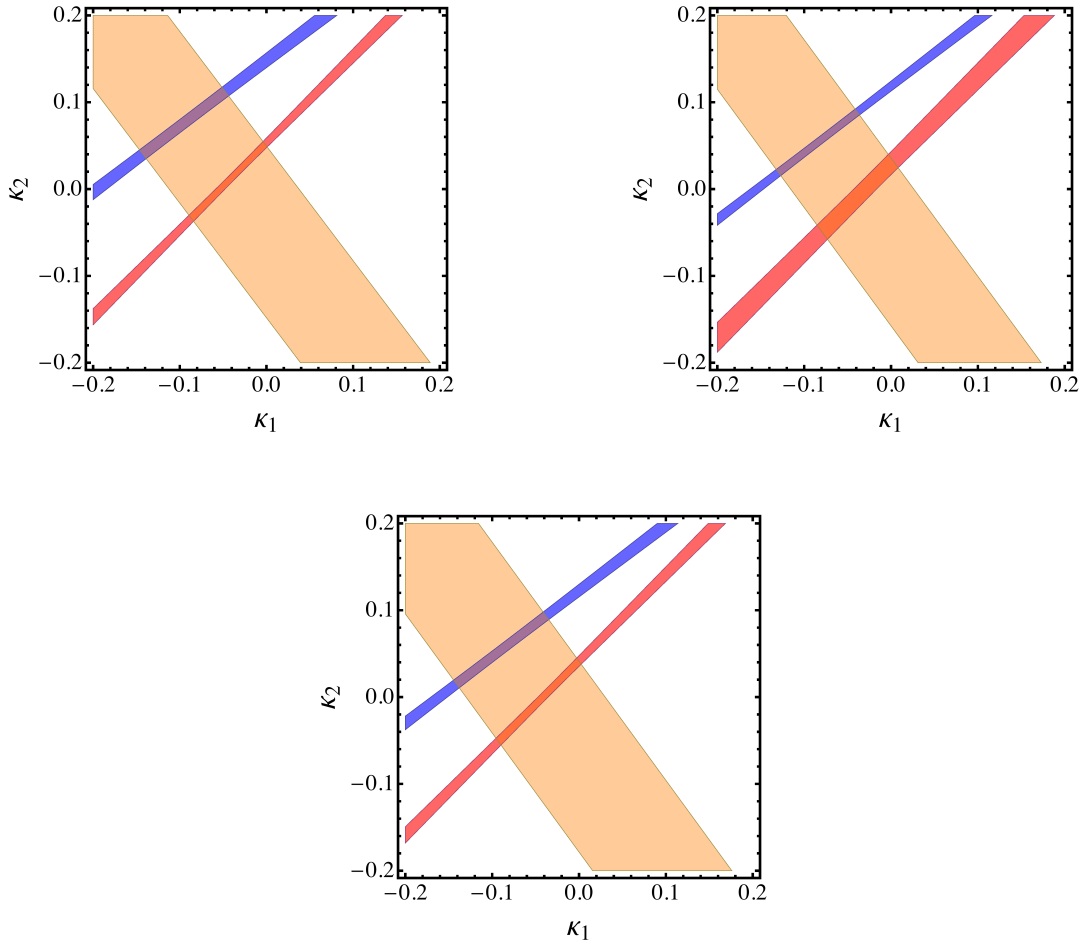

FIGURE 17.12. Correlation coefficient constraints for April 2012 scans I, II and III. The band of negative slope comes from a direct comparison of Eq. 16.15 with the values of $\kappa^{\mathcal{L}}$ measured for the luminous region. The width of the band directly reflects the errors on this measurement. The bands of positive slope come from comparing the analytical expressions for $d\langle x\rangle/dh_y$ and $d\langle y\rangle/dh_x$ in the case of beam crossing angle (Eqs. E.4 and E.6) with the corresponding fitted slopes of Figs. 17.6, 17.7 and 17.8. The widths come from the fit errors, though the errors from the constrained individual beam widths have also been propagated through. The consistency of these constraints is rather poor, compared with March 2011 and July 2012. This is likely to be attributable to the use of a linear model where the data clearly have non-linear features, however, the constraints still point to very small linear x-y coupling, which has negligible impact on the luminosity error.

17.3.3. July 2012. The residual crossing angles for July 2012 were inconsequential again, as corroborated by the last two plots in Figs. 17.13 – 17.18. Indeed, the nominal crossing angles for this set of scans were zero by design. Table 17.4 shows all the input data used and required for the associated linear coupling analysis. One again, the quantities are all BCID-averaged (over X-Y scan *pairs* in the case of $\kappa^{\mathcal{L}}$) with the error quoted as the standard deviation of the values that went into these averages.

There are distinct regions of linear behaviour in the central scan regions, as shown in Figs. 17.13 – 17.18, which is perhaps the reason for good consistency of the finally determined correlation coefficients in Fig. 17.21. The intermediate determination of the individual beam widths is shown in Figs. 17.19 and 17.20. Once again, the errors determined from the individual width constraints are propagated into the plots constraining the values of $\kappa_{1,2}$ for each scan.

The plots are presented in the same way as for March 2011 and April 2012, so the reader is referred to the text in Sec. 17.3.1 for a description. Furthermore, the widths of the constraint bands are also determined in the same way.

TABLE 17.4. Table of input parameters for the July 2012 analysis. Errors on Σ values are standard deviations across all BCIDs, whilst the actual value is taken to be the BCID-average. Errors on $\kappa^{\mathcal{L}}$ values are standard deviations across all scan points with the actual value given by the average across all scan points in a given X-Y scan *pair*.

Parameter	Value
Σ_x^{IV}	$(120 \pm 2)\,\mu$m
Σ_y^{IV}	$(125 \pm 3)\,\mu$m
Σ_x^{V}	$(124 \pm 2)\,\mu$m
Σ_y^{V}	$(128 \pm 3)\,\mu$m
Σ_x^{VI}	$(123 \pm 3)\,\mu$m
Σ_y^{VI}	$(128 \pm 3)\,\mu$m
Σ_x^{VII}	$(144 \pm 4)\,\mu$m
Σ_y^{VII}	$(163 \pm 4)\,\mu$m
Σ_x^{VIII}	$(121 \pm 3)\,\mu$m
Σ_y^{VIII}	$(127 \pm 2)\,\mu$m
Σ_x^{IX}	$(153 \pm 5)\,\mu$m
Σ_y^{IX}	$(180 \pm 7)\,\mu$m
$\kappa_{\mathrm{IV}}^{\mathcal{L}}$	-0.004 ± 0.010
$\kappa_{\mathrm{V}}^{\mathcal{L}}$	-0.002 ± 0.010
$\kappa_{\mathrm{VI}}^{\mathcal{L}}$	-0.003 ± 0.011
$\kappa_{\mathrm{VII}}^{\mathcal{L}}$	0.02 ± 0.08
$\kappa_{\mathrm{VIII}}^{\mathcal{L}}$	-0.001 ± 0.012
$\kappa_{\mathrm{IX}}^{\mathcal{L}}$	0.01 ± 0.12

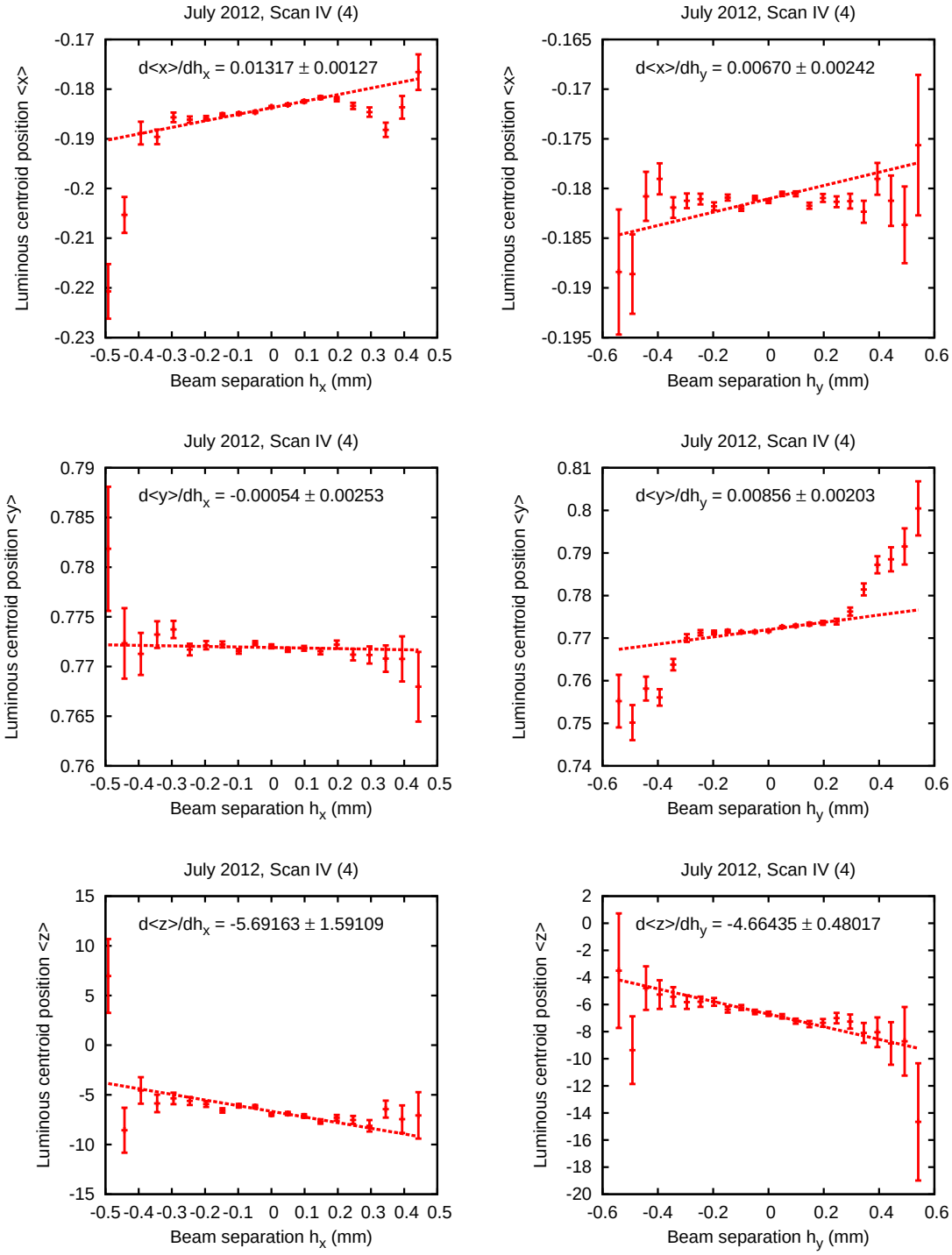

FIGURE 17.13. July 2012 Scan IV data. The linear fit is to the central scan points corresponding to separations $\leq$ 0.1 mm. The errors on the luminous centroid positions are of statistical origin only.

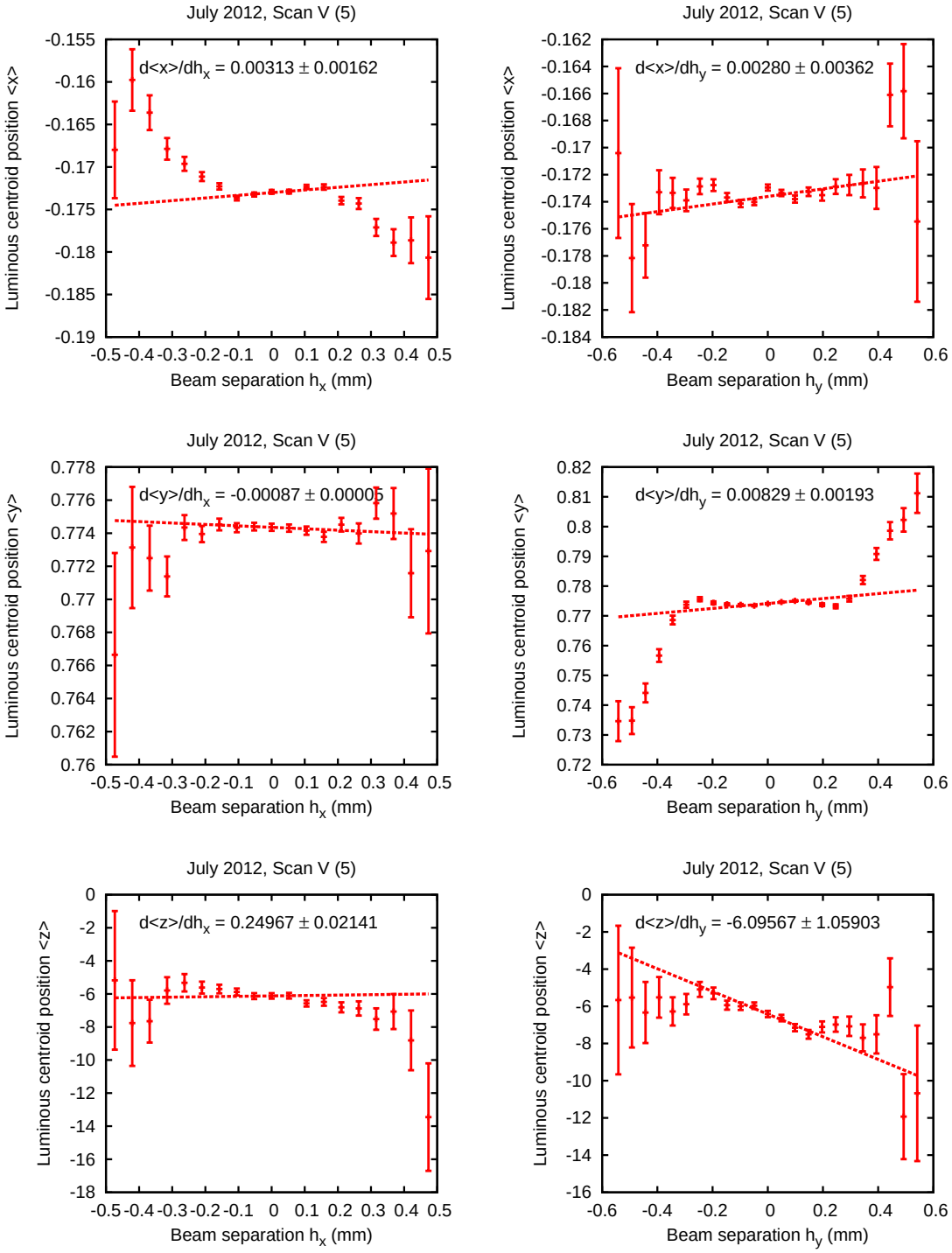

FIGURE 17.14. July 2012 Scan V data. The linear fit is to the central scan points corresponding to separations ≤ 0.1 mm. The errors on the luminous centroid positions are of statistical origin only.

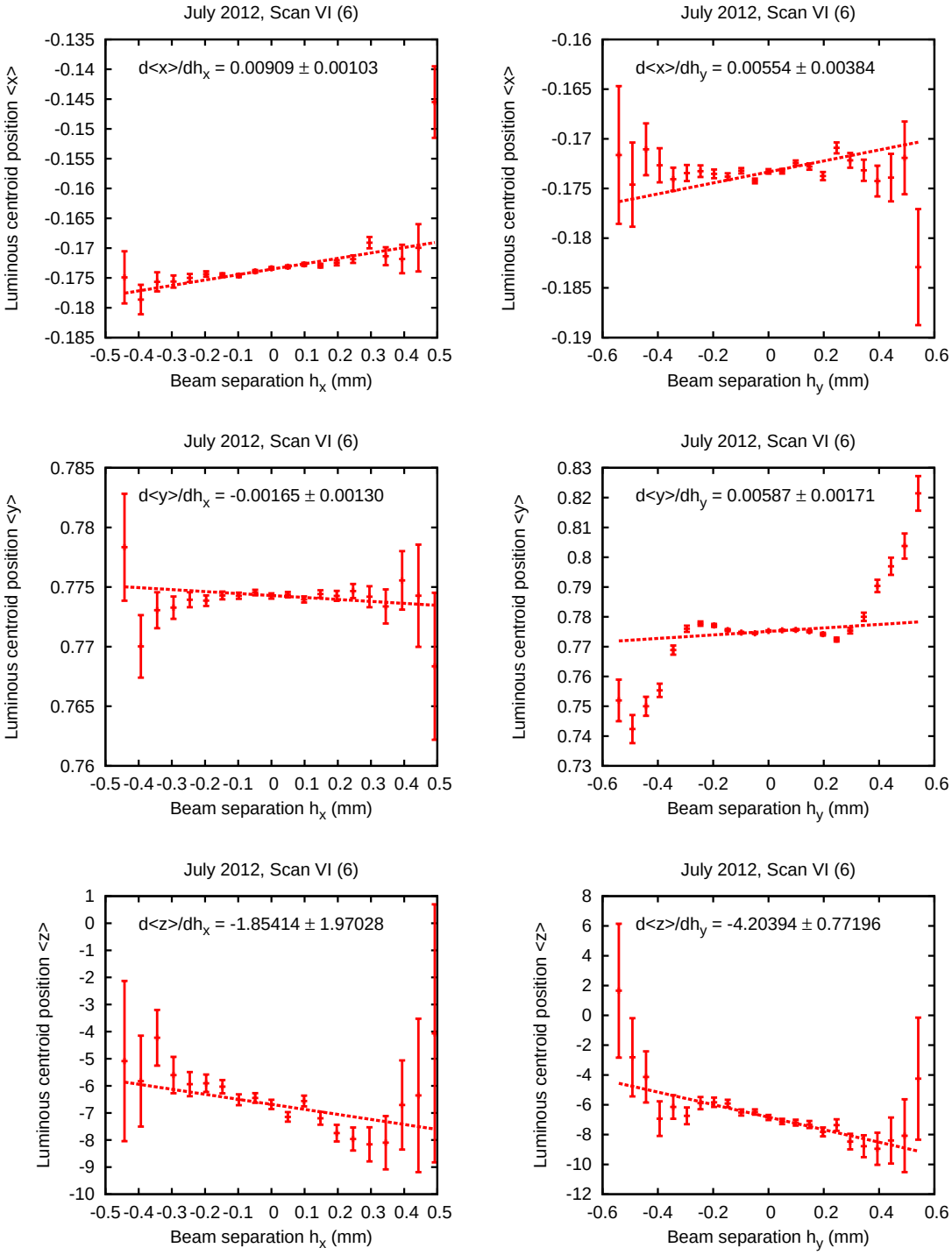

FIGURE 17.15. July 2012 Scan VI data. The linear fit is to the central scan points corresponding to separations $\leq$ 0.1 mm. The errors on the luminous centroid positions are of statistical origin only.

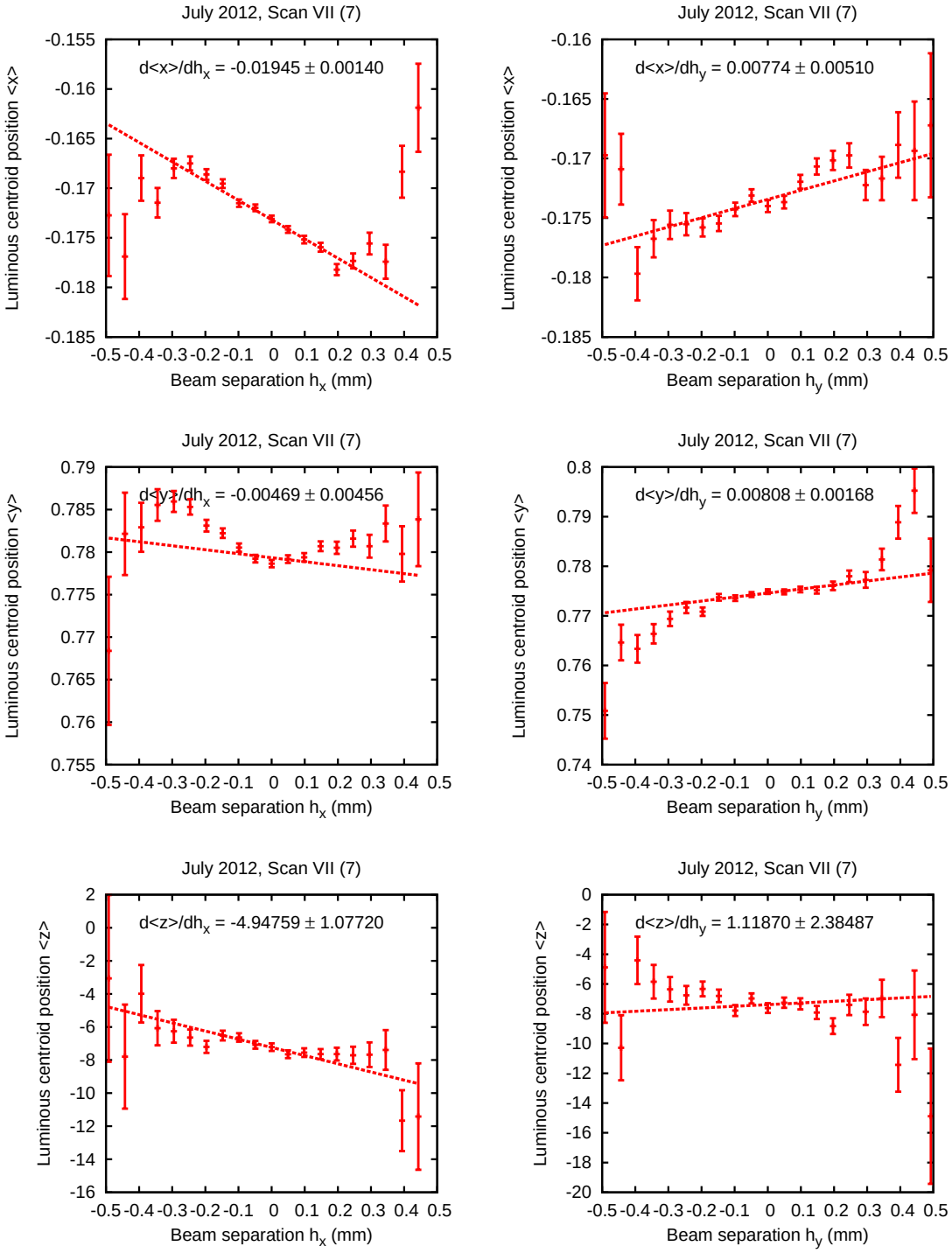

FIGURE 17.16. July 2012 Scan VII data. The linear fit is to the central scan points corresponding to separations ≤ 0.1 mm. The errors on the luminous centroid positions are of statistical origin only.

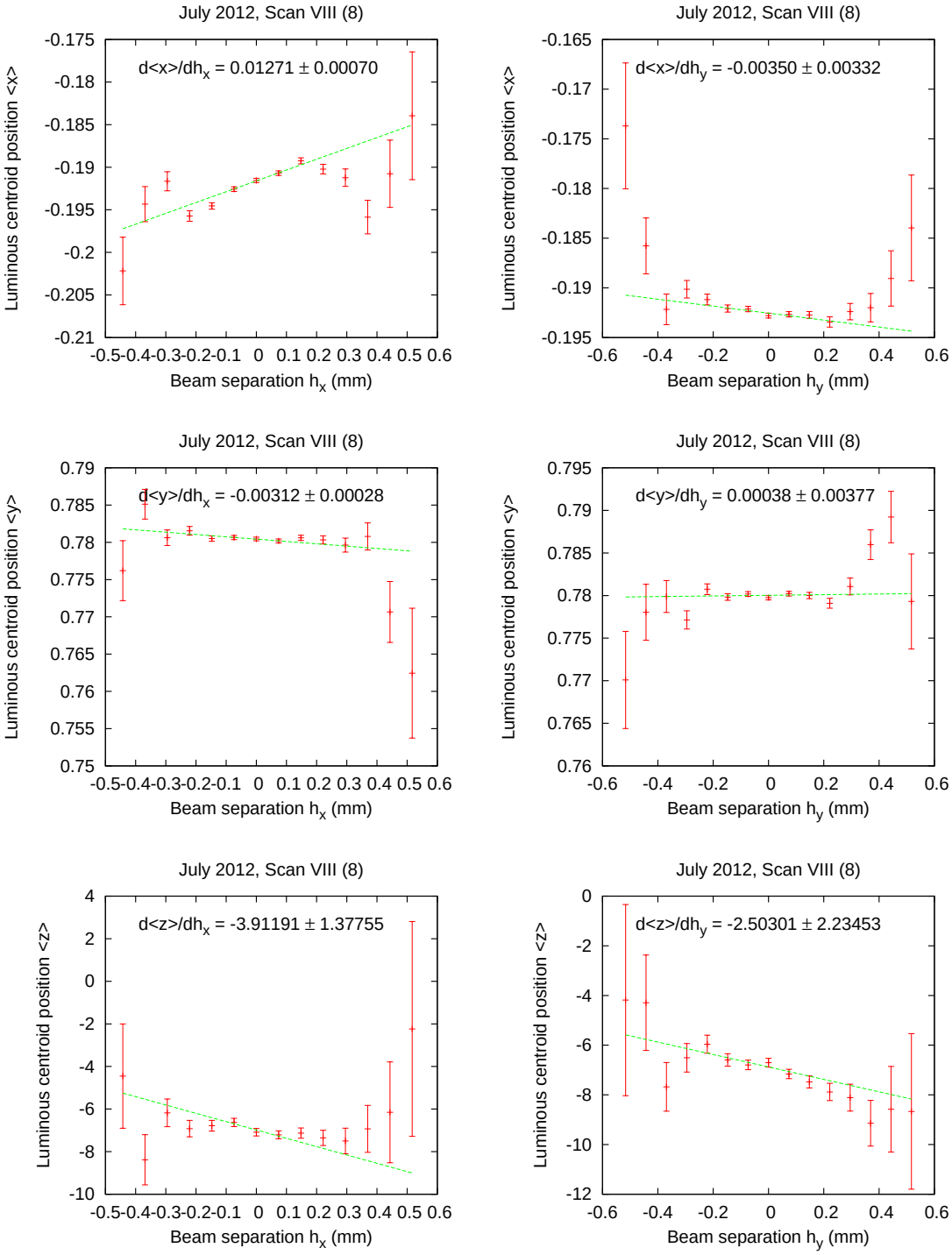

FIGURE 17.17. July 2012 Scan VIII data. The linear fit is to the central scan points corresponding to separations $\leq$ 0.1 mm. The errors on the luminous centroid positions are of statistical origin only.

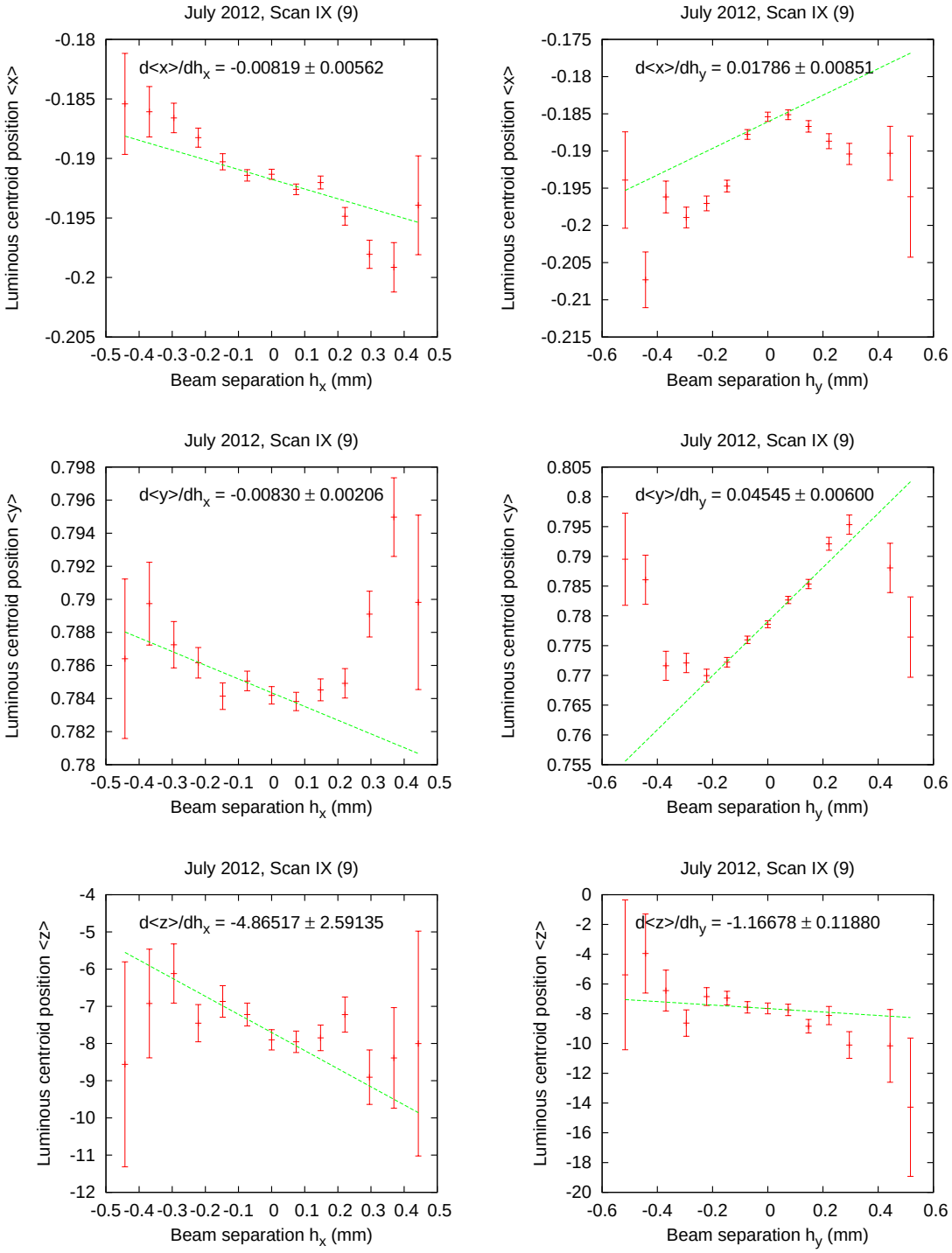

FIGURE 17.18. July 2012 Scan IX data. The linear fit is to the central scan points corresponding to separations ≤ 0.1 mm. The errors on the luminous centroid positions are of statistical origin only.

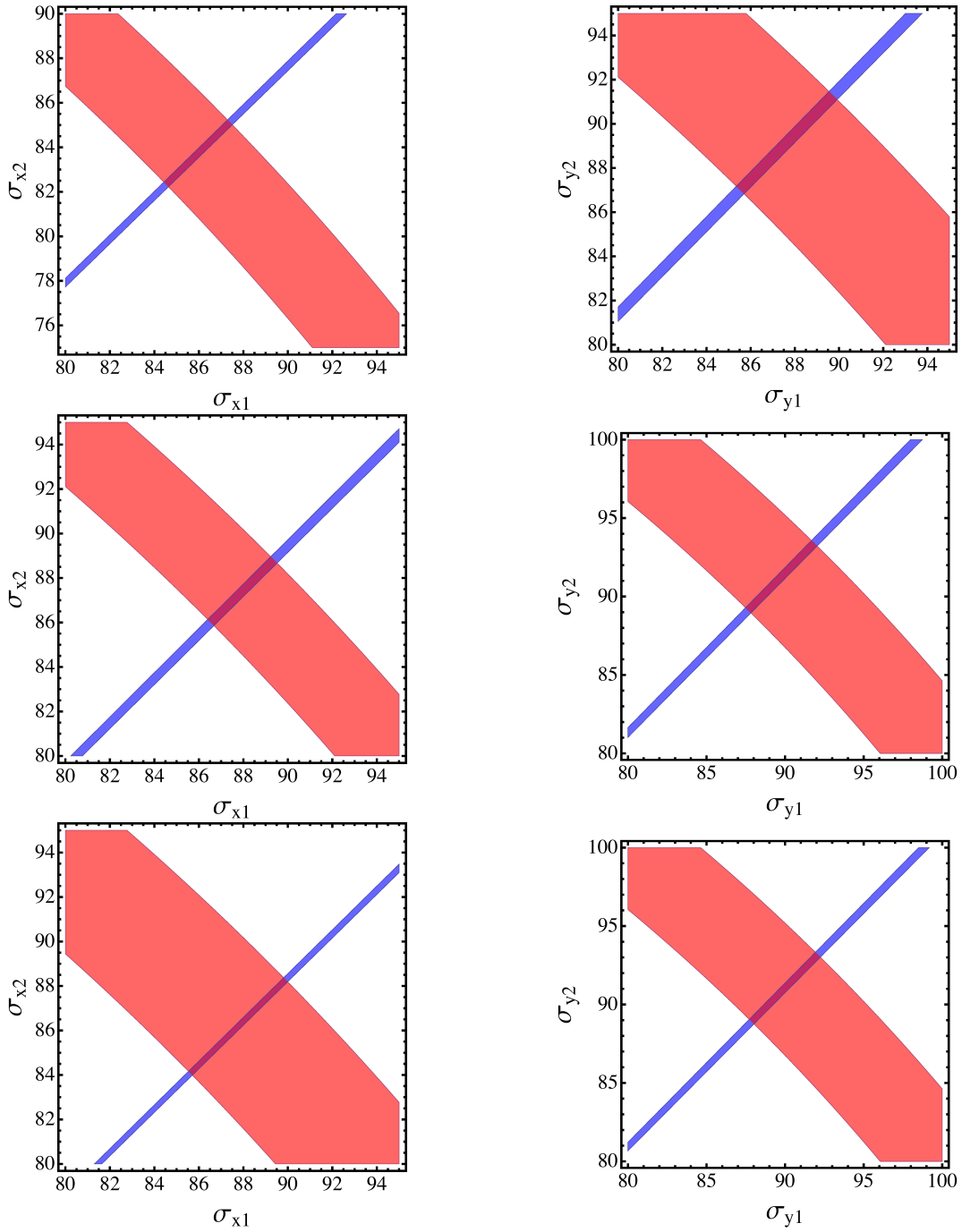

FIGURE 17.19. Constrained individual beam widths for scans IV – VI, performed in July 2012. The constraints are determined by a direct comparison between the fitted slopes of Figs. 17.13, 17.14 and 17.15 with Eqs. 16.10 and 16.13 (producing the bands with positive slope) in addition to supplementary information given by the measured values of Σ_x and Σ_y, the convolved beam widths (bands with negative slope). The errors directly represent either the fit errors for the gradients, or the error on the convolved beam width, as explained in the text.

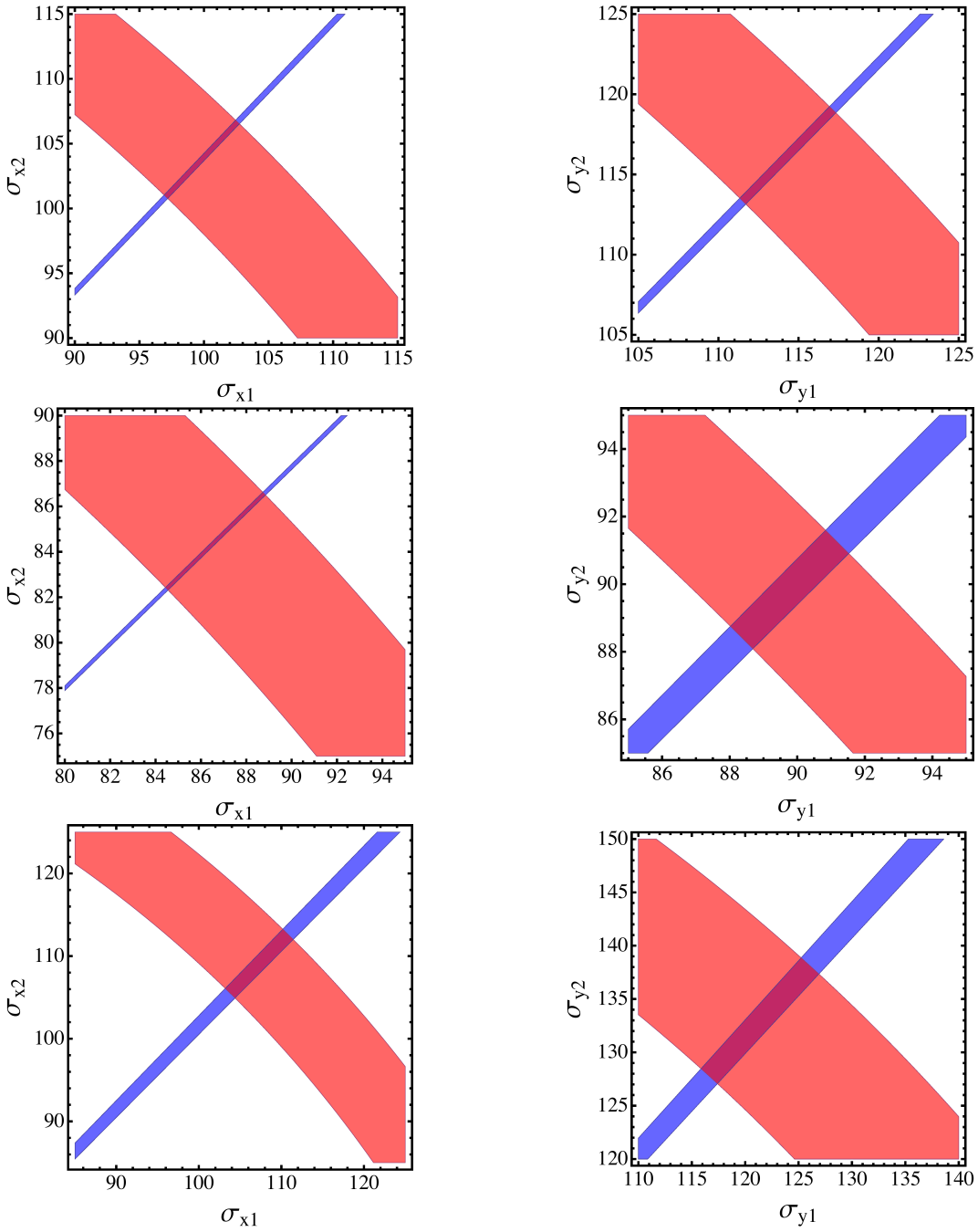

FIGURE 17.20. Constrained individual beam widths for scans VII – IX, performed in July 2012. The constraints are determined by a direct comparison between the fitted slopes of Fig. 17.16, 17.17 and 17.18 with Eqs. 16.10 and 16.13 (producing the bands with positive slope) in addition to supplementary information given by the measured values of Σ_x and Σ_y, the convolved beam widths (bands with negative slope). The errors directly represent either the fit errors for the gradients, or the error on the convolved beam width, as explained in the text.

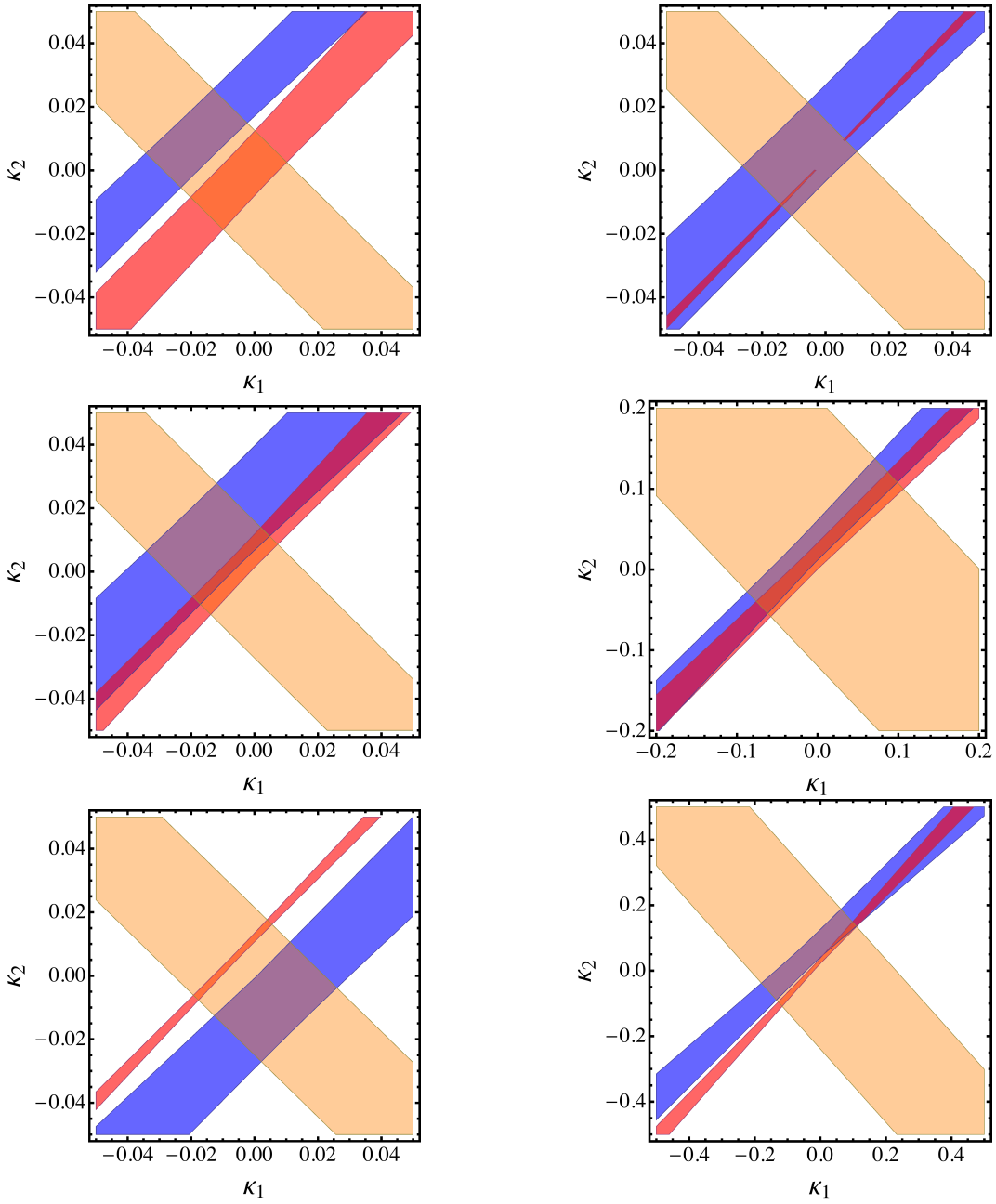

FIGURE 17.21. Constrained individual linear x-y correlation coefficients for scans IV – IX, performed in July 2012. The bands of negative slope come from a direct comparison of Eq. 16.15 with the values of $\kappa^{\mathcal{L}}$ measured for the luminous region. The widths of the bands directly reflect the errors on these measurements. The bands of positive slope come from comparing the analytical expressions for $d\langle x\rangle/dh_y$ (blue) and $d\langle y\rangle/dh_x$ (red) with the corresponding fitted slopes of Figs. 17.13 — 17.18. The widths come from the fit errors and the propagated errors from the constrained individual beam widths.

17.4. Compilation of all vdM scan results

The following tables collect all the results of beam width determinations across in-plane scans from October 2010 to July 2012. Since $\kappa_{1,2}$ values are often determined with inconsistencies present in the relevant constraint plots, they are not tabulated here, and the figures themselves may be used. That said, the values of $\kappa_{1,2}$ have been shown to be consistently negligible as far as the luminosity error is concerned.

TABLE 17.5. October 2010 widths (μm)

Scan	IV	V
σ_{x1}	60.9 ± 1.0	60.6 ± 1.0
σ_{y1}	58.7 ± 1.0	58.7 ± 1.0
σ_{x2}	53.3 ± 1.0	53.8 ± 1.0
σ_{y2}	57.8 ± 1.0	57.8 ± 1.0

TABLE 17.6. March 2011 widths (μm) and correlation coefficients

Scan	I	II
σ_{x1}	166 ± 12	143 ± 11
σ_{y1}	179 ± 14	155 ± 13
σ_{x2}	158 ± 11	140 ± 11
σ_{y2}	173 ± 13	149 ± 12
κ_1	-0.03 ± 0.02	-0.03 ± 0.01
κ_2	0.06 ± 0.02	0.05 ± 0.01

TABLE 17.7. May 2011 widths (μm)

Scan	VII	VIII
σ_{x1}	40.2 ± 1.0	40.2 ± 1.0
σ_{y1}	40.9 ± 1.0	40.9 ± 1.0
σ_{x2}	40.4 ± 1.0	40.4 ± 1.0
σ_{y2}	42.6 ± 1.0	42.6 ± 1.0

TABLE 17.8. April 2012 widths (μm)

Scan	I	II	III
σ_{x1}	17.6 ± 0.3	17.6 ± 0.2	18.4 ± 0.2
σ_{y1}	16.2 ± 0.3	16.0 ± 0.3	16.4 ± 0.3
σ_{x2}	17.6 ± 0.3	18.0 ± 0.2	18.8 ± 0.2
σ_{y2}	21.3 ± 0.2	21.4 ± 0.2	22.0 ± 0.2

TABLE 17.9. July 2012 widths (μm) and correlation coefficients

Scan	IV	V	VI	VII	VIII	IX
σ_{x1}	86.0 ± 1.4	88.0 ± 1.4	87.9 ± 2.0	99.9 ± 2.7	86.6 ± 2.2	107 ± 4
σ_{y1}	87.9 ± 1.9	89.9 ± 1.9	89.9 ± 2.1	115 ± 3	89.9 ± 1.3	121 ± 5
σ_{x2}	83.8 ± 1.4	87.4 ± 1.4	86.2 ± 2.1	104 ± 3	84.4 ± 2.2	109 ± 4
σ_{y2}	89.3 ± 2.1	91.4 ± 2.0	91.1 ± 2.1	116 ± 3	90.0 ± 1.3	133 ± 5
κ_1	-0.01 ± 0.02	-0.01 ± 0.02	-0.01 ± 0.02	0.02 ± 0.05	0 ± 0.02	0 ± 0.02
κ_2	0 ± 0.02	0 ± 0.02	0 ± 0.02	0.02 ± 0.05	0 ± 0.02	0 ± 0.02

The transverse size of a single beam may be written in terms of the normalized emittance ϵ_{N}, the value of the interaction-point beta function β^*, and the Lorentz factor of the beam particles γ, as

$$\sigma_{\mathrm{b}} = \sqrt{\frac{\epsilon_{\mathrm{N}}\,\beta^*}{\gamma}}\,, \tag{17.14}$$

with γ determined simply from $E = \gamma mc^2$, taking $m = m_{\mathrm{proton}}$ and $E = E_{\mathrm{beam}}$. It should be noted that the individual beam widths determined in this manner are indeed only very approximate, owing to the combination of instrumental systematics and beta function uncertainties which together are at the $\pm 20\%$ level. Nonetheless, it is interesting to compare the width results listed in Tables 17.5—17.9 above with the widths determined from Eq. 17.14 taking the *design* emittance $\epsilon_{\mathrm{N}} = 3.75\,\mu\mathrm{m} \cdot \mathrm{rad}$ and the nominal beta functions. The results are collected in Table 17.10 for comparison.

TABLE 17.10. Approximate individual beam widths determined from the LHC design emittance and nominal beta functions.

Scan	β^* (m) [nominal]	E_{beam} (TeV)	γ	σ_{b} (μm) [approx.]
October 2010	3.5	3.5	3730	59
March 2011	11	3.5	3730	105
May 2011	1.5	3.5	3730	39
April 2012	0.6	4	4263	23
July 2012	11	4	4263	98

17.5. Discussion of results and conclusions

An obvious shortcoming of the analysis presented here is that it is BCID blind. Concurrent studies within ATLAS have shown that the corresponding plots showing the movement of the luminous centroid during a scan vary from one colliding BCID to the next. A more thorough analysis would repeat the procedure but on a BCID-specific level.

We can derive a rough estimate the uncertainty on the determination of the individual beam widths, owing to this bunch-by-bunch averaging, by appealing to the variation in the convolved beam widths Σ determined on a bunch-by-bunch basis from the vdM scans. Making the approximation that beams 1 and 2 are of equal width σ (in either direction) we have the relation $\Sigma = \sqrt{2}\,\sigma$. We consequently have $\delta\sigma = \delta\Sigma/\sqrt{2}$, where δ denotes the

uncertainty on the given quantity. Considering, for example, the October 2010 scans, we took $\delta\Sigma = 1\,\mu$m which implies $\delta\sigma \approx 0.7\,\mu$m. A typical individual beam width determined for these scans is $\sigma \approx (60 \pm 1)\,\mu$m, therefore implying an additional uncertainty at the $0.7/60 \approx 1\%$ level.

This study is indicative of negligibly small *linear* x-y correlations in all of the scans considered, and therefore it is predicted that these correlations should have little impact on the determination of the error of the respective luminosity calibrations, as shown explicitly for October 2010 and May 2011 scans in Chap. 16 (also [**115**]). *Non-linear* effects do still have a large impact.

It would be interesting to see if SMOG data from LHCb were consistent with the beam asymmetry indicated in Table 17.8.

A general remark, regarding the error analysis, is that the errors on the luminous centroid positions (e.g. in Fig. 17.18, but indeed for all such plots in this thesis) are entirely statistical in nature, and systematics due to vertex resolution, for example, are *not* included. Furthermore, the quoted errors on Σ values in all cases are the standard deviations across all bunches in the fill, for a given scan, and therefore do not contain systematics either. Furthermore, the distance scale error, $\lesssim 1\%$, is also assumed to be negligible throughout this analysis.

It has already been stated that the single-Gaussian model is incapable of describing the non-linear data seen in many of the vdM scans, since this model generates only linear predictions for the movement of the luminous centroid with respect to beam separation. Nonetheless, the single-Gaussian formalism remains important, for several reasons:

- The analytic solubility of the model offers a lot of intuition about the expected behaviour of the luminous centroid movements, in the presence of x-y correlation, beam crossing angles, and asymmetric beam sizes. Furthermore, it provides insight as to which parameters are important in describing the salient phenomena, and especially where certain approximations are valid, allowing one to make progress with extracting individual beam information from knowledge only of the movement of the maximum of the convolved bunch densities.
- It offers a robust method for confining a region of parameter space that, when substituted into the model, reproduce the central scan data in the large number of cases where these data are linear.
- More sophisticated models may not offer the luxury of a fully analytical solution, so numerical methods must be sought. Extensions to the single-Gaussian model will in general have much larger parameter spaces (often at least double in dimensionality) and may thus require significant computing time. The results of the single-Gaussian model may be used as a starting point in parameter space for improvement and optimization in a more sophisticated numerical model.

It is hoped that the compilation of results in Sec. 17.4 will prove to be useful for either current or future analyses of the vdM scan data. The current issue for the luminosity error may now be restated: $\kappa_{1,2}$ values tend to be inconsequential, but the non-linear tails present in the data give rise to new problems. The *principal* aim of this analysis

has therefore changed from just determining the linear correlation coefficients. Now it is hoped that the analytical formalism itself may be used in finding good starting points for future vdM scans in experiments across the LHC.

During the writing of the original note for this analysis, a note has become available which the reader here may wish to consult [**124**].

CHAPTER 18

Concluding remarks

I have approached my studies within the *ATLAS luminosity measurement task force* from an analytical perspective, in order to complement numerical studies also performed within the group. It is quite clear that, while an analytical approach can only take us so far in terms of yielding a solution to a given model, it certainly offers much insight for such soluble models, beyond that of a purely numerical analysis. Contrarily, while a purely numerical approach may not rigorously expound the interplay between various properties of the beams and its manifestation as salient beamspot phenomena, it certainly allows us to obtain results for models of far greater complexity than the single-Gaussian model studied in this thesis would permit. It is my hope that the analytical methods I have developed will continue to complement future numerical studies and provide insight for the study of more complicated models, which the data clearly demand.

The single-Gaussian model is a *linear* model, in that it is capable of describing only those phenomena pertaining to the movements of the luminous centroid which are linear functions of beam separation. The data clearly display non-linear 'tails' however. A particularly beautiful example of this is the horizontal luminous centroid position vs. horizontal beam separation, for Scan 2 data of March 2011 (see Fig. 18.1).

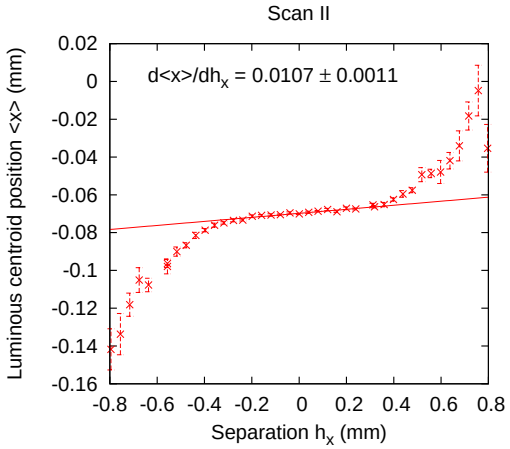

FIGURE 18.1. An example of non-linear tails in beamspot data: The horizontal luminous centroid position vs. horizontal beam separation for Scan 2 of March 2011

Fitting exclusively to the tails of these data, as opposed to the central scan region, it is clear we would determine different values for the individual beam parameters. A model that has received much numerical scrutiny is the so-called 'double-Gaussian' model, in

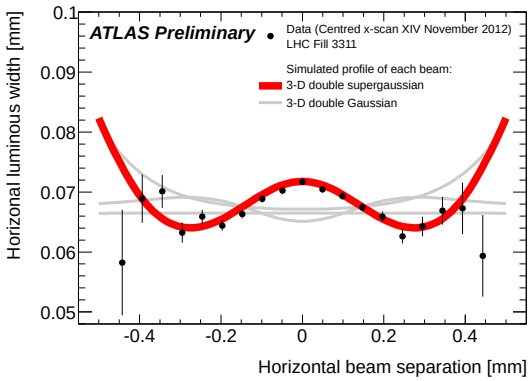

FIGURE 18.2. Data calling for a model beyond Gaussians: The horizontal luminous width vs. horizontal beam separation for Scan 14 of November 2012 [**112**]

which the individual beams are modelled according to the weighted sum of two Gaussians, as

$$\rho(x;\sigma_1,\sigma_2,w) = w\,\rho_1(x;\sigma_1) + (1-w)\,\rho(x;\sigma_2)\,, \tag{18.1}$$

where $\rho_i(x;\sigma_i)$ is a Gaussian function of width σ_i—for the three dimensional case, we consider a position vector $\vec{x}$ and a covariance matrix $\underline{\sigma}_i$. Typically one Gaussian is taken to be 'wide' while the other is taken to be 'narrow'. In this case, the narrow Gaussian then controls the dynamics of the beamspot phenomena at small scan separations, and is therefore analogous to the single-Gaussian, while the wide Gaussian has different parameters and controls the dynamics of the beamspot phenomena in the tails of the scan data. In principle, the transition between the two régimes is therefore smooth, as is observed in the data.

A significant shortcoming of the double-Gaussian model is the multiplicity of the parameter space, which more-than-doubles: we require an additional set of parameters describing the second Gaussian, along with a weight, for each beam. I have described ways in which the parameters may be decoupled from one-another, namely by focusing exclusively on central scan data and high-separation scan data separately which, one might hope, would mitigate this complication to a significant extent. Arbitrarily many Gaussians may be added together in this manner, but it is far from clear that this would be a sensible approach, given the aforementioned considerations. Already, the double-Gaussian model places us in a situation where an analytical approach has not yet offered exact solutions for the various beamspot phenomena—although I have studied the double-Gaussian model to quite some extent in this manner in order to identify the specific problems—so the bulk of study has been largely numerically driven.

A particularly interesting phenomenon is presented in Scan 14 data of November 2012 although it is by no means exclusive to these data. The grey curves in Fig. 18.2 are produced within the framework of the double-Gaussian model, and are various attempts to model all data points simultaneously *by hand*. The take-home point is that the double-Gaussian is incapable of modelling a significant feature of the data: the width of the luminous region *decreases* as the beams become separated. The kurtosis of a distribution is

a measure of how it bulges[1], with a Gaussian having a kurtosis of precisely zero. Gaussians have the remarkable property that the width of a product of two Gaussians is independent of their relative separation.

The product of two *double*-Gaussians may have a width which varies as the relative separation of the double-Gaussians varies, owing to the non-zero kurtosis of the double-Gaussian. However, this width may only ever *increase* with increasing separation, since the sum of two (different) Gaussians is *platykurtic*; i.e. broader than a Gaussian. In order for the width of the product of two functions to *decrease* with increasing relative separation, we require they be *leptokurtic*; i.e. narrower than a Gaussian. For this reason I have proposed a modification to the single-Gaussian model, introducing a new parameter ϵ, which directly modifies the kurtosis of the original Gaussian:

$$\rho(x;\sigma,\epsilon) = \mathcal{N}\,\exp\left[-\frac{1}{2}\left(\frac{|x|}{\sigma}\right)^{2+\epsilon}\right] \tag{18.2}$$

This function apparently carries the name 'super-Gaussian' [**125**]. For $\epsilon > 0$ the function becomes leptokurtic, and for $\epsilon < 0$ it becomes platykurtic. It is interesting to note the limit $\epsilon \to \infty$ yields the top-hat function, with the piecewise definition

$$\rho(x;\sigma,\epsilon) = \begin{cases} 1 & \text{for } |x| < \sigma \\ 0 & \text{for } |x| > \sigma \end{cases} \tag{18.3}$$

The function has since been used as a candidate model of beam profiles in numerical simulations, and the red curve in Fig. 18.2 shows the striking agreement with data that may be achieved for a suitable choice of ϵ. It would appear that certain non-linear phenomena may be adequately described with the introduction of only a single new parameter. It would undoubtedly be very interesting to learn of a potential reason, rooted in accelerator physics, as to why this functional form for the beam profiles might be anticipated.

[1]Etymology: modern Latin, < Greek κύρτωσις a bulging, convexity, < κυρτός bulging, convex. Source: Oxford English Dictionary

APPENDIX A

Explicit calculations

The calculations presented in this appendix follow those given in [**35, 60, 126**], and are reproduced here for the benefit of the reader.

A.1. Drell–Yan in the Born approximation

The incoming partons have momenta $p_1 = (E, \mathbf{p})$ and $p_2 = (E, -\mathbf{p})$ since the collision is collinear and the scattering is considered in a frame where the incoming partons have equal energies. Finally, the scattering energy is defined by $s := (p_1 + p_2)^2$ and so we deduce $2E = \sqrt{s}$.

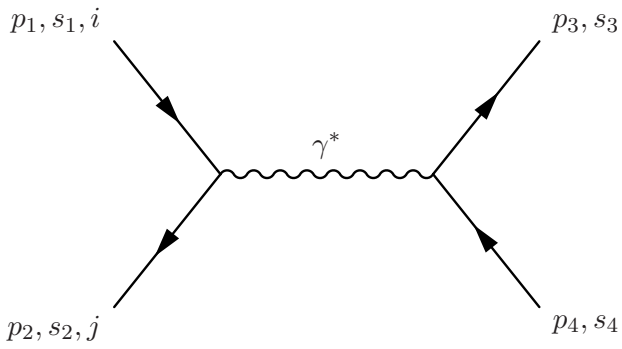

FIGURE A.1. The partonic amplitude for the Drell-Yan process in the Born approximation. Only the process in which a virtual photon, γ^*, is exchanged is considered for the sake of simplicity.

Figure A.1 shows the partonic Feynman diagram for the Drell-Yan process at $\mathcal{O}\left(\alpha^2\right)$, corresponding to the Born approximation. The amplitude corresponding to this diagram may be written down using the tree-level Feynman rules, Fig. 2.1, and one obtains

$$\mathcal{M}_0 = i\, Q_f\, (e\, \mu^\epsilon)^2\, \delta_{ij}\, \frac{1}{q^2}\, \bar{u}_3\, \gamma^\alpha\, v_4\, \bar{v}_2\, \gamma_\alpha\, u_1, \tag{A.1}$$

where $q = p_1 + p_2 = p_3 + p_4$, and u_1, $\bar{v}_2$, $\bar{u}_3$ and v_4 are shorthand for the Dirac spinors $u_1(p_1, s_1)$, $\bar{v}_2(p_2, s_2)$, $\bar{u}_3(p_3, s_3)$ and $v_4(p_4, s_4)$ respectively, where $p_{1,\ldots,4}$ are momenta, $s_{1,\ldots,4}$ label spin quantum numbers and the Roman indices label quark and anti-quark colours. The arbitrary mass scale μ has been introduced to retain a dimensionless coupling e. It is possible to drop the $i\epsilon$ prescription in the photon propagator, given that $q^2 \neq 0$, ever. Furthermore, the calculation proceeds in $d = 4 - 2\epsilon$ space-time dimensions, in order to provide a regularization scheme for divergent integrals that we anticipate will appear when

one considers $\mathcal{O}(\alpha_\mathrm{s})$ corrections. The complex conjugate amplitude, relabelling dummy indices so as to avoid ambiguity, is therefore

$$\mathcal{M}_0^\dagger = -i\,Q_f\,(e\,\mu^\epsilon)^2\,\delta_{ij}\,\frac{1}{q^2}\,\bar{v}_4\,\gamma^\beta\,u_3\,\bar{u}_1\,\gamma_\beta\,v_2, \tag{A.2}$$

where an obvious extension of the aforementioned spinor shorthand has been used. The squared amplitude for the partonic process depicted in Fig. A.1 therefore becomes

$$\begin{aligned}|\mathcal{M}_0|^2 = Q_f^2\,(e\,\mu^\epsilon)^4\,\delta_{ij}^2\,\frac{1}{q^4} \\ \times\mathrm{Tr}\big[u_1\,\bar{u}_1\,\gamma_\beta\,v_2\,\bar{v}_2\,\gamma_\alpha\big]\mathrm{Tr}\big[u_3\,\bar{u}_3\,\gamma^\alpha\,v_4\,\bar{v}_4\,\gamma^\beta\big],\end{aligned} \qquad \text{(no summation on } i,j) \tag{A.3}$$

after writing the spinor–matrix products inside traces then exploiting the freedom of cyclic permutation permitted by traces. Since the goal is to obtain the inclusive and unpolarized cross-section, one now averages initial spins and colours, and sums over final spins, as such:

$$\begin{aligned}\overline{|\mathcal{M}_0|^2} &= \left(\frac{1}{2}\sum_{s_1}\frac{1}{2}\sum_{s_2}\right)\left(\sum_{s_3}\sum_{s_4}\right)\left(\frac{1}{N_\mathrm{c}}\sum_{i=1}^{N_\mathrm{c}}\frac{1}{N_\mathrm{c}}\sum_{j=1}^{N_\mathrm{c}}\right)|\mathcal{M}_0|^2 \\ &= \frac{1}{N_\mathrm{c}}\,\frac{Q_f^2\,(e\,\mu^\epsilon)^4}{4\,q^4}\,\mathrm{Tr}\big[\not{p}_1\,\gamma_\beta\,\not{p}_2\,\gamma_\alpha\big]\mathrm{Tr}\big[\not{p}_3\,\gamma^\alpha\,\not{p}_4\,\gamma^\beta\big] \\ &= \frac{1}{N_\mathrm{c}}\,\frac{Q_f^2\,(e\,\mu^\epsilon)^4}{4\,q^4}\,Q_{\alpha\beta}\,L^{\alpha\beta}.\end{aligned} \tag{A.4}$$

In the second line, the completeness relations for spinors (in the massless limit) have been used:

$$\sum_s u(p,s)\,\bar{u}(p,s) = \not{p} + m \qquad \text{and} \qquad \sum_s v(p,s)\,\bar{v}(p,s) = \not{p} - m\,. \tag{A.5}$$

Using standard techniques, the traces are evaluated and become

$$Q_{\alpha\beta} = 4\big[p_{1\alpha}\,p_{2\beta} + p_{1\beta}\,p_{2\alpha} - p_1\cdot p_2\,g_{\alpha\beta}\big] \tag{A.6}$$

and

$$L^{\alpha\beta} = 4\big[p_3^\alpha\,p_4^\beta + p_3^\beta\,p_4^\alpha - p_3\cdot p_4\,g^{\alpha\beta}\big]. \tag{A.7}$$

Our aim for this calculation is to compute the total cross-section and, for that, we will make a simplifying assumption. We assume that the lepton tensor may be decomposed as follows:

$$L^{\alpha\beta} = (A\,q^2\,g^{\alpha\beta} + B\,q^\alpha\,q^\beta)L(q^2); \tag{A.8}$$

i.e. it depends only on the momentum $q = p_3 + p_4$. We will discuss the validity of this decomposition further, below. We will not be differential in the individual directions of the outgoing leptons this way, but this is not necessary if we are seeking the total cross-section anyway. To conserve current,

$$q_\alpha\,L^{\alpha\beta} = q_\beta\,L^{\alpha\beta} = 0, \tag{A.9}$$

we require $B = -A$ and we pick $A = 1$ and $B = -1$. Furthermore, since the quark traces must themselves obey current conservation, $q^\alpha\,Q_{\alpha\beta} = q^\beta\,Q_{\alpha\beta} = 0$, only the term

proportional to $g^{\alpha\beta}$ in $L^{\alpha\beta}$ contributes to

$$L^{\alpha\beta}\,Q_{\alpha_\beta} = q^2\,g^{\alpha\beta}\,Q_{\alpha\beta}\,L(q^2) \tag{A.10}$$

and, therefore, it is only necessary to compute the trace, Q^α_α. This will significantly simplify the algebra when we come to computing traces for the real and virtual corrections. The traces of these tensors are, using Eqs. A.6 and A.7,

$$\begin{aligned} g_{\alpha\beta}\,L^{\alpha\beta} &= 2\,(2-d)\,q^2 \\ &= g_{\alpha\beta}\,(q^2\,g^{\alpha\beta} - q^\alpha\,q^\beta)\,L(q^2) = q^2\,(d-1)\,L(q^2) \\ \Rightarrow \qquad q^2\,L(q^2) &= \frac{2\,(2-d)\,q^2}{d-1} \end{aligned} \tag{A.11}$$

and

$$Q^\alpha_\alpha = 2\,(2-d)\,q^2, \tag{A.12}$$

and therefore

$$L^{\alpha\beta}\,Q_{\alpha\beta} = \frac{4\,(2-d)^2\,q^4}{d-1}. \tag{A.13}$$

It is now time to consider the two-body phase-space in d dimensions. It is a direct generalization of the usual two-body phase-space in 4D and is written, using $q = p_3 + p_4$,

$$d\mathrm{PS}_2 = \int (2\pi)^d\,\delta^d(p_3 + p_4 - q)\,\frac{d^{d-1}\mathbf{p}_3}{(2\pi)^{d-1}2E_3}\,\frac{d^{d-1}\mathbf{p}_4}{(2\pi)^{d-1}2E_4}. \tag{A.14}$$

d of the integrals are somewhat trivial because, in collaboration with the d-dimensional δ function, they amount to overall energy and momentum conservation. However, it is good to perform these integrals in a manifestly covariant manner using the identity

$$\int dp_0\,\delta(p^2 - m^2)\,\theta(p_0) = \frac{1}{2E(\mathbf{p})}, \tag{A.15}$$

where $\theta(p_0)$ is the Heaviside step function. The two-body phase-space may now be written

$$\begin{aligned} d\mathrm{PS}_2 &= 2\pi \int \delta^d(p_3 + p_4 - q)\,\frac{d^{d-1}\mathbf{p}_3}{(2\pi)^{d-1}2E_3}\,d^d p_4\,\delta(p_4^2)\,\theta(p_{4,0}) \\ &= 2\pi\,\frac{d^{d-1}\mathbf{p}_3}{(2\pi)^{d-1}2E_3}\,\delta\left((q-p_3)^2\right), \end{aligned} \tag{A.16}$$

after integrating over p_4. Since the quantity $(q-p_3)^2$ is Lorentz-invariant, we may evaluate it in any frame. The frame in which $q = (M, \mathbf{0})$ is particularly useful, so $(q-p_3)^2 = M^2 - 2ME_3$. Now $\delta\big((q-p_3)^2\big) = \delta(E_3 - M/2)/2M$. Further rewriting the integral measure for $\mathbf{p}_3$ in terms of polar coordinates in d dimensions, i.e.

$$d^{d-1}\mathbf{p}_3 = |\mathbf{p}_3|^{d-2}\,d|\mathbf{p}_3|\,d\Omega_{d-2} = E_3^{d-2}\,dE_3\,d\Omega_{d-2}, \tag{A.17}$$

we obtain

$$d\mathrm{PS}_2 = \frac{M^{d-2}\,d\Omega_{d-2}}{(4\pi)^{d-2}\,2M^2}\,, \tag{A.18}$$

after integrating over E_3. Finally, introducing the flux factor for collinear particle scattering

$$\frac{1}{F} = \frac{1}{2s}, \tag{A.19}$$

where $s = (p_1 + p_2)^2$, we have all the pieces we need to write down the inclusive partonic cross-section:

$$d\hat{\sigma}_0 = \frac{1}{F}\,\overline{|\mathcal{M}|^2}\,d\mathrm{PS}_2\,. \tag{A.20}$$

The phase-space integral over the surface of the $(d-2)$-sphere[1] may be evaluated immediately, and is a standard result:

$$\int d\Omega_{d-2} = \frac{2\pi^{(d-1)/2}}{\Gamma\left(\frac{d-1}{2}\right)}, \tag{A.21}$$

since the matrix element does not depend upon the angles of the outgoing leptons, according to our simplification of the tensor product, and so

$$\int d\mathrm{PS}_2 = \frac{1}{8\pi}\left(\frac{4\pi}{M^2}\right)^{\epsilon}\frac{\Gamma(1-\epsilon)}{\Gamma(2-2\epsilon)}\,, \tag{A.22}$$

where the duplication formula

$$\Gamma(z)\,\Gamma\left(z+\frac{1}{2}\right) = 2^{1-2z}\,\sqrt{\pi}\,\Gamma(2z) \tag{A.23}$$

with $z = 1-\epsilon$ has been used. The final partonic cross-section, in $d = 4-2\epsilon$ dimensions, is then

$$\begin{aligned} Q_f^2\,\hat{\sigma}_0(s) &= \frac{1}{2s}\,\frac{Q_f^2\,(e\,\mu^{\epsilon})^4}{N_\mathrm{c}}\,\frac{(2-d)^2}{d-1}\int d\mathrm{PS}_2 \\ &= \frac{1}{2s}\,\frac{Q_f^2\,(e\,\mu^{\epsilon})^4}{N_\mathrm{c}}\,\frac{(2-d)^2}{d-1}\,\frac{1}{8\pi}\left(\frac{4\pi}{M^2}\right)^{\epsilon}\frac{\Gamma(1-\epsilon)}{\Gamma(2-2\epsilon)} \\ &= \left(\frac{4\pi}{M^2}\right)^{\epsilon}\frac{4\,\pi\,Q_f^2\,\alpha^2\,\mu^{4\epsilon}}{N_\mathrm{c}\,s}\,\frac{(1-\epsilon)^2}{(3-2\epsilon)}\,\frac{\Gamma(1-\epsilon)}{\Gamma(2-2\epsilon)} \end{aligned} \tag{A.24}$$

using $\alpha = e^2/4\pi$, and factoring out the only flavour-dependent quantity, Q_f^2, for later convenience. Using the identity $\int dM^2\,\delta(s-M^2) = 1$, we can make our result differential in the mass of the lepton pair, M^2:

$$\frac{d\hat{\sigma}_0}{dM^2} = \frac{\hat{\sigma}_0}{s}\,\delta\left(1-\frac{M^2}{s}\right). \tag{A.25}$$

This form will be useful later.

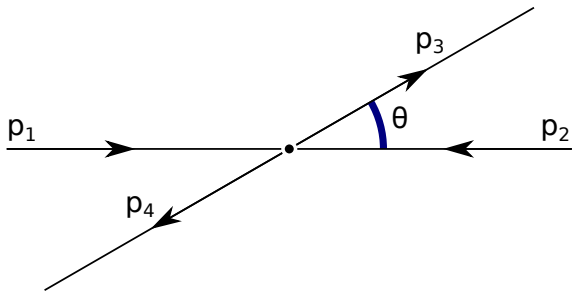

FIGURE A.2. The scattering angle used in the $2 \to 2$ scattering process.

[1] I use 'n-sphere' in the topologists' sense. For example, a 2-sphere is the familiar object embedded in 3D space.

We now discuss the validity of the decomposition assumed for the lepton tensor in Eq. A.10, when computing the total cross-section. At the Born level I would like to prove the equivalence of this simplification for the total cross-section. For this discussion we temporarily revert back to $d = 4$ dimensions, and note that Eq. A.24 becomes

$$\hat{\sigma}_0 = \frac{4\pi\, Q_f^2\, \alpha^2}{3\, N_\mathrm{c}\, s}. \tag{A.26}$$

Now, without the simplification, the tensor contraction in Eq. A.10 is, in $d = 4$ dimensions,

$$\begin{aligned} Q_{\alpha\beta}\, L^{\alpha\beta} &= 16\, [2p_1 \cdot p_4\, p_2 \cdot p_3 + 2p_1 \cdot p_3\, p_2 \cdot p_4] \\ &= 32\, E^4 \left[(1 + \cos\theta)^2 + (1 - \cos\theta)^2\right] \\ &= 64\, E^4 \left[1 + \cos^2\theta\right], \end{aligned} \tag{A.27}$$

where θ is the angle between $\mathbf{p}_1$ and $\mathbf{p}_3$ or, equivalently, between $\mathbf{p}_2$ and $\mathbf{p}_4$, as shown in Fig. A.2. Given this definition, $p_1 \cdot p_3 = p_2 \cdot p_4 = E^2(1 - \cos\theta)$ and $p_1 \cdot p_4 = p_2 \cdot p_3 = E^2(1 + \cos\theta)$, where E is the energy of each particle in the frame for which the collision is symmetric. Since the particles collide head-on, and the leptons are produced back-to-back, we also have $p_1 \cdot p_2 = p_3 \cdot p_4 = 2E^2$. Once again, all particles participating in the scattering process are assumed to be massless.

Finally, we again write the cross-section according to Eq. A.20, but this time using Eq. A.18, in the limit $d \to 4$, and using Eq. A.4 for the matrix element, but with $L^{\alpha\beta}\, Q_{\alpha\beta}$ given in Eq. A.27. Putting this together, we have

$$\begin{aligned} \hat{\sigma}_0 &= \frac{Q_f^2\, e^4}{2s\, N_\mathrm{c}\, 4q^4}\, 64\, E^4 \int (1 + \cos^2\theta)\, \frac{d(\cos\theta)\, d\phi}{8(2\pi)^2} \\ &= \frac{4\pi\, Q_f^2\, \alpha^2}{3\, N_\mathrm{c}\, s}, \end{aligned} \tag{A.28}$$

which is the same as Eq. A.24.

A.2. Real corrections to Drell–Yan

We now consider the emission of a single gluon during the Drell-Yan annihilation process. The kinematics of the $2 \to 3$ scattering process $q\,\bar{q} \to g\,\ell^+\,\ell^-$ is shown in Fig. A.3. The emitted gluon momentum is k, and the gluon makes an angle θ with respect to the beam axis, defined by the direction of p_1. The lepton pair recoils against the gluon with total time-like momentum q, such that $p_1 + p_2 = k + q$, and $q^2 = M^2$, where M is the invariant mass of the lepton pair.

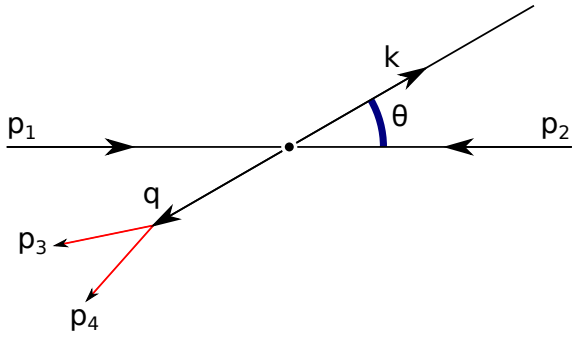

FIGURE A.3. Kinematics of the $2 \to 3$ scattering process for real emission. The momentum of the lepton *pair* is the time-like $q = p_3 + p_4$, where $q^2 = M^2$. The lepton pair recoils against gluon emission, whose momentum is k, and which makes an angle θ with respect to the beam-line.

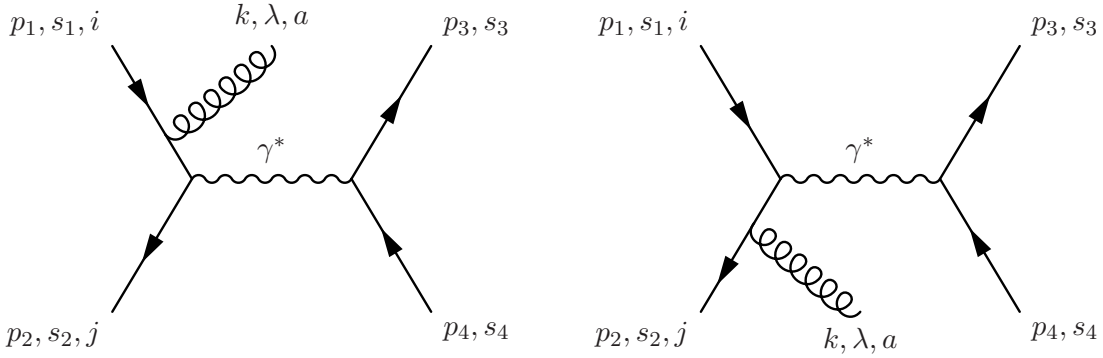

FIGURE A.4. The two real diagrams contributing to the Drell–Yan annihilation process at $\mathcal{O}(\alpha_s)$. External particle momenta and quantum numbers have been labelled.

The amplitudes for the two real processes shown in Fig. A.4 are

$$\mathcal{M}_1 = -i\,Q_f\,(e\,\mu^\epsilon)^2\,g_s\,\mu^\epsilon\,T^a_{ji}\,\bar{u}_3\,\gamma^\alpha\,v_4\,\frac{1}{q^2}\,\frac{\bar{v}_2\,\gamma_\alpha\,(\not{p}_1 - \not{k})\,\gamma^\mu\,u_1}{[(p_1-k)^2 + i\epsilon]}\,\epsilon^{*a}_\mu \tag{A.29}$$

and

$$\mathcal{M}_2 = -i\,Q_f\,(e\,\mu^\epsilon)^2\,g_s\,\mu^\epsilon\,T^a_{ji}\,\bar{u}_3\,\gamma^\alpha\,v_4\,\frac{1}{q^2}\,\frac{\bar{v}_2\,\gamma^\mu\,(-\not{p}_2 + \not{k})\,\gamma_\alpha\,u_1}{[(p_2-k)^2 + i\epsilon]}\,\epsilon^{*a}_\mu. \tag{A.30}$$

Additional shorthand for the gluon polarization has been introduced: $\epsilon^{*a}_\mu \equiv \epsilon^{*a}_\mu(k,\lambda)$, where λ is the quantum number specifying its polarization, a indexes its colour, and k is its momentum. Again, the squared amplitude that appears in the definition of the

inclusive unpolarized cross-section is obtained by averaging over quantum numbers of the initial state and summing those of the final state. In the case of real emission, one has the additional sums over the polarizations and colours of the gluon. Therefore

$$\overline{|\mathcal{M}|^2} = \left(\frac{1}{2}\sum_{s_1}\frac{1}{2}\sum_{s_2}\right)\left(\sum_{s_3}\sum_{s_3}\right)\left(\frac{1}{N_\mathrm{c}}\sum_{i=1}^{N_\mathrm{c}}\frac{1}{N_\mathrm{c}}\sum_{j=1}^{N_\mathrm{c}}\right)\left(\sum_{a,b}\sum_{\lambda}\right)|\mathcal{M}|^2. \tag{A.31}$$

The square of the sum of amplitudes is

$$\begin{aligned}|\mathcal{M}_1+\mathcal{M}_2|^2 = Q_f^2\,(e\,\mu^\epsilon)^4\,(g_\mathrm{s}\,\mu^\epsilon)^2\,T^b_{ij}\,T^a_{ji}\,\mathrm{Tr}\left[u_3\,\bar{u}_3\,\gamma^\alpha\,v_4\,\bar{v}_4\,\gamma^\beta\right]\,\frac{1}{q^4}\,\epsilon^{*a}_\mu\,\epsilon^b_\nu \\ \times\Bigg\{\frac{\mathrm{Tr}\left[u_1\,\bar{u}_1\,\gamma^\nu\,(\not{p}_1-\not{k})\,\gamma_\beta\,v_2\,\bar{v}_2\,\gamma_\alpha\,(\not{p}_1-\not{k})\,\gamma^\mu\right]}{[(p_1-k)^2+i\epsilon]^2} \\ +\frac{\mathrm{Tr}\left[u_1\,\bar{u}_1\,\gamma_\beta\,(-\not{p}_2+\not{k})\,\gamma^\nu\,v_2\,\bar{v}_2\,\gamma^\mu\,(-\not{p}_2+\not{k})\,\gamma_\alpha\right]}{[(p_2-k)^2+i\epsilon]^2} \\ +2\mathrm{Re}\left[\frac{\mathrm{Tr}\left[u_1\,\bar{u}_1\,\gamma_\beta\,(-\not{p}_2+\not{k})\,\gamma^\nu\,v_2\,\bar{v}_2\,\gamma_\alpha\,(\not{p}_1-\not{k})\,\gamma^\mu\right]}{[(p_1-k)^2+i\epsilon][(p_2-k)^2+i\epsilon]}\right]\Bigg\},\end{aligned} \tag{A.32}$$

where new dummy indices have been introduced for the complex conjugate amplitudes, as before, and the interference term has been written $\mathcal{M}_1^*\,\mathcal{M}_2+\mathcal{M}_1\,\mathcal{M}_2^*=2\mathrm{Re}\,[\mathcal{M}_2^*\,\mathcal{M}_1]$. A summation over repeated Greek (Lorentz) indices is implicit, but I will explicitly show the summation over Roman (colour) indices. The sum over gluon polarization states amounts to the replacement

$$\sum_\lambda \epsilon^{*a}_\mu\,\epsilon^b_\nu \to -\delta^{ab}\,g_{\mu\nu}, \tag{A.33}$$

implicitly assuming the Feynman gauge choice. Then, the averaging over initial quark colours and summing over gluon colours results in

$$\begin{aligned}\left(\frac{1}{N_\mathrm{c}}\sum_{i=1}^{N_\mathrm{c}}\frac{1}{N_\mathrm{c}}\sum_{j=1}^{N_\mathrm{c}}\right)\left(\sum_{a,b}\right)\,T^b_{ij}\,T^a_{ji}\,\delta^{ab} &= \frac{1}{N_\mathrm{c}^2}\sum_{i=1}^{N_\mathrm{c}}\left(\sum_a\sum_{j=1}^{N_\mathrm{c}}T^a_{ij}\,T^a_{ji}\right) \\ &= \frac{1}{N_\mathrm{c}^2}\sum_{i=1}^{N_\mathrm{c}}C_\mathrm{F}\,\delta_{ii} = \frac{1}{N_\mathrm{c}}\,C_\mathrm{F}\,.\end{aligned} \tag{A.34}$$

Finally, as always, the completeness relations for massless Dirac spinors allow the spin sums to be replaced by $u_1\,\bar{u}_1\to\not{p}_1$, $v_2\,\bar{v}_2\to\not{p}_2$, $u_3\,\bar{u}_3\to\not{p}_3$ and $v_4\,\bar{v}_4\to\not{p}_4$ in the traces. Now, we may write the square of the sum of amplitudes as

$$\overline{|\mathcal{M}_1+\mathcal{M}_2|^2} = Q_f^2\,(e\,\mu^\epsilon)^4\,(g_\mathrm{s}\,\mu^\epsilon)^2\,\frac{1}{N_\mathrm{c}}\,C_\mathrm{F}\,\frac{(-1)}{4\,q^4}\,L^{\alpha\beta}\,\left\{Q^1_{\alpha\beta}+Q^2_{\alpha\beta}+2\mathrm{Re}\left[Q^3_{\alpha\beta}\right]\right\}, \tag{A.35}$$

where

$$Q^1_{\alpha\beta} = \frac{\mathrm{Tr}\left[\not{p}_1\,\gamma_\mu\,(\not{p}_1-\not{k})\,\gamma_\beta\,\not{p}_2\,\gamma_\alpha\,(\not{p}_1-\not{k})\,\gamma^\mu\right]}{[(p_1-k)^2+i\epsilon]^2}, \tag{A.36}$$

$$Q^2_{\alpha\beta} = \frac{\mathrm{Tr}\left[\not{p}_1\,\gamma_\beta\,(-\not{p}_2+\not{k})\,\gamma_\mu\,\not{p}_2\,\gamma^\mu\,(-\not{p}_2+\not{k})\,\gamma_\alpha\right]}{[(p_2-k)^2+i\epsilon]^2} \tag{A.37}$$

and

$$Q^3_{\alpha\beta} = \frac{\mathrm{Tr}\left[\not{p}_1\,\gamma_\beta\,(-\not{p}_2+\not{k})\,\gamma_\mu\,\not{p}_2\,\gamma_\alpha\,(\not{p}_1-\not{k})\,\gamma^\mu\right]}{[(p_1-k)^2+i\epsilon][(p_2-k)^2+i\epsilon]}. \tag{A.38}$$

As before, we are interested in the inclusive cross-section integrated over all directions of the outgoing leptons, which permits the decomposition of the lepton trace, as in Eq. A.8. Again, this requires one to compute only the traces of the tensors in Eq. A.36 to A.38, which are reported below, in $d = 4 - 2\epsilon$ space-time dimensions:

$$Q^{1\,\alpha}_{\ \ \alpha} = \frac{8\,u\,(1-\epsilon)^2}{t}, \tag{A.39}$$

$$Q^{2\,\alpha}_{\ \ \alpha} = \frac{8\,t\,(1-\epsilon)^2}{u} \tag{A.40}$$

and

$$Q^{3\,\alpha}_{\ \ \alpha} = \frac{8\,(1-\epsilon)\,(M^2\,s - t\,u\,\epsilon)}{t\,u}, \tag{A.41}$$

in terms of the Mandelstam variables $s = (p_1+p_2)^2$, $t = (p_1-k)^2$ and $u = (p_2-k)^2$. Note that $k^2 = 0$ since the gluon is real. Their sum, as in Eq. A.35, is then

$$Q^{1\,\alpha}_{\ \ \alpha} + Q^{2\,\alpha}_{\ \ \alpha} + 2\mathrm{Re}\left[Q^{3\,\alpha}_{\ \ \alpha}\right] = 8\,(1-\epsilon)\,\left[\frac{2\,M^2\,s}{t\,u} + \left(\frac{t}{u}+\frac{u}{t}\right)\,(1-\epsilon) - 2\,\epsilon\right]. \tag{A.42}$$

It is now time to consider the phase-space. The challenge this time will be in handling the three-body phase space

$$d\mathrm{PS}_3 = \frac{d^{d-1}\mathbf{p}_3}{(2\pi)^{d-1}2E_3}\,\frac{d^{d-1}\mathbf{p}_4}{(2\pi)^{d-1}2E_4}\,\frac{d^{d-1}\mathbf{k}}{(2\pi)^{d-1}2E_k}\,(2\pi)^d\,\delta^d(p_3+p_4+k-p_1-p_2), \tag{A.43}$$

where $k = (E_k, \mathbf{k})$ is the four-momentum of the gluon. The phase-space for the two leptons can be decoupled by introducing the momentum q, as in

$$d\mathrm{PS}_3 = \frac{d^{d-1}\mathbf{p}_3}{(2\pi)^{d-1}2E_3}\,\frac{d^{d-1}\mathbf{p}_4}{(2\pi)^{d-1}2E_4}\,\frac{d^{d-1}\mathbf{k}}{(2\pi)^{d-1}2E_k}\,d^dq\,(2\pi)^d\,\delta^d(p_3+p_4-q)\,\delta^d(q+k-p_1-p_2). \tag{A.44}$$

Now the identity

$$\int dM^2\,\delta(q^2-M^2)\,\theta(q_0) = 1 \tag{A.45}$$

is inserted into Eq. A.44. The Heaviside function is trivially satisfied since, from $q = p_3+p_4$, we see that $q_0 = E_3+E_4 > 0$. Furthermore, q is time-like: $q^2 = 2\,p_3\cdot p_4 > 0$, so the argument of the δ-function can always be satisfied for a particular choice of M. We can now write

$$\begin{aligned} d\mathrm{PS}_3 &= d\mathrm{PS}_2^\ell\,dM^2\,d^dq\,\delta(q^2-M^2)\,\frac{d^{d-1}\mathbf{k}}{(2\pi)^{d-1}2E_k}\,\delta^d(q+k-p_1-p_2) \\ &=: d\mathrm{PS}_2^\ell\,\frac{dM^2}{2\pi}\,d\mathrm{PS}_2, \end{aligned} \tag{A.46}$$

thereby defining $d\mathrm{PS}_2$, where the lepton phase-space, denoted by ℓ,

$$d\mathrm{PS}_2^\ell = \frac{d^{d-1}\mathbf{p}_3}{(2\pi)^{d-1}2E_3}\,\frac{d^{d-1}\mathbf{p}_4}{(2\pi)^{d-1}2E_4}\,(2\pi)^d\,\delta^d(p_3+p_4-q) \tag{A.47}$$

is just the usual two-body phase-space. We have thus succeeding in factorizing the three-body phase-space, necessarily making us differential in the squared invariant mass, M^2, of the lepton pair. Since we have been utilizing a decomposition of the lepton tensor that produces no angular dependence of the final-state leptons, we may completely integrate

$d\mathrm{PS}_2$ as before. In addition, the reader is reminded that

$$L^{\alpha\beta}\,Q^i_{\alpha\beta} = \frac{2\,(2-d)\,q^2}{d-1}\;\; Q^{i\,\alpha}_{\;\;\alpha}\,, \tag{A.48}$$

as before.

The differential partonic cross-section for real emission may now be written

$$\begin{aligned} d\hat{\sigma}^{\mathrm{R}}_{q\bar{q}} &= \hat{\sigma}_0\,(g_\mathrm{s}\,\mu^\epsilon)^2\,(-1)\,C_\mathrm{F}\,\frac{dM^2}{2\pi}\,d\mathrm{PS}_2\,\frac{\left\{\,Q^{1\,\alpha}_{\;\;\alpha} + Q^{2\,\alpha}_{\;\;\alpha} + 2\mathrm{Re}\left[\,Q^{3\,\alpha}_{\;\;\alpha}\right]\right\}}{2\,(2-d)\,q^2} \\ &= \hat{\sigma}_0\,(4\,\alpha_\mathrm{s})\,\mu^{2\epsilon}\,C_\mathrm{F}\,\frac{dM^2}{M^2}\,d\mathrm{PS}_2\,\left[\frac{2\,M^2\,s}{t\,u} + \left(\frac{t}{u}+\frac{u}{t}\right)\,(1-\epsilon) - 2\,\epsilon\right], \end{aligned} \tag{A.49}$$

where the definition of $\hat{\sigma}_0$ in Eq. A.24 has been used, along with $\alpha_\mathrm{s} = g_\mathrm{s}/4\pi$ and $d = 4-2\epsilon$. The angular integration for the remaining phase space will not be trivial, since both the gluon and lepton *pair* have a particular direction. Using $p_1 + p_2 = (2E, \mathbf{0}) = (\sqrt{s}, \mathbf{0})$, we write

$$\begin{aligned} d\mathrm{PS}_2 &= \frac{d^{d-1}\mathbf{k}}{(2\pi)^{d-1}2E_k}\,(2\pi)\,d^dq\,\delta(q^2-M^2)\,\delta^d(q+k-p_1-p_2) \\ &= \frac{E_k^{d-3}\,dE_k\,d\Omega_{d-2}}{2\,(2\pi)^{d-2}}\,\delta\left(s - 2E_k\sqrt{s} - M^2\right). \end{aligned} \tag{A.50}$$

Now we set $d = 4-2\epsilon$ and define the fraction $z := M^2/s$, to obtain

$$d\mathrm{PS}_2 = \frac{1}{32\pi^2}\left[\frac{(4\pi)^2}{M^2}\right]^\epsilon z^\epsilon\,(1-z)^{1-2\epsilon}\,d\Omega_{d-2}, \tag{A.51}$$

where the identity $\delta(a\,x) = \delta(x)/|a|$ has also been used. The differential angular measure, extended to arbitrarily higher dimension, is written iteratively as

$$d\Omega_{d-2} = d\theta_{d-3}\,(\sin\theta_{d-3})^{d-3}\,d\Omega_{d-3}, \qquad (\text{c.f. } d\Omega_2 = \sin\theta\,d\theta\,d\phi) \tag{A.52}$$

and so

$$\int d\Omega_{d-2} = \frac{2\pi^{1-\epsilon}}{\Gamma(1-\epsilon)}\int_0^\pi d\theta\,(\sin\theta)^{1-2\epsilon}, \tag{A.53}$$

after integrating over all but one polar angle using

$$\int d\Omega_{d-3} = \frac{2\pi^{(d-2)/2}}{\Gamma\left(\frac{d-2}{2}\right)} \tag{A.54}$$

and relabelling $\theta_{d-3} \to \theta$. In anticipation that the integral representation of the Beta function will be of use, this is further re-expressed by introducing $y = \frac{1}{2}(1+\cos\theta)$, such that

$$\int_0^\pi d\theta\,(\sin\theta)^{1-2\epsilon} = \frac{2}{4^\epsilon}\int_0^1 dy\,[y(1-y)]^{-\epsilon}, \tag{A.55}$$

and the phase-space becomes

$$d\mathrm{PS}_2 = \frac{1}{8\pi}\left(\frac{4\pi}{M^2}\right)^\epsilon\,\frac{z^\epsilon\,(1-z)^{1-2\epsilon}}{\Gamma(1-\epsilon)}\int_0^1 [y\,(1-y)]^{-\epsilon}\,dy. \tag{A.56}$$

The Mandelstam variables t and u must also be written in terms of M^2, y and z. We may start with

$$t = (p_1 - k)^2 = -2\,E\,E_k\,(1+\cos\theta) = -2\sqrt{s}\,\left(\frac{s-M^2}{2\sqrt{s}}\right)\,y, \tag{A.57}$$

using $E_k = (s-M^2)/2\sqrt{s}$, which has already been constrained by the δ-function in Eq. A.50. Substituting $s \to M^2/z$ gives

$$t = -\frac{M^2\,y\,(1-z)}{z}, \tag{A.58}$$

and a similar exercise gives

$$u = -\frac{M^2\,(1-y)\,(1-z)}{z}. \tag{A.59}$$

Finally, one obtains

$$\begin{aligned} d\hat{\sigma}^{\rm R}_{q\bar{q}} = \hat{\sigma}_0\,\frac{\alpha_{\rm s}}{2\pi}\,C_{\rm F}\,\frac{dM^2}{M^2}\,\left(\frac{4\,\pi\,\mu^2}{M^2}\right)^{\epsilon}\,\frac{z^{\epsilon}\,(1-z)^{1-2\epsilon}}{\Gamma(1-\epsilon)} \\ \times\int_0^1 dy\,[y(1-y)]^{-\epsilon}\,\left[\frac{2z}{y\,(1-y)\,(1-z)^2} + \left(\frac{y}{1-y}+\frac{1-y}{y}\right)(1-\epsilon) - 2\,\epsilon\right] \end{aligned} \tag{A.60}$$

for the real contribution to the annihilation Drell-Yan process. The integrals over y may be performed immediately by using the integral representation of the Beta function, expressed further in terms of Gamma functions:

$$\mathrm{B}(m,n) := \int_0^1 y^{m-1}\,(1-y)^{n-1}\,dy = \frac{\Gamma(m)\,\Gamma(n)}{\Gamma(m+n)}, \tag{A.61}$$

for $\mathrm{Re}(m), \mathrm{Re}(n) > 0$. Four integrals one has to perform are

$$I_1 = \int_0^1 dy\,y^{-(1+\epsilon)}(1-y)^{-(1+\epsilon)} = \frac{[\Gamma(-\epsilon)]^2}{\Gamma(-2\epsilon)} = -\frac{2}{\epsilon}\,\frac{[\Gamma(1-\epsilon)]^2}{\Gamma(1-2\epsilon)}, \tag{A.62}$$

$$I_2 = \int_0^1 dy\,y^{1-\epsilon}\,(1-y)^{-(1+\epsilon)} = \frac{\Gamma(2-\epsilon)\,\Gamma(-\epsilon)}{\Gamma(2-2\epsilon)} = -\frac{1}{\epsilon}\,\frac{(1-\epsilon)}{(1-2\epsilon)}\,\frac{[\Gamma(1-\epsilon)]^2}{\Gamma(1-2\epsilon)}, \tag{A.63}$$

$$I_3 = \int_0^1 dy\,y^{-(1+\epsilon)}\,(1-y)^{1-\epsilon} = \frac{\Gamma(-\epsilon)\,\Gamma(2-\epsilon)}{\Gamma(2-2\epsilon)} = I_2 \tag{A.64}$$

and

$$I_4 = \int_0^1 dy\,y^{-\epsilon}\,(1-y)^{-\epsilon} = \frac{[\Gamma(1-\epsilon)]^2}{\Gamma(2-2\epsilon)} = \frac{1}{(1-2\epsilon)}\,\frac{[\Gamma(1-\epsilon)]^2}{\Gamma(1-2\epsilon)}, \tag{A.65}$$

where the identity $z\,\Gamma(z) \equiv \Gamma(1+z)$ has been extensively used to obtain the final equalities. Introducing the notation

$$D(\epsilon) := \left(\frac{4\,\pi\,\mu^2}{M^2}\right)^{\epsilon}\,\frac{\Gamma(1-\epsilon)}{\Gamma(1-2\epsilon)}, \tag{A.66}$$

we may write

$$\begin{aligned} d\hat{\sigma}^{\rm R}_{q\bar{q}} &= \hat{\sigma}_0\,\frac{\alpha_{\rm s}}{2\pi}\,C_{\rm F}\,\frac{dM^2}{M^2}\,D(\epsilon)\,z^{\epsilon}\,(1-z)^{1-2\epsilon}\,\left(-\frac{2}{\epsilon}\right)\,\left[\frac{2z}{(1-z)^2}+1\right] \\ &= \hat{\sigma}_0\,\frac{\alpha_{\rm s}}{2\pi}\,C_{\rm F}\,\frac{dM^2}{M^2}\,D(\epsilon)\,z^{\epsilon}\,\left(-\frac{2}{\epsilon}\right)\,\frac{1+z^2}{(1-z)^{1+2\epsilon}}. \end{aligned} \tag{A.67}$$

In order to obtain the total cross-section, one would have to integrate this real contribution over all M^2 or, equivalently, over z from $z = 0$ to $z = 1$. Clearly, the integral is not convergent on this closed interval, because the integrand diverges for $z \to 1$. We will see that the virtual contribution is divergent, containing poles in ϵ, but this contributes only for $z = 1$ since, without real emission, the invariant mass of the lepton pair $M^2 = s$. We therefore proceed to isolate the divergence in the real contribution at $z = 1$, by use of the 'plus prescription', which I present below.

Consider the integral

$$I = \int_0^1 dz \, \frac{f(z)}{(1-z)^{1+2\epsilon}}, \tag{A.68}$$

where ϵ is small and positive. The integrand is divergent as $z \to 1$, so we isolate this divergence by writing $f(z) = [f(z) - f(1)] + f(1)$, to obtain

$$\begin{aligned} I &= \int_0^1 dz \, \frac{[f(z) - f(1)]}{(1-z)^{1+2\epsilon}} + f(1) \int_0^1 dz \, (1-z)^{-(1+2\epsilon)} \\ &= \left\{ \int_0^1 dz \, \frac{[f(z) - f(1)]}{(1-z)^{1+2\epsilon}} \right\} - \frac{1}{2\epsilon} \, f(1) \\ &= \int_0^1 dz \, \left\{ \frac{f(z)}{[(1-z)^{1+2\epsilon}]_+} - \frac{1}{2\epsilon} \, f(z) \, \delta(1-z) \right\}, \end{aligned} \tag{A.69}$$

where the 'plus prescription' notation $f(z)/g(x)_+ \equiv [f(z) - f(1)]/g(x)$ has been introduced. I have also introduced the δ-function, to maintain a single integral over z. One expands $(1-z)^{-(1+2\epsilon)}$ about $\epsilon = 0$, namely

$$(1-z)^{-(1+2\epsilon)} = (1-z)^{-1} \left[1 - 2\epsilon \log(1-z) + \dots \right] . \tag{A.70}$$

Therefore an identification can be made, which is understood to be valid only under integration:

$$\frac{1}{(1-z)^{1+2\epsilon}} \equiv \frac{1}{(1-z)_+} - 2\epsilon \left[\frac{\log(1-z)}{1-z} \right]_+ - \frac{1}{2\epsilon} \, \delta(1-z). \tag{A.71}$$

We note that $D(\epsilon)$ has no poles in ϵ, for

$$D(\epsilon) = 1 + \epsilon \left[\log(4\pi) - \gamma_{\mathrm{E}} + \log\left(\frac{\mu^2}{M^2} \right) \right] + \mathcal{O}(\epsilon^2). \tag{A.72}$$

Neither does $z^\epsilon = 1 + \epsilon \log(z) + \dots$, and therefore we are left to expand

$$-\frac{2}{\epsilon} \, \frac{1+z^2}{(1-z)^{1+2\epsilon}}, \tag{A.73}$$

dropping all terms proportional to ϵ^n, for $n \geq 1$. Upon doing so, one at last obtains the textbook expression for the real contribution to the Drell-Yan annihilation process:

$$d\hat{\sigma}^{\mathrm{R}}_{q\bar{q}} = \hat{\sigma}_0 \, \frac{\alpha_{\mathrm{s}}}{2\pi} \, C_{\mathrm{F}} \, \frac{dM^2}{M^2} \, D(\epsilon) \, \mathcal{F}_{q\bar{q}}(z), \tag{A.74}$$

with

$$\mathcal{F}_{q\bar{q}}(z) = \frac{2}{\epsilon^2} \, \delta(1-z) - \frac{2}{\epsilon} \, \frac{1+z^2}{(1-z)_+} + 4\,(1+z^2) \left[\frac{\log(1-z)}{1-z} \right]_+ - 2\log(z) \, \frac{1+z^2}{1-z}. \tag{A.75}$$

The plus prescription is dropped on the final term, since $\log(1) = 0$.

A.3. Virtual corrections to Drell–Yan

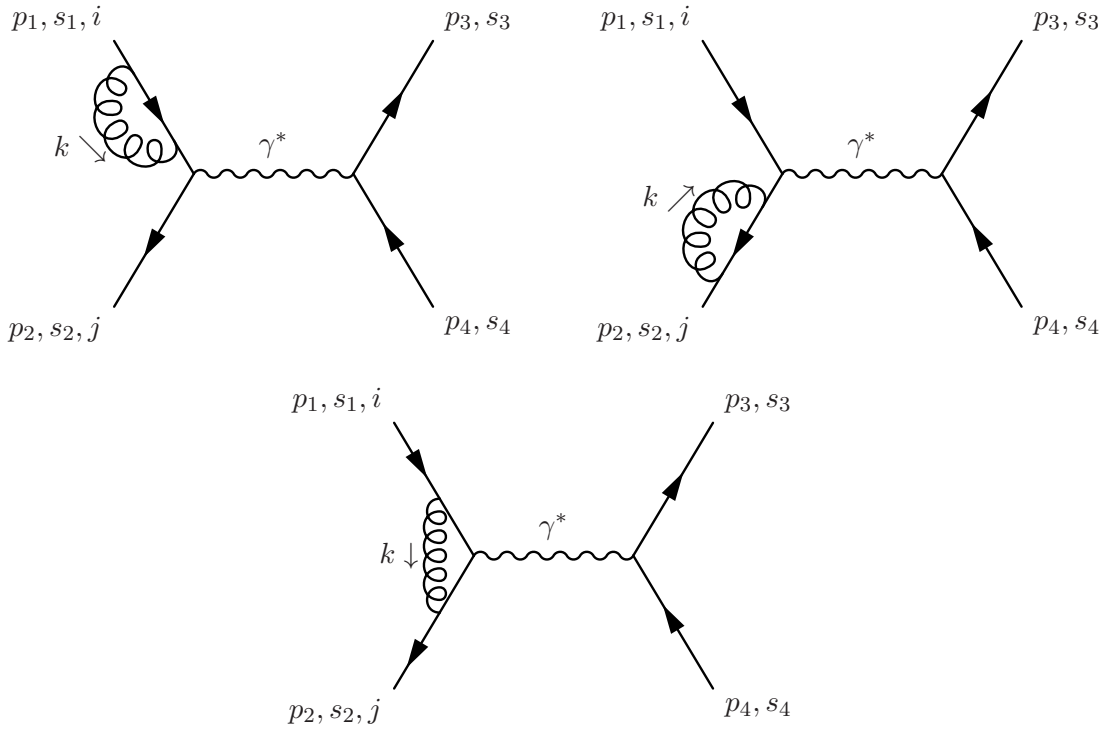

FIGURE A.5. The three virtual diagrams contributing to the Drell–Yan process at $\mathcal{O}(\alpha_\mathrm{s})$. External particle momenta and quantum numbers have been labelled.

In this section I compute the one-loop virtual QCD contributions to the annihilation Drell-Yan process $q\bar{q} \to \gamma^* \ell^+ \ell^-$. The relevant diagrams are shown in Fig. A.5. The amplitudes for these diagrams are, with a summation over the gluon and quark colour indices a and k implied,

$$\begin{aligned}\mathcal{M}_1^\mathrm{V} = {} & Q_f \, (e\,\mu^\epsilon)^2 \, (g_\mathrm{s}\,\mu^\epsilon)^2 \, T^a_{jk} \, T^a_{ki} \, \bar{u}_3 \, \gamma^\alpha \, v_4 \\ & \times \frac{1}{q^2} \int \frac{d^d k}{(2\pi)^d} \, \bar{v}_2 \, \gamma_\alpha \, S_\mathrm{F}(p_1) \, \gamma^\nu \, S_\mathrm{F}(p_1 - k) \, \gamma^\mu \, u_1 \, D_{\mathrm{F}\mu\nu}(k),\end{aligned} \tag{A.76}$$

$$\begin{aligned}\mathcal{M}_2^\mathrm{V} = {} & Q_f \, (e\,\mu^\epsilon)^2 \, (g_\mathrm{s}\,\mu^\epsilon)^2 \, T^a_{jk} \, T^a_{ki} \, \bar{u}_3 \, \gamma^\alpha \, v_4 \\ & \times \frac{1}{q^2} \int \frac{d^d k}{(2\pi)^d} \, \bar{v}_2 \, \gamma^\nu \, S_\mathrm{F}(-(p_2 - k)) \, \gamma^\mu \, S_\mathrm{F}(-p_2) \, \gamma_\alpha \, u_1 \, D_{\mathrm{F}\mu\nu}(k)\end{aligned} \tag{A.77}$$

and

$$\begin{aligned}\mathcal{M}_3^\mathrm{V} = {} & Q_f \, (e\,\mu^\epsilon)^2 \, (g_\mathrm{s}\,\mu^\epsilon)^2 \, T^a_{jk} \, T^a_{ki} \, \bar{u}_3 \, \gamma^\alpha \, v_4 \\ & \times \frac{1}{q^2} \int \frac{d^d k}{(2\pi)^d} \, \bar{v}_2 \, \gamma^\nu \, S_\mathrm{F}(-(p_2 + k)) \, \gamma_\alpha \, S_\mathrm{F}(p_1 - k) \, \gamma^\mu \, u_1 \, D_{\mathrm{F}\mu\nu}(k),\end{aligned} \tag{A.78}$$

where $D_{\mathrm{F}\mu\nu}(k)$ comes from the gluon propagator in a general covariant gauge, and is given by

$$D_{\mathrm{F}\mu\nu}(k) = \frac{1}{k^2 + i\epsilon}\left(g_{\mu\nu} - (1-\eta)\,\frac{k_\mu\,k_\nu}{k^2+i\epsilon}\right). \tag{A.79}$$

Introducing the quark *self-energy* insertion, we may write $\mathcal{M}_1^{\mathrm{V}}$, for instance, as

$$\mathcal{M}_1^{\mathrm{V}} = Q_f\,(e\,\mu^\epsilon)^2\,\delta_{ij}\,\bar{u}_3\,\gamma^\alpha\,v_4\,\frac{1}{q^2}\,\bar{v}_2\,\gamma_\alpha\,S_{\mathrm{F}}(p_1)\,\Sigma(p_1)\,u_1, \tag{A.80}$$

where the insertion is

$$\begin{aligned}\Sigma(p) = {} & (g_{\mathrm{s}}\,\mu^\epsilon)^2\,C_{\mathrm{F}}\left\{\int\frac{d^dk}{(2\pi)^d}\frac{\gamma_\mu(\not{p}-\not{k})\gamma^\mu}{[(p-k)^2+i\epsilon][k^2+i\epsilon]}\right.\\ & \left. -(1-\eta)\int\frac{d^dk}{(2\pi)^d}\frac{\not{k}(\not{p}-\not{k})\not{k}}{[(p-k)^2+i\epsilon][k^2+i\epsilon]^2}\right\} = (g_{\mathrm{s}}\,\mu^\epsilon)^2\,C_{\mathrm{F}}\,(I_1+I_2).\end{aligned} \tag{A.81}$$

We focus initially on the first integral in this expression, where the numerator of the integrand is

$$\gamma_\mu(\not{p}-\not{k})\gamma^\mu = (2-d)(\not{p}-\not{k})\,. \tag{A.82}$$

Using Feynman's parameterization, the denominator can be first re-expressed:

$$\begin{aligned}\frac{1}{[(p-k)^2+i\epsilon][k^2+i\epsilon]} &= \int_0^1\frac{dz}{\left[z[(p-k)^2+i\epsilon]+(1-z)[k^2+i\epsilon]\right]^2}\\ &= \int_0^1\frac{dz}{[(k-z\,p)^2+i\epsilon]^2},\end{aligned} \tag{A.83}$$

where, to obtain the last equality, one completes the square and uses $p^2=0$. This suggests we introduce the momentum $\ell = k - z\,p$ and apply the shift $k \to \ell + z\,p$ in the numerator of the integrand, Eq. A.82. The integral measure is invariant under this shift, i.e. $d^dk = d^d\ell$, and so the integral becomes

$$I_1 = (2-d)\int_0^1 dz\int\frac{d^d\ell}{(2\pi)^d}\frac{(1-z)\not{p}-\not{\ell}}{[\ell^2+i\epsilon]^2} = 0\,. \tag{A.84}$$

The integral is over symmetric limits, so the contribution associated with the odd term $\not{\ell}$ in the numerator evaluates to zero, and this term may be immediately dropped. The remainder of the integral also evaluates to zero because there is no explicit mass scale in the integrand. To see this more clearly, the integral over ℓ is re-written as the sum of two parts, introducing an arbitrary mass scale Λ:

$$\begin{aligned}\int\frac{d^d\ell}{(2\pi)^d}\frac{1}{[\ell^2+i\epsilon]} &= \int\frac{d^d\ell}{(2\pi)^d}\left(\frac{1}{[\ell^2+i\epsilon]}-\frac{1}{[\ell^2-\Lambda^2]^2}\right)+\int\frac{d^d\ell}{(2\pi)^d}\frac{1}{[\ell^2-\Lambda^2]^2}\\ &= \frac{i}{16\pi^2}\left(\frac{1}{\epsilon_{\mathrm{UV}}}-\gamma_{\mathrm{E}}+\log 4\pi-\log\Lambda^2\right)\\ &\quad+\frac{i}{16\pi^2}\left(\frac{1}{\epsilon_{\mathrm{IR}}}+\gamma_{\mathrm{E}}-\log 4\pi+\log\Lambda^2\right)\\ &= 0,\end{aligned} \tag{A.85}$$

where the second line may be verified by explicit computation. Since we are working in $d = 4-2\epsilon$ dimensions, the quantity $\epsilon_{\mathrm{UV}} = \epsilon$ regulates the ultraviolet divergences

whilst $\epsilon_{\rm IR} = -\epsilon$ (such that $d = 4 + 2\epsilon_{\rm IR}$) regulates the infrared divergences. This can be seen by considering which integration limit is responsible for the divergence in each case. Dimensional regularization has systematically regulated both divergences simultaneously and clearly the two divergences cancel. The physical content of this result is that the masslessness of the theory is a feature that is not destroyed under quantum corrections.

Moving now to the second integral term in Eq. A.81, we consider the numerator

$$\not{k}(\not{p} - \not{k})\not{k} = (\not{k}\not{p} - k^2)\not{k} = (2k \cdot p - \not{p}\not{k} - k^2)\not{k}, \tag{A.86}$$

which reduces to

$$(2k \cdot p - k^2)\not{k} = -(p-k)^2\not{k} \tag{A.87}$$

when multiplied from the left by $\not{p}$, as in Eq. A.80, where the $\not{p}$ comes from $S_{\rm F}(p)$, and using $p^2 = 0$. In the limit $\epsilon \to 0$, part of the numerator cancels part of the denominator, and one is left with

$$I_2 = (1-\eta)\int \frac{d^dk}{(2\pi)^d}\frac{(p-k)^2\not{k}}{[(p-k)^2 + i\epsilon][k^2+i\epsilon]^2} \to (1-\eta)\int \frac{d^dk}{(2\pi)^d}\frac{\not{k}}{[k^2+i\epsilon]^2}. \tag{A.88}$$

Since the integrand is purely odd, and the range of integration is between symmetric limits, this evaluates to exactly zero. Since the quark self-energy insertion is universal, the same steps to eliminate this contribution in the massless theory from the second diagram of Fig. A.5 follow immediately, and thus the only diagram left to consider is the QCD vertex correction of Fig. A.5.

It may be worth pausing for a moment. We have seen that the virtual corrections corresponding to the quark self-energy play no rôle here. In summary, the quantum loop corrections to the quark propagators do not generate quark masses in a theory that was initially massless, and there is no gauge-dependent contribution from these diagrams either. Since the gauge-dependence is only required to cancel out in the sum of all relevant amplitudes, the final remaining amplitude for the vertex correction *must* be independent of η to ensure this is the case. We now move to compute this final contribution.

In order to compute the inclusive unpolarized cross-section we must average over initial spins and quark colours, and sum over final spins. Having done this, the interference of these amplitudes with that of the Born approximation, $\mathcal{M}_0$, is an $\mathcal{O}(\alpha_{\rm s})$ contribution and gives

$$\begin{aligned}\overline{\mathcal{M}_3^{\rm V}\,\mathcal{M}_0^\dagger} &= \left(\frac{1}{2}\sum_{s_1}\frac{1}{2}\sum_{s_2}\right)\left(\sum_{s_3}\sum_{s_4}\right)\left(\frac{1}{N_{\rm c}}\sum_{i=1}^{N_{\rm c}}\frac{1}{N_{\rm c}}\sum_{j=1}^{N_{\rm c}}\right)\mathcal{M}_3^{\rm V}\,\mathcal{M}_0^\dagger \\ &= -i\frac{1}{N_{\rm c}}\frac{Q_f^2\,(e\,\mu^\epsilon)^4\,(g_{\rm s}\,\mu^\epsilon)^2\,C_{\rm F}}{4\,q^4}Q^{\rm V}_{\alpha\beta}L^{\alpha\beta},\end{aligned} \tag{A.89}$$

where $T^a_{jk}\,T^a_{ki} = C_{\rm F}\,\delta_{ij}$ has been used, $L_{\alpha\beta}$ is that given in Eq. A.7, and where

$$Q^{\rm V}_{\alpha\beta} = \int \frac{d^dk}{(2\pi)^d}\frac{{\rm Tr}\left[\not{p}_1\,\gamma_\beta\,\not{p}_2\,\gamma^\nu\,(\not{p}_2 + \not{k})\,\gamma_\alpha\,(\not{k} - \not{p}_1)\,\gamma^\mu\right]}{[(p_2+k)^2+i\epsilon][(p_1-k)^2+i\epsilon][k^2+i\epsilon]}\left(g_{\mu\nu} - (1-\eta)\,\frac{k_\mu\,k_\nu}{k^2+i\epsilon}\right) \tag{A.90}$$

contains the integrals and traces one has to perform.

According to Eq. A.10, one has only to compute $Q^{\mathrm{V}\,\alpha}_{\ \ \alpha} = g^{\alpha\beta} Q^{\mathrm{V}}_{\alpha\beta}$. After contracting all Lorentz indices in Eq. A.90 and taking the trace, the quantity $Q^{\mathrm{V}\,\alpha}_{\ \ \alpha}$ becomes

$$\begin{aligned} Q^{\mathrm{V}\,\alpha}_{\ \ \alpha} = 4(2-d) \int \frac{d^dk}{(2\pi)^d} \frac{[(d-4)k^2\, p_1\cdot p_2 + 4(k\cdot p_1 + p_1\cdot p_2)(k\cdot p_2 - p_1\cdot p_2)]}{[(p_2+k)^2+i\epsilon][(p_1-k)^2+i\epsilon][k^2+i\epsilon]} \\ - 4(2-d)(1-\eta) \int \frac{d^dk}{(2\pi)^d} \frac{(k-p_1)^2\,(k+p_2)^2\, p_1\cdot p_2}{[(p_2+k)^2+i\epsilon][(p_1-k)^2+i\epsilon][k^2+i\epsilon]^2}\,. \end{aligned} \tag{A.91}$$

Focusing for a moment on the second integral here, in the limit $\epsilon \to 0$ there is some significant cancellation between terms in the numerator and the denominator, and this term becomes

$$4\,(d-2)\,(1-\eta)\, p_1\cdot p_2 \int \frac{d^dk}{(2\pi)^d} \frac{1}{[k^2+i\epsilon]^2} = 0\,, \tag{A.92}$$

which we know by now is exactly zero due to the lack of any mass scale. Reassuringly, the dependence of the calculation on the arbitrary gauge parameter η has disappeared in all three diagrams of Fig. A.5, and we will be left with a gauge invariant expression for the virtual QCD corrections at $\mathcal{O}(\alpha_{\mathrm{s}})$. All that remains is to compute the integral in the first term in Eq. A.91, which is the only non-zero contribution to these one-loop virtual QCD corrections.

As it stands, the integrand does not simplify any further. Therefore, in the usual manner, one can use Feynman's parameterization to re-express the denominator as follows:

$$\frac{1}{[(p_2+k)^2+i\epsilon][(p_1-k)^2+i\epsilon][k^2+i\epsilon]} = 2! \int_0^1 dz_1 \int_0^1 dz_2 \int_0^1 dz_3\, \frac{\delta(z_1+z_2+z_3-1)}{D^3}, \tag{A.93}$$

where

$$D = z_1[(p_2+k)^2+i\epsilon] + z_2[(p_1-k)^2+i\epsilon] + z_3[k^2+i\epsilon]. \tag{A.94}$$

Now, performing the integral over z_3 amounts to the replacement $z_3 \to 1-z_1-z_2$ in D, by virtue of the δ-function. Note, however, that the remaining integration limits must be adjusted accordingly in order to make this replacement with impunity. One can now write

$$\begin{aligned} D &= k^2 - 2(z_2\, p_1 - z_1\, p_2)\cdot k + i\epsilon \\ &= (k - z_2\, p_1 + z_1\, p_2)^2 + 2 z_1\, z_2\, p_1\cdot p_2 + i\epsilon, \end{aligned} \tag{A.95}$$

by completing the square. This suggests we shift the momentum k by introducing a new momentum $\ell = k - z_2\, p_1 + z_1\, p_2$. The first integral in Eq. A.91, making the change of variables $k \to \ell + z_2\, p_1 - z_1\, p_2$ and using $d = 4 - 2\epsilon$, becomes

$$Q^{\mathrm{V}\,\alpha}_{\ \ \alpha} = -8\,(1-\epsilon)\, 2! \int_0^1 dz_1 \int_0^{1-z_1} dz_2 \int \frac{d^d\ell}{(2\pi)^d} \frac{\mathcal{N}}{[\ell^2 + z_1\, z_2\, s + i\,\epsilon]^3}, \tag{A.96}$$

with the numerator given by

$$\begin{aligned} \mathcal{N} &= -2\,\epsilon\,\ell^2\, p_1\cdot p_2 + 4\,\ell\cdot p_1\,\ell\cdot p_2 + 4\,(p_1\cdot p_2)^2\,[\epsilon\, z_1\, z_2 - (z_1-1)\,(z_2-1)] \\ &= -\epsilon\,\ell^2\, s + 4\,\ell\cdot p_1\,\ell\cdot p_2 - s^2\,[(1-\epsilon)\, z_1\, z_2 + 1 - z_1 - z_2], \end{aligned} \tag{A.97}$$

where $s = (p_1+p_2)^2 = 2\, p_1\cdot p_2$ has been used and terms linear in ℓ have been dropped since they integrate to zero over the symmetric limits of the integral. Exploiting the isotropy

of the integral, one may also make the replacement

$$\ell^\mu \ell^\nu \to \frac{\ell^2\, g^{\mu\nu}}{d} = \frac{\ell^2\, g^{\mu\nu}}{4-2\epsilon}, \tag{A.98}$$

so we can now write

$$Q^{\rm V}{}_\alpha^\alpha = -8\,(1-\epsilon)\,2!\,s\int_0^1 dz_1 \int_0^{1-z_1} dz_2 \left\{ \frac{(1-\epsilon)^2}{2-\epsilon}\, I_4 - s[(1-\epsilon)z_1\, z_2 + 1 - z_1 - z_2]\, I_3 \right\} \tag{A.99}$$

in terms of the standard integrals

$$I_3 = \int \frac{d^d\ell}{(2\pi)^d} \frac{1}{[\ell^2 - \Delta^2 + i\,\epsilon]^3} = \frac{-i}{(4\pi)^{2-\epsilon}} \frac{\Gamma(1+\epsilon)}{2} \frac{1}{(\Delta^2)^{1+\epsilon}} \tag{A.100}$$

and

$$I_4 = \int \frac{d^d\ell}{(2\pi)^d} \frac{\ell^2}{[\ell^2 - \Delta^2 + i\,\epsilon]^3} = \frac{i}{(4\pi)^{2-\epsilon}} (2-\epsilon) \frac{\Gamma(\epsilon)}{2} \frac{1}{(\Delta^2)^{\epsilon}}, \tag{A.101}$$

where $\Delta^2 = -z_1\, z_2\, s$.

Putting everything together, we obtain

$$\begin{aligned}
\overline{\mathcal{M}_3^{\rm V} \mathcal{M}_0^\dagger} &= \overline{|\mathcal{M}_0|^2}\, \frac{\alpha_{\rm s}\, \mu^{2\epsilon}\, C_{\rm F}\, (4\pi)^\epsilon}{4\pi\, q^2} \\
&\qquad \times 4\, s \int_0^1 dz_1 \int_0^{1-z_1} dz_2 \left\{ (1-\epsilon)^2\, \frac{\Gamma(\epsilon)}{2}\, \frac{1}{(\Delta^2)^\epsilon} \right. \\
&\qquad \left. +\; s\,[(1-\epsilon)\, z_1\, z_2 + 1 - z_1 - z_2]\, \frac{\Gamma(1+\epsilon)}{2}\, \frac{1}{(\Delta^2)^{1+\epsilon}} \right\} \\
&= \overline{|\mathcal{M}_0|^2}\, \frac{\alpha_{\rm s}}{2\pi}\, C_{\rm F} \left(\frac{4\,\pi\,\mu^2}{-s} \right)^\epsilon \frac{s}{q^2} \\
&\qquad \times \Gamma(1+\epsilon) \int_0^1 dz_1 \int_0^{1-z_1} dz_2\, \frac{1}{(z_1\, z_2)^\epsilon} \left\{ \frac{(1-\epsilon)^2}{\epsilon} - \frac{[(1-\epsilon)\, z_1\, z_2 + 1 - z_1 - z_2]}{z_1\, z_2} \right\}
\end{aligned} \tag{A.102}$$

In the final equality I have used $\Gamma(\epsilon) = \Gamma(1+\epsilon)/\epsilon$.

One may now make the change of variables $z_2 \to (1-z_1)\, x$, to render the integration limits 0 and 1 on both integrals, preparing us for use of the integral representation of the Beta function, Eq. A.61:

$$\begin{aligned}
&\int_0^1 dz_1 \int_0^{1-z_1} dz_2\, \frac{1}{(z_1\, z_2)^\epsilon} \left\{ \frac{(1-\epsilon)^2}{\epsilon} - \frac{[(1-\epsilon)\, z_1\, z_2 + 1 - z_1 - z_2]}{z_1\, z_2} \right\} \\
&\qquad = \int_0^1 dz_1 \int_0^1 dx \left\{ (1-z_1)^{1-\epsilon}\, z_1^{-\epsilon}\, x^{-\epsilon} \left[\frac{(1-\epsilon)^2}{\epsilon} - (1-\epsilon) \right] \right. \\
&\qquad\qquad \left. - (1-z_1)^{1-\epsilon}\, z_1^{-(1+\epsilon)}\, x^{-(1+\epsilon)}\, (1-x) \right\} \\
&\qquad = \left[\frac{(1-\epsilon)^2}{\epsilon} - (1-\epsilon) \right] {\rm B}(1-\epsilon, 2-\epsilon)\, {\rm B}(1-\epsilon, 1) - {\rm B}(-\epsilon, 2-\epsilon)\, {\rm B}(-\epsilon, 2) \\
&\qquad = \frac{1}{2} \left[-\frac{2}{\epsilon^2} - \frac{3}{\epsilon} - \frac{8}{1-2\epsilon} \right] \frac{\Gamma^2(1-\epsilon)}{\Gamma(1-2\epsilon)}.
\end{aligned} \tag{A.103}$$

The phase space, $d\mathrm{PS}_2$ is exactly the same as in the Born calculation and, of course, the flux factor is common to all three pieces. With the result above, it follows that

$$\begin{aligned} d\hat{\sigma}^{\mathrm{V}} &= \frac{1}{F}\, 2\,\mathrm{Re}\left[\overline{\mathcal{M}^{\mathrm{V}}\,\mathcal{M}_0^{\dagger}}\right]\, d\mathrm{PS}_2 \\ &= \hat{\sigma}_0\,\frac{\alpha_{\mathrm{s}}}{2\pi}\,C_{\mathrm{F}}\,\mathrm{Re}\left[\left(\frac{4\pi\,\mu^2}{-s}\right)^{\epsilon}\right]\,\frac{\Gamma(1+\epsilon)\,\Gamma^2(1-\epsilon)}{\Gamma(1-2\epsilon)}\,\left(-\frac{2}{\epsilon^2}-\frac{3}{\epsilon}-\frac{8}{1-2\epsilon}\right)\frac{s}{q^2} \\ &= \hat{\sigma}_0\,\frac{\alpha_{\mathrm{s}}}{2\pi}\,C_{\mathrm{F}}\,\frac{dM^2}{M^2}\,D(\epsilon)\left[-\frac{2}{\epsilon^2}-\frac{3}{\epsilon}+\left(\frac{2\pi^2}{3}-8\right)\right]\,\delta(1-z)\,, \end{aligned} \tag{A.104}$$

where I have used $D(\epsilon)$ given in Eq. A.66, inserted the identity in the form $\int dM^2\,\delta(s-M^2)$, with $z=M^2/s$, and used the expansion

$$(-1)^{\epsilon}\,\Gamma(1+\epsilon)\,\Gamma(1-\epsilon)\,\left(-\frac{2}{\epsilon^2}-\frac{3}{\epsilon}-\frac{8}{1-2\epsilon}\right) = -\frac{2}{\epsilon^2}-\frac{3+2i\pi}{\epsilon}-8-3i\pi+\frac{2\pi^2}{3} \tag{A.105}$$

before finally taking the real part.

A.4. The collinear splitting function

In this section I demonstrate the universality of the collinear $q \to q + g$ splitting function, P_{qq}, that appeared in the calculation of Drell-Yan at NLO, multiplying the simple pole $1/\epsilon$ which had to be absorbed into a redefinition of the PDFs. This discussion follows very closely that originally given in [**35**] for the case of $d = 4$ dimensions, and is reproduced here for the benefit of the reader.

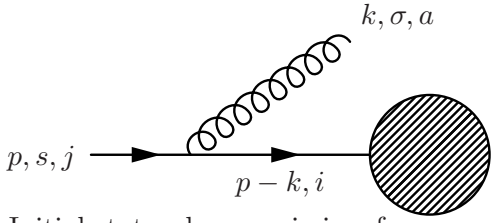

FIGURE A.6. Initial-state gluon emission for an arbitrary hard process $\mathcal{M}_i^n$, which may contain n additional gluons but which may not interfere with the gluon k. Momenta and quantum numbers have been labelled.

One begins by writing down the matrix element for the process shown in Fig. A.6, where a collinear gluon is emitted from an initial state quark:

$$\mathcal{M}_j^{n+1} = \sum_i \mathcal{M}_i^n \, i \frac{\not{p} - \not{k}}{(p-k)^2 + i\epsilon} \, i \, g_{\rm s} \, \mu^\epsilon \, t_{ij}^a \, \gamma^\mu \, u(p,s) \, \epsilon_\mu^*(k,\sigma) \, . \tag{A.106}$$

Averaging over the colours and polarization states of the incoming quark, and summing over those of the gluon, the squared matrix element becomes

$$\begin{aligned} \overline{|\mathcal{M}^{n+1}|^2} &= \left(\frac{1}{N_{\rm c}} \sum_j \frac{1}{2} \sum_s \right) \sum_{a,\sigma} \left| \mathcal{M}_j^{n+1} \right|^2 \\ &= g_{\rm s}^2 \, \mu^{2\epsilon} \, \frac{C_{\rm F}}{N_{\rm c}} \sum_{i,i'} \delta_{ii'} \\ &\quad \times \frac{1}{2} \sum_s \left[\bar{u}(p,s) \, \gamma^\nu \, \frac{\not{p} - \not{k}}{(p-k)^2 + i\epsilon} \; \mathcal{M}_{i'}^{n\,\dagger} \; \mathcal{M}_i^n \, \frac{\not{p} - \not{k}}{(p-k)^2 + i\epsilon} \, \gamma^\mu \, u(p,s) \right] \\ &\quad \times \left(-g_{\mu\nu} + \frac{k_\mu \, n_\nu + n_\mu \, k_\nu}{n \cdot k} \right) , \end{aligned} \tag{A.107}$$

where

$$\sum_j \sum_a t_{ij}^a \, t_{ji'}^a = C_{\rm F} \, \delta_{ii'} \tag{A.108}$$

and

$$\sum_\sigma \epsilon_\mu^*(k,\sigma) \, \epsilon_\nu(k,\sigma) \to -g_{\mu\nu} + \frac{k_\mu \, n_\nu + n_\mu \, k_\nu}{n \cdot k} \tag{A.109}$$

has been used, taking $n^2 = 0$. Taking the trace of the quantity in square brackets (since this is just a number) one can permute the Dirac γ-matrices within and, using the completeness relation for the $u(p,s)$ spinor, one obtains

$$\overline{\left| \mathcal{M}_j^{n+1} \right|^2} = g_{\rm s}^2 \, \mu^{2\epsilon} \, \frac{C_{\rm F}}{N_{\rm c}} \sum_i T_i, \tag{A.110}$$

where, dropping the $i\epsilon$ prescription,

$$\begin{aligned} T_i &= \frac{1}{2}\ \mathrm{Tr}\left[\mathcal{M}_i^n\,\frac{\not p-\not k}{(p-k)^2}\,\gamma^\mu\,\not p\,\gamma^\nu\,\frac{\not p-\not k}{(p-k)^2}\ \mathcal{M}_i^{n\,\dagger}\right]\left(-g_{\mu\nu}+\frac{k_\mu\,n_\nu+n_\mu\,k_\nu}{n\cdot k}\right)\\ &= \frac{1}{2}\,\frac{1}{(2\,p\cdot k)^2}\ \mathrm{Tr}\left[\mathcal{M}_i^n\,(\not p-\not k)\left(-\gamma^\mu\,\not p\,\gamma_\mu+\frac{\not k\,\not p\,\not n+\not n\,\not p\,\not k}{n\cdot k}\right)(\not p-\not k)\ \mathcal{M}_i^{n\,\dagger}\right]\\ &= \frac{1}{2}\,\frac{1}{(2\,p\cdot k)^2}\ \mathrm{Tr}\left[\mathcal{M}_i^n\Big((d-2)\,(\not p-\not k)\,\not p\,(\not p-\not k)\right.\\ &\qquad\qquad\left.+\frac{1}{n\cdot k}(\not p-\not k)\,(\not k\,\not p\,\not n+\not n\,\not p\,\not k)\,(\not p-\not k)\Big)\ \mathcal{M}_i^{n\,\dagger}\right]. \end{aligned} \tag{A.111}$$

In the last line I have used the Clifford algebra in d space-time dimensions. The following identities may be shown, again using the Clifford algebra in d space-time dimensions, and assuming $p^2=k^2=0$:

$$(\not p-\not k)\,\not p\,(\not p-\not k)=2\,(p\cdot k)\,\not k \tag{A.112}$$

$$(\not p-\not k)\,(\not k\,\not p\,\not n+\not n\,\not p\,\not k)\,(\not p-\not k)=2\,(p\cdot k)\,\left[4\,(n\cdot p)\,\not p-2\,(k\cdot n)\,\not p+2\,(k\cdot p)\,\not n-2\,(n\cdot p)\,\not k\right] \tag{A.113}$$

Therefore, T_i becomes

$$T_i=\frac{1}{2\,(p\cdot k)\,(n\cdot k)}\ \mathrm{Tr}\left[\mathcal{M}_i^n\ \left(n\cdot(k-p)\,(\not k-\not p)+(n\cdot p)\,\not p+(k\cdot p)\,\not n-\epsilon\,(n\cdot k)\,\not k\right)\ \mathcal{M}_i^{n\,\dagger}\right], \tag{A.114}$$

in $d=4-2\epsilon$ space-time dimensions.

The task now is to evaluate this trace as far as possible. We will opt to retain only those terms required to obtain the leading logarithmic dependence in the collinear limit. In order to simplify the task of obtaining the collinear limit, the Sudakov decomposition is introduced. The quark momentum after the emission is assumed to be some fraction z of the initial quark momentum, plus a small amount transverse to its original direction.

$$\begin{aligned} q^\mu &= p^\mu-k^\mu\\ &= z\,p^\mu+\beta\,n^\mu-k_\perp^\mu\\ \Rightarrow\qquad k^\mu &= p^\mu-q^\mu\\ &= (1-z)\,p^\mu-\beta\,n^\mu+k_\perp^\mu. \end{aligned} \tag{A.115}$$

By definition, $k_\perp\cdot p=0$, and we may choose n to be the gauge vector and to also satisfy $k_\perp\cdot n=0$. Thus, the quantity β may be thought of as the appropriate scale factor required to retain a massless gluon, which may be determined by insisting that $k^2=0$:

$$\begin{aligned} k^2 &= (1-z)^2\,p^2+\beta^2\,n^2+k_\perp^2-2\,(1-z)\,\beta\,p\cdot n-2\,\beta\,n\cdot k_\perp+2\,(1-z)\,p\cdot k_\perp\\ &= k_\perp^2-2\,(1-z)\,\beta\,p\cdot n=0 \end{aligned} \tag{A.116}$$

on account of $p^2=k^2=0$, and choosing the gauge vector such that $n^2=0$, as we've done already in the replacement for the gluon polarization sum, Eq. A.109. We may thus solve for β, to obtain

$$\beta=-\frac{k_\mathrm{T}^2}{2\,(1-z)\,p\cdot n}, \tag{A.117}$$

where the parameterization $k_\perp=(0,\mathbf{k}_\mathrm{T})$ has been adopted, and $k_\mathrm{T}=|\mathbf{k}_\mathrm{T}|$.

Finally, using

$$n \cdot k = (1-z)\, n \cdot p, \tag{A.118}$$

$$k \cdot p = k_{\mathrm{T}}^2/2\,(1-z), \tag{A.119}$$

$$n \cdot (k-p) = -z\,(n \cdot p) \tag{A.120}$$

$$\text{and} \quad \not{k} - \not{p} = -z\,\not{p} - \beta\,\not{n} + \not{k}_\perp, \tag{A.121}$$

which follow directly from Eq. A.115, the trace becomes

$$\begin{aligned} T_i &= \frac{1}{k_{\mathrm{T}}^2}\ \mathrm{Tr}\left[\mathcal{M}_i^n\ \left((1+z^2)\,\not{p} + \frac{k_{\mathrm{T}}^2}{2\,p\cdot n}\,\not{n} - z\,\not{k}_\perp - \epsilon\,(1-z)\,\not{k}\right)\ \mathcal{M}_i^{n\,\dagger}\right] \\ &= \frac{1}{k_{\mathrm{T}}^2}\left[(1+z^2) - \epsilon\,(1-z)^2\right]\ 2\,\overline{|\mathcal{M}_i^n(p-k)|^2}\,R_{\mathrm{F}}\,, \end{aligned} \tag{A.122}$$

where the final equality is obtained after using $\not{k} = (1-z)\,\not{p} + \mathcal{O}(k_{\mathrm{T}})$ and dropping all $\mathcal{O}(k_{\mathrm{T}})$ terms. The factor two is to account for spin averaging, and

$$|\mathcal{M}_i^n(p-k)|^2 = \mathrm{Tr}\left[z\,\not{p}\,\mathcal{M}_i^n(p-k)\,(\mathcal{M}_i^n)^\dagger(p-k)\right]\,. \tag{A.123}$$

Furthermore, $\mathcal{M}_i^n(p-k) \approx \mathcal{M}_i^n(z\,p)$, up to $\mathcal{O}(k_{\mathrm{T}})$ corrections. The ratio $R_{\mathrm{F}} = 1/z$ is to account for the change in flux factors.

The phase space for the additional gluon may be written

$$d\mathrm{PS} = \frac{d^{d-1}\mathbf{k}}{(2\pi)^{d-1}2E_k} = \frac{1}{2\,(2\pi)^{3-2\epsilon}}\,\frac{dE_k}{E_k}\,|\mathbf{k}|^{2-2\epsilon}\,d\Omega_{d-2}. \tag{A.124}$$

In the collinear approximation, Eq. A.52 reads

$$d\Omega_{d-2} \approx d\theta\,\theta^{1-2\epsilon}\,d\Omega_{d-3}. \tag{A.125}$$

Taking $d = 4-2\epsilon$ space-time dimensions, $\int d\Omega_{d-3} = 2\pi^{1-\epsilon}/\Gamma(1-\epsilon)$, using Eq. A.54. Noting that $k_{\mathrm{T}} = |\mathbf{k}|\sin\theta \approx |\mathbf{k}|\theta$, and writing the energy of the gluon as a fraction of the initial quark's energy, i.e. $E_k = E_p\,(1-z)$, one finally obtains for the phase space

$$d\mathrm{PS} = \frac{1}{16\pi^2}\,\frac{(4\pi)^\epsilon}{\Gamma(2-\epsilon)}\,\frac{dz}{(1-z)}\,dk_{\mathrm{T}}^{2-2\epsilon}. \tag{A.126}$$

Therefore, one has

$$\overline{\left|\mathcal{M}_j^{n+1}\right|^2} = \frac{\alpha_{\mathrm{s}}}{2\pi}\left(\frac{4\pi\mu^2}{k_{\mathrm{T}}^2}\right)^\epsilon\,\frac{dk_{\mathrm{T}}^2}{k_{\mathrm{T}}^2}\,C_{\mathrm{F}}\left[\frac{1+z^2}{1-z} - \epsilon\,(1-z)\right]dz\,\frac{1}{N_{\mathrm{c}}}\sum_i\,\overline{\left|\mathcal{M}_i^n\right|^2}\,. \tag{A.127}$$

APPENDIX B

Mathematical appendix

B.1. Integral representations of Heaviside step functions

It follows from the definition of the Dirac δ-function that

$$\int_{-A}^{A} dp\,\delta(p-a)\,f(p) = \begin{cases} f(a) & \text{if} \quad -A < a < A \\ 0 & \text{otherwise} \end{cases} \\ = f(a)\,\Theta(A-|a|)\,. \tag{B.1}$$

Combining this with the integral representation of the Dirac δ-function in Fourier space, i.e.

$$\delta(p-a) = \frac{1}{2\pi}\int_{-\infty}^{\infty} e^{i\,x\,(p-a)}\,dx\,, \tag{B.2}$$

one establishes that, taking $f(p)=1$,

$$\begin{aligned} \Theta(A-|a|) &= \frac{1}{2\pi}\int_{-\infty}^{\infty} dx \int_{-A}^{A} dp\, e^{i\,x\,(p-a)} \\ &= \frac{1}{\pi}\int_{-\infty}^{\infty} \frac{dx}{x}\,\sin(x\,A)\;e^{-i\,x\,a} \\ &= \frac{2}{\pi}\int_{0}^{\infty} \frac{dx}{x}\,\sin(x\,A)\;e^{i\,x\,a} + \frac{2\,i}{\pi}\,\ln\left[\frac{(a-A)^2}{(a+A)^2}\right], \end{aligned} \tag{B.3}$$

using $e^{i\,\theta} = \cos\theta + i\,\sin\theta$ and exploiting the parity of the integrand. Upon making the replacements $A \to \phi^*\,M$ and $a \to \sum_i k_{\mathrm{T}i}\,\sin\phi_i$, and implicitly taking the real part, one obtains Eq. 4.105.

B.2. Special functions

B.2.1. The Euler Gamma function. The Euler Gamma function may be defined as

$$\Gamma(z) := \int_0^\infty t^{z-1}\, e^{-t}\, dt \quad \text{for } \operatorname{Re} z > 0\,. \tag{B.4}$$

Integrating by parts the corresponding integral form of $\Gamma(z+1)$ reveals

$$\Gamma(z+1) = z\,\Gamma(z)\,. \tag{B.5}$$

As such, it is related to the factorial as

$$\Gamma(n+1) = n! \quad \text{for } n \in \mathbb{N}\,. \tag{B.6}$$

A common occurrence when dealing with d-dimensional spheres is $\Gamma\left(\frac{1}{2}\right)$. Letting $t = r^2$ and using symmetric limits, permitted by the parity of the integrand, one obtains the Gaussian integral

$$\Gamma\left(\frac{1}{2}\right) = \int_\infty^\infty e^{-r^2}\, dr = \sqrt{\pi}\,. \tag{B.7}$$

B.2.2. The Beta function. The Beta function may be defined as

$$B(m,n) := \frac{\Gamma(m)\,\Gamma(n)}{\Gamma(m+n)}\,, \tag{B.8}$$

which is symmetric under the exchange $m \leftrightarrow n$. Taking the numerator in integral form and changing variables through $t = z\,\alpha$ and $u = z\,(1-\alpha)$, one obtains

$$\begin{aligned}
\Gamma(m)\,\Gamma(n) &= \int_0^\infty t^{m-1}\, e^{-t}\, dt \int_0^\infty u^{n-1}\, e^{-u}\, du \\
&= \int_0^\infty z^{m+n-1}\, e^{-z}\, dz \int_0^1 \alpha^{m-1}\,(1-\alpha)^{n-1}\, d\alpha \\
&= \Gamma(m+n) \int_0^1 \alpha^{m-1}\,(1-\alpha)^{n-1}\, d\alpha
\end{aligned} \tag{B.9}$$

and so

$$B(m,n) = \int_0^1 \alpha^{m-1}\,(1-\alpha)^{n-1}\, d\alpha\,. \tag{B.10}$$

It is often useful to identify such integrals as a form of the Beta function, writing them subsequently in terms of Gamma functions.

B.2.3. The Euler–Mascheroni constant. The Euler–Mascheroni constant is defined as

$$\gamma_{\mathrm{E}} := \lim_{N\to\infty} \left[\sum_{n=1}^{N} - \log N \right]\,, \tag{B.11}$$

i.e. the limiting difference between the harmonic series and the natural logarithm. The series expansion of $\Gamma(\epsilon)$ about $\epsilon = 0$ involves this quantity and is

$$\frac{1}{\epsilon} - \gamma_{\mathrm{E}} + \frac{1}{12}\left(6\,\gamma_{\mathrm{E}}^2 + \pi^2\right)\epsilon + \mathcal{O}(\epsilon^2)\,. \tag{B.12}$$

B.3. Azimuthal integration of radiation function

Here it is shown that

$$\begin{aligned}\int \frac{d\phi}{2\pi}\,\tilde{W}^k_{[i]j} &\equiv \int \frac{d\phi}{2\pi}\left[\frac{(i,j)}{(i,k)\,(k,j)}+\frac{1}{(i,k)}-\frac{1}{(j,k)}\right]\\ &= \frac{2}{(i,k)}\,\Theta[\cos\theta_{ik}-\cos\theta_{ij}]\,,\end{aligned} \tag{B.13}$$

where $(a,b)=1-\cos\theta_{ab}$, by following the derivation which may be found in [**48**]. Energies are assumed to have already been factored out, and so we have $a=(1,\mathbf{a})$. The integration is over the azimuth of $\mathbf{k}$, about the direction of $\mathbf{i}$. First, pick the directions of $\mathbf{i}$, $\mathbf{j}$ and $\mathbf{k}$ to be

$$\mathbf{i} = (0,0,1) \tag{B.14}$$

$$\mathbf{j} = (\sin\theta_{ij}, 0, \cos\theta_{ij}) \tag{B.15}$$

$$\text{and} \qquad \mathbf{k} = (\sin\theta_{ik}\,\cos\phi, \sin\theta_{ik}\,\sin\phi, \cos\theta_{ik})\,. \tag{B.16}$$

The angle between $\mathbf{j}$ and $\mathbf{k}$ is then $\mathbf{j}\cdot\mathbf{k}$, so

$$(j,k) = 1-\cos\theta_{jk} = A - B\,\cos\phi\,, \tag{B.17}$$

where

$$A = 1-\cos\theta_{ij}\,\cos\theta_{ik} \tag{B.18}$$

$$\text{and} \qquad B = \sin\theta_{ij}\,\sin\theta_{ik}\,. \tag{B.19}$$

Consider the integral

$$I = \int_0^{2\pi}\frac{d\phi}{(j,k)} = \int_0^{2\pi}\frac{d\phi}{A-B\,\cos\phi}\,. \tag{B.20}$$

Introducing $z=e^{i\phi}$, this may be written

$$I = \frac{2}{i\,B}\oint\frac{dz}{(z_+-z)\,(z-z_-)} \tag{B.21}$$

where $z_\pm = A/B \pm \sqrt{A^2/B^2-1}$, and the contour is the anticlockwise unit circle in the complex plane. The only pole to reside within this contour is at $z=z_-$. Therefore, by Cauchy's residue theorem,

$$I = \frac{2}{i\,B}\,2\,\pi\,i\,\frac{1}{(z_+-z_-)} = 2\,\pi\,\frac{1}{\sqrt{A^2-B^2}}\,. \tag{B.22}$$

Using this result in Eq. B.13, and the fact that

$$\sqrt{A^2-B^2} = |\cos\theta_{ij}-\cos\theta_{ik}|\,, \tag{B.23}$$

gives

$$\begin{aligned}\int \frac{d\phi}{2\pi}\,\tilde{W}^{r\,k}_{[i]j} &= \frac{(i,j)}{(i,k)}\int \frac{d\phi}{2\pi}\,\frac{1}{(k,j)} + \frac{1}{(i,k)} - \int \frac{d\phi}{2\pi}\,\frac{1}{(k,j)} \\ &= \frac{1}{(i,k)}\left[1 - \frac{\cos\theta_{ij} - \cos\theta_{ik}}{|\cos\theta_{ij} - \cos\theta_{ik}|}\right] \\ &= \begin{cases} 0 & \text{if } \cos\theta_{ij} \geq \cos\theta_{ik} \\ 2 & \text{if } \cos\theta_{ij} < \cos\theta_{ik} \end{cases} \\ &= \frac{2}{(i,k)}\,\Theta[(i,j) - (i,k)]\,.\end{aligned} \tag{B.24}$$

B.4. NNLL approximation

Aspects of this calculation are a reproduction of that originally presented in [**66**]. My hope is that the additional working presented herein will provide insight for the interested reader.

The aim here is to show that, to the desired accuracy, one may replace

$$\left(1 - e^{i\,b\,x}\right) \to \Theta\left(|x| - \frac{1}{b}\right) \tag{B.25}$$

in

$$R(b) = \int_{Q_0}^{M} \frac{dk_{\rm T}}{k_{\rm T}}\, F\left(\alpha_{\rm s}\,\ln\frac{k_{\rm T}}{M}\right)\left(1 - e^{i\,b\,x}\right), \tag{B.26}$$

where $x = k_{\rm T}\,\sin\phi/M$. Further discussion may also be found in [**66**]. We begin by considering the more general integral

$$I = \int_{\Delta_{\rm min}}^{\Delta_{\rm max}} \frac{d\Delta}{\Delta}\, F\left(\alpha_{\rm s}\,\ln\Delta\right)\left(1 - e^{i\,b\,v\,\Delta}\right). \tag{B.27}$$

Given that one can generate the single logarithmic terms, of which F is a function, using

$$\left.\frac{d\Delta^{\epsilon}}{d\epsilon}\right|_{\epsilon=0} = \ln\Delta\,, \tag{B.28}$$

we may write I as

$$I = F\left(\alpha_{\rm s}\,\frac{d}{d\epsilon}\right)\int_{\Delta_{\rm min}}^{\Delta_{\rm max}} \frac{d\Delta\,\Delta^{\epsilon}}{\Delta}\left(1 - e^{i\,b\,v\,\Delta}\right)\Big|_{\epsilon=0} = F\left(\alpha_{\rm s}\,\frac{d}{d\epsilon}\right)(I_1 - I_2)\Big|_{\epsilon=0}\,, \tag{B.29}$$

where

$$I_1 = \int_{\Delta_{\rm min}}^{\Delta_{\rm max}} \frac{d\Delta\,\Delta^{\epsilon}}{\Delta} = \frac{\Delta_{\rm max}^{\epsilon} - \Delta_{\rm min}^{\epsilon}}{\epsilon} \tag{B.30}$$

and

$$I_2 = \int_{\Delta_{\rm min}}^{\Delta_{\rm max}} \frac{d\Delta\,\Delta^{\epsilon}}{\Delta}\, e^{i\,b\,v\,\Delta}\,, \tag{B.31}$$

the latter of which is the focus of our attention.

We consider I_2 to be the 'A' leg of the integral around the closed contour, γ, shown in Fig. B.1. Since this contour encloses no poles in the variable of integration, Δ,

$$I_\gamma = \oint_\gamma \frac{d\Delta\,\Delta^{\epsilon}}{\Delta}\, e^{i\,b\,v\,\Delta} = I_A + I_B + I_C + I_D + I_R = 0\,. \tag{B.32}$$

Along this contour, $\mathrm{Im}\,\Delta \geq 0$, so $e^{i\,b\,v\,\Delta} = e^{i\,b\,v\,\mathrm{Re}\,\Delta}\,e^{-\,b\,v\,\mathrm{Im}\,\Delta}$ does not become large, provided that $b\,v \geq 0$. Furthermore, since $0 < \epsilon \ll 1$,

$$\frac{\Delta^{\epsilon}}{\Delta} \to 0 \qquad \text{as} \qquad |\Delta| \to \infty\,. \tag{B.33}$$

Thus, the contribution to the integral from the contour piece 'R' is $I_R = 0$.

The contribution from the contour piece 'C',

$$I_C = \int_{i\,\infty}^{i\,\Delta_{\rm min}} \frac{d\Delta\,\Delta^{\epsilon}}{\Delta}\, e^{i\,b\,v\,\Delta}\,, \tag{B.34}$$

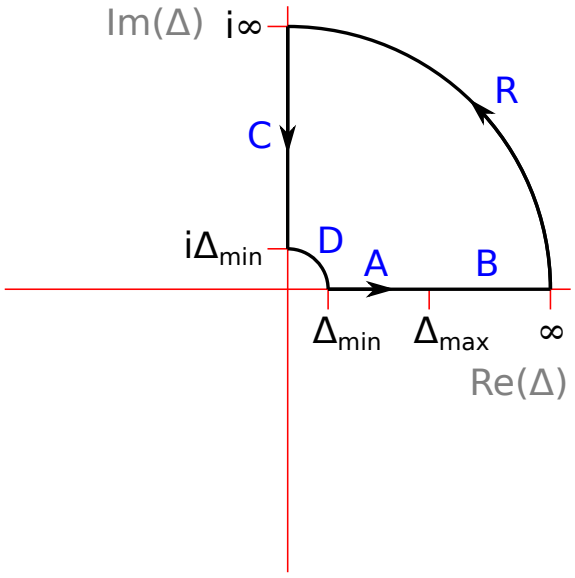

FIGURE B.1. A closed contour in the Re(Δ)–Im(Δ) plane, within which the integrand of Eq. B.32 contains no poles.

may be brought into a more convenient form by changing the variable of integration to $t = -i\,b\,v\,\Delta$. As such,

$$I_C = -\left(\frac{i}{b\,v}\right)^{\epsilon} \int_{b\,v\,\Delta_{\rm min}}^{\infty} dt\, t^{\epsilon-1}\, e^{-t} = -\left(\frac{i}{b\,v}\right)^{\epsilon} \Gamma(\epsilon, b\,v\,\Delta_{\rm min})\,, \tag{B.35}$$

where $\Gamma(\epsilon, b\,v\,\Delta_{\rm min})$ is the incomplete Γ function. Performing a series expansion about $x = 0$, we have

$$\Gamma(\epsilon, x) = \Gamma(\epsilon) - \frac{x^{\epsilon}}{\epsilon} + \ldots\,, \tag{B.36}$$

and so, in the limit $\Delta_{\rm min} \to 0$, we have

$$I_C = -\left(\frac{i}{b\,v}\right)^{\epsilon} \Gamma(\epsilon) + \frac{(i\,\Delta_{\rm min})^{\epsilon}}{\epsilon}\,. \tag{B.37}$$

The integration around the quarter circle 'D' may be evaluated by writing $\Delta = \Delta_{\rm min}\, e^{i\,\theta}$, and changing the variable of integration to θ. Thus

$$I_D = \int_D \frac{d\Delta\,\Delta^{\epsilon}}{\Delta}\, e^{i\,b\,v\,\Delta} = \int_{\pi/2}^{0} i\,d\theta\,\Delta_{\rm min}^{\epsilon}\, e^{i\,\epsilon\,\theta}\, e^{i\,b\,v\,\Delta_{\rm min}\,\cos\theta}\, e^{-\,b\,v\,\Delta_{\rm min}\,\sin\theta}\,. \tag{B.38}$$

Taking $\Delta_{\rm min}$ to be sufficiently small, this is simply

$$I_D = i\,\Delta_{\rm min}^{\epsilon} \int_{\pi/2}^{0} d\theta\, e^{i\,\epsilon\,\theta} = \frac{\Delta_{\rm min}^{\epsilon} - (i\,\Delta_{\rm min})^{\epsilon}}{\epsilon} \tag{B.39}$$

The final contribution is from the contour piece 'B'. To the accuracy we desire, this does not contribute. The logarithmic enhancements are in the ratio $\Delta_{\rm max}/\Delta_{\rm min}$, and so the contribution from I_B is beyond our accuracy.

Taking all the contributions together, we have

$$I_2 \equiv I_A = -I_C - I_D = -\frac{\Delta_{\rm min}^{\epsilon}}{\epsilon} + \left(\frac{i}{b\,v}\right)^{\epsilon} \Gamma(\epsilon)\,. \tag{B.40}$$

Using, for small ϵ,

$$i^\epsilon\,\Gamma(\epsilon) = \frac{1}{\epsilon} - \gamma_{\rm E} + \frac{i\,\pi}{2} = \frac{1-\epsilon\,\gamma_{\rm E}}{\epsilon} + \frac{i\,\pi}{2} \approx \frac{e^{-\epsilon\,\gamma_{\rm E}}}{\epsilon} + \frac{i\,\pi}{2}\,, \tag{B.41}$$

we have

$$\mathrm{Re}(I_2) = -\frac{\Delta_{\rm min}^\epsilon}{\epsilon} + \frac{1}{\epsilon}\left(\frac{e^{-\gamma_{\rm E}}}{b\,v}\right)^\epsilon\,, \tag{B.42}$$

and so

$$I = I_1 - I_2 = \frac{\Delta_{\rm max}^\epsilon - (\bar{b}\,v)^{-\epsilon}}{\epsilon}\,, \tag{B.43}$$

where $\bar{b} = b\,e^{\gamma_{\rm E}}$. This is precisely I_1, but with $\Delta_{\rm min} \to 1/(\bar{b}\,v)$. Therefore, we may replace

$$1 - e^{i\,b\,v\,\Delta} \to \Theta\left(\Delta - \frac{1}{\bar{b}\,v}\right) \tag{B.44}$$

up to NNLL accuracy in our expression for $R(b)$, for $v > 0$. For general v, one obtains Eq. B.25 where $x = v\,\Delta$.

APPENDIX C

Control plots for resummed predictions

C.1. Cancellation of logs for DØ predictions

C.1.1. Predictions in peak region.

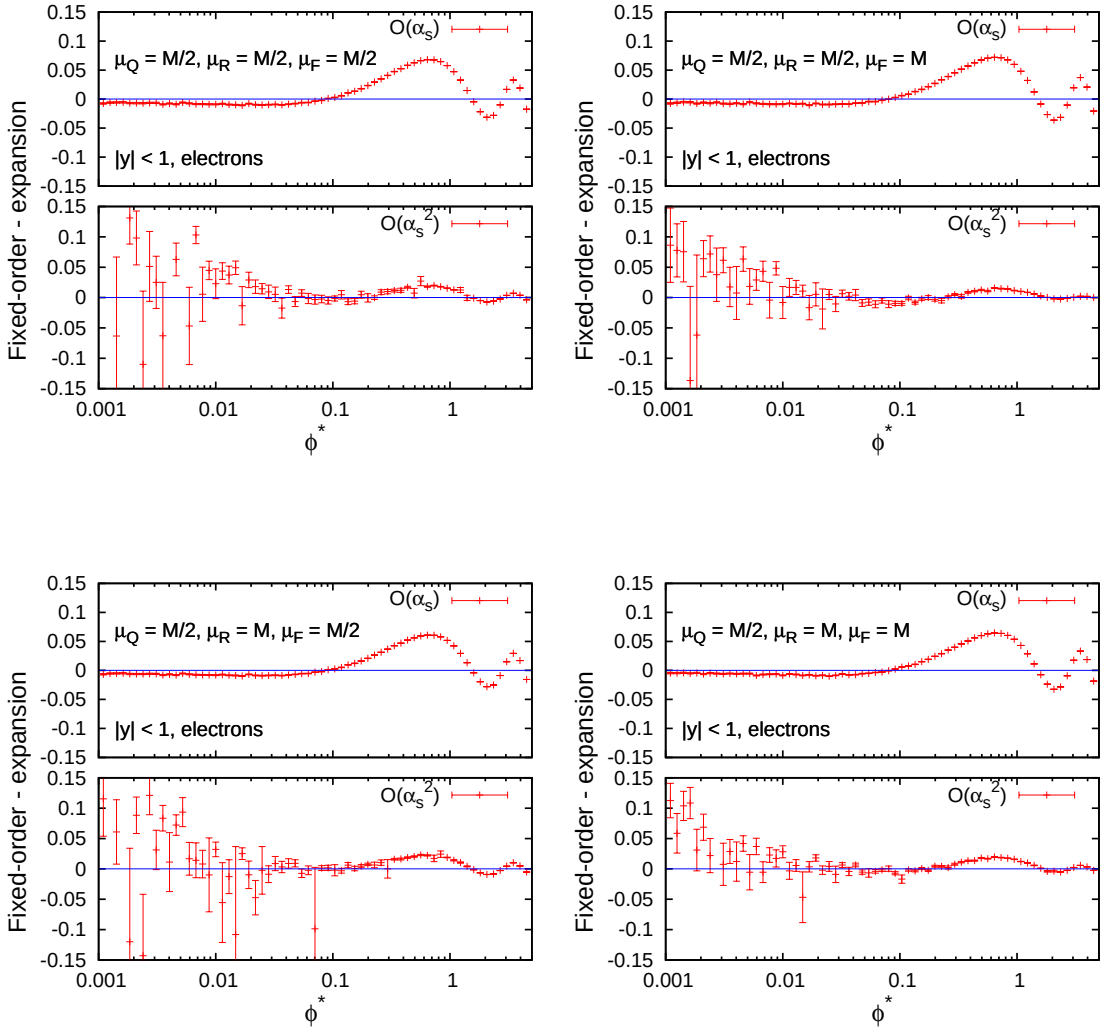

FIGURE C.1. Plots showing the cancellation of large logarithms between the fixed-order component and the expansion of the resummation, for DØ data in the $Z \to ee$ channel around the resonance and the rapidity range $|y| < 1$. The scale $\mu_Q = M/2$.

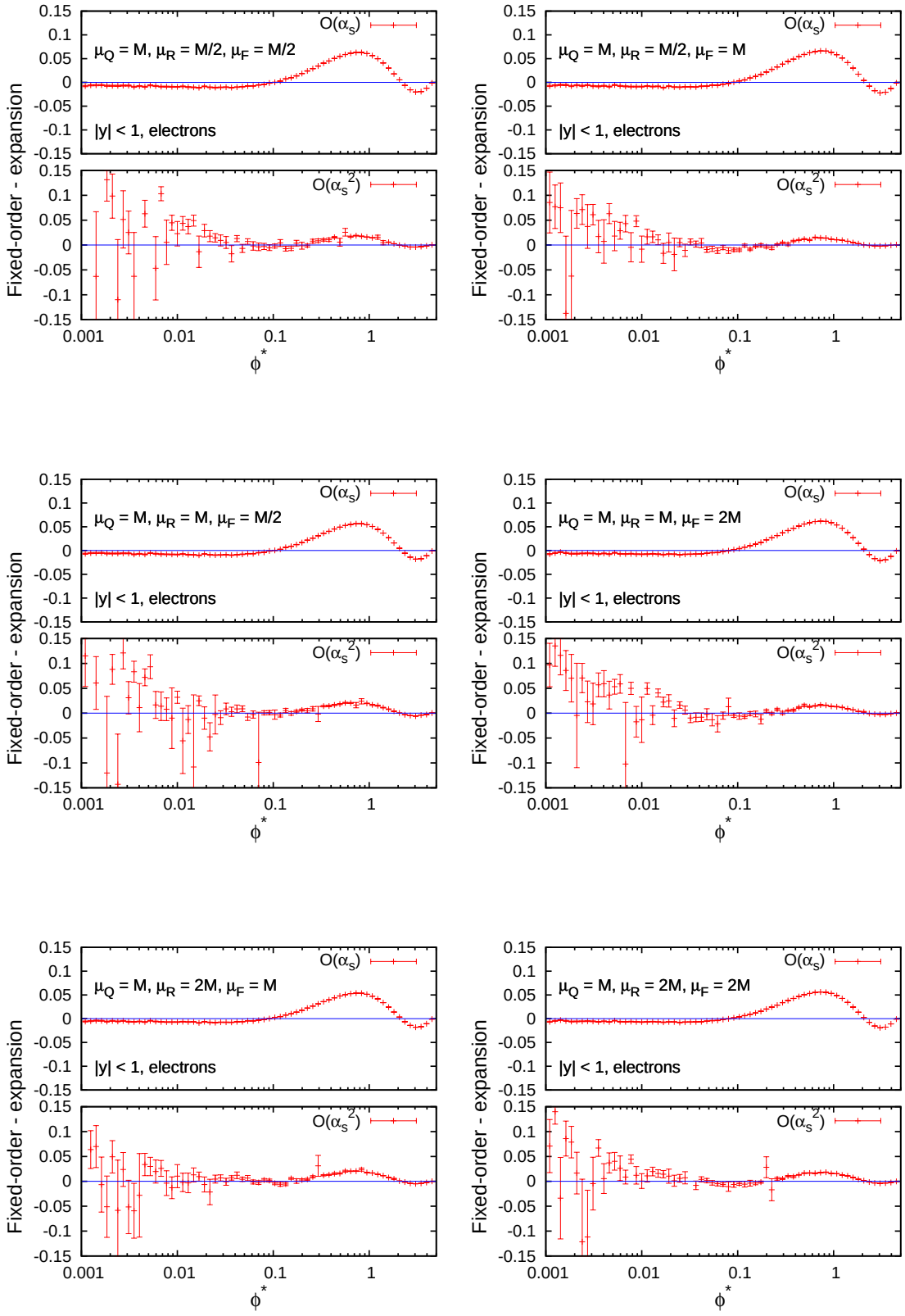

FIGURE C.2. Plots showing the cancellation of large logarithms between the fixed-order component and the expansion of the resummation, for DØ data in the $Z \to ee$ channel around the resonance and the rapidity range $|y| < 1$. The scale $\mu_Q = M$.

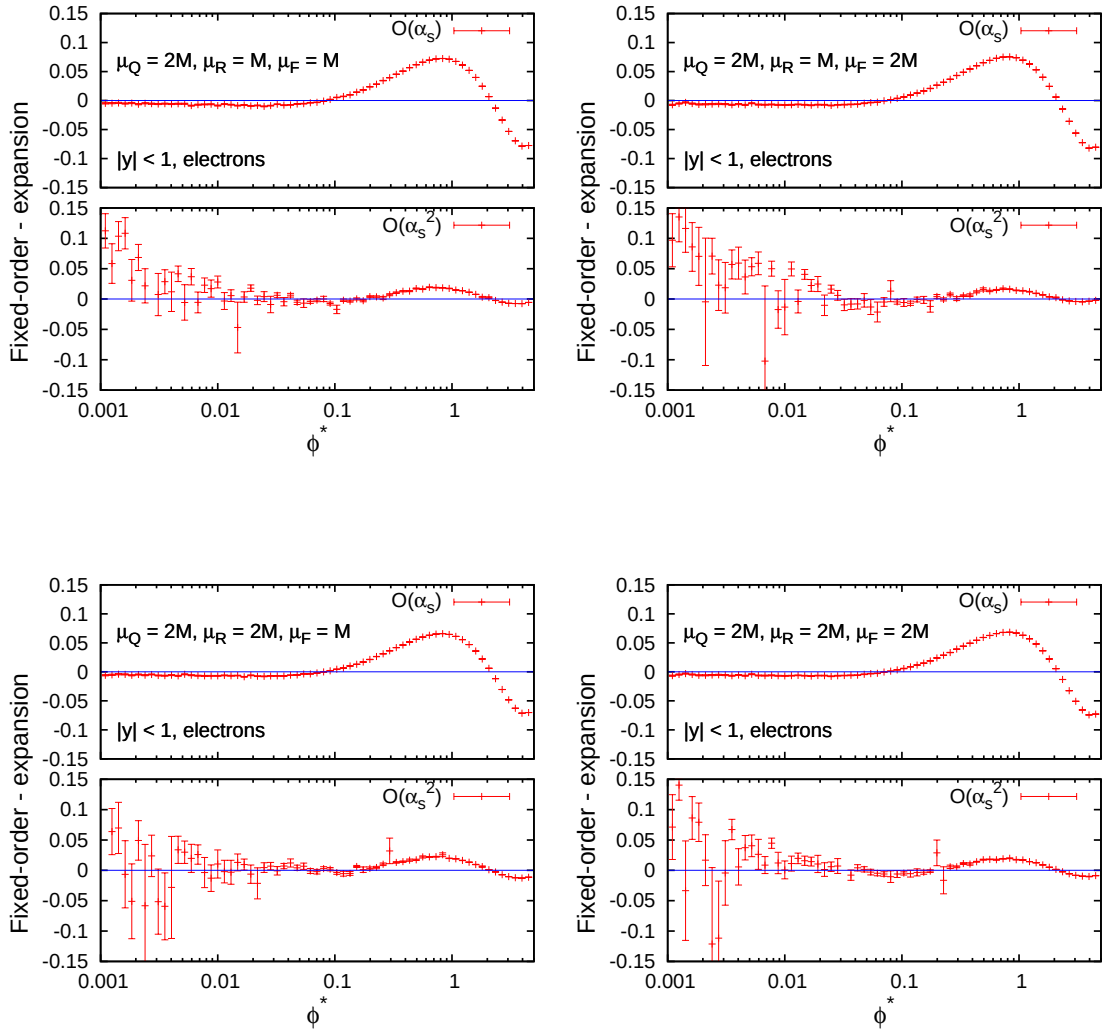

FIGURE C.3. Plots showing the cancellation of large logarithms between the fixed-order component and the expansion of the resummation, for DØ data in the $Z \to ee$ channel around the resonance and the rapidity range $|y| < 1$. The scale $\mu_Q = 2M$.

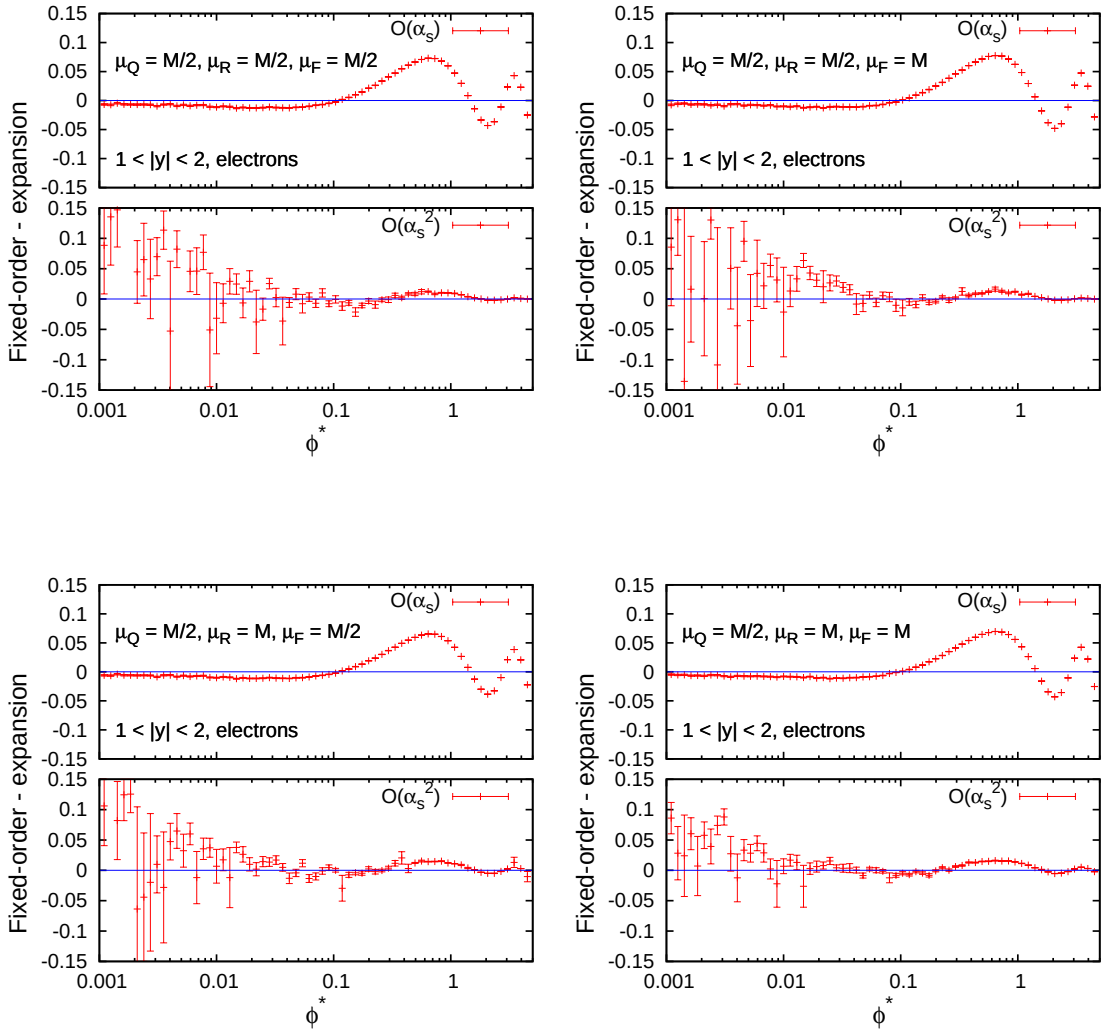

FIGURE C.4. Plots showing the cancellation of large logarithms between the fixed-order component and the expansion of the resummation, for DØ data in the $Z \to ee$ channel around the resonance and the rapidity range $1 < |y| < 2$. The scale $\mu_Q = M/2$.

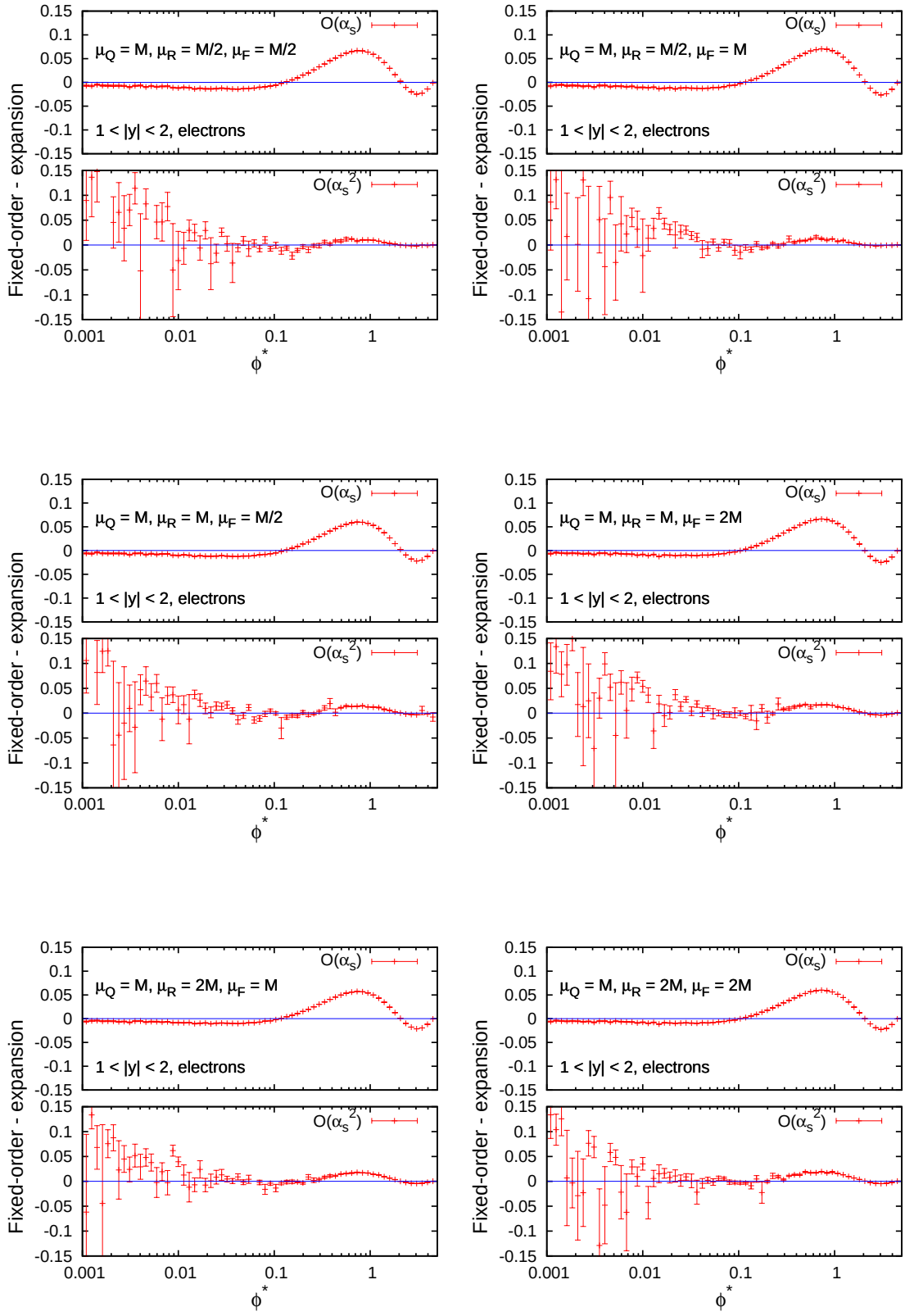

FIGURE C.5. Plots showing the cancellation of large logarithms between the fixed-order component and the expansion of the resummation, for DØ data in the $Z \to ee$ channel around the resonance and the rapidity range $1 < |y| < 2$. The scale $\mu_Q = M$.

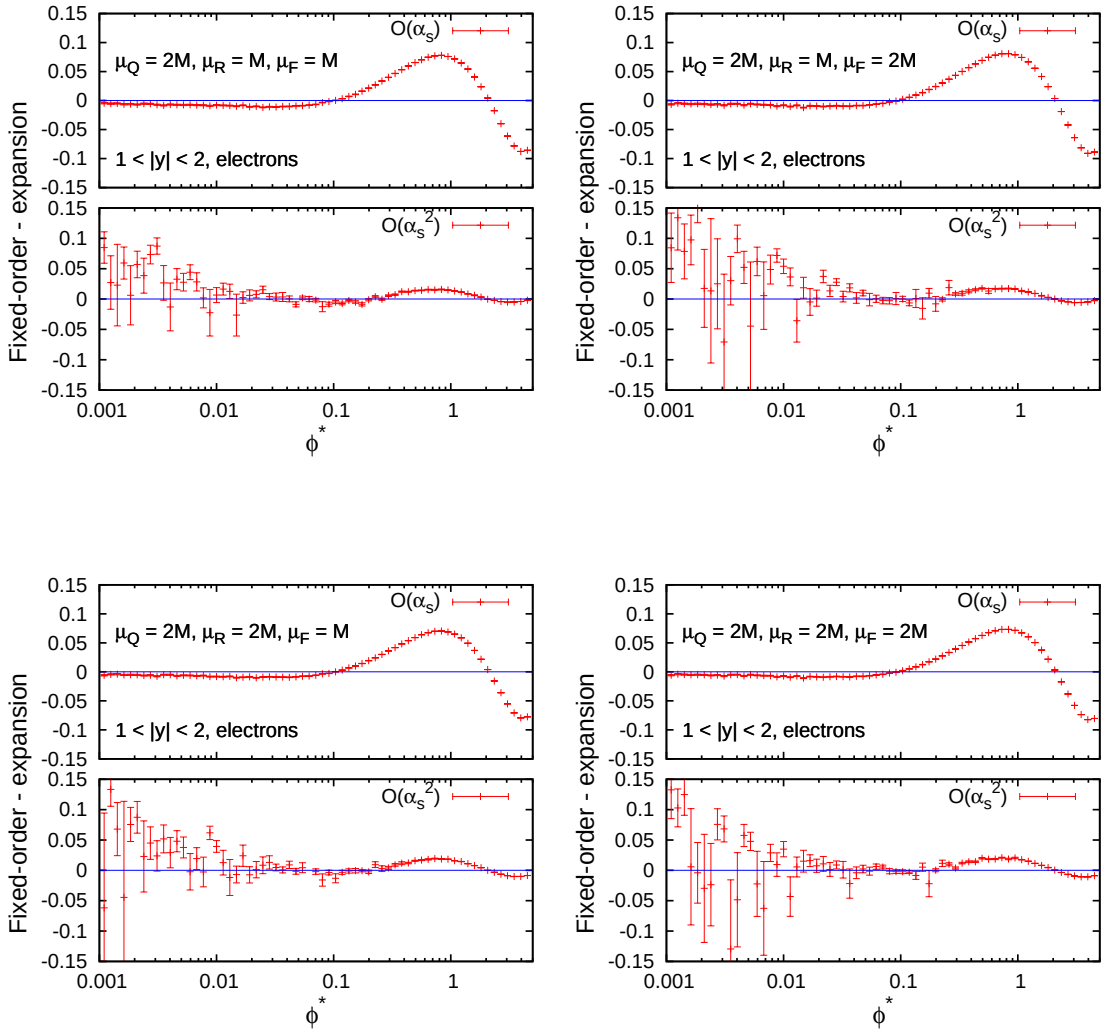

FIGURE C.6. Plots showing the cancellation of large logarithms between the fixed-order component and the expansion of the resummation, for DØ data in the $Z \to ee$ channel around the resonance and the rapidity range $1 < |y| < 2$. The scale $\mu_Q = 2M$.

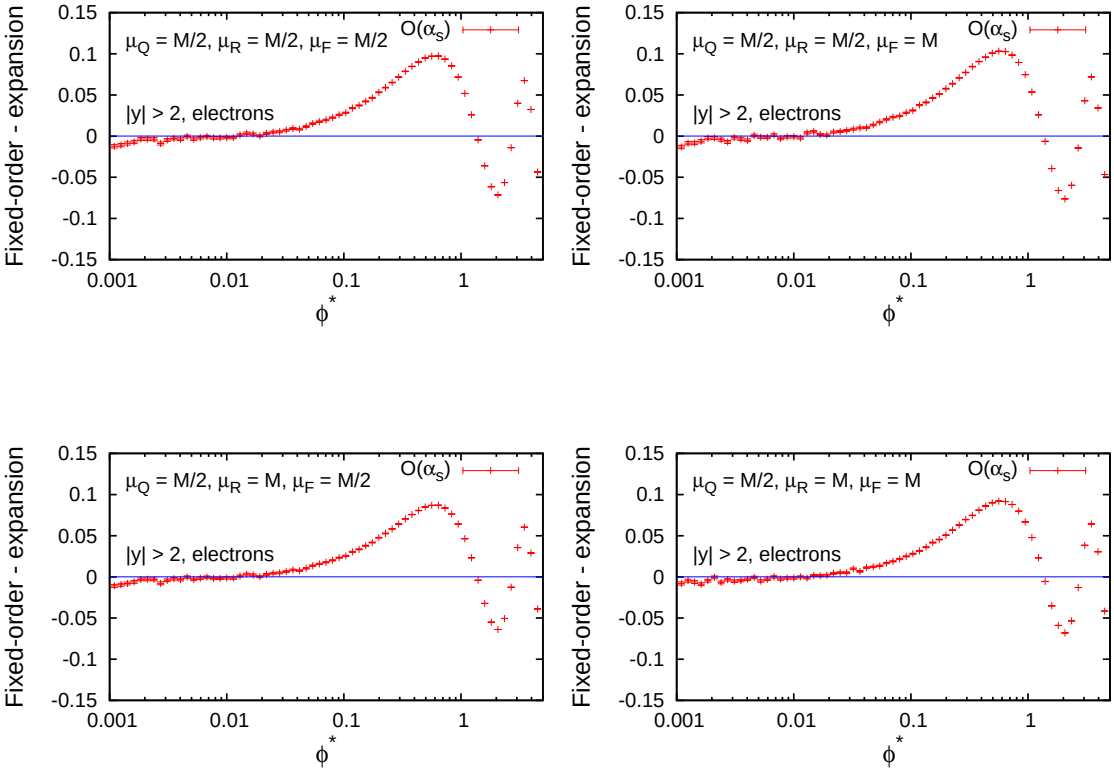

FIGURE C.7. Plots showing the cancellation of large logarithms between the fixed-order component and the expansion of the resummation, for DØ data in the $Z \to ee$ channel around the resonance and the rapidity range $|y| > 2$. The scale $\mu_Q = M/2$.

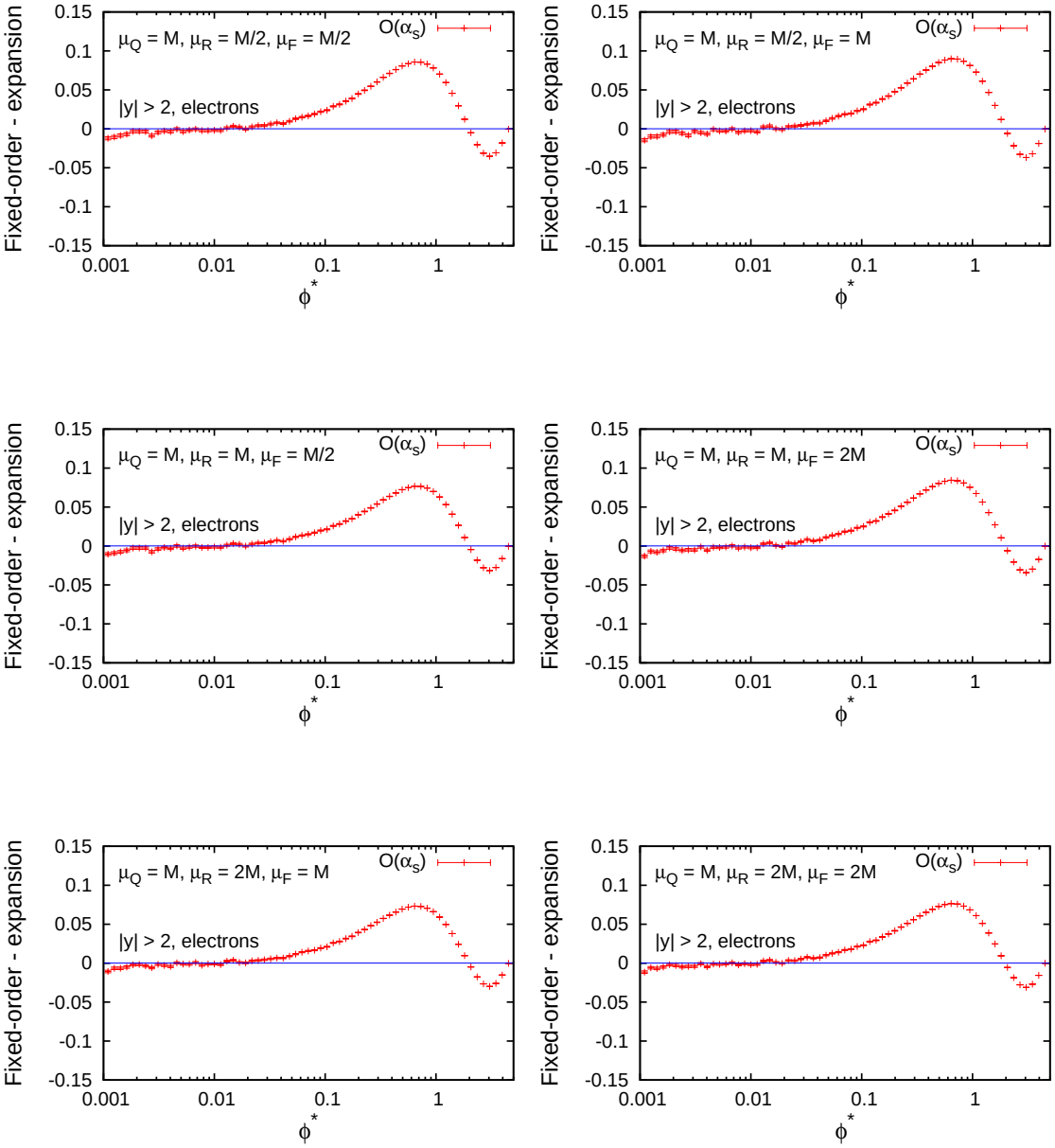

FIGURE C.8. Plots showing the cancellation of large logarithms between the fixed-order component and the expansion of the resummation, for DØ data in the Z $\to ee$ channel around the resonance and the rapidity range $|y| > 2$. The scale $\mu_Q = M$.

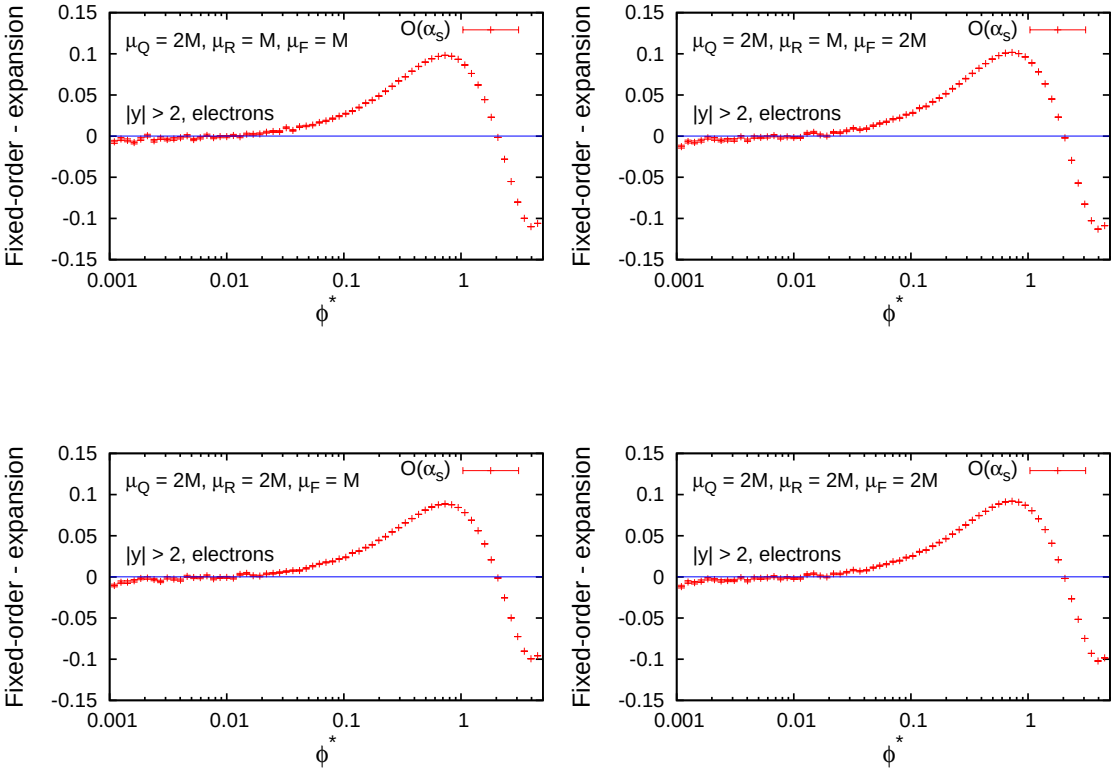

FIGURE C.9. Plots showing the cancellation of large logarithms between the fixed-order component and the expansion of the resummation, for DØ data in the $Z \to ee$ channel around the resonance and the rapidity range $|y| > 2$. The scale $\mu_Q = 2M$.

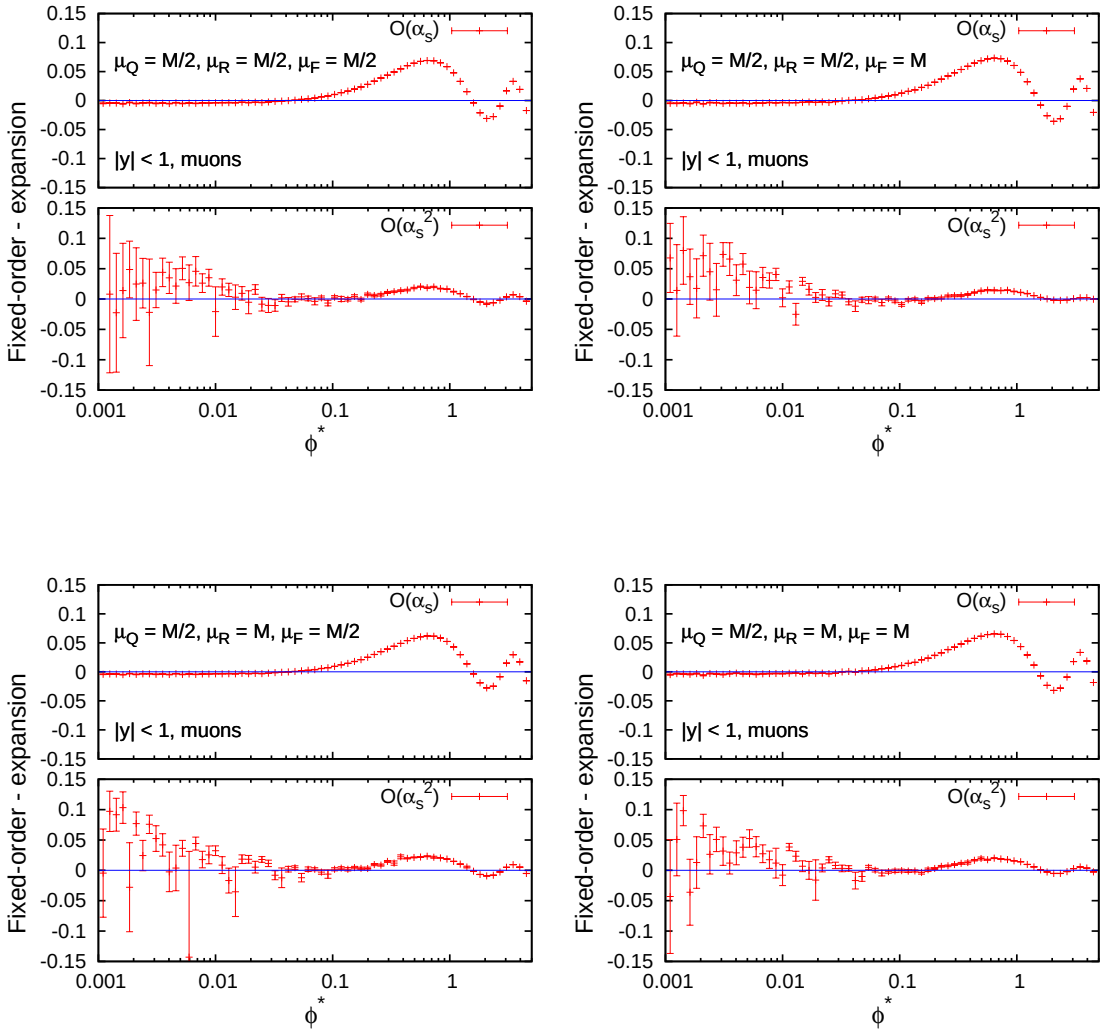

FIGURE C.10. Plots showing the cancellation of large logarithms between the fixed-order component and the expansion of the resummation, for DØ data in the $Z \to \mu\mu$ channel around the resonance and the rapidity range $|y| < 1$. The scale $\mu_Q = M/2$.

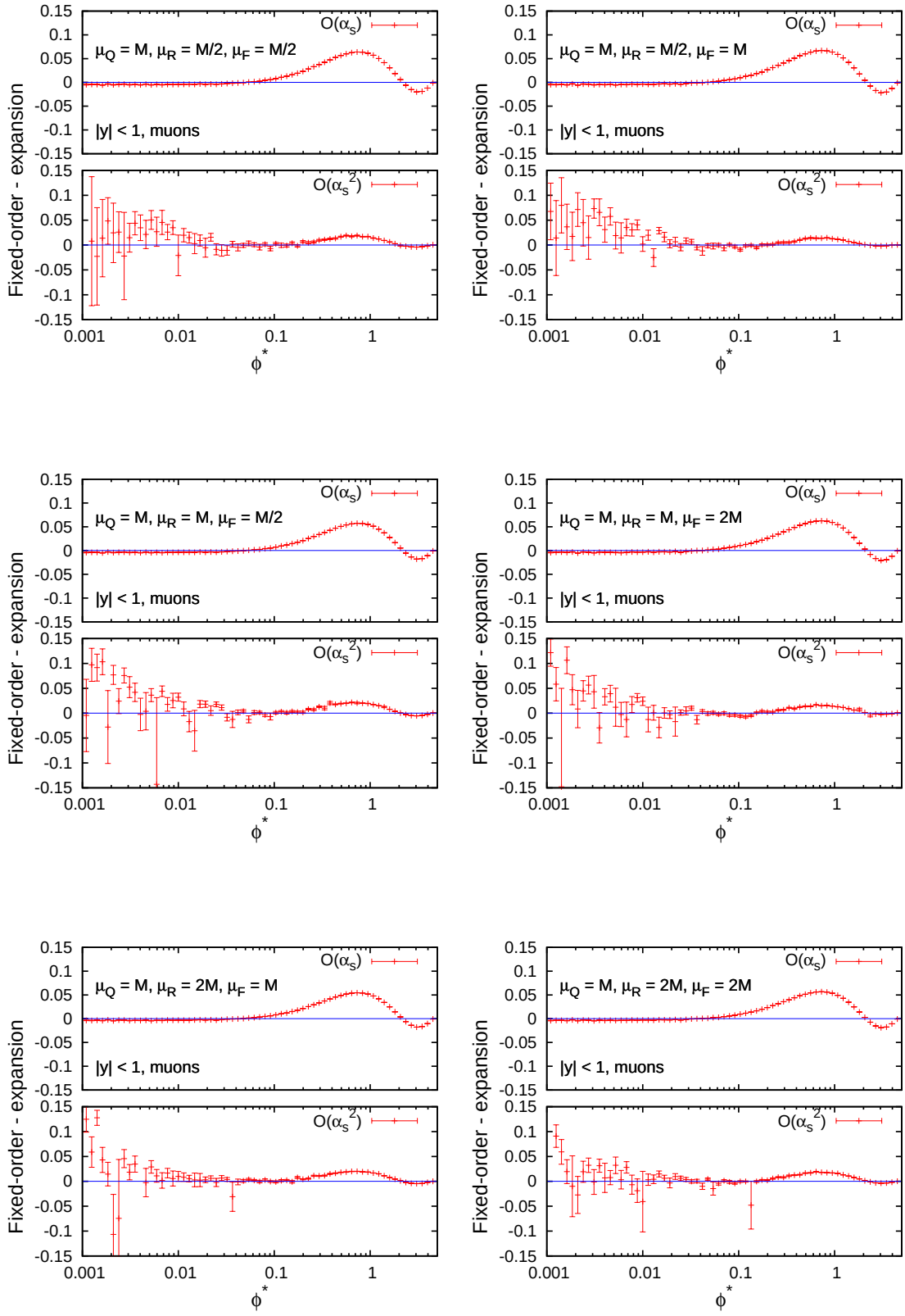

FIGURE C.11. Plots showing the cancellation of large logarithms between the fixed-order component and the expansion of the resummation, for DØ data in the $Z \to \mu\mu$ channel around the resonance and the rapidity range $|y| < 1$. The scale $\mu_Q = M$.

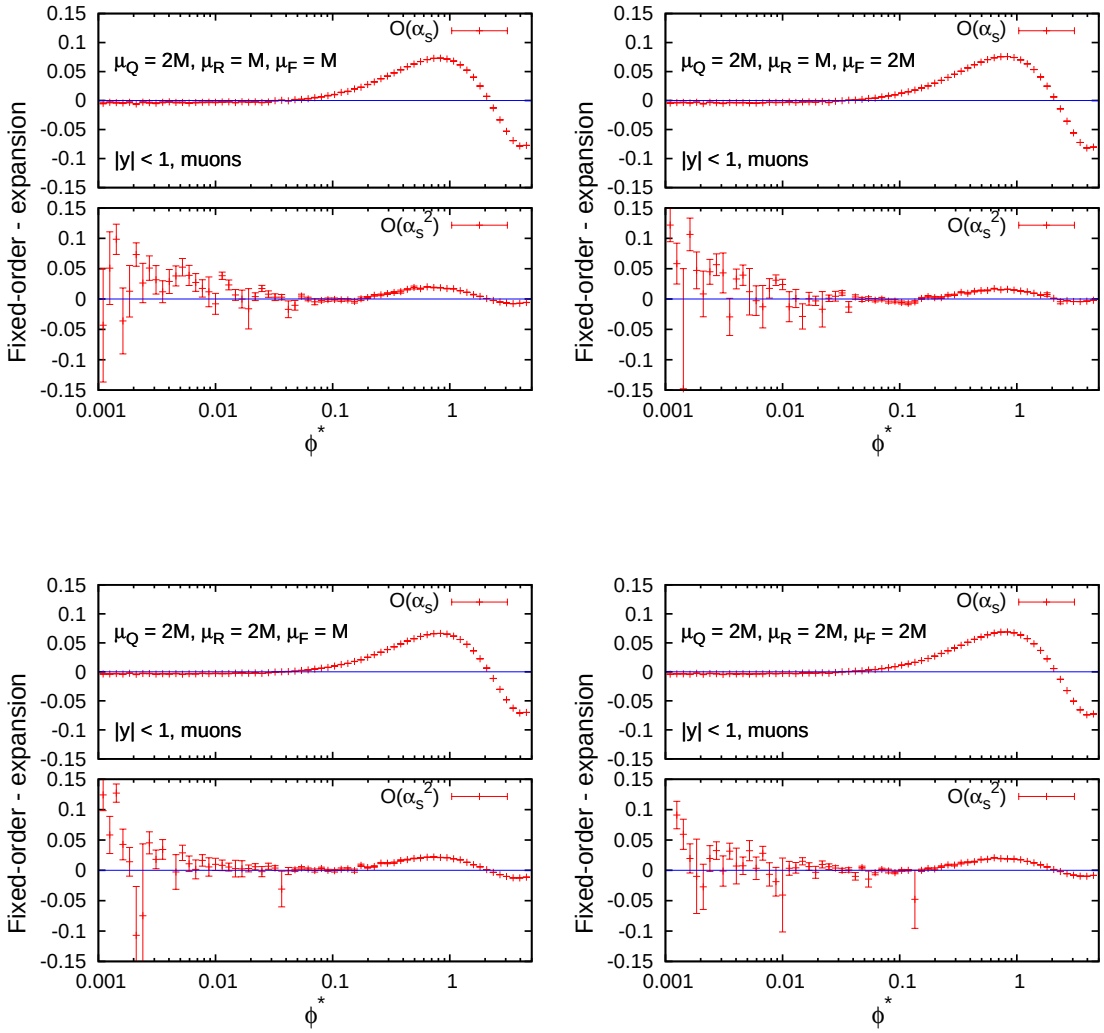

FIGURE C.12. Plots showing the cancellation of large logarithms between the fixed-order component and the expansion of the resummation, for DØ data in the $Z \to \mu\mu$ channel around the resonance and the rapidity range $|y| < 1$. The scale $\mu_Q = 2M$.

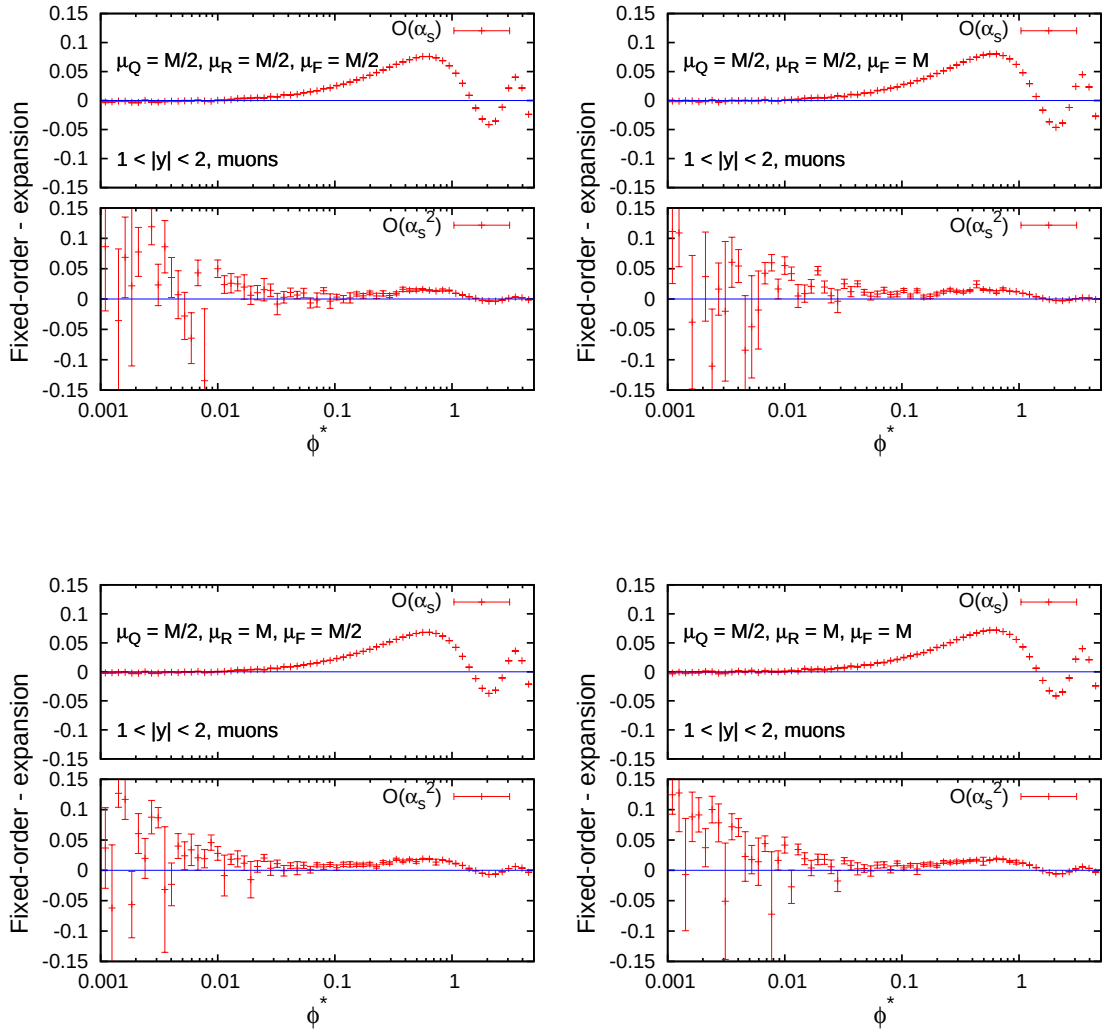

FIGURE C.13. Plots showing the cancellation of large logarithms between the fixed-order component and the expansion of the resummation, for DØ data in the $Z \to \mu\mu$ channel around the resonance and the rapidity range $1 < |y| < 2$. The scale $\mu_Q = M/2$.

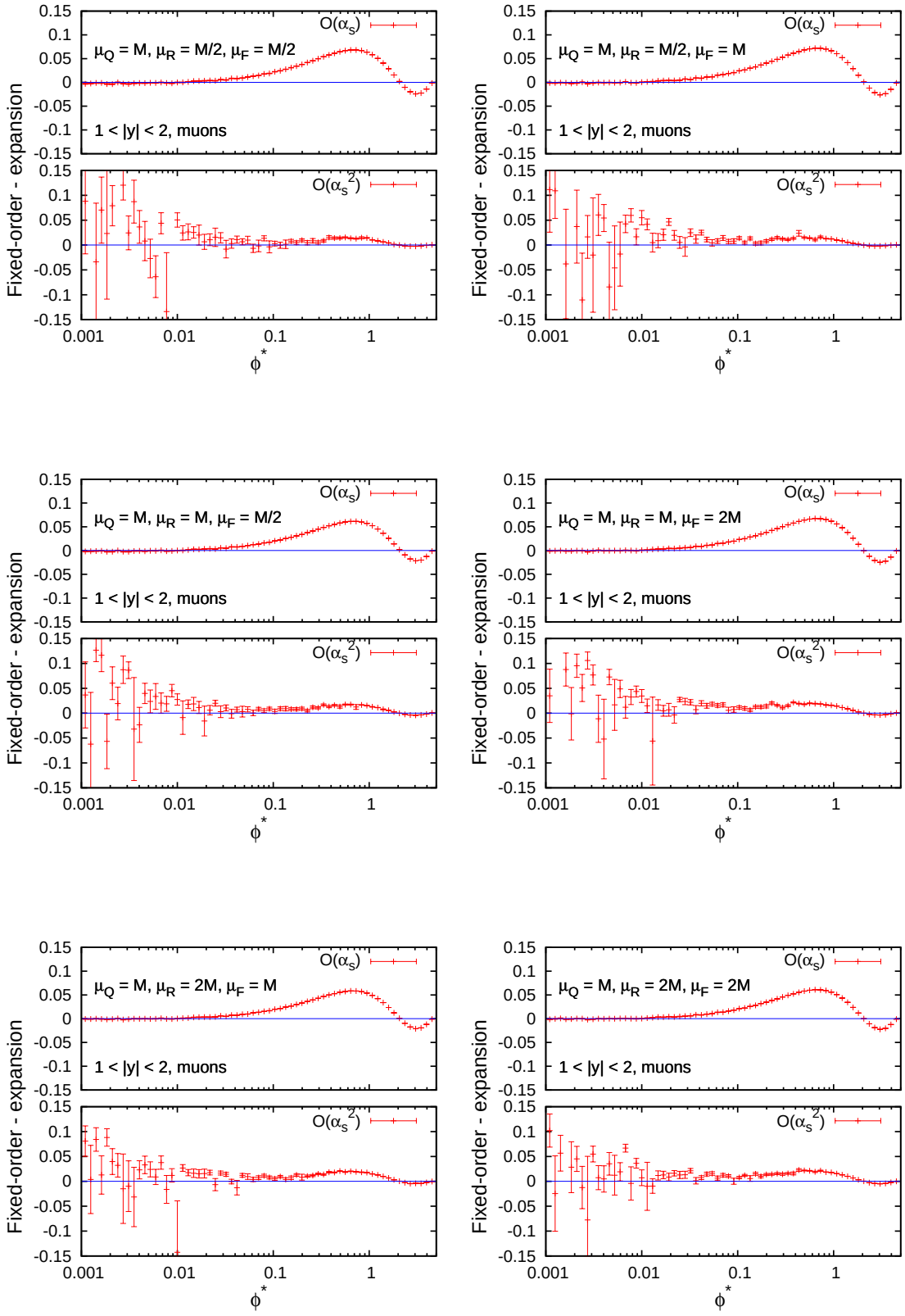

FIGURE C.14. Plots showing the cancellation of large logarithms between the fixed-order component and the expansion of the resummation, for DØ data in the $Z \to \mu\mu$ channel around the resonance and the rapidity range $1 < |y| < 2$. The scale $\mu_Q = M$.

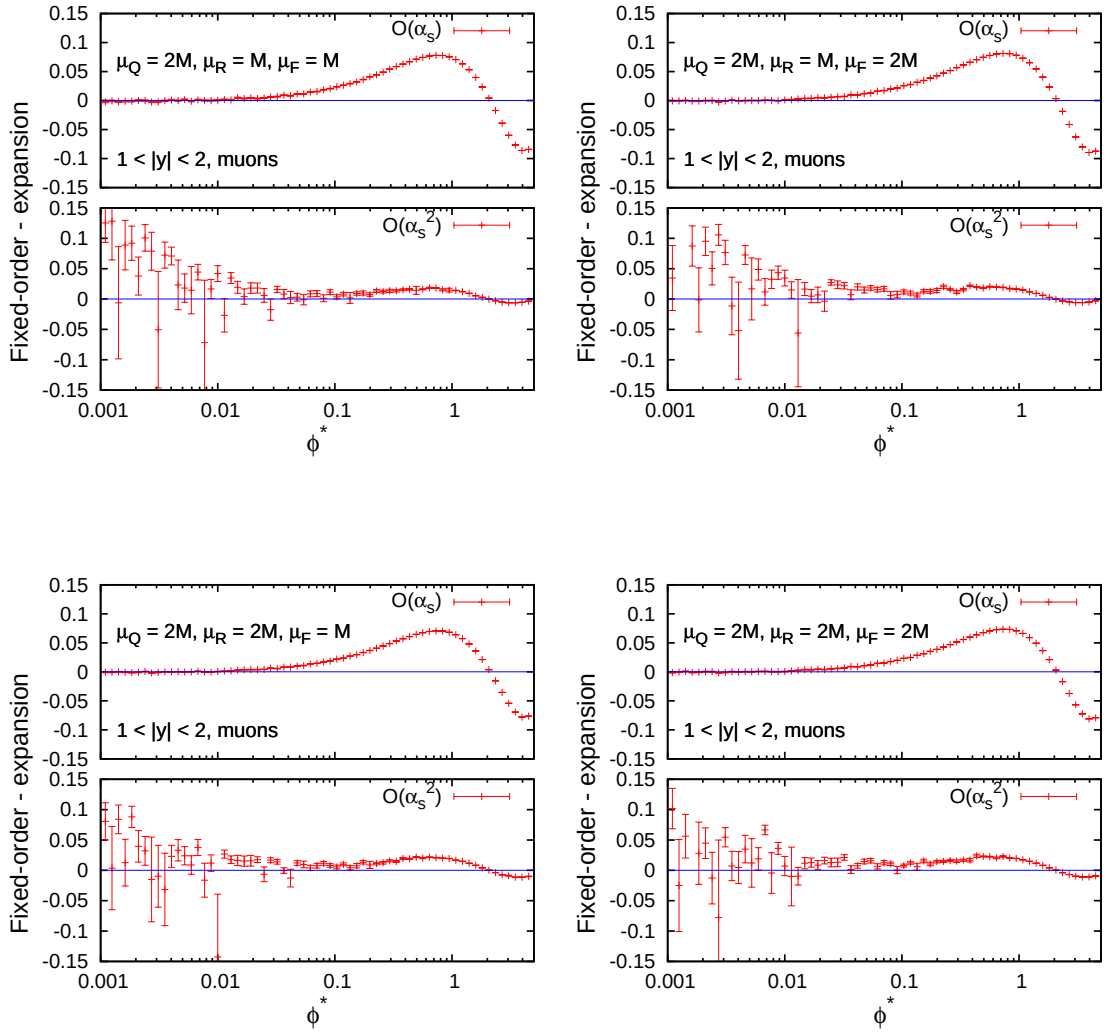

FIGURE C.15. Plots showing the cancellation of large logarithms between the fixed-order component and the expansion of the resummation, for DØ data in the $Z \to \mu\mu$ channel around the resonance and the rapidity range $1 < |y| < 2$. The scale $\mu_Q = 2M$.

C.1.2. Prediction at low mass.

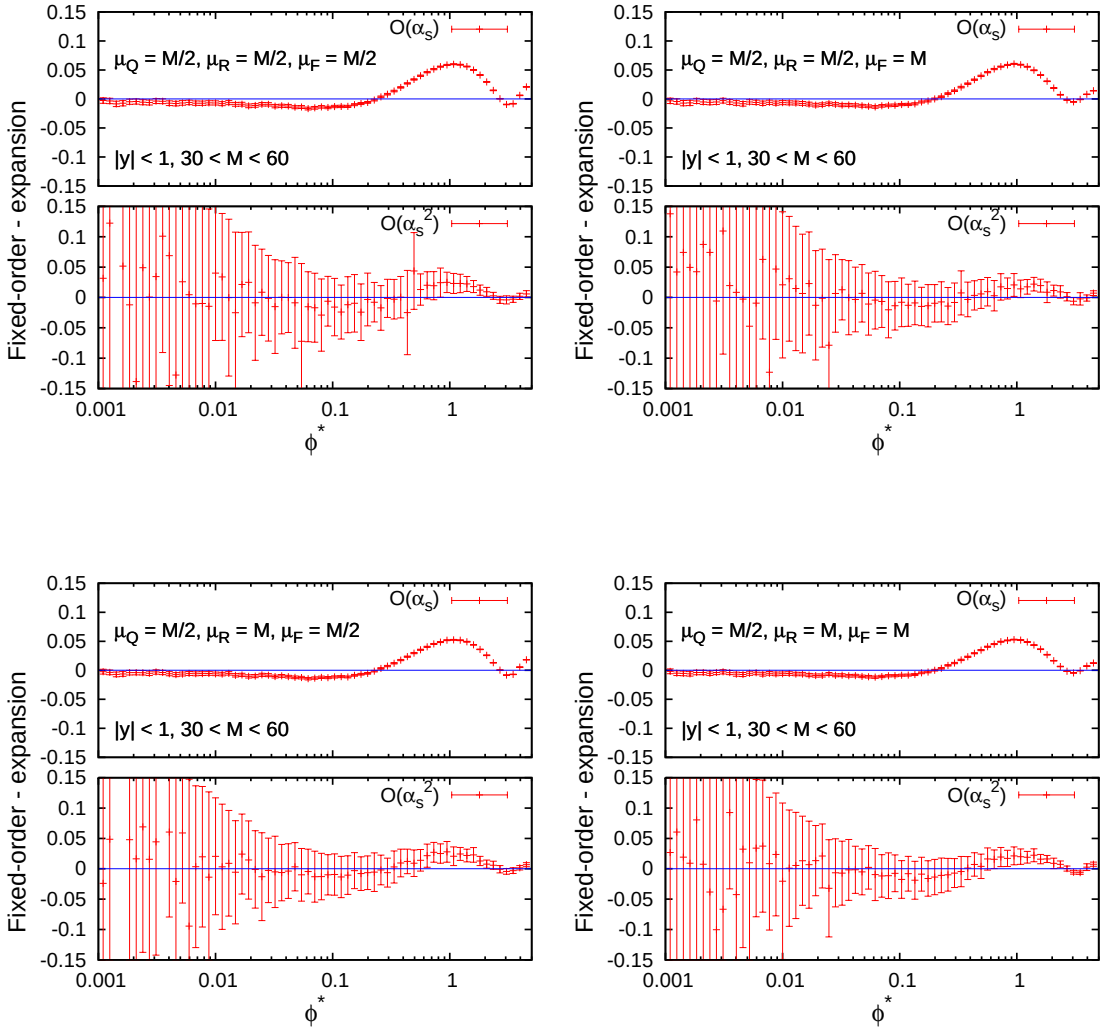

FIGURE C.16. Plots showing the cancellation of large logarithms between the fixed-order component and the expansion of the resummation, for DØ data at low invariant mass and the rapidity range $|y| < 1$. The scale $\mu_Q = M/2$.

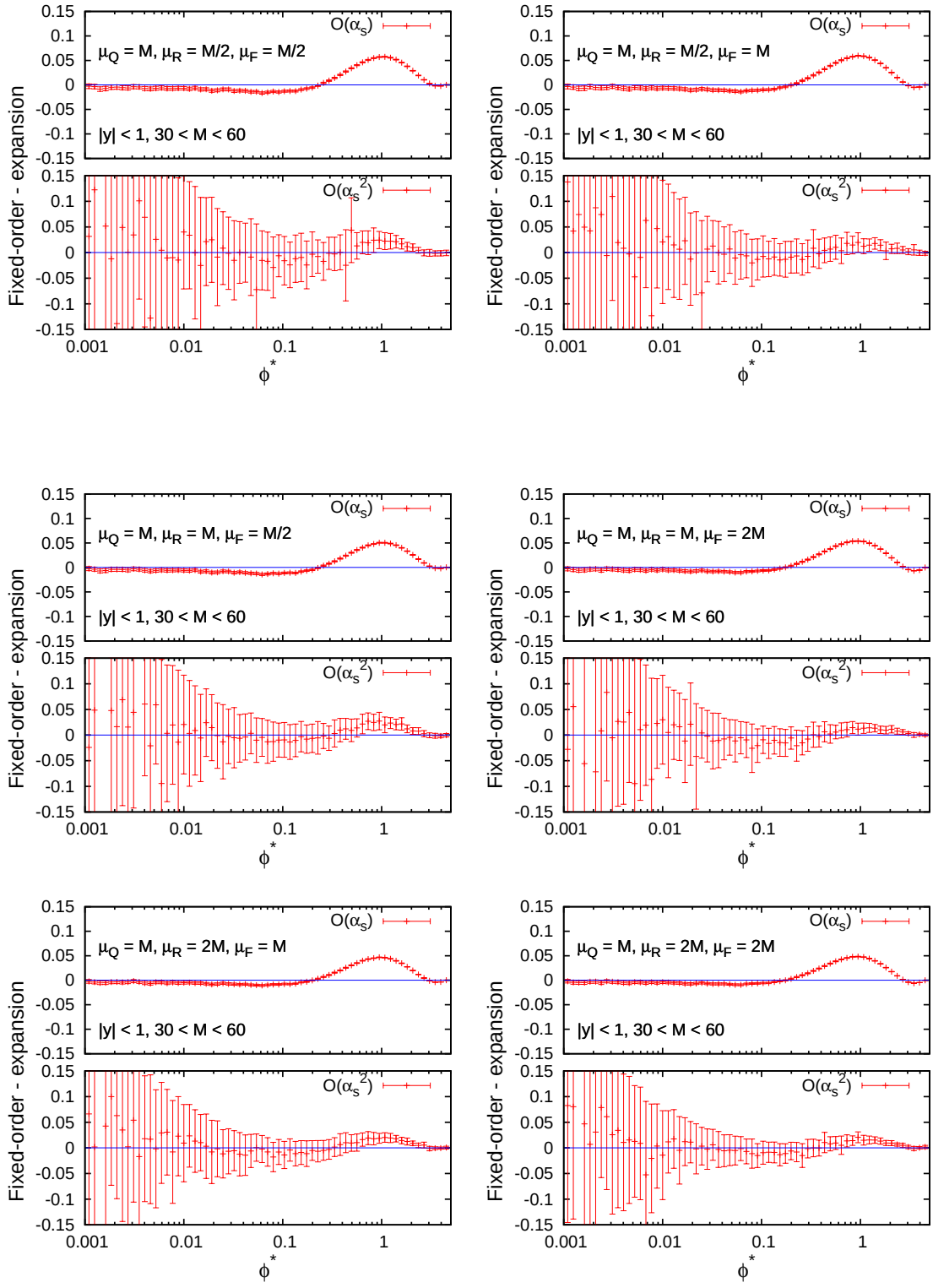

FIGURE C.17. Plots showing the cancellation of large logarithms between the fixed-order component and the expansion of the resummation, for DØ data at low invariant mass and the rapidity range $|y| < 1$. The scale $\mu_Q = M$.

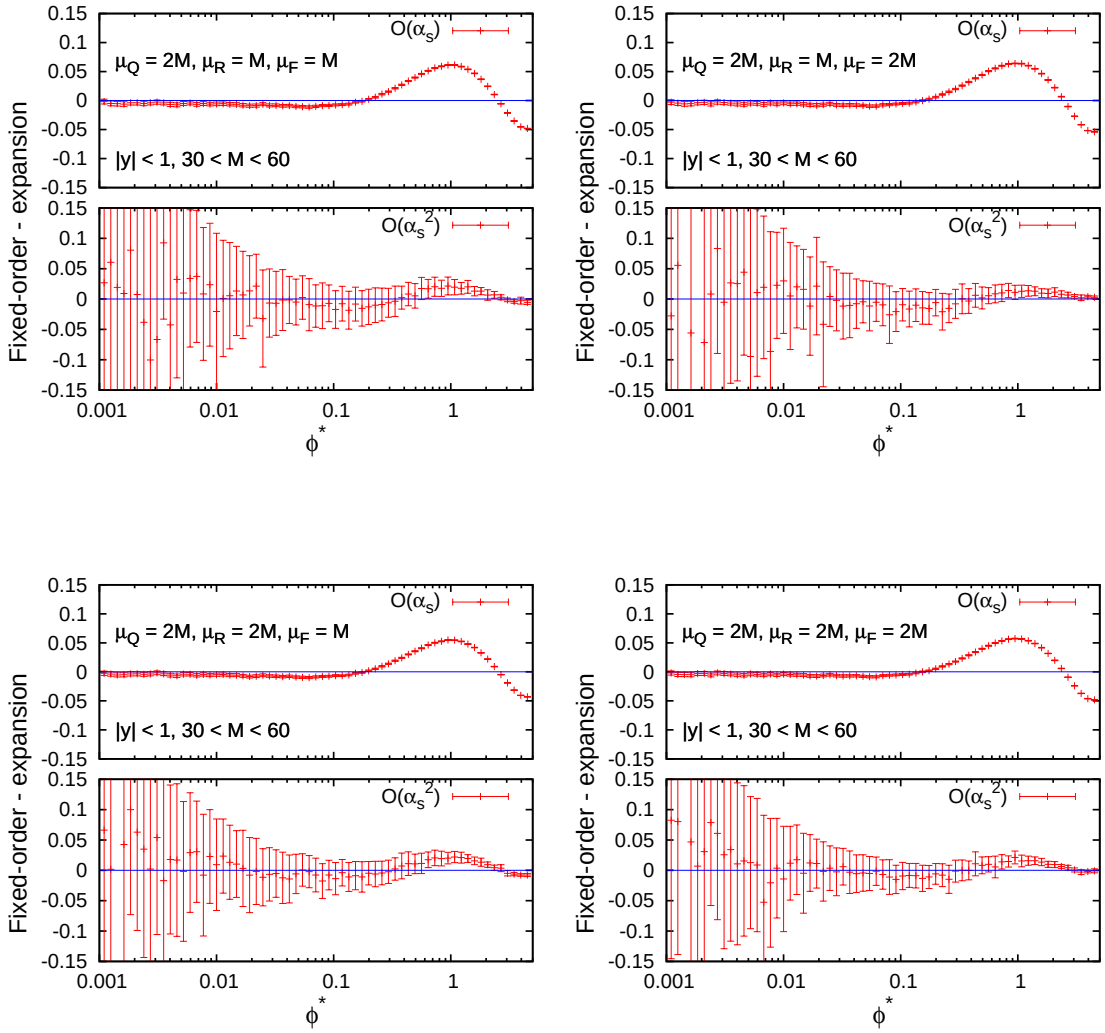

FIGURE C.18. Plots showing the cancellation of large logarithms between the fixed-order component and the expansion of the resummation, for DØ data at low invariant mass and the rapidity range $|y| < 1$. The scale $\mu_Q = 2M$.

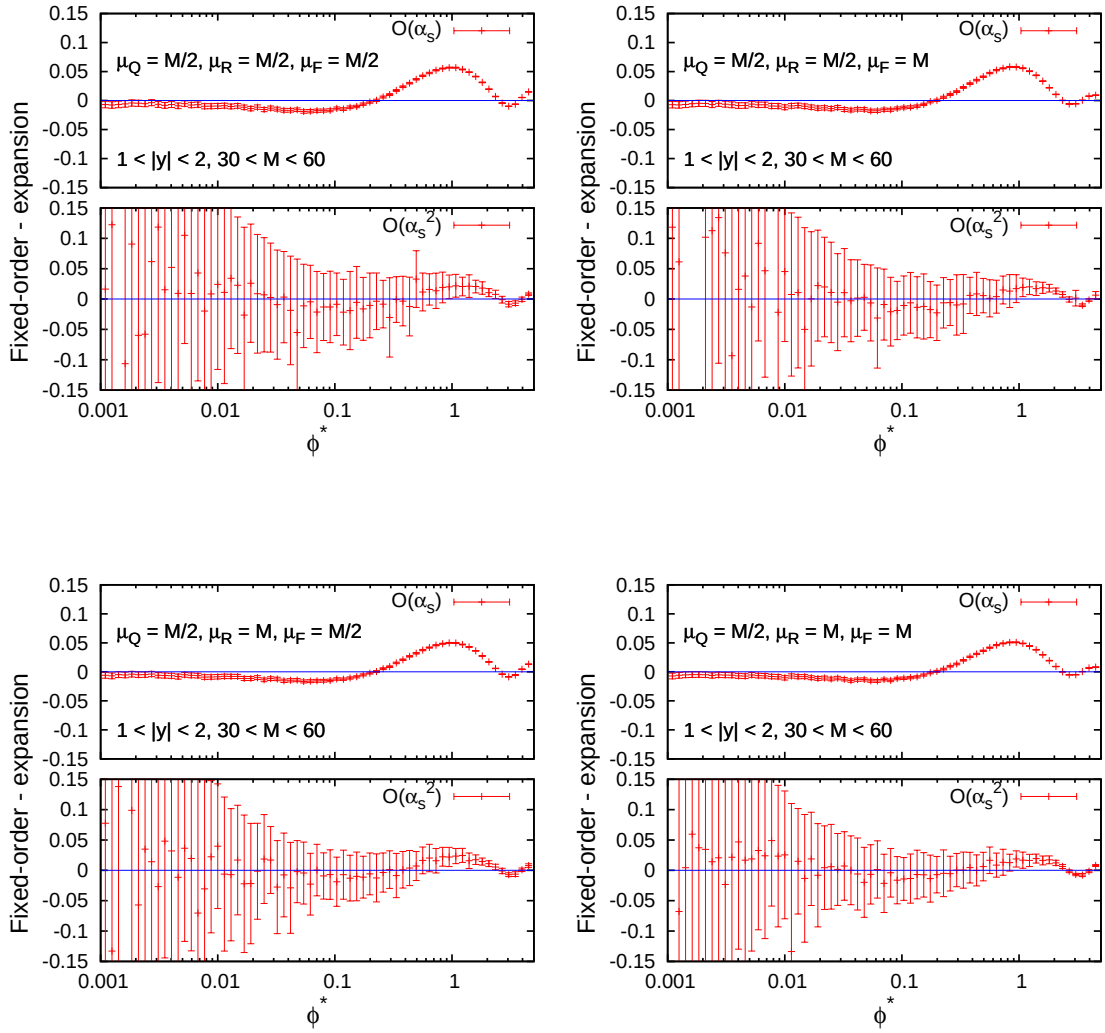

FIGURE C.19. Plots showing the cancellation of large logarithms between the fixed-order component and the expansion of the resummation, for DØ data at low invariant mass and the rapidity range $1 < |y| < 2$. The scale $\mu_{\mathrm{Q}} = M/2$.

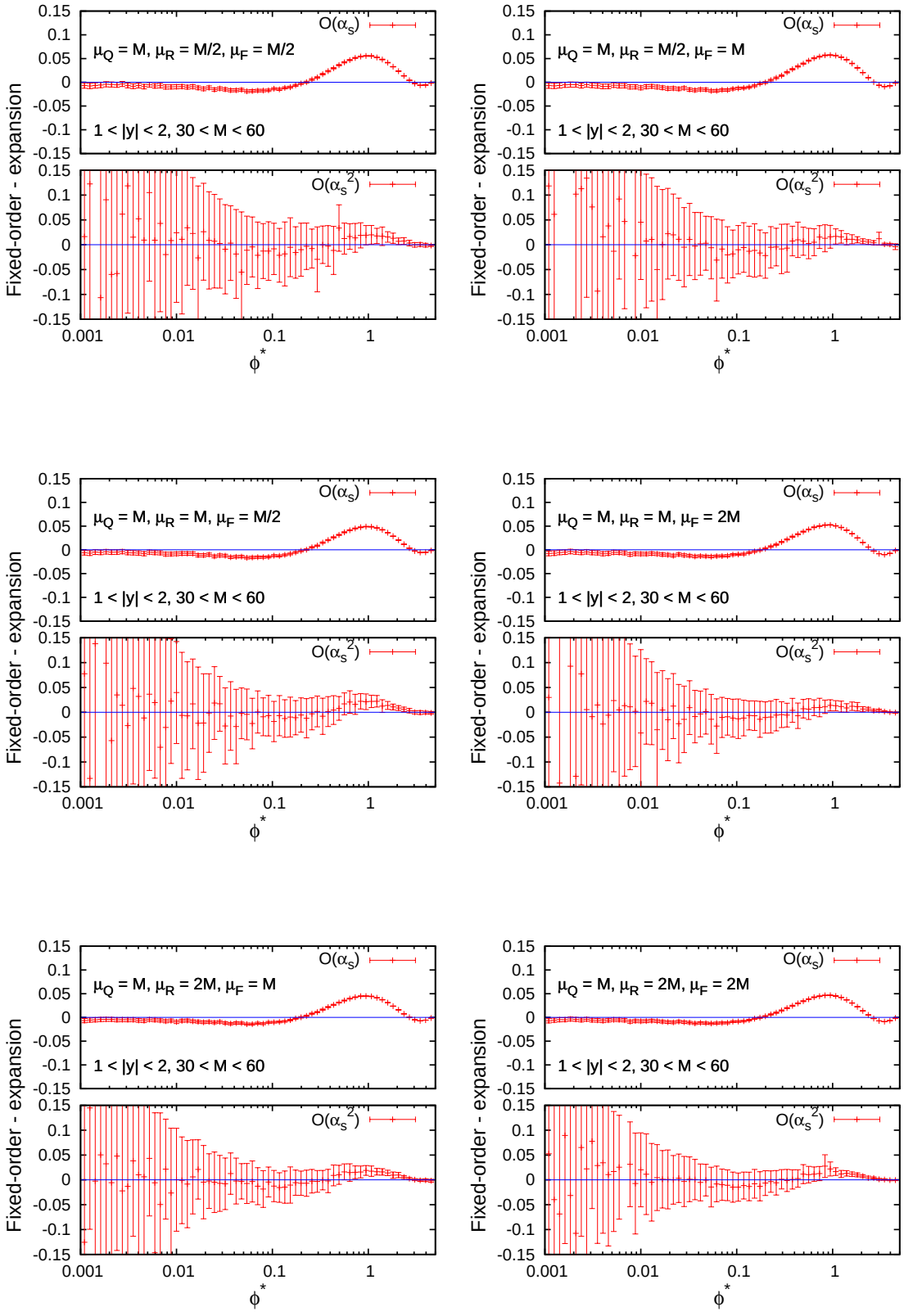

FIGURE C.20. Plots showing the cancellation of large logarithms between the fixed-order component and the expansion of the resummation, for DØ data at low invariant mass and the rapidity range $1 < |y| < 2$. The scale $\mu_Q = M$.

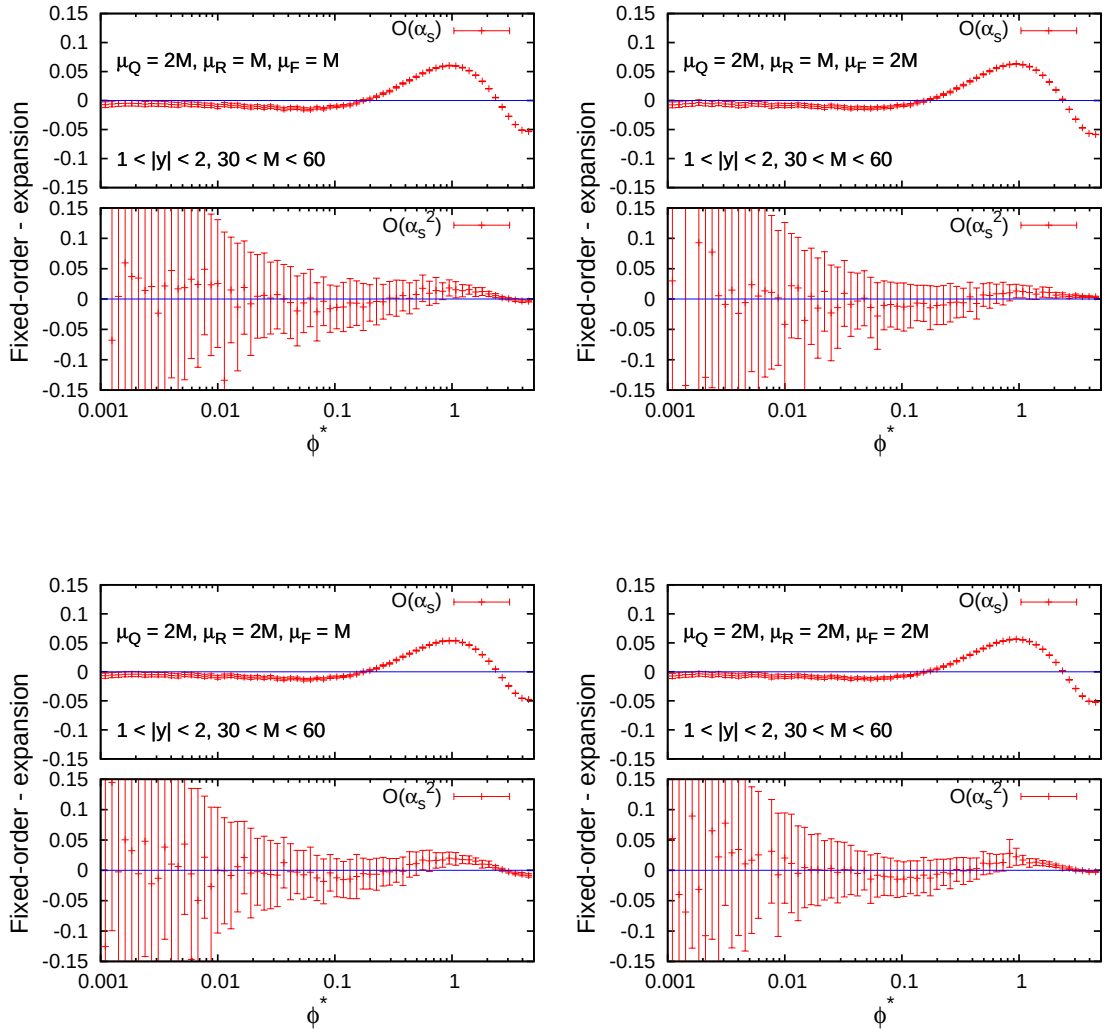

FIGURE C.21. Plots showing the cancellation of large logarithms between the fixed-order component and the expansion of the resummation, for DØ data at low invariant mass and the rapidity range $1 < |y| < 2$. The scale $\mu_{\mathrm{Q}} = 2M$.

C.2. Cancellation of logs for ATLAS predictions

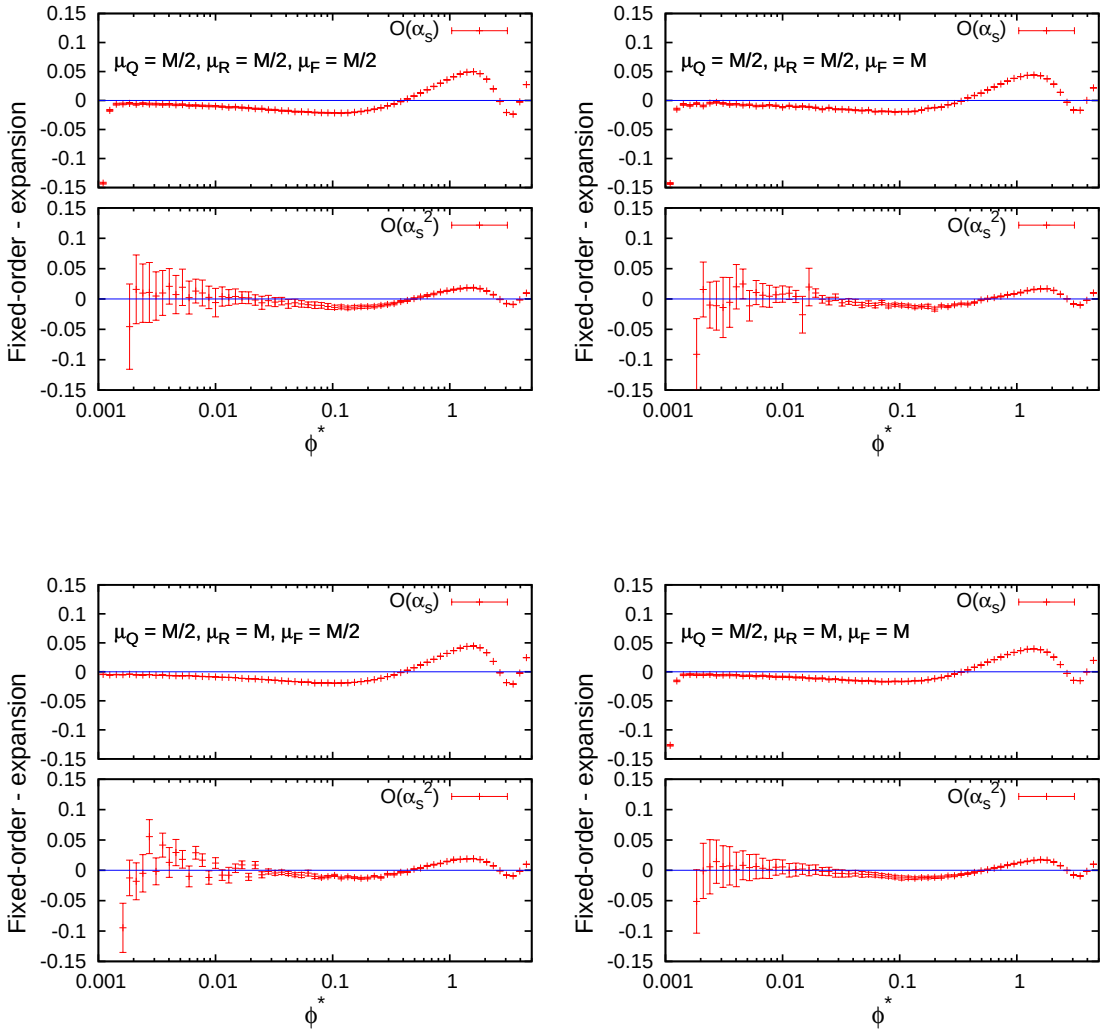

FIGURE C.22. Plots showing the cancellation of large logarithms between the fixed-order component and the expansion of the resummation, for the predicted ATLAS ϕ^* distributions with $\mu_Q = M/2$.

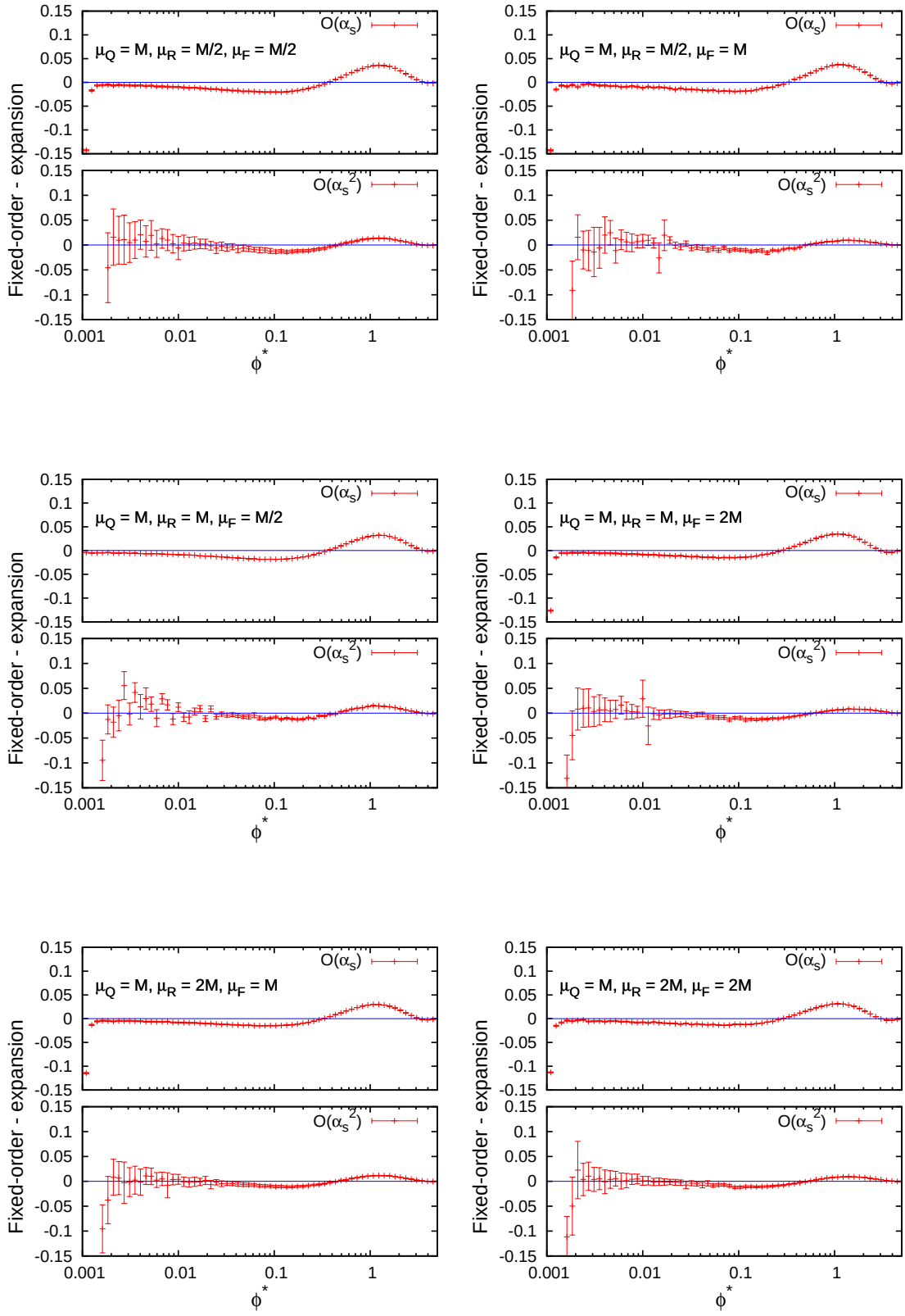

FIGURE C.23. Plots showing the cancellation of large logarithms between the fixed-order component and the expansion of the resummation, for the predicted ATLAS ϕ^* distributions with $\mu_Q = M$.

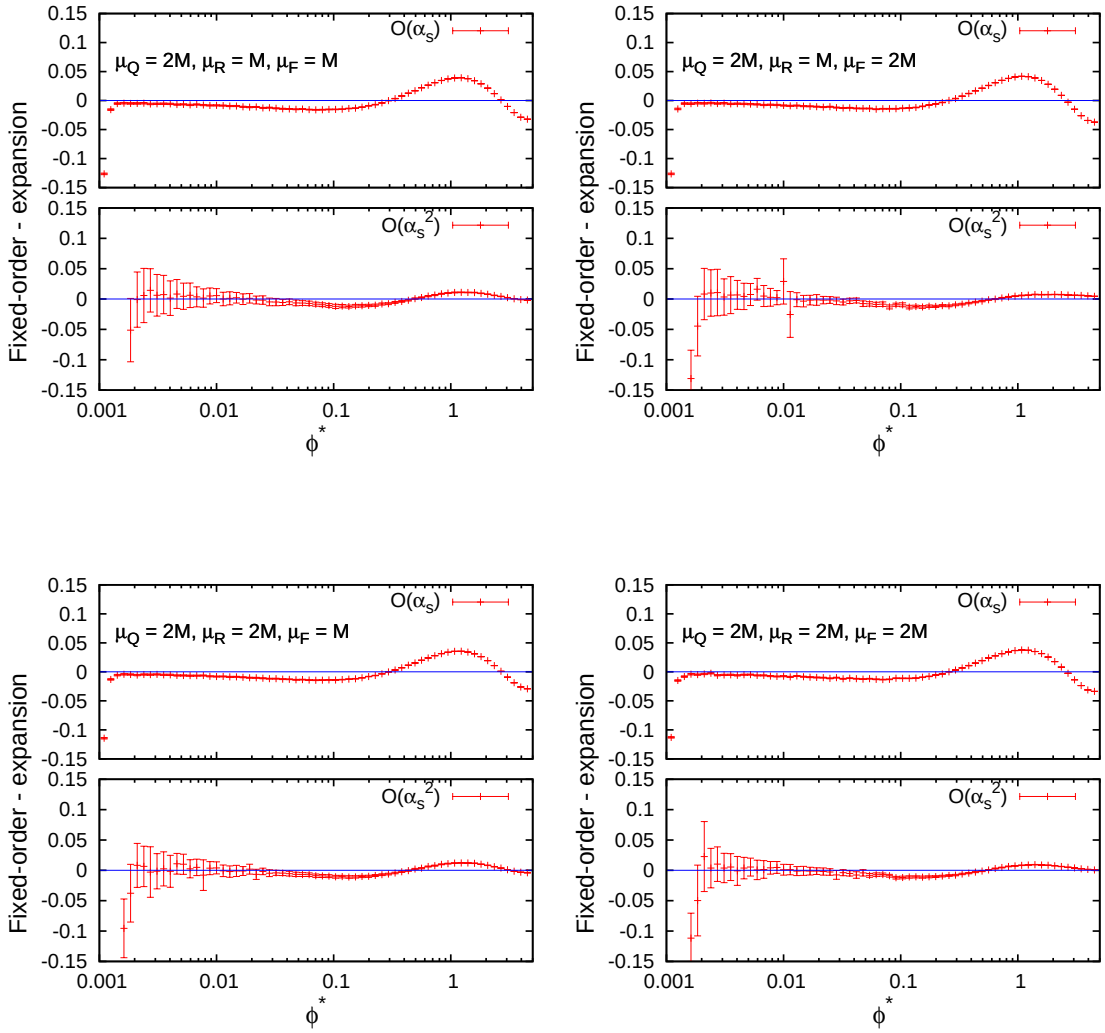

FIGURE C.24. Plots showing the cancellation of large logarithms between the fixed-order component and the expansion of the resummation, for the predicted ATLAS ϕ^* distributions with $\mu_Q = 2M$.

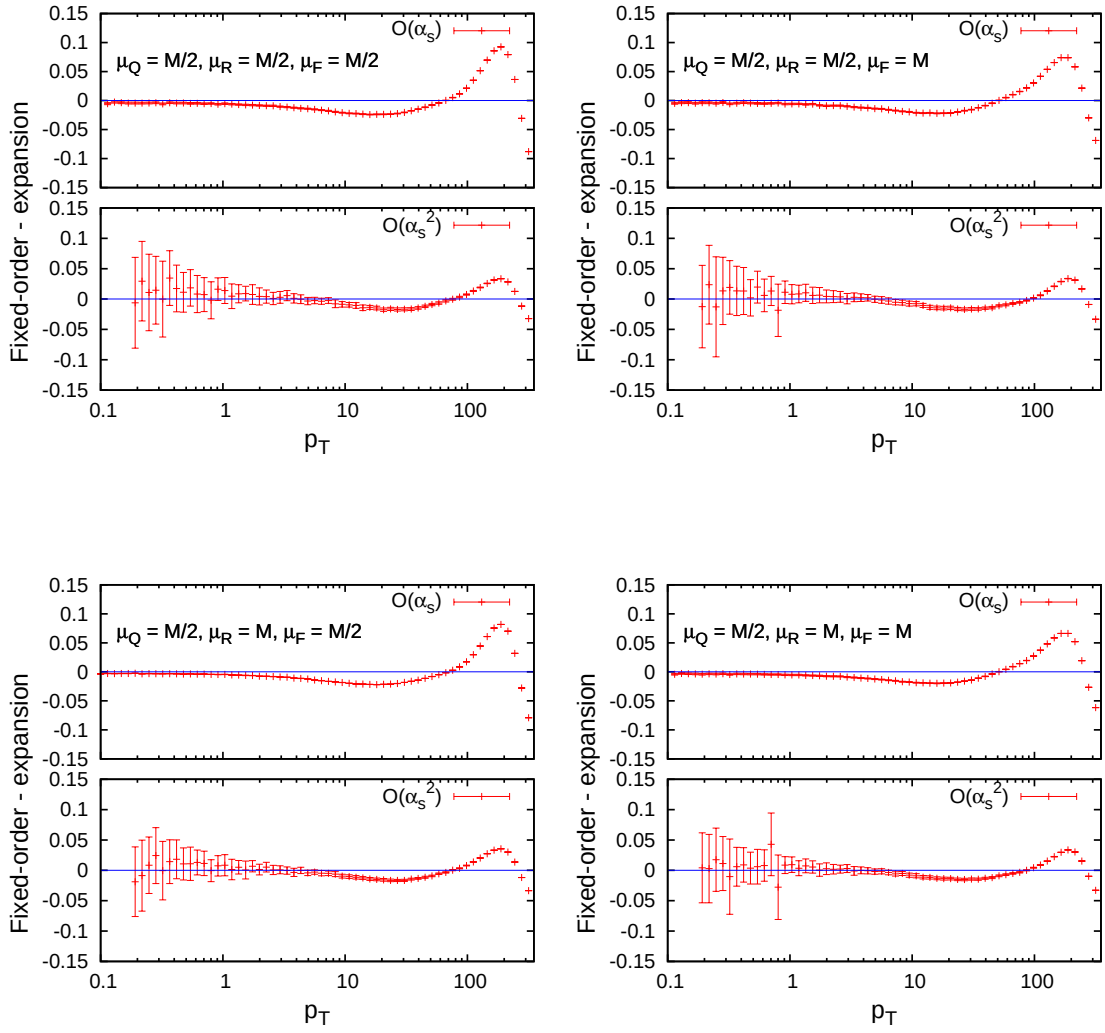

FIGURE C.25. Plots showing the cancellation of large logarithms between the fixed-order component and the expansion of the resummation, for the ATLAS Q_{T} distributions with $\mu_{\mathrm{Q}} = M/2$.

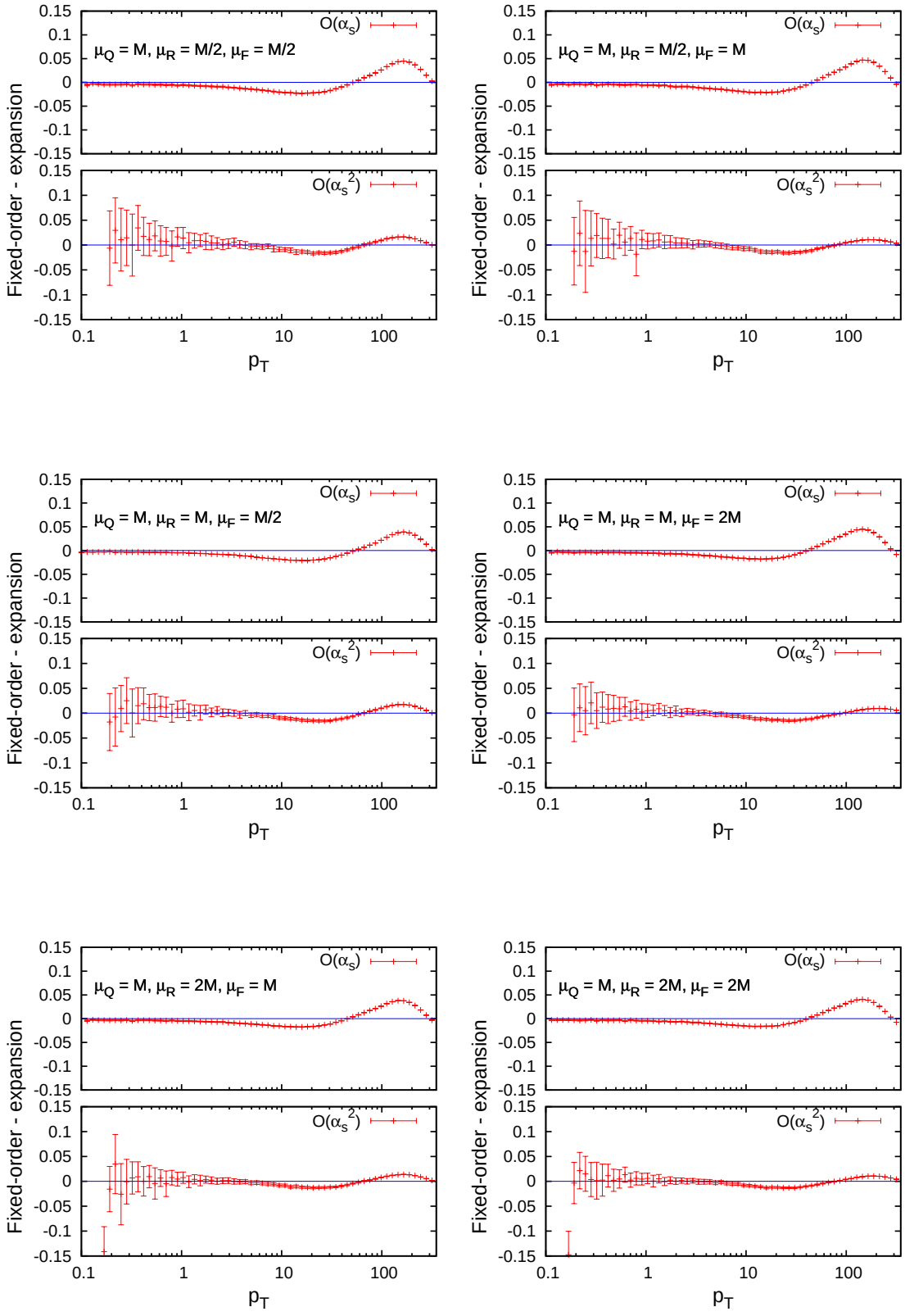

FIGURE C.26. Plots showing the cancellation of large logarithms between the fixed-order component and the expansion of the resummation, for the ATLAS Q_{T} distributions with $\mu_{\mathrm{Q}} = M$.

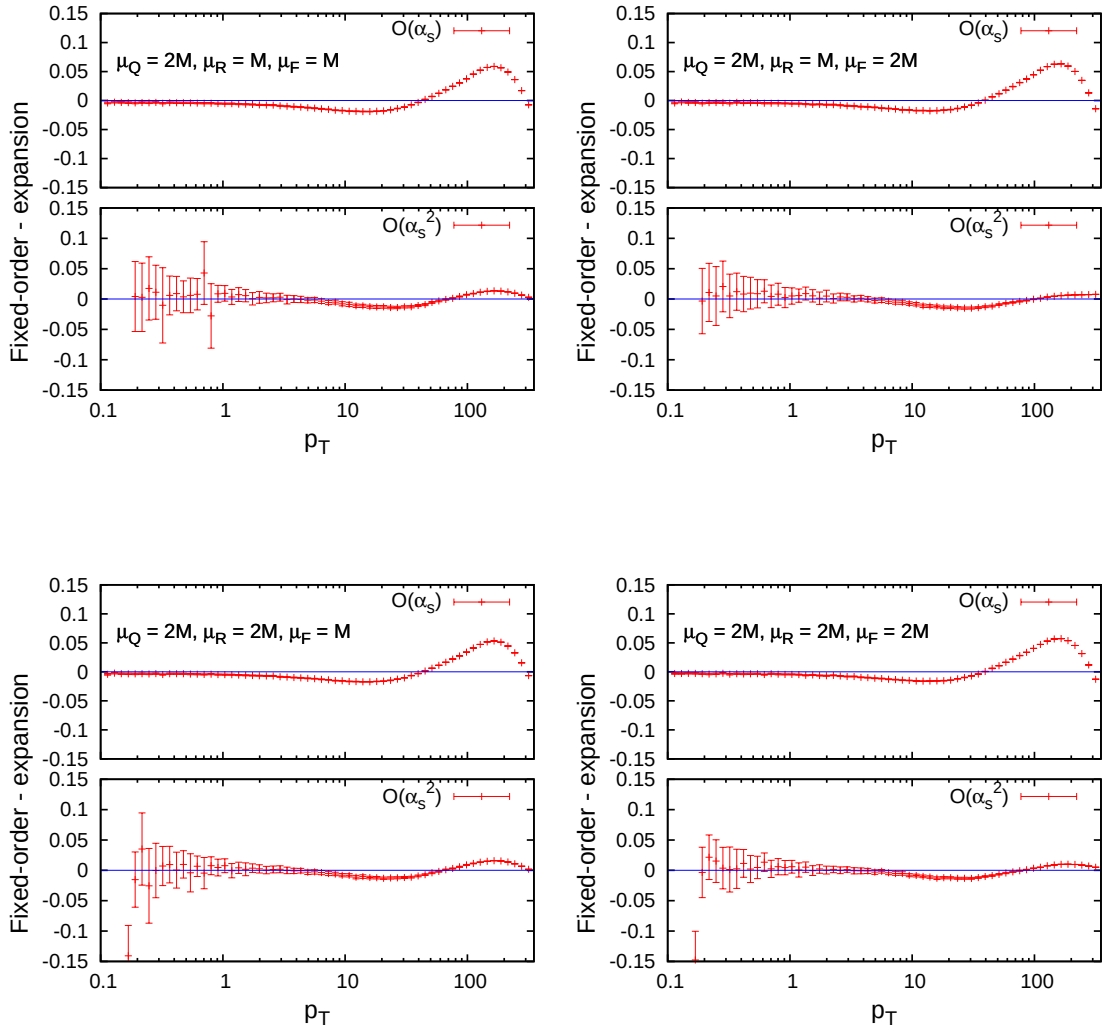

FIGURE C.27. Plots showing the cancellation of large logarithms between the fixed-order component and the expansion of the resummation, for the ATLAS Q_{T} distributions with $\mu_{\mathrm{Q}} = 2M$.

C.3. Cancellation of logs for CMS predictions

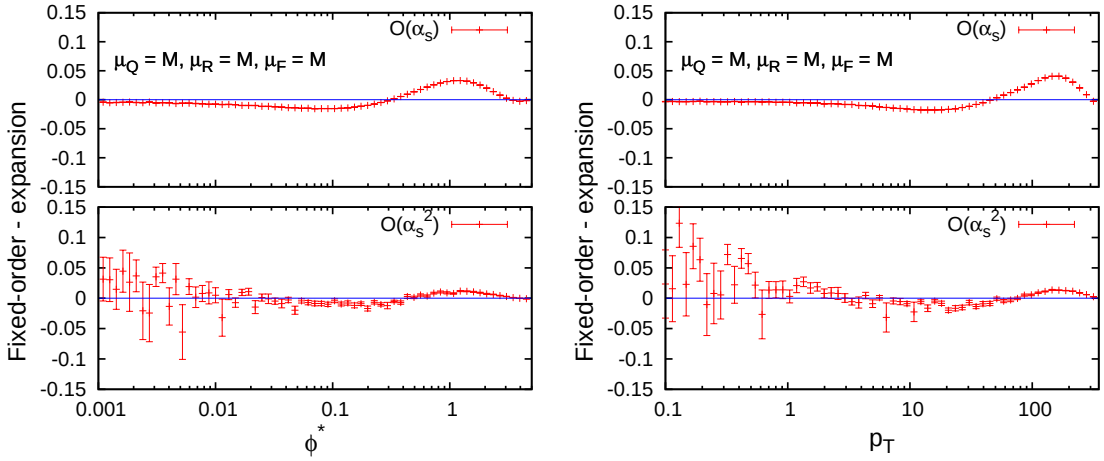

FIGURE C.28. Plots showing the cancellation of large logarithms between the fixed-order component and the expansion of the resummation, for the predicted CMS ϕ^* and Q_{T} distributions with the central scale choices.

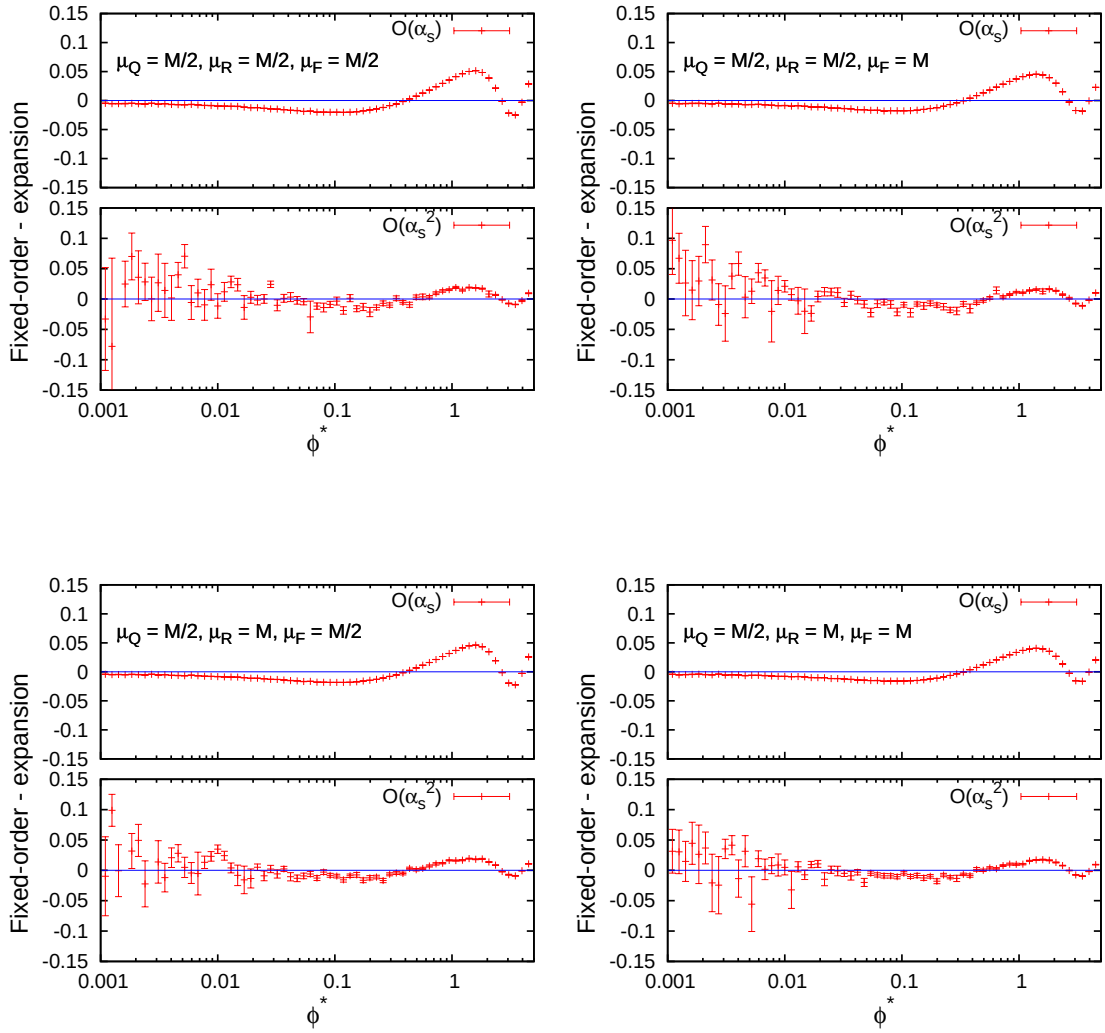

FIGURE C.29. Plots showing the cancellation of large logarithms between the fixed-order component and the expansion of the resummation, for the predicted CMS ϕ^* distributions with $\mu_Q = M/2$.

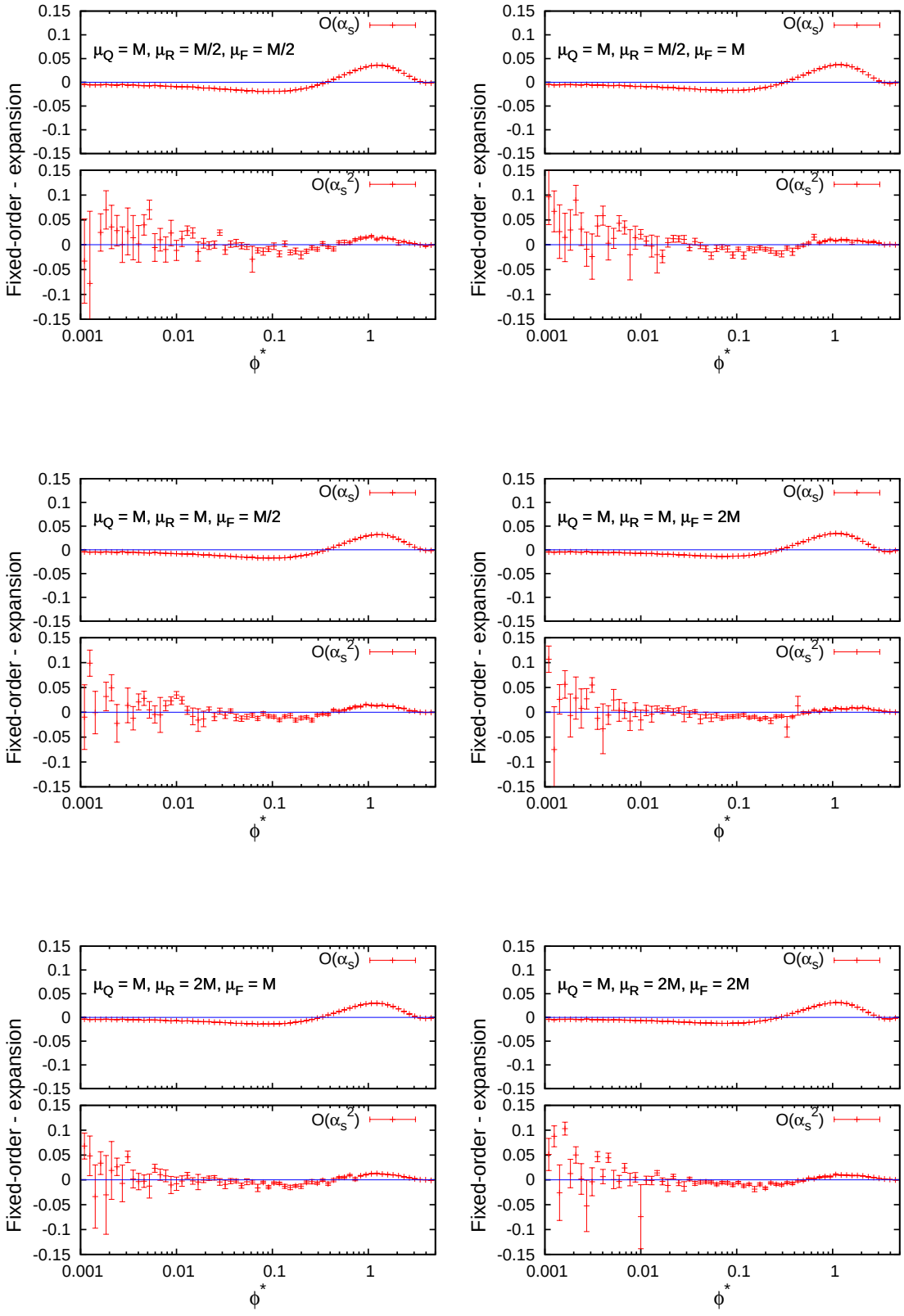

FIGURE C.30. Plots showing the cancellation of large logarithms between the fixed-order component and the expansion of the resummation, for the predicted CMS ϕ^* distributions with $\mu_Q = M$.

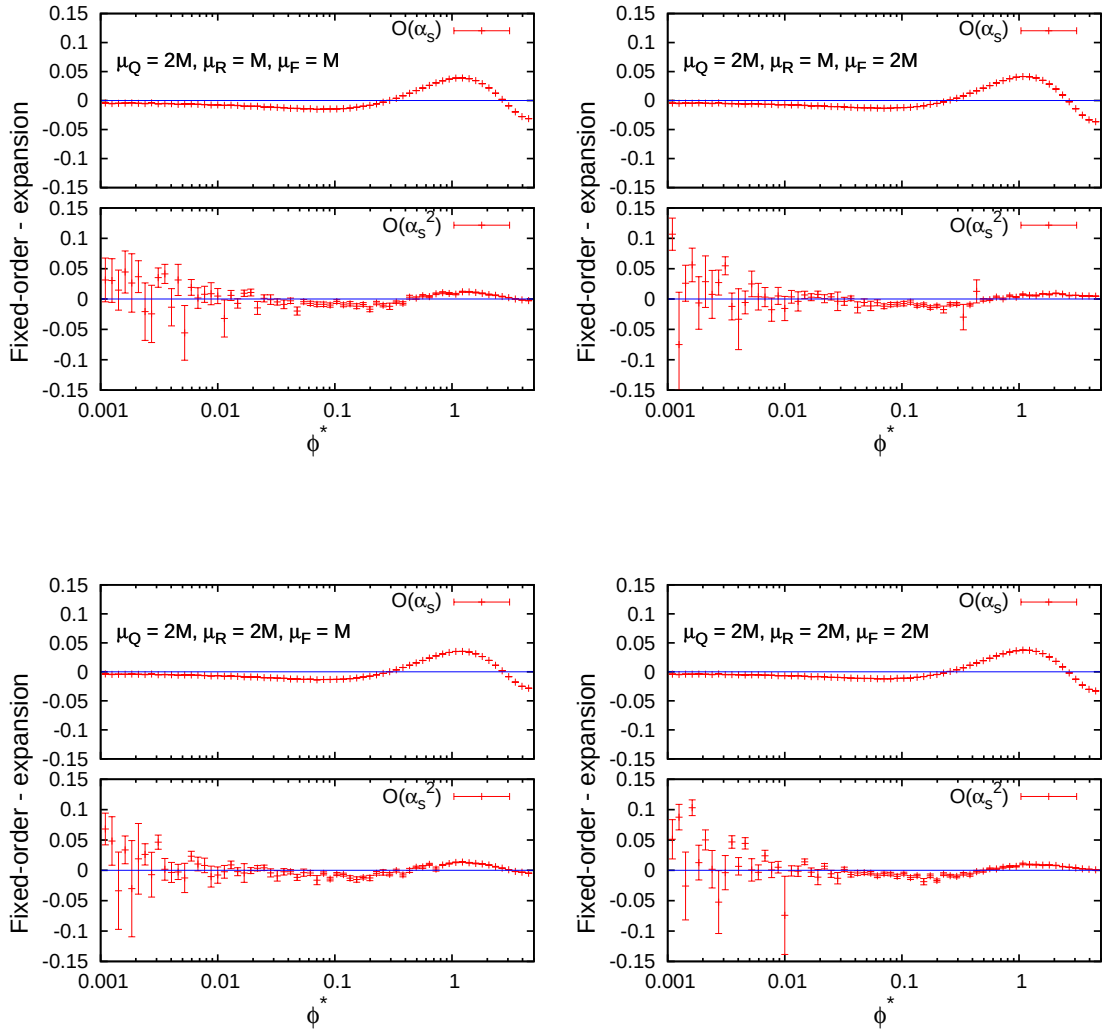

FIGURE C.31. Plots showing the cancellation of large logarithms between the fixed-order component and the expansion of the resummation, for the predicted CMS ϕ^* distributions with $\mu_Q = 2M$.

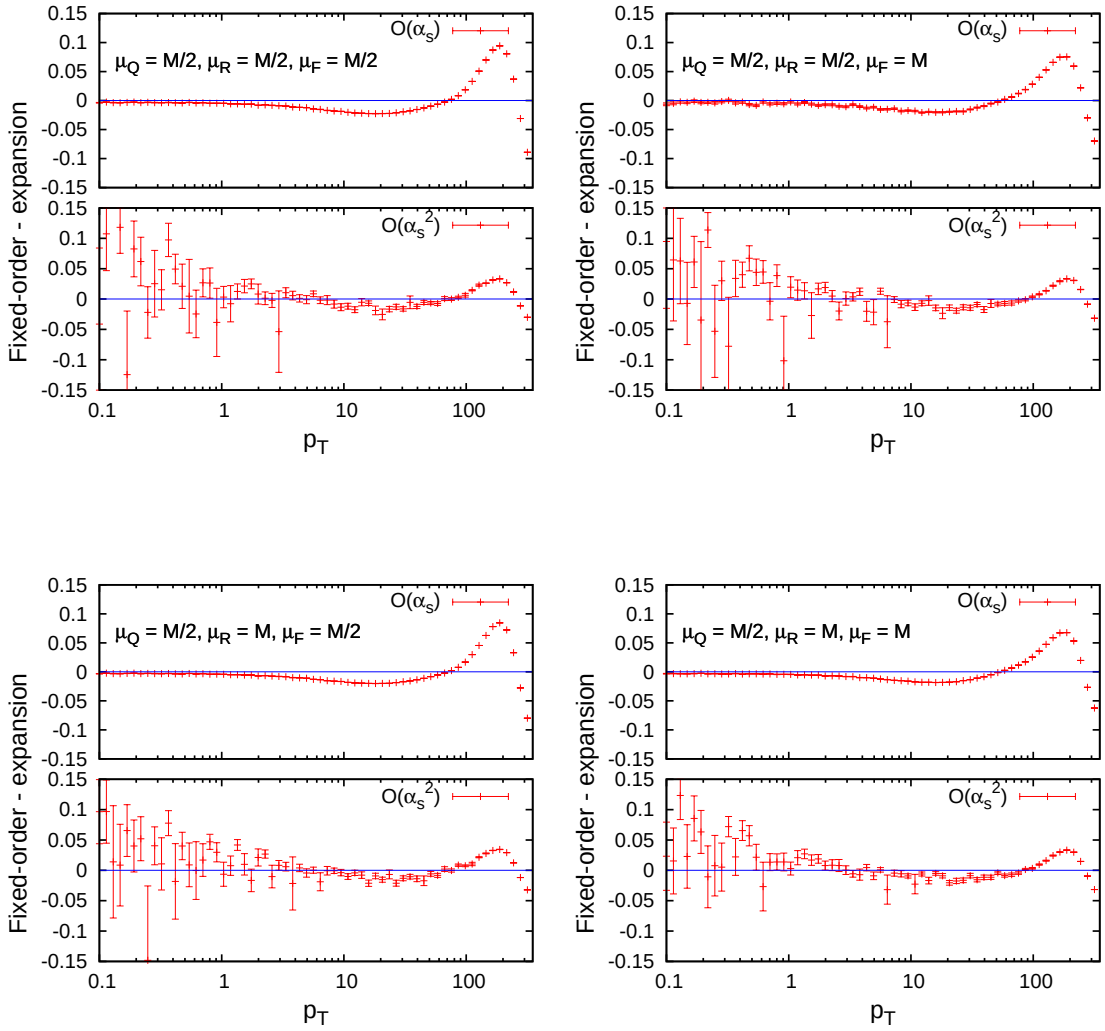

FIGURE C.32. Plots showing the cancellation of large logarithms between the fixed-order component and the expansion of the resummation, for the CMS Q_{T} distributions with $\mu_{\mathrm{Q}} = M/2$.

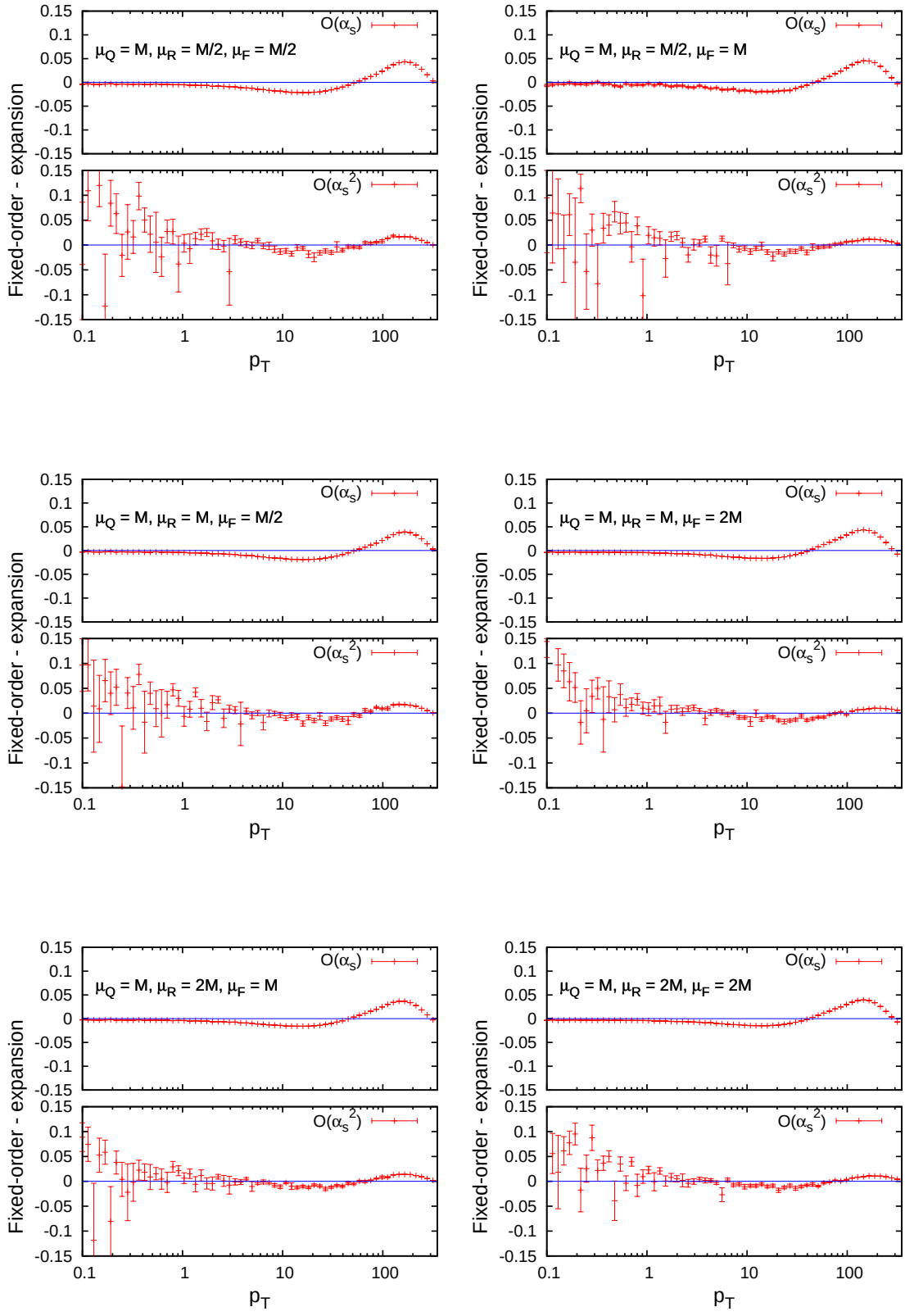

FIGURE C.33. Plots showing the cancellation of large logarithms between the fixed-order component and the expansion of the resummation, for the CMS Q_{T} distributions with $\mu_{\mathrm{Q}} = M$.

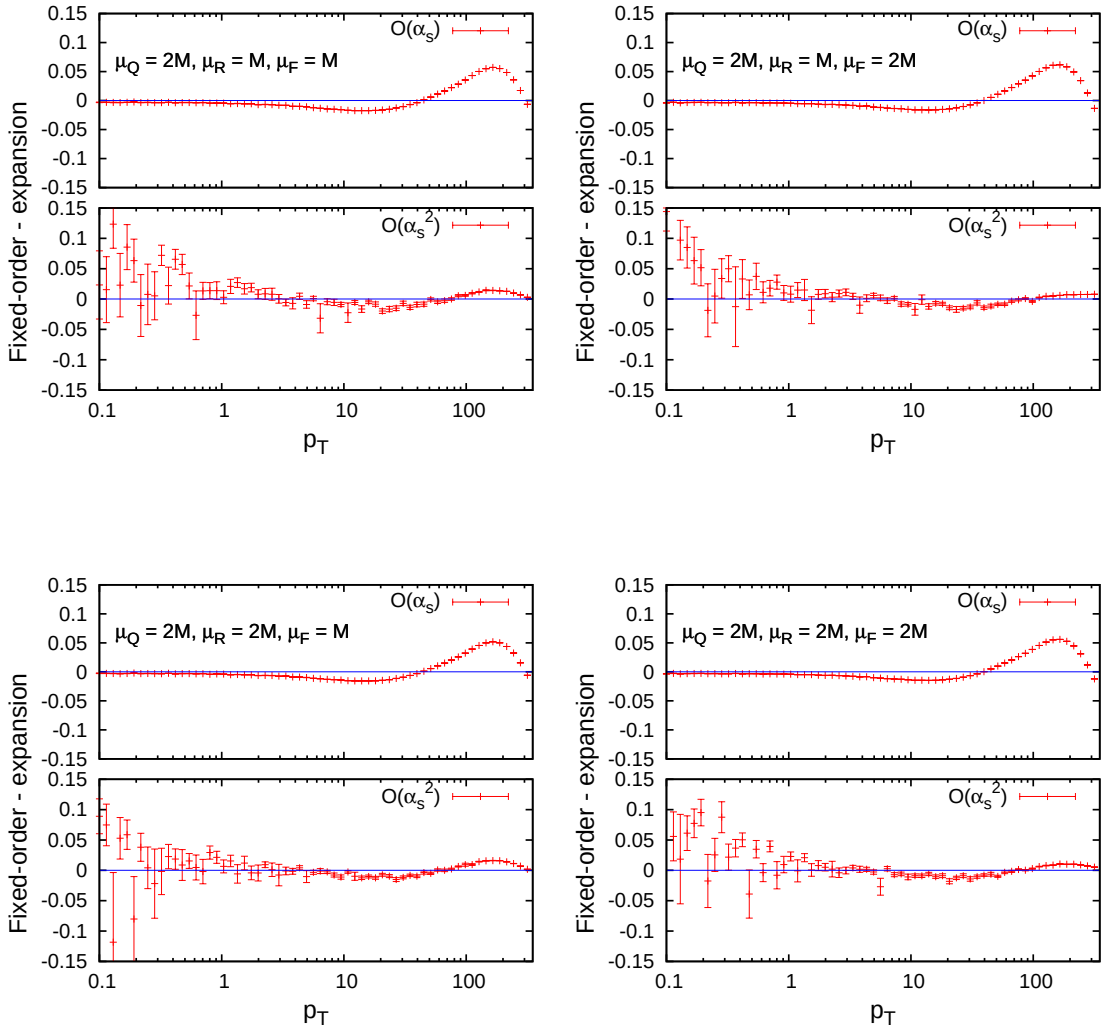

FIGURE C.34. Plots showing the cancellation of large logarithms between the fixed-order component and the expansion of the resummation, for the CMS Q_{T} distributions with $\mu_{\mathrm{Q}} = 2M$.

APPENDIX D

Azimuthal distribution of muons

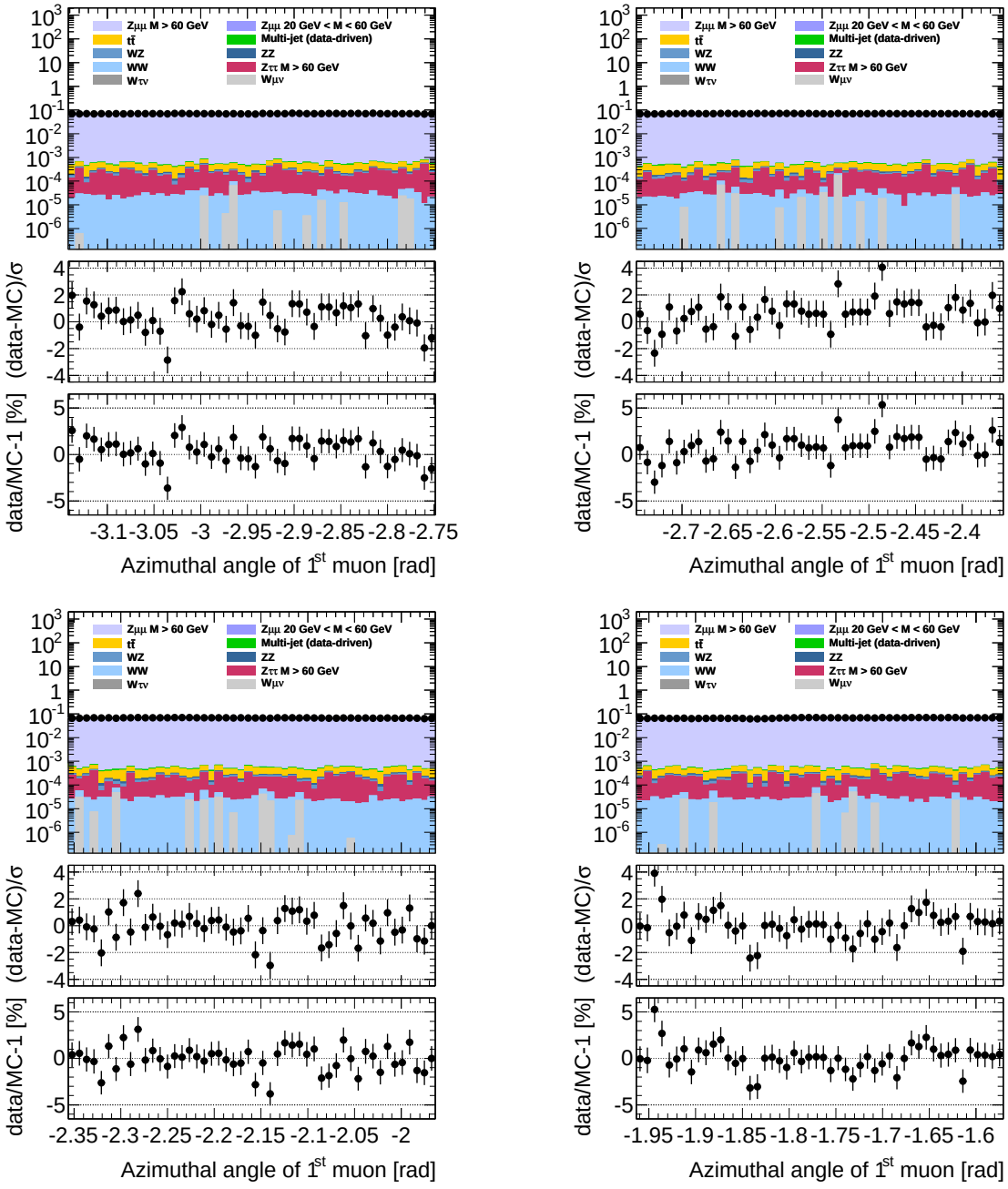

FIGURE D.1. The finely binned distributions of the azimuthal angle of the leading muon, covering the range $-\pi < \theta < -\pi/2$

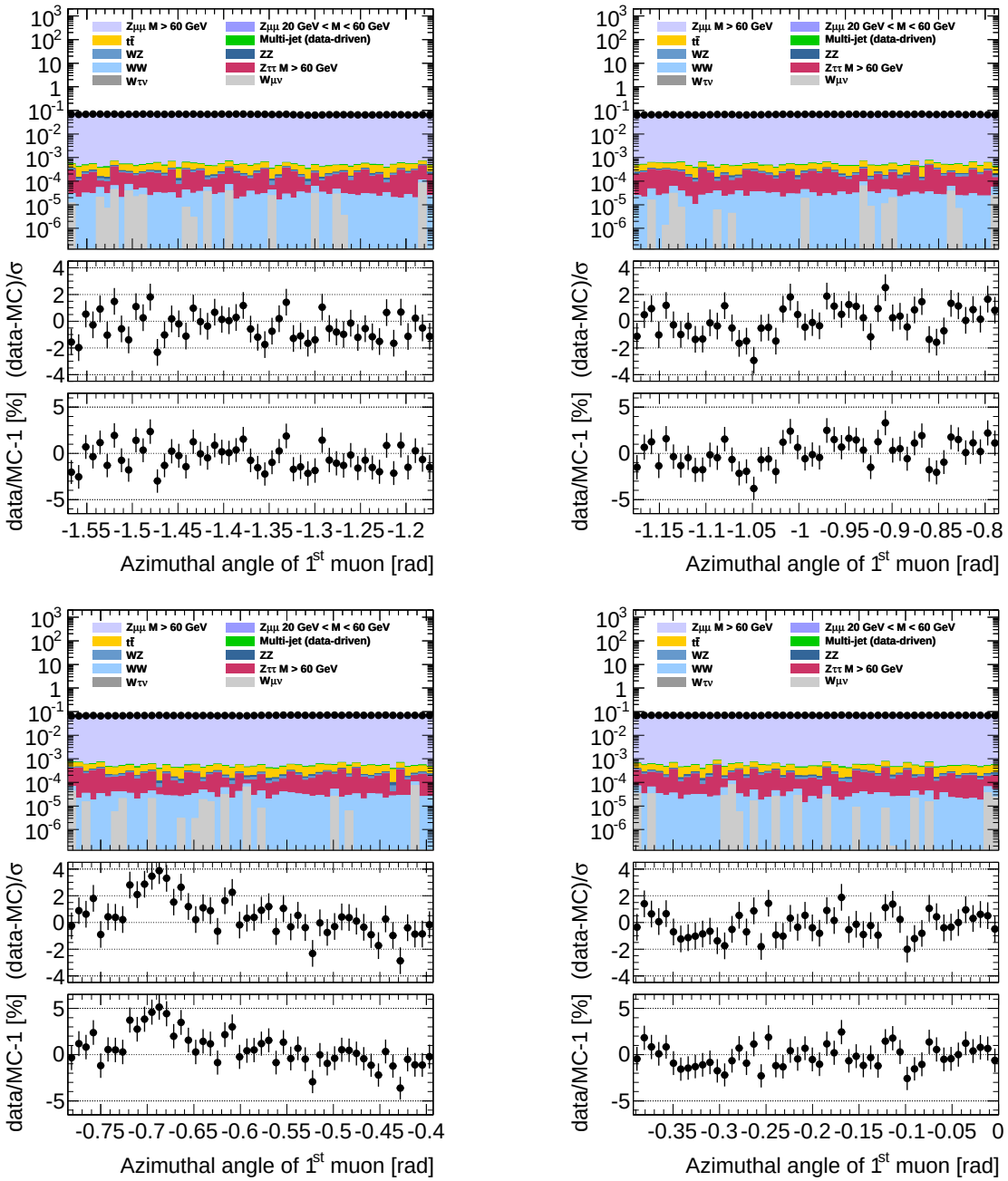

FIGURE D.2. The finely binned distributions of the azimuthal angle of the leading muon, covering the range $-\pi/2 < \theta < 0$

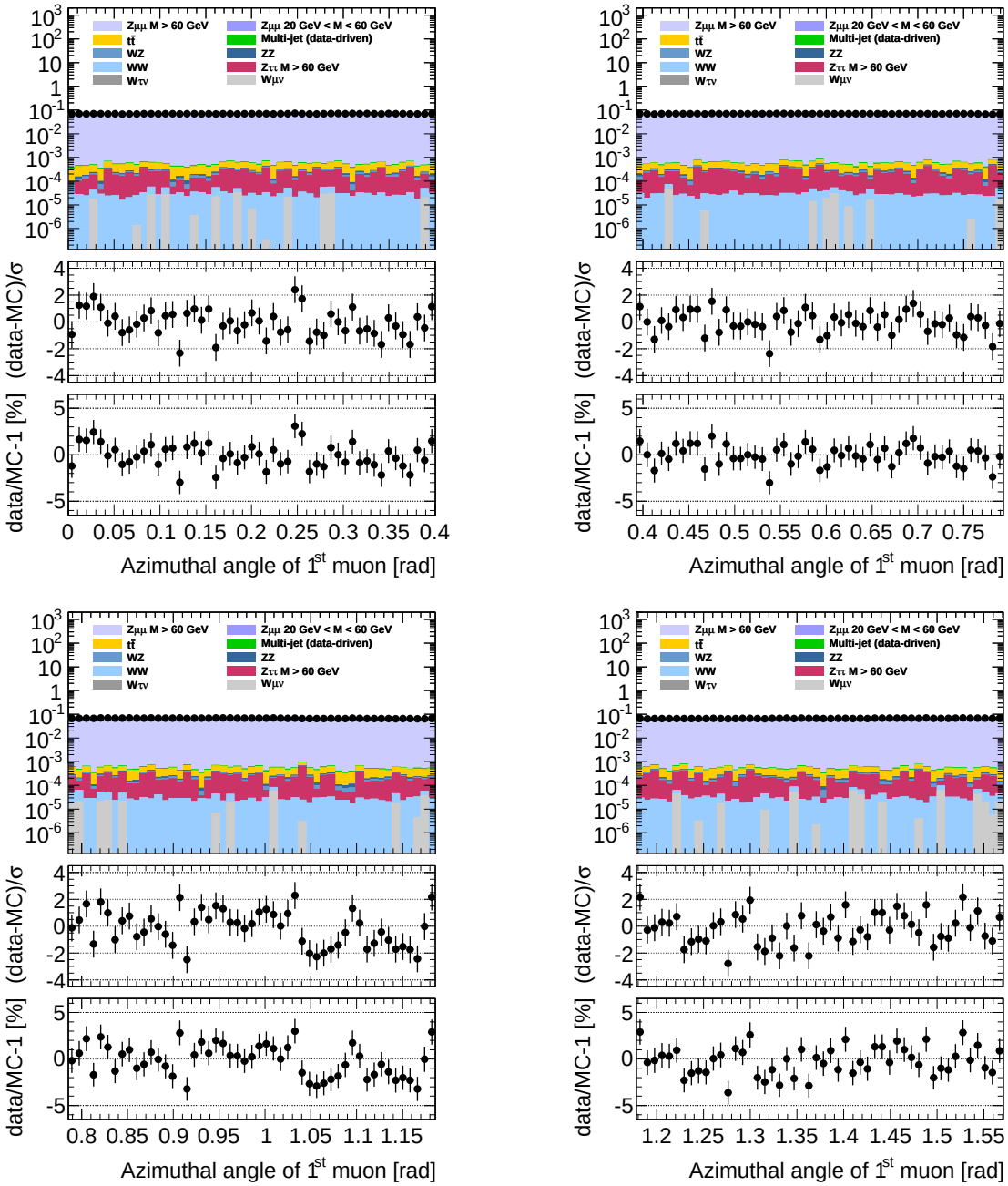

FIGURE D.3. The finely binned distributions of the azimuthal angle of the leading muon, covering the range $0 < \theta < \pi/2$

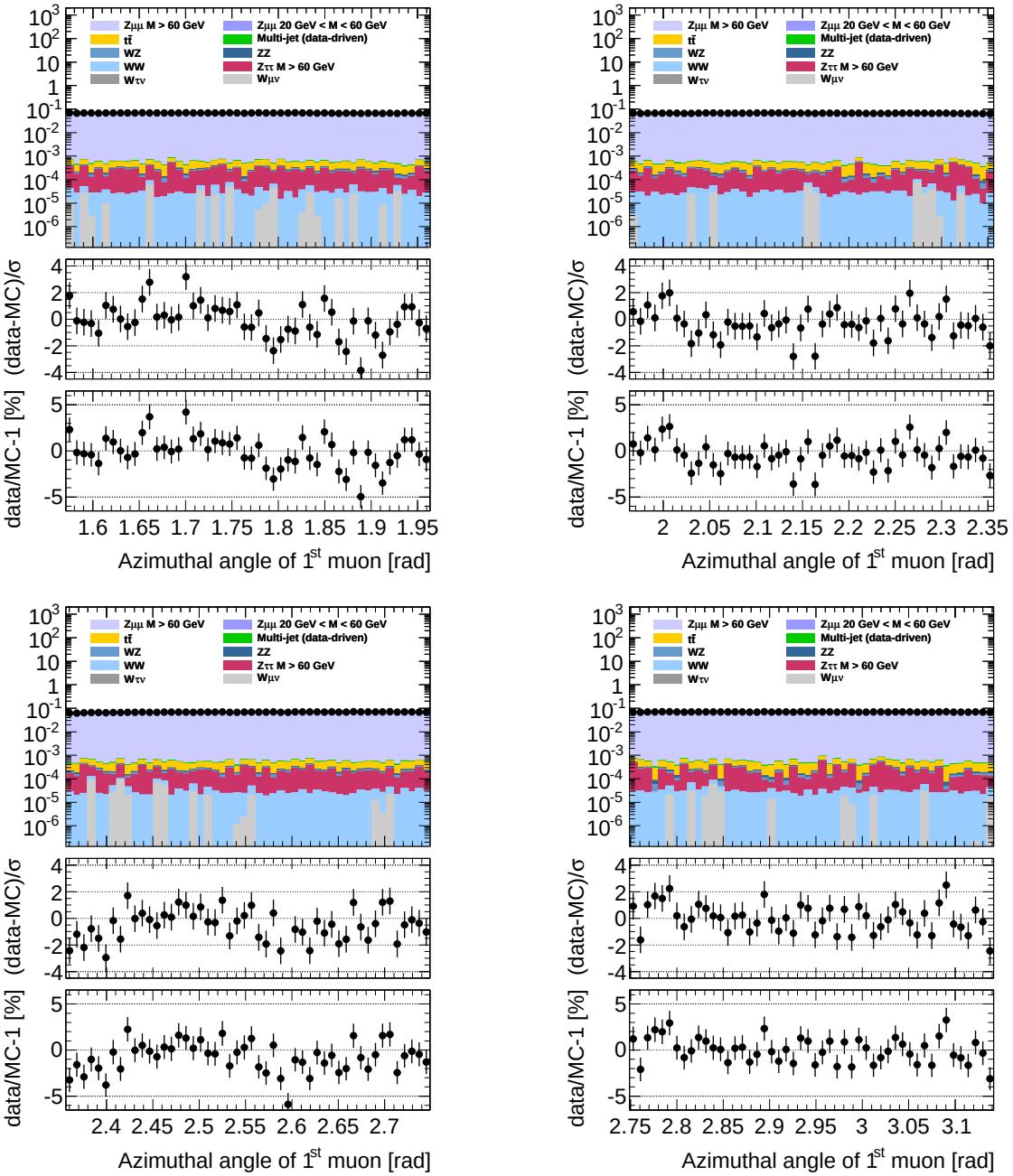

FIGURE D.4. The finely binned distributions of the azimuthal angle of the leading muon, covering the range $\pi/2 < \theta < \pi$

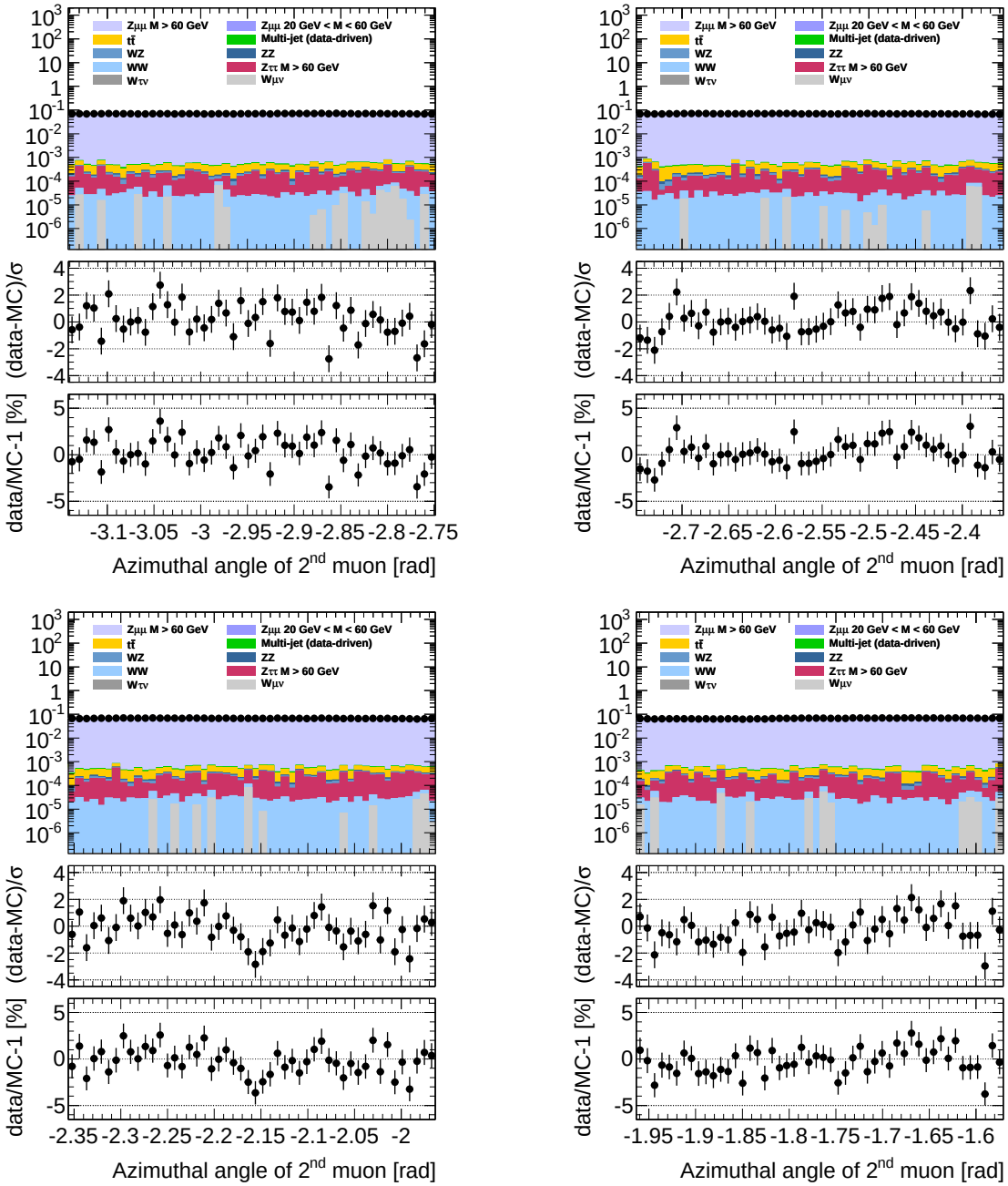

FIGURE D.5. The finely binned distributions of the azimuthal angle of the sub-leading muon, covering the range $-\pi < \theta < -\pi/2$

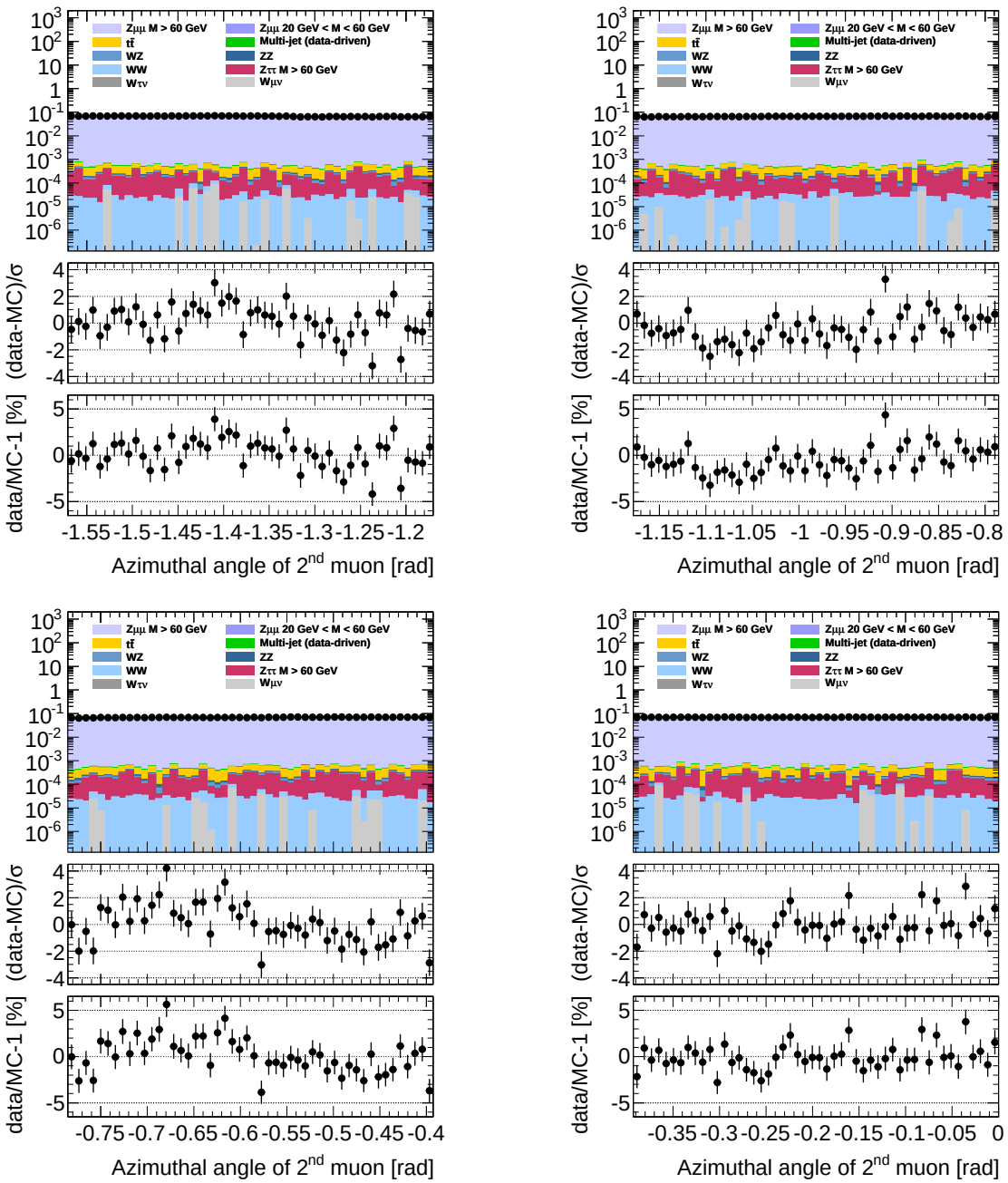

FIGURE D.6. The finely binned distributions of the azimuthal angle of the sub-leading muon, covering the range $-\pi/2 < \theta < 0$

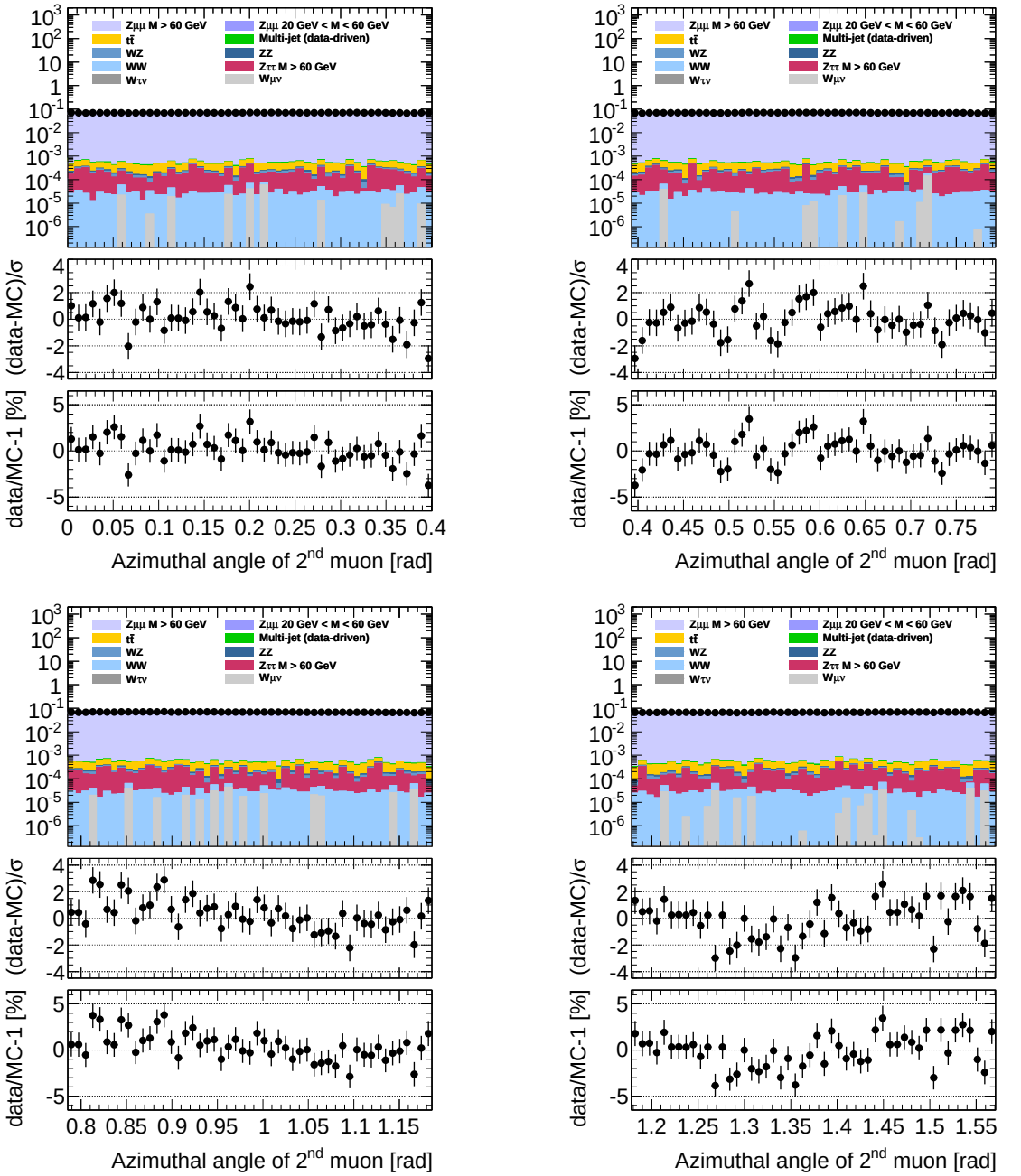

FIGURE D.7. The finely binned distributions of the azimuthal angle of the sub-leading muon, covering the range $0 < \theta < \pi/2$

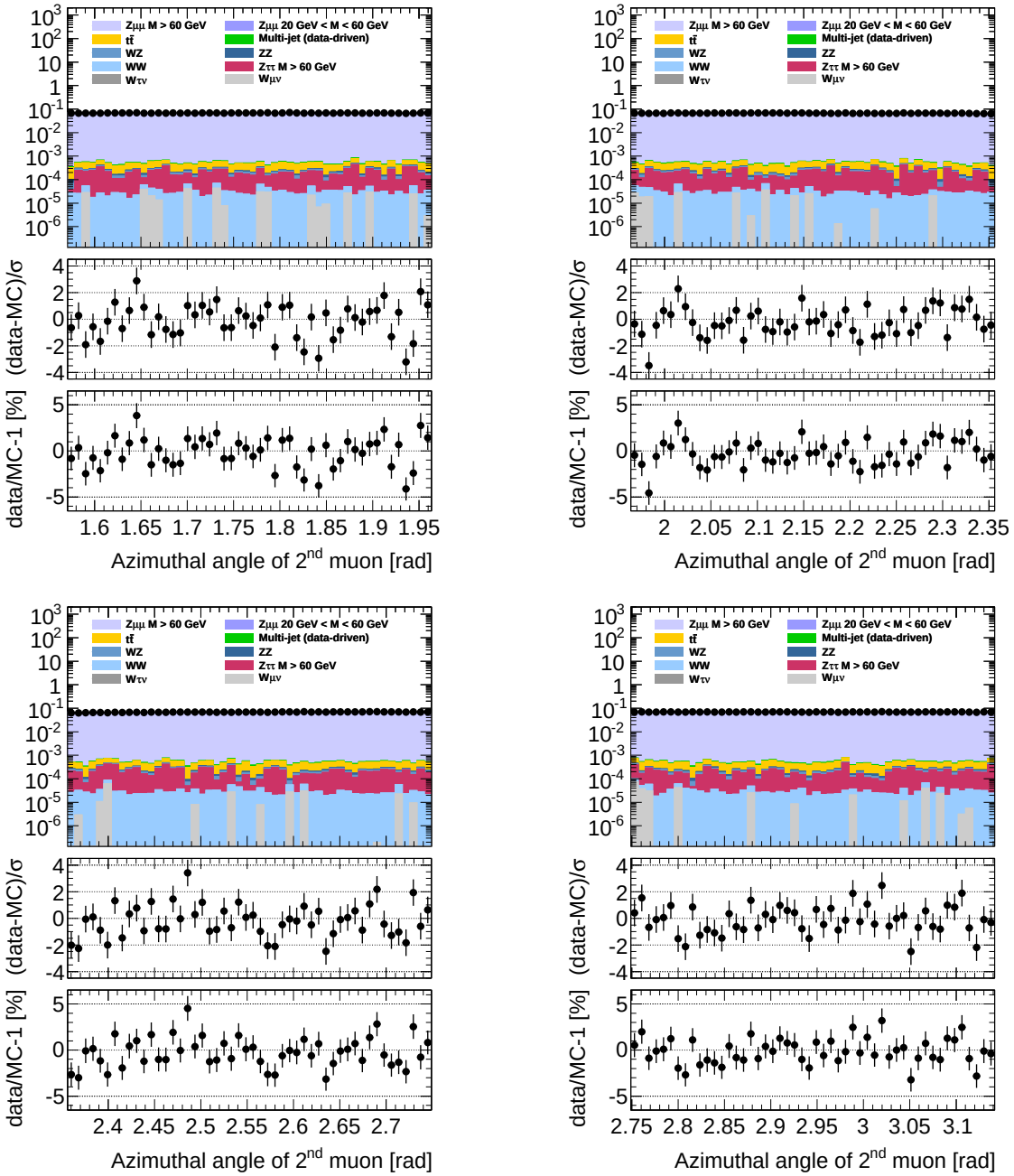

FIGURE D.8. The finely binned distributions of the azimuthal angle of the sub-leading muon, covering the range $\pi/2 < \theta < \pi$

APPENDIX E

Luminosity

E.1. Optimized $\sigma_{\text{vis}}^{\text{AND}}$ plots

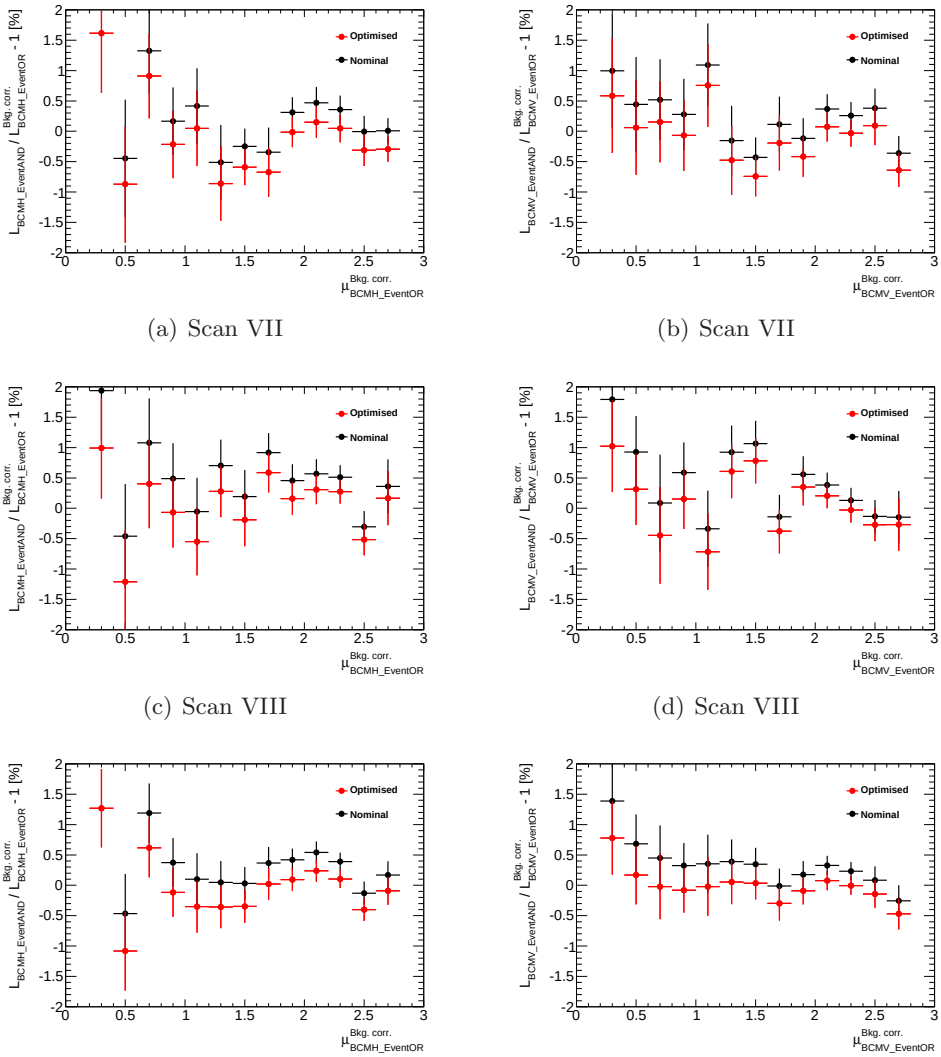

(a) Scan VII (b) Scan VII

(c) Scan VIII (d) Scan VIII

(e) Scans VII and VIII (f) Scans VII and VIII

FIGURE E.1. These plots show the effect of optimizing $\sigma_{\text{vis}}^{\text{AND}}$ on the AND-over-OR luminosity ratios, in bins of μ. In all instances, the μ values quoted for the OR algorithm have been background-corrected. The values determined from these optimization studies are summarized in Table 15.2.

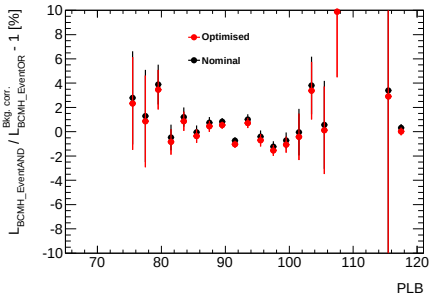

(a) Scan VII x

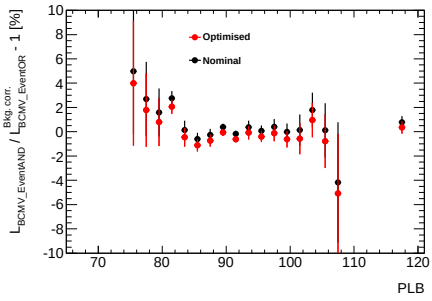

(b) Scan VII x

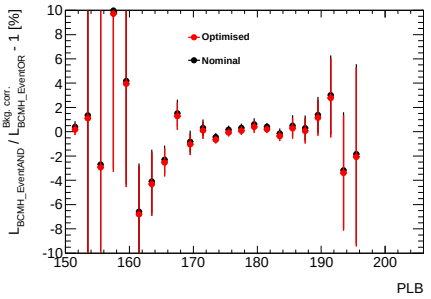

(c) Scan VII y

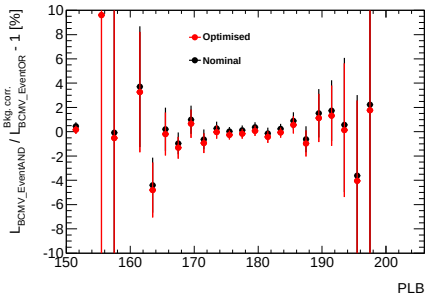

(d) Scan VII y

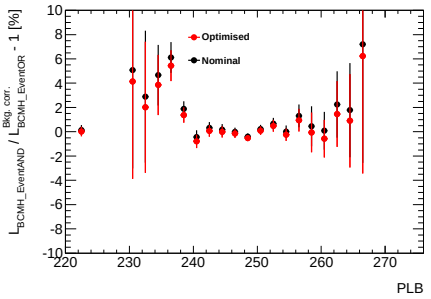

(e) Scan VIII x

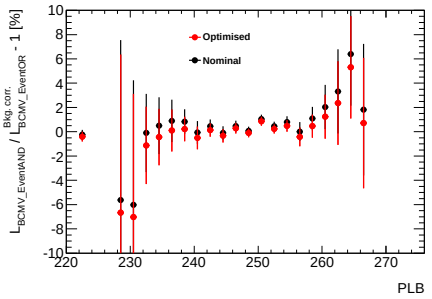

(f) Scan VIII x

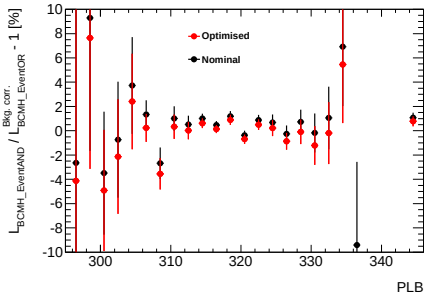

(g) Scan VIII y

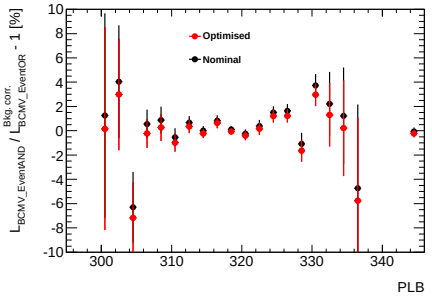

(h) Scan VIII y

FIGURE E.2. These plots show the effect of optimizing $\sigma_{\text{vis}}^{\text{AND}}$ on the AND-over-OR luminosity ratios, in bins corresponding to pseudo-lumiblocks (PLBs), which is equivalent to bins in nominal beam separation, since each scan point corresponds to a distinct PLB. In all instances, the luminosity determined according to the OR algorithm has had a background correction applied. The values determined from these optimization studies are summarized in Table 15.2.

E.2. Systematics due to non-zero α_{xz}

Table E.1 shows how the gradients of linear movement of the luminous centroid change for various discrete crossing angles, α_{xz}. The final two columns express the change as a percentage *difference* to the value of the observable obtained for $\alpha_{xz} = 0$. Note, fitted values of $dz/dh_{x,y}$ provide direct constraints on this crossing angle. All quantities are calculated using a numerical model employing the single-Gaussian beam profiles described in this note. Percentage changes found for $\alpha_{xz} = 20\,\mu$rad are used as the systematic in determining the widths of the bands in Fig. 16.7(e), as explained in Sec. 16.5. In particular, these Monte Carlo results were derived by assuming the values in the 'May scan VII' column of Table 16.4, and the 'May' column of Table 16.6, where σ_z is taken to be 69 mm for both beams, and $\alpha_{yz} = 120\,\mu$rad.

TABLE E.1. This table shows changes in Monte Carlo observables with respect to discrete changes in the α_{xz} crossing angle. Note well, that all values quoted are the *absolute* value (i.e. the modulus) of those determined.

α_{xz} (μrad)	0	20	40	20 (%)	40 (%)
$\lvert d\langle x\rangle/dh_x\rvert$	$1.5 \cdot 10^{-2}$	$1.5 \cdot 10^{-2}$	$1.5 \cdot 10^{-2}$	$\sim 0\%$	$\sim 0\%$
$\lvert d\langle y\rangle/dh_x\rvert$	$1.9 \cdot 10^{-4}$	$3.5 \cdot 10^{-4}$	$4.3 \cdot 10^{-4}$	84%	130%
$\lvert d\langle z\rangle/dh_x\rvert$	1.6	$2.7 \cdot 10^{1}$	$4.1 \cdot 10^{1}$	1500%	2400%
$\lvert d\langle x\rangle/dh_y\rvert$	$1.8 \cdot 10^{-4}$	$2.7 \cdot 10^{-4}$	$3.2 \cdot 10^{-4}$	52%	78%
$\lvert d\langle y\rangle/dh_y\rvert$	$2.3 \cdot 10^{-2}$	$2.3 \cdot 10^{-2}$	$2.3 \cdot 10^{-2}$	$\sim 0\%$	$\sim 0\%$
$\lvert d\langle z\rangle/dh_y\rvert$	$1.6 \cdot 10^{2}$	$1.6 \cdot 10^{2}$	$1.6 \cdot 10^{2}$	$\sim 0\%$	$\sim 0\%$

E.3. Luminous centroid movements with non-zero beam crossing angle

The equations corresponding to Eqs. 16.10 – 16.13, but in the presence of a single beam crossing angle (i.e. $\alpha_{xz} = 0$ and $\alpha_{yz} \neq 0$, for instance) may be derived according to the method set out in Sec. 17.2. They are summarized for the benefit of the reader below. The dots (...) are to remind the reader a series expansion has been performed, and *higher* terms have been neglected.

To begin with, it is interesting to see how the z-position of the luminous centroid, denoted $\langle z \rangle$, gains a dependence on h_x and h_y. The z-movement during a scan *in* the crossing plane is the easiest to understand:

$$\frac{d\langle z \rangle}{dh_y} = \frac{\alpha_{yz}\,\sigma_z^2}{2\big(\sigma_{y,1}^2 + \sigma_{y,2}^2\big)} + \ldots \tag{E.1}$$

It should be noted that $d\langle z \rangle / dh_x$, the z-movement during a scan *out* of the crossing plane, gains this dependence *via* the linear x-y coupling:

$$\frac{d\langle z \rangle}{dh_x} = \frac{\alpha_{yz}\,\sigma_z^2\,\big(\kappa_1\,\sigma_{x,1}\,\sigma_{y,1} + \kappa_2\,\sigma_{x,2}\,\sigma_{y,2}\big)}{2\big(\sigma_{x,1}^2 + \sigma_{x,2}^2\big)\,\big(\sigma_{y,1}^2 + \sigma_{y,2}^2\big)} + \ldots \tag{E.2}$$

In the following, the label 'no xing' indicates the corresponding quantity in Eqs. 16.10 – 16.13, where crossing angles were *not* included. The quantity $d\langle x \rangle / dh_x$ remains unaffected, since the assumed crossing plane is (y, z), not (x, z):

$$\frac{d\langle x \rangle}{dh_x} = \frac{\sigma_{x,1}^2 - \sigma_{x,2}^2}{2\big(\sigma_{x,1}^2 + \sigma_{x,2}^2\big)} + \ldots = \left.\frac{d\langle x \rangle}{dh_x}\right|_{\text{no xing}} \tag{E.3}$$

The changes to the remaining movements are neatly summarized in terms of the quantity $d\langle z \rangle / dh_y$, above:

$$\begin{aligned} \frac{d\langle x \rangle}{dh_y} &= \frac{\sigma_{x,1}\,\sigma_{x,2}\,\big(\kappa_2\,\sigma_{x,1}\,\sigma_{y,2} - \kappa_1\,\sigma_{x,2}\,\sigma_{y,1}\big)}{\big(\sigma_{x,1}^2 + \sigma_{x,2}^2\big)\,\big(\sigma_{y,1}^2 + \sigma_{y,2}^2\big)} \left(1 - \frac{\alpha_{yz}^2\,\sigma_z^2}{2\big(\sigma_{y,1}^2 + \sigma_{y,2}^2\big)}\right) + \ldots \\ &= \left(1 - \alpha_{yz}\,\frac{d\langle z \rangle}{dh_y}\right) \left.\frac{d\langle x \rangle}{dh_y}\right|_{\text{no xing}} \end{aligned} \tag{E.4}$$

and

$$\frac{d\langle y \rangle}{dh_y} = \frac{\sigma_{y,2}^2 - \sigma_{y,1}^2}{2\big(\sigma_{y,1}^2 + \sigma_{y,2}^2\big)} \left(1 - \frac{\alpha_{yz}^2\,\sigma_z^2}{2\big(\sigma_{y,1}^2 + \sigma_{y,2}^2\big)}\right) + \ldots = \left(1 - \alpha_{yz}\,\frac{d\langle z \rangle}{dh_y}\right) \left.\frac{d\langle y \rangle}{dh_y}\right|_{\text{no xing}}, \tag{E.5}$$

except in

$$\frac{d\langle y \rangle}{dh_x} = \big[1 + \mathcal{O}\left(\alpha_{yz}^2\right)\big] \left.\frac{d\langle y \rangle}{dh_x}\right|_{\text{no xing}}, \tag{E.6}$$

where one recognizes that the quantity $\big(d\langle y \rangle / dh_x\big)_{\text{no xing}}$ already depends on $\kappa_{1,2}$ to first order, and so the (cumbersome) $\mathcal{O}\big(\alpha_{yz}^2\big)$ correction terms may be neglected if we work to the same order as the (simple) $\mathcal{O}\big(\alpha_{yz}^2\big)$ correction term in Eq. E.5. One can indeed verify this numerically, and in fact the same should be true of Eq. E.4, which is presented above to $\mathcal{O}\big(\alpha_{yz}^2\,\kappa_{1,2}\big)$. Finally, it should be noted that this is consistent with the notion that one requires a crossing angle in *both* planes in order to significantly impact the determination of the linear x-y coupling coefficients.

E.4. When does crossing angle become negligible?

It has been mentioned in the text that one can deduce whether or not one needs to consider any beam crossing angle by observing the plots for $d\langle z\rangle/dh_{x_i}$, where $x_i \in \{x, y\}$. To make this statement quantitative, the scale at which one should judge these plots is derived below.

Observing Eqs. E.4 and E.5, above, we see that the effect of a single crossing angle becomes important when $\alpha_{yz}^2\,\sigma_z^2 \sim 2\left(\sigma_{y,1}^2 + \sigma_{y,2}^2\right) = 2\,\Sigma_y^2$. The converse statement is that one can neglect the crossing angle when

$$\alpha_{yz}\,\sigma_z \ll \sqrt{2}\,\Sigma_y. \tag{E.7}$$

Using the definition of $d\langle z\rangle/dh_y$ in Eq. E.1, one can rewrite this expression as

$$\frac{d\langle z\rangle}{dh_y} \ll \frac{\sigma_z}{\sqrt{2}\,\Sigma_y}, \tag{E.8}$$

and thus obtain a quantitative statement for when one can ignore the crossing angle, in terms of quantities already known *a priori*. For example, the residual crossing angles may be ignored in the July 2012 scans because $\sigma_z \approx 90$ mm and $\Sigma_y \approx 150\,\mu$m, thus $d\langle z\rangle/dh_y$ should be much smaller than ~ 420. From the final plot in Fig. 17.13, for example, one sees that $|d\langle z\rangle/dh_y| \approx 5$, justifying the neglect of α_{yz} in the analysis.

Bibliography

[1] S. D. Drell and T. -M. Yan, "Massive Lepton Pair Production in Hadron-Hadron Collisions at High-Energies," Phys. Rev. Lett. **25** (1970) 316 [Erratum-ibid. **25** (1970) 902].

[2] W. J. Stirling and M. R. Whalley, "A Compilation of Drell-Yan cross-sections," J. Phys. G **19** (1993) D1.

[3] R. K. Ellis, D. A. Ross and S. Veseli, "Vector boson production in hadronic collisions," Nucl. Phys. B **503** (1997) 309 [hep-ph/9704239].

[4] R. K. Ellis and S. Veseli, "W and Z transverse momentum distributions: Resummation in q_T space," Nucl. Phys. B **511** (1998) 649 [hep-ph/9706526].

[5] T. Affolder *et al.* [CDF Collaboration], "The transverse momentum and total cross section of e^+e^- pairs in the Z boson region from $p\bar{p}$ collisions at $\sqrt{s} = 1.8$ TeV," Phys. Rev. Lett. **84** (2000) 845 [hep-ex/0001021].

[6] B. Abbott *et al.* [D0 Collaboration], "Measurement of the inclusive differential cross section for Z bosons as a function of transverse momentum in $\bar{p}p$ collisions at $\sqrt{s} = 1.8$ TeV," Phys. Rev. D **61** (2000) 032004 [hep-ex/9907009].

[7] G. Bozzi, S. Catani, G. Ferrera, D. de Florian and M. Grazzini, "Transverse-momentum resummation: A Perturbative study of Z production at the Tevatron," Nucl. Phys. B **815** (2009) 174 [arXiv:0812.2862 [hep-ph]].

[8] G. Bozzi, S. Catani, G. Ferrera, D. de Florian and M. Grazzini, "Production of Drell-Yan lepton pairs in hadron collisions: Transverse-momentum resummation at next-to-next-to-leading logarithmic accuracy," Phys. Lett. B **696** (2011) 207 [arXiv:1007.2351 [hep-ph]].

[9] Y. L. Dokshitzer, D. Diakonov and S. I. Troian, "On the Transverse Momentum Distribution of Massive Lepton Pairs," Phys. Lett. B **79** (1978) 269.

[10] G. Altarelli, G. Parisi and R. Petronzio, "Transverse Momentum of Muon Pairs Produced in Hadronic Collisions," Phys. Lett. B **76** (1978) 356.

[11] G. Parisi and R. Petronzio, "Small Transverse Momentum Distributions in Hard Processes," Nucl. Phys. B **154** (1979) 427.

[12] C. T. H. Davies and W. J. Stirling, "Nonleading Corrections to the Drell-Yan Cross-Section at Small Transverse Momentum," Nucl. Phys. B **244** (1984) 337.

[13] C. T. H. Davies, B. R. Webber and W. J. Stirling, "Drell-Yan Cross-Sections at Small Transverse Momentum," Nucl. Phys. B **256** (1985) 413.

[14] J. C. Collins, D. E. Soper and G. F. Sterman, "Transverse Momentum Distribution in Drell-Yan Pair and W and Z Boson Production," Nucl. Phys. B **250** (1985) 199.

[15] A. Banfi, S. Redford, M. Vesterinen, P. Waller and T. R. Wyatt, "Optimisation of variables for studying dilepton transverse momentum distributions at hadron colliders," Eur. Phys. J. C **71** (2011) 1600 [arXiv:1009.1580 [hep-ex]].

[16] A. Banfi, M. Dasgupta and S. Marzani, "QCD predictions for new variables to study dilepton transverse momenta at hadron colliders," Phys. Lett. B **701** (2011) 75 [arXiv:1102.3594 [hep-ph]].

[17] A. Banfi, M. Dasgupta, S. Marzani and L. Tomlinson, "Probing the low transverse momentum domain of Z production with novel variables," JHEP **1201** (2012) 044 [arXiv:1110.4009 [hep-ph]].

[18] A. Banfi, M. Dasgupta, S. Marzani and L. Tomlinson, "Predictions for Drell-Yan ϕ^* and Q_T observables at the LHC," Phys. Lett. B **715** (2012) 152 [arXiv:1205.4760 [hep-ph]].

[19] V. M. Abazov *et al.* [D0 Collaboration], "Precise study of the Z/γ^* boson transverse momentum distribution in $p\bar{p}$ collisions using a novel technique," Phys. Rev. Lett. **106** (2011) 122001 [arXiv:1010.0262 [hep-ex]].

[20] G. Aad *et al.* [ATLAS Collaboration], "Measurement of angular correlations in Drell-Yan lepton pairs to probe Z/gamma* boson transverse momentum at sqrt(s)=7 TeV with the ATLAS detector," Phys. Lett. B **720** (2013) 32 [arXiv:1211.6899 [hep-ex]].

[21] S. Catani, L. Trentadue, G. Turnock and B. R. Webber, "Resummation of large logarithms in e+ e- event shape distributions," Nucl. Phys. B **407** (1993) 3.

[22] S. Catani, D. de Florian and M. Grazzini, "Universality of nonleading logarithmic contributions in transverse momentum distributions," Nucl. Phys. B **596** (2001) 299 [hep-ph/0008184].

[23] D. de Florian and M. Grazzini, "Next-to-next-to-leading logarithmic corrections at small transverse momentum in hadronic collisions," Phys. Rev. Lett. **85** (2000) 4678 [hep-ph/0008152].

[24] G. Bozzi, S. Catani, D. de Florian and M. Grazzini, "The q(T) spectrum of the Higgs boson at the LHC in QCD perturbation theory," Phys. Lett. B **564** (2003) 65 [hep-ph/0302104].

[25] G. Bozzi, S. Catani, D. de Florian and M. Grazzini, "Transverse-momentum resummation and the spectrum of the Higgs boson at the LHC," Nucl. Phys. B **737** (2006) 73 [hep-ph/0508068].

[26] T. Becher and M. Neubert, "Drell-Yan production at small q_T, transverse parton distributions and the collinear anomaly," Eur. Phys. J. C **71** (2011) 1665 [arXiv:1007.4005 [hep-ph]].

[27] T. Muta, "Foundations of quantum chromodynamics. Second edition," World Sci. Lect. Notes Phys. **57** (1998) 1.

[28] T. P. Cheng and L. F. Li, "Gauge Theory Of Elementary Particle Physics," Oxford, Uk: Clarendon (1984) 536 P. (Oxford Science Publications)

[29] L. D. Faddeev and V. N. Popov, "Feynman Diagrams for the Yang-Mills Field," Phys. Lett. B **25** (1967) 29.

[30] G. 't Hooft and M. J. G. Veltman, "Regularization and Renormalization of Gauge Fields," Nucl. Phys. B **44** (1972) 189.

[31] N. N. Bogoliubov, O. S. Parasiuk and , "On the Multiplication of the causal function in the quantum theory of fields," Acta Math. **97** (1957) 227.

[32] K. Hepp, "Proof of the Bogolyubov-Parasiuk theorem on renormalization," Commun. Math. Phys. **2** (1966) 301.

[33] W. Zimmermann, "The power counting theorem for minkowski metric," Commun. Math. Phys. **11** (1968) 1.

[34] W. Zimmermann, "Convergence of Bogolyubov's method of renormalization in momentum space," Commun. Math. Phys. **15** (1969) 208 [Lect. Notes Phys. **558** (2000) 217].

[35] G. Dissertori, I. G. Knowles and M. Schmelling, "High energy experiments and theory," (International series of monographs on physics. 115)

[36] J. C. Taylor, "Ward Identities and Charge Renormalization of the Yang-Mills Field," Nucl. Phys. B **33** (1971) 436.

[37] A. A. Slavnov, "Ward Identities in Gauge Theories," Theor. Math. Phys. **10** (1972) 99 [Teor. Mat. Fiz. **10** (1972) 153].

[38] G. 't Hooft, "Dimensional regularization and the renormalization group," Nucl. Phys. B **61** (1973) 455.

[39] S. Weinberg, "New approach to the renormalization group," Phys. Rev. D **8** (1973) 3497.

[40] S. A. Larin and J. A. M. Vermaseren, "The Three loop QCD Beta function and anomalous dimensions," Phys. Lett. B **303** (1993) 334 [hep-ph/9302208].

[41] A. J. Buras, E. G. Floratos, D. A. Ross and C. T. Sachrajda, "Asymptotic Freedom Beyond the Leading Order," Nucl. Phys. B **131** (1977) 308.

[42] S. Catani and M. Grazzini, "Infrared factorization of tree level QCD amplitudes at the next-to-next-to-leading order and beyond," Nucl. Phys. B **570** (2000) 287 [hep-ph/9908523].

[43] B. I. Ermolaev and V. S. Fadin, "Log - Log Asymptotic Form of Exclusive Cross-Sections in Quantum Chromodynamics," JETP Lett. **33** (1981) 269 [Pisma Zh. Eksp. Teor. Fiz. **33** (1981) 285].

[44] A. H. Mueller, "On the Multiplicity of Hadrons in QCD Jets," Phys. Lett. B **104** (1981) 161.

[45] Y. L. Dokshitzer, V. S. Fadin and V. A. Khoze, "Double Logs of Perturbative QCD for Parton Jets and Soft Hadron Spectra," Z. Phys. C **15** (1982) 325.

[46] V. S. Fadin, "Double Logarithmic Asymptotics Of The Cross-sections Of E+ E- Annihilation Into Quarks And Gluons. (in Russian)," Yad. Fiz. **37** (1983) 408.

[47] A. Bassetto, M. Ciafaloni and G. Marchesini, "Jet Structure and Infrared Sensitive Quantities in Perturbative QCD," Phys. Rept. **100** (1983) 201.

[48] R. K. Ellis, W. J. Stirling and B. R. Webber, "QCD and collider physics," Camb. Monogr. Part. Phys. Nucl. Phys. Cosmol. **8** (1996) 1.

[49] G. Marchesini and B. R. Webber, "Monte Carlo Simulation of General Hard Processes with Coherent QCD Radiation," Nucl. Phys. B **310** (1988) 461.

[50] A. Banfi, G. P. Salam and G. Zanderighi, "Principles of general final-state resummation and automated implementation," JHEP **0503** (2005) 073 [hep-ph/0407286].

[51] M. Dasgupta and G. P. Salam, "Resummation of nonglobal QCD observables," Phys. Lett. B **512** (2001) 323 [hep-ph/0104277].

[52] M. Dasgupta and G. P. Salam, "Accounting for coherence in interjet E(t) flow: A Case study," JHEP **0203** (2002) 017 [hep-ph/0203009].

[53] G. Altarelli and G. Parisi, "Asymptotic Freedom in Parton Language," Nucl. Phys. B **126** (1977) 298.

[54] R. Devenish and A. Cooper-Sarkar, "Deep inelastic scattering," Oxford, UK: Univ. Pr. (2004) 403 p

[55] Y. L. Dokshitzer, "Calculation of the Structure Functions for Deep Inelastic Scattering and e+ e- Annihilation by Perturbation Theory in Quantum Chromodynamics.," Sov. Phys. JETP **46** (1977) 641 [Zh. Eksp. Teor. Fiz. **73** (1977) 1216].

[56] V. N. Gribov and L. N. Lipatov, "Deep inelastic e p scattering in perturbation theory," Sov. J. Nucl. Phys. **15** (1972) 438 [Yad. Fiz. **15** (1972) 781].

[57] J. C. Collins, D. E. Soper and G. F. Sterman, "Factorization of Hard Processes in QCD," Adv. Ser. Direct. High Energy Phys. **5** (1988) 1 [hep-ph/0409313].

[58] P. Aurenche and J. Lindfors, "QCD Corrections to Direct Lepton Production in Hadronic Collisions," Nucl. Phys. B **185** (1981) 274.

[59] G. Altarelli, R. K. Ellis and G. Martinelli, "Leptoproduction and Drell-Yan Processes Beyond the Leading Approximation in Chromodynamics," Nucl. Phys. B **143** (1978) 521 [Erratum-ibid. B **146** (1978) 544].

[60] B. Potter, "Calculational Techniques in Perturbative QCD: The Drell-Yan Process,"

[61] A. Banfi, M. Dasgupta and R. M. Duran Delgado, "The a(T) distribution of the Z boson at hadron colliders," JHEP **0912** (2009) 022 [arXiv:0909.5327 [hep-ph]].

[62] D. de Florian and M. Grazzini, "The Structure of large logarithmic corrections at small transverse momentum in hadronic collisions," Nucl. Phys. B **616** (2001) 247 [hep-ph/0108273].

[63] M. Vesterinen and T. R. Wyatt, "A Novel Technique for Studying the Z Boson Transverse Momentum Distribution at Hadron Colliders," Nucl. Instrum. Meth. A **602** (2009) 432 [arXiv:0807.4956 [hep-ex]].

[64] W. Furmanski and R. Petronzio, "Singlet Parton Densities Beyond Leading Order," Phys. Lett. B **97** (1980) 437.

[65] S. Catani, B. R. Webber and G. Marchesini, "QCD coherent branching and semi-inclusive processes at large x," Nucl. Phys. B **349** (1991) 635.

[66] A. Banfi, P. F. Monni, G. P. Salam and G. Zanderighi, "Higgs and Z-boson production with a jet veto," Phys. Rev. Lett. **109** (2012) 202001 [arXiv:1206.4998 [hep-ph]].

[67] G. P. Salam and J. Rojo, "A Higher Order Perturbative Parton Evolution Toolkit (HOPPET)," Comput. Phys. Commun. **180** (2009) 120 [arXiv:0804.3755 [hep-ph]].

[68] M. R. Whalley, D. Bourilkov and R. C. Group, "The Les Houches accord PDFs (LHAPDF) and LHAGLUE," hep-ph/0508110.

[69] J. M. Campbell and R. K. Ellis, "Next-to-leading order corrections to W^+ 2 jet and Z^+ 2 jet production at hadron colliders," Phys. Rev. D **65** (2002) 113007 [hep-ph/0202176].

[70] S. Catani, L. Cieri, G. Ferrera, D. de Florian and M. Grazzini, "Vector boson production at hadron colliders: a fully exclusive QCD calculation at NNLO," Phys. Rev. Lett. **103** (2009) 082001 [arXiv:0903.2120 [hep-ph]].

[71] K. Melnikov and F. Petriello, "Electroweak gauge boson production at hadron colliders through O(alpha(s)**2)," Phys. Rev. D **74** (2006) 114017 [hep-ph/0609070].

[72] R. Gavin, Y. Li, F. Petriello and S. Quackenbush, "FEWZ 2.0: A code for hadronic Z production at next-to-next-to-leading order," Comput. Phys. Commun. **182** (2011) 2388 [arXiv:1011.3540 [hep-ph]].

[73] C. Balazs and C. P. Yuan, "Soft gluon effects on lepton pairs at hadron colliders," Phys. Rev. D **56** (1997) 5558 [hep-ph/9704258].

[74] P. M. Nadolsky, D. R. Stump and C. P. Yuan, "Phenomenology of multiple parton radiation in semiinclusive deep inelastic scattering," Phys. Rev. D **64** (2001) 114011 [hep-ph/0012261].

[75] S. Berge, P. M. Nadolsky, F. Olness and C. -P. Yuan, "Transverse momentum resummation at small x for the Tevatron and CERN LHC," Phys. Rev. D **72** (2005) 033015 [hep-ph/0410375].

[76] V. M. Abazov *et al.* [D0 Collaboration], "Measurement of the shape of the boson transverse momentum distribution in $p\bar{p} \to Z/\gamma^* \to e^+e^- + X$ events produced at $\sqrt{s}$=1.96-TeV," Phys. Rev. Lett. **100** (2008) 102002 [arXiv:0712.0803 [hep-ex]].

[77] J. Pumplin, D. R. Stump, J. Huston, H. L. Lai, P. M. Nadolsky and W. K. Tung, "New generation of parton distributions with uncertainties from global QCD analysis," JHEP **0207** (2002) 012 [hep-ph/0201195].

[78] A. D. Martin, W. J. Stirling, R. S. Thorne and G. Watt, "Parton distributions for the LHC," Eur. Phys. J. C **63** (2009) 189 [arXiv:0901.0002 [hep-ph]].

[79] G. Aad *et al.* [ATLAS Collaboration], "Measurement of the transverse momentum distribution of Z/gamma* bosons in proton-proton collisions at $\sqrt{s} = 7$ TeV with the ATLAS detector," Phys. Lett. B **705** (2011) 415 [arXiv:1107.2381 [hep-ex]].

[80] S. Catani, M. Ciafaloni and F. Hautmann, "High-energy factorization and small x heavy flavor production," Nucl. Phys. B **366** (1991) 135.

[81] J. C. Collins and R. K. Ellis, "Heavy quark production in very high-energy hadron collisions," Nucl. Phys. B **360** (1991) 3.

[82] S. M. Aybat, J. C. Collins, J. W. Qiu and T. C. Rogers, "The QCD Evolution of the Sivers Function," Phys. Rev. D **85** (2012) 034043 [arXiv:1110.6428 [hep-ph]].

[83] S. Chatrchyan *et al.* [CMS Collaboration], "Measurement of the Rapidity and Transverse Momentum Distributions of Z Bosons in pp Collisions at $\sqrt{s} = 7$ TeV," Phys. Rev. D **85** (2012) 032002 [arXiv:1110.4973 [hep-ex]].

[84] A. Guffanti and G. E. Smye, "Nonperturbative effects in the W and Z transverse momentum distribution," JHEP **0010** (2000) 025 [hep-ph/0007190].

[85] Y. L. Dokshitzer, G. Marchesini and B. R. Webber, "Nonperturbative effects in the energy energy correlation," JHEP **9907** (1999) 012 [hep-ph/9905339].

[86] F. Landry, R. Brock, P. M. Nadolsky and C. P. Yuan, "Tevatron Run-1 Z boson data and Collins-Soper-Sterman resummation formalism," Phys. Rev. D **67** (2003) 073016 [hep-ph/0212159].

[87] M. Guzzi, P. M. Nadolsky and B. Wang, "Nonperturbative contributions to a resummed leptonic angular distribution in inclusive neutral vector boson production," arXiv:1309.1393 [hep-ph].

[88] G. A. Ladinsky and C. P. Yuan, "The Nonperturbative regime in QCD resummation for gauge boson production at hadron colliders," Phys. Rev. D **50** (1994) 4239 [hep-ph/9311341].

[89] P. B. Arnold and M. H. Reno, "The Complete Computation of High p(t) W and Z Production in 2nd Order QCD," Nucl. Phys. B **319** (1989) 37 [Erratum-ibid. B **330** (1990) 284].

[90] A. Kulesza, G. F. Sterman and W. Vogelsang, "Joint resummation in electroweak boson production," Phys. Rev. D **66** (2002) 014011 [hep-ph/0202251].

[91] S. Catani, M. L. Mangano, P. Nason and L. Trentadue, "The Resummation of soft gluons in hadronic collisions," Nucl. Phys. B **478** (1996) 273 [hep-ph/9604351].

[92] P. W. Higgs, "Broken Symmetries and the Masses of Gauge Bosons," Phys. Rev. Lett. **13** (1964) 508.

[93] S. Catani and M. Grazzini, "QCD transverse-momentum resummation in gluon fusion processes," Nucl. Phys. B **845** (2011) 297 [arXiv:1011.3918 [hep-ph]].

[94] A. D. Pilkington, private communication

[95] S. Mantry and F. Petriello, "Transverse Momentum Distributions from Effective Field Theory with Numerical Results," Phys. Rev. D **83** (2011) 053007 [arXiv:1007.3773 [hep-ph]].

[96] T. Becher, M. Neubert and D. Wilhelm, "Electroweak Gauge-Boson Production at Small q_T: Infrared Safety from the Collinear Anomaly," JHEP **1202** (2012) 124 [arXiv:1109.6027 [hep-ph]].

[97] G. Aad *et al.* [ATLAS Collaboration], "The ATLAS Experiment at the CERN Large Hadron Collider," JINST **3** (2008) S08003.

[98] P. Nason, "A New method for combining NLO QCD with shower Monte Carlo algorithms," JHEP **0411** (2004) 040 [hep-ph/0409146].

[99] S. Frixione, P. Nason and C. Oleari, "Matching NLO QCD computations with Parton Shower simulations: the POWHEG method," JHEP **0711** (2007) 070 [arXiv:0709.2092 [hep-ph]].

[100] S. Alioli, P. Nason, C. Oleari and E. Re, "NLO vector-boson production matched with shower in POWHEG," JHEP **0807** (2008) 060 [arXiv:0805.4802 [hep-ph]].

[101] S. Alioli, P. Nason, C. Oleari and E. Re, "A general framework for implementing NLO calculations in shower Monte Carlo programs: the POWHEG BOX," JHEP **1006** (2010) 043 [arXiv:1002.2581 [hep-ph]].

[102] T. Sjostrand, S. Mrenna and P. Z. Skands, "PYTHIA 6.4 Physics and Manual," JHEP **0605** (2006) 026 [hep-ph/0603175].

[103] T. Sjostrand, S. Mrenna and P. Z. Skands, "A Brief Introduction to PYTHIA 8.1," Comput. Phys. Commun. **178** (2008) 852 [arXiv:0710.3820 [hep-ph]].

[104] S. Frixione and B. R. Webber, "Matching NLO QCD computations and parton shower simulations," JHEP **0206** (2002) 029 [hep-ph/0204244].

[105] J. M. Butterworth, J. R. Forshaw and M. H. Seymour, "Multiparton interactions in photoproduction at HERA," Z. Phys. C **72** (1996) 637 [hep-ph/9601371].

[106] T. Gleisberg, S. Hoeche, F. Krauss, M. Schonherr, S. Schumann, F. Siegert and J. Winter, "Event generation with SHERPA 1.1," JHEP **0902** (2009) 007 [arXiv:0811.4622 [hep-ph]].

[107] G. Corcella, I. G. Knowles, G. Marchesini, S. Moretti, K. Odagiri, P. Richardson, M. H. Seymour and B. R. Webber, "HERWIG 6: An Event generator for hadron emission reactions with interfering gluons (including supersymmetric processes)," JHEP **0101** (2001) 010 [hep-ph/0011363].

[108] S. Agostinelli *et al.* [GEANT4 Collaboration], "GEANT4: A Simulation toolkit," Nucl. Instrum. Meth. A **506** (2003) 250.

[109] G. Aad *et al.* [ATLAS Collaboration], "The ATLAS Simulation Infrastructure," Eur. Phys. J. C **70** (2010) 823 [arXiv:1005.4568 [physics.ins-det]].

[110] H. L. Lai, M. Guzzi, J. Huston, Z. Li, P. M. Nadolsky, J. Pumplin and C.-P. Yuan, "New parton distributions for collider physics," Phys. Rev. D **82** (2010) 074024 [arXiv:1007.2241 [hep-ph]].

[111] The ATLAS Luminosity Measurement Task Force, "Preliminary Luminosity Determination in pp Collisions at sqrt(s) = 8 TeV using the ATLAS Detector in 2012," ATL-COM-LUM-2012-013

[112] Luminosity Public Results, `https://twiki.cern.ch/twiki/bin/view/AtlasPublic/LuminosityPublicResults`, [22 Sep 2014]

[113] G. Aad *et al.* [ATLAS Collaboration], "Improved luminosity determination in *pp* collisions at $\sqrt{s} = 7$ TeV using the ATLAS detector at the LHC," Eur. Phys. J. C **73** (2013) 2518 [arXiv:1302.4393 [hep-ex]].

[114] L. Tomlinson, "A study on the drift in the BCM-reported luminosity and the recalibration of the visible cross-section," ATL-COM-LUM-2013-019.

[115] L. Tomlinson, "The effect of linear transverse coupling on the luminosity calibration by the van der Meer method," ATL-COM-LUM-2012-011.

[116] L. Tomlinson, "An analytical determination of the parameters of the single-Gaussian model of bunch densities and their impact on the luminosity calibration by the van der Meer method," ATL-COM-LUM-2013-009.

[117] [ATLAS Collaboration], "Luminosity Determination in pp Collisions at sqrt(s) = 7 TeV using the ATLAS Detector in 2011," ATLAS-CONF-2011-116.

[118] S. van der Meer, "Calibration of the Effective Beam Height in the ISR," CERN-ISR-PO-68-31.

[119] V. Balagura, "Notes on van der Meer Scan for Absolute Luminosity Measurement," Nucl. Instrum. Meth. A **654** (2011) 634 [arXiv:1103.1129 [physics.ins-det]].

[120] S. Pagan Griso, "Numerical simulation," `svn+ssh://spagan@svn.cern.ch/reps/spgrepo/Atlas/BeamStudies/trunk/`

[121] Y. Cai, "Luminosity of asymmetric e+ e- collider with coupling lattices," hep-ph/0007052.

[122] S. M. White, "Determination of the Absolute Luminosity at the LHC," CERN-THESIS-2010-139, LAL-10-154.

[123] S. N. Webb & T. R. Wyatt, private communication

[124] M. Ferro-Luzzi, "Luminosity and luminous region shape for pure Gaussian bunches," LHCb-PUB-2012-016.

[125] F. J. Decker, "Beam distributions beyond RMS," SLAC-PUB-6684.

[126] C.-P. Yuan, "A NLO Calculation of pQCD: Total Cross Section of $P\bar{P} \to W^+ + X$," CTEQ Summer School, June 2002.